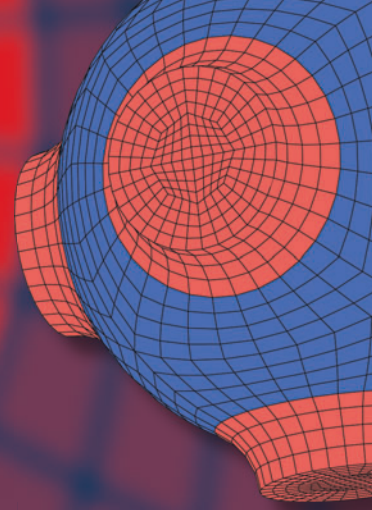


Advanced Structured Materials

Holm Altenbach  
Erasmus Carrera  
Gennady Kulikov *Editors*



# Analysis and Modelling of Advanced Structures and Smart Systems

 Springer

# **Advanced Structured Materials**

Volume 81

## **Series editors**

Andreas Öchsner, Southport Queensland, Australia

Lucas F. M. da Silva, Porto, Portugal

Holm Altenbach, Magdeburg, Germany

More information about this series at <http://www.springer.com/series/8611>

Holm Altenbach · Erasmo Carrera  
Gennady Kulikov  
Editors

# Analysis and Modelling of Advanced Structures and Smart Systems

 Springer

*Editors*

Holm Altenbach  
Faculty of Mechanical Engineering  
Otto-von-Guericke-University Magdeburg  
Magdeburg  
Germany

Gennady Kulikov  
Laboratory of Intelligent Materials  
and Structures  
Tambov State Technical University  
Tambov  
Russia

Erasmus Carrera  
Mechanical and Aerospace Engineering  
Politecnico di Torino  
Turin  
Italy

ISSN 1869-8433

ISSN 1869-8441 (electronic)

Advanced Structured Materials

ISBN 978-981-10-6764-8

ISBN 978-981-10-6895-9 (eBook)

<https://doi.org/10.1007/978-981-10-6895-9>

Library of Congress Control Number: 2017960198

© Springer Nature Singapore Pte Ltd. 2018

This work is subject to copyright. All rights are reserved by the Publisher, whether the whole or part of the material is concerned, specifically the rights of translation, reprinting, reuse of illustrations, recitation, broadcasting, reproduction on microfilms or in any other physical way, and transmission or information storage and retrieval, electronic adaptation, computer software, or by similar or dissimilar methodology now known or hereafter developed.

The use of general descriptive names, registered names, trademarks, service marks, etc. in this publication does not imply, even in the absence of a specific statement, that such names are exempt from the relevant protective laws and regulations and therefore free for general use.

The publisher, the authors and the editors are safe to assume that the advice and information in this book are believed to be true and accurate at the date of publication. Neither the publisher nor the authors or the editors give a warranty, express or implied, with respect to the material contained herein or for any errors or omissions that may have been made. The publisher remains neutral with regard to jurisdictional claims in published maps and institutional affiliations.

Printed on acid-free paper

This Springer imprint is published by Springer Nature

The registered company is Springer Nature Singapore Pte Ltd.

The registered company address is: 152 Beach Road, #21-01/04 Gateway East, Singapore 189721, Singapore

# Preface

The book contains selected papers presented at the 8<sup>th</sup> International Conference "Design, Modelling and Experiments of Advanced Structures and Systems" (DeMEASS) which was held in Moscow, Russia in May 2017. The topics of this conference series centers on *Advanced Structures and Intelligent Systems* in its various aspects:

- Smart Materials: Piezoelectric, Ferroelectric, Ferroelastic and Magnetostrictive Materials, Shape Memory Alloys and Active Polymers,
- Functionally Graded Materials,
- Multi-Functional Materials and Structures,
- Coupled Multi-Field Problems,
- Design and Modelling of Sensors and Actuators
- Adaptive Structures

The spirit of the conference is to collect international experts in one single venue and to promote intensive and fruitful discussions among the participants.

After the reviewing process 16 papers were accepted. These contributions have been prepared by authors from different countries, among them Austria, Belarus, France, Germany, Italy, Poland and Russia. The papers are printed in alphabetical order with respect to the surname of the first author.

We gratefully acknowledge the efforts put in by all contributors for the successful completion of the book at hand. In addition, we are indebted to Dr.-Ing. Sascha Duzek and Dr.-Ing. Fabian Duvigneau (Institute für Mechanik, Otto-von-Guericke-Universität Magdeburg) for their technical support concerning different L<sup>A</sup>T<sub>E</sub>X applications. Last but not least, we want to sincerely thank Dr. Christoph Baumann (Springer Publisher) for supporting this book project.

Magdeburg, Torino, Tambov  
October 2017

*Holm Altenbach  
Erasmus Carrera  
Gennady Kulikov*

# Contents

<b>1</b>	<b>Bending of a Three-Layered Plate with Surface Stresses</b> . . . . .	1
	Holm Altenbach and Victor A. Eremeyev	
1.1	Introduction . . . . .	1
1.2	Surface Elasticity . . . . .	2
1.3	Equilibrium of a Symmetric Three-Layered Plate . . . . .	3
1.3.1	Static Equations for a Three-Dimensional Plate-Like Solid	3
1.3.2	Transition to the Two-Dimensional Static Equations . . . . .	5
1.3.3	Effective Stiffness Parameters . . . . .	6
1.4	Conclusions and Future Steps . . . . .	8
	References . . . . .	9
<b>2</b>	<b>A Numerical Study on the Potential of Acoustic Metamaterials</b> . . . . .	11
	Fabian Duvigneau and Sascha Duzcek	
2.1	Introduction . . . . .	11
2.2	Models for the Parametric Studies . . . . .	14
2.3	Numerical Results . . . . .	18
2.3.1	Influence of the Distribution of the Spherical Inclusions . . . . .	18
2.3.2	Influence of the Material Properties of the Spherical Inclusions . . . . .	24
2.3.3	Influence of a Fixed Density-Volume-Product . . . . .	25
2.3.4	Influence of the Volume of the Inclusions . . . . .	27
2.3.5	Influence of the Number of Layers with Different Material Properties . . . . .	28
2.3.6	Discussion . . . . .	29
2.4	Conclusions . . . . .	30
	References . . . . .	32
<b>3</b>	<b>Electromechanical Degradation of Piezoelectric Patches</b> . . . . .	35
	Hassan Elahi, Marco Eugeni, and Paolo Gaudenzi	
3.1	Introduction . . . . .	35
3.2	Experimentation . . . . .	37

3.3	Results and Discussions . . . . .	40
3.4	Conclusions . . . . .	42
	References . . . . .	43
<b>4</b>	<b>Hybrid-Mixed Solid-Shell Element for Stress Analysis of Laminated Piezoelectric Shells through Higher-Order Theories . . . . .</b>	<b>45</b>
	Gennady M. Kulikov, Svetlana V. Plotnikova, and Erasmo Carrera	
4.1	Introduction . . . . .	46
4.2	Sampling Surface Shell Formulation . . . . .	48
4.3	Hu-Washizu Variational Equation . . . . .	50
4.4	Hybrid-Mixed Solid-Shell Element Formulation . . . . .	52
4.5	Numerical Examples . . . . .	57
	4.5.1 Three-Layer Piezoelectric Cylindrical Shell . . . . .	57
	4.5.2 Three-Layer Piezoelectric Spherical Shell . . . . .	61
4.6	Conclusions . . . . .	65
	References . . . . .	65
<b>5</b>	<b>Finite Element Approach for Composite Magneto-Piezoelectric Materials Modeling in ACELAN-COMPOS Package . . . . .</b>	<b>69</b>
	Natalia V. Kurbatova, Dmitry K. Nadolin, Andrey V. Nasedkin, Pavel A. Oganessian, and Arcady N. Soloviev	
5.1	Introduction . . . . .	70
5.2	Piezomagnetolectric Boundary Problems . . . . .	71
5.3	Finite Element Approximations . . . . .	73
5.4	Homogenization of Two-Phase Piezomagnetolectric Materials . . . . .	75
5.5	Inhomogenous Polarization . . . . .	78
5.6	Three-Dimensional Models for Composite Materials . . . . .	81
5.7	Conclusions . . . . .	86
	References . . . . .	87
<b>6</b>	<b>Robust Displacement and Mixed CUF-Based Four-Node and Eight-Node Quadrilateral Plate Elements . . . . .</b>	<b>89</b>
	Thi Huyen Cham Le, Michele D'Ottavio, Philippe Vidal, and Olivier Polit	
6.1	Introduction . . . . .	89
6.2	Variable Kinematics Plate Model . . . . .	93
	6.2.1 Variational Statements . . . . .	93
	6.2.1.1 The Principle of Virtual Displacements . . . . .	93
	6.2.1.2 Reissner's Mixed Variational Theorem . . . . .	94
	6.2.2 Variable Kinematics Assumptions . . . . .	95
	6.2.3 The Stress and Strain Fields . . . . .	96
	6.2.3.1 PVD Formulation . . . . .	97
	6.2.3.2 RMVT Formulation . . . . .	97
6.3	Finite Element Approximations . . . . .	98
	6.3.1 Displacement-Based Finite Elements . . . . .	98
	6.3.2 RMVT-Based Finite Elements . . . . .	101



6.4	Numerical Results . . . . .	102
6.4.1	Eigenvalues of the Stiffness Matrix . . . . .	103
6.4.2	Transverse Shear Locking Test . . . . .	106
6.4.2.1	PVD Based Elements: ED2 Model . . . . .	107
6.4.2.2	RMVT Based Elements: EM2 and EM2c Models . . . . .	109
6.4.2.3	Effectiveness of the QC4/CL8 Approach for Variable Kinematics Models . . . . .	110
6.4.3	The Distortion Tests . . . . .	111
6.4.3.1	The Square Plate Test . . . . .	111
6.4.3.2	The Circular Plate Test . . . . .	112
6.5	Conclusion . . . . .	113
	Appendix1 . . . . .	115
	Appendix2 . . . . .	115
	References . . . . .	116
<b>7</b>	<b>Effect of Magnetic Field on Free and Forced Vibrations of Laminated Cylindrical Shells Containing Magnetorheological Elastomers . . . . .</b>	<b>119</b>
	Gennadi Mikhasev, Ihnat Mlechka, and Svetlana Maevskaya	
7.1	Introduction . . . . .	120
7.2	Structure of Laminated Shell . . . . .	121
7.3	Basic Hypotheses . . . . .	123
7.4	Governing Equations . . . . .	124
7.4.1	Governing Equations in Terms of Stress Resultants and Couples . . . . .	124
7.4.2	Governing Equations in Terms of Displacements . . . . .	126
7.4.3	Equations of Technical Shell Theory . . . . .	127
7.4.4	Error of Governing Equations . . . . .	129
7.5	Free Vibrations of MRE-based Laminated Cylindrical Shells and Panels . . . . .	130
7.5.1	Lengthy Simply Supported Cylinders . . . . .	130
7.5.2	Medium-Length Cylindrical Panels . . . . .	134
7.5.3	Vibrations of Medium-Length Cylindrical Shells in Nonuniform Magnetic Field . . . . .	136
7.6	Forced Vibrations . . . . .	141
7.7	Conclusions . . . . .	145
	References . . . . .	146
<b>8</b>	<b>Impact-Induced Internal Resonance Phenomena in Nonlinear Doubly Curved Shallow Shells with Rectangular Base . . . . .</b>	<b>149</b>
	Yury A. Rossikhin (†), Marina V. Shitikova, and Mohammed Salih Khalid	
8.1	Introduction . . . . .	149
8.2	Problem Formulation and Governing Equations . . . . .	152
8.3	Method of Solution . . . . .	156

- 8.3.1 Solution of Equations at Order of  $\varepsilon$  ..... 157
- 8.3.2 Solution of Equations at Order of  $\varepsilon^2$  ..... 159
- 8.3.3 Impact-induced internal resonance  $\omega_1 = 2\omega_2$  ..... 159
  - 8.3.3.1 Initial Conditions ..... 165
  - 8.3.3.2 Contact Force and Shell’s Deflection at the Point of Impact ..... 168
- 8.3.4 Solution of Equations at Order of  $\varepsilon^3$  ..... 170
  - 8.3.4.1 Impact-Induced Three-to-One Internal Resonance ..... 171
  - 8.3.4.2 Phase Portraits ..... 175
  - 8.3.4.3 Initial Conditions ..... 180
  - 8.3.4.4 The Contact Force and Shell’s Deflection at the Point of Contact ..... 181
- 8.4 Conclusion ..... 183
- References ..... 185
- Appendix ..... 187

**9 Ferrous Material Fill: Magnetization Channels, Layer-by-Layer and Average Permeability, Element-to-Element Field** ..... 191

Anna A. Sandulyak, Darya A. Sandulyak, Vera A. Ershova, and Alexander V. Sandulyak

- 9.1 Introduction. Qualitative Assessment of Typical Intervals for the Volume Fraction of a Ferrous Component ..... 192
- 9.2 Quantitative Assessment of Characteristic Intervals for the Volume Fraction of a Ferrous Component and its Values for the Filling Materials ..... 193
- 9.3 Selective (in the Form of Chains of Channels) Magnetization of Ferrous Material. Concept of Layer-Tube Channels ..... 194
- 9.4 Data of the In-Channel (Core and Layer-Tube) Magnetic Flux, Average Induction, and Permeability ..... 196
- 9.5 Magnetizing Channel Layer Tubes: Local Permeability, Radial Profile ..... 199
- 9.6 Magnetization Channel Core: Average Magnetic Permeability . . . . 201
- 9.7 Generalized Dependencies for Comparison of the Calculated and Experimental Data ..... 203
- 9.8 Magnetization Channel and Harness of the Channels (in the Ferromaterial Filling): Average Magnetic Permeability ..... 204
- 9.9 The Physical Meaning of the Profile Permeability. Relative Field Strength Between Ferroelements ..... 206
- 9.10 Conclusions ..... 208
- References ..... 209

**10 Modeling and Simulation of a Chemically Stimulated Hydrogel Bilayer Bending Actuator** ..... 211

Martin Sobczyk and Thomas Wallmersperger

- 10.1 Introduction ..... 211

10.2	Chemo-Electro-Mechanical Field Formulation . . . . .	213
10.2.1	Chemical Field . . . . .	214
10.2.2	Electrical Field . . . . .	214
10.2.3	Mechanical Field . . . . .	215
10.2.4	Numerical Solution Procedure . . . . .	216
10.3	Numerical Simulation of a Chemically Stimulated Bilayer . . . . .	217
10.4	Conclusion . . . . .	224
	References . . . . .	224
<b>11</b>	<b>Mathematical Modelling of Piezoelectric Generators on the Base of the Kantorovich Method . . . . .</b>	<b>227</b>
	Arkadiy N. Soloviev, Valerii A. Chebanenko, and Ivan A. Parinov	
11.1	Introduction . . . . .	227
11.2	Mathematical Modelling of PEG . . . . .	229
11.2.1	The Boundary-Value Problem in the Theory of Electroelasticity . . . . .	229
11.2.2	Modeling of Cantilever Type PEGs . . . . .	230
11.2.2.1	Numerical Experiment . . . . .	238
11.2.2.2	Comparison with Finite Element . . . . .	240
11.2.2.3	Parametric Studies . . . . .	242
11.2.3	Modelling of Stack Type PEG . . . . .	247
11.2.3.1	Parametric Studies . . . . .	251
11.2.3.2	Comparison With Finite Element . . . . .	255
11.3	Summary . . . . .	255
	References . . . . .	257
<b>12</b>	<b>Modeling of Dielectric Elastomers Accounting for Electrostriction by Means of a Multiplicative Decomposition of the Deformation Gradient Tensor . . . . .</b>	<b>259</b>
	Elisabeth Staudigl, Michael Krommer, and Alexander Humer	
12.1	Introduction . . . . .	259
12.2	Electromechanical Coupling by Electrostatic Force . . . . .	261
12.2.1	Kinematics in Nonlinear Elasticity . . . . .	261
12.2.2	Electro-Elastic Balance Laws . . . . .	263
12.2.2.1	Maxwell Equation and Electric Body Forces . . . . .	263
12.2.2.2	Conservation Laws . . . . .	264
12.2.3	Lagrangian (Material) Framework . . . . .	266
12.2.4	Constitutive Relations . . . . .	267
12.3	Electromechanical Coupling Using a Multiplicative Decomposition of the Deformation Gradient Tensor . . . . .	269
12.3.1	Total Stress . . . . .	272
12.3.2	Intermediate Configuration . . . . .	273
12.4	Electrostriction . . . . .	274
12.4.1	Homogeneously Deformed Plate . . . . .	276
12.4.1.1	Plane Stress . . . . .	277
12.4.1.2	Incompressibility . . . . .	277

	12.4.1.3	Electrostatic Force	278
	12.4.1.4	Traction Boundary Condition	279
12.5		Electromechanical Stability	280
	12.5.1	Stiffening Effect of Electrodes	285
12.6		Conclusion and Outlook	287
		References	288
<b>13</b>		<b>Mechanics of Axially Moving Structures at Mixed Eulerian-Lagrangian Description</b>	<b>291</b>
		Yury Vetyukov	
13.1		Introduction	291
13.2		Linear Waves in a Moving String	293
13.3		Large Vibrations of an Axially Moving String	294
	13.3.1	Mixed Eulerian-Lagrangian Description of the Kinematics of Motion	296
	13.3.2	Mixed Form of the Variational Equation of Virtual Work	297
	13.3.3	Finite Element Approximation	298
	13.3.4	Lagrange's Equation of Motion of the Second Kind	299
	13.3.5	Example Solution	300
13.4		Finite Deformations of an Axially Moving Plate	302
	13.4.1	Kinematic Description	303
	13.4.2	Deformation and Strain Energy	305
	13.4.3	Finite Element Scheme	308
	13.4.4	Benchmark Problem	310
	13.4.5	Time Stepping and Boundary Conditions	311
	13.4.6	Simulation of a Moving Plate	313
13.5		Mixed Eulerian-Lagrangian Formulation in the Analysis of a Belt Drive	315
	13.5.1	Problem Statement	316
	13.5.2	Problem-Specific Coordinate System	317
	13.5.3	Mixed Lagrangian-Eulerian Kinematic Description	319
	13.5.4	Finite Element Approximation and Energy	319
	13.5.5	Simulation Results	320
	13.5.6	Work in Progress and Outlook	321
		References	323
<b>14</b>		<b>A software platform for the analysis of porous die-cast parts using the finite cell method</b>	<b>327</b>
		Mathias Würkner, Sascha Duczek, Harald Berger, Heinz Köppe, Ulrich Gabbert	
14.1		Introduction	327
14.2		The Finite Cell Method	329
	14.2.1	Fundamentals of the Finite Cell Method	329
	14.2.2	Numerical Integration	332
14.3		Concept of the Software Platform	333
14.4		Trouble Shooting the STL Data Set	335

14.5	Verification of the Software Platform .....	337
14.6	Summary and Outlook .....	339
	References .....	341
<b>15</b>	<b>Refined One-Dimensional Models for the Multi-Field Analysis of Layered Smart Structures .....</b>	<b>343</b>
	<b>Enrico Zappino and Erasmo Carrera</b>	
15.1	Introduction .....	343
15.2	Thermo-Piezo-Elastic One-Dimensional Model .....	346
15.2.1	Kinematic Approximation .....	347
15.2.1.1	Classical Beam Models .....	347
15.2.1.2	Refined One-Dimensional Models .....	348
15.2.1.3	Taylor Expansion Models (TE) .....	349
15.2.1.4	Lagrange Expansion Models (LE).....	349
15.2.2	Geometrical Relations.....	350
15.2.3	Constitutive Relations .....	351
15.2.4	Governing Equation .....	352
15.2.5	Loading Vector .....	354
15.2.6	Rotation and Assembly of the Fundamental Nucleus ....	355
15.2.7	The Stiffness Matrix Assembly .....	356
15.3	Numerical Results.....	356
15.3.1	Piezo-Elastic Model Assessment .....	357
15.3.2	Cantilever Beams with Piezo-Patches .....	358
15.3.3	Thermo-Piezo-Elastic Model Assessment .....	361
15.4	Conclusions .....	363
	References .....	363

# List of Contributors

Holm Altenbach

Institut für Mechanik, Otto-von-Guericke-Universität Magdeburg, Universitätsplatz 2,  
39106 Magdeburg, Germany, e-mail: holm.altenbach@ovgu.de

Harald Berger

Institut für Mechanik, Otto-von-Guericke-Universität Magdeburg, Universitätsplatz 2,  
39106 Magdeburg, Germany, e-mail: harald.berger@ovgu.de

Erasmus Carrera

*Mul<sup>2</sup>Team*, Politecnico di Torino, Corso Duca degli Abruzzi 24, Torino, Italy, e-mail:  
erasmo.carrera@polito.it

Valerii A. Chebanenko

Southern Scientific Center of Russian Academy of Science, Chekhov st., 41,  
Rostov-on-Don, Russia, e-mail: valera.chebanenko@yandex.ru

Michele D'Ottavio

UPL, Univ Paris Nanterre, LEME, 50 Rue de Sèvres, 92410 Ville d'Avray, France,  
e-mail: mdottavi@parisnanterre.fr

Sascha Duczec

Institut für Mechanik, Otto-von-Guericke-Universität Magdeburg, Universitätsplatz 2,  
39106 Magdeburg, Germany, e-mail: sascha.duczec@ovgu.de

Fabian Duvigneau

Institut für Mechanik, Otto-von-Guericke-Universität Magdeburg, Universitätsplatz 2,  
39106 Magdeburg, Germany, e-mail: fabian.duvigneau@ovgu.de

Hassan Elahi

Department of Mechanical and Aerospace Engineering, Sapienza University of  
Rome, Italy, e-mail: hassan.elahi@uniroma1.it

Victor A. Eremeyev  
Gdańsk University of Technology, ul. Gabriela Narutowicza 11/12, 80-233 Gdańsk,  
Poland & South Federal University, Milchakova str. 8a, 344090 Rostov on Don,  
Russia, e-mail: eremeyev.victor@gmail.com

Vera A. Ershova  
Moscow Technological University, Moscow, Stromynka 20, Russia, e-mail:  
v.ershova@mail.ru

Marco Eugeni  
Department of Mechanical and Aerospace Engineering, Sapienza University of  
Rome, Italy, e-mail: marco.eugeni@uniroma1.it

Ulrich Gabbert  
Institut für Mechanik, Otto-von-Guericke-Universität Magdeburg, Universitätsplatz 2,  
39106 Magdeburg, Germany, e-mail: ulrich.gabbert@ovgu.de

Paolo Gaudenzi  
Department of Mechanical and Aerospace Engineering, Sapienza University of  
Rome, Italy, e-mail: paolo.gaudenzi@uniroma1.it

Alexander Humer  
Institute of Technical Mechanics, Johannes Kepler University Linz, Altenbergerstraße  
69, A-4040 Linz, Austria, e-mail: alexander.humer@jku.at

Mohammed Salih Khalid  
Research Center of Wave Dynamics, Voronezh State Technical University, Voronezh  
394006, Russia, e-mail: Khalid\_bus@yahoo.com

Heinz Köppe  
Institut für Mechanik, Otto-von-Guericke-Universität Magdeburg, Universitätsplatz 2,  
39106 Magdeburg, Germany, e-mail: heinz.koeppe@ovgu.de

Michael Krommer  
Institute of Mechanics and Mechatronics, TU Wien, Getreidemarkt 9, A-1060  
Vienna, Austria, e-mail: michael.krommer@tuwien.ac.at

Gennady M. Kulikov  
Laboratory of Intelligent Materials and Structures, Tambov State Technical  
University, Sovetskaya Street, 106, Tambov 392000, Russia, e-mail: gmkulikov@  
mail.ru

Natalia V. Kurbatova  
Southern Federal University, Institute of Mathematics, Mechanics and Computer  
Science, Milchakova Street 8a, Rostov-on-Don, 344090, Russia, e-mail:  
nvk-ru@yandex.ru

Thi Huyen Cham Le  
UPL, Univ Paris Nanterre, LEME, 50 Rue de Sèvres, 92410 Ville d'Avray, France,  
e-mail: thihuyencham.le@parisnanterre.fr

Svetlana Maevskaya  
Vitebsk State University, 210030 Vitebsk, Belarus, e-mail: svetlanamaevsckaya@ya.ru

Gennadi Mikhasev  
Belarusian State University, 220030 Minsk, Belarus, e-mail: mikhasev@bsu.by

Ihnat Mlechka  
Belarusian State University, 220030 Minsk, Belarus, e-mail: ignat.mlechka@gmail.com

Dmitry K. Nadolin  
Southern Federal University, Institute of Mathematics, Mechanics and Computer Science, Milchakova Street 8a, Rostov-on-Don, 344090, Russia, e-mail: nadolin@yandex.ru

Andrey V. Nasedkin  
Southern Federal University, Institute of Mathematics, Mechanics and Computer Science, Milchakova Street 8a, Rostov-on-Don, 344090, Russia, e-mail: nasedkin@math.sfedu.ru

Pavel A. Oganessian  
Southern Federal University, Institute of Mathematics, Mechanics and Computer Science, Milchakova Street 8a, Rostov-on-Don, 344090, Russia, e-mail: wolwerine@yandex.ru

Ivan Anatolievich Parinov  
I. I. Vorovich Institute of Mathematics, Mechanics and Computer Sciences, Southern Federal University, Milchakov st., 8A, Rostov-on-Don, Russia, e-mail: parinov\_ia@mail.ru

Svetlana V. Plotnikova  
Laboratory of Intelligent Materials and Structures, Tambov State Technical University, Sovetskaya Street, 106, Tambov 392000, Russia, e-mail:

Olivier Polit  
UPL, Univ Paris Nanterre, LEME, 50 Rue de Sèvres, 92410 Ville d'Avray, France, e-mail: opolit@parisnanterre.fr

Yury A. Rossikhin (†)  
Research Center of Wave Dynamics, Voronezh State Technical University, Voronezh 394006, Russia

Alexander V. Sandulyak  
Moscow Technological University, Moscow, Stromynka 20, Russia, e-mail: a.sandulyak@mail.ru

Anna A. Sandulyak  
Moscow Technological University, Moscow, Stromynka 20, Russia, e-mail: anna.sandulyak@mail.ru



Darya A. Sandulyak

Moscow Technological University, Moscow, Stromynka 20, Russia, e-mail:  
d.sandulyak@mail.ru

Marina V. Shitikova

Research Center of Wave Dynamics, Voronezh State Technical University, Voronezh  
394006, Russia, e-mail: mvs@vgasu.vrn.ru

Martin Sobczyk

Technische Universität Dresden, Institut für Festkörpermechanik, 01062 Dresden,  
Germany, e-mail: martin.sobczyk@tu-dresden.de

Arcady N. Soloviev

Don State Technical University, Gagarin sq., 1 & I. I. Vorovich Institute of  
Mathematics, Mechanics and Computer Sciences, Southern Federal University,  
Milchakov st., 8A, Rostov-on-Don, Russia, e-mail: solovievarc@gmail.com

Elisabeth Staudigl

Institute of Mechanics and Mechatronics, TU Wien, Getreidemarkt 9, A-1060  
Vienna, Austria, e-mail: elisabeth.staudigl@tuwien.ac.at

Yury Vetyukov

Institute of Mechanics and Mechatronics, Vienna University of Technology,  
Getreidemarkt 9, 1060 Vienna, Austria, e-mail: yury.vetyukov@tuwien.ac.at

Philippe Vidal

UPL, Univ Paris Nanterre, LEME, 50 Rue de Sèvres, 92410 Ville d'Avray, France,  
e-mail: pvidal@parisnanterre.fr

Thomas Wallmersperger

Technische Universität Dresden, Institut für Festkörpermechanik, 01062 Dresden,  
Germany, e-mail: thomas.wallmersperger@tu-dresden.de

Mathias Würkner

Institut für Mechanik, Otto-von-Guericke-Universität Magdeburg, Universitätsplatz 2,  
39106 Magdeburg, Germany, e-mail: mathias.wuerkner@ovgu.de

Enrico Zappino

*Mul<sup>2</sup>Team*, Politecnico di Torino, Corso Duca degli Abruzzi 24, Torino, Italy, e-mail:  
enrico.zappino@polito.it

# Chapter 1

## Bending of a Three-Layered Plate with Surface Stresses

Holm Altenbach and Victor A. Eremeyev

**Abstract** We discuss here the bending deformations of a three-layered plate taking into account surface and interfacial stresses. The first-order shear deformation plate theory and the Gurtin-Murdoch model of surface stresses will be considered and the formulae for stiffness parameters of the plate are derived. Their dependence on surface elastic moduli will be analyzed.

### 1.1 Introduction

Recently with respect to developments in the technologies of nanostructured materials the interest grows to surface elasticity and models which explicitly take into account surface stresses. For example, the model presented in Gurtin and Murdoch (1975, 1978) found many applications in micro- and nanomechanics, see Duan et al (2009); Wang et al (2011); Javili et al (2013); Altenbach et al (2013); Eremeyev (2016) and the reference therein. In particular, it can forecast the positive size-effect (Altenbach et al, 2011) that is stiffening at the nanoscale. The Gurtin-Murdoch model is also used for modification of models of plates and shells to the nanoscale, see for example Altenbach et al (2010a); Altenbach and Eremeyev (2011); Altenbach et al (2012); Ru (2016).

Here we discuss the dependence of elastic properties including bending stiffness of an elastic three-layered plate with interfacial and surface stresses acting on layer interfaces and plate faces. First we briefly introduce the Gurtin–Murdoch model

---

Holm Altenbach

Otto-von-Guericke-Universität Magdeburg, Universitätsplatz 2, 39106 Magdeburg, Germany  
e-mail: holm.altenbach@ovgu.de

Victor A. Eremeyev

Gdańsk University of Technology, ul. Gabriela Narutowicza 11/12, 80-233 Gdańsk, Poland &  
South Federal University, Milchakova str. 8a, 344090 Rostov on Don, Russia  
e-mail: eremeyev.victor@gmail.com

of surface elasticity. Then we apply it to a three-layered plate-like solid. Finally, using the through-the thickness procedure we derive the modified two-dimensional constitutive equations.

## 1.2 Surface Elasticity

Following Gurtin and Murdoch (1975, 1978) let us briefly introduce the surface elasticity model. This model is the generalization of the surface tension known in the theory of capillarity (Rowlinson and Widom, 2003). From the physical point of view the Gurtin–Murdoch model corresponds to an elastic solid with an elastic membrane perfectly glued on its surface. The stress resultants acting in the membrane are the surface stresses. So, for the model it is necessary to introduce constitutive equations both in the bulk and at the surface. Considering layered media or media with inclusions one can also introduce interfacial stresses acting on the interfaces between layers or between inclusions and matrix material.

For infinitesimal deformations the equilibrium equations and the boundary conditions of the surface elasticity take the following form:

- equilibrium for the bulk material

$$\nabla \cdot \boldsymbol{\sigma} + \rho \mathbf{f} = \mathbf{0} \quad (1.1)$$

- equilibrium for the surface

$$(\mathbf{n} \cdot \boldsymbol{\sigma} - \nabla_S \cdot \boldsymbol{\tau})|_{\Omega_S} = \mathbf{t} \quad (1.2)$$

- boundary conditions for the displacements

$$\mathbf{u}|_{\Omega_u} = \mathbf{u}_0 \quad (1.3)$$

- boundary condition for the traction (surface force vector)

$$\mathbf{n} \cdot \boldsymbol{\sigma}|_{\Omega_t} = \mathbf{t}. \quad (1.4)$$

Here  $\boldsymbol{\sigma}$  is the stress tensor,  $\nabla$  the three-dimensional (3D) nabla operator,  $\nabla_S$  the surface (2D) nabla operator,  $\boldsymbol{\tau}$  the surface stress tensor acting on the surfaces  $\Omega_S$ ,  $\mathbf{u}$  the displacement vector,  $\mathbf{f}$  and  $\mathbf{t}$  the body force and surface force vectors, respectively, and  $\rho$  the mass density. On  $\Omega_u$  the displacements are given, whereas on  $\Omega_t$  the surface stresses  $\mathbf{S}$  are absent,  $\Omega \equiv \partial V = \Omega_u \cup \Omega_S \cup \Omega_t$ ,  $V$  is the body volume, and  $\mathbf{r}$  is the position vector. Equation (1.2) is the extension of the Young-Laplace equation. In fact, the presence of surface stresses in (1.2) may change dramatically the behaviour of solutions of the boundary-value problem (1.1)–(1.4). Note that hereinafter we use the direct tensor calculus Lebedev et al (2010).

For an interface  $\Omega_I$  with interfacial stresses  $\boldsymbol{\tau}_I$  we have the following compatibility conditions

$$(\mathbf{n} \cdot [[\boldsymbol{\sigma}]] - \nabla_S \cdot \boldsymbol{\tau}_I)|_{\Omega_I} = \mathbf{0}, \quad [[\mathbf{u}]]|_{\Omega_I} = \mathbf{0}, \quad (1.5)$$

where  $[[\boldsymbol{\sigma}]]$  denotes a jump of discontinuity in stresses across the interfaces. Here we consider perfect interfaces that is without slipping or delamination at the interface. Other models are discussed, for example, in Nazarenko et al (2017).

In what follows we consider isotropic materials only and neglect residual surface stresses. In this case the stress and surface stress tensors are given by the following constitutive equations

$$\boldsymbol{\sigma} = 2\mu\boldsymbol{\varepsilon} + \lambda\text{Tr}\boldsymbol{\varepsilon}\mathbf{I}, \quad (1.6)$$

$$\boldsymbol{\tau} = 2\mu_S\mathbf{e} + \lambda_S\mathbf{A}\text{tr}\mathbf{e} \quad (1.7)$$

with

$$\boldsymbol{\varepsilon} = \frac{1}{2} [\nabla\mathbf{u} + (\nabla\mathbf{u})^T], \quad (1.8)$$

$$\mathbf{e} = \frac{1}{2} [\nabla_S\mathbf{u} \cdot \mathbf{A} + \mathbf{A} \cdot (\nabla_S\mathbf{u})^T], \quad (1.9)$$

where  $\boldsymbol{\varepsilon}$  and  $\mathbf{e}$  are the strain and surface strain tensors, respectively,  $\lambda$  and  $\mu$  are the Lamé parameters,  $\lambda_S$  and  $\mu_S$ , which are called the surface Lamé parameters,  $\mathbf{A} \equiv \mathbf{I} - \mathbf{n} \otimes \mathbf{n}$  with the unit normal  $\mathbf{n}$ ,  $\otimes$  is the tensor (diadic) product, and  $\mathbf{I}$  is the 3D unit tensor.

## 1.3 Equilibrium of a Symmetric Three-Layered Plate

### 1.3.1 Static Equations for a Three-Dimensional Plate-Like Solid

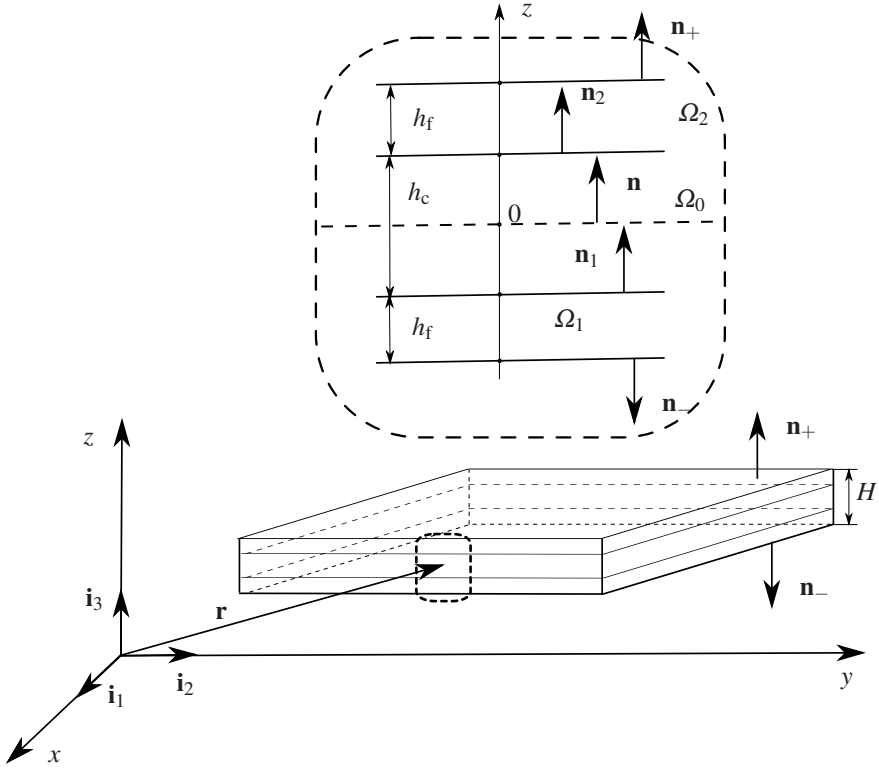
Let us consider an equilibrium state of an elastic plate of thickness  $H$  shown in Fig. 1.1. For simplicity we discuss the symmetric in the thickness direction plate. Here  $h_f$  is the thickness of faces,  $h_c$  is the thickness of the plate core, so  $H = 2h_f + h_c$ . The orientation of normal vectors to faces and interfaces is shown in Fig. 1.1. We introduce the Cartesian coordinates  $x, y, z$  and the corresponding unit base vectors  $\mathbf{i}_k$ . In what follows we apply the Einstein summation rule over repeating indices. The Latin indices take as usual values 1, 2, 3 whereas the Greek indices are equal to 1, 2. The surface stresses act on the faces  $\Omega_{\pm}$  whereas the interfacial stresses are given on the interfaces  $\Omega_1$  and  $\Omega_2$ . Thus,  $\Omega_S = \Omega_+ \cup \Omega_-$ ,  $\Omega_I = \Omega_1 \cup \Omega_2$ .

Summarizing all static equations for the plate-like solid we become the following system of equations

- equilibrium for the bulk

$$\nabla \cdot \boldsymbol{\sigma} + \rho\mathbf{f} = \mathbf{0}, \quad (1.10)$$

- equilibrium on the surfaces



**Fig. 1.1:** Three-layered plate with surface and interfacial stresses.

$$(\mathbf{n}_\pm \cdot \boldsymbol{\sigma} - \nabla_S \cdot \boldsymbol{\tau}_\pm)|_{\Omega_\pm} = \mathbf{t}_\pm, \quad (1.11)$$

- boundary conditions

$$\mathbf{u}|_{\Omega_u} = \mathbf{u}_0, \quad \mathbf{n} \cdot \boldsymbol{\sigma}|_{\Omega_t} = \mathbf{t}, \quad (1.12)$$

- jump conditions

$$(\mathbf{n}_\alpha \cdot [[\boldsymbol{\sigma}]] - \nabla_S \cdot \boldsymbol{\tau}_\alpha)|_{\Omega_\alpha} = \mathbf{0}, \quad [[\mathbf{u}]]|_{\Omega_\alpha} = \mathbf{0}, \quad \alpha = 1, 2. \quad (1.13)$$

Here we introduce surface stresses  $\boldsymbol{\tau}_\pm$  and interfacial stresses  $\boldsymbol{\tau}_\alpha$ . For the latter we use the following constitutive relations

$$\boldsymbol{\tau}_\pm = 2\mu_\pm \mathbf{e} + \lambda_\pm \mathbf{A} \text{tr} \mathbf{e}, \quad (1.14)$$

$$\boldsymbol{\tau}_\alpha = 2\mu_\alpha \mathbf{e} + \lambda_\alpha \mathbf{A} \text{tr} \mathbf{e}. \quad (1.15)$$

where  $\lambda_\pm$  and  $\mu_\pm$ ,  $\lambda_\alpha$  and  $\mu_\alpha$  are the surface and interfacial elastic moduli, respectively.

From the positive definiteness of the surface and interface strain energy densities it follows the restrictions (Altenbach et al, 2010b)

$$\mu_{\pm} > 0, \quad \lambda_{\pm} + \mu_{\pm} > 0, \quad \mu_{\alpha} > 0, \quad \lambda_{\alpha} + \mu_{\alpha} > 0, \quad \alpha = 1, 2.$$

With the classic inequalities  $\mu > 0$ ,  $3\lambda + 2\mu > 0$  the latter constraints result in existence and uniqueness of weak solutions of surface elasticity.

### 1.3.2 Transition to the Two-Dimensional Static Equations

In the literature are known various 3D into 2D reduction techniques, see, e.g., Altenbach and Eremeyev (2017a). Here we consider the through-the-thickness integration procedure described in detail in Libai and Simmonds (1998); Chróscielewski et al (2004); Lebedev et al (2010). This technique was applied for plates and shells at the nanoscale, see Altenbach et al (2010a); Altenbach and Eremeyev (2011); Altenbach et al (2012); Altenbach and Eremeyev (2017b).

First, integrating over the thickness (1.10) and taking into account (1.11) and (1.13) we obtain 2D equilibrium vectorial equation

$$\nabla_S \cdot \mathbf{T} + \nabla_S \cdot \boldsymbol{\tau}_+ + \nabla_S \cdot \boldsymbol{\tau}_- + \sum_{\alpha=1}^2 \nabla_S \cdot \boldsymbol{\tau}_{\alpha} + \mathbf{q} = \mathbf{0}, \quad (1.16)$$

where  $\mathbf{q} = \langle \rho \mathbf{f} \rangle + \mathbf{t}_+ + \mathbf{t}_-$ ,  $\mathbf{T} = \langle \mathbf{A} \cdot \boldsymbol{\sigma} \rangle$ , and

$$\langle (\dots) \rangle = \int_{-H/2}^{H/2} (\dots) dz \equiv \sum_{i=1}^3 \int_{z_{i-1}}^{z_i} (\dots) dz.$$

The tensor  $\mathbf{T}$  is the classical stress resultant tensor. Here  $z_i$  (the Latin index only in this case takes the values  $i = 0, 1, 2, 3$ ) are the coordinates of the interfaces counted from the middle surface of the plate, see Fig. 1.1,

$$z_0 = -H/2, \quad z_1 = -h_c/2, \quad z_2 = h_c/2, \quad z_3 = H/2, \quad H = 2h_f + h_c.$$

Then, cross-multiplying 3D equilibrium equation (1.10) by  $z_i \mathbf{i}_3$  from the left and again integrating the result over the thickness we obtain

$$\nabla_S \cdot \mathbf{M} + \mathbf{T}_{\times} + \sum_{i=0}^3 z_i \mathbf{i}_3 \times (\nabla_S \cdot \boldsymbol{\tau}_i) + \mathbf{c} = \mathbf{0}, \quad (1.17)$$

where

$$\mathbf{c} = \mathbf{i}_3 \times (\mathbf{t}_+ - \mathbf{t}_-)H/2 + \langle z \rho \mathbf{i}_3 \times \mathbf{f} \rangle, \quad \mathbf{M} = -\langle z \mathbf{A} \cdot \boldsymbol{\sigma} \times \mathbf{i}_3 \rangle,$$

and  $\mathbf{T}_{\times}$  is the vectorial invariant of  $\mathbf{T}$ . For example, for a diad it is defined as follows  $(\mathbf{a} \otimes \mathbf{b})_{\times} = \mathbf{a} \times \mathbf{b}$ , where  $\times$  stands for the cross product. In (1.17) for consistency we denote  $\boldsymbol{\tau}_+ = \boldsymbol{\tau}_3$  and  $\boldsymbol{\tau}_- = \boldsymbol{\tau}_0$ .

Equations (1.16) and (1.17) are the local balance equations for the momentum and the moment of momentum. The presence of surface and interfacial stresses result in additional terms in (1.16) and (1.17). Introducing the effective stress resultant and couple stress tensors by formulae

$$\mathbf{T}^* = \mathbf{T} + \mathbf{T}_S, \quad \mathbf{M}^* = \mathbf{M} + \mathbf{M}_S,$$

where

$$\mathbf{T}_S = \sum_{i=0}^3 \boldsymbol{\tau}_i, \quad \mathbf{M}_S = - \sum_{i=0}^3 z_i \boldsymbol{\tau}_i \times \mathbf{i}_3,$$

we transform the equilibrium equations into the form

$$\nabla_S \cdot \mathbf{T}^* + \mathbf{q} = \mathbf{0}, \quad \nabla_S \cdot \mathbf{M}^* + \mathbf{T}_X^* + \mathbf{c} = \mathbf{0}. \quad (1.18)$$

Note that (1.18) have a form of the equilibrium equations within the first-order shear-deformable plate theory (Altenbach, 2000; Altenbach and Eremeyev, 2017a).

### 1.3.3 Effective Stiffness Parameters

Using the typical ansatz of the first-order shear-deformable plate theory we assume that

$$\mathbf{u}(x, y, z) = \mathbf{v}(x, y) - z \boldsymbol{\vartheta}(x, y), \quad \mathbf{i}_3 \cdot \boldsymbol{\vartheta} = 0. \quad (1.19)$$

This approximation means that we consider a five-parameter plate theory with three translations and two rotations. With (1.19) we obtain

$$\mathbf{e} = \mathbf{E} - z \mathbf{K}, \quad (1.20)$$

$$\mathbf{E} = \frac{1}{2} \left[ \nabla_S \mathbf{v} \cdot \mathbf{A} + \mathbf{A} \cdot (\nabla_S \mathbf{v})^T \right], \quad (1.21)$$

$$\mathbf{K} = \frac{1}{2} \left[ \nabla_S \boldsymbol{\vartheta} + (\nabla_S \boldsymbol{\vartheta})^T \right]. \quad (1.22)$$

In what follows for simplicity we consider the plate with equal surface and interfacial properties, so  $\lambda_\alpha = \lambda_I$ ,  $\mu_\alpha = \mu_I$ ,  $\lambda_\pm = \lambda_S$  and  $\mu_\pm = \mu_S$ .

For  $\mathbf{T}$  and  $\mathbf{M}$  we use the standard constitutive equations (Altenbach et al, 2010a; Altenbach and Eremeyev, 2017a)

$$\mathbf{T} = C_1 \mathbf{E} + C_2 \text{Atr} \mathbf{E} + \Gamma \boldsymbol{\gamma} \otimes \mathbf{i}_3, \quad (1.23)$$

$$\mathbf{M} = -(D_1 \mathbf{K} + D_2 \text{Atr} \mathbf{K}) \times \mathbf{i}_3. \quad (1.24)$$

Here  $C_\alpha$  and  $D_\beta$  are the tangent and bending stiffness parameters, whereas  $\Gamma$  is the transverse shear stiffness. In particular,  $C_1 + C_2$  and  $D_1 + D_2$  give the classic tangent and bending stiffness, respectively,

$$C = C_1 + C_2, \quad D = D_1 + D_2.$$

The stiffness parameters for a three-layered plate are given by formulae (Altenbach, 2000)

$$C_1 = 2C_{22}, \quad C_2 = C_{11} - C_{22},$$

$$D_1 = 2D_{22}, \quad D_2 = D_{33} - D_{22},$$

$$\Gamma = \ell^2 D_{22},$$

$$C_{11} = \frac{1}{2} \left( \frac{2E_f h_f}{1 - \nu_f} + \frac{E_c h_c}{1 - \nu_c} \right), \quad C_{22} = \frac{1}{2} \left( \frac{2E_f h_f}{1 + \nu_f} + \frac{E_c h_c}{1 + \nu_c} \right),$$

$$D_{22} = \frac{1}{24} \left[ \frac{E_f (H^3 - h_c^3)}{1 + \nu_f} + \frac{E_c h_c^3}{1 + \nu_c} \right], \quad D_{33} = \frac{1}{24} \left[ \frac{E_f (H^3 - h_c^3)}{1 - \nu_f} + \frac{E_c h_c^3}{1 - \nu_c} \right],$$

where  $\ell$  is the minimal positive root of the following equation

$$\mu_0 \cos \ell \frac{h_f}{2} \cos \ell \frac{h_c}{2} - \sin \ell \frac{h_f}{2} \sin \ell \frac{h_c}{2} = 0, \quad \mu_0 = \mu_c / \mu_f,$$

$E_c$  and  $E_f$ ,  $\nu_c$  and  $\nu_f$ ,  $\mu_c$  and  $\mu_f$  are the Young moduli, Poisson ratios, and shear moduli of the shell core and faces, respectively. As a result, the tangent and bending stiffness parameters for a three-layered plate are

$$C = \frac{2E_f h_f}{1 - \nu_f^2} + \frac{E_c h_c}{1 - \nu_c^2}, \quad D = \frac{1}{12} \left[ \frac{E_f (H^3 - h_c^3)}{1 - \nu_f^2} + \frac{E_c h_c^3}{1 - \nu_c^2} \right].$$

Calculating  $\mathbf{T}_S$  and  $\mathbf{M}_S$  we get

$$\mathbf{T}_S = 4(\mu_S + \mu_I) \mathbf{E} + 2(\lambda_S + \lambda_I) \mathbf{Atr} \mathbf{E},$$

$$\mathbf{M}_S = - \left[ (H^2 \mu_S + h_c^2 \mu_I) \mathbf{K} + \frac{1}{2} (H^2 \lambda_S + h_c^2 \lambda_I) \mathbf{Atr} \mathbf{K} \right] \times \mathbf{i}_3.$$

As a result,  $\mathbf{T}^*$  and  $\mathbf{M}^*$  take the form of (1.23) and (1.24) with effective stiffness parameters

$$C_1^* = C_1 + 2\mu_S + 2\mu_I, \quad C_2^* = C_2 + 2\lambda_S + 2\lambda_I,$$

$$D_1^* = D_1 + H^2 \mu_S + \frac{1}{2} h_c^2 \mu_I, \quad D_2^* = D_2 + \frac{1}{2} H^2 \lambda_S + \frac{1}{2} h_c^2 \lambda_I.$$

The effective tangent and bending stiffness take the values

$$C^* = C_1^* + C_2^* = C + 4\mu_S + 2\lambda_S + 4\mu_I + 2\lambda_I, \quad (1.25)$$

$$D^* = D_1^* + D_2^* = D + H^2 \mu_S + \frac{1}{2} H^2 \lambda_S + h_c^2 \mu_I + \frac{1}{2} h_c^2 \lambda_I. \quad (1.26)$$



Obviously, the presence of surface and interfacial stresses leads to the stiffening of the plate that is to the positive size-effect. Let us note that surface stresses do not affect  $\Gamma$ . The stiffening is significant if the shell thickness has the same order as the characteristic length parameter  $d = (2\mu_S + \lambda_S)/E_{f,c}$ , i.e. when  $H \sim d$ . Note that for the three-layered plate there are few length-scale parameters related to surface and interfacial elastic moduli. Let us for simplicity assume that  $\mu_\alpha = \mu_\pm = \mu_S$  and  $\lambda_\alpha = \lambda_\pm = \lambda_S$  that is when the interfacial and surface moduli are equal. In addition as an example we consider  $t_{hf} = h_c = h$ , so  $H = 3h$ , and  $E_c = E_f = E$ ,  $\nu_c = \nu_f = \nu$ . Then we get

$$C = \frac{3Eh}{1-\nu^2}, \quad D = \frac{9}{4} \frac{Eh^3}{1-\nu^2},$$

$$C^* = C + 8\mu_S + 4\lambda_S, \quad D^* = D + 10h^2\mu_S + 5h^2\lambda_S.$$

As a result, the ratios of stiffness parameters at the nanoscale and at the macroscale have the form

$$\frac{C^*}{C} = 1 + K_1 \frac{d}{h}, \quad \frac{D^*}{D} = 1 + K_2 \frac{d}{h}, \quad (1.27)$$

where  $K_1 = \frac{4}{3}(1-\nu^2)$ ,  $K_2 = \frac{20}{9}(1-\nu^2)$ . The hyperbolic form of Eqs (1.27) coincides with the scaling law proposed for nanomaterials by Wang et al (2006). For a general case the qualitative dependencies of  $C^*/C$  and  $D^*/D$  on  $d/h$  are similar to considered simplified case.

## 1.4 Conclusions and Future Steps

Here we discussed the statics for a three-layered elastic plate undergoing small deformations taking into account surface and interfacial stresses. The Gurtin–Murdoch model of surface elasticity was applied. For the derivation of the two-dimensional constitutive equations for stress resultants we utilized the through-the-thickness integration procedure. Finally, we found the expressions for effective stiffness parameters. It is interesting that the surface elastic moduli influence on the tangent and bending stiffness but do not affect the transverse shear stiffness.

The presented results can be generalized in few directions. In particular, inelastic behavior such as surface viscoelasticity could be considered as in Altenbach et al (2012). The residual/initial surface stresses may significantly change the elastic response (Altenbach et al, 2013; Altenbach and Eremeyev, 2017b), for example, this may lead to self-instabilities (Wang and Zhao, 2009). In addition, non-perfect surfaces and interfaces with surface elasticity can be considered as in Eremeyev (2016); Eremeyev et al (2016). Modelling of surface and interfacial phenomena is also possible on the base of the strain gradient elasticity (Mindlin, 1965), see also dell’Isola and Seppecher (1995, 1997); dell’Isola et al (2012) for description of contact interactions. This unified approach could also useful for description of

surface and interfacial stresses in layered structures. In particular, similar the theory of capillarity (Rowlinson and Widom, 2003; de Gennes, 1981) this approach may lead to the derivation of the constitutive equations for surface and interfacial stresses.

**Acknowledgements** V.A.E. acknowledges financial support from the Russian Science Foundation under the grant *Methods of microstructural nonlinear analysis, wave dynamics and mechanics of composites for research and design of modern metamaterials and elements of structures made on its base* (No 15-19-10008).

## References

- Altenbach H (2000) An alternative determination of transverse shear stiffnesses for sandwich and laminated plates. *Int J Solids Struct* 37(25):3503–3520
- Altenbach H, Eremeyev V (2017a) Thin-walled structural elements: Classification, classical and advanced theories, new applications. In: Altenbach H, Eremeyev V (eds) *Shell-like Structures: Advanced Theories and Applications*, CISM Courses and Lectures, vol 572, Springer, Cham, pp 1–62
- Altenbach H, Eremeyev VA (2011) On the shell theory on the nanoscale with surface stresses. *Int J Engng Sci* 49(12):1294–1301
- Altenbach H, Eremeyev VA (2017b) On the elastic plates and shells with residual surface stresses. *Proc IUTAM* 21:25–32
- Altenbach H, Eremeyev VA, Morozov NF (2010a) On equations of the linear theory of shells with surface stresses taken into account. *Mech Solids* 45(3):331–342
- Altenbach H, Eremeyev VA, Lebedev LP (2010b) On the existence of solution in the linear elasticity with surface stresses. *ZAMM* 90(3):231–240
- Altenbach H, Eremeyev VA, Lebedev LP (2011) On the spectrum and stiffness of an elastic body with surface stresses. *ZAMM* 91(9):699–710
- Altenbach H, Eremeyev VA, Morozov NF (2012) Surface viscoelasticity and effective properties of thin-walled structures at the nanoscale. *Int J Engng Sci* 59:83–89
- Altenbach H, Eremeyev VA, Morozov NF (2013) On the influence of residual surface stresses on the properties of structures at the nanoscale. In: Altenbach H, Morozov NF (eds) *Surface Effects in Solid Mechanics*, *Adv. Struct. Mat.*, vol 30, Springer, Heidelberg, pp 21–32
- Chróścielewski J, Makowski J, Pietraszkiewicz W (2004) *Statics and Dynamics of Multifolded Shells. Nonlinear Theory and Finite Element Method* (in Polish). Wydawnictwo IPPT PAN, Warszawa
- dell’Isola F, Seppecher P (1995) The relationship between edge contact forces, double forces and interstitial working allowed by the principle of virtual power. *C R de l’Académie des sciences Série Iib, Mécanique, physique, astronomie* 321:303–308
- dell’Isola F, Seppecher P (1997) Edge contact forces and quasi-balanced power. *Meccanica* 32(1):33–52
- dell’Isola F, Seppecher P, Madeo A (2012) How contact interactions may depend on the shape of Cauchy cuts in Nth gradient continua: approach “à la d’Alembert”. *ZAMP* 63(6):1119–1141
- Duan H, Wang J, Karimloo BL (2009) Theory of elasticity at the nanoscale. *Adv Appl Mech* 42:1–68
- Eremeyev VA (2016) On effective properties of materials at the nano- and microscales considering surface effects. *Acta Mech* 227(1):29–42
- Eremeyev VA, Rosi G, Naili S (2016) Surface/interfacial anti-plane waves in solids with surface energy. *Mech Res Comm* 74:8–13
- de Gennes PG (1981) Some effects of long range forces on interfacial phenomena. *J Physique Lettres* 42(16):377–379

- Gurtin ME, Murdoch AI (1975) A continuum theory of elastic material surfaces. *Arch Ration Mech Anal* 57(4):291–323
- Gurtin ME, Murdoch AI (1978) Surface stress in solids. *Int J Solids Struct* 14(6):431–440
- Javili A, McBride A, Steinmann P (2013) Thermomechanics of solids with lower-dimensional energetics: On the importance of surface, interface, and curve structures at the nanoscale. A unifying review. *Appl Mech Rev* 65(1):010,802
- Lebedev LP, Cloud MJ, Eremeyev VA (2010) *Tensor Analysis with Applications in Mechanics*. World Scientific, New Jersey
- Libai A, Simmonds JG (1998) *The Nonlinear Theory of Elastic Shells*, 2nd edn. Cambridge University Press, Cambridge
- Mindlin RD (1965) Second gradient of strain and surface-tension in linear elasticity. *Int J Solids Struct* 1(4):417–438
- Nazarenko L, Stolarski H, Altenbach H (2017) A definition of equivalent inhomogeneity applicable to various interphase models and various shapes of inhomogeneity. *Proc IUTAM* 21:63 – 70
- Rowlinson JS, Widom B (2003) *Molecular Theory of Capillarity*. Dover, New York
- Ru CQ (2016) A strain-consistent elastic plate model with surface elasticity. *Cont Mech Thermodyn* 28(1–2):263–273
- Wang J, Huang Z, Duan H, Yu S, Feng X, Wang G, Zhang W, Wang T (2011) Surface stress effect in mechanics of nanostructured materials. *Acta Mech Solida Sin* 24(1):52–82
- Wang J, Duan HL, Huang ZP, Karihaloo BL (2006) A scaling law for properties of nano-structured materials. *Proc Roy Soc A* 462(2069):1355–1363
- Wang Z, Zhao Y (2009) Self-instability and bending behaviors of nano plates. *Acta Mech Solida Sin* 22(6):630–643

# Chapter 2

## A Numerical Study on the Potential of Acoustic Metamaterials

Fabian Duvigneau and Sascha Duczek

**Abstract** In the present contribution we are going to investigate a special class of acoustic metamaterials, i.e. synthetic foams with spherical inclusions. This study is motivated by the need for an improved acoustical behavior of engines and vehicles which is one important criterion for the automotive industry. In this context, innovative materials offering a high damping efficiency over a wide frequency range are becoming more and more important. Since there is an innumerable selection of different absorbing materials with an equally large range of properties numerical studies are inevitable for their assessment. In the paper at hand, we look at a special class of such materials in which the influence of the inclusions on the acoustical behavior is examined in detail. To this end, we vary the size, mass density, number and position of spherical inclusions. Here, the main goal is to improve the damping properties in comparison to conventional materials which can be bought off the shelf. In that regard, the lower frequency range is of special interest to us. The results show that a random distribution of the inclusions should be favored while for the other parameters values that are centered within the investigated interval are recommended.

### 2.1 Introduction

In general, there are two main approaches for improving the acoustic behavior of arbitrary parts: (i) active and (ii) passive methods. Active methods require an external energy supply in order to drive actuators that are able to excite the structure and create destructive interferences of elastic and acoustic waves (Gabbert et al, 2017). To achieve an efficient damping the vibrations of the structure have to be measured first before a suitable control strategy can be applied. A wide variety of control concepts

---

Fabian Duvigneau · Sascha Duczek  
Institut für Mechanik, Otto-von-Guericke-Universität Magdeburg, Universitätsplatz 2, 39106 Magdeburg, Germany  
e-mail: fabian.duvigneau@ovgu.de, sascha.duczek@ovgu.de

with automotive applications can be found in the literature, e.g., active structural acoustic control (ASAC) of an oil pan (Ringwelski et al, 2011), active noise control (ANC) of the cabin noise within a car (Schirmacher et al, 2007) or active vibration control (AVC) of a rear axle to avoid gear whining (Troge et al, 2016). However, today passive concepts are still more popular in industrial applications due to their inherent simplicity, the absence of an additional energy supply, the costs, the failure safety and the fact that active concepts are only efficient in the low frequency range.

In the context of passive methods the geometry of the part is often modified to eliminate sound transmission paths and hence, to reduce the resulting sound radiation of the structure. This can be achieved by adding mass or stiffeners to specific locations where also alternative materials, such as synthetic or metal foams (Schrader et al, 2015), are employed. In the wide body of literature also more exotic approaches such as the use of granular materials (Duvigneau et al, 2016a) can be found. Here, a sandwich panel with a honeycomb core was utilized to intelligently distribute the granular material. This methodology leads to an improved damping behavior in conjunction with a high stiffness to mass ratio (Koch et al, 2017b). In this context, it was shown that a granular medium made of light and highly elastic rubber is very effective for vibration damping (Koch et al, 2017a).

Even today it is unfortunately still common practice to focus on targets such as fuel consumption, power output, mass and design aspects when optimizing automotive parts. In this context the acoustic performance of vehicles is often neglected and therefore, we need concepts to tackle this issue after the final design has already been approved. Typically acoustic problems are only detected experimentally when an expensive prototype has been build and an extensive testing campaign is conducted. At this stage in the development process it is, however, almost prohibitive to propose fundamental changes in the design and hence, alternative methods need to be employed until the acoustic behavior is finally part of initial considerations. First steps in this direction are taken in Duvigneau et al (2016b,d), where a holistic workflow for the acoustic evaluation of a combustion engine is developed. However, nowadays it is still common practice to mitigate observed acoustic problems of prototypes by applying damping materials to acoustically conspicuous components. In Duvigneau et al (2016c) it is exemplarily shown that an encapsulation of an engine is a very efficient approach to significantly reduce the noise emission of a vehicle. Here, the main challenge is to balance the need for an improved acoustic emission behavior with mass considerations. The additional mass caused by the installation of an encapsulation should be naturally as low as possible. An additional consideration is the available space which is in modern vehicles rather limited such that the dimensioning of the encapsulation needs to be adapted to these requirements.

Due to the mentioned issues one important aspect when designing passive noise reduction approaches is to improve the damping properties of the deployed materials. They need to have a high damping ratio over a wide frequency range while being both light and thin. The classical approach for noise control applications is to utilize homogeneous heavy foils made of high density viscoelastic materials such as bitumen or butyl rubber. These foils are mainly applied at locations where the noise emission is rather high such as large planar faces. Here, they increase the

transmission loss through material damping (described by the loss factor) and the additional mass (lower vibration amplitudes). Because of the large-area application of these materials there is still quite some room for improvement left. Therefore, heterogeneous materials have been in the focus of investigations recently. Such material systems include polyurethane (PUR) and melamine foams or microfiber materials which provide a high material damping due to the additional interactions at the fluid-solid-interface. Their advantage compared to previously discussed materials is the comparably low density (which naturally leads to low mass gains). Generally speaking, the characteristic value of the acoustic effect, provided by homogeneous materials, is governed by the thickness only, whereas porous (heterogeneous) materials offer much more freedom to be tailored for specific applications. Parameters such as the mean pore size, the porosity (volume fraction) and the reticulation rate can significantly influence the acoustic performance. These influence parameters can be adjusted by chemists or process engineers during the manufacturing process. By adding an additional mass layer at the surface of the heterogeneous material the dissipation effect is increased even further. Now, the material system represents a mass-spring-damper system. These bimaterial foam systems have been extensively investigated in a previous study (Schrader et al, 2016). A remarkable feature of the investigated foams is that the added mass layer is created by impregnating only a part of the base material. This procedure is very flexible in terms of penetration depth and achievable density.

Special classes of heterogeneous materials are the so-called acoustic metamaterials. In the following, we discuss an important group of these metamaterials, which is made of locally resonant structures. Generally, they consist of a soft matrix phase featuring stiff mass inclusions with different weights and sizes. In various studies it has been shown that the mass inclusions within the elastic matrix cause frequency bands with high transmission losses or absorption coefficients (Liu et al, 2000, 2005; Fuller and Saux, 2012; Idrisi et al, 2010; Deymier, 2013; Sheng et al, 2017; Lu et al, 2009); this behavior is analogous to bandgap phenomena in phononic crystals (Jensen, 2011; Zhang et al, 2006; Zhao et al, 2013). The frequency bands with increased transmission losses depend on both the mass of the inclusion and its location (Fuller and Saux, 2012; Idrisi et al, 2010; Deymier, 2013). One important feature that is demonstrated in the cited literature is the ability to increase the transmission loss especially in the low frequency range where classical passive approaches do not work satisfactorily. Therefore, a simple inclusion of “resonant” masses within a conventional damping material can lead to significant gains in terms of the suppression of sound emission. In general, it is suggested to distribute inclusions with different masses at various locations within the elastic matrix to achieve a notable sound energy dissipation in a broader frequency range.

Another approach to design metamaterials has been introduced in Sui et al (2015). Here, a lightweight honeycomb structure was covered with an elastic membrane. This material shows a high transmission loss at low frequencies which can be attributed to the effect of the membrane. In Schrader et al (2017a) this method was seized and combined with two additional metamaterial concepts. First, only the honeycomb-membrane system was investigated to obtain reference measurements. In a second

step the honeycombs were filled with PUR foam. Finally, mass inclusions were placed in the honeycomb cells before filling these cells with foam as in the previous step. Honeycomb structures combined with PUR foam show significant sound pressure level reductions in a frequency range from 0.5 to 2 kHz. These reductions are notably higher than the ones gained with a simple PUR foam of the same thickness. The honeycomb plate with the surface membrane alone does not show these effects either. A further improvement is gained by the use of the mass inclusions within the honeycombs, especially the concept with a large number of small-sized mass inclusions surrounded by the PUR foam shows a high sound pressure level reduction.

In Schrader et al (2017a) another concept which is inspired by applications in room acoustics has been proposed. The fundamental idea is based on the application of perforated acoustic panels which contain large air cavities beyond the interface. In this concept the energy is dissipated by friction between the moving air particles and the solid perforated plate. Schrader et al (2017a) applied this idea to PUR foams. In their approach large cavities were introduced into the foam structure and covered by micro-perforated membranes. The membrane was micro-perforated, as the perforations have to be rather small in order to devise an efficient material system (Fuchs, 2007). The operating principle is based on the physical concept of a Helmholtz resonator whose efficiency depends on the friction losses in the micro-perforations. The theory of noise reduction by micro-perforated absorbers was originally developed by Maa (1998). This idea was further extended by Zhang and Gu (1997) who suggested employing a structure featuring a double-layered micro-perforated absorber. The specific feature of such a design is that it exhibits two absorption maxima.

In the present contribution a metamaterial based on spherical inclusions that combines the benefits of a low mass density with an improved noise absorption compared to conventional damping materials (especially at low frequencies) is proposed and studied in detail. In Fig. 2.1 a possible design of the proposed metamaterial which is attached to a rectangular plate is shown. Here, three layers of inclusions which are distributed in a structured fashion are depicted. The investigated material system increases the energy dissipation within the polyurethane base material (foam) by adding additional masses. The basic idea is to create a local mass-spring-damper system which is able to attenuate the vibrations. In the following sections the acoustic efficacy of the proposed metamaterial is investigated for several configurations differing in weight, size and location of the spherical inclusions within the PUR foam.

## 2.2 Models for the Parametric Studies

In this section the road map for our numerical investigations is explained, the used models are presented and in the following Sect. 2.3 selected results that are representative of the behavior for the proposed metamaterial are discussed. The results are obtained by numerical simulations using the finite element method (FEM)

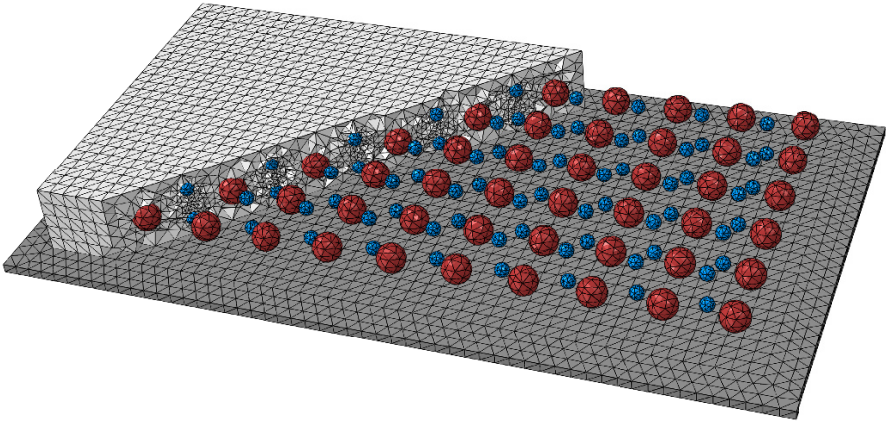
(Zienkiewicz and Taylor, 2000; Hughes, 1987) which is the dominating tool to solve partial differential equations arising in many different branches of engineering.

In Fig. 2.2 the setup for the numerical experiments is depicted. On the left hand side the FE-model of the plate with the metamaterial attached to its surface is shown. The dimensions of the model are compiled in Table 2.1. In this model structural

Table 2.1: Dimensions of the structural model

	length	width	thickness $t$
Aluminum plate	440 mm	240 mm	5 mm
Metamaterial	400 mm	200 mm	40 mm

damping is used, which assumes that the damping forces  $F_D$  are opposed to the velocity and are proportional to the forces  $F_S$  caused by stressing the structure. The damping forces are  $F_D = i \cdot \delta \cdot F_S$  wherein  $\delta$  is the structural damping factor and  $i$  is the imaginary unit. The corresponding damping factors  $\delta$  of the different materials, which are used within the FE-model, are listed in Table 2.2. As Dirichlet boundary conditions we fixed the displacements in all spatial directions at the four corner nodes



**Fig. 2.1:** Example of an acoustic metamaterial attached on a rectangular plate

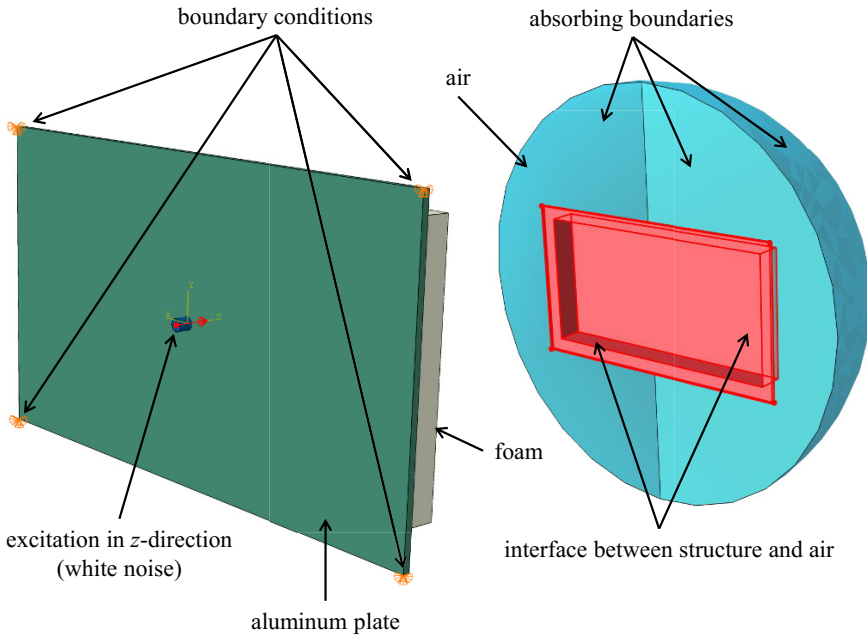
Table 2.2: Material properties of the numerical reference model

	aluminium	foam	inclusions
Young's modulus	70000 N/mm <sup>2</sup>	5 N/mm <sup>2</sup>	5000 N/mm <sup>2</sup>
Density	2.7 g/cm <sup>3</sup>	0.05 g/cm <sup>3</sup>	0.5 g/cm <sup>3</sup>
Poisson ratio	0.3	0.3	0.3
Structural damping	0.01	0.05	0.0

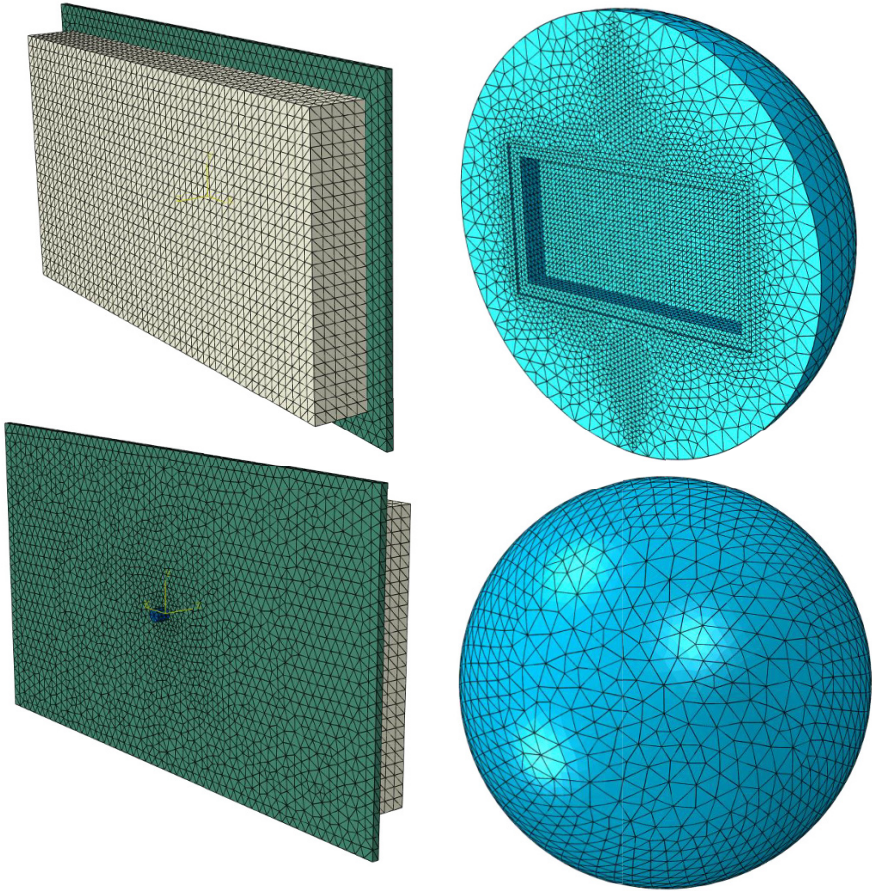


of the backside of the aluminum plate. In experiments the excitation is typically applied by means of a shaker and therefore, we introduce the Neumann boundary conditions by attaching an aluminum cylinder (height: 10 mm, radius 5 mm) at the centroid of the backside of the aluminum plate. This procedure is identical to the experimental setup that was used in a previous study (Schrader et al, 2017b). A white noise signal with an amplitude of 1 N is generated to excite the structure in the whole frequency range of interest. The numerical analysis is executed in the frequency domain due to the computational costs of a fully transient analysis in the time domain.

On the right hand side of Fig. 2.3 the FE-model of the air volume surrounding the structure is depicted. The spherical air volume needed to compute the sound pressure distribution has a radius of 330 mm. Consequently, for frequencies higher than 1.55 kHz the far field assumption (approximately 1.5 times the wavelength) already holds within the discretized domain. To reduce the computational effort the surrounding fluid volume is modeled only as a hemisphere. Due to the geometric complexity of the micro-structure of metamaterials both the structural and the acoustic domain are discretized by means of tetrahedral finite elements with quadratic shape functions (10-node tetrahedra). The maximum element size of the structural model is set to 8 mm which corresponds to 8 nodes per wavelength of the maximum



**Fig. 2.2:** Simulation model of the plate, foam and air including interface and boundary conditions



**Fig. 2.3:** FE-models of the aluminum plate with the attached foam layer and the surrounding air

frequency. At the interface between both models (structural-acoustic interface) a conforming mesh is generated and the element size is then slowly increased towards the periphery of the hemisphere where a maximum element size of 30 mm is reached. In Duvigneau (2017) it was shown that this discretization is still reasonable due to the much finer discretized interface. For the acoustic problem free-field conditions are assumed and therefore, the outer boundary of the air volume are modeled as absorbing boundaries (impedance based absorbing boundary conditions(Givoli, 2008)). At the structural-acoustic interface the air is excited through the surface velocities of the vibrating structure, which have been calculated in a previous analysis step. Due to the conformal interface mesh the interpolation of the results is trivial. To further reduce the computational effort an uncoupled acoustic simulation is executed, i.e. the influence of the vibrating air on the aluminum plate and the metamaterial

is neglected. The geometrical dimensions, the mesh parameters, the boundary and loading conditions are identical for all investigated configurations. Thus, we ensure that the results are comparable as the only influence is now related to the changes made with respect to the metamaterial. Here, we primarily change the geometry (volume), distribution (number, location) and material properties (density, Young's modulus) of the spherical inclusions.

In Table 2.2 the material properties of aluminum, PUR foam and the initial data for the inclusions are compiled. If not stated otherwise this data set is used in all numerical simulations. For the sake of clarity, all important parameters describing the models used in our numerical analyses in Sect. 2.3 are compiled in Table 2.3. Here, all details such as the number of spherical inclusions, their diameter and their material properties (mass density  $\rho$ , Young's modulus  $E$ ) are listed. Note, that the Poisson's ratio  $\nu$  is set to 0.3 for all constituents (see Table 2.2). From these information the additional mass can be computed, although we have to bear in mind that the mass of the fully foam filled structure needs to be taken into consideration. That means that we have to compute the mass of the inclusions and subtract the mass of the foam that originally occupied this space. The values  $\Delta x$ ,  $\Delta y$  and  $\Delta z$  describe the spacing between adjacent spheres measured from centroid to centroid (for structured arrangements only). If only one layer of spheres is deployed  $\Delta z$  gives the distance between the centroid of the sphere and the bottom surface of the foam structure.

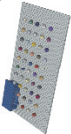

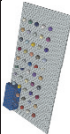
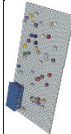
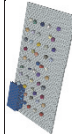
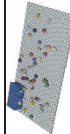
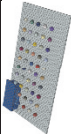
## 2.3 Numerical Results

In the current section we comprehensively discuss selected results of our numerical investigations that are representative of the behavior of the proposed metamaterial.

### 2.3.1 Influence of the Distribution of the Spherical Inclusions

In this section we investigate six different configurations which are depicted in Fig. 2.4. All models contain 50 spherical inclusions with a diameter of 15 mm while only their distribution (with respect to the location) is varied. One important question we want to answer by executing this study is whether the positioning with respect to the out-of-plane direction ( $z$ -axis, height) or the in-plane positioning ( $x$ - $y$ -plane) is more significant for the damping behavior. In a previous investigation (Schrader et al, 2017b) it was suggested that the former effect would be dominant.

Table 2.3: Parameters for the numerical models used in the parametric investigations. The spacing of the inclusions is given in terms of the variables  $a = 36.4$  mm,  $b = 33.3$  mm and  $t = 40$  mm (thickness of the metamaterial).

#	Geometry	Number of inclusions	Diameter	Mass density	Young's modulus	Added mass	$\Delta x$	$\Delta y$	$\Delta z$
Sect. 2.3.1									
1		50, 1 layer 5x10	15 mm	0.5 g/cm <sup>3</sup>	5,000 N/mm <sup>2</sup>	39.8 g	a	b	0.5t
2		50, 1 layer 5x10	15 mm	0.5 g/cm <sup>3</sup>	5,000 N/mm <sup>2</sup>	39.8 g	a	b	0.25t
3		50, 1 layer 5x10	15 mm	0.5 g/cm <sup>3</sup>	5,000 N/mm <sup>2</sup>	39.8 g	a	b	0.75t
4		50, random distribution in-plane	15 mm	0.5 g/cm <sup>3</sup>	5,000 N/mm <sup>2</sup>	39.8 g	-	-	0.5t
5		50, random distribution out-of-plane	15 mm	0.5 g/cm <sup>3</sup>	5,000 N/mm <sup>2</sup>	39.8 g	a	b	-
6		50, random distribution in all directions	15 mm	0.5 g/cm <sup>3</sup>	5,000 N/mm <sup>2</sup>	39.8 g	-	-	-
Sect. 2.3.2									
7		50, 1 layer 5x10	15 mm	0.1 g/cm <sup>3</sup>	5,000 N/mm <sup>2</sup>	4.42 g	a	b	0.5t

Continued on next page...

Table 2.3 – continued from previous page.

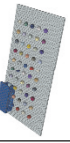
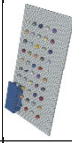
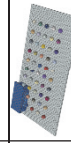
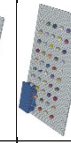
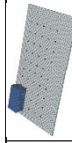
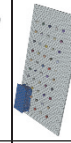
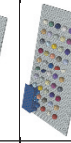
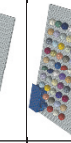

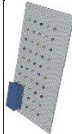
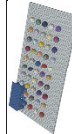
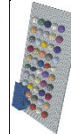
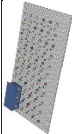
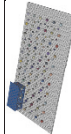
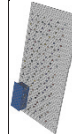
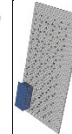
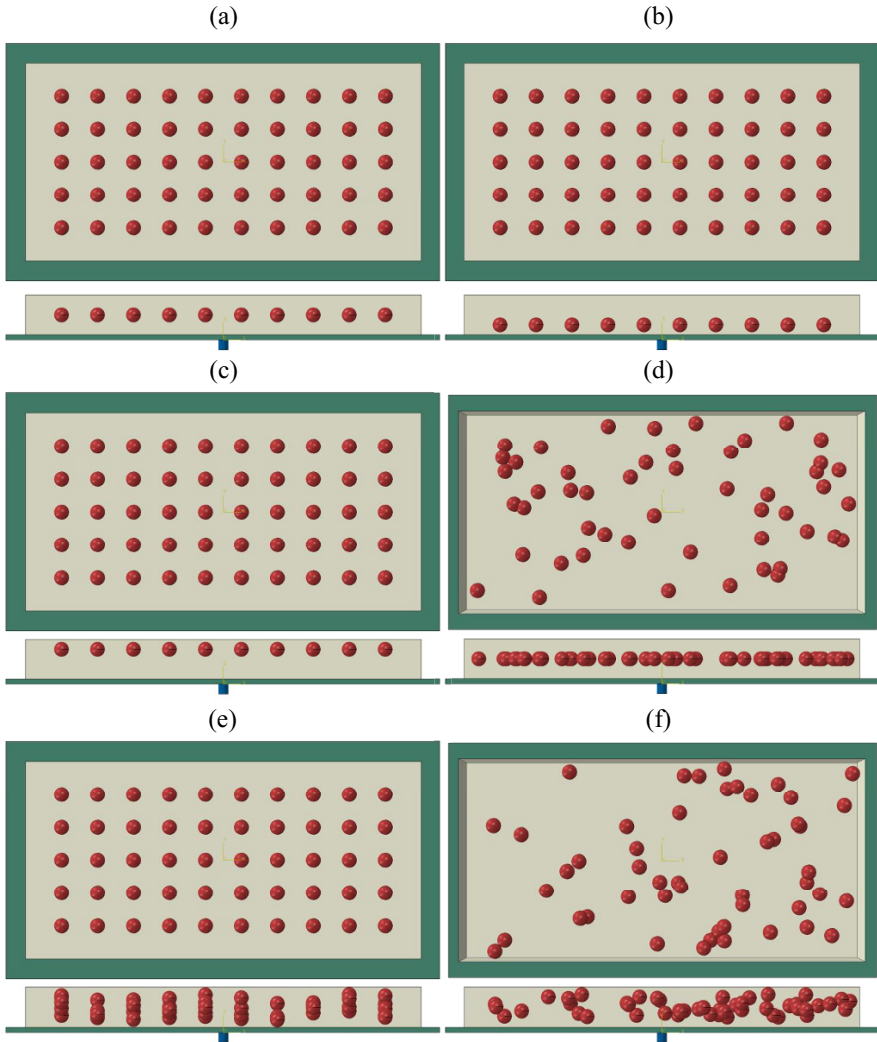
#	Geometry	Number of inclusions	Diameter	Mass density	Young's modulus	Added mass	$\Delta x$	$\Delta y$	$\Delta z$
8		50, 1 layer 5x10	15 mm	1.0 g/cm <sup>3</sup>	5,000 N/mm <sup>2</sup>	83.9 g	a	b	0.5t
9		50, 1 layer 5x10	15 mm	5.0 g/cm <sup>3</sup>	5,000 N/mm <sup>2</sup>	437.4 g	a	b	0.5t
10		50, 1 layer 5x10	15 mm	0.5 g/cm <sup>3</sup>	500 N/mm <sup>2</sup>	39.8 g	a	b	0.5t
11		50, 1 layer 5x10	15 mm	0.5 g/cm <sup>3</sup>	50,000 N/mm <sup>2</sup>	39.8 g	a	b	0.5t
Sect. 2.3.3									
12		50, 1 layer 5x10	5 mm	13.5 g/cm <sup>3</sup>	5,000 N/mm <sup>2</sup>	39.8 g	a	b	0.5t
13		50, 1 layer 5x10	10 mm	1.6875 g/cm <sup>3</sup>	5,000 N/mm <sup>2</sup>	39.8 g	a	b	0.5h
14		50, 1 layer 5x10	20 mm	0.2109 g/cm <sup>3</sup>	5,000 N/mm <sup>2</sup>	39.8 g	a	b	0.5t
15		50, 1 layer 5x10	25 mm	0.108 g/cm <sup>3</sup>	5,000 N/mm <sup>2</sup>	39.8 g	a	b	0.5t
Continued on next page...									

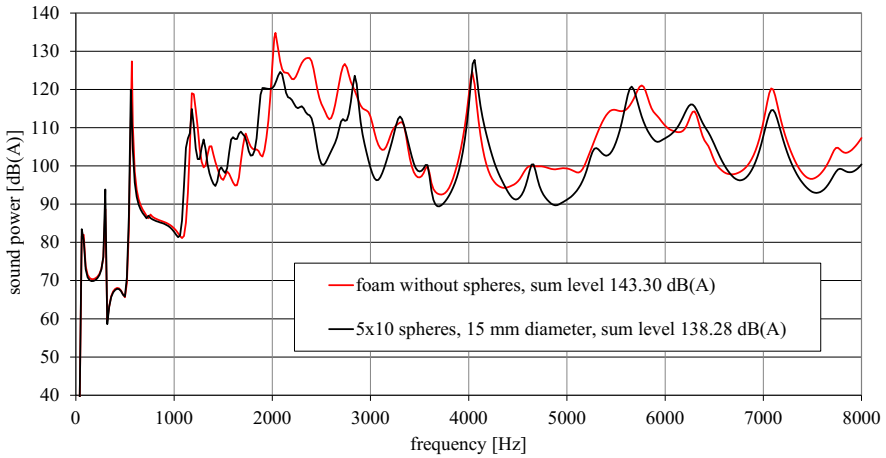
Table 2.3 – continued from previous page.

#	Geometry	Number of inclusions	Diameter	Mass density	Young's modulus	Added mass	$\Delta x$	$\Delta y$	$\Delta z$
Sect. 2.3.4									
16		50, 1 layer 5x10	5 mm	0.5 g/cm <sup>3</sup>	5,000 N/mm <sup>2</sup>	1.47 g	a	b	0.5t
17		50, 1 layer 5x10	10 mm	0.5 g/cm <sup>3</sup>	5,000 N/mm <sup>2</sup>	11.8 g	a	b	0.5t
18		50, 1 layer 5x10	20 mm	0.5 g/cm <sup>3</sup>	5,000 N/mm <sup>2</sup>	94.2 g	a	b	0.5t
19		50, 1 layer 5x10	25 mm	0.5 g/cm <sup>3</sup>	5,000 N/mm <sup>2</sup>	184.1 g	a	b	0.5t
Sect. 2.3.5									
20		166, 3 layers (5x10, 6x11, 5x10)	6/10/6 mm	0.5 g/cm <sup>3</sup>	5,000 N/mm <sup>2</sup>	20.6 g	a	b	0.25t
21		166, 3 layers (5x10, 6x11, 5x10)	6/10/6 mm	5.0/0.5/5.0 g/cm <sup>3</sup>	5,000 N/mm <sup>2</sup>	71.5 g	a	b	0.25t
22		166, 3 layers (5x10, 6x11, 5x10)	6 mm	0.5 g/cm <sup>3</sup>	5,000 N/mm <sup>2</sup>	8.4 g	a	b	0.25t
23		166, 3 layers (5x10, 6x11, 5x10)	6 mm	0.5/5.0/0.5 g/cm <sup>3</sup>	5,000 N/mm <sup>2</sup>	42.0 g	a	b	0.25t



**Fig. 2.4:** Investigated configurations (top and side view of the sphere position in the foam). The models from Table 2.3 which are used for the analyses are: configuration 1 (a), configuration 2 (b), configuration 3 (c), configuration 4 (d), configuration 5 (e), configuration 6 (f)

Configuration 1 (see Fig. 2.4) is used to generate a reference solution against which all other numerical results are compared in the remainder of the chapter. The results for the sound power level, computed using configuration 1 and a pure PUR foam, are summarized in Fig. 2.5. We observe that the resulting sum level of the A-weighted sound power is decreased by 5 dB(A) when using this simple metamaterial.



**Fig. 2.5:** Sound power levels of configuration 1 in comparison to a foam without mass inclusions

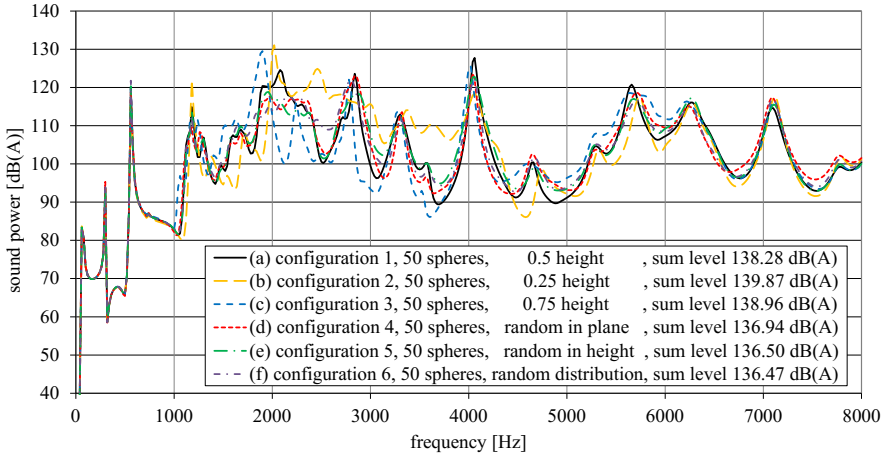
The value of the sound power level is calculated on the surface of the hemispherical air volume. Although, a significant overall reduction is generally observed, but there are also small frequency bands where the amplitudes of the sound power level are actually increased by introducing spherical inclusions.

Still the overall results are quite satisfactory with a large amplitude reduction of more than 10 dB(A) between 2 and 3 kHz. If we look at the results of the aluminum plate that is covered with PUR foam only we observe that this frequency band is actually the most critical due to the high amplitudes that are exhibited. Consequently, we were able to achieve the best reduction in amplitudes in a range where it is of special significance for the chosen structure. These remarkable results have been obtained by simply adding inclusions in a structured fashion to an existing damping material.

In the following paragraphs we will settle what advantages can be gained by introducing more advanced arrangements of the spherical inclusions. To this end, the distribution of the 50 spheres is now varied in different steps.

In Fig. 2.6 the computed sound power levels for all six different configurations (see Fig. 2.4) within the frequency interval from 0 to 8 kHz are depicted. In the legend important information such as the distribution of the inclusions and the sum level of the A-weighted sound power are listed. First, we compare the three regular arrangements of the inclusions (see Fig. 2.4 (a) to (c) – configuration 1, 2, 3). In this case, we observe that the best results over the investigated frequency range are obtained, if the spheres are located in the midplane of the plate. Furthermore, we note that a larger distance to the aluminum plate for configuration 3 is advantageous compared to configuration 2 where the spheres are located almost directly above the base plate. However, if we merely consider the sum levels the random distribution in configurations 4 to 6 lead to an improved noise radiation behavior. In our example



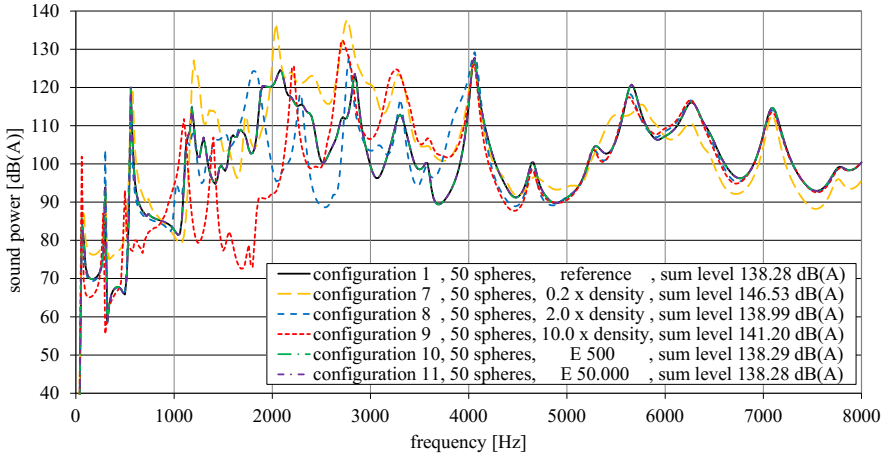


**Fig. 2.6:** Sound power levels of the configurations 1, 2, 3, 4, 5 and 6

a random distribution over the height while a regular one within the plane seems to be a viable choice, as the sum level of configuration 5 is actually almost the same as that of configuration 6. This highlights the fact that the distribution over the height of the damping material is more important than the in-plane one. These findings are also supported by the experimentally drawn conclusions (Schrader et al, 2017b). From a manufacturing point of view (automation of the process) it is also advantageous if a random distribution only needs to be achieved over the height while the in-plane one is structured. Therefore, from our point of view this arrangement constitutes the best choice. In addition, it is remarkable that the behavior in the low frequency range, below 1 kHz, is hardly influenced by the inclusions at all. In the frequency range from 1 kHz to 5 kHz a significant variation in the results can be seen. This is the frequency range where an optimized design can lead to a notable reduction in noise radiation. Above 6 kHz there is again no significant difference between the individual configurations in Fig. 2.6.

### 2.3.2 Influence of the Material Properties of the Spherical Inclusions

In the current subsection we are going to investigate the influence of the material properties on the noise radiation behavior of the acoustic metamaterial. To this end, the Young's modulus and the mass density of the spherical inclusions are varied for configuration 1 (see Table 2.3). Consequently, configurations 1, 7, 8, 9, 10 and 11 are in the focus of this section.

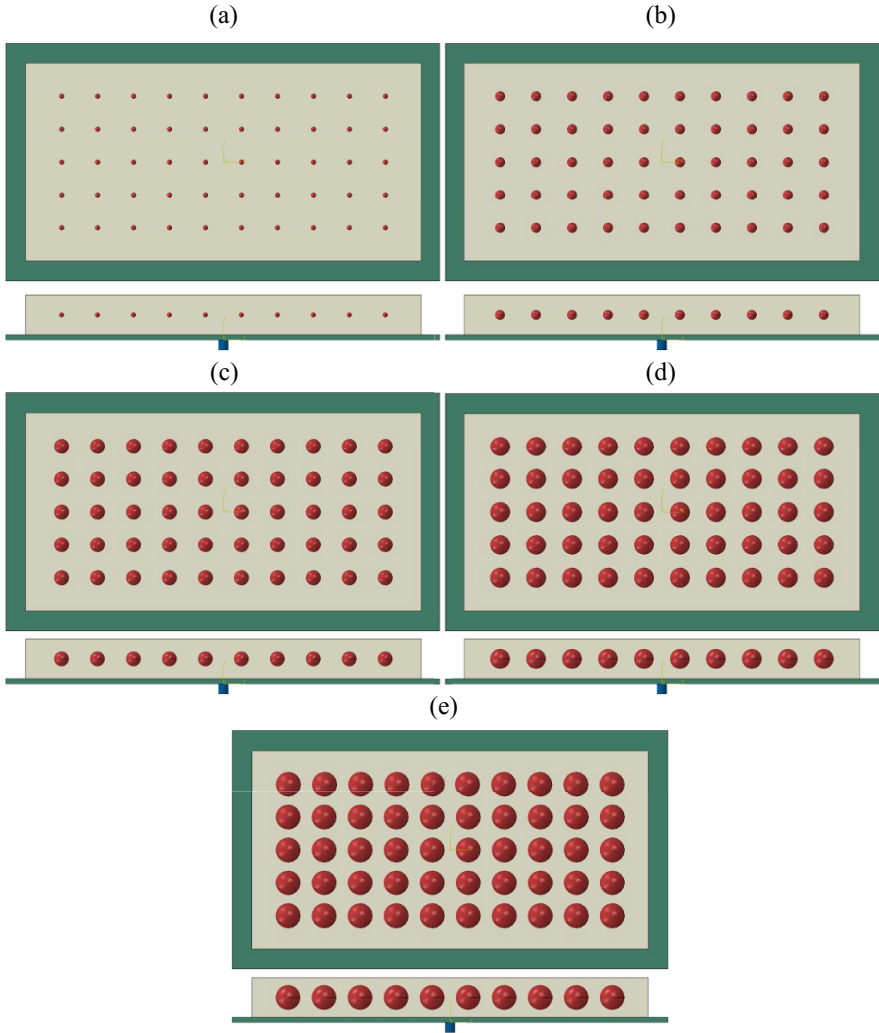


**Fig. 2.7:** Sound power levels of the configurations 1, 7, 8, 9, 10 and 11 (density and Young's modulus variations based on configuration 1)

In Fig. 2.7 the numerical results for the variation of the material properties are shown. The first conclusion that can be drawn is that the variation of the Young's modulus does not seem to have any notable influence on the results. This behavior can be attributed to the fact that the difference in stiffness between the foam and the inclusions is too large such that the inclusions act as rigid bodies even if the Young's modulus is decreased to only  $500 \text{ N/mm}^2$ . A second conclusion is that higher density values show an influence on the radiated sound power for frequencies below 4.5 kHz. Only if the density is drastically decreased an effect over the whole investigated frequency range is visible. For our example the lowest chosen density leads to the worst results but also an increased density compared to the initial configuration leads to deteriorated results. This is caused by the fact that these inclusions (with higher density) elevate some resonance peaks in the critical frequency range. This, of course, results in a higher sum level, even if the amplitudes in other frequency ranges are significantly reduced. This behavior is nicely observed in the frequency range from 1.2 to 2.2 kHz where the sound power level is reduced up to 35 dB(A) for the configuration with 10-times the density (dashed red line) and still the computed sum level is rather unsatisfactorily high, as the sum level is dominated almost only by the most important peaks.

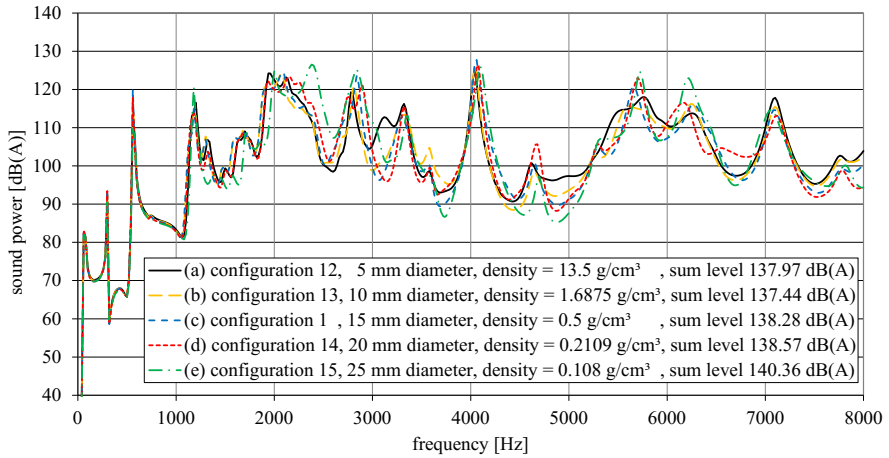
### 2.3.3 Influence of a Fixed Density-Volume-Product

In the next step, the product of density times volume is kept constant, i.e. the added mass is identical for all five different configurations depicted in Fig. 2.8. In our example the additional mass amounts to 39.8 g. The aim of the current investigations



**Fig. 2.8:** Five different configurations with a fixed density-volume-ratio (top and side view of the sphere position in the foam). The models which are used for the analyses are: configuration 12 (a), configuration 13 (b), configuration 1 (c), configuration 14 (d), configuration 15 (e)

is to answer the question, whether the added mass or the geometrical dimension of the spherical inclusions exerts the dominant influence on the vibration behavior of the structure. If the volume of the sphere is changed, so is the spring constant, assuming that we interpret the inclusion and the foam as a spring-mass-system.



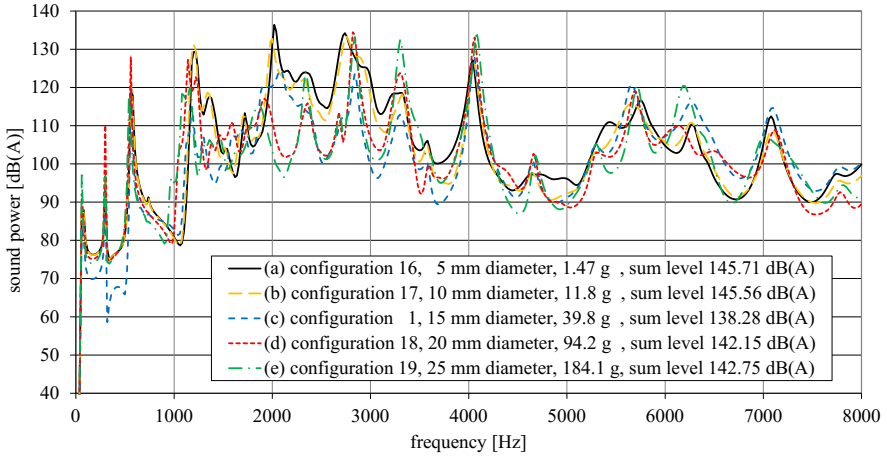
**Fig. 2.9:** Sound power levels of the configurations 12, 13, 1, 14 and 15 (constant density-volume-product based on configuration 1)

In Fig. 2.9 the computed A-weighted sound power levels for the five configurations depicted in Fig. 2.8 are plotted. It can easily be seen that the qualitative behavior is rather similar, but in some frequency ranges there are significant differences. It can be inferred that larger spheres (with a lower density) seem to be disadvantageous as they considerably reduce the volume of the absorbing foam layer. This in turn also leads to a stiffer spring which increases the eigenfrequency of the single spring-mass system. In the current investigation the spheres with a diameter of 10 mm deliver the best results.

### 2.3.4 Influence of the Volume of the Inclusions

In the current subsection the five different configurations that have been introduced in Sect. 2.3.3 are studied again, but this time the mass density is fixed to  $0.5 \text{ g/cm}^3$  which corresponds to the value of configuration 1 (see Fig. 2.8 (c)). Since now the mass density is constant and volume is different for each example, so are the additional masses. Therefore, the values of the added masses are also given in the legend of Fig. 2.10.

When evaluating the results that are plotted in Fig. 2.10 we note that the configurations 16 and 17 are almost without effect which can be attributed to the negligible additional mass in comparison to the pure foam. Especially in the critical frequency range between 2.0 and 2.8 kHz the vibration behavior is quite poor. However, the two configurations 18 and 19 exhibit large amplitude reductions of up to 20 dB(A) compared to the reference configuration 1. For all that the higher additional masses still cause elevated amplitudes at some other frequencies (e.g. at 2.9, 3.3 or 4.1 kHz).



**Fig. 2.10:** Sound power levels of the configurations 16, 17, 1, 18 and 19 (constant density with different volumes of the spherical inclusions)

This effect can be explained by the fact that large inclusions significantly reduce the volume of the absorbing foam. Thus, the energy dissipation caused by the foam is also decreased. For this reason, we conclude that the spherical inclusions with a diameter of 15 mm are an acceptable compromise for our example.

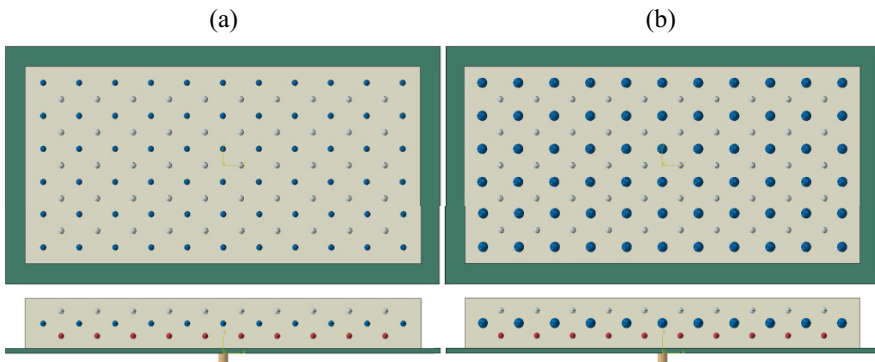
### 2.3.5 Influence of the Number of Layers with Different Material Properties

In the current section we investigate the effect of three layers of inclusions where in each layer the spheres are made of a different material. The models are illustrated in Fig. 2.11. In the top and bottom layers again  $5 \times 10$  spherical inclusions are added to the foam, while in the middle layer  $6 \times 11$  spheres are used. Consequently, the inclusions in adjacent layers are shifted. The diameter of the inclusions is set to 6 mm for configuration 20 and 21, whereas the two arrangements only differ in the densities of the spheres. Considering the second model, configuration 22 and 23 (different densities of the inclusions), the diameter of all spheres that are in the middle layer is increased to 10 mm. The material properties of the added masses can be taken from Table 2.2. However, note that the density is varied between 0.5 and 5.0 g/cm<sup>3</sup>. The actual parameters for each simulation are listed in Table 2.3. In Fig. 2.12 the results for the sound power are depicted. Since the additional mass is an important aspect for such materials, as mentioned in the introduction, it is also given in the legend of that figure.

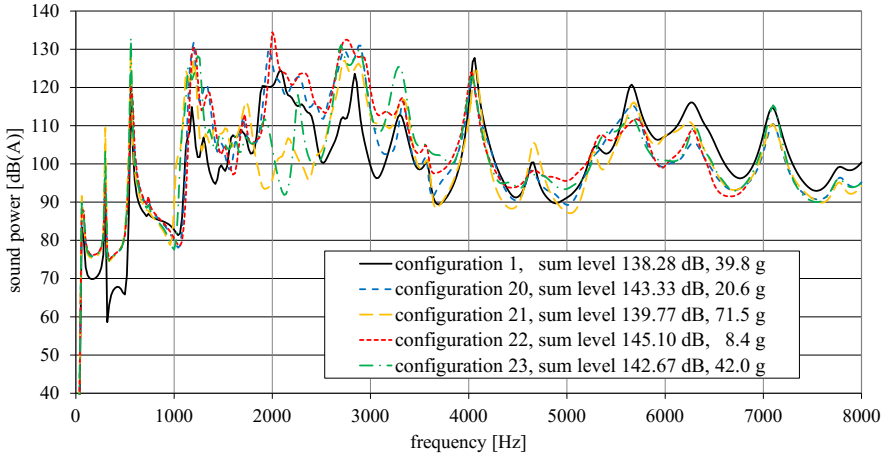
Surprisingly the results depicted in Fig. 2.12 convey that there is no increased attenuation of the resulting sound radiation due to the number of additional layers and consequently a much higher number of spherical inclusions. Compared to the reference configuration the sound power level is not even slightly reduced but in contrast always elevated for the tested setups. It might be concluded that inclusions with a diameter of only 6 or 10 mm are too small and light (the mass density is  $0.5 \text{ g/cm}^3$ ) to have a significant effect. In the reference configuration spheres with a diameter of 15 mm have been utilized. When the density of the spherical inclusions is increased from  $0.5$  to  $5.0 \text{ g/cm}^3$  they are actually heavier than the inclusions in the reference model and therefore, one might conclude that this distribution of the spheres is detrimental. However, to verify this assumption additional parametric studies need to be conducted. In case the mass density is increased for the outer or the middle layer the damping results are improved but they are still worse than the reference configuration and hold another disadvantage as more mass is added to the system.

### 2.3.6 Discussion

The conducted parametric studies show that each parameter such as the position, the mass density, the volume and the number of inclusions can have a significant effect on the resulting sound power level. Moreover, we observed that too many or too large inclusions have a negative influence on the radiated sound power. As the overall mass of a passive damping approach is naturally limited, the added mass is also restricted. To find an optimal solution for the presented problem we are



**Fig. 2.11:** Configurations with three layers of regular positioned mass inclusions, which differ in the material properties and the size of the middle layer. The models which are used for the analyses are: configurations 20, 21 (a) and configurations 22, 23 (b)



**Fig. 2.12:** Sound power levels of the configurations 1, 20, 21, 22 and 23

going to deploy computational optimization techniques for future studies. Here, the distribution, the material properties and the geometry of the inclusions will be varied under the constraint of a restricted additional mass and volume. Thus, the potentials and limits of this type of metamaterials can be assessed with respect to its lightweight potential and achievable sound reduction.

The observations reported in the contribution at hand are supported by experimental findings that have been published in Schrader et al (2017a). In comparable experimental measurements it was shown that an arrangement of inclusions far from the damped surface leads to an increased damping effect in a higher frequency range (Schrader et al, 2017a). Furthermore, a concept with a large number of added masses was rejected as being inefficient (Schrader et al, 2017a) similar to the results presented in Sect. 2.3.5.

## 2.4 Conclusions

In this contribution we investigated the potential of a special class of acoustic metamaterials by means of numerical simulations (FEM). Our focus lay on locally resonant structures consisting of an elastic matrix material in combination with spherical inclusions (added masses). Our exemplary application case is a soft synthetic foam made of polyurethane with much stiffer inclusions within. These inclusions have been varied in size, material properties, number and position. Here, it was shown that this type of acoustic metamaterials is well suited to increase the damping effect compared to that of the base material. Depending on the tuned arrangement of inclusions it is both possible to influence the damping properties only in certain frequency bands or over the whole frequency range of interest. A strong correlation between

the influence parameters of the spherical mass inclusions (size, material properties, number and position) and the resulting sound power level was observed. That is to say, we have to be careful when designing such an acoustic metamaterial as an arbitrary distribution of inclusions with arbitrary parameters could result in a worse performance compared to the base material. Consequently, it is of utmost importance to design efficient and robust numerical tools for the dimensioning of these materials. A first step in this direction was made in this contribution.

In the parametric studies we observed that the stiffness of the inclusions has a negligible effect on the achieved sound absorption. Due to the vastly different mechanical impedances of both materials all investigated inclusions acted as rigid bodies within the soft elastic foam. On the other hand, a variation of the mass density of the spherical inclusions or their location cause a significant difference in the radiated sound power in a frequency range between 1 and 5 kHz. Both below 1 kHz and above 6 kHz the different tested configurations displayed hardly any changes in the resulting sound power levels. For our example problem the sound radiation is deteriorated if the mass density is chosen too high or too low. Consequently, this parameter should be optimized for future applications. Moreover, it was verified that the product of mass density and volume has an influence on the sound absorption. In this context, it has been found that the spherical inclusions should be neither too small nor too big as the obtained results have been much worse compared to our reference configuration. For this reason, the size of the inclusions is a second parameter that calls for an optimization. In regard to the positioning of the inclusions we can state that the out-of-plane direction is seemingly more important than the in-plane directions. Therefore, the position might be a third parameter that should be investigated by means of a numerical optimization technique, although random distributions have in general attained favorable results in our parametric studies.

Finally, the presented results have been validated with experimental measurements that have been published previously. The most important conclusions that we have drawn from the parametric studies are supported by the experimental evidence. With the help of the knowledge derived from the observations of this contribution initial design proposals for this class of acoustic metamaterials can be given. Therewith, we are able to achieve an improved damping behavior with a minimum gain in mass.

Future research activities in the direction of acoustic metamaterials will include a fully automated numerical optimization to determine the optimal configuration. To this end, a sophisticated python script has been developed to automatically generate the finite element model for arbitrary arrangements. The parameters that should be included in the optimization process are the number of inclusions, the number of layers, the size, the position and the material properties of the inclusions. The objective function will be the resulting sound power level of the overall system. We hope that the results of the optimization process will help us to answer the following questions:

1. How many inclusions should be added to the base material?
2. How many layers of inclusions should be added?
3. Which distribution of inclusions should be deployed to obtain the best possible results?



#### 4. Which material should be chosen for the inclusions?

In the current study it was demonstrated that one layer featuring 50 spherical inclusions performs better than several layers with a much greater number of added masses. In general, this might not be true considering that the randomly distributed configurations lead to the best overall results.

After the numerical optimization has been executed a prototype of the optimal configuration will be produced and compared to both the best configurations determined in the current contribution and to the foam material without any modifications. The experimental measurements will be conducted in an acoustic far field room which is equipped with a microphone array and far field microphones. The aim is to validate that the computed optimal solution exhibits a significantly improved damping behavior compared to all other previous configurations.

Another interesting point for future studies is naturally the investigation of the influence of the inclusion shape on the damping behavior. Therefore, different simple shapes such as arbitrary ellipsoids could be studied in contrast to arbitrarily shaped (convex) inclusions generated by means of Voronoi diagrams.

**Acknowledgements** The presented work is part of the joint project COMO “Competence in Mobility”, which is financially supported by the European Funds for Regional Development (EFRE) as well as the German State of Saxony-Anhalt. This support is gratefully acknowledged.

We would also like to thank our colleague Peter Schrader from the Institute of Mobile Systems (Otto-von-Guericke-Universität Magdeburg) for numerous fruitful discussions, the successful co-operation during the last years and the execution of the experiments, which supported our efforts to gain a deeper insight into the acoustical behavior of metamaterials and their most important influence parameters.

## References

- Deymier PA (2013) *Acoustic Metamaterials and Phononic Crystals*. Springer-Verlag Berlin Heidelberg
- Duvigneau F (2017) Ganzheitliche simulationsbasierte Bewertung der Akustik von automobilen Antrieben. No. 467 in *Fortschritt-Berichte VDI, Reihe 20*, VDI-Verlag GmbH, Düsseldorf
- Duvigneau F, Koch S, Woschke E, Gabbert U (2016a) An effective vibration reduction concept for automotive applications based on granular-filled cavities. *Journal of Vibration and Control*
- Duvigneau F, Liefold S, Höchstetter M, Verhey JL, Gabbert U (2016b) Analysis of simulated engine sounds using a psychoacoustic model. *Journal of Sound and Vibration* 366:544–555
- Duvigneau F, Luft T, Hots J, Verhey JL, Rottengruber H, Gabbert U (2016c) Thermo-acoustic performance of full engine encapsulations - a numerical, experimental and psychoacoustic study. *Journal of Applied Acoustics* 102:79–87
- Duvigneau F, Nitzschke S, Woschke E, Gabbert U (2016d) A holistic approach for the vibration and acoustic analysis of combustion engines including hydrodynamic interactions. *Archive of Applied Mechanics* 86(11):1887–1900
- Fuchs HV (2007) *Schallabsorber und Schalldämpfer*. Springer-Verlag Berlin Heidelberg New York
- Fuller C, Saux TD (2012) Sound absorption using poro-elastic acoustic metamaterials. In: *Internoise 2012 conference proceedings*
- Gabbert U, Duvigneau F, Ringwelski S (2017) Noise control of vehicle drive systems. *FACTA UNIVERSITATIS, Series: Mechanical Engineering* 15(2):183–200

- Givoli D (2008) Computational absorbing boundaries. In: Marburg S, Nolte B (eds) *Computational Acoustics of Noise Propagation in Fluids*, Springer-Verlag, Berlin, pp 145–166
- Hughes TJR (1987) *The Finite Element Method: Linear Static and Dynamic Finite Element Analysis*. Prentice-Hall, New Jersey
- Idrisi K, Johnson ME, Theurich D, Carneal JP (2010) A study on the characteristic behavior of mass inclusions added to a poro-elastic layers. *Journal of Sound and Vibration* 329:4136–4148
- Jensen JS (2011) *Waves and vibrations in inhomogeneous structures: Bandgaps and optimal designs*. PhD thesis, Technical University of Denmark
- Koch S, Duvigneau F, Duczek S, Woschke E (2017a) Vibration reduction in automotive applications based on the damping effect of granular material. In: *Automotive Acoustics Conference 2017*, 4. Internationale ATZ-Fachtagung Fahrzeugakustik
- Koch S, Duvigneau F, Orszulik R, Gabbert U, Woschke E (2017b) Partial filling of a honeycomb structure by granular materials for vibration and noise reduction. *Journal of Sound and Vibration* 393:30–40, DOI <http://dx.doi.org/10.1016/j.jsv.2016.11.024>
- Liu Z, Zhang X, Mao Y, Zhu YY, Yang Z, Chan CT, Sheng P (2000) Locally resonant sonic materials. *Science* 289:1734–1736
- Liu Z, Chan CT, Sheng P (2005) Analytic model of phononic crystals with local resonances. *Physical Review B* 71:1–8
- Lu MH, Feng L, Chen YF (2009) Phononic crystals and acoustic metamaterials. *Materials today* 12:34–42
- Maa DY (1998) Potential of microperforated panel absorber. *Journal of the Acoustical Society of America* 104:2861–2866
- Ringwelski S, Luft T, Gabbert U (2011) Piezoelectric controlled noise attenuation of engineering systems. *Journal of Theoretical and applied mechanics* 49(3):859–878
- Schirmacher R, Lippold R, Steinbach F, Walter F (2007) *Praktische Aspekte beim Einsatz von ANC-Systemen in PKW*. In: *Fortschritte der Akustik, DAGA*
- Schrader P, Duvigneau F, Luft T, Gabbert U, Rottengruber H (2015) Development, Simulation and Experimental Investigation of a Function-Integrated and Foam Damped Oil Pan for a Two Cylinder Diesel Engine. In: *44th International Congress and Exposition on Noise Control Engineering - InterNoise 2015*, San Francisco
- Schrader P, Duvigneau F, Orszulik R, Rottengruber H, Gabbert U (2016) A numerical and experimental study on the noise absorption behavior of functionally graded materials considering geometrical and material influences. In: *45th International Congress and Exposition on Noise Control Engineering - InterNoise*
- Schrader P, Duvigneau F, Rottengruber H, Gabbert U (2017a) The noise reduction potential of lightweight acoustic metamaterials – A numerical and experimental study. In: *Automotive Acoustics Conference 2017*, 4. Internationale ATZ-Fachtagung Fahrzeugakustik
- Schrader P, Duvigneau F, Rottengruber H, Gabbert U (2017b) Passive Reduktion der Schallabstrahlung von Oberflächen durch Anwendung von Metamaterialstrukturen. In: *43. Jahrestagung für Akustik - DAGA*
- Sheng P, Mei J, Liu Z, Wen W (2017) Dynamic mass density and acoustic metamaterials. *Physica B* 394:256–261
- Sui N, Yan X, Huang TY, Xu J, Yuan FG, Jing Y (2015) A lightweight yet sound-proof honeycomb acoustic metamaterial. *Applied Physics Letters* 106:1–4
- Troge J, Drossel WG, Lochmahr M, Zumach S (2016) Reducing rear axle gear whine noise inside a car by influencing the structure-borne sound transfer path using structurally integrated piezo-actuators. In: *Proceedings of the 22nd International Congress on Acoustics - ICA*
- Zhang G, Jackson T, Lafond E, Deymier P, Vasseur J (2006) Evidence of surface acoustic wave band gaps in the phononic crystals created on thin plates. *Applied Physics Letters* 88:3pp.
- Zhang ZM, Gu XT (1997) The theoretical and application study on a double layer microperforated sound absorption structure. *Journal of Sound and Vibration* 215:399–405
- Zhao M, Xie YZ, Zhang XG, Gao J (2013) Band gaps of Lamb waves propagating in one-dimensional periodic and nesting Fibonacci superlattices thin plates. *Thin Solid Films* 546:439–442

Zienkiewicz OC, Taylor RL (2000) *The Finite Element Method: Volume 1 The Basis*. Butterworth Heinemann, London

# Chapter 3

## Electromechanical Degradation of Piezoelectric Patches

Hassan Elahi, Marco Eugeni, and Paolo Gaudenzi

**Abstract** Piezoelectric materials (PZT) are widely used as smart structure in various aerospace applications because of their sensing, actuating and energy harvesting abilities. In this research work, the degradation of the electromechanical properties of a PZT material after various mechanical and thermal shocking conditions is experimentally studied. In particular, the relationship between resistance and peak to peak voltage of Lead Zirconate Titanate (PZT-5A4E) to the degradation factor at variable frequencies and thermo-mechanical shocking conditions is considered. This research provides novel mechanism for characterizing smart structures using Mechanical Quality Factor.

### 3.1 Introduction

Degradation of electromechanical properties in a piezoelectric material is of great interest for design engineers as well as for maintenance engineer. Energy harvesting using a piezoelectric patch is the process in which energy is generated from external stresses and utilized as electrical energy for powering sensors or actuators or stored in batteries for lateral tasks. Electrostatics, electromagnetic and piezoelectric are most famous mechanisms of electricity generation via vibration energy; among them piezoelectricity is the best one because of performance and their manufacturability in nano, micro and macro scales (Gaudenzi, 2009; Cook-Chennault et al, 2008). Generation of electric potential from mechanical stress i.e., direct piezoelectric effect and generation of mechanical vibrations from applied electric potential i.e., converse piezoelectric effect is discovered by Jacques Curie and Pierre Curie in 1880 (Safari and Akdogan, 2008). For the application of a piezoelectric patch as a sensor is an application of direct piezoelectric effect whereas usage of piezoelectric patch as

---

Hassan Elahi · Marco Eugeni · Paolo Gaudenzi  
Department of Mechanical and Aerospace Engineering, Sapienza University of Rome, Italy  
e-mail: hassan.elahi@uniroma1.it, paolo.gaudenzi@uniroma1.it

a transducer is an application of converse effect (Gaudenzi, 2009). From last few decades a large quantity of research works have been done on piezoelectric materials because of their voltage actuation abilities and their applications in fields of smart structures, micro electro-mechanical systems, aerospace, structural health monitoring, etc. (Paliwal et al, 2015; Gaudenzi et al, 2015; Gaudenzi and Facchini, 2013).

Piezoelectric energy harvesters, vibrators, strain gauges, accelerometers that transform one form of energy into another as well as work as transducer can be used for remote sensing and electronic embedded devices. For electro-mechanical actuation like solenoid operating valves, piezoelectric materials play a vital role and their maintenance or replacement in a given equipment is critical (Chen et al, 2012; Waqar et al, 2017; Sasaki and Shimamura, 2001). Experimentation on piezoelectric patches was begin from 1984 which lead base for this phenomenon Häsler et al (1984). Experimentation on polyvinylidene difluoride (PVDF) specimen was done to know the effect of frequency loading at high and low amplitude (Schmidt, 1992; Gull et al, 2017). Various studies has been performed to harvest energy from smart structures using human body and to drive low power electronic equipments from these piezoelectric harvesters (Antaki et al, 1994). The effect of electromechanical degradation is declared as one of the most important phenomenon in piezoelectricity for characterizing smart structures, energy harvesters, integration of sensors and actuators for structural health monitoring specially for aerospace field (Facchini et al, 2015; Gaudenzi et al, 2014). In 2014 an experimental investigation was carried out by using piezoelectric patch over wide range of variable electrical loading conditions to harvest energy (Xiao et al, 2014).

In designing of piezoelectric sensors and actuators mechanical quality factors play a vital role because it indicates energy loss in the form of impedance over resistance in a piezoelectric patch (Montero De Espinosa et al, 1992; Liu et al, 2015). With increase in frequency the mechanical quality factor of PZT patch decrease i.e., varies from 3700 to 930 with frequency variation of 158 kHz to 1.18 MHz (DeVoe, 2001; Elahi et al, 2014). A new class of piezoelectric ceramics has been reported having higher mechanical quality factor which vibrates at frequency loading of 1.7 MHz and have greater applications in ultrasonics transducers (Butt et al, 2017; Elahi et al, 2016). Till date the manufacturing and maintenance of piezoelectric patches is on hit and trial method which not only takes a longer time as well as is more expensive. These practices are not in accordance to the modern industry development, these practices can be carried out with some computerized numerical solution software for theoretical prediction of properties for transducers. Currently, Finite Element Analysis (FEA) is acting as important tool for researchers for prediction of electromechanical properties and mechanical quality factor (Gaudenzi and Bathe, 1995; Lampani et al, 2012; Tralli et al, 2005). Modeling capabilities have been also developed which allow finite element techniques to simulate the behavior the coupled electro-elastic behavior of these materials with increasing accuracy both in the linear and non linear case for 3D solids, and for structural elements like plates and shells (Pasquali and Gaudenzi, 2012, 2015).

The prediction of electrical and mechanical properties plays a vital role in characterizing the piezoelectric material and they are influenced by operating and testing

conditions (Uchino et al, 2011). The aim of this research is to investigate and analyze the degradation and mechanical quality factor of a rectangular shaped piezoelectric patch i.e., Lead Zirconate titanate at variable frequency, resistance and mechanical loading conditions with respect to mechanical characteristics and electronic response. The response of peak to peak voltage generated by the piezoelectric patch and factors effecting it are also analyzed. Experimental campaign and experimental setup are explained in Sect. 3.2. In Sect. 3.3 the experimental results are presented and discussed. Finally, in Sect. 3.4 some final remarks are given.

## 3.2 Experimentation

Experimentation was performed in specifically designed test rig. The samples are all rectangular PZT-patch of 1.20cm length, 0.60cm width and 0.3cm thickness. The selected material is the Lead Zirconate Titanate (PZT-5A4E) because of its good dielectric, ferroelectric and piezoelectric properties, see Table 3.1 for a resume of its mechanical and electrical properties.

Table 3.1: Lead Zirconate Titanate (PZT-5A4E) mechanical and electrical properties

$C_{11}$	$121.0 \cdot 10^9$ Pa	$C_{12}$	$75.4 \cdot 10^9$ Pa
$C_{13}$	$75.2 \cdot 10^9$ Pa	$C_{33}$	$111.0 \cdot 10^9$ Pa
$C_{44}$	$21.1 \cdot 10^9$ Pa	$d_{15}$	$584.0 \cdot 10^{-12}$ m/V
$d_{31}$	$-171.0 \cdot 10^{-12}$ m/V	$d_{33}$	$374 \cdot 10^{-12}$ m/V
$e_{31}$	$-5.4$ C/m <sup>2</sup>	$e_{33}$	$15.8$ C/m <sup>2</sup>
$e_{15}$	$12.3$ C/m <sup>2</sup>	$\epsilon_{11}$	$8.1 \cdot 10^9$ F/m
$\epsilon_{33}$	$7.346 \cdot 10^9$ F/m		

Experimental setup was designed in such a way that load cell was mounted on the base composite structure that was used for the construction of satellite to calculate the force or load acting on a piezoelectric patch. Piezoelectric patches were placed between copper electrodes that were surrounded by mica sheet to provide thermal and electrical insulation. For the sake of thermal shocking heat filament element was used and to analyze temperature at any instance or spot, laser temperature gun was used. To shock piezoelectric electrically at various frequency and resistances, function generator and decade box were used. For mechanical loading DC motor was used with a screw mechanism to control the amount of force acting on it. To analyze the overall result digital oscilloscope was used with data acquisition system. We used the function generator (HAMEG-8150) to measure the performance of the commercial PZT patch at various sinusoidal frequencies and voltage amplitudes and a 25 N electromagnetic shaker(Model-F10/Z820WA) with a wide frequency range to provide sinusoidal vibrating load conditions so that we could measure the dynamic and static responses of the material. We monitored the applied load using a load cell

(HYTEK) placed at the bottom layer of the specimen. We also used an impedance analyzer(HP-4294A) connected with a switch box circuit to measure the impedance, resonance, and anti-resonance frequency. We prepared an oscillator circuit to produce a very low distortion frequency signal and used a simple energy harvesting circuit (AC to DC converter) to measure the DC voltage across the harvester. Figure 3.1 shows a rectifier circuit consisting of four diodes connected to the piezoelectric ring. To measure the current through the ring, we stored in a capacitor a  $1\text{ k}\Omega$  resistor connected in series and the generated electrical potential. To avoid any noise or other adjacent environment effects, we placed the experimental setup on an insulated bench and monitored the dynamic and static response of the piezoelectric material on a digital oscilloscope (GPS-1072B). Experimental setup is shown in Fig. 3.2, circuit diagram is shown in Fig. 3.3 while Fig. 3.1 represents controlling mechanism of mechanical load shocking to PZT patch via DC motor respectively Elahi et al (2014). Boundary conditions of piezoelectric patch are considered to be fixed at one end and alternating stress is applied from other end as shown in Fig. 3.4.

Mechanical stimulus is applied on alternate basis to the PZT. For this purpose a circuit is specifically designed to alternate the stress via DC Motor by setting its RPM and geometry of shaft as shown in Fig. 3.5. Resonating frequency ( $f_a$ ) and anti-resonating frequency ( $f_b$ ) was determined by a circuit method Elahi et al (2014). The capacitance (C) was determined via capacitance meter and the mechanical quality

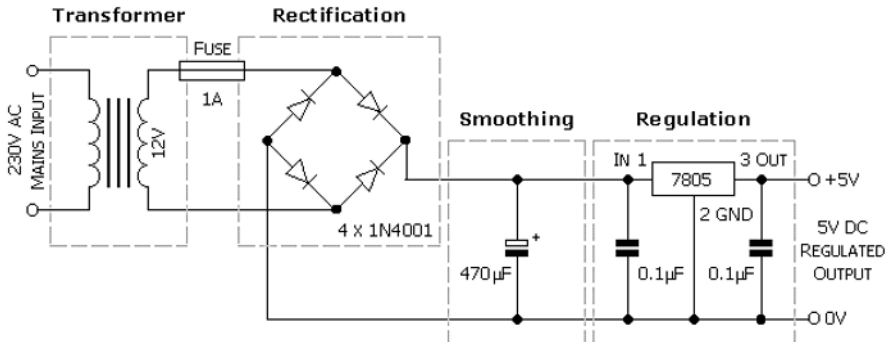


Fig. 3.1: Circuit diagram for controlling the mechanical load via DC Motor

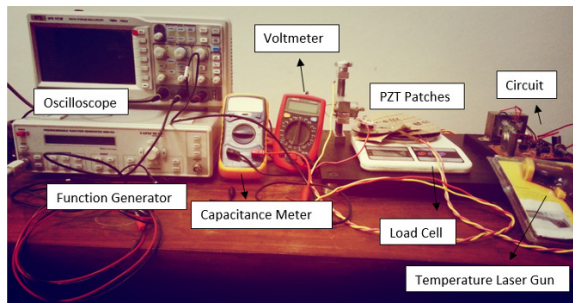
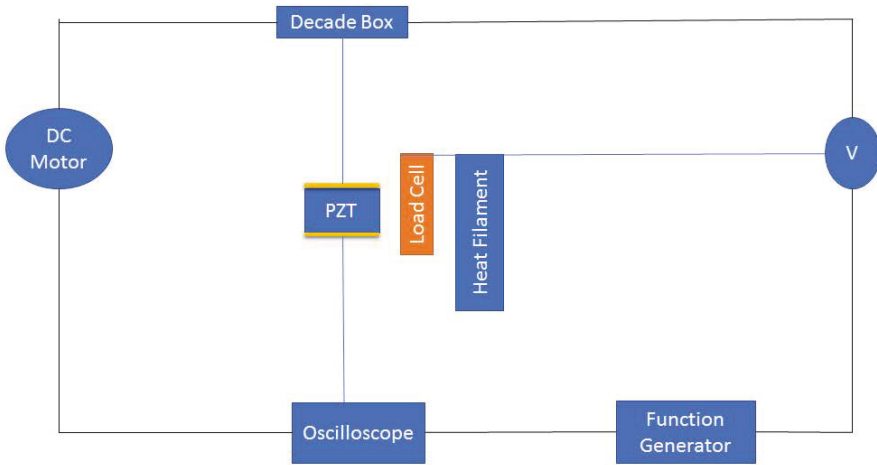
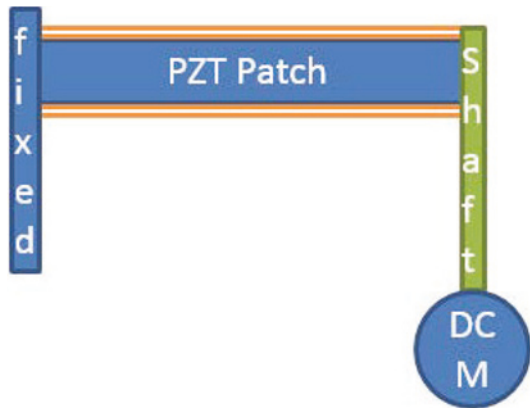


Fig. 3.2 Experimental Setup



**Fig. 3.3:** Circuit diagram for experimental campaign

**Fig. 3.4** Schematic diagram of experimentation



factor ( $Q_m$ ) was calculated by using equations 3.1 to 3.4 Elahi et al (2014)

$$Q_m = \frac{X_c}{R} \tag{3.1}$$

As impedance is given by

$$X_c = \frac{1}{2\pi fC} \tag{3.2}$$

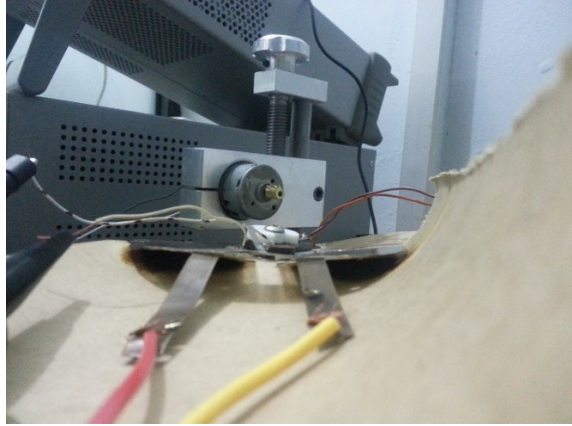
the Mechanical Quality Factor is defined as

$$Q_m = \frac{1}{2\pi\delta fRC} \tag{3.3}$$

where:



**Fig. 3.5** Experimental setup for alternate mechanical stress application



$$\delta f = f_b - f_a \quad (3.4)$$

### 3.3 Results and Discussions

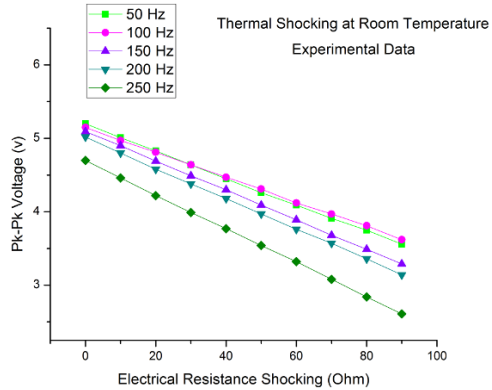
During the experimentation it is observed that by increasing temperature, the peak to peak voltage increases but by increasing frequency the output peak to peak voltage decreases. For maximum results optimization has to be done by increasing temperature, decreasing resistance, and decreasing frequency. Experimentation is performed at temperatures varying from  $20^\circ\text{C}$  to  $180^\circ\text{C}$  temperature, resistance varies from  $0\ \Omega$  to  $90\ \Omega$ , and frequency ranges from  $50\ \text{Hz}$  to  $250\ \text{Hz}$ . The results obtained are shown in the figures of this section.

Extensive experimentation has been performed to analyze degradation of electromechanical properties. For each data point, 23 times experiments have been performed with new piezoelectric patch of the same geometry in order to cater the effect of polarization. These experiments were performed up to 2500 stress cycles in order to analyze the phenomenon of degradation. The response was negligible before 300 stress cycles and it shows pretty fast response after this limit up to 1500 stress cycles. After 1498 stress cycles within given conditions material degraded it is electromechanical properties. So for maintenance engineer it is necessary to replace piezoelectric patches before this level of stress in described conditions.

Figure 3.6 represents the experimental data on electrical resistance shocking ( $0\ \Omega$  to  $100\ \Omega$ ) versus peak to peak voltage at various Frequency loading ( $50\ \text{Hz}$  to  $250\ \text{Hz}$ ) at room temperature ( $25^\circ\text{C}$ ) under stress cycles from 300 to 1500. It can be analyzed that with increase in stress cycles, frequency and resistance the degradation of properties starts and because of this factor the peak to peak voltage of piezoelectric patch decreases. It exhibits a negative linear behavior.

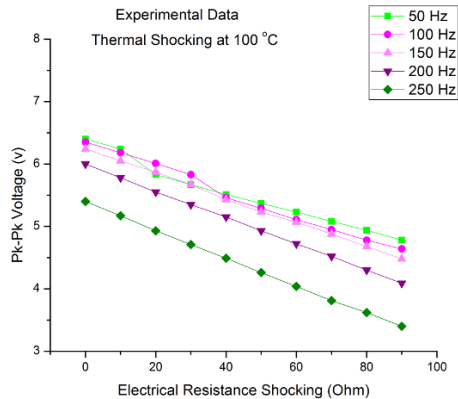
Figure 3.7 represents the experimental data on electrical resistance shocking ( $0\ \Omega$  to  $100\ \Omega$ ) versus peak to peak voltage at various Frequency loading ( $50\ \text{Hz}$  to  $250\ \text{Hz}$ )

**Fig. 3.6** Experimental data on Electrical Resistance Shocking vs. Pk-Pk voltage at various Frequency shocking at room temperature



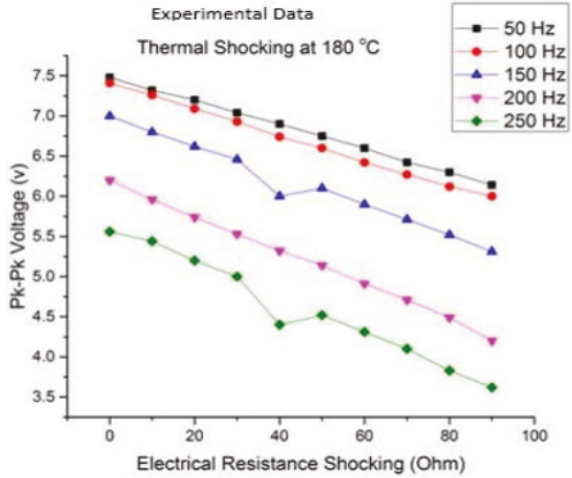
at 100° C temperature under stress cycles from 300 to 1500. It can be analyzed that with increase in stress cycles, frequency and resistance the degradation of properties starts and because of this factor the peak to peak voltage of piezoelectric patch decreases. It exhibits some disruption between 30 Ω to 50 Ω resistance shocking because of some irruption in polarization of piezoelectric patch.

Figure 3.8 represents the experimental data on electrical resistance shocking (0 Ω to 100 Ω) verses peak to peak voltage at various Frequency loading (50 Hz to 250 Hz) at 180° C temperature under stress cycles from 300 to 1500. It can be analyzed that with increase in stress cycles, frequency and resistance the degradation of properties starts and because of this factor the peak to peak voltage of piezoelectric patch decreases. It exhibits some disruption between 30 Ω to 50 Ω resistance shocking at 150 Hz and 250 Hz of frequency because of some irruption in polarization of piezoelectric patch.



**Fig. 3.7** Experimental data on Electrical Resistance Shocking vs Pk-Pk voltage at various Frequency shocking at 100°C Thermal Shocking

**Fig. 3.8** Experimental data on Electrical Resistance Shocking vs Pk-Pk voltage at various Frequency shocking at 180°C Thermal Shocking



**Fig. 3.9** Experimental data on Mechanical Quality Factor vs. Mechanical Load

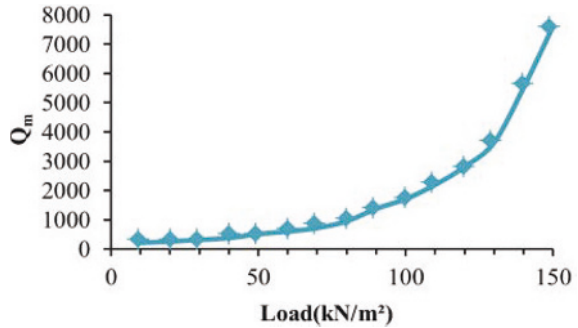


Figure 3.9 represents the Mechanical Quality Factor as well as peak to peak voltage generated by a piezoelectric patch increases with the increase in load ( $kNm^{-2}$ ). It reaches up to it's maximum value of 7900 at 150 ( $kNm^{-2}$ ) at room temperature and at constant frequency loading of 50 Hz.

### 3.4 Conclusions

In this research work electromechanical degradation of piezoelectric materials is analyzed experimentally as well as numerically. On the basis of the results obtained following conclusions can be made. On increasing the resistance from 0 Ohm to 100 Ohm the voltage generated by piezoelectric patch i.e., Lead Zirconate Titanate decreases at variable frequency shocking conditions from 50Hz to 250Hz. The maximum drop of voltage generated was observed at 100 Ohm of resistance and 250 Hz of frequency. The relationship between voltage generated and electrical resistance shocking at variable fixed frequency is negative linear behavior. Voltage

generated goes on increasing with increase in mechanical loading with the increase in resistance which depicts output voltage is mainly dependent on mechanical loading rather than resistance or frequency shocking. The efficiency of piezoelectric patch increase with mechanical loading because of the in mechanical quality factor. No significant degradation was observed before 50 Hz of frequency shocking and 300 stress cycles. Experimentation and numerical simulations were within 10 percent of error, FEM model is correct and good for future studies.

## References

- Antaki JF, Bertocci GE, Green EC, Nadeem A, Rintoul T, Kormos RL, Griffith BP (1994) A gait-powered autologous battery charging system for artificial organs. *ASAIO Journal (American Society for Artificial Internal Organs)* 41(3):M588–95
- Butt Z, Anjum Z, Sultan A, Qayyum F, Ali HMK, Mehmood S (2017) Investigation of electrical properties and mechanical quality factor of piezoelectric material (pzt-4a). *Journal of Electrical Engineering and Technology* 12(2):846–851
- Chen Xr, Yang Tq, Wang W, Yao X (2012) Vibration energy harvesting with a clamped piezoelectric circular diaphragm. *Ceramics International* 38:S271–S274
- Cook-Chennault KA, Thambi N, Sastry AM (2008) Powering MEMS portable devices—A review of non-regenerative and regenerative power supply systems with special emphasis on piezoelectric energy harvesting systems. *Smart Materials and Structures* 17(4):043,001
- DeVoe DL (2001) Piezoelectric thin film micromechanical beam resonators. *Sensors and Actuators A: Physical* 88(3):263–272
- Elahi H, Pasha RA, Khan MZ (2014) Experimental determination of mechanical quality factor of lead zirconate titanate (PZT-5A4E) by equivalent circuit method under various thermal and resistance conditions. *University of Engineering and Technology Taxila Technical Journal* 19(II):1–4
- Elahi H, Israr A, Khan MZ, Ahmad S (2016) Robust vehicle suspension system by converting active and passive control of a vehicle to semi-active control system analytically. *Journal of Automation and Control Engineering* 4(4):300–304
- Facchini G, Bernardini L, Atek S, Gaudenzi P (2015) Use of the wavelet packet transform for pattern recognition in a structural health monitoring application. *Journal of Intelligent Material Systems and Structures* 26(12):1513–1529
- Gaudenzi P (2009) *Smart Structures: Mathematical Modelling and Applications*. Wiley
- Gaudenzi P, Bathe KJ (1995) An iterative finite element procedure for the analysis of piezoelectric continua. *Journal of Intelligent Material Systems and Structures* 6(2):266–273
- Gaudenzi P, Facchini G (2013) Wireless structural sensing. In: *SMART'13: Smart Materials and Structures*, Trans Tech Publications, Advanced Materials Research, vol 745, pp 155–165
- Gaudenzi P, Bernabei M, Dati E, de Angelis G, Marrone M, Lampani L (2014) On the evaluation of impact damage on composite materials by comparing different ndi techniques. *Composite Structures* 118(1):257–266
- Gaudenzi P, Nardi D, Chiappetta I, Atek S, Lampani L, Pasquali M, Sarasini F, Tirilló J, Valente T (2015) Sparse sensing detection of impact-induced delaminations in composite laminates. *Composite Structures* 133(Supplement C):1209 – 1219
- Gull MA, Elahi H, Marwat M, Waqar S (2017) A new approach to classification of upper limb and wrist movements using eeg signals. In: *Biomedical Engineering (BioMed), 2017 13th IASTED International Conference on, IEEE*, pp 181–194
- Häslér E, Stein L, Harbauer G (1984) Implantable physiological power supply with PVDF film. *Ferroelectrics* 60(1):277–282

- Lampani L, Grillo R, Gaudenzi P (2012) Finite element models of piezoelectric actuation for active flow control. *Acta Astronautica* 71
- Liu G, Zhang S, Jiang W, Cao W (2015) Losses in ferroelectric materials. *Materials Science and Engineering: R: Reports* 89:1–48
- Montero De Espinosa F, San Emeterio J, Sanz P (1992) Summary of the measurement methods of  $q_m$  for piezoelectric materials. *Ferroelectrics* 128(1):61–66
- Paliwal N, Mukhija N, Bhatia D (2015) Design and optimization of high quality factor mems piezoelectric resonator with pseudo electrodes. In: *Reliability, Infocom Technologies and Optimization (ICRITO)(Trends and Future Directions)*, 2015 4th International Conference on, IEEE, pp 1–5
- Pasquali M, Gaudenzi P (2012) A nonlinear formulation of piezoelectric plates. *Journal of Intelligent Material Systems and Structures* 23(15):1713–1723
- Pasquali M, Gaudenzi P (2015) A nonlinear formulation of piezoelectric shells with complete electro-mechanical coupling. *Meccanica* 50(10):2471–2486
- Safari A, Akdogan EK (2008) *Piezoelectric and Acoustic Materials for Transducer Applications*. Springer Science & Business Media
- Sasaki Y, Shimamura T (2001) Piezoelectric vibrators. US Patent 6,191,524
- Schmidt VH (1992) Piezoelectric energy conversion in windmills. In: *Ultrasonics Symposium, 1992, Proceedings, IEEE*, pp 897–904
- Tralli A, Olivier M, Sciacovelli D, Gaudenzi P (2005) Modelling of active space structures for vibration control. In: Fletcher K (ed) *Proceedings of the European Conference on Spacecraft Structures, Materials and Mechanical Testing 2005*, vol 581, pp 1–7
- Uchino K, Zhuang Y, URAL SO (2011) Loss determination methodology for a piezoelectric ceramic: new phenomenological theory and experimental proposals. *Journal of Advanced Dielectrics* 1(1):17–31
- Waqar S, Asad S, Ahmad S, Abbas CA, Elahi H (2017) Effect of drilling parameters on hole quality of Ti-6Al-4V titanium alloy in dry drilling. In: *Materials Science Forum*, vol 880, pp 33–36
- Xiao Z, Yang T, Dong Y, Wang X (2014) Energy harvester array using piezoelectric circular diaphragm for broadband vibration. *Applied Physics Letters* 104(22):223,904

## Chapter 4

# Hybrid-Mixed Solid-Shell Element for Stress Analysis of Laminated Piezoelectric Shells through Higher-Order Theories

Gennady M. Kulikov, Svetlana V. Plotnikova, and Erasmo Carrera

**Abstract** A geometrically exact hybrid-mixed four-node piezoelectric solid-shell element by using the sampling surfaces (SaS) method is developed. The SaS formulation is based on choosing inside the layers the arbitrary number of SaS parallel to the middle surface and located at Chebyshev polynomial nodes in order to introduce the displacements and electric potentials of these surfaces as basic shell unknowns. The external surfaces and interfaces are also included into a set of SaS because of the variational formulation. Such a choice of unknowns with the consequent use of Lagrange polynomials in the through-thickness approximations of displacements, strains, electric potential and electric field leads to a very compact piezoelectric shell element formulation. To implement the efficient analytical integration throughout the element, the enhanced assumed natural strain (ANS) method is employed. The proposed hybrid-mixed four-node piezoelectric shell element is based on the Hu-Washizu variational equation and exhibits a superior performance in the case of coarse meshes. It could be useful for the three-dimensional (3D) stress analysis of thick and thin doubly-curved laminated piezoelectric shells since the SaS formulation gives the possibility to obtain the numerical solutions with a prescribed accuracy, which asymptotically approach the exact solutions of piezoelectricity as the number of SaS tends to infinity.

---

Gennady M. Kulikov · Svetlana V. Plotnikova  
Laboratory of Intelligent Materials and Structures, Tambov State Technical University, Sovetskaya Street, 106, Tambov 392000, Russia  
e-mail: [gmkulikov@mail.ru](mailto:gmkulikov@mail.ru)

Erasmo Carrera  
Department of Mechanical and Aerospace Engineering, Politecnico di Torino, Corso Duca degli Abruzzi 24, 10129, Turin, Italy  
e-mail: [erasmo.carrera@polito.it](mailto:erasmo.carrera@polito.it)

## 4.1 Introduction

A large number of works has been carried out on 3D continuum-based finite elements (Sze and Yao, 2000; Sze et al, 2000; Lee et al, 2003; Zheng et al, 2004; Klinkel and Wagner, 2006, 2008; Kulikov and Plotnikova, 2008; Lentzen, 2009) that can handle the analysis of thin laminated piezoelectric shells satisfactorily. These elements are typically defined by two layers of nodes at the bottom and top surfaces with three translational and one electric degrees of freedom (DOF) per node and known as 6-parameter piezoelectric solid-shell elements because of the total number of translational DOF. Unfortunately, the 6-parameter solid-shell element formulation based on the complete 3D constitutive equations of piezoelectricity is deficient because thickness locking occurs. This is due to the fact that the linear displacement field in the thickness direction results in a constant transverse normal strain, which in turn causes artificial stiffening of the shell element in the case of non-vanishing Poisson's ratios. To prevent thickness locking, the 3D constitutive equations have to be modified employing the generalized plane stress conditions (Lee et al, 2003; Kulikov and Plotnikova, 2008). The hybrid stress method (Sze and Yao, 2000; Sze et al, 2000) in which the transverse normal stress is constant through the shell thickness and the enhanced assumed strain method in which the transverse normal strain is enriched in the thickness direction by a linear term (Zheng et al, 2004; Klinkel and Wagner, 2006, 2008; Lentzen, 2009) can be also utilized.

An efficient way of using the complete 3D constitutive equations for the analysis of piezoelectric shells is to employ the first-order equivalent single layer (ESL) theory with seven translational DOF (Kulikov and Plotnikova, 2010, 2011a). The 7-parameter ESL shell model is based on choosing six displacements and two electric potentials of the bottom and top surfaces and a transverse displacement of the middle surface as basic shell unknowns. Such a model is optimal with respect to the number of DOF. The more general 9-parameter ESL shell model is based on considering the external and middle surfaces and choosing the displacements and electric potentials of these surfaces as shell unknowns (Kulikov and Plotnikova, 2011b, 2015). Such choice of unknowns with the consequent use of Lagrange polynomials of the second order in the through-thickness approximations of displacements, strains, electric potential and electric field leads to a robust piezoelectric shell formulation. Moreover, this approach allows the derivation of the objective strain-displacement equations, which exactly represent all rigid-body shell motions in any convected curvilinear coordinate system. Taking into account that the displacement vectors of reference surfaces are resolved in the middle surface frame, the higher-order shell formulation with nine DOF is very promising for developing the exact geometry or geometrically exact (GeX) piezoelectric solid-shell elements. The term GeX implies that the parametrization of the middle surface is known a priori and, therefore, the coefficients of the first and second fundamental forms are taken exactly at element nodes.

Note that the above solid-shell elements (Sze and Yao, 2000; Sze et al, 2000; Lee et al, 2003; Zheng et al, 2004; Klinkel and Wagner, 2006, 2008; Kulikov and Plotnikova, 2008; Lentzen, 2009; Kulikov and Plotnikova, 2010, 2011a,b, 2015) do not describe properly the transverse stresses in a laminated piezoelectric shell.

To calculate them a post-processing stress recovery technique has to be employed. However, to evaluate the distribution of transverse stresses through the thickness of the laminated piezoelectric shell, higher-order layer-wise (LW) models have to be utilized. Robust GeX nine-node piezoelectric shell elements with a variable number of DOF per node have been developed in contributions (Carrera et al, 2011, 2014; Cinefra et al, 2015; Carrera and Valvano, 2017) through Carrera's unified formulation (Carrera, 1999, 2003). The shear and membrane locking phenomena (Carrera et al, 2014; Cinefra et al, 2015; Carrera and Valvano, 2017) are prevented by using the MITC technique (Bathe and Dvorkin, 1986; Bathe et al, 2003). These finite elements exhibit an excellent performance and can be recommended for the 3D stress analysis of piezoelectric shells. At the same time, Cinefra et al (2015) report that the piezoelectric shell element based on the fourth-order LW theory does not provide the continuity of the transverse normal stress and electric displacement on interfaces especially in the case of thin shells.

The present paper is intended to overcome the aforementioned difficulties and develop a piezoelectric solid-shell element that makes it possible to evaluate all stress and electric displacement components effectively for thick and very thin shells. To solve such a problem, the GeX four-node solid-shell element using the sampling surface (SaS) method (Kulikov and Plotnikova, 2013) is proposed. The SaS formulation is based on choosing inside the  $n$ th layer  $I_n$  not equally spaced surfaces  $\Omega^{(n)1}, \Omega^{(n)2}, \dots, \Omega^{(n)I_n}$  parallel to the middle surface in order to introduce the displacements and electric potentials of these surfaces as basic shell variables, where  $I_n \geq 3$ . Such choice of unknowns with the consequent use of Lagrange polynomials of degree  $I_n - 1$  in the assumed distributions of displacements, strains, electric potential and electric field through the thickness yields a very compact piezoelectric shell formulation. Recently, the SaS formulation has been employed to analyze analytically the electroelastic and thermoelectroelastic stress fields in laminated and functionally graded shells (Kulikov and Plotnikova, 2014; Kulikov et al, 2015; Kulikov and Plotnikova, 2017). However, the piezoelectric shell elements via the SaS technique have not been developed yet.

The origin of the SaS concept can be traced back to contributions (Kulikov, 2001; Kulikov and Carrera, 2008) in which three, four and five equally spaced SaS are utilized. The SaS formulation with an arbitrary number of equispaced SaS is considered in (Kulikov and Plotnikova, 2011d). The more general approach with the SaS located at Chebyshev polynomial nodes (roots of the Chebyshev polynomial) (Bakhvalov, 1977) was developed later (Kulikov and Plotnikova, 2013, 2014) because the SaS formulation with equispaced SaS does not work properly with the higher-order Lagrange interpolation. The use of the Chebyshev polynomial nodes improves significantly the behavior of the higher-degree Lagrange polynomials since such choice makes possible to minimize uniformly the error due to the Lagrange interpolation. This fact gives an opportunity to calculate the displacements and stresses with a prescribed accuracy employing the sufficiently large number of SaS. Thus, the solutions based on the SaS concept can asymptotically approach the 3D exact solutions of piezoelectricity as the number of SaS tends to infinity.



Here, the GeX hybrid-mixed four-node piezoelectric solid-shell element formulation is developed with the SaS located inside the layers at Chebyshev polynomial nodes (Kulikov and Plotnikova, 2013). To circumvent shear and membrane locking, the assumed interpolations of displacement-independent strains and stresses are utilized through the Hu-Washizu variational principle. Such an approach exhibits an excellent performance in the case of coarse mesh configurations and has computational advantages compared to conventional isoparametric hybrid-mixed piezoelectric solid-shell element formulations (Sze and Yao, 2000; Sze et al, 2000; Lee et al, 2003; Zheng et al, 2004; Klinkel and Wagner, 2006, 2008), because it reduces the computational cost of the numerical integration in the evaluation of the element stiffness matrix. This is due to the fact that all element matrices require only direct substitutions, i.e., no expensive numerical matrix inversion is needed. Second, the GeX four-node solid-shell element formulation is based on the effective analytical integration throughout the finite element by using the enhanced ANS method (Kulikov and Plotnikova, 2015, 2011c). The latter has a great meaning for the numerical modeling of doubly-curved shells with variable curvatures.

## 4.2 Sampling Surface Shell Formulation

Consider a laminated shell of the thickness  $h$ . Let the middle surface  $\Omega$  be described by orthogonal curvilinear coordinates  $\theta_1$  and  $\theta_2$ , which refer to the lines of principal curvatures of its surface. The coordinate  $\theta_3$  is oriented along the unit vector  $\mathbf{e}_3(\theta_1, \theta_2)$  normal to the middle surface. We introduce the following notations:  $\mathbf{e}_\alpha(\theta_1, \theta_2)$  are the orthonormal base vectors of the middle surface;  $A_\alpha(\theta_1, \theta_2)$  are the coefficients of the first fundamental form;  $k_\alpha(\theta_1, \theta_2)$  are the principal curvatures of the middle surface;  $c_\alpha = 1 + k_\alpha\theta_3$  are the components of the shifter tensor;  $c_\alpha^{(n)i_n}(\theta_1, \theta_2)$  are the components of the shifter tensor at SaS defined as

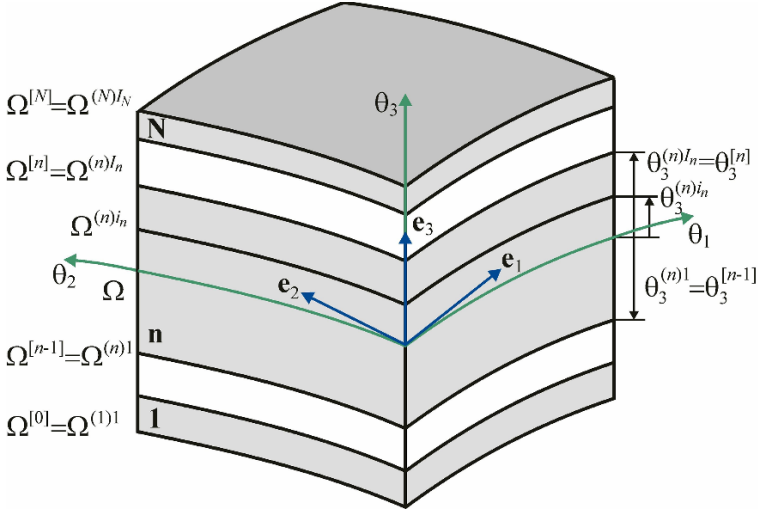
$$c_\alpha^{(n)i_n} = c_\alpha(\theta_3^{(n)i_n}) = 1 + k_\alpha\theta_3^{(n)i_n}, \quad (4.1)$$

where  $\theta_3^{(n)i_n}$  are the transverse coordinates of the SaS inside the  $n$ th layer given by

$$\theta_3^{(n)1} = \theta_3^{[n-1]}, \quad \theta_3^{(n)I_n} = \theta_3^{[n]}, \quad (4.2)$$

$$\theta_3^{(n)m_n} = \frac{1}{2}(\theta_3^{[n-1]} + \theta_3^{[n]}) - \frac{1}{2}h_n \cos\left(\pi \frac{2m_n - 3}{2(I_n - 2)}\right), \quad (4.3)$$

in which  $\theta_3^{[n-1]}$  and  $\theta_3^{[n]}$  are the transverse coordinates of interfaces  $\Omega^{[n-1]}$  and  $\Omega^{[n]}$  depicted in Fig. 4.1;  $h_n = \theta_3^{[n]} - \theta_3^{[n-1]}$  is the thickness of the  $n$ th layer. Here and in the following derivations, the index  $n$  identifies the correspondence of any quantity to the  $n$ th layer and runs from 1 to  $N$ , where  $N$  is the number of layers;  $N_{\text{SaS}} = \sum_n I_n - N + 1$  is the total number of SaS; the indices  $i_n$  and introduced later  $j_n, k_n$  identify the correspondence of any quantity to the SaS of the  $n$ th layer and run from 1 to  $I_n$ ; the



**Fig. 4.1:** Geometry of the laminated shell

index  $m_n$  identifies the belonging of any quantity to the inner SaS of the  $n$ th layer and runs from 2 to  $I_n - 1$ ; Latin indices  $i, j, k, l$  range from 1 to 3; Greek indices  $\alpha, \beta$  range from 1 to 2.

*Remark 4.1.* It is seen from Eq. (4.3) that the transverse coordinates of inner SaS  $\theta_3^{(n)I_n}$  coincide with the coordinates of Chebyshev polynomial nodes. This fact has a great meaning for the convergence of the SaS method.

The through-thickness SaS approximations (Kulikov and Plotnikova, 2013) can be written as

$$\left[ u_i^{(n)} \quad \varepsilon_{ij}^{(n)} \quad \sigma_{ij}^{(n)} \quad \varphi^{(n)} \quad E_i^{(n)} \right] = \sum_{i_n} L^{(n)i_n} \left[ u_i^{(n)i_n} \quad \varepsilon_{ij}^{(n)i_n} \quad \sigma_{ij}^{(n)i_n} \quad \varphi^{(n)i_n} \quad E_i^{(n)i_n} \right], \quad (4.4)$$

where  $u_i^{(n)}$ ,  $\varepsilon_{ij}^{(n)}$ ,  $\sigma_{ij}^{(n)}$ ,  $\varphi^{(n)}$ ,  $E_i^{(n)}$  are the displacements, strains, stresses, electric potential and electric field of the  $n$ th layer;  $u_i^{(n)i_n}(\theta_1, \theta_2)$ ,  $\varepsilon_{ij}^{(n)i_n}(\theta_1, \theta_2)$ ,  $\sigma_{ij}^{(n)i_n}(\theta_1, \theta_2)$ ,  $\varphi^{(n)i_n}(\theta_1, \theta_2)$  and  $E_i^{(n)i_n}(\theta_1, \theta_2)$  are the displacements, strains, electric potential and electric field of SaS of the  $n$ th layer  $\Omega^{(n)i_n}$ ;  $L^{(n)i_n}(\theta_3)$  are the Lagrange basis polynomials of degree  $I_n - 1$  related to the  $n$ th layer:

$$L^{(n)i_n} = \prod_{j_n \neq i_n} \frac{\theta_3 - \theta_3^{(n)j_n}}{\theta_3^{(n)i_n} - \theta_3^{(n)j_n}}. \quad (4.5)$$

In the orthonormal basis  $\mathbf{e}_i$ , the relations between strains and displacements of SaS of the  $n$ th layer are written as

$$2\varepsilon_{\alpha\beta}^{(n)i_n} = \frac{1}{c_\beta^{(n)i_n}} \lambda_{\alpha\beta}^{(n)i_n} + \frac{1}{c_\alpha^{(n)i_n}} \lambda_{\beta\alpha}^{(n)i_n},$$

$$2\varepsilon_{\alpha 3}^{(n)i_n} = \frac{1}{c_\alpha^{(n)i_n}} \lambda_{3\alpha}^{(n)i_n} + \beta_\alpha^{(n)i_n}, \quad \varepsilon_{33}^{(n)i_n} = \beta_3^{(n)i_n}, \quad (4.6)$$

where  $\lambda_{i\alpha}^{(n)i_n}(\theta_1, \theta_2)$  are the strain parameters of SaS of the  $n$ th layer;  $\beta_i^{(n)i_n}(\theta_1, \theta_2)$  are the values of the derivative of displacements with respect to thickness coordinate on SaS:

$$\lambda_{\alpha\alpha}^{(n)i_n} = \frac{1}{A_\alpha} u_{\alpha,\alpha}^{(n)i_n} + B_\alpha u_\beta^{(n)i_n} + k_\alpha u_3^{(n)i_n} \quad \text{for } \beta \neq \alpha,$$

$$\lambda_{\beta\alpha}^{(n)i_n} = \frac{1}{A_\alpha} u_{\beta,\alpha}^{(n)i_n} - B_\alpha u_\alpha^{(n)i_n} \quad \text{for } \beta \neq \alpha,$$

$$\lambda_{3\alpha}^{(n)i_n} = \frac{1}{A_\alpha} u_{3,\alpha}^{(n)i_n} - k_\alpha u_\alpha^{(n)i_n}, \quad B_\alpha = \frac{1}{A_\alpha A_\beta} A_{\alpha\beta} \quad \text{for } \beta \neq \alpha, \quad (4.7)$$

$$\beta \quad (4.8)$$

where the symbol  $(\dots)_i$  stands for the partial derivatives with respect to coordinates  $\theta_i$ ;  $M^{(n)j_n} = L_{,3}^{(n)j_n}$  are the derivatives of Lagrange basis polynomials, which are calculated at the SaS as follows:

$$M^{(n)j_n}(\theta_3^{(n)i_n}) = \frac{1}{\theta_3^{(n)j_n} - \theta_3^{(n)i_n}} \prod_{k_n \neq i_n, j_n} \frac{\theta_3^{(n)i_n} - \theta_3^{(n)k_n}}{\theta_3^{(n)j_n} - \theta_3^{(n)k_n}} \quad \text{for } j_n \neq i_n,$$

$$M^{(n)i_n}(\theta_3^{(n)i_n}) = - \sum_{j_n \neq i_n} M^{(n)j_n}(\theta_3^{(n)i_n}). \quad (4.9)$$

In the orthonormal basis  $\mathbf{e}_i$ , the relations between the electric field and electric potentials of the SaS of the  $n$ th layer (Kulikov and Plotnikova, 2013) are expressed as

$$E_\alpha^{(n)i_n} = - \frac{1}{A_\alpha c_\alpha^{(n)i_n}} \varphi_{,\alpha}^{(n)i_n},$$

$$E_3^{(n)i_n} = - \sum_{j_n} M^{(n)j_n}(\theta_3^{(n)i_n}) \varphi^{(n)j_n}. \quad (4.10)$$

### 4.3 Hu-Washizu Variational Equation

The proposed hybrid-mixed piezoelectric solid-shell element is based on the modified Hu-Washizu variational equation of piezoelectricity in which displacements, strains, stresses and electric potential are utilized as independent variables (Kulikov and Plotnikova, 2015):

$$\delta J = 0, \quad (4.11)$$

$$J = \iint_{\Omega} \sum_n \int_{\theta_3^{[n-1]}}^{\theta_3^{[n]}} \left[ \frac{1}{2} \eta_{ij}^{(n)} C_{ijkl}^{(n)} \eta_{kl}^{(n)} - E_k^{(n)} e_{kij}^{(n)} \eta_{ij}^{(n)} - \frac{1}{2} E_i^{(n)} \epsilon_{ij}^{(n)} E_j^{(n)} - \sigma_{ij}^{(n)} (\eta_{ij}^{(n)} - \epsilon_{ij}^{(n)}) \right] dV - W, \quad (4.12)$$

where  $dV = A_1 A_2 c_1 c_2 d\theta_1 d\theta_2 d\theta_3$  is the infinitesimal volume element;  $\epsilon_{ij}^{(n)}$  and  $\eta_{ij}^{(n)}$  are the displacement-dependent and displacement-independent strains of the  $n$ th layer;  $C_{ijkl}^{(n)}$ ,  $e_{kij}^{(n)}$  and  $\epsilon_{ij}^{(n)}$  are the elastic, piezoelectric and dielectric constants of the  $n$ th layer;  $W$  is the work done by external electromechanical loads. As usual, the summation on repeated Latin indices is implied.

Following the SaS technique (4.4), we introduce the next assumption of the hybrid-mixed solid-shell element formulation. Assume that the displacement-independent strains are distributed through the thickness of the  $n$ th layer by

$$\eta_{ij}^{(n)} = \sum_{i_n} L^{(n)i_n} \eta_{ij}^{(n)i_n}, \quad (4.13)$$

where  $\eta_{ij}^{(n)i_n}(\theta_1, \theta_2)$  are the displacement-independent strains of SaS of the  $n$ th layer.

Substituting the through-thickness distributions (4.4) and (4.13) in Eq. (4.12) and introducing

$$\Lambda^{(n)i_n j_n} = \int_{\theta_3^{[n-1]}}^{\theta_3^{[n]}} L^{(n)i_n} L^{(n)j_n} c_1 c_2 d\theta_3, \quad (4.14)$$

one can write the Hu-Washizu mixed functional in terms of SaS variables as

$$J = \iint_{\Omega} \sum_n \sum_{i_n} \sum_{j_n} \Lambda^{(n)i_n j_n} \left[ \frac{1}{2} (\eta^{(n)i_n})^T \mathbf{C}^{(n)} \boldsymbol{\eta}^{(n)j_n} - (\mathbf{E}^{(n)i_n})^T \mathbf{e}^{(n)} \boldsymbol{\eta}^{(n)j_n} - \frac{1}{2} (\mathbf{E}^{(n)i_n})^T \boldsymbol{\epsilon}^{(n)} \mathbf{E}^{(n)j_n} - (\boldsymbol{\sigma}^{(n)i_n})^T (\boldsymbol{\eta}^{(n)j_n} - \boldsymbol{\epsilon}^{(n)j_n}) \right] A_1 A_2 d\theta_1 d\theta_2 - W, \quad (4.15)$$

where

$$\begin{aligned} \boldsymbol{\epsilon}^{(n)i_n} &= \left[ \epsilon_{11}^{(n)i_n} \quad \epsilon_{22}^{(n)i_n} \quad \epsilon_{33}^{(n)i_n} \quad 2\epsilon_{12}^{(n)i_n} \quad 2\epsilon_{13}^{(n)i_n} \quad 2\epsilon_{23}^{(n)i_n} \right]^T, \\ \boldsymbol{\eta}^{(n)i_n} &= \left[ \eta_{11}^{(n)i_n} \quad \eta_{22}^{(n)i_n} \quad \eta_{33}^{(n)i_n} \quad 2\eta_{12}^{(n)i_n} \quad 2\eta_{13}^{(n)i_n} \quad 2\eta_{23}^{(n)i_n} \right]^T, \\ \boldsymbol{\sigma}^{(n)i_n} &= \left[ \sigma_{11}^{(n)i_n} \quad \sigma_{22}^{(n)i_n} \quad \sigma_{33}^{(n)i_n} \quad \sigma_{12}^{(n)i_n} \quad \sigma_{13}^{(n)i_n} \quad \sigma_{23}^{(n)i_n} \right]^T, \\ \mathbf{E}^{(n)i_n} &= \left[ E_1^{(n)i_n} \quad E_2^{(n)i_n} \quad E_3^{(n)i_n} \right]^T, \end{aligned}$$

$$\begin{aligned}
\mathbf{C}^{(n)} &= \begin{bmatrix} C_{1111}^{(n)} & C_{1122}^{(n)} & C_{1133}^{(n)} & C_{1112}^{(n)} & 0 & 0 \\ C_{2211}^{(n)} & C_{2222}^{(n)} & C_{2233}^{(n)} & C_{2212}^{(n)} & 0 & 0 \\ C_{3311}^{(n)} & C_{3322}^{(n)} & C_{3333}^{(n)} & C_{3312}^{(n)} & 0 & 0 \\ C_{1211}^{(n)} & C_{1222}^{(n)} & C_{1233}^{(n)} & C_{1212}^{(n)} & 0 & 0 \\ 0 & 0 & 0 & 0 & C_{1313}^{(n)} & C_{1323}^{(n)} \\ 0 & 0 & 0 & 0 & C_{2313}^{(n)} & C_{2323}^{(n)} \end{bmatrix}, \\
\mathbf{e}^{(n)} &= \begin{bmatrix} 0 & 0 & 0 & 0 & e_{113}^{(n)} & e_{123}^{(n)} \\ 0 & 0 & 0 & 0 & e_{213}^{(n)} & e_{223}^{(n)} \\ e_{311}^{(n)} & e_{322}^{(n)} & e_{333}^{(n)} & e_{312}^{(n)} & 0 & 0 \end{bmatrix}, \\
\boldsymbol{\epsilon}^{(n)} &= \begin{bmatrix} \epsilon_{11}^{(n)} & \epsilon_{12}^{(n)} & 0 \\ \epsilon_{21}^{(n)} & \epsilon_{22}^{(n)} & 0 \\ 0 & 0 & \epsilon_{33}^{(n)} \end{bmatrix}. \tag{4.16}
\end{aligned}$$

#### 4.4 Hybrid-Mixed Solid-Shell Element Formulation

The finite element formulation is based on a simple interpolation of the shell via GeX four-node piezoelectric solid-shell elements

$$u_i^{(n)i_n} = \sum_r N_r u_{ir}^{(n)i_n}, \quad \varphi^{(n)i_n} = \sum_r N_r \varphi_r^{(n)i_n}, \tag{4.17}$$

where  $N_r(\xi_1, \xi_2)$  are the bilinear shape functions of the element;  $u_{ir}^{(n)i_n}$  and  $\varphi_r^{(n)i_n}$  are the displacements and electric potentials of SaS  $\mathcal{Q}^{(n)i_n}$  at element nodes;  $\xi_1, \xi_2$  are the normalized curvilinear coordinates  $\theta_1, \theta_2$  (Fig. 4.2); the nodal index  $r$  runs from 1 to 4.

To implement the efficient analytical integration throughout the finite element, the enhanced ANS method (Kulikov and Plotnikova, 2011c) is adopted

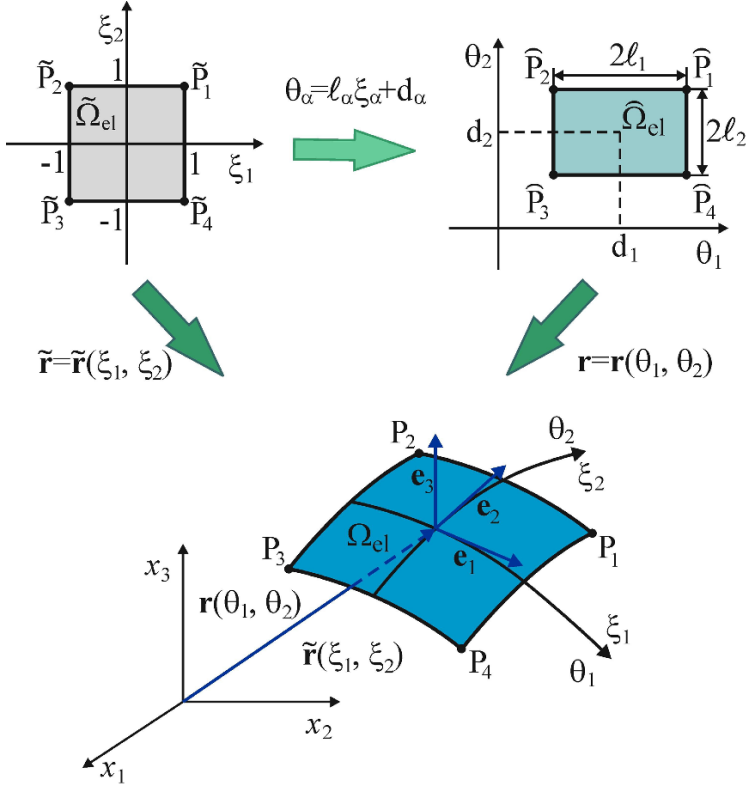
$$\boldsymbol{\epsilon}^{(n)i_n} = \sum_r N_r \boldsymbol{\epsilon}_r^{(n)i_n}, \tag{4.18}$$

$$\boldsymbol{\epsilon}_r^{(n)i_n} = [\boldsymbol{\epsilon}_{11r}^{(n)i_n} \ \boldsymbol{\epsilon}_{22r}^{(n)i_n} \ \boldsymbol{\epsilon}_{33r}^{(n)i_n} \ 2\boldsymbol{\epsilon}_{12r}^{(n)i_n} \ 2\boldsymbol{\epsilon}_{13r}^{(n)i_n} \ 2\boldsymbol{\epsilon}_{23r}^{(n)i_n}]^T,$$

$$\mathbf{E}^{(n)i_n} = \sum_r N_r \mathbf{E}_r^{(n)i_n}, \tag{4.19}$$

$$\mathbf{E}_r^{(n)i_n} = [E_{1r}^{(n)i_n} \ E_{2r}^{(n)i_n} \ E_{3r}^{(n)i_n}]^T,$$

where  $\boldsymbol{\epsilon}_{ijr}^{(n)i_n}$  and  $E_{ir}^{(n)i_n}$  are the strains and electric field of SaS of the  $n$ th layer at element nodes.



**Fig. 4.2:** Biunit square in  $(\xi_1, \xi_2)$ -space mapped into the middle surface of the GeX four-node solid-shell element in  $(x_1, x_2, x_3)$ -space

*Remark 4.2.* The main idea of such approach can be traced back to the ANS method developed by many scientists for the isoparametric finite element formulation (Bathe and Dvorkin, 1986; Hughes and Tezduyar, 1981; Macneal, 1982; Park and Stanley, 1986; Ko et al, 2017; Betsch and Stein, 1995). In contrast with above formulation, we treat the term ANS in a broader sense. In the proposed GeX four-node solid-shell element formulation, all components of the displacement-dependent strain tensor and electric field are assumed to vary bilinearly throughout the biunit square in  $(\xi_1, \xi_2)$ -space. This implies that instead of the expected *non-linear* interpolations due to Eqs. (4.6), (4.7) and (4.10) the more suitable *bilinear* interpolations (4.18) and (4.19) are utilized.

The strain vectors of the SaS at element nodes can be expressed as

$$\boldsymbol{\varepsilon}_r^{(n)i_n} = \mathbf{B}_{ur}^{(n)i_n} \mathbf{U}, \quad (4.20)$$

where  $\mathbf{B}_{u_r}^{(n)i_n}$  are the constant inside the finite element matrices of order  $6 \times 12N_{\text{SaS}}$ ;  $\mathbf{U}$  is the element displacement vector given by

$$\begin{aligned} \mathbf{U} &= [\mathbf{U}_1^T \mathbf{U}_2^T \mathbf{U}_3^T \mathbf{U}_4^T]^T, \\ \mathbf{U}_r &= \left[ (\mathbf{u}_r^{[0]})^T (\mathbf{u}_r^{(1)2})^T \dots (\mathbf{u}_r^{(1)I_1-1})^T (\mathbf{u}_r^{[1]})^T (\mathbf{u}_r^{(2)2})^T \right. \\ &\quad \left. \dots (\mathbf{u}_r^{(N-1)I_{N-1}-1})^T (\mathbf{u}_r^{[N-1]})^T (\mathbf{u}_r^{(N)2})^T \dots (\mathbf{u}_r^{(N)I_N-1})^T (\mathbf{u}_r^{[N]})^T \right]^T, \\ \mathbf{u}_r^{[m]} &= [u_{1r}^{[m]} u_{2r}^{[m]} u_{3r}^{[m]}]^T, \quad \mathbf{u}_r^{(n)m_n} = [u_{1r}^{(n)m_n} u_{2r}^{(n)m_n} u_{3r}^{(n)m_n}]^T, \end{aligned} \quad (4.21)$$

where  $u_{ir}^{[m]}$  are the displacements of external surfaces and interfaces at element nodes ( $m = 0, 1, \dots, N$ ).

The electric field vectors of SaS at element nodes are

$$\mathbf{E}_r^{(n)i_n} = -\mathbf{B}_{\varphi_r}^{(n)i_n} \boldsymbol{\Phi}, \quad (4.22)$$

where  $\mathbf{B}_{\varphi_r}^{(n)i_n}$  are the constant inside the finite element matrices of order  $3 \times 4N_{\text{SaS}}$ ;  $\boldsymbol{\Phi}$  is the element electric field vector defined as

$$\begin{aligned} \boldsymbol{\Phi} &= [\boldsymbol{\Phi}_1^T \boldsymbol{\Phi}_2^T \boldsymbol{\Phi}_3^T \boldsymbol{\Phi}_4^T]^T, \\ \boldsymbol{\Phi}_r &= [\varphi_r^{[0]} \varphi_r^{(1)2} \dots \varphi_r^{(1)I_1-1} \varphi_r^{[1]} \varphi_r^{(2)2} \\ &\quad \dots \varphi_r^{(N-1)I_{N-1}-1} \varphi_r^{[N-1]} \varphi_r^{(N)2} \dots \varphi_r^{(N)I_N-1} \varphi_r^{[N]}]^T, \end{aligned} \quad (4.23)$$

where  $\varphi_r^{[m]}$  are the electric potentials of external surfaces and interfaces at element nodes.

From a computational point of view, it is convenient to write the ANS interpolation (4.18) in the following form:

$$\boldsymbol{\varepsilon}^{(n)i_n} = \sum_{r_1, r_2} (\xi_1)^{r_1} (\xi_2)^{r_2} \boldsymbol{\varepsilon}_{r_1 r_2}^{(n)i_n}, \quad \boldsymbol{\varepsilon}_{r_1 r_2}^{(n)i_n} = \mathbf{B}_{ur_1 r_2}^{(n)i_n} \mathbf{U}, \quad (4.24)$$

where

$$\begin{aligned} \boldsymbol{\varepsilon}_{r_1 r_2}^{(n)i_n} &= [\boldsymbol{\varepsilon}_{11r_1 r_2}^{(n)i_n} \boldsymbol{\varepsilon}_{22r_1 r_2}^{(n)i_n} \boldsymbol{\varepsilon}_{33r_1 r_2}^{(n)i_n} 2\boldsymbol{\varepsilon}_{12r_1 r_2}^{(n)i_n} 2\boldsymbol{\varepsilon}_{13r_1 r_2}^{(n)i_n} 2\boldsymbol{\varepsilon}_{23r_1 r_2}^{(n)i_n}]^T, \\ \mathbf{B}_{u00}^{(n)i_n} &= \frac{1}{4} (\mathbf{B}_{u1}^{(n)i_n} + \mathbf{B}_{u2}^{(n)i_n} + \mathbf{B}_{u3}^{(n)i_n} + \mathbf{B}_{u4}^{(n)i_n}), \\ \mathbf{B}_{u01}^{(n)i_n} &= \frac{1}{4} (\mathbf{B}_{u1}^{(n)i_n} + \mathbf{B}_{u2}^{(n)i_n} - \mathbf{B}_{u3}^{(n)i_n} - \mathbf{B}_{u4}^{(n)i_n}), \\ \mathbf{B}_{u10}^{(n)i_n} &= \frac{1}{4} (\mathbf{B}_{u1}^{(n)i_n} - \mathbf{B}_{u2}^{(n)i_n} - \mathbf{B}_{u3}^{(n)i_n} + \mathbf{B}_{u4}^{(n)i_n}), \end{aligned}$$

$$\mathbf{B}_{u11}^{(n)i_n} = \frac{1}{4} \left( \mathbf{B}_{u1}^{(n)i_n} - \mathbf{B}_{u2}^{(n)i_n} + \mathbf{B}_{u3}^{(n)i_n} - \mathbf{B}_{u4}^{(n)i_n} \right). \quad (4.25)$$

Here, and below the indices  $r_1$  and  $r_2$  run from 0 to 1. The same concerns the ANS interpolation (4.19), that is,

$$\mathbf{E}^{(n)i_n} = \sum_{r_1, r_2} (\xi_1)^{r_1} (\xi_2)^{r_2} \mathbf{E}_{r_1 r_2}^{(n)i_n}, \quad \text{with} \quad \mathbf{E}_{r_1 r_2}^{(n)i_n} = -\mathbf{B}_{\varphi r_1 r_2}^{(n)i_n} \boldsymbol{\Phi}, \quad (4.26)$$

where

$$\begin{aligned} \mathbf{E}_{r_1 r_2}^{(n)i_n} &= \left[ E_{1r_1 r_2}^{(n)i_n} \ E_{2r_1 r_2}^{(n)i_n} \ E_{3r_1 r_2}^{(n)i_n} \right]^T, \\ \mathbf{B}_{\varphi 00}^{(n)i_n} &= \frac{1}{4} \left( \mathbf{B}_{\varphi 1}^{(n)i_n} + \mathbf{B}_{\varphi 2}^{(n)i_n} + \mathbf{B}_{\varphi 3}^{(n)i_n} + \mathbf{B}_{\varphi 4}^{(n)i_n} \right), \\ \mathbf{B}_{\varphi 01}^{(n)i_n} &= \frac{1}{4} \left( \mathbf{B}_{\varphi 1}^{(n)i_n} + \mathbf{B}_{\varphi 2}^{(n)i_n} - \mathbf{B}_{\varphi 3}^{(n)i_n} - \mathbf{B}_{\varphi 4}^{(n)i_n} \right), \\ \mathbf{B}_{\varphi 10}^{(n)i_n} &= \frac{1}{4} \left( \mathbf{B}_{\varphi 1}^{(n)i_n} - \mathbf{B}_{\varphi 2}^{(n)i_n} - \mathbf{B}_{\varphi 3}^{(n)i_n} + \mathbf{B}_{\varphi 4}^{(n)i_n} \right), \\ \mathbf{B}_{\varphi 11}^{(n)i_n} &= \frac{1}{4} \left( \mathbf{B}_{\varphi 1}^{(n)i_n} - \mathbf{B}_{\varphi 2}^{(n)i_n} + \mathbf{B}_{\varphi 3}^{(n)i_n} - \mathbf{B}_{\varphi 4}^{(n)i_n} \right). \end{aligned} \quad (4.27)$$

To overcome shear and membrane locking and introduce no spurious zero energy modes, the robust displacement-independent strain and stress interpolations are utilized:

$$\boldsymbol{\eta}^{(n)i_n} = \sum_{r_1+r_2 < 2} (\xi_1)^{r_1} (\xi_2)^{r_2} \mathbf{Q}_{r_1 r_2} \boldsymbol{\eta}_{r_1 r_2}^{(n)i_n}, \quad (4.28)$$

$$\begin{aligned} \boldsymbol{\eta}_{00}^{(n)i_n} &= \left[ \psi_1^{(n)i_n} \ \psi_2^{(n)i_n} \ \psi_3^{(n)i_n} \ \psi_4^{(n)i_n} \ \psi_5^{(n)i_n} \ \psi_6^{(n)i_n} \right]^T, \\ \boldsymbol{\eta}_{01}^{(n)i_n} &= \left[ \psi_7^{(n)i_n} \ \psi_9^{(n)i_n} \ \psi_{11}^{(n)i_n} \right]^T, \quad \boldsymbol{\eta}_{10}^{(n)i_n} = \left[ \psi_8^{(n)i_n} \ \psi_{10}^{(n)i_n} \ \psi_{12}^{(n)i_n} \right]^T, \end{aligned}$$

$$\boldsymbol{\sigma}^{(n)i_n} = \sum_{r_1+r_2 < 2} (\xi_1)^{r_1} (\xi_2)^{r_2} \mathbf{Q}_{r_1 r_2} \boldsymbol{\sigma}_{r_1 r_2}^{(n)i_n}, \quad (4.29)$$

$$\begin{aligned} \boldsymbol{\sigma}_{00}^{(n)i_n} &= \left[ \mu_1^{(n)i_n} \ \mu_2^{(n)i_n} \ \mu_3^{(n)i_n} \ \mu_4^{(n)i_n} \ \mu_5^{(n)i_n} \ \mu_6^{(n)i_n} \right]^T, \\ \boldsymbol{\sigma}_{01}^{(n)i_n} &= \left[ \mu_7^{(n)i_n} \ \mu_9^{(n)i_n} \ \mu_{11}^{(n)i_n} \right]^T, \quad \boldsymbol{\sigma}_{10}^{(n)i_n} = \left[ \mu_8^{(n)i_n} \ \mu_{10}^{(n)i_n} \ \mu_{12}^{(n)i_n} \right]^T, \end{aligned}$$

where  $\mathbf{Q}_{r_1 r_2}$  are the projective matrices given by

$$\mathbf{Q}_{00} = \begin{bmatrix} 1 & 0 & 0 & 0 & 0 & 0 \\ 0 & 1 & 0 & 0 & 0 & 0 \\ 0 & 0 & 1 & 0 & 0 & 0 \\ 0 & 0 & 0 & 1 & 0 & 0 \\ 0 & 0 & 0 & 0 & 1 & 0 \\ 0 & 0 & 0 & 0 & 0 & 1 \end{bmatrix}, \quad \mathbf{Q}_{01} = \begin{bmatrix} 1 & 0 & 0 \\ 0 & 0 & 0 \\ 0 & 1 & 0 \\ 0 & 0 & 0 \\ 0 & 0 & 1 \\ 0 & 0 & 0 \end{bmatrix}, \quad \mathbf{Q}_{10} = \begin{bmatrix} 0 & 0 & 0 \\ 1 & 0 & 0 \\ 0 & 1 & 0 \\ 0 & 0 & 0 \\ 0 & 0 & 0 \\ 0 & 0 & 1 \end{bmatrix}. \quad (4.30)$$



*Remark 4.3.* The assumed interpolations (4.28) and (4.29) provide a correct rank of the element stiffness matrix.

Substituting interpolations (4.17), (4.24), (4.26), (4.28) and (4.29) in the Hu-Washizu variational equation (4.11) and (4.15), replacing the metric product  $A_1 A_2$  in surface integrals by its value at the element center and integrating analytically throughout the finite element, the following equilibrium equations of the GeX hybrid-mixed four-node solid-shell element are obtained:

$$\boldsymbol{\eta}_{r_1 r_2}^{(n) i_n} = \mathbf{Q}_{r_1 r_2}^T \mathbf{B}_{u r_1 r_2}^{(n) i_n} \mathbf{U} \text{ for } r_1 + r_2 < 2, \quad (4.31)$$

$$\boldsymbol{\sigma}_{r_1 r_2}^{(n) i_n} = \mathbf{Q}_{r_1 r_2}^T \left( \mathbf{C}^{(n)} \mathbf{Q}_{r_1 r_2} \boldsymbol{\eta}_{r_1 r_2}^{(n) i_n} + (\mathbf{e}^{(n)})^T \mathbf{B}_{\varphi r_1 r_2}^{(n) i_n} \boldsymbol{\Phi} \right) \text{ for } r_1 + r_2 < 2, \quad (4.32)$$

$$\sum_n \sum_{i_n} \sum_{j_n} \Lambda^{(n) i_n j_n} \sum_{r_1+r_2 < 2} \frac{1}{3^{r_1+r_2}} (\mathbf{B}_{u r_1 r_2}^{(n) i_n})^T \mathbf{Q}_{r_1 r_2} \boldsymbol{\sigma}_{r_1 r_2}^{(n) j_n} = \mathbf{F}_u, \quad (4.33)$$

$$\begin{aligned} \sum_n \sum_{i_n} \sum_{j_n} \Lambda^{(n) i_n j_n} \sum_{r_1+r_2 < 2} \frac{1}{3^{r_1+r_2}} (\mathbf{B}_{\varphi r_1 r_2}^{(n) i_n})^T (\mathbf{e}^{(n)} \mathbf{Q}_{r_1 r_2} \boldsymbol{\eta}_{r_1 r_2}^{(n) j_n} \\ - \boldsymbol{\epsilon}^{(n)} \mathbf{B}_{\varphi r_1 r_2}^{(n) j_n} \boldsymbol{\Phi}) = \mathbf{F}_\varphi, \end{aligned} \quad (4.34)$$

where  $\mathbf{F}_u$  and  $\mathbf{F}_\varphi$  are the element-wise mechanical and electric surface vectors.

Eliminating vectors  $\boldsymbol{\eta}_{r_1 r_2}^{(n) i_n}$  and  $\boldsymbol{\sigma}_{r_1 r_2}^{(n) i_n}$  from Eqs. (4.31)-(4.34), one arrives at the system of linear equations

$$\begin{bmatrix} \mathbf{K}_{uu} & \mathbf{K}_{u\varphi} \\ \mathbf{K}_{\varphi u} & \mathbf{K}_{\varphi\varphi} \end{bmatrix} \begin{bmatrix} \mathbf{U} \\ \boldsymbol{\Phi} \end{bmatrix} = \begin{bmatrix} \mathbf{F}_u \\ \mathbf{F}_\varphi \end{bmatrix}, \quad (4.35)$$

where  $\mathbf{K}_{uu}$ ,  $\mathbf{K}_{u\varphi}$ ,  $\mathbf{K}_{\varphi u} = \mathbf{K}_{u\varphi}^T$  and  $\mathbf{K}_{\varphi\varphi}$  are the mechanical, piezoelectric and dielectric stiffness matrices defined as

$$\begin{aligned} \mathbf{K}_{uu} &= \sum_n \sum_{i_n} \sum_{j_n} \Lambda^{(n) i_n j_n} \sum_{r_1+r_2 < 2} \frac{1}{3^{r_1+r_2}} (\mathbf{B}_{u r_1 r_2}^{(n) i_n})^T \mathbf{Q}_{r_1 r_2} \mathbf{Q}_{r_1 r_2}^T \mathbf{C}^{(n)} \mathbf{Q}_{r_1 r_2} \mathbf{Q}_{r_1 r_2}^T \mathbf{B}_{u r_1 r_2}^{(n) j_n}, \\ \mathbf{K}_{u\varphi} &= \sum_n \sum_{i_n} \sum_{j_n} \Lambda^{(n) i_n j_n} \sum_{r_1+r_2 < 2} \frac{1}{3^{r_1+r_2}} (\mathbf{B}_{u r_1 r_2}^{(n) i_n})^T \mathbf{Q}_{r_1 r_2} \mathbf{Q}_{r_1 r_2}^T (\mathbf{e}^{(n)})^T \mathbf{B}_{\varphi r_1 r_2}^{(n) j_n}, \\ \mathbf{K}_{\varphi\varphi} &= - \sum_n \sum_{i_n} \sum_{j_n} \Lambda^{(n) i_n j_n} \sum_{r_1+r_2 < 2} \frac{1}{3^{r_1+r_2}} (\mathbf{B}_{\varphi r_1 r_2}^{(n) i_n})^T \boldsymbol{\epsilon}^{(n)} \mathbf{B}_{\varphi r_1 r_2}^{(n) j_n}. \end{aligned} \quad (4.36)$$

*Remark 4.4.* It is worth noting that all stiffness matrices are evaluated without the expensive numerical matrix inversion that is impossible in available isoparametric hybrid-mixed finite element formulations.

## 4.5 Numerical Examples

The performance of the developed GeX four-node piezoelectric solid-shell element denoted by GeXPS4 element is evaluated with the help of several exact solutions of piezoelectricity extracted from the literature (Heyliger, 1997; Chen et al, 2001).

### 4.5.1 Three-Layer Piezoelectric Cylindrical Shell

Consider a simply supported three-layer cylindrical shell with equal ply thicknesses under the imposed transverse deformation on the top surface

$$u_3^+ = u_0 \sin \frac{\pi \theta_1}{L} \cos 2\theta_2, \quad (4.37)$$

where  $L$  is the length of the shell and  $u_0 = 10^{-8}$  m. The both outer layers are composed of PZT-4 with the material properties presented in Table 4.1 and Heyliger (1997). The middle layer is made of fictitious material (Heyliger, 1997) with elastic constants exactly half of PZT-4 and the piezoelectric and dielectric constants exactly double of those of PZT-4. The bottom and top surfaces are assumed to be electrically grounded and traction free.

Table 4.1: Elastic, piezoelectric and dielectric properties of materials\*

Material	PZT-4 (Heyliger, 1997)	PZT-4 (Dunn and Taya, 1994)	BaTiO <sub>3</sub> (Dunn and Taya, 1994)
$C_{1111}$ , GPa	139.0	139.0	150.0
$C_{2222}$ , GPa	139.0	139.0	150.0
$C_{3333}$ , GPa	115.0	115.0	146.0
$C_{1122}$ , GPa	77.8	77.8	66.0
$C_{1133}$ , GPa	74.3	74.3	66.0
$C_{2233}$ , GPa	74.3	74.3	66.0
$C_{1313}$ , GPa	25.6	25.6	44.0
$C_{2323}$ , GPa	25.6	25.6	44.0
$C_{1212}$ , GPa	30.6	30.6	42.0
$e_{311}$ , C/m <sup>2</sup>	-5.2	-5.2	-4.35
$e_{322}$ , C/m <sup>2</sup>	-5.2	-5.2	-4.35
$e_{333}$ , C/m <sup>2</sup>	15.08	15.1	17.5
$e_{113}$ , C/m <sup>2</sup>	12.72	12.7	11.4
$e_{223}$ , C/m <sup>2</sup>	12.72	12.7	11.4
$\epsilon_{11}/\epsilon_0$	1475	730	1115
$\epsilon_{22}/\epsilon_0$	1475	730	1115
$\epsilon_{33}/\epsilon_0$	1300	635	1260

\* Vacuum permittivity  $\epsilon_0=8.854$  pF/m

Due to symmetry of the problem, only one octant of the shell ( $L/2 \leq \theta_1 \leq L$ ,  $0 \leq \theta_2 \leq \pi/2$ ) is modeled by a regular mesh consisting of  $48 \times 96$  GeXPS4 elements. To compare the results with the exact solution of Heyliger (1997), we take  $L = R^+ = 0.01$  m and introduce the scaled variables as functions of the dimensionless thickness coordinate as follows:

$$\begin{aligned}
\bar{u}_1 &= 10^{11} \times u_1(L, 0, z), \quad \bar{u}_3 = 10^{11} \times u_3(L/2, 0, z), \\
\bar{\sigma}_{11} &= 10^{-3} \times \sigma_{11}(L/2, 0, z), \quad \bar{\sigma}_{22} = 10^{-3} \times \sigma_{22}(L/2, 0, z), \\
\bar{\sigma}_{13} &= 10^{-3} \times \sigma_{13}(L, 0, z), \quad \bar{\sigma}_{23} = 10^{-3} \times \sigma_{23}(L/2, \pi/4, z), \\
\bar{\sigma}_{33} &= 10^{-3} \times \sigma_{33}(L/2, 0, z), \\
\bar{\varphi} &= \varphi(L/2, 0, z), \quad \bar{D}_3 = 10^6 \times D_3(L/2, 0, z), \quad z = \theta_3/h,
\end{aligned} \tag{4.38}$$

where  $R^+$  is the radius of the top cylindrical surface.

Tables 4.2 and 4.3 list the results of the convergence study due to increasing the number of SaS  $I_n$  inside each layer for two values of the slenderness ratio  $S = R^+/h$ . A comparison with the exact SaS solution (Kulikov and Plotnikova, 2013) is also given. Fig. 4.3 shows the distributions of displacements, transverse stresses, electric potential and electric displacement through the thickness for different slenderness ratios by taking five SaS for each layer. These results demonstrate convincingly the high potential of the proposed GeX hybrid-mixed solid-shell element formulation. This is due to the facts that the boundary conditions on external surfaces for the transverse stresses and the continuity conditions on interfaces for the transverse stresses and electric displacement are satisfied for thick and thin shells properly.

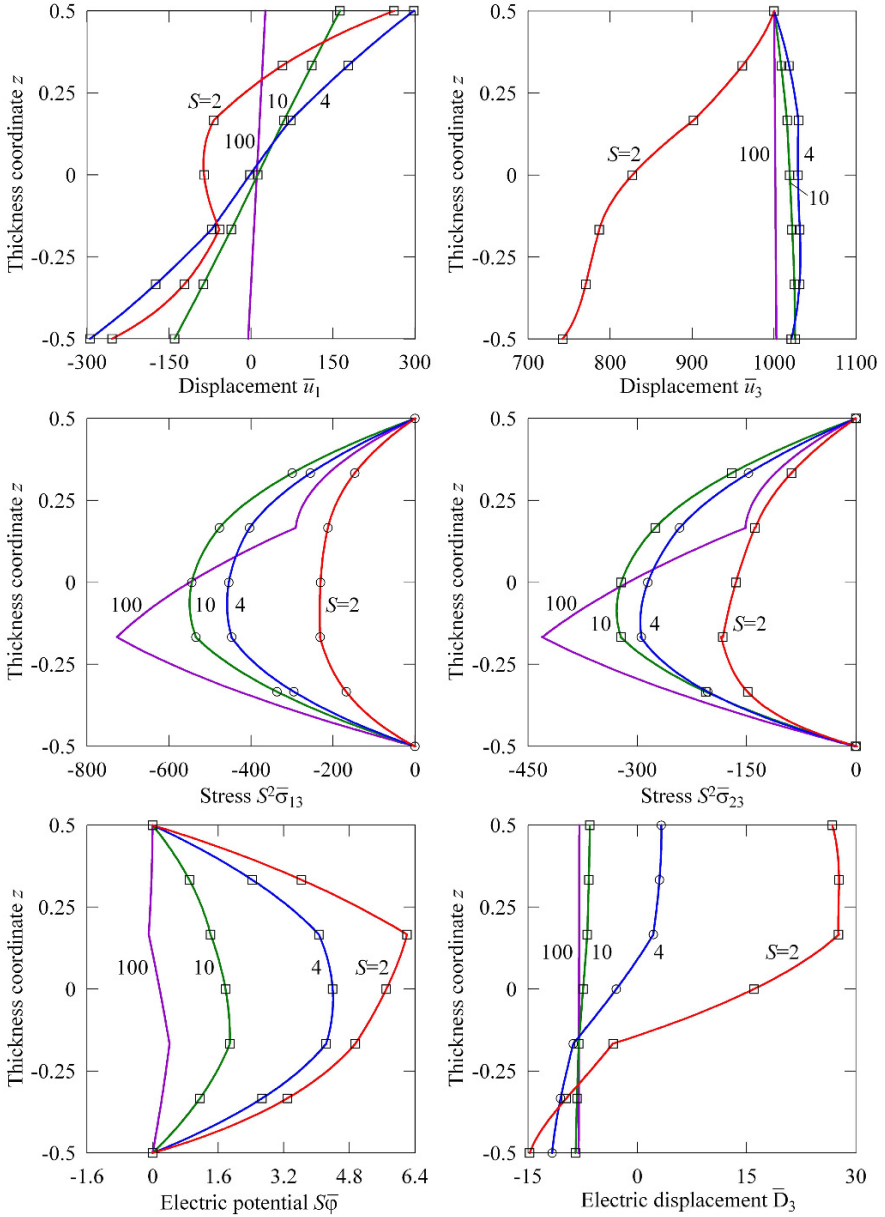
The results of the convergence study due to mesh refinement are presented in Fig. 4.4. The analytical answer is provided by the exact SaS solution (Kulikov and Plotnikova, 2013). In this study, we consider five regular meshes with  $3 \times 6$ ,  $6 \times 12$ ,  $12 \times 24$ ,  $24 \times 48$  and  $48 \times 96$  finite elements, which are characterized by the mesh parameter  $k$  running from 1 to 5. It is seen that the GeXPS4 element behaves well even in the case of coarse meshes except for the transverse normal stress for thin shells.

Table 4.2: Results for a three-layer cylindrical shell with  $S = 2$  under mechanical loading

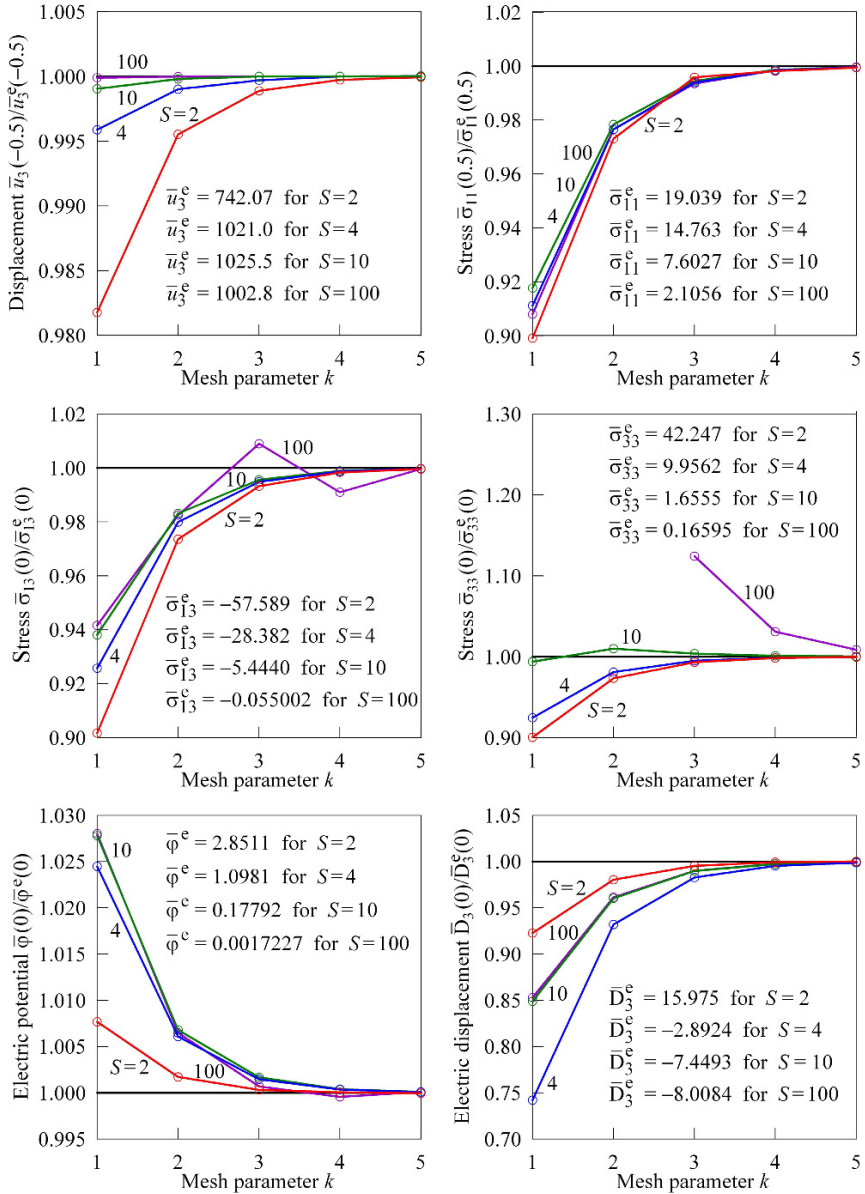
$I_n$	$\bar{u}_1(-0.5)$	$\bar{u}_3(-0.5)$	$\bar{\varphi}(0)$	$\bar{\sigma}_{22}(-0.5)$	$\bar{\sigma}_{13}(0)$	$\bar{\sigma}_{23}(0)$	$\bar{\sigma}_{33}(0)$	$\bar{D}_3(0)$
3	-251.6	740.2	2.849	-136.3	-56.80	-40.70	40.48	15.22
4	-254.6	742.2	2.851	-131.2	-57.71	-40.98	42.50	16.11
5	-254.3	742.1	2.851	-127.9	-57.57	-41.20	42.23	15.98
Exact	-254.3	742.1	2.851	-127.7	-57.59	-41.21	42.25	15.98

Next, we study the same three-layer piezoelectric cylindrical shell subjected to electric loading on the top surface whereas the bottom surface is electrically grounded

$$\varphi^- = 0, \quad \varphi^+ = \varphi_0 \sin \frac{\pi\theta_1}{L} \cos 2\theta_2, \tag{4.39}$$



**Fig. 4.3:** Through-thickness distributions of displacements, transverse shear stresses, electric potential and electric displacement for a three-layer cylindrical shell subjected to mechanical loading for  $I_1 = I_2 = I_3 = 5$ : GeXPS4 element (—), exact SaS solution (Kulikov and Plotnikova, 2013) (○) and Heyliger's exact 3D solution (Heyliger, 1997) (□)



**Fig. 4.4:** Convergence study due to mesh refinement for a three-layer cylindrical shell subjected to mechanical loading for  $I_1 = I_2 = I_3 = 5$ ; the reference solution (—) is provided by the exact SaS solution (Kulikov and Plotnikova, 2013)

Table 4.3: Results for a three-layer cylindrical shell with  $S = 10$  under mechanical loading

$I_n$	$\bar{u}_1(-0.5)$	$\bar{u}_3(-0.5)$	$\bar{\varphi}(0)$	$\bar{\sigma}_{22}(-0.5)$	$\bar{\sigma}_{13}(0)$	$\bar{\sigma}_{23}(0)$	$\bar{\sigma}_{33}(0)$	$\bar{D}_3(0)$
3	-139.7	1026.	0.1780	-1.784	-5.352	-3.168	1.691	-7.452
4	-139.7	1026.	0.1779	-1.591	-5.445	-3.216	1.659	-7.444
5	-139.7	1026.	0.1779	-1.574	-5.443	-3.220	1.656	-7.445
Exact	-139.7	1026.	0.1779	-1.564	-5.440	-3.221	1.656	-7.449

where  $\varphi_0 = 10$  V. The external surfaces are assumed to be traction free. Here, again one octant of the shell is modeled by a regular mesh with  $48 \times 96$  GeXPS4 elements.

Table 4.4 lists the results of the convergence study for the moderately thick shell by increasing the number of SaS  $I_n$  inside each layer. The obtained results are compared with the exact SaS solution (Kulikov and Plotnikova, 2013). Figure 4.5 shows the through-thickness distributions of displacements, transverse stresses, electric potential and electric displacement (4.38) for different slenderness ratios  $S$  by choosing five SaS for each layer. It is seen that the boundary conditions on bottom and top surfaces and the continuity conditions at interfaces for transverse stresses and electric displacement are satisfied again correctly.

Table 4.4: Results for a three-layer cylindrical shell with  $S = 10$  under electric loading

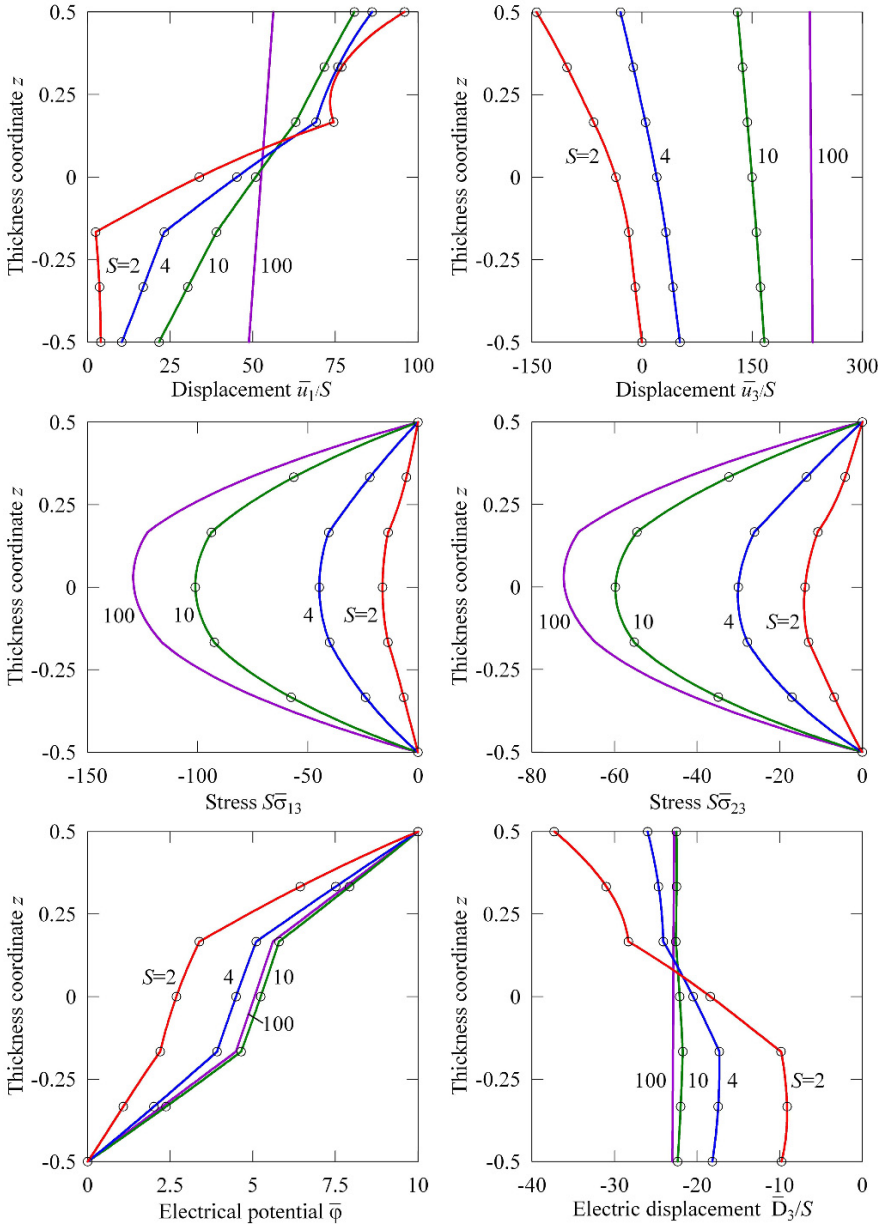
$I_n$	$\bar{u}_1(-0.5)$	$\bar{u}_3(-0.5)$	$\bar{\varphi}(0)$	$\bar{\sigma}_{11}(-0.5)$	$\bar{\sigma}_{13}(0)$	$\bar{\sigma}_{23}(0)$	$\bar{\sigma}_{33}(0)$	$\bar{D}_3(0)$
3	216.2	1664.	5.239	-12.12	-9.910	-5.866	-1.527	-221.2
4	216.1	1664.	5.239	-12.14	-10.11	-5.979	-1.535	-221.1
5	216.1	1664.	5.239	-12.14	-10.11	-5.977	-1.535	-221.1
Exact	216.2	1665.	5.239	-12.15	-10.11	-5.979	-1.545	-221.2

### 4.5.2 Three-Layer Piezoelectric Spherical Shell

Consider a three-layer piezoelectric spherical shell with ply thicknesses  $[0.4h/0.2h/0.4h]$  subjected to a localized uniform pressure symmetrically distributed on the top surface by

$$p_3^+ = -p_0 \text{ for } 0 \leq \theta_1 \leq \theta_0, \quad \pi - \theta_0 \leq \theta_1 \leq \pi \text{ and } 0 \leq \theta_2 \leq 2\pi, \quad (4.40)$$

where  $\theta_1$  and  $\theta_2$  are the spherical coordinates of the middle surface;  $p_0 = 1 \text{ N/m}^2$  and  $\theta_0 = \arccos(0.75)$ . The bottom and top layers are made of the  $\text{BaTiO}_3$  whereas the middle layer of the PZT-4 with the material properties given in Table 4.4 and (Dunn



**Fig. 4.5:** Through-thickness distributions of displacements, transverse shear stresses, electric potential and electric displacement for a three-layer cylindrical shell subjected to electric loading for  $I_1 = I_2 = I_3 = 5$ : GeXPS4 element (—) and exact SaS solution (Kulikov and Plotnikova, 2013) (○)

Table 4.5: Results for a three-layer piezoelectric spherical shell with  $R/h = 1.5$ 

$I_n$	$\bar{u}_1(0.5)$	$\bar{u}_3(0.5)$	$\bar{\varphi}(0.5)$	$\bar{\sigma}_{11}(0.5)$	$\bar{\sigma}_{22}(0.5)$	$\bar{\sigma}_{13}(0)$	$\bar{\sigma}_{33}(0)$	$\bar{D}_3(0)$
3	-0.7592	-3.572	4.131	-10.98	-9.862	-0.5407	-4.367	-1.062
5	-0.7655	-3.582	4.119	-10.78	-9.725	-0.5491	-4.370	-1.097
7	-0.7655	-3.582	4.120	-10.79	-9.738	-0.5490	-4.370	-1.096
9	-0.7655	-3.582	4.120	-10.79	-9.738	-0.5490	-4.370	-1.096

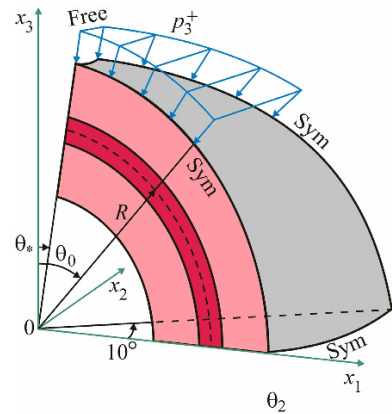
and Taya, 1994). This problem is a good benchmark to test the proposed analytical integration scheme because in the literature an exact 3D solution is available (Chen et al, 2001).

Owing to symmetry, we consider a part of the shell ( $\theta_* \leq \theta_1 \leq 90^\circ$ ,  $0 \leq \theta_2 \leq 10^\circ$ ) depicted in Fig. 4.6, which is modeled by a fine mesh with  $450 \times 1$  GeXPS4 elements to describe correctly the boundary conditions on external surfaces and the continuity conditions at interfaces for transverse components of stresses and electric displacement, where  $\theta_* = 0.001^\circ$ . To analyze the results efficiently, we introduce the following dimensionless variables as functions of the thickness coordinate:

$$\begin{aligned}
 \bar{u}_1 &= 10c_{44}u_1(\pi/6, 0, z)/RS p_0, & \bar{u}_3 &= 10c_{44}u_3(\pi/6, 0, z)/RS p_0, \\
 \bar{\sigma}_{11} &= 10\sigma_{11}(\pi/6, 0, z)/S p_0, & \bar{\sigma}_{22} &= 10\sigma_{22}(\pi/6, 0, z)/S p_0, \\
 \bar{\sigma}_{13} &= 10\sigma_{13}(\pi/6, 0, z)/p_0, & \bar{\sigma}_{33} &= \sigma_{33}(\pi/6, 0, z)/p_0, \\
 \bar{\varphi} &= 100e_{33}\varphi(\pi/6, 0, z)/Rp_0, & \bar{D}_3 &= 10Sc_{44}D_3(\pi/6, 0, z)/e_{33}p_0, & z &= \theta_3/h,
 \end{aligned} \tag{4.41}$$

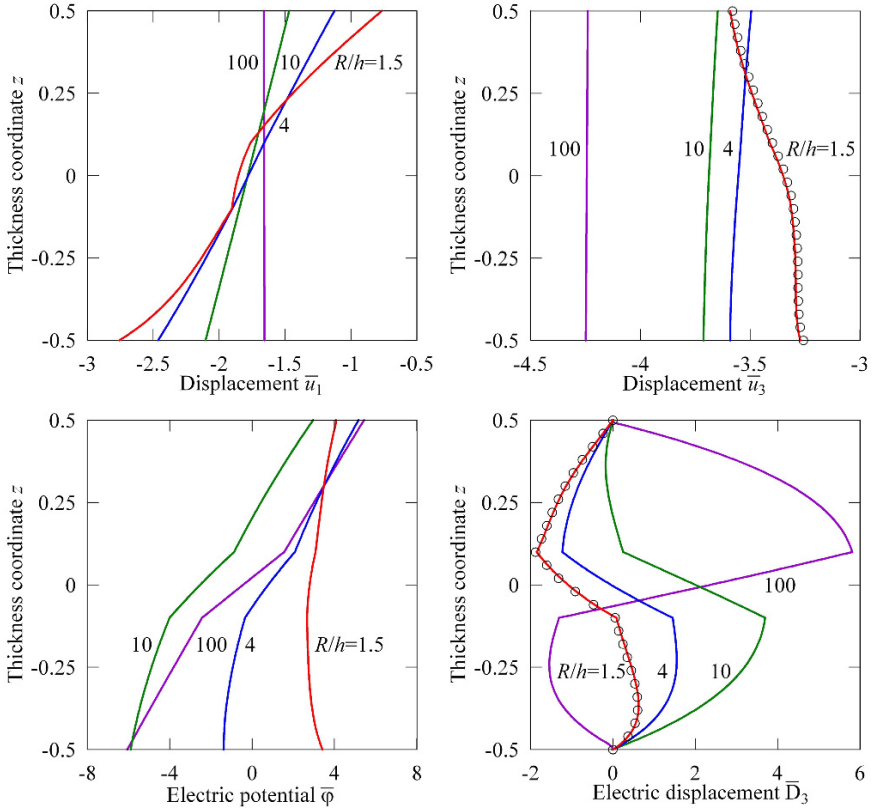
where  $S = R/h$  is the slenderness ratio;  $R = 1$  m is the radius of the middle surface;  $c_{44} = 44.0$  GPa and  $e_{33} = 17.5$  C/m<sup>2</sup> are the representative moduli.

The data listed in Table 4.5 show that the GeXPS4 element allows reproducing the 3D solution of piezoelectricity (Chen et al, 2001) for a thick spherical shell with a high accuracy by using the sufficiently large number of SaS inside the layers. Figures



**Fig. 4.6** A part of the three-layer piezoelectric spherical shell modeled by regular  $k \times 1$  meshes





**Fig. 4.7:** Through-thickness distributions of displacements, electric potential and electric displacement for a three-layer piezoelectric spherical shell for  $I_1 = I_2 = I_3 = 9$ : GeXPS4 element (—) and exact 3D solution (Chen et al, 2001) (○)

4.7 and 4.8 display the distributions of displacements, electric potential, electric displacement and stresses (4.41) through the thickness for various slenderness ratios by choosing nine SaS inside each layer. A comparison with the exact 3D solution (Chen et al, 2001) is also presented. One can see that the results for a thick shell are very close.

Figure 4.9 shows the results of the convergence study through the use of the normalized transverse displacement, electric potential and stresses for thick and thin shells with nine SaS for each layer. The regular  $30k \times 1$  meshes are utilized with the mesh parameter  $k$  that runs from 1 to 5. The reference values for the displacement, electric potential and stresses are listed in Table 4.6. They have been obtained by using a fine  $450 \times 1$  mesh. As can be seen, the GeXPS4 element demonstrates again good convergence characteristics.

Table 4.6: Reference values of basic variables for a three-layer piezoelectric spherical shell for  $I_1 = I_2 = I_3 = 9$  by using a fine  $450 \times 1$  mesh

$S$	$\bar{u}_3^{\text{ref}}(0.5)$	$\bar{\varphi}^{\text{ref}}(0.5)$	$\bar{\sigma}_{11}^{\text{ref}}(0.5)$	$\bar{\sigma}_{33}^{\text{ref}}(0)$
1.5	-3.582	4.120	-10.79	-0.5490
4	-3.486	4.607	-8.748	-0.4539
10	-3.638	2.970	-8.544	-0.4037
100	-4.239	5.429	-5.589	-0.4870

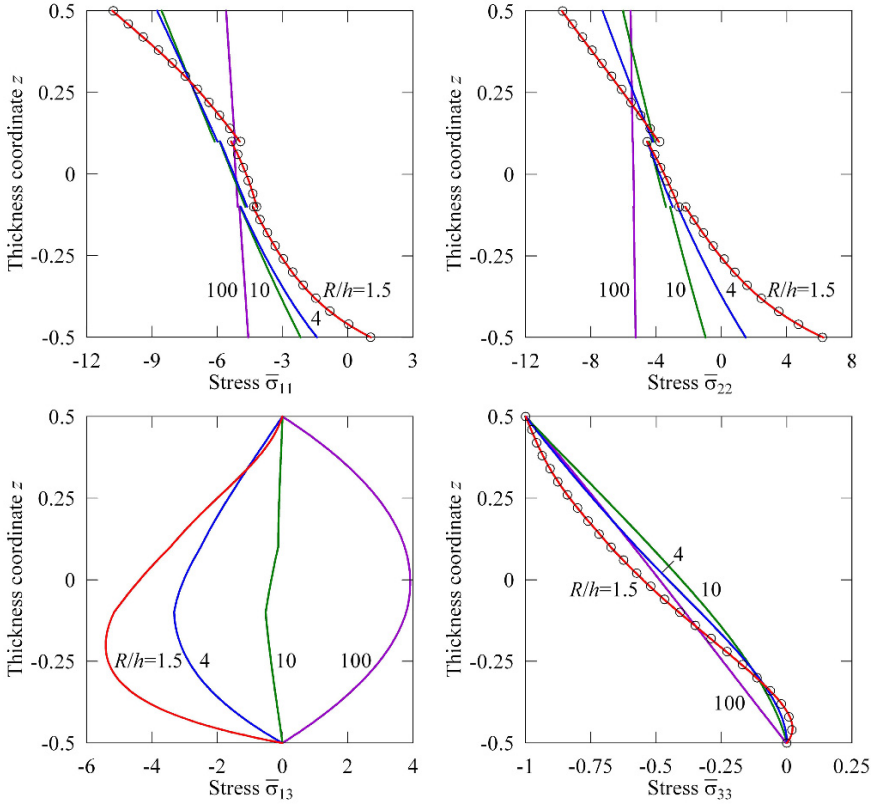
## 4.6 Conclusions

The paper presents a geometrically exact hybrid-mixed four-node piezoelectric solid-shell element (GeXPS4) based on the SaS formulation in which displacements and electric potentials of SaS are utilized as fundamental shell unknowns. The SaS are located at Chebyshev polynomial nodes inside the layers and interfaces as well that improves significantly the behavior of the higher-order Lagrange interpolations. To implement the efficient analytical integration throughout the element, the enhanced ANS method for all components of the strain tensor and electric field is employed. The feature of the GeXPS4 element is that the element stiffness matrices are evaluated without the use of expensive numerical matrix inversion. As a result, the GeXPS4 element exhibits a superior performance in the case of coarse mesh configurations. Therefore, it can be recommended for the 3D stress analysis of thick and thin doubly-curved shells.

**Acknowledgements** This work was supported by the Russian Ministry of Education and Science (Grants No. 9.1148.2017/4.6 and 9.4914.2017/6.7).

## References

- Bakhvalov NS (1977) Numerical Methods: Analysis, Algebra, Ordinary Differential Equations. MIR, Moscow
- Bathe KJ, Dvorkin EN (1986) A formulation of general shell elements—the use of mixed interpolation of tensorial components. *Int J Numer Meth Engng* 22(3):697–722
- Bathe KJ, Lee PS, Hiller JF (2003) Towards improving the MITC9 shell element. *Comput Struct* 81(8):477–489
- Betsch P, Stein E (1995) An assumed strain approach avoiding artificial thickness straining for a non-linear 4-node shell element. *Comm Num Meth Engng* 11(11):899–909
- Carrera E (1999) Multilayered shell theories accounting for layerwise mixed description. Part 1: Governing equations. *AIAA J* 37(9):1107–1116
- Carrera E (2003) Theories and finite elements for multilayered plates and shells: A unified compact formulation with numerical assessment and benchmarking. *Arch Comput Meth Engng* 10(3):215–296



**Fig. 4.8:** Through-thickness distribution of stresses for a three-layer piezoelectric spherical shell for  $I_1 = I_2 = I_3 = 9$ : GeXPS4 element (—) and exact 3D solution (Chen et al, 2001) (o)

Carrera E, Valvano S (2017) Analysis of laminated composite structures with embedded piezoelectric sheets by variable kinematic shell elements. *J Intel Mater Systems Struct* online:1–29, DOI 10.1177/1045389X17704913

Carrera E, Brischetto S, Nali P (2011) *Plates and Shells for Smart Structures: Classical and Advanced Theories for Modeling and Analysis*. John Wiley & Sons Ltd, Chichester

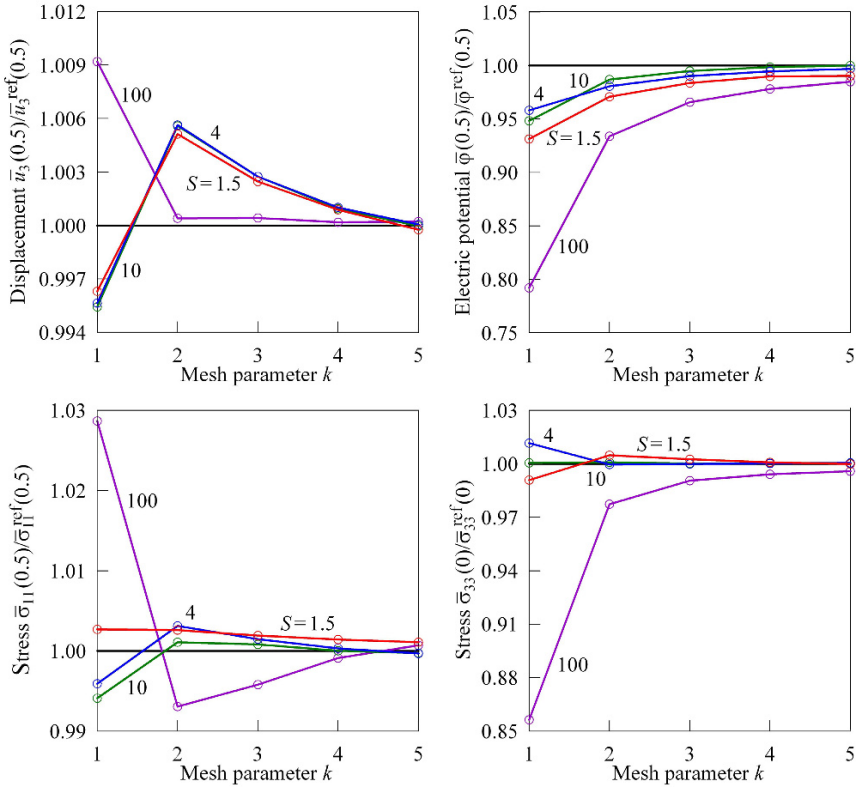
Carrera E, Cinefra M, Petrolo M, Zappino E (2014) *Finite Element Analysis of Structures Through Unified Formulation*. John Wiley & Sons Ltd, Chichester

Chen WQ, Ding HJ, Xu RQ (2001) Three-dimensional static analysis of multi-layered piezoelectric hollow spheres via the state space method. *Int J Solids Struct* 38(28):4921–4936

Cinefra M, Carrera E, Valvano S (2015) Variable kinematic shell elements for the analysis of electro-mechanical problems. *Mech Adv Mater Struct* 22:77–106

Dunn ML, Taya M (1994) Electroelastic field concentrations in and around inhomogeneities in piezoelectric solids. *Trans ASME J Appl Mech* 61(2):474–475

Heyliger P (1997) A note on the static behavior of simply supported laminated piezoelectric cylinders. *Int J Solids Struct* 34(29):3781 – 3794



**Fig. 4.9:** Convergence study due to mesh refinement for a three-layer spherical shell for  $I_1 = I_2 = I_3 = 9$ ; the reference solution (—) is provided by Table 4.6

Hughes TJR, Tezduyar TE (1981) Finite elements based upon Mindlin plate theory with particular reference to the four-node bilinear isoparametric element. *Trans ASME J Appl Mech* 48(3):587–596

Klinkel S, Wagner W (2006) A geometrically non-linear piezoelectric solid shell element based on a mixed multi-field variational formulation. *Int J Numer Meth Eng* 65(3):349–382

Klinkel S, Wagner W (2008) A piezoelectric solid shell element based on a mixed variational formulation for geometrically linear and nonlinear applications. *Comp Struct* 86(1):38 – 46

Ko Y, Lee PS, Bathe KJ (2017) A new MITC4+ shell element. *Comput Struct* 182:404–418

Kulikov GM (2001) Refined global approximation theory of multilayered plates and shells. *J Eng Mech* 127(2):119–125

Kulikov GM, Carrera E (2008) Finite deformation higher-order shell models and rigid-body motions. *Int J Solids Struct* 45(11):3153–3172

Kulikov GM, Plotnikova SV (2008) Geometrically exact four-node piezoelectric solid-shell element. *Mech Adv Mater Struct* 15(3-4):199–207

Kulikov GM, Plotnikova SV (2010) Solution of a coupled problem of thermopiezoelectricity based on a geometrically exact shell element. *Mech Comp Mater* 46(4):349–364

- Kulikov GM, Plotnikova SV (2011a) Exact geometry piezoelectric solid-shell element based on the 7-parameter model. *Mech Adv Mater Struct* 18(2):133–146
- Kulikov GM, Plotnikova SV (2011b) Finite rotation piezoelectric exact geometry solid-shell element with nine degrees of freedom per node. *Comput Mater Continua* 23:233–264
- Kulikov GM, Plotnikova SV (2011c) Non-linear exact geometry 12-node solid-shell element with three translational degrees of freedom per node. *Int J Numer Meth Engng* 88(13):1363–1389
- Kulikov GM, Plotnikova SV (2011d) On the use of a new concept of sampling surfaces in shell theory. In: Altenbach H, Eremeyev VA (eds) *Shell-like Structures: Non-classical Theories and Applications*, Springer, Berlin, Heidelberg, pp 715–726
- Kulikov GM, Plotnikova SV (2013) A sampling surfaces method and its application to three-dimensional exact solutions for piezoelectric laminated shells. *Int J Solids Struct* 50(11):1930–1943
- Kulikov GM, Plotnikova SV (2014) Exact electroelastic analysis of functionally graded piezoelectric shells. *Int J Solids Struct* 51(1):13–25
- Kulikov GM, Plotnikova SV (2015) The use of 9-parameter shell theory for development of exact geometry 12-node quadrilateral piezoelectric laminated solid-shell elements. *Mech Adv Mater Struct* 22(6):490–502
- Kulikov GM, Plotnikova SV (2017) Assessment of the sampling surfaces formulation for thermo-electroelastic analysis of layered and functionally graded piezoelectric shells. *Mech Adv Mater Struct* 24(5):392–409
- Kulikov GM, Mamontov AA, Plotnikova SV (2015) Coupled thermoelectroelastic stress analysis of piezoelectric shells. *Compos Struct* 124:65–76
- Lee S, Goo NS, Park HC, Yoon KJ, Cho C (2003) A nine-node assumed strain shell element for analysis of a coupled electro-mechanical system. *Smart Mater Struct* 12:355–362
- Lentzen S (2009) Nonlinearly coupled thermopiezoelectric modelling and FE-simulation of smart structures. No. 419 in *Fortschritt-Berichte VDI, Reihe 20*, VDI-Verlag GmbH, Düsseldorf
- Macneal RH (1982) Derivation of element stiffness matrices by assumed strain distributions. *Nuclear Engineering and Design* 70(1):3–12
- Park KC, Stanley GM (1986) A curved  $C^0$  shell element based on assumed natural-coordinate strains. *Trans ASME J Appl Mech* 53(2):278–290
- Sze KY, Yao LQ (2000) A hybrid stress ANS solid-shell element and its generalization for smart structure modelling. Part I: Solid-shell element formulation. *Int J Numer Meth Eng* 48:545–564
- Sze KY, Yao LQ, Yi S (2000) A hybrid stress ANS solid-shell element and its generalization for smart structure modelling. Part II: Smart structure modelling. *Int J Numer Meth Eng* 48:565–582
- Zheng S, Wang X, Chen W (2004) The formulation of a refined hybrid enhanced assumed strain solid shell element and its application to model smart structures containing distributed piezoelectric sensors/actuators. *Smart Mater Struct* 13:N43–N50

# Chapter 5

## Finite Element Approach for Composite Magneto-Piezoelectric Materials Modeling in ACELAN-COMPOS Package

Natalia V. Kurbatova, Dmitry K. Nadolin, Andrey V. Nasedkin, Pavel A. Oganessian, and Arcady N. Soloviev

**Abstract** The problem of material properties identification for modern active composites is closely connected to the state of the art methods of design and manufacturing using composite and smart materials. This chapter deals with computer design of multiscale two-phase piezomagnetolectric (magnetolectric) bulk composites in finite element software ACELAN-COMPOS. These composites consist of piezomagnetic and piezoelectric fractions of irregular structures. The complex approach for the homogenization problem of such composites include the effective moduli method, computer modeling of the representative volumes with microstructure features, and the finite element technologies for solving the static problems for the representative volumes. Representative volumes are widely used as geometrical models for such problems. The three-dimensional application is demonstrated for piezomagnetolectric and piezoelectric materials. A specific set of boundary conditions applied to the representative volume enables us to determine effective moduli of the material. The first step of such modeling consists in describing a material distribution inside the representative volumes with a known percentage of each material. Three algorithms were created to simulate random material distribution for specific patterns: biphasic composite with connectivity of each phase, granules of predefined size and regular rods.

---

Natalia V. Kurbatova, Dmitry K. Nadolin, Andrey V. Nasedkin, Pavel A. Oganessian  
Southern Federal University, Institute of Mathematics, Mechanics and Computer Science,  
Milchakova Street 8a, Rostov-on-Don, 344090, Russia  
e-mail: [nvk-ru@yandex.ru](mailto:nvk-ru@yandex.ru), [nadolin@yandex.ru](mailto:nadolin@yandex.ru), [nasedkin@math.sfedu.ru](mailto:nasedkin@math.sfedu.ru), [wolwerine@yandex.ru](mailto:wolwerine@yandex.ru)

Arcady N. Soloviev  
Don State Technical University, Department of Theoretical and Applied Mechanics, Gagarin sq., 1,  
Rostov-on-Don, 344000, Russia  
e-mail: [solovievarc@gmail.com](mailto:solovievarc@gmail.com)

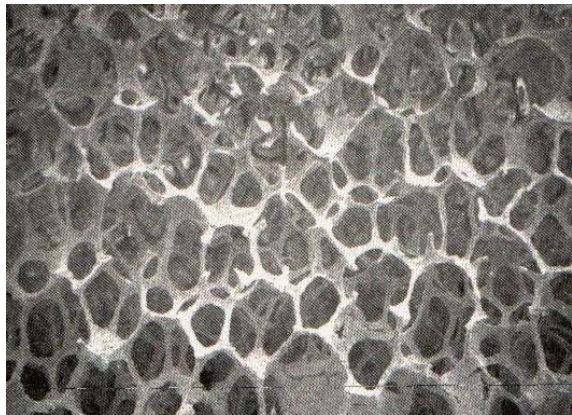
## 5.1 Introduction

Inhomogeneous and porous active materials are widely used in modern material science and technique. Thus, two-phase piezomagnetolectric (magnetolectric) composites consisting of active piezoelectric and piezomagnetic phases demonstrate the ability to mutual transformation of magnetic and electric fields, although each separate phase does not have such property. Modern magnetolectric composites have high effectiveness of the magnetolectric transformation, relatively high temperatures of phase transitions and long process life (Nan et al, 2008).

Piezoceramic composite materials and, in particular, porous piezoceramic materials also have been actively developed in the last years (Ringgaard et al, 2015; Rybyanets, 2010, 2011). Porous piezoceramics have a lower impedance than dense ceramics. Therefore, the impedance mismatch between the piezoelectric device and the surrounding acoustic medium is decreased. On the other hand, its longitudinal piezomodulus  $d_{33}$ , which determines the efficiency of mechanical and electrical energy transformations for thickness vibrations, remains almost the same as for the dense piezoceramics. This properties allows to create high-intensity ultrasound transducers.

Recently magnetolectric composites became of interest to many researchers which resulted in considerable increase in the number of works devoted to the modeling of the effective properties of these composites (see Lee et al, 2005; Li, 2000; Nan et al, 2008; Tang and Yu, 2008; Zhang and Soh, 2005, etc.). Piezoelectric composites are studied much better (see Bowen et al, 2001; Iyer and Venkatesh, 2014; Martínez-Ayuso et al, 2017; Nguyen et al, 2016; Ramesh et al, 2005; Rybyanets, 2010; Rybyanets et al, 2015; Topolov and Bowen, 2009, etc.). Example of such materials can be seen in Figs. 5.1 and 5.2.

Mathematical models of such materials are complicated and usually require additional modeling step to define physical properties of composite. In this paper we consider homogenization models and the finite element method as a tool for



**Fig. 5.1** Scanning electron microscope (SEM) picture of a high-porous PZT material with 95 % of porosity synthesized by foam reticulation technique.



**Fig. 5.2:** Piezoceramics with different size of pores and pores percentage.

representative volume modeling and properties identification of piezoelectric and magnetolectric materials.

## 5.2 Piezomagnetolectric Boundary Problems

In ACELAN we use the original models of piezomagnetolectric (magnetolectric) materials with damping similar described in Nasedkin et al (2014).

Let  $\Omega$  be a region occupied by a piezomagnetolectric material;  $\Gamma = \partial\Omega$  is the boundary of the region;  $\mathbf{n}$  is the vector of the external unit normal to  $\Gamma$ ;  $\mathbf{x} = \{x_1, x_2, x_3\}$ ;  $t$  is the time;  $\mathbf{u} = \mathbf{u}(\mathbf{x}, t)$  is the vector of mechanical displacements;  $\varphi = \varphi(\mathbf{x}, t)$  is the electric potential;  $\phi = \phi(\mathbf{x}, t)$  is the magnetic potential. The system of differential equations for piezomagnetolectric body with damping effects in  $\Omega$  can be written in the following vector–matrix form

$$\mathbf{L}^*(\nabla) \cdot \mathbf{T} + \rho \mathbf{f} = \rho(\ddot{\mathbf{u}} + \alpha_d \dot{\mathbf{u}}), \quad \nabla \cdot \mathbf{D} = \sigma_\Omega, \quad \nabla \cdot \mathbf{B} = 0, \quad (5.1)$$

$$\mathbf{T} = \mathbf{c} \cdot (\mathbf{S} + \beta_d \dot{\mathbf{S}}) - \mathbf{e}^* \cdot \mathbf{E} - \mathbf{h}^* \cdot \mathbf{H}, \quad (5.2)$$

$$\mathbf{D} + \zeta_d \dot{\mathbf{D}} = \mathbf{e} \cdot (\mathbf{S} + \zeta_d \dot{\mathbf{S}}) + \boldsymbol{\kappa} \cdot \mathbf{E} + \boldsymbol{\alpha} \cdot \mathbf{H}, \quad (5.3)$$

$$\mathbf{B} + \gamma_d \dot{\mathbf{B}} = \mathbf{h} \cdot (\mathbf{S} + \gamma_d \dot{\mathbf{S}}) + \boldsymbol{\alpha}^* \cdot \mathbf{E} + \boldsymbol{\mu} \cdot \mathbf{H}, \quad (5.4)$$

$$\mathbf{S} = \mathbf{L}(\nabla) \cdot \mathbf{u}, \quad \mathbf{E} = -\nabla\varphi, \quad \mathbf{H} = -\nabla\phi, \quad (5.5)$$

$$\mathbf{L}^*(\nabla) = \begin{bmatrix} \partial_1 & 0 & 0 & 0 & \partial_3 & \partial_2 \\ 0 & \partial_2 & 0 & \partial_3 & 0 & \partial_1 \\ 0 & 0 & \partial_3 & \partial_2 & \partial_1 & 0 \end{bmatrix}. \quad (5.6)$$

Here  $\mathbf{L}(\mathbf{a})$  is a matrix operator for the vector  $\mathbf{a}$ ,  $\mathbf{L}^*(\mathbf{a})$  is the transposed operator,  $\mathbf{T} = \{\sigma_{11}, \sigma_{22}, \sigma_{33}, \sigma_{23}, \sigma_{13}, \sigma_{12}\}$  denotes the array of the stress components;  $\mathbf{S} = \{\varepsilon_{11},$



$\varepsilon_{22}, \varepsilon_{33}, 2\varepsilon_{23}, 2\varepsilon_{13}, 2\varepsilon_{12}$  is the array of the strain components;  $\mathbf{D}$  and  $\mathbf{E}$  are the electric flux density vector or the electric displacement vector and the electric field vector;  $\mathbf{B}$  and  $\mathbf{H}$  are the magnetic flux density vector and the magnetic field vector;  $\rho$  is the mass density of the material;  $\mathbf{c} = \mathbf{c}^{E,H}$  is the  $6 \times 6$  matrix of elastic stiffness moduli;  $\mathbf{e} = \mathbf{e}^H$  is the  $3 \times 6$  matrix of piezoelectric moduli;  $\mathbf{h} = \mathbf{h}^E$  is the the  $3 \times 6$  matrix of magnetostriction moduli (piezomagnetic moduli);  $\boldsymbol{\kappa} = \boldsymbol{\kappa}^{S,H} = \boldsymbol{\varepsilon}^{S,H}$  is the the  $3 \times 3$  matrix of dielectric permittivity moduli;  $\boldsymbol{\alpha} = \boldsymbol{\alpha}^S$  is the  $3 \times 3$  matrix of magnetoelectric coupling coefficients;  $\boldsymbol{\mu} = \boldsymbol{\mu}^{S,E}$  is the  $3 \times 3$  matrix of magnetic permeability moduli;  $\alpha_d, \beta_d, \zeta_d, \gamma_d$  are the damping coefficients;  $\mathbf{f}$  is the vector of mass forces;  $\sigma_Q$  is the density of free electric charges (usually,  $\sigma_Q = 0$ );  $(\dots)^*$  is the transpose operation;  $(\dots) : (\dots)$  is the double scalar product operation.

We suppose that the material moduli have the usual symmetry properties:  $c_{\alpha\beta} = c_{\beta\alpha}$ ,  $\kappa_{kl} = \kappa_{lk}$ ,  $\mu_{kl} = \mu_{lk}$ . In addition to this for the positive definiteness of the intrinsic energy for the piezomagnetolectric medium the following inequalities must be satisfied ( $\forall \mathbf{S}, \mathbf{E}, \mathbf{H}$ ),  $\exists W_0 > 0$ :

$$\mathbf{S}^* \cdot \mathbf{c} \cdot \mathbf{S} + \mathbf{E}^* \cdot \boldsymbol{\kappa} \cdot \mathbf{E} + 2\mathbf{E}^* \cdot \boldsymbol{\alpha} \cdot \mathbf{H} + \mathbf{H}^* \cdot \boldsymbol{\mu} \cdot \mathbf{H} \geq W_0(\mathbf{S}^* \cdot \mathbf{S} + \mathbf{E}^* \cdot \mathbf{E} + \mathbf{H}^* \cdot \mathbf{H}).$$

In Eqs. (5.1)–(5.6) for the piezomagnetolectric material, we use a generalized Rayleigh method of damping evaluation, see Belokon et al (2002); Nasedkin (2010) for the case of piezoelectric material and Nasedkin et al (2014) for the case of thermopiezomagnetolectric material with equations in tensor form. When  $\zeta_d = \gamma_d = 0$  in Eqs. (5.3), (5.4), we have the model for taking into account of mechanical damping in piezomagnetolectric media which is adopted in the case of elastic and piezoelectric materials in several well-known finite element packages. A more complicated model (5.2)–(5.4) extends Kelvin's model to the case of piezomagnetolectric media. It has been shown that the model (5.1)–(5.6) with  $\beta_d = \zeta_d = \gamma_d$  satisfies the conditions of the energy dissipation and has the possibility to apply the mode superposition method for transient and harmonic problems.

The boundary and the initial conditions should be added to the system of differential equations (5.1)–(5.6). The boundary conditions are of three types: mechanical, electric and magnetic. To formulate the mechanical boundary conditions we assume that the boundary  $\Gamma$  is divided in two subsets  $\Gamma_\sigma$  and  $\Gamma_u$  ( $\Gamma = \Gamma_\sigma \cup \Gamma_u$ ). We will assume that at the part of the boundary  $\Gamma_\sigma$  the vector of mechanical stress  $\mathbf{p}_\Gamma$  is known

$$\mathbf{L}^*(\mathbf{n}) \cdot \mathbf{T} = \mathbf{p}_\Gamma, \quad \mathbf{x} \in \Gamma_\sigma. \quad (5.7)$$

On the remaining part  $\Gamma_u$  of the boundary  $\Gamma$  we pose known the mechanical displacements vector  $\mathbf{u}_\Gamma$

$$\mathbf{u} = \mathbf{u}_\Gamma, \quad \mathbf{x} \in \Gamma_u, \quad (5.8)$$

where  $\mathbf{L}^*(\mathbf{n})$  is the matrix as in (5.6) with replace  $\partial_k$  by  $n_k$ . To set the electric boundary conditions we assume that the surface  $\Gamma$  is also subdivided in two subsets:  $\Gamma_D$  and  $\Gamma_\varphi$  ( $\Gamma = \Gamma_D \cup \Gamma_\varphi$ ). The regions  $\Gamma_D$  does not contain electrodes and hold the following conditions

$$\mathbf{n} \cdot \mathbf{D} = -\sigma_\Gamma, \quad \mathbf{x} \in \Gamma_D, \quad (5.9)$$

where  $\sigma_\Gamma$  is the known surface density of electric charge, and usually,  $\sigma_\Gamma = 0$ . The subset  $\Gamma_\varphi$  is the union of  $M + 1$  regions  $\Gamma_{\varphi_j}$  ( $j \in J_Q \cup J_V$ ,  $J_Q = \{1, 2, \dots, m\}$ ,  $J_V = \{0, m, m + 1, \dots, M\}$ ), that does not border on each other and are covered with infinitely thin electrodes. At these regions we set the following boundary for the electrical field conditions

$$\varphi = \Phi_j, \quad \mathbf{x} \in \Gamma_{\varphi_j}, \quad j \in J_Q, \quad (5.10)$$

$$\int_{\Gamma_{\varphi_j}} \mathbf{n} \cdot \mathbf{D} d\Gamma = -Q_j, \quad I_j = \pm \dot{Q}_j, \quad \mathbf{x} \in \Gamma_{\varphi_j}, \quad j \in J_Q, \quad (5.11)$$

$$\varphi = V_j, \quad \mathbf{x} \in \Gamma_{\varphi_j}, \quad j \in J_V, \quad \Gamma_{j0} \neq \emptyset, \quad (5.12)$$

where the variables  $\Phi_j$ ,  $V_j$  do not depend on  $\mathbf{x}$ ;  $Q_j$  is the overall electric charge on  $\Gamma_{\varphi_j}$ , and the sign " $\pm$ " in (5.11) is chosen in accordance with the accepted direction of the current  $I_j$  in the electric circuit. For magnetic boundary condition we suppose that on the boundary  $\Gamma$  hold the following condition

$$\mathbf{n} \cdot \mathbf{B} = 0, \quad \mathbf{x} \in \Gamma. \quad (5.13)$$

For transient problems it is also necessary to pose initial conditions, which can be written as

$$\mathbf{u} = \mathbf{u}_*(\mathbf{x}), \quad \dot{\mathbf{u}} = \mathbf{v}_*(\mathbf{x}), \quad \varphi = \varphi_*(\mathbf{x}), \quad \phi = \phi_*(\mathbf{x}), \quad t = 0, \quad \mathbf{x} \in \Omega, \quad (5.14)$$

where  $\mathbf{u}_*(\mathbf{x})$ ,  $\mathbf{v}_*(\mathbf{x})$ ,  $\varphi_*(\mathbf{x})$ ,  $\phi_*(\mathbf{x})$  are the known initial values of the corresponding fields.

Equations (5.1)–(5.14) represent the statement of the transient problem for piezomagnetolectric body with the generalized Rayleigh damping. We can also consider the particular cases of this model without tacking into account the connectivity between some physical fields (models of piezoelectric, piezomagnetic, and elastic materials).

### 5.3 Finite Element Approximations

For solving problems for the piezomagnetolectric body in weak forms we will use classical finite element approximation techniques (Bathe and Wilson, 1976; Zienkewicz and Morgan, 1983). Let  $\Omega_h$  be a region of the corresponding finite element mesh  $\Omega_h \subseteq \Omega$ ,  $\Omega_h = \cup_k \Omega^{ek}$ , where  $\Omega^{ek}$  is a separate finite element with number  $k$ . On the finite element mesh  $\Omega_h = \cup_k \Omega^{ek}$  we will find the approximation to the weak solution  $\{\mathbf{u}_h \approx \mathbf{u}, \varphi_h \approx \varphi, \phi_h \approx \phi\}$  for the transient problem in the form

$$\mathbf{u}_h(\mathbf{x}, t) = \mathbf{N}_u^*(\mathbf{x}) \cdot \mathbf{U}(t), \quad \varphi_h(\mathbf{x}, t) = \mathbf{N}_\varphi^*(\mathbf{x}) \cdot \Phi(t), \quad \phi_h(\mathbf{x}, t) = \mathbf{N}_\phi^*(\mathbf{x}) \cdot \mathbf{A}(t), \quad (5.15)$$

where  $\mathbf{N}_u^*$  is the matrix of the shape functions for the displacements,  $\mathbf{N}_\varphi^*$  is the row vector of the shape functions for the electric potential,  $\mathbf{N}_\phi^*$  is the row vector of the shape functions for the magnetic potential,  $\mathbf{U}(t)$ ,  $\Phi(t)$ ,  $\mathbf{A}(t)$  are the global vectors of the nodal displacements, the electric potential, and the magnetic potential, respectively.

In accordance with conventional finite element technique we approximate the continuous weak formulation by the problem in finite-dimensional spaces. Substituting (5.15) and similar representations for project functions into the weak formulation of the problem for the magnetoelectric body on  $\Omega_h$ , without taking into account the principal boundary conditions we obtain

$$\mathbf{M}_{uu} \cdot \ddot{\mathbf{U}} + \mathbf{C}_{uu} \cdot \dot{\mathbf{U}} + \mathbf{K}_{uu} \cdot \mathbf{U} + \mathbf{K}_{u\varphi} \cdot \Phi + \mathbf{K}_{u\phi} \cdot \mathbf{A} = \mathbf{F}_u, \quad (5.16)$$

$$-\mathbf{K}_{u\varphi}^* \cdot (\mathbf{U} + \zeta_d \dot{\mathbf{U}}) + \mathbf{K}_{\varphi\varphi} \cdot \Phi + \mathbf{K}_{\varphi\phi} \cdot \mathbf{A} = \mathbf{F}_\varphi + \zeta_d \mathbf{F}_\varphi^t, \quad (5.17)$$

$$-\mathbf{K}_{u\phi}^* \cdot (\mathbf{U} + \gamma_d \dot{\mathbf{U}}) + \mathbf{K}_{\varphi\phi}^* \cdot \Phi + \mathbf{K}_{\phi\phi} \cdot \mathbf{A} = 0, \quad (5.18)$$

with the initial conditions

$$\mathbf{U}(0) = \mathbf{U}_0, \quad \dot{\mathbf{U}}(0) = \mathbf{U}_0^t, \quad \Phi(0) = \Phi_0, \quad \mathbf{A}(0) = \mathbf{A}_0, \quad (5.19)$$

where the vector of the nodal initial displacements  $\mathbf{U}_0$ , the vector of the nodal initial velocities  $\mathbf{U}_0^t$ , the vector of the nodal initial electric potentials  $\Phi_0$ , and the vector of the nodal initial magnetic potentials  $\mathbf{A}_0$  are derived from the corresponding continuous initial conditions (5.14).

Here,  $\mathbf{M}_{uu} = \sum^a \mathbf{M}_{uu}^{ek}$ ,  $\mathbf{C}_{uu} = \sum^a \mathbf{C}_{uu}^{ek}$ ,  $\mathbf{K}_{uu} = \sum^a \mathbf{K}_{uu}^{ek}$ ,  $\mathbf{K}_{u\varphi} = \sum^a \mathbf{K}_{u\varphi}^{ek}$ ,  $\mathbf{K}_{u\phi} = \sum^a \mathbf{K}_{u\phi}^{ek}$  etc. are the global matrices, obtained from the assembly of the corresponding element matrices. The element matrices are provided in the following form:

$$\mathbf{M}_{uu}^{ek} = \int_{\Omega^{ek}} \rho \mathbf{N}_u^e \cdot \mathbf{N}_u^{e*} d\Omega, \quad \mathbf{C}_{uu}^{ek} = \alpha_d \mathbf{M}_{uu}^{ek} + \beta_d \mathbf{K}_{uu}^{ek}, \quad (5.20)$$

$$\mathbf{K}_{uu}^{ek} = \int_{\Omega^{ek}} \mathbf{B}_u^{e*} \cdot \mathbf{c} \cdot \mathbf{B}_u^e d\Omega, \quad \mathbf{K}_{u\varphi}^{ek} = \int_{\Omega^{ek}} \mathbf{B}_u^{e*} \cdot \mathbf{e}^* \cdot \mathbf{B}_\varphi^e d\Omega, \quad (5.21)$$

$$\mathbf{K}_{\varphi\varphi}^{ek} = \int_{\Omega^{ek}} \mathbf{B}_\varphi^{e*} \cdot \boldsymbol{\kappa} \cdot \mathbf{B}_\varphi^e d\Omega, \quad \mathbf{K}_{\varphi\phi}^{ek} = \int_{\Omega^{ek}} \mathbf{B}_\varphi^{e*} \cdot \boldsymbol{\alpha} \cdot \mathbf{B}_\phi^e d\Omega, \quad (5.22)$$

$$\mathbf{K}_{\phi\phi}^{ek} = \int_{\Omega^{ek}} \mathbf{B}_\phi^{e*} \cdot \boldsymbol{\mu} \cdot \mathbf{B}_\phi^e d\Omega, \quad \mathbf{B}_u^e = \mathbf{L}(\nabla) \cdot \mathbf{N}_u^{e*}, \quad \mathbf{B}_\varphi^e = \nabla \mathbf{N}_\varphi^{e*}, \quad \mathbf{B}_\phi^e = \nabla \mathbf{N}_\phi^{e*}, \quad (5.23)$$

where  $\mathbf{N}_u^{e*}$ ,  $\mathbf{N}_\varphi^{e*}$ ,  $\mathbf{N}_\phi^{e*}$  are the matrices and the row vectors of approximate shape functions, respectively, defined on separate finite elements. The vectors  $\mathbf{F}_u$ ,  $\mathbf{F}_\varphi$ ,  $\mathbf{F}_\phi$  in (5.16), (5.17) are obtained from the boundary conditions, the corresponding right parts of the weak statements, and the finite element approximations.

Note that in ACELAN we use an effective algorithm for symmetric positive definite and quasi-definite matrices (Belokon et al, 2000, 2002; Nasedkin, 2010) for solving finite element Eqs. (5.16)–(5.18) (Benzi et al, 2005; Benzi and Wathen, 2008; Vanderbei, 1995). For example we can use the Newmark method for integrating Cauchy problem (5.16)–(5.19) with symmetric quasidefinite effective stiffness matrices in a formulation where the velocities and the accelerations at the time layers are not given explicitly (Belokon et al, 2002; Nasedkin, 2010). We can also implement in a symmetric form the most important procedures of finite element technologies such as the rotations of the degrees of freedom, the realizations of mechanical and electric boundary conditions, etc. ACELAN package also provides a two-dimensional version (Fig. 5.3) for non-homogeneously polarized materials.

### 5.4 Homogenization of Two-Phase Piezomagnetolectric Materials

Let  $\Omega$  be a representative volume of a two-phase composite heterogeneous body composed of two materials  $\Omega_e$  and  $\Omega_m$  ( $\Omega = \Omega_e \cup \Omega_m$ ), where the phase  $\Omega_e$  has the piezoelectric properties and the phase  $\Omega_m$  has the piezomagnetic properties. Both phases  $\Omega_e$  and  $\Omega_m$  can consist of separate, generally speaking, disjointed subregions  $\Omega_e = \cup_i \Omega_{ei}$ ,  $\Omega_m = \cup_j \Omega_{ej}$ , that in the aggregate have common boundaries and do not

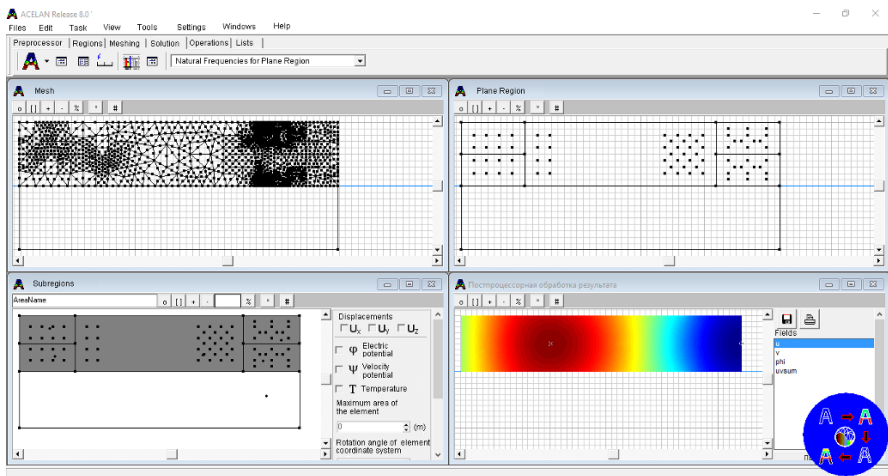


Fig. 5.3: 2D ACELAN package graphical user interface.

overlap each other. Thus, here we consider a two-phase mixture composite with piezoelectric and piezomagnetic fractions.

We assume that the both phases separately do not have magnetoelectric coupling. Then, for static homogenization problem we have the following system of equations

$$\mathbf{L}^*(\nabla) \cdot \mathbf{T} = 0, \quad \nabla \cdot \mathbf{D} = 0, \quad \nabla \cdot \mathbf{B} = 0, \quad (5.24)$$

$$\mathbf{T} = \mathbf{c} \cdot \mathbf{S} - \mathbf{e}^* \cdot \mathbf{E} - \mathbf{h}^* \cdot \mathbf{H}, \quad (5.25)$$

$$\mathbf{D} = \mathbf{e} \cdot \mathbf{S} + \boldsymbol{\kappa} \cdot \mathbf{E} + \boldsymbol{\alpha} \cdot \mathbf{H}, \quad (5.26)$$

$$\mathbf{B} = \mathbf{h} \cdot \mathbf{S} + \boldsymbol{\alpha}^* \cdot \mathbf{E} + \boldsymbol{\mu} \cdot \mathbf{H}, \quad (5.27)$$

$$\mathbf{S} = \mathbf{L}(\nabla) \cdot \mathbf{u}, \quad \mathbf{E} = -\nabla\varphi, \quad \mathbf{H} = -\nabla\phi, \quad (5.28)$$

where  $\mathbf{c} = \mathbf{c}_a$ ,  $\mathbf{e} = \mathbf{e}_a$ ,  $\mathbf{h} = \mathbf{h}_a$ ,  $\boldsymbol{\kappa} = \boldsymbol{\kappa}_a$ ,  $\boldsymbol{\alpha} = \boldsymbol{\alpha}_a$ ,  $\boldsymbol{\mu} = \boldsymbol{\mu}_a$  for  $\mathbf{x} \in \Omega_a$ ,  $a = e, m$ .

We note that  $\mathbf{e}_m = 0$  and  $\boldsymbol{\alpha}_m = 0$  for  $\mathbf{x} \in \Omega_m$ ,  $\mathbf{h}_e = 0$  and  $\boldsymbol{\alpha}_e = 0$  for  $\mathbf{x} \in \Omega_e$ , that is both phases separately do not have magnetoelectric coupling. However for composite magnetoelectric medium due to the coupling of the magnetic and mechanical fields at the piezomagnetic phase  $\Omega_m$  and the coupling of the electric and mechanical fields at the piezoelectric phase  $\Omega_e$  as the result we get the coupling of magnetic and electric fields that does not exist at each separate phase.

We will determine the effective moduli  $\tilde{\mathbf{c}}$ ,  $\tilde{\mathbf{e}}$ ,  $\tilde{\mathbf{h}}$ ,  $\tilde{\boldsymbol{\kappa}}$ ,  $\tilde{\boldsymbol{\alpha}}$ ,  $\tilde{\boldsymbol{\mu}}$  by the following technique (Nasedkin, 2014a,b) similarly for elastic and piezoelectric composites. Let us put some “equivalent” homogeneous piezomagnetoelastic medium  $\Omega$  with the effective moduli  $\tilde{\mathbf{c}}$ ,  $\tilde{\mathbf{e}}$ ,  $\tilde{\mathbf{h}}$ ,  $\tilde{\boldsymbol{\kappa}}$ ,  $\tilde{\boldsymbol{\alpha}}$ ,  $\tilde{\boldsymbol{\mu}}$  into correspondence with initial heterogeneous medium. The constitutive equations for “equivalent” medium, similar to (5.25)–(5.27) for static problem, are given in the forms (with (5.28)):

$$\mathbf{T} = \tilde{\mathbf{c}} \cdot \mathbf{S} - \tilde{\mathbf{e}}^* \cdot \mathbf{E} - \tilde{\mathbf{h}}^* \cdot \mathbf{H}, \quad (5.29)$$

$$\mathbf{D} = \tilde{\mathbf{e}} \cdot \mathbf{S} + \tilde{\boldsymbol{\kappa}} \cdot \mathbf{E} + \tilde{\boldsymbol{\alpha}} \cdot \mathbf{H}, \quad (5.30)$$

$$\mathbf{B} = \tilde{\mathbf{h}} \cdot \mathbf{S} + \tilde{\boldsymbol{\alpha}}^* \cdot \mathbf{E} + \tilde{\boldsymbol{\mu}} \cdot \mathbf{H}. \quad (5.31)$$

We consider the static magnetoelastoelectric problems for representative volume with Eqs. (5.24)–(5.28) for composite medium and with Eqs. (5.24), (5.29)–(5.31), (5.28) for homogeneous medium, and with the following boundary conditions at the external boundary  $\Gamma = \partial\Omega$

$$\mathbf{u} = \mathbf{L}^*(\mathbf{x}) \cdot \mathbf{S}_0, \quad \varphi = -\mathbf{x} \cdot \mathbf{E}_0, \quad \phi = -\mathbf{x} \cdot \mathbf{H}_0, \quad \mathbf{x} \in \Gamma, \quad (5.32)$$

where  $\mathbf{S}_0 = \{\varepsilon_{011}, \varepsilon_{022}, \varepsilon_{033}, 2\varepsilon_{023}, 2\varepsilon_{013}, 2\varepsilon_{012}\}$ ;  $\varepsilon_{0ij}$  are some constant values that do not depend on  $\mathbf{x}$ ;  $\mathbf{E}_0$  and  $\mathbf{H}_0$  are some constant vectors.

Thus, the static problem for an “equivalent” medium is the problem with the effective moduli. It is obvious that the solution of the problem (5.24), (5.29)–(5.31), (5.28), (5.32) has the following form:  $\mathbf{u} = \mathbf{u}_0$ ,  $\mathbf{u}_0 = \mathbf{L}^*(\mathbf{x}) \cdot \mathbf{S}_0$ ,  $\varphi = \varphi_0$ ,  $\varphi_0 = -\mathbf{x} \cdot \mathbf{E}_0$ ,  $\phi = \phi_0$ ,  $\phi_0 = -\mathbf{x} \cdot \mathbf{H}_0$ ,  $\mathbf{S} = \mathbf{S}_0$ ,  $\mathbf{E} = \mathbf{E}_0$ ,  $\mathbf{H} = \mathbf{H}_0$ ,  $\mathbf{T} = \mathbf{T}_0$ ,  $\mathbf{T}_0 = \tilde{\mathbf{c}} \cdot \mathbf{S}_0 - \tilde{\mathbf{e}}^* \cdot \mathbf{E}_0 - \tilde{\mathbf{h}}^* \cdot \mathbf{H}_0$ ,  $\mathbf{D} = \mathbf{D}_0$ ,  $\mathbf{D}_0 = \tilde{\mathbf{e}} \cdot \mathbf{S}_0 + \tilde{\mathbf{k}} \cdot \mathbf{E}_0 + \tilde{\mathbf{a}} \cdot \mathbf{H}_0$ ,  $\mathbf{B} = \mathbf{B}_0$ ,  $\mathbf{B}_0 = \tilde{\mathbf{h}} \cdot \mathbf{S}_0 + \tilde{\mathbf{a}}^* \cdot \mathbf{E}_0 + \tilde{\mathbf{\mu}} \cdot \mathbf{H}_0$ .

From the solution of problem (5.24)–(5.28), (5.32) for a heterogeneous representative volume we find the fields  $\boldsymbol{\varepsilon}$ ,  $\mathbf{E}$ ,  $\mathbf{H}$ ,  $\boldsymbol{\sigma}$ ,  $\mathbf{D}$  and  $\mathbf{B}$ . We note that for problem for a heterogeneous medium the equalities  $\langle \boldsymbol{\varepsilon} \rangle = \boldsymbol{\varepsilon}_0$ ,  $\langle \mathbf{E} \rangle = \mathbf{E}_0$  and  $\langle \mathbf{H} \rangle = \mathbf{H}_0$  hold (Kurbatova et al, 2017; Nasedkin, 2014a,b; Nasedkin and Shevtsova, 2011), where the broken brackets denote the volume-averaged quantities

$$\langle (\dots) \rangle = \frac{1}{|\Omega|} \int_{\Omega} (\dots) d\Omega. \quad (5.33)$$

For problem for the heterogeneous medium we accept the following equations for the determination of effective moduli:  $\langle \mathbf{T} \rangle = \mathbf{T}_0$ ,  $\langle \mathbf{D} \rangle = \mathbf{D}_0$ ,  $\langle \mathbf{B} \rangle = \mathbf{B}_0$ . Note that due to Kurbatova et al (2017); Nasedkin (2014a,b); Nasedkin and Shevtsova (2011) the average energies are equal for both heterogeneous and “equivalent” homogeneous piezomagnetolectric media:  $\langle \mathbf{T} \cdot \mathbf{S} + \mathbf{D} \cdot \mathbf{E} + \mathbf{B} \cdot \mathbf{H} \rangle / 2 = (\mathbf{T}_0 \cdot \mathbf{S}_0 + \mathbf{D}_0 \cdot \mathbf{E}_0 + \mathbf{B}_0 \cdot \mathbf{H}_0) / 2$ .

Now, by using Eqs. (5.32), we can select such boundary conditions, that enable us to obtain obvious expressions for the effective moduli. Indeed, setting in (5.32)

$$\mathbf{S}_0 = S_0 \mathbf{p}_{\zeta}, \quad \zeta = 1, 2, \dots, 6, \quad S_0 = \text{const}, \quad \mathbf{E}_0 = 0, \quad \mathbf{H}_0 = 0, \quad (5.34)$$

where  $\zeta$  is fixed index ranging from 1 to 6;  $\mathbf{p}_{\zeta}$  is the vector from six-dimensional basic set for the components of the strain tensor basic set;  $\mathbf{p}_j = \mathbf{e}_j \mathbf{e}_j$ ,  $j = 1, 2, 3$ ;  $\mathbf{p}_4 = (\mathbf{e}_2 \mathbf{e}_3 + \mathbf{e}_3 \mathbf{e}_2) / 2$ ;  $\mathbf{p}_5 = (\mathbf{e}_1 \mathbf{e}_3 + \mathbf{e}_3 \mathbf{e}_1) / 2$ ;  $\mathbf{p}_6 = (\mathbf{e}_1 \mathbf{e}_2 + \mathbf{e}_2 \mathbf{e}_1) / 2$ ;  $\mathbf{e}_j$  are the basic vectors of the Cartesian coordinate system. From the solution of problem (5.24)–(5.28), (5.32), (5.34) we obtain the calculation formulas for the effective elastic stiffness moduli, piezoelectric moduli and piezomagnetic moduli:

$$\tilde{c}_{\beta\zeta} = \langle T_{\beta} \rangle / S_0, \quad \beta = 1, \dots, 6, \quad \tilde{d}_{j\zeta} = \langle D_j \rangle / S_0, \quad \tilde{h}_{j\zeta} = \langle B_j \rangle / S_0, \quad j = 1, 2, 3. \quad (5.35)$$

If we assume that  $E_0 = \text{const}$  in Eq. (5.32)

$$\mathbf{S}_0 = 0, \quad \mathbf{E}_0 = E_0 \mathbf{e}_m, \quad m = 1, 2, 3, \quad \mathbf{H}_0 = 0, \quad (5.36)$$

then from the solution of problem (5.24)–(5.28), (5.32), (5.36) we find the effective piezoelectric moduli, dielectric permittivity moduli and magnetolectric coupling coefficients

$$\tilde{e}_{m\beta} = -\langle T_{\beta} \rangle / E_0, \quad \beta = 1, 2, \dots, 6, \quad \tilde{k}_{jm} = \langle D_j \rangle / E_0, \quad \tilde{a}_{jm} = \langle B_j \rangle / E_0, \quad j = 1, 2, 3. \quad (5.37)$$

If we assume that  $H_0 = \text{const}$  in Eq. (5.32)

$$\mathbf{S}_0 = 0, \quad \mathbf{E}_0 = 0, \quad \mathbf{H}_0 = H_0 \mathbf{e}_l \quad l = 1, 2, 3, \quad (5.38)$$

then from the solution of problem (5.24)–(5.28), (5.32), (5.38) we find the effective piezomagnetic moduli, magnetoelectric coupling coefficients and magnetic permeability moduli

$$\tilde{h}_{l\beta} = -\langle T_\beta \rangle / H_0, \quad \beta = 1, 2, \dots, 6, \quad \tilde{\alpha}_{jl} = \langle D_j \rangle / H_0, \quad \tilde{\mu}_{jl} = \langle B_j \rangle / H_0, \quad j = 1, 2, 3. \quad (5.39)$$

Thus, we can find the full set of the effective moduli of piezomagnetolectric composite mediim with arbitrary anisotropy class. For that we solve six problems (5.24)–(5.28), (5.32), (5.34), obtain the solutions of these problems, calculate the averaged by (5.33) mechanical stresses, electric flux densities, magnetic flux densities, and find the moduli from (5.35). Similarly, we solve three problems (5.24)–(5.28), (5.32), (5.36), obtain the solutions of these problems, and find the moduli from (5.37). Finally we solve three problems (5.24)–(5.28), (5.32), (5.38), obtain the solutions of these problems, and find the moduli from (5.39). Note, that the quantities  $\langle T_\beta \rangle$ ,  $\langle D_j \rangle$  and  $\langle B_j \rangle$  in ((5.35), (5.37), (5.39) are different, since they are calculated from the solutions of the problems (5.24)–(5.28), (5.32) with different boundary conditions (5.32): (5.34), (5.36) and (5.38).

For the homogenization problems for two-phase piezomagnetolectric composites in ACELAN-COMPOS package we can also use other less popular boundary conditions. Namely, instead of principal boundary conditions (5.32) with linear functions we can accept natural boundary conditions with constant quantities  $\mathbf{T}_0$ ,  $\mathbf{D}_0$  and  $\mathbf{B}_0$

$$\mathbf{L}^*(\mathbf{n}) \cdot \mathbf{T} = \mathbf{L}^*(\mathbf{n}) \cdot \mathbf{T}_0, \quad \mathbf{n} \cdot \mathbf{D} = \mathbf{n} \cdot \mathbf{D}_0, \quad \mathbf{n} \cdot \mathbf{B} = \mathbf{n} \cdot \mathbf{B}_0, \quad \mathbf{x} \in \Gamma, \quad (5.40)$$

and the mixed boundary conditions from (5.32), (5.40)

$$\mathbf{L}^*(\mathbf{n}) \cdot \mathbf{T} = \mathbf{L}^*(\mathbf{n}) \cdot \mathbf{T}_0, \quad \varphi = -\mathbf{x} \cdot \mathbf{E}_0, \quad \mathbf{n} \cdot \mathbf{B} = \mathbf{n} \cdot \mathbf{B}_0, \quad \mathbf{x} \in \Gamma, \quad (5.41)$$

or

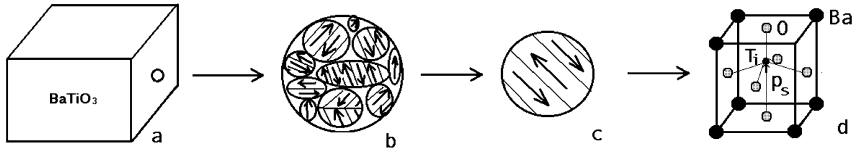
$$\mathbf{u} = \mathbf{L}^*(\mathbf{x}) \cdot \mathbf{S}_0, \quad \mathbf{n} \cdot \mathbf{D} = \mathbf{n} \cdot \mathbf{D}_0, \quad \mathbf{n} \cdot \mathbf{B} = \mathbf{n} \cdot \mathbf{B}_0, \quad \mathbf{x} \in \Gamma, \quad (5.42)$$

or the other boundary conditions with use the relation  $\phi = -\mathbf{x} \cdot \mathbf{H}_0$  instead of  $\mathbf{n} \cdot \mathbf{B} = \mathbf{n} \cdot \mathbf{B}_0$  in (5.32), (5.40)–(5.42).

In ACELAN-COMPOS package we can also consider the particular cases of this model without taking into account the connectivity between some physical fields. For example, we can obtain the model of piezoelectric material, if we assume  $\mathbf{h} = 0$ ,  $\boldsymbol{\alpha}$  in (5.24), (5.25), and if we ignore the equations for magnetic fields.

## 5.5 Inhomogenous Polarization

The possibility to solve polarization definition problems in package ACELAN is based on the study by A.S. Skaliukh (Belokon and Skaliuh, 2010; Skaliukh et al, 2015; Soloviev et al, 2015). In this study a representative volume of polycrystalline



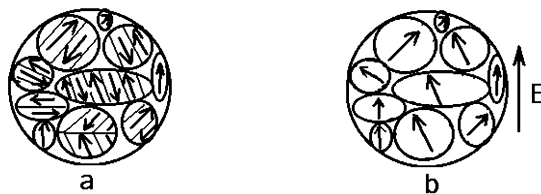
**Fig. 5.4:** Structure of perovskite-type polycrystalline ferroelectric material on example of barium titanate ceramic: a – ceramic sample; b – representative volume; c – dipoles in the crystallite; d – nuclear cell (Belokon and Skaliuh, 2010).

ferroelectric continuum which contains a great number of crystallites is analyzed. Each crystallite contains a great number of domains, and each domain has a set of cells with the same direction of spontaneous polarization, as shown in Fig. 5.4.

Each of the domains in the ferroelectric phase has the spontaneous polarization  $\mathbf{p}_s$  and the spontaneous deformation  $\varepsilon_s$ , and one of the principal axes coincides with the direction of the spontaneous polarization. The domain switching process begins inside all crystallites when the electric field  $\mathbf{E}$  is applied to the sample. All domains are arranged in a direction close to the direction of the electric field as the internal crystalline structure allows them. Fig. 5.5a shows a representative volume in the depolarized state, and Fig. 5.5b shows the pattern distribution of the domains after polarization. It was established experimentally that the domain switching begins only when the electric field reaches certain "threshold" values.

Numerical experiments were conducted with plain piezoelectric transducer (see Fig. 5.6) with stress free boundaries and with electrodes on upper and lower surfaces on the transducer. Material was PZT-4, the model included a study of damping with coefficients  $\alpha = 2.7 \cdot 10^{-2}$ ,  $\beta = \zeta = 3.84 \cdot 10^{-8}$ . Length of the rod was 1 cm, its thickness changed in numerical experiments from 0.025 to 0.200 cm. Oscillations were excited by the voltage of 200 V.

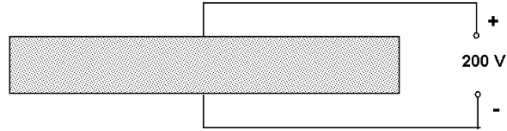
The first part of the study consisted in analyzing mode shapes of the rod. In this research the longitudinal oscillations with coupled electro-mechanical fields were observed. We suggested that the polarization field corresponded to the strain field. This type of functions can be described as  $F(x) = \sin(\pi kx/l)$ , where  $l$  is the length of the rod. Effectiveness of piezoelectric device can be estimated by electro-mechanical coupling coefficient. We used the following representation:



**Fig. 5.5** Direction of the vectors of spontaneous polarization in domains: a – before polarization; b – after polarization Belokon and Skaliuh (2010).



**Fig. 5.6** Scheme of piezoelectric rod.

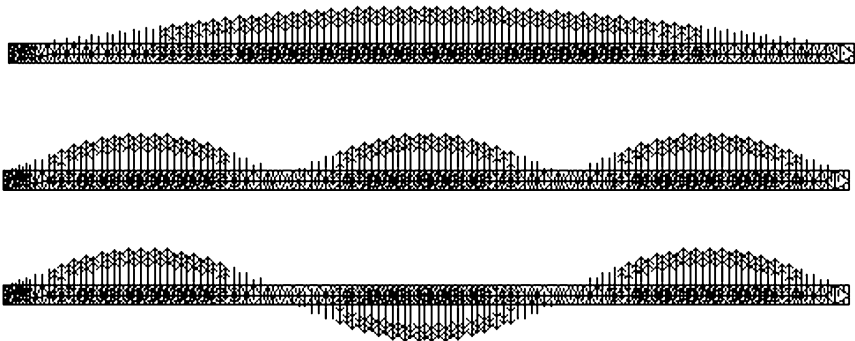


$$K^2 = \frac{f_a^2 - f_r^2}{f_a^2}, \tag{5.43}$$

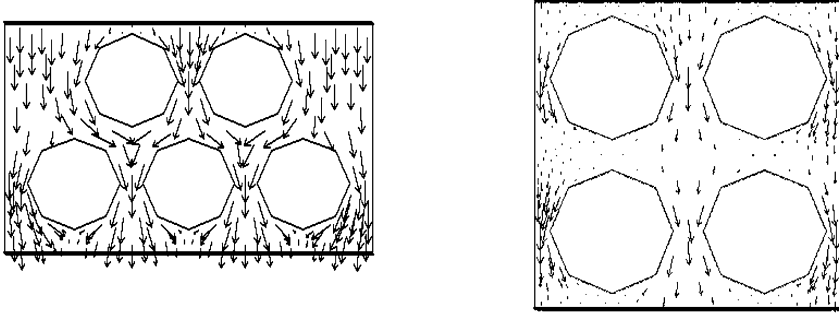
where  $f_r$  is the resonance frequency and  $f_a$  is the antiresonance frequency. Some of observed polarization fields are present in Fig. 5.7.

Three resonance and antiresonance frequencies were analyzed for each case of polarization field. We estimated effectiveness of the transducer by comparing electro-mechanical coupling coefficient of the heterogeneously polarized specimen with a uniformly polarized one. Frequency differences between different cases were less than 5 %, but electro-mechanical coupling coefficient growth was large in some cases. For the first eigenmode no better scheme was found than the case of polarization field shown in Fig. 5.7 (top). Fig. 5.7 (middle) shows the most effective polarization field obtained for the second mode, and Fig. 5.7 (bottom) shows the best field for the third mode. In all cases the specimens of different thickness were analyzed.

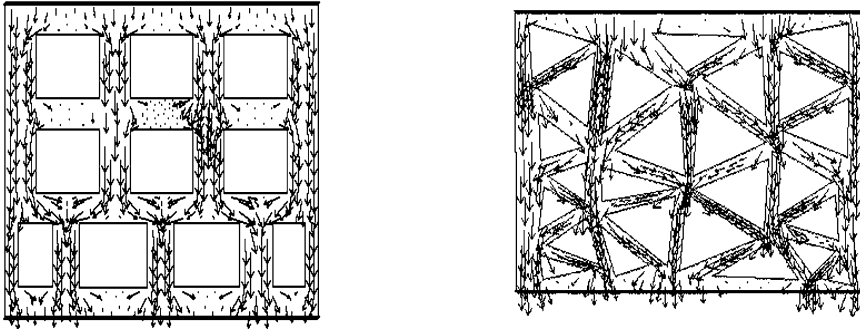
In most cases the polarization of porous ceramics is considered as uniform over the body, directed along the applied electric field. However numerical experiments with finite element models in ACELAN package showed that in some cases these observation do not take place. Let us consider some example of the representative volumes. Top and bottom sides of the bodies have electrodes. Potentials applied to these electrodes creates polarization field in the material, transforming ceramics into



**Fig. 5.7:** Some inhomogeneous polarization fields.



**Fig. 5.8:** Polarized porous ceramics with round pores.



**Fig. 5.9:** Polarized porous ceramics with different types of pores.

piezoceramics. Pores are modeled as void areas without any material. Figures 5.8 and 5.9 shows examples of polarization field in bodies with different geometry and porosity percentage.

These models demonstrates that there are areas in the bodies where polarization direction is not the same with applied external field. In some areas there are no polarization at all. This fact has significant influence on piezoelectric properties of the bodies. Detailed study is presented in Vernigora et al (2011).

### 5.6 Three-Dimensional Models for Composite Materials

In 3D models the most common way to build a representative volume is to simulate a cube with predefined or randomized geometrical entities inside (Skaliukh et al, 2015). Representative volume technique is widely used in material science. Specialized module ACELAN-COMPOS consists of common finite element library, representative

volume generator and graphical user interface (GUI) for user interaction. The user has possibilities to choose among one of three basic two-phase models of material distribution in ACELAN package (Fig. 5.10): granules in the matrix, composites with two connected phases and rods (pillars) in the matrix. Each model is based on the enumeration algorithm which decides if the finite element belongs to material *A* or to material *B*.

ACELAN package was developed using .NET platform and C#. ACELAN has advanced program interfaces for exporting and importing models and meshes in .stl, .inp, .gmsh formats, and internal binary format developed for the package. ACELAN package has fully functional models for finite element analysis of generic meshes, but the main feature of new ACELAN-COMPOS package concern to design of active composites with tacking into account their internal structures.

In case of different types of materials in single composite (e.g. elastic and piezo-electric, piezomagnetic and piezoelectric, etc.) the number of degrees of freedom for each material can be different. This fact is taken into account during the assembly of global stiffness matrix to reduce its size.

Three algorithms were created to describe random material distribution for specific patterns: biphasic composite with connectivity of each phase, granules of predefined size, and rods of the second material in the matrix. Both patterns are inspired by well-known classes of composites: the first one can be classified as 3-3 or mixed (bulk) composite, the second one – as 3-0 composite, and last case as 3-1 composite (rods in polymer) in terms described by Newnham et al (1978).

Let us assume that the representative volume consists of clusters, each cluster consists of 512 equal cubes which are elements with regular distribution. Each cluster is randomly generated and placed in the representative volume. The number of clusters can vary from 1 to  $8n$ , as far as we suggest that all clusters are of the

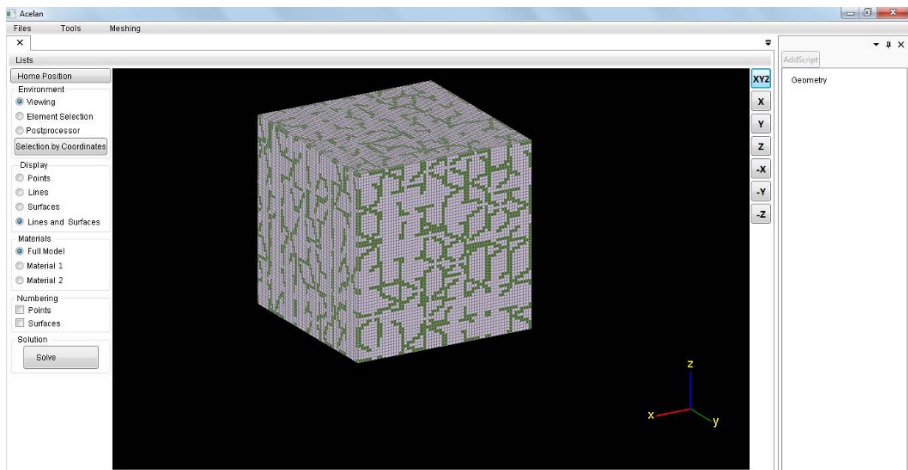


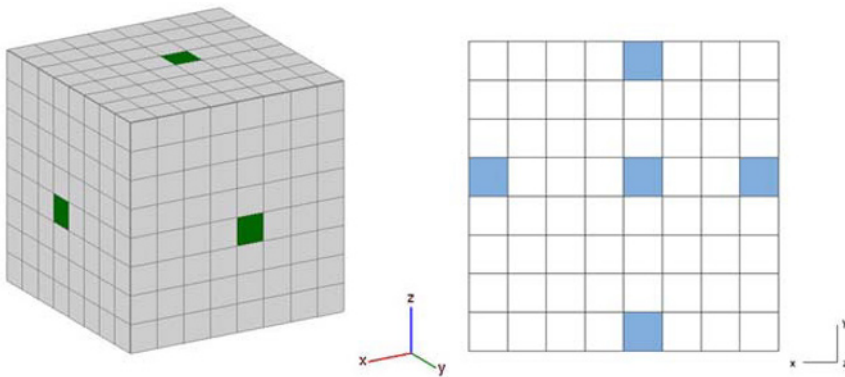
Fig. 5.10: 3D ACELAN package graphical user interface.

same size and the shape of the volume is predefined. The presented algorithms can be modified by changing assumptions about cluster size. Let's also state that the connectivity of material is a possibility to reach any element of the phase from any other element of the phase by passing through planes of elements. Connection of edges or nodes is not regarded as connectivity. Key point is considered as an element with predefined materials that cannot be changed. To make a random distribution of a biphasic composite made from materials *A* and *B*, we place 8 key points of the material *A* near each of the cube vertices and a starting point somewhere inside the cluster.

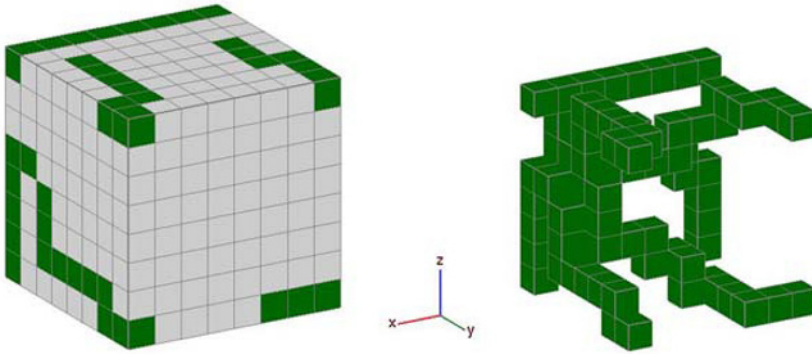
The connectivity of material *B* inside the cluster is guaranteed by the algorithm, the connectivity between clusters is achieved by adding 6 key points of material *B*, one for each external plane of cluster (Fig. 5.11). After that we make the shortest path between the starting point and the key point of the material *A*. The shortest path gives us about 15 % of the material *A* (Fig. 5.12). After that we add more elements to the path until the needed percentage reached.

The iterative process of adding new elements to the material *A* selects possible candidates on each step. The candidate element is an element that does not belong to the material *A* and can be removed from material *B* without disrupting the connectivity of the materials. Selecting such candidates is a basic problem of the graph theory. After the set of candidates is build, the algorithm randomly selects one candidate, adds it to the material *A* and starts the next iteration. A 2D example of a single step of this process is presented in Fig. 5.13. Examples of different representative volumes are shown in Fig. 5.14.

The described algorithm can be used independently in each part of the representative volume starting from  $d = 4$ . This fact allows us to use simple parallel computational techniques to increase the speed of numerical calculations. The sec-

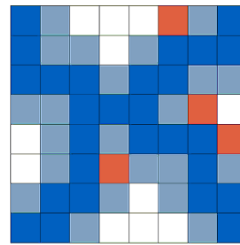


**Fig. 5.11:** Green elements represent material *B*, gray elements represent material *A*. The key points of the material *B* guarantee that the neighboring elements are connected by both phases.



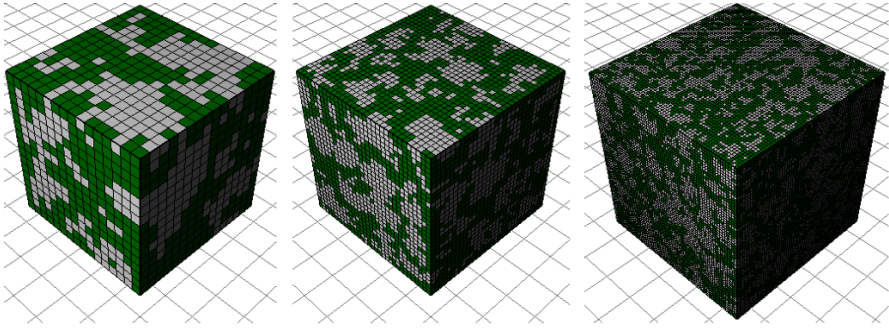
**Fig. 5.12:** Green elements represent material A, gray elements represent material B. Initial distribution (up to 15 % of material A).

**Fig. 5.13** The layer of the representative volume during some algorithm step of materials distribution. Dark blue color denotes the material A, light blue color denotes the candidates to be added to the material A, red color denotes the candidates that would disrupt the connectivity of the material B if added to A, and white denotes the material B.

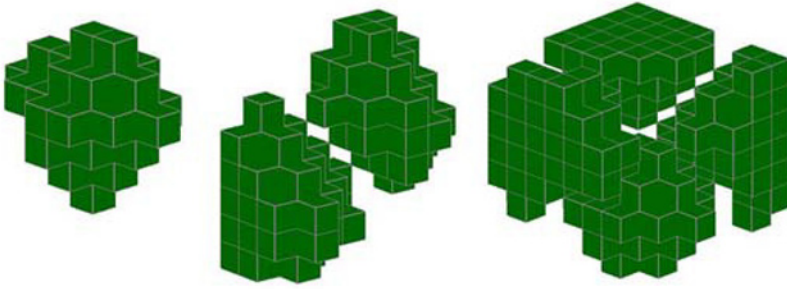


ond algorithm is designed for the cases where material or pores are distributed in the form of isolated areas in the shape of granules. Granular composites are widely used in engineering and industry. As an example we consider granular composite polyester resin with the addition of calcium carbonate with mixtures of magnesium carbonate in the form of granules. The maximal and minimal sizes and overall percentage of granules can be set as input. On each step of iteration process, we select random key point in the cluster, with restriction that forbids the merging of granules (Fig. 5.15). Using this restriction, we select candidates for the next element to join the granule. There are up to six possible directions (Fig. 5.16) in which we can add new element. Random distribution for each candidate allows us to construct granules of natural form. 3D examples shown in Fig. 5.17.

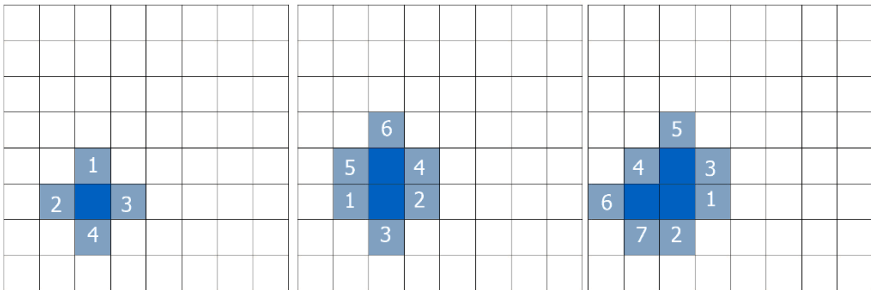
The third type of representative volume contains rods placed in the skeleton of the main material. This is a straightforward algorithm based on placing 2D pattern on the bottom of the volume and extruding it through the body (Fig. 5.18).



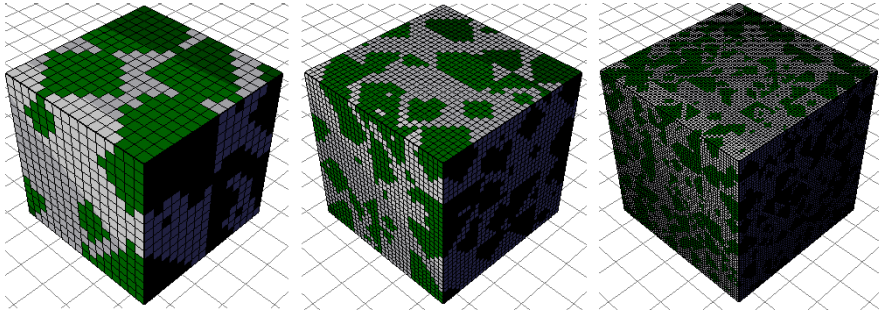
**Fig. 5.14:** Different representative volumes with two phases for composites of 3–3 connectivities.



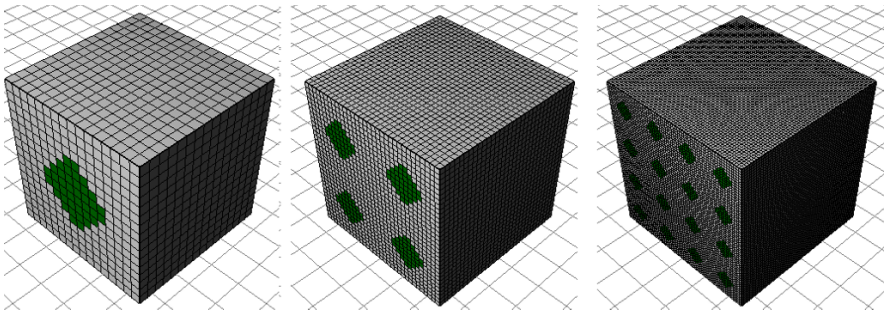
**Fig. 5.15:** Granules are distinguished by 1 element thick area.



**Fig. 5.16:** Adding elements to the granule in 2D case.



**Fig. 5.17:** Example: granular composite polyester resin with the addition of calcium carbonate with mixtures of magnesium carbonate in the form of granules. The maximal and minimal sizes and overall percentage of granules can be set as user input.



**Fig. 5.18:** Rods of different size in representative volumes with different meshes.

## 5.7 Conclusions

In the current paper we have described the models of active (piezomagnetolectric and piezoelectric) composites and the possibilities of their simulation in the finite element software ACELAN and ACELAN-COMPOS.

The presented methods and programs are capable of solving the problems of definition of effective material characteristics for representative volumes with electroelastic and magnetoelastic properties. Both 2D and 3D cases we considered in the developed algorithms. Different types of the material distribution inside the representative volume were simulated in the mesh generating module. ACELANs program interfaces allows us to use generated meshes and models from external software packages and to use the imported meshes from other CAD/CAE software. ACELAN-COMPOS package allows us to determine the properties of two-phase active materials with 3–0, 3–3 and 3–1 connectivities.

Future possibilities of ACELAN-COMPOS package will be associated with the other types of the representative volumes and with the modeling of surface effects

and surface finite elements for piezoelectric and piezomagnetolectric composite media on the micro- and nanoscale (Eremeyev and Nasedkin, 2017; Nasedkin, 2017).

**Acknowledgements** This work was supported by the Ministry of Education and Science of Russia, competitive part of state assignment, No. 9.1001.2017/PCh.

## References

- Bathe K, Wilson EL (1976) *Numerical Methods in Finite Elements Analysis*. Prentice-Hall, Englewood Cliffs, N
- Belokon AV, Skaliuh AS (2010) *Mathematical Modeling of Irreversible Processes of Polarization* (in Russ.). FIZMATLIT, Moscow
- Belokon AV, Eremeyev VA, Nasedkin AV, Solov'yev AN (2000) Partitioned schemes of the finite-element method for dynamic problems of acoustoelectroelasticity. *Journal of Applied Mathematics and Mechanics* 64(3):367–377
- Belokon AV, Nasedkin AV, Solov'yev AN (2002) New schemes for the finite-element dynamic analysis of piezoelectric devices. *Journal of Applied Mathematics and Mechanics* 66(3):481–490
- Benzi M, Wathen AJ (2008) Some preconditioning techniques for saddle point problems. In: Schilders WHA, van der Vorst HA, Rommes J (eds) *Model Order Reduction: Theory, Research Aspects and Applications*, Springer, Berlin, Heidelberg, *Mathematics in Industry*, vol 13, pp 195–211
- Benzi M, Golub GH, Liesen J (2005) Numerical solution of saddle point problems. *Acta Numerica* 14:1–137
- Bowen CR, Perry A, Kara H, Mahon SW (2001) Analytical modelling of 3-3 piezoelectric composites. *Journal of the European Ceramic Society* 21(10):1463–1467
- Eremeyev VA, Nasedkin AV (2017) Mathematical models and finite element approaches for nanosized piezoelectric bodies with uncoupled and coupled surface effects. In: Sumbatyan MA (ed) *Wave Dynamics and Composite Mechanics for Microstructured Materials and Metamaterials*, Springer, Singapore, *Advanced Structured Materials*, vol 59, pp 1–18
- Iyer S, Venkatesh TA (2014) Electromechanical response of (3-0,3-1) particulate, fibrous, and porous piezoelectric composites with anisotropic constituents: A model based on the homogenization method. *International Journal of Solids and Structures* 51(6):1221–1234
- Kurbatova NV, Nadolin DK, Nasedkin AV, Nasedkina AA, Oganeyan PA, Skaliukh AS, Soloviev AN (2017) Mathematical models and finite element approaches for nanosized piezoelectric bodies with uncoupled and coupled surface effects. In: Sumbatyan MA (ed) *Models of active bulk composites and new opportunities of ACELAN finite element package*. In: *Methods of wave dynamics and mechanics of composites for analysis of microstructured materials and metamaterials*, Springer, Singapore, *Advanced Structured Materials*, vol 59, pp 133–158
- Lee J, Boyd JG, Lagoudas DC (2005) Effective properties of three-phase electro-magneto-elastic composites. *International Journal of Engineering Science* 43(10):790–825
- Li JY (2000) Magneto-electroelastic multi-inclusion and inhomogeneity problems and their applications in composite materials. *International Journal of Engineering Science* 38(18):1993–2011
- Martínez-Ayuso G, Friswell MI, Adhikari S, Khodaparast HH, Berger H (2017) Homogenization of porous piezoelectric materials. *International Journal of Solids and Structures* 113(Supplement C):218–229
- Nan CW, Bichurin MI, Dong S, Viehland D, Srinivasan G (2008) Multiferroic magnetoelectric composites: Historical perspective, status, and future directions. *Journal of Applied Physics* 103(3):031,101
- Nasedkin A (2014a) Modeling of magnetoelectric composites by effective moduli and finite element methods. theoretical approaches. *Ferroelectrics* 461(1):106–112



- Nasedkin A (2017) Size-dependent models of multiferroic materials with surface effects. *Ferroelectrics* 509(1):57–63
- Nasedkin AV (2010) Some finite element methods and algorithms for solving acousto-piezoelectric problems. In: Paronov IA (ed) *Piezoceramic Materials and Devices*, Nova Science Publ., NY, pp 177–218
- Nasedkin AV (2014b) Multiscale computer design of piezomagnetolectric mixture composite structures. *AIP Conference Proceedings* 1627(1):64–69
- Nasedkin AV, Shevtsova MS (2011) Improved finite element approaches for modeling of porous piezocomposite materials with different connectivity. In: Paronov IA (ed) *Ferroelectrics and Superconductors: Properties and Applications*, Nova Science Publ., NY, pp 231–254
- Nasedkin AV, Skaliukh AS, Soloviev AN (2014) New models of coupled active materials for finite element package ACELAN. *AIP Conference Proceedings* 1637(1):714–723
- Newnham RE, Skinner DP, Cross LE (1978) Connectivity and piezoelectric-pyroelectric composites. *Materials Research Bulletin* 13(5):525–536
- Nguyen BV, Challagulla KS, Venkatesh TA, Hadjiloizi DA, Georgiades AV (2016) Effects of porosity distribution and porosity piezoelectric foams. *Smart Materials and Structures* 25(12):125,028
- Ramesh R, Kara H, Bowen CR (2005) Finite element modelling of dense and porous piezoceramic disc hydrophones. *Ultrasonics* 43(3):173–181
- Ringgaard E, Lautzenhiser F, Bierregaard LM, Zawada T, Molz E (2015) Development of porous piezoceramics for medical and sensor applications. *Materials* 8(12):8877–8889
- Rybyanets AN (2010) Ceramic piezocomposites: modeling, technology, characterization. In: Paronov IA (ed) *Piezoceramic Materials and Devices*, Nova Science Publ., NY, pp 115–174
- Rybyanets AN (2011) Porous piezoceramics: theory, technology, and properties. *IEEE Transactions on Ultrasonics, Ferroelectrics, and Frequency Control* 58(7):1492–1507
- Rybyanets AN, Nasedkin AV, Naumenko AA, Shvetsova NA, Lugovaya MA, Petrova EI (2015) Optimization of finite element models for porous ceramic piezoelements by piezoelectric resonance analysis method. In: Paronov IA, Chang SH, Theerakulpisut S (eds) *Advanced Materials – Studies and Applications*, Nova Science Publ., NY, pp 147–168
- Skaliukh AS, Soloviev AN, Oganessian PA (2015) Modeling of piezoelectric elements with inhomogeneous polarization in acelan. *Ferroelectrics* 483(1):95–101
- Soloviev AN, Oganessian PA, Skaliukh AS (2015) Modeling of piezoelectric elements with inhomogeneous polarization by using acelan. In: Paronov IA, Chang SH, Theerakulpisut S (eds) *Advanced Materials – Studies and Applications*, Nova Science Publ., NY, pp 169–192
- Tang T, Yu W (2008) Variational asymptotic homogenization of heterogeneous electromagnetoelastic materials. *International Journal of Engineering Science* 46(8):741–757
- Topolov VY, Bowen CR (2009) *Electromechanical Properties in Composites Based on Ferroelectrics*. Springer, London
- Vanderbei RJ (1995) Symmetric quasidefinite matrices. *SIAM Journal on Optimization* 5(1):100–113
- Vernigora GD, Lupeiko TG, Skaliukh AS, Soloviev AN (2011) About polarization and effective properties identification for porous ceramics. *DSTU Herald (Russ edition)* 11(4 (55)):462–469
- Zhang ZK, Soh AK (2005) Micromechanics predictions of the effective moduli of magneto-electroelastic composite materials. *European Journal of Mechanics - A/Solids* 24(6):1054–1067
- Zienkiewicz OC, Morgan K (1983) *Finite Elements and Approximation*. John Wiley and Sons, N.Y.

# Chapter 6

## Robust Displacement and Mixed CUF-Based Four-Node and Eight-Node Quadrilateral Plate Elements

Thi Huyen Cham Le, Michele D'Ottavio, Philippe Vidal, and Olivier Polit

**Abstract** This paper presents two classes of new four-node and eight-node quadrilateral finite elements for composite plates. Variable kinematics plate models are formulated in the framework of Carrera's Unified Formulation, which encompass Equivalent Single Layer as well as Layer-Wise models, with the variables that are defined by polynomials up to 4th order along the thickness direction  $z$ . The two classes refer to two variational formulations that are employed to derive the finite elements matrices, namely the Principle of Virtual Displacement (PVD) and Reissner's Mixed Variational Theorem (RMVT). For the PVD based elements, the main novelty consists in the extension of two field compatible approximations for the transverse shear strain field, referred to as QC4 and CL8 interpolations, which eliminate the shear locking pathology by constraining only the  $z$ -constant transverse shear strain terms, to all variable kinematics plate elements. Moreover, for the first time the QC4 and CL8 interpolations are introduced for the transverse shear stress field within RMVT based elements. Preliminary numerical studies are proposed on homogeneous isotropic plates that demonstrate the absence of spurious modes and of locking problems as well as the enhanced robustness with respect to distorted element shapes. The new QC4 and CL8 variable kinematics plate elements display excellent convergence rates and yield accurate responses for both, thick and thin plates.

### 6.1 Introduction

Composite laminates and sandwich structures are increasingly used in engineering application because of their excellent mechanical properties such as high specific stiffness and strength. Due to geometric considerations, these structures are often

---

Thi Huyen Cham Le · Michele D'Ottavio · Philippe Vidal · Olivier Polit  
UPL, Univ Paris Nanterre, LEME, 50 Rue de Sèvres, 92410 Ville d'Avray, France  
e-mail: thi.huyencham.le@parisnanterre.fr, mdottavi@parisnanterre.fr  
e-mail: pvidal@parisnanterre.fr, opolit@parisnanterre.fr

© Springer Nature Singapore Pte Ltd. 2018  
H. Altenbach et al. (eds.), *Analysis and Modelling of Advanced Structures and Smart Systems*, Advanced Structured Materials 81,  
[https://doi.org/10.1007/978-981-10-6895-9\\_6](https://doi.org/10.1007/978-981-10-6895-9_6)

described by two-dimensional plate or shell models for the design and simulation aspects. It is necessary to develop the computational models for accurate knowledge of both global and local response. However, the classical approaches, i.e., the Classical Laminate Plate Theory (CLPT) and the First-order Shear Deformation Theory (FSDT) (Reddy, 2004), are not sufficient for a predictive and accurate modeling due to complicating effects, such as anisotropy, heterogeneity and transverse shear compliance. Based on Kirchhoff-Love assumptions, CLPT neglects transverse shear deformation in the laminates. FSDT is based on Reissner-Mindlin plate theory and the transverse shear strain is assumed to be constant over the entire plate thickness. A shear correction factor is thus required to tune the accuracy of transverse shear deformation of the model.

Various two-dimensional plate theories categorize into two groups as (i) Equivalent Single Layer (ESL) and (ii) Layer-Wise (LW) models (Reddy, 1993). In the ESL approach, the number of unknowns is independent of the number of layers constituting the plate. CLPT, FSDT and the high-order shear deformation theories (HSDT) are mostly used for ESL models. HSDT are constructed by enhancing the kinematics for the transverse shear deformation and retaining the plane stress condition. No shear correction factors are required in HSDT. Several representative HSDT have been developed, e.g., Reddy's third-order theory (Reddy, 1984) and the Sinus model of Touratier (1991). An overview of ESL models can be found in Sayyad and Ghugal. (2015).

By employing a single approximation for the displacement field across all layers of the laminate, the continuity of the transverse shear and normal stress at the interface between adjacent layers with different material properties cannot be fulfilled. Zig-Zag theories describe a piece-wise continuous displacement field in the thickness direction and are, hence, able to satisfy the interlaminar continuity condition for the transverse stresses (Demasi, 2012). Note that several Zig-Zag theories have been proposed, which do not exactly fulfill the interlaminar continuity of transverse stresses, see, e.g., Barut et al (2013). The paper by Carrera (2003a) reviews several independent ways of introducing Zig-Zag theories proposed for the analysis of multilayered plates and shells. An interesting approach relies on the use of Reissner's Mixed Variational Theorem (RMVT) (Reissner, 1984), which allows to introduce independent approximations for the displacement and transverse stress fields (Carrera, 2001). Tessler (2015) proposed a Zig-Zag theory by employing RMVT in a two-step procedure. In the context of RMVT, the so-called Murakami's Zig-Zag function (MZZF) provides a simple means for representing displacement fields with a slope discontinuity at the layers' interfaces (Murakami, 1986). More recently, MZZF has been used to enhance displacement-based ESL models (Carrera, 2004; Vidal and Polit, 2011).

More accurate predictions of short wavelength responses, however, require an explicit representation of individual layers, which calls for a LW approach, see, e.g., the seminal paper by Sun and Whitney (1973) and the comprehensive discussion by Robbins Jr and Reddy (1993). Several works develop the LW models within a displacement-based approach (Reddy, 1987; Ferreira, 2005) and within the mixed

RMVT formulation (Toledano and Murakami, 1987; Carrera, 1998, 2000; Rao and Desai, 2004).

The resulting computational model of a LW approach has a number of unknowns that depends on the number of constituting layers, which can become very large. Several approaches have been thus proposed in order to reduce the computational cost by limiting the use of the expensive high-order models to small regions hosting the local stress gradient of interest, while lower-order models are used for large portions of the structure characterized by smooth, long wavelength gradients. In the framework of the finite element method we can mention the direct interface coupling (Robbins Jr and Reddy, 1996; Carrera et al, 2013), which can be enhanced on the basis of an extended variational formulation (Wenzel et al, 2014), the transition element approach (Feng and Hoa, 1998; Carrera et al, 2017), and the overlapping mesh approach based on Arlequin method (Hu et al, 2009).

A flexible manner for introducing a general description of two-dimensional formulations for modeling the composite structures has been proposed by Carrera thanks to a dedicated Unified Formulation (Carrera, 2003b). By an extensive use of compact index notations, Carrera's Unified Formulation (CUF) permits to implement a series of hierarchical, variable kinematics models within a single program by using a limited number of model-invariant  $3 \times 3$  *fundamental nuclei*. In CUF, the model is constructed by using the order  $N$  for the polynomial expansion for all unknown functions; different models can be then obtained upon penalizing some specific terms (Carrera et al, 2014, 2015). Further generalizations of CUF have been proposed in Demasi (2008, 2010, 2013); Botshekanan Dehkordi et al (2013); D'Ottavio (2016); D'Ottavio et al (2016).

The first FEM application of variable kinematics CUF models has been proposed by Carrera and Demasi (2002a,b), where the matrices of plate elements have been obtained by referring to the weak forms expressed by the Principle of Virtual Displacement (PVD) and Reissner's Mixed Variational Theorem (RMVT). The displacement field can be described in an ESL or LW manner, with the possibility of superposing MZZF to an ESL description, whereas transverse stresses are always described in an LW sense. Four-, eight- and nine-node elements have been presented with  $C^0$  isoparametric interpolations for all unknown functions.

A robust finite element (FE) should overcome numerical pathologies, i.e., it should have only six rigid body modes without spurious zero-energy modes and it should be free from numerical lacks that could degrade the solution's accuracy in case of distorted element geometries or extreme thickness ratios.

It is well known that  $C^0$  isoparametric displacement approximations for shear deformable plates cause a spurious over-constraint in the thin-plate limit, which dramatically underestimates the bending deformation: the transverse shear locking. Several techniques have been proposed in order to prevent this pathology affecting FSDT-based plate/shell element, most of which can be stated from hybrid-mixed approaches (Pian and Sumihara, 1995). The most commonly used techniques are reduced integration methods, which, however, entail spurious zero-energy modes (Belytschko et al, 2000), and so-called B-bar techniques (Hughes, 1987), which employ a specific constraint for transverse shear strain field. Examples of such B-bar

methods are given by the so-called Kirchhoff mode (Hughes and Tezduyar, 1981), the Assumed Natural Strain (ANS) method (MacNeal, 1982; Park et al, 1989), the Mixed Interpolation of Tensorial Components (MITC) approach (Bathe and Dvorkin, 1985), the interpolations constructed using the field-consistency paradigm (Somashekar et al, 1987), the Discrete Shear elements (Batoz and Lardeur, 1989) or the Discrete Shear Gap (DSG) elements (Bletzinger et al, 2000).

All methods mentioned above were developed for FSDT kinematics and only few works are available on variable kinematics models. A selective reduced quadrature has been used in Robbins Jr and Reddy (1993); Carrera and Demasi (2002a); D'Ottavio et al (2006). Rectangular four- and nine-node elements have been proposed upon extending the MITC approach to CUF-based displacement-based models (Carrera et al, 2010; Cinefra et al, 2013). Kulikov and Plotnikova (2016) proposed a four-node quadrilateral plate element employing a hybrid-mixed ANS approach in conjunction with a variable kinematics approach formulated in terms of Sampling Surfaces (SaS). In these works, *all* transverse shear strain terms issued from the high-order kinematics are constrained according to the adopted MITC or ANS approach. However, since high-order shear deformation terms depend on the plate thickness and will vanish in thin-plate limit, the locking behavior is produced by the first-order Reissner-Mindlin kinematics only. As a matter of fact, the convergence rates of CUF elements do not depend on the polynomial order  $N$  defining the plate kinematics (D'Ottavio et al, 2006).

Concerning RMVT-based elements, it is worth reporting the hybrid-mixed developments by Li (1989); Pian and Li (1990); Hoa and Feng (1998), whose assumed transverse stress fields lead to robust finite elements for laminated plates. More recently, nine-node plate/shell element have been proposed in which the MITC technique is employed to interpolate the transverse shear stresses (Chinosi et al, 2013; Cinefra et al, 2014).

Based on the classical CUF-based FEM of Carrera and Demasi (2002a,b), the authors have recently proposed a new robust four-node quadrilateral plate element (Le et al, 2017): a special transverse shear locking correction, denoted QC4, is formulated by referring to the field consistency paradigm and applied only to the thickness-independent part of the transverse shear strain. This method was firstly proposed by Polit *et al* for FSDT (Polit et al, 1994), and subsequently extended to a refined Sinus-based kinematics (Polit et al, 2012). The previous paper (Le et al, 2017) was limited to four-node elements and to displacement-based CUF models. The purpose of this paper is to extend the methodology for obtaining robust FE to eight-node finite elements as well as to variable kinematics CUF models based on the mixed RMVT formulation.

This paper is organized as follows: the CUF-based variable kinematics approach is recalled in Sect. 6.2 and the QC4 and CL8 FE approximations are presented for displacement- and mixed-based formulations in Sect. 6.3. The numerical results are discussed in Sect. 6.4, where a comprehensive investigation is proposed that concerns the rank of the stiffness matrix, the robustness of the element with respect to length-to-thickness ratio and mesh distortion. Finally, Sect. 6.5 summarizes the main conclusions and proposes an outlook towards further studies.

## 6.2 Variable Kinematics Plate Model

Let us consider a multilayered plate occupying the domain  $V = \Omega \times \left\{ -\frac{e}{2} \leq x_3 \leq \frac{e}{2} \right\}$  in a Cartesian coordinate system  $(x, y, z) = (x_i)$ , see Fig. 6.1. Unless otherwise stated, Latin indices range in  $\{1, 2, 3\}$ , Greek indices range in  $\{1, 2\}$  and tensorial repeated index convention is employed.  $\Omega$  is the reference surface of arbitrary shape lying in the  $(x_1, x_2)$ -plane located for convenience at  $x_3 \equiv z = 0$ . The plate has constant thickness  $e$ , which is composed of  $k = 1, 2, \dots, N_L$  orthotropic, elastic and perfectly bonded layers, each with a thickness  $e^{(k)}$  and with an orientation of the material orthotropy axes defined by the rotation angle  $\theta^{(k)}$  about the thickness direction  $z$ .

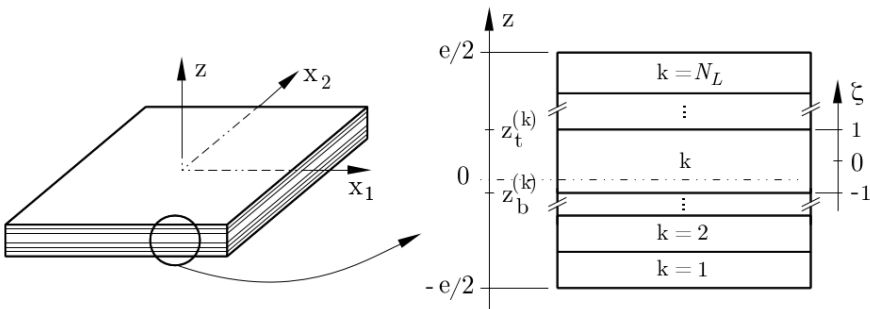
### 6.2.1 Variational Statements

The weak forms of the governing equations suitable for obtaining the FE matrices are derived from variational statements. The plate models are constructed by referring to the displacement-based approach expressed by the PVD as well as to the mixed approach expressed by the RMVT.

#### 6.2.1.1 The Principle of Virtual Displacements

The displacement-based approach is expressed in terms of admissible virtual displacement  $\delta u_i$  as

$$\iint_{\Omega} \left\{ \int_{-e/2}^{e/2} \delta \epsilon_{\alpha\beta}^{(G)} \sigma_{\alpha\beta}^{(H)} + \delta \epsilon_{i3}^{(G)} \sigma_{i3}^{(H)} \right\} dz \, dx \, dy = \iint_{\Omega} \delta u_i \bar{t}_i \, dx \, dy \quad (6.1)$$



**Fig. 6.1:** Coordinates and notation used for the description of the composite plate.

where the imposed surface loads are denoted by  $\bar{l}_i$ . Eq. (6.1) yields the weak form of the equilibrium equations and traction boundary conditions once the strain field is related to the displacement by the geometric relations (superscript  $G$ )

$$\epsilon_{\alpha\beta}^{(G)} = \frac{1}{2}(u_{\alpha,\beta} + u_{\beta,\alpha}); \quad \epsilon_{i3}^{(G)} = \frac{1}{2}(u_{i,3} + u_{3,i}) \quad (6.2)$$

and the in-plane and transverse stresses are defined by means of the linear elastic constitutive law in terms of the actual strains (superscript  $H$ )

$$\begin{bmatrix} \bar{\sigma}_{\alpha\beta}^{(H)} \\ \bar{\sigma}_{i3}^{(H)} \end{bmatrix} = \begin{bmatrix} \tilde{C}_{\alpha\beta\lambda\mu} & \tilde{C}_{\alpha\beta j3} \\ \tilde{C}_{i3\lambda\mu} & \tilde{C}_{i3 j3} \end{bmatrix} \begin{bmatrix} \bar{\epsilon}_{\lambda\mu}^{(G)} \\ \bar{\epsilon}_{j3}^{(G)} \end{bmatrix} \quad (6.3)$$

Exploiting the symmetry of the stress and strain tensors, Voigt compact notation is introduced for using the conventional matrix notation instead of the more cumbersome tensor notation for the description of the constitutive law Eq. (6.3). The constitutive law is obviously defined for each layer  $k$  for it depends on the layer's orthotropic elastic properties  $C_{PQ}^{(k)}$  ( $P, Q \in \{1, 6\}$  according to Voigt notation) and on the orientation angle  $\theta^{(k)}$ . The generic layer  $k$  is thus assumed to have a monoclinic material symmetry in the plate's reference frame  $(x_\alpha, z)$ .

### 6.2.1.2 Reissner's Mixed Variational Theorem

In the framework of RMVT, the transverse stresses  $\sigma_{i3}$  are assumed as independent variables. The weak form of the problem can be written in terms of admissible virtual displacement  $\delta u_i$  and of virtual transverse stresses  $\delta\sigma_{i3}$  as

$$\iint_{\Omega} \left\{ \int_{-e/2}^{e/2} \delta\epsilon_{\alpha\beta}^{(G)} \sigma_{\alpha\beta}^{(H)} + \delta\epsilon_{i3}^{(G)} \sigma_{i3} + \delta\sigma_{i3} (\epsilon_{i3}^{(G)} - \epsilon_{i3}^{(H)}) \right\} dz \, dx \, dy = \iint_{\Omega} \delta u_i \bar{l}_i \, dx \, dy \quad (6.4)$$

where the transverse strains denoted by  $\epsilon_{i3}^{(H)}$  and in-plane stresses  $\sigma_{\alpha\beta}^{(H)}$  are evaluated by the following mixed constitutive law

$$\begin{bmatrix} \bar{\sigma}_{\alpha\beta}^{(H)} \\ \bar{\epsilon}_{i3}^{(H)} \end{bmatrix} = \begin{bmatrix} C_{\alpha\beta\lambda\mu} & C_{\alpha\beta j3} \\ C_{i3\lambda\mu} & C_{i3 j3} \end{bmatrix} \begin{bmatrix} \bar{\epsilon}_{\lambda\mu}^{(G)} \\ \bar{\sigma}_{j3} \end{bmatrix} \quad (6.5)$$

where

$$\begin{cases} C_{\alpha\beta\lambda\mu} &= \tilde{C}_{\alpha\beta\lambda\mu} - \tilde{C}_{\alpha\beta i3} \tilde{C}_{i3 j3}^{-1} \tilde{C}_{j3\lambda\mu} \\ C_{\alpha\beta i3} &= \tilde{C}_{\alpha\beta j3} \tilde{C}_{j3 i3}^{-1} \\ C_{i3\alpha\beta} &= -\tilde{C}_{i3 j3}^{-1} \tilde{C}_{j3\alpha\beta} \\ C_{i3 j3} &= \tilde{C}_{i3 j3}^{-1} \end{cases} \quad (6.6)$$

Voigt notation is again employed to express Eq. (6.5) and Eq. (6.6) in terms of matrices instead of fourth-order tensors. Eq. (6.4) yields the weak form of the equilibrium equations, of the traction boundary conditions and of the constitutive equations related to only the transverse stresses, i.e., the second row of Eq. (6.5). Subsidiary conditions are the geometric relations Eq. (6.2) and the constitutive equations associated to the in-plane stresses, i.e., the first row of Eq. (6.5).

## 6.2.2 Variable Kinematics Assumptions

According to Carrera's Unified Formulation (CUF), the two-dimensional variable kinematics plate model is formulated upon separating the in-plane variables  $x_\alpha$  from the thickness direction  $z$ , along which a generic variable  $g$ , which may be a component of the displacement field or of the transverse stress field, i.e.,  $g \in \{u_i, \sigma_{i3}\}$ , is *a priori* postulated by known functions  $F(z)$ :

$$g(x_\alpha, z) = F_\tau(z) \hat{g}_\tau(x_\alpha), \quad (6.7)$$

where  $\tau = 0, 1, \dots, N$  is the summation index and the order of expansion  $N$  is a free parameter of the formulation. In this work  $N$  can range from 1 to 4, in agreement with the classical CUF implementation (Carrera and Demasi, 2002a).

In order to deal with both ESL and LW descriptions within a unique notation, it is convenient to refer to a layer-specific thickness coordinate  $z_k \in \{z_b^{(k)}, z_t^{(k)}\}$  that ranges between the  $z$ -coordinates of the bottom (subscript  $b$ ) and top (subscript  $t$ ) planes delimiting the  $k^{\text{th}}$  layer, see Fig. 6.1. Equation (6.7) can thus be formally re-written for each layer as

$$g^{(k)}(x_\alpha, z_k) = F_t(z_k) \hat{g}_t^{(k)}(x_\alpha) + F_b(z_k) \hat{g}_b^{(k)}(x_\alpha) + F_r(z_k) \hat{g}_r^{(k)}(x_\alpha) \quad (6.8)$$

with  $\tau = t, b, r$  and  $r = 2, \dots, N$ . The variable  $g$  for the whole multilayered stack is then defined through an opportune assembly procedure of the layer-specific contributions  $g^{(k)}$ , which depends on the ESL or LW description.

In an ESL approach, the thickness functions are defined as Taylor-type expansion and only one variable  $\hat{g}_\tau$  is used for the whole multilayer, i.e., the layer index ( $k$ ) in Eq. (6.8) may be dropped off and the following thickness functions are used:

$$F_b = 1, \quad F_t = z^N, \quad F_r = z^r \quad (r = 2, \dots, N-1) \quad (6.9)$$

The ESL description can be enhanced by including the Zig-Zag function  $F_{ZZ}(z)$  proposed by Murakami (1986) in order to allow slope discontinuities at layers' interfaces. In this case, the Zig-Zag function replaces the highest expansion order and the following functions are used:

$$F_b = 1, \quad F_t = F_{ZZ}(z), \quad F_r = z^r \quad (r = 2, \dots, N-1) \quad (6.10)$$



where Murakami's ZigZag Function (MZZF) is defined as

$$F_{ZZ}(z) = (-1)^k \zeta_k(z) \quad \text{with} \quad \zeta_k(z) = \frac{2}{z_t^{(k)} - z_b^{(k)}} \left( z - \frac{z_t^{(k)} + z_b^{(k)}}{2} \right) \quad (6.11)$$

Note that  $F_{ZZ}(z)$  is expressed in terms of the non-dimensional layer-specific coordinate  $-1 \leq \zeta_k \leq +1$  and it provides a linear piecewise function of bi-unit amplitude across the thickness of each layer  $k$ .

The assumptions for a LW description are formulated in each layer  $k$  as in Eq. (6.8), where the thickness functions are defined by linear combinations of Legendre polynomials  $P_r(\zeta_k)$  as follows:

$$\begin{aligned} F_t(\zeta_k) &= \frac{P_0(\zeta_k) + P_1(\zeta_k)}{2}; & F_b(\zeta_k) &= \frac{P_0(\zeta_k) - P_1(\zeta_k)}{2}; \\ F_r(\zeta_k) &= P_r(\zeta_k) - P_{r-2}(\zeta_k) \quad (r = 2, \dots, N) \end{aligned} \quad (6.12)$$

where  $\zeta_k$  is the non-dimensional coordinate introduced in Eq. (6.11). The Legendre polynomials of degree 0 and 1 are  $P_0(\zeta_k) = 1$  and  $P_1(\zeta_k) = \zeta_k$ , respectively; higher-order polynomials are defined according to the following recursive formula:

$$P_{n+1}(\zeta_k) = \frac{(2n+1)\zeta_k P_n(\zeta_k) - nP_{n-1}(\zeta_k)}{n+1} \quad (6.13)$$

which leads to the following expressions for the polynomials employed if  $N = 4$ :

$$P_2(\zeta_k) = \frac{3\zeta_k^2 - 1}{2}; \quad P_3(\zeta_k) = \frac{5\zeta_k^3 - 3\zeta_k}{2}; \quad P_4(\zeta_k) = \frac{35\zeta_k^4}{8} - \frac{15\zeta_k^2}{4} + \frac{3}{8} \quad (6.14)$$

It is finally emphasized that the chosen thickness functions for a LW model satisfy the following properties

$$\begin{aligned} \zeta_k = 1: & \quad F_t = 1, \quad F_b = 0, \quad F_r = 0 \\ \zeta_k = -1: & \quad F_t = 0, \quad F_b = 1, \quad F_r = 0 \end{aligned} \quad (6.15)$$

Therefore,  $\hat{g}_t^{(k)}$  and  $\hat{g}_b^{(k)}$  are the physical displacement or transverse stress components at the top and bottom of the  $k^{\text{th}}$  layer, respectively, and  $F_t(\zeta_k)$  and  $F_b(\zeta_k)$  are the corresponding linear Lagrange interpolation functions.

### 6.2.3 The Stress and Strain Fields

The contributions to the strain and stress fields in each layer  $k$  are identified with respect to the in-plane ( $p$ ), i.e., membrane and bending, transverse normal ( $n$ ) and transverse shear ( $s$ ) deformation of the plate:

$$\begin{aligned}
\vec{\epsilon}_p^{(k)} &= [\epsilon_1^{(k)} \ \epsilon_2^{(k)} \ \epsilon_6^{(k)}]; & \vec{\epsilon}_n^{(k)} &= \epsilon_3^{(k)}; & \vec{\epsilon}_s^{(k)} &= [\epsilon_5^{(k)} \ \epsilon_4^{(k)}] \\
\vec{\sigma}_p^{(k)} &= [\sigma_1^{(k)} \ \sigma_2^{(k)} \ \sigma_6^{(k)}]; & \vec{\sigma}_n^{(k)} &= \sigma_3^{(k)}; & \vec{\sigma}_s^{(k)} &= [\sigma_5^{(k)} \ \sigma_4^{(k)}]
\end{aligned} \tag{6.16}$$

where Voigt notation has been used.

### 6.2.3.1 PVD Formulation

Recalling the separation of the in-plane variables from the thickness direction, employed for expressing the assumed displacement field as in Eq. (6.8), the bending, transverse normal and transverse shear components of the strains in the displacement-based formulation are recast in the following matrix notation

$$\begin{aligned}
\vec{\epsilon}_p(x_\alpha, z_k) &= F p_{ut}(z_k) \vec{V}_\tau^{(k)}(x_\alpha) \\
\vec{\epsilon}_n(x_\alpha, z_k) &= F n_{ut}(z_k) \vec{V}_\tau^{(k)}(x_\alpha) \\
\vec{\epsilon}_s(x_\alpha, z_k) &= F s_{ut}(z_k) \vec{V}_\tau^{(k)}(x_\alpha)
\end{aligned} \tag{6.17}$$

where  $\vec{V}_\tau^{(k)}(x_\alpha)$  is the generalized strain vector of each layer defined as

$$\vec{V}_\tau^{(k)}(x_\alpha) = \left[ \hat{u}_{1\tau}^{(k)} \ \hat{u}_{1\tau,1}^{(k)} \ \hat{u}_{1\tau,2}^{(k)} \ ; \ \hat{u}_{2\tau}^{(k)} \ \hat{u}_{2\tau,1}^{(k)} \ \hat{u}_{2\tau,2}^{(k)} \ ; \ \hat{u}_{3\tau}^{(k)} \ \hat{u}_{3\tau,1}^{(k)} \ \hat{u}_{3\tau,2}^{(k)} \right]^T \tag{6.18}$$

In order to introduce the transverse shear locking correction proposed in the next section, the transverse shear strain field given in Eq. (6.17) is split into the classical  $z$ -constant contribution  $\vec{\gamma}^0$  of standard FSDT, and a contribution  $\vec{\gamma}^h$  that depends on the thickness coordinate  $z$  and is related to high-order terms:

$$\vec{\epsilon}_s(x_\alpha, z_k) = \gamma^0(x_\alpha) + \gamma^h(x_\alpha, z_k) = F s_{ut}^0 \vec{V}_\tau^{(k)}(x_\alpha) + F s_{ut}^h(z_k) \vec{V}_\tau^{(k)}(x_\alpha) \tag{6.19}$$

Note that  $F s_{ut}^0$  is a matrix containing only constant values for all  $z$ -dependency is contained in the matrix  $F s_{ut}^h(z_k) = F s_{ut}(z_k) - F s_{ut}^0$ . The explicit expressions for the matrices  $F p_{ut}$ ,  $F n_{ut}$ ,  $F s_{ut}$  and  $F s_{ut}^0$  can be found in Le et al (2017). The stress field is obtained by the linear elastic constitutive law Eq. (6.3).

### 6.2.3.2 RMVT Formulation

In addition to the compatible strains defined by Eq. (6.17), the transverse stress components are expressed in CUF as follows

$$\begin{aligned}
\vec{\sigma}_n(x_\alpha, z_k) &= F n_{\sigma\tau}(z_k) \vec{S}_\tau^{(k)}(x_\alpha) \\
\vec{\sigma}_s(x_\alpha, z_k) &= F s_{\sigma\tau}(z_k) \vec{S}_\tau^{(k)}(x_\alpha)
\end{aligned} \tag{6.20}$$

where  $\vec{S}_\tau^{(k)}(x_\alpha)$  is the generalized transverse stress vector of each layer defined as

$$\vec{S}_\tau^{(k)}(x_\alpha) = \left[ \hat{\sigma}_{13_\tau}^{(k)} \ ; \ \hat{\sigma}_{23_\tau}^{(k)} \ ; \ \hat{\sigma}_{33_\tau}^{(k)} \right]^T \quad (6.21)$$

and

$$Fn_{\sigma\tau} = \begin{bmatrix} 0 & 0 & F_\tau \end{bmatrix}, \quad Fs_{\sigma\tau} = \begin{bmatrix} 0 & F_\tau & 0 \\ F_\tau & 0 & 0 \end{bmatrix} \quad (6.22)$$

The conjugated in-plane stresses as well as the transverse strains defined in terms of the in-plane strains and of the transverse stresses are expressed by the mixed constitutive law Eq. (6.5).

### 6.3 Finite Element Approximations

It is well known that the isoparametric interpolation for the transverse shear field applied to the classical displacement-based formulation leads to a locking phenomenon because of the incompatibility of the polynomial spaces defined by the sum of  $\hat{u}_{\alpha\tau}$  and the in-plane derivative  $\hat{u}_{3_\tau,\alpha}$  ( $\alpha = 1, 2$  for  $\gamma_{13}^0$  and  $\gamma_{23}^0$ , respectively) (Polit et al, 2012). The locking pathology is associated only to the  $z$ -constant part, because higher-order contributions depend on the plate thickness and vanish naturally in the thin plate limit. Thus a new field-compatible interpolation for the four-node element is constructed for the  $z$ -constant part  $\vec{\gamma}^0$ : this is an extension to arbitrary variable kinematics plate models of the approach proposed in Polit et al (1994) for FSdT plate elements and in Polit et al (2012) to a refined plate element.

The formulation for the four-node quadrilateral FE for PVD-based CUF plate models has been reported in Le et al (2017). Therefore, this section presents at first the eight-node quadrilateral FE approximation, referred to as CL8 approximation, for avoiding transverse shear locking problems and minimizing the convergence rate loss for distorted meshes in the framework of PVD-based plate models. Subsequently, the QC4 and CL8 interpolations are employed to approximate the transverse shear stresses in the context of RMVT-based plate elements.

#### 6.3.1 Displacement-Based Finite Elements

The CL8 interpolation is constructed as follows:

- In order to enhance the element's robustness for distorted shapes, the  $z$ -constant part of transverse shear strain components is written in the element's natural coordinate system  $(\xi, \eta) \in [-1, +1]^2$  as:

$$\begin{bmatrix} \gamma_\xi^0(\xi, \eta) \\ \gamma_\eta^0(\xi, \eta) \end{bmatrix}^{(k)} = Fs_{u\tau}^0 \vec{U}_\tau^{(k)}(\xi, \eta) \quad (6.23)$$

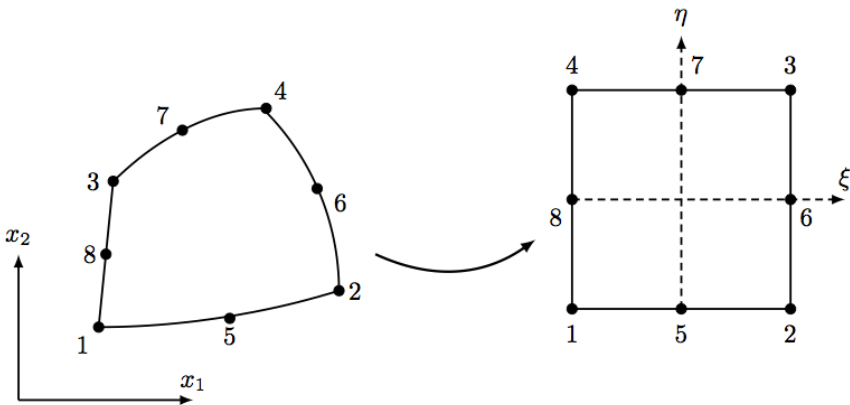
where

$$\vec{U}_\tau^{(k)}(\xi, \eta) = \left[ \hat{u}_{\xi\tau}^{(k)} \hat{u}_{\xi\tau,\xi}^{(k)} \hat{u}_{\xi\tau,\eta}^{(k)} \ ; \ \hat{u}_{\eta\tau}^{(k)} \hat{u}_{\eta\tau,\xi}^{(k)} \hat{u}_{\eta\tau,\eta}^{(k)} \ ; \ \hat{u}_{3\tau}^{(k)} \hat{u}_{3\tau,\xi}^{(k)} \hat{u}_{3\tau,\eta}^{(k)} \right]^T \quad (6.24)$$

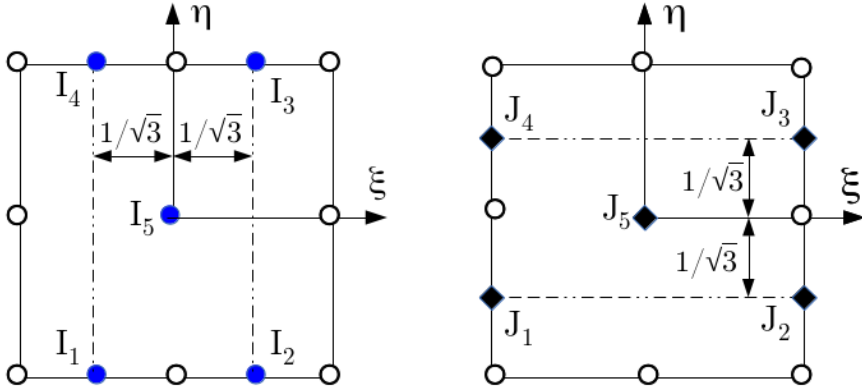
is the projection onto the reduced natural coordinates  $\xi, \eta$  of the generalized strain vector  $\vec{V}_\tau^{(k)}$ .

- The field-compatible approximation shall be constructed upon enhancing the polynomial space of the transverse deflection  $\hat{u}_{3\tau}^{(k)}$  so that its derivative matches the serendipity quadratic approximation of the in-plane displacements  $\hat{u}_{\xi\tau}^{(k)}$  and  $\hat{u}_{\eta\tau}^{(k)}$  that contribute to the  $z$ -constant reduced transverse shear strains  $\gamma_\xi^0$  and  $\gamma_\eta^0$ . For this, a cubic polynomial interpolation is assumed for  $\hat{u}_{3\tau}^{(k)}$  by introducing four supplementary DOFs,  $(\hat{u}_{3\tau,\xi})_5^{(k)}$ ,  $(\hat{u}_{3\tau,\eta})_6^{(k)}$ ,  $(\hat{u}_{3\tau,\xi})_7^{(k)}$  and  $(\hat{u}_{3\tau,\eta})_8^{(k)}$ , which correspond to the tangential derivatives of  $\hat{u}_{3\tau}$  with respect to the natural coordinates at the mid-side nodes of the reference domain, see Fig. 6.2. The supplementary DOFs are subsequently expressed in terms of the DOFs at the nodes by imposing a linear variation of the  $z$ -constant reduced tangential transverse shear strain at each side of the elementary domain:  $\gamma_\xi^0$  should be linear along  $\xi$  at  $\eta = \pm 1$  and  $\gamma_\eta^0$  should be linear along  $\eta$  at  $\xi = \pm 1$ . The resulting eight-node FE shall be denoted CL8 due to the initial Cubic approximation for  $\hat{u}_{3\tau}$  and the subsequent Linear constraint imposed on the tangential transverse shear strains at the element’s edges Polit et al (1994).
- The new field-compatible interpolation for  $\gamma_\xi^0, \gamma_\eta^0$  is defined by the polynomial basis obtained from the intersection sets of monomial terms in  $\xi$  and  $\eta$ :

$$\begin{aligned} \mathcal{B}(\gamma_\xi^0) &= \mathcal{B}(u_{\xi\tau}) \cap \mathcal{B}(u_{3\tau,\xi}) = \{1, \xi, \eta, \xi\eta, \eta^2\} \\ \mathcal{B}(\gamma_\eta^0) &= \mathcal{B}(u_{\eta\tau}) \cap \mathcal{B}(u_{3\tau,\eta}) = \{1, \xi, \eta, \xi\eta, \xi^2\} \end{aligned} \quad (6.25)$$



**Fig. 6.2:** Eight-node element in the physical Cartesian frame  $x_1, x_2$  and in the natural frame  $\xi, \eta$ .



**Fig. 6.3:** Sampling points for CL8 finite element.

- According to the polynomial basis, five sampling points are required for each reduced transverse shear strains as illustrated in Fig. 6.3, see also Polit et al (1994). The  $z$ -constant reduced transverse shear strains are then obtained as follows

$$\gamma_{\xi}^0(\xi, \eta) = \sum_{I=1}^5 C_{\xi I}(\xi, \eta) \gamma_{\xi I}^0 ; \quad \gamma_{\eta}^0(\xi, \eta) = \sum_{J=1}^5 C_{\eta J}(\xi, \eta) \gamma_{\eta J}^0 \quad (6.26)$$

where the interpolating functions  $C_{\xi I}$  and  $C_{\eta J}$  are given Appendix 1.

- The physical transverse shear strains are finally deduced from the reduced transverse shear strains in the reference domain as

$$\begin{bmatrix} \gamma_{13}^0(x_{\alpha}) \\ \gamma_{23}^0(x_{\alpha}) \end{bmatrix} = J^{-1} \begin{bmatrix} \gamma_{\xi}^0(\xi, \eta) \\ \gamma_{\eta}^0(\xi, \eta) \end{bmatrix} \quad (6.27)$$

where

$$J = \begin{bmatrix} x_{1,\xi} & x_{2,\xi} \\ x_{1,\eta} & x_{2,\eta} \end{bmatrix} \quad (6.28)$$

is the Jacobian matrix that will be evaluated at the  $3 \times 3$  Gauss points used for integrating the stiffness matrix.

The expression for the CL8 approximation for the  $z$ -constant transverse shear strain field can be finally written as

$$\vec{\gamma}^0 = J^{-1} F s_{u\tau}^0 \bar{B}_i \vec{q}_{\tau i}^{(k)} \quad (6.29)$$

where  $\vec{q}_{\tau i}^{(k)} = [u_{1\tau}^{(k)} u_{2\tau}^{(k)} u_{3\tau}^{(k)}]_i^T$  is the DOF vector of the node  $i$  related to the layer  $k$  and the expansion order index  $\tau$ .  $\bar{B}_i$  ( $i = 1, 8$ ) is the matrix containing the modified CL8 interpolation functions and their derivatives with respect to the physical coordinates  $x_{\alpha}$ . The explicit expression of the  $\bar{B}_i$  matrices can be found in Appendix 2.

Starting from the integral expression Eq. (6.1), the isoparametric FE interpolations are introduced for the in-plane and transverse normal strain energy contributions, and the QC4/CL8 interpolations are introduced for the transverse shear strain energy contributions. The integral over the thickness is carried out upon assembling all layers' contributions in the appropriate manner depending on the ESL or LW description (Carrera and Demasi, 2002a,b); the integral over the in-plane domain of each finite element constituting the mesh is carried out numerically. The weak form of the equilibrium equations issued from the PVD yields thus the following standard matrix system for each finite element

$$K \vec{q} = \vec{f} \quad (6.30)$$

where  $\vec{q}$  and  $\vec{f}$  are the vectors of the nodal displacements and nodal forces. These elemental arrays are subsequently assembled over the whole mesh following the standard FEM procedure.

### 6.3.2 RMVT-Based Finite Elements

After introducing FE interpolations for the displacement and transverse stress fields, carrying out the integrals across the thickness (including the assembly over all layers) and the integrals over the element domain  $\Omega_e$ , the RMVT integral Eq. (6.4) yields the following matrix system for each finite element

$$\begin{bmatrix} K_{uu} & K_{u\sigma} \\ K_{u\sigma}^T & K_{\sigma\sigma} \end{bmatrix} \begin{bmatrix} \vec{q} \\ \vec{g} \end{bmatrix} = \begin{bmatrix} \vec{f} \\ \vec{0} \end{bmatrix} \quad (6.31)$$

where  $\vec{q}$  and  $\vec{g}$  are the vectors of the nodal displacements and nodal transverse stresses, respectively, and  $\vec{f}$  is the nodal force vector, see also Carrera and Demasi (2002a,b). The first hyper-row corresponds to the virtual variations of the displacements and represents the weak form of the equilibrium equation for the finite element, the second hyper-row corresponds to the virtual variation of the transverse stresses and represents the weak form of the transverse part of the constitutive equation of the finite element. The element contributions expressed by Eq. (6.31) can be directly assembled for the whole FE mesh, which leads to a mixed system whose unknowns are the displacements and transverse stresses at each node of the mesh.

An alternative strategy consists in statically condensing out the nodal stress unknowns of each finite element according to

$$\vec{g} = -K_{\sigma\sigma}^{-1} K_{u\sigma}^T \vec{q} \quad (6.32a)$$

which defines a mixed-hybrid formulation with only displacement DOF according to

$$\vec{K}_C \vec{q} = \vec{f} \quad \text{with} \quad \vec{K}_C = \vec{K}_{uu} - \vec{K}_{u\sigma} \vec{K}_{\sigma\sigma}^{-1} \vec{K}_{u\sigma}^T \quad (6.32b)$$

The mixed-hybrid formulation Eq. (6.32) yields an element that suffers transverse shear locking if isoparametric interpolations are used for both, the displacement and the transverse stress fields (Zienkiewicz and Taylor, 2000). In order to enhance the element robustness, several strategies may be devised. One of these consists in adopting the previously discussed QC4/CL8 interpolation for the  $z$ -constant transverse shear strains inside the  $K_{uu}$  matrix, i.e., in correcting the compatible transverse shear strain field as in the conventional displacement-based FEM. A more interesting approach is to take profit of the mixed nature of the RMVT statement and to adopt an opportune interpolation scheme for the transverse shear stresses in conjunction with standard isoparametric interpolations for the displacement and transverse normal stress fields. It turns out that adopting the QC4 and CL8 interpolations for the transverse shear stresses yields a shear-locking-free mixed-hybrid finite element, see also Hoa and Feng (1998); Li (1989); Zienkiewicz and Taylor (2000). Therefore, the following interpolation is used in the natural reference frame for the reduced transverse shear stresses

$$\sigma_{\xi}(\xi, \eta) = \sum_{I=1}^{n_p} C_{\xi I}(\xi, \eta) \sigma_{\xi I} ; \quad \sigma_{\eta}(\xi, \eta) = \sum_{J=1}^{n_p} C_{\eta J}(\xi, \eta) \sigma_{\eta J} \quad (6.33)$$

where  $n_p$  ( $n_p = 2$  for QC4 and  $n_p = 5$  for CL8) is the number of sampling points, which are located at the mid-sides of the edges for the four-node element (Le et al, 2017) and as illustrated in Fig. 6.3 for the eight-node element. An opportune tensorial transformation by means of the Jacobian matrix is required to map the reduced transverse shear stresses onto the physical domain.

## 6.4 Numerical Results

Several numerical benchmark problems are considered for displaying the accuracy and robustness of the proposed QC4 and CL8 CUF-based plate elements. The classical CUF acronyms are used for naming the various plate models: the polynomial order  $N$  is appended to a string that identifies whether the description of the displacement field is ESL (E{D,M}N), Zig-Zag (E{D,M}ZN) or LW (L{D,M}N). A capital “D” is used for PVD-based elements, while capital “M” identifies RMVT-based elements. In these latter models, the transverse stress field is always described in a LW sense. If the mixed-hybrid formulation is used for RMVT-based elements, a “c” is appended at the end of the model acronym.

Since the objective of this paper is focused on the performance of the FE approximation, the problems involve a simple homogeneous and isotropic plate. At first, the properties of the stiffness matrix are considered via an eigenvalue analysis. Subsequently, the convergence rate for thin and thick plates is investigated. Finally, the sensitivity with respect to distorted element shapes is assessed through numerical tests conducted on a square plate with distorted mesh and a circular plate. Most of the numerical tests are performed with an ESL model with expansion order  $N = 2$ ,

which retains the three-dimensional constitutive law and avoids the occurrence of spurious Poisson locking. Table 6.1 lists the acronyms used for denoting the various configurations of boundary conditions and type of loading. Whenever possible, the computational model is reduced through application of opportune symmetry boundary conditions on the displacement field.

Present results are compared against solutions obtained with the following isoparametric approaches:

- ISO full-integrated isoparametric element
- ISO-SI isoparametric element with selective integration

All elements are implemented as user subroutines into the commercial ABAQUS software. A dedicated pre-processing tool allows to prepare the FE model within the ABAQUS/CAE graphical interface. Therefore, the conventional shell elements of ABAQUS will be included in the comparison, which are the general-purpose four-node elements S4 and S4R and the thick-shell eight-node element S8R. It should be noted that the S4 and S4R elements can be used for modeling thin and thick shells and both use the same transverse shear treatment, which consists in a modified version of the MITC4 assumed strain method with one Gauss point evaluation plus hourglass stabilization; the primary difference between the S4 and S4R elements is in their membrane strain field treatment (N., 2016). According to N. (2016), the use of the the S8R element should be limited to shells with non-negligible transverse shear flexibility and within a regular mesh.

### 6.4.1 Eigenvalues of the Stiffness Matrix

The eigenvalues of the stiffness matrix of a square element are analyzed for a thin and a thick plate, according to the following configuration

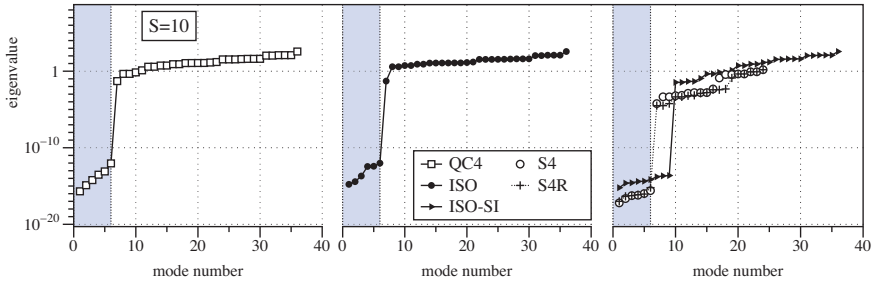
- geometry square element  $a \times a$  ( $a = 1$ ), thickness  $e = 10^{-n}$  ( $n = 1, 3$ )
- material properties isotropic with  $E = 10.92$  and  $\nu = 0.3$

The eigenvalues of four-node displacement-based elements (ED2 model) are reported for thick and thin plates in Figs. 6.4 and 6.5, respectively. The eigenvalues of the ABAQUS general-purpose elements S4 and S4R (FSDT model) are also presented. The proposed graphics allow to recognize at a glance the eigenvalues associated to rigid-body modes as well as the gap between them and those associated to deformation modes. It is apparent that the present full integrated QC4 and ISO

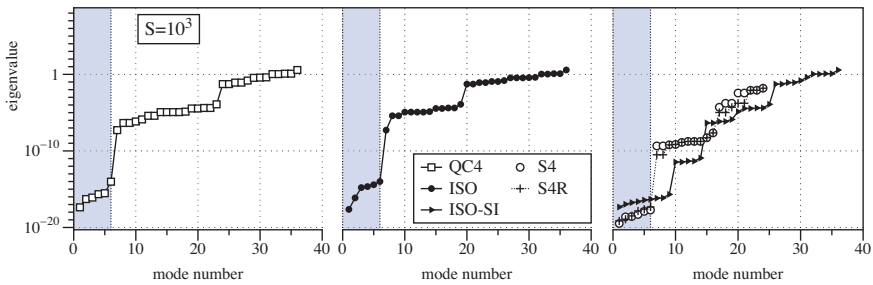
Boundary conditions	Loading
(SA) Simply supported	(P) Uniform load $q_0$ at top surface
(CL) Clamped	(C) Concentrated force $\bar{P}$ at plate center

Table 6.1: Acronyms for boundary conditions and type of loading.





**Fig. 6.4:** Eigenvalues of the stiffness matrix for thick plate ( $S = 10$ ): ED2 model, four-node FE.

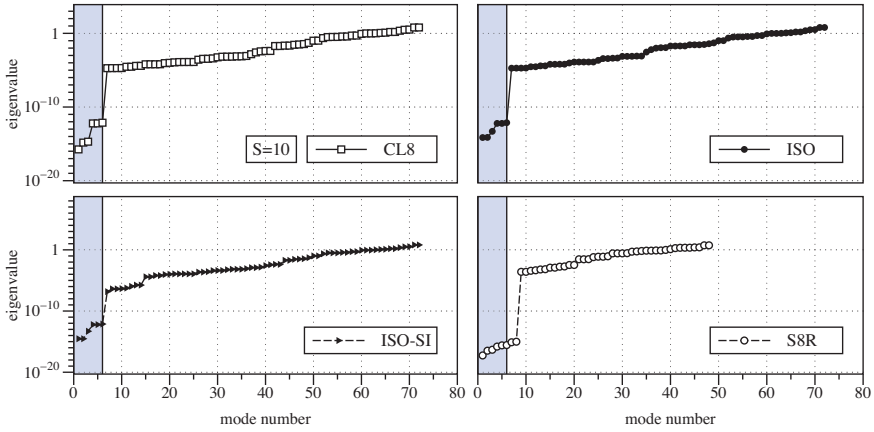


**Fig. 6.5:** Eigenvalues of the stiffness matrix for thin plate ( $S = 1000$ ): ED2 model, four-node FE.

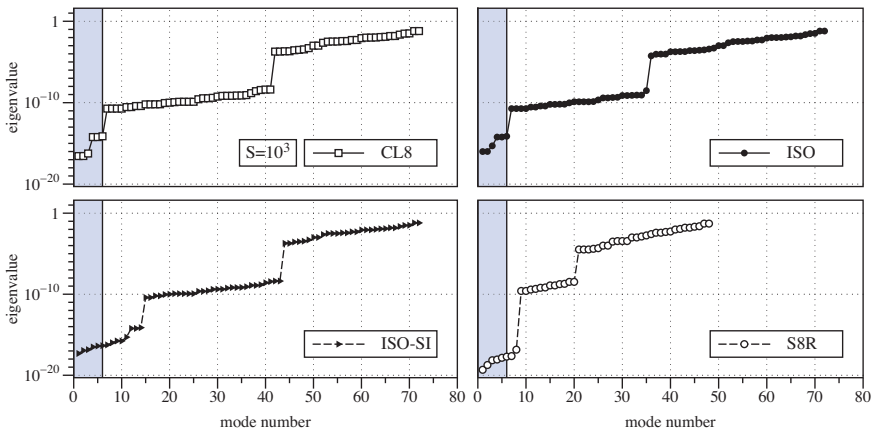
elements have the correct number of rigid-body modes (i.e., 6) regardless of the element’s slenderness  $S = a/e$ . Similarly, the ABAQUS elements S4 and S4R do not show hourglass modes. On the contrary, the selective reduced integration scheme entails 3 spurious zero-energy modes, which indicates the possibility of an unstable behavior of both, thick and thin elements.

The same analysis is conducted on the eight-node PVD-based finite elements and the eigenvalues obtained for the thick ( $S = 10$ ) and thin ( $S = 10^3$ ) elements are reported in Figs. 6.6 and 6.7, respectively. As expected, the full integrated CL8 and ISO elements have six rigid-body modes independently of the plate thickness. The selective integrated eight-node element appears to have a correct rank in the thick plate case, but shows several spurious zero-energy modes in the thin plate case. The stiffness matrix of the ABAQUS S8R element shows two spurious zero-energy modes for both, the thick and the thin plate cases.

The eigenvalues of the stiffness matrix of a four-node mixed RMVT-based element are reported in Fig. 6.8 for a thick plate case and an EM2 model. The resulting FE has 36 transverse stress DOF and 36 displacement DOF, the mixed matrix has thus 72 eigenvalues. The left graphic of Fig. 6.8 reports the 36 eigenvalues that are negative and associated to the transverse stress DOF, which are thus shown to play the role

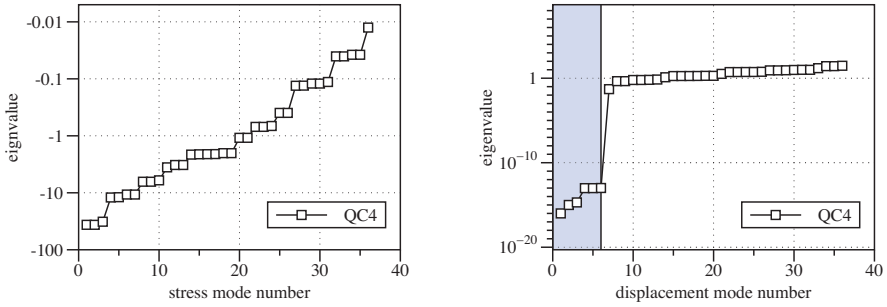


**Fig. 6.6:** Eigenvalues of the stiffness matrix for thick plate ( $S = 10$ ): ED2 model, eight-node FE.



**Fig. 6.7:** Eigenvalues of the stiffness matrix for thin plate ( $a/e = 1000$ ): ED2 model, eight-node FE.

of Lagrange multipliers. The graphic on the right of Fig. 6.8 displays the positive eigenvalues that are associated to the displacement DOF and shows that the proposed mixed FE with a QC4 interpolation of the transverse shear stresses has a correct rank with 6 eigenvalues that are numerically zero. It may be noted that mixed finite elements derived from Hellinger-Reissner principle possess negative eigenvalues that are related to displacement DOF, see, e.g., Mijuca (2004). Figure 6.9 reports the eigenvalues of the stiffness matrices for a mixed-hybrid 4-node element in which the transverse shear stresses are approximated either with the isoparametric or with the QC4 interpolation (the displacement field and the transverse normal stress are



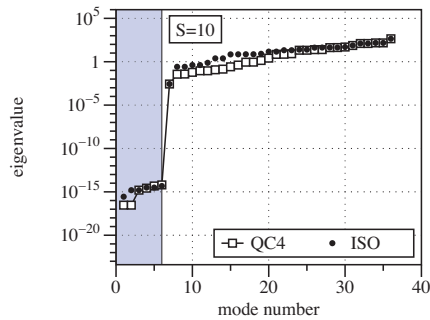
**Fig. 6.8:** Negative (left) and positive (right) eigenvalues of the stiffness matrix for thick plate ( $S = 10$ ) for the full mixed EM2 model with QC4 interpolation for the transverse shear stresses.

interpolated with an isoparametric scheme). In either case, 36 positive eigenvalues are recovered, 6 of which are numerically zero. It is worth noticing that the spectra of the ISO-EM2c and of the ISO-ED2 stiffness matrices are very similar.

### 6.4.2 Transverse Shear Locking Test

A numerical test is carried out to assess the sensitivity of the proposed QC4 and CL8 elements to the transverse shear locking. The test is described as follows:

- geometry                      square plate  $a \times a$  ( $a = 1$ ), thickness  $e = 10^{-n}$  with  $n \in \{0, 4\}$
- boundary conditions      (SA) on all sides
- loading                        (P)
- material properties        isotropic with  $E = 10.92$  and  $\nu = 0.3$
- mesh                            regular with  $N = 1, 2, 4, 8, 16, 32$  (see Fig. 6.10)



**Fig. 6.9** Eigenvalues of the stiffness matrices of a mixed-hybrid 4-node EM2c element with QC4 and ISO approximations for the transverse shear stresses ( $S = 10$ ).

results transverse displacement  $U_3$  at the center of the plate  
 reference values Kirchhoff-Love theory (Timoshenko and Woinowsky-Krieger, 1959):  

$$U_3^a(a/2, a/2, 0) = 0.00406 q_0 \frac{da^4}{dr} e^3 D \text{ (with } D = \frac{E}{12(1-\nu^2)})$$

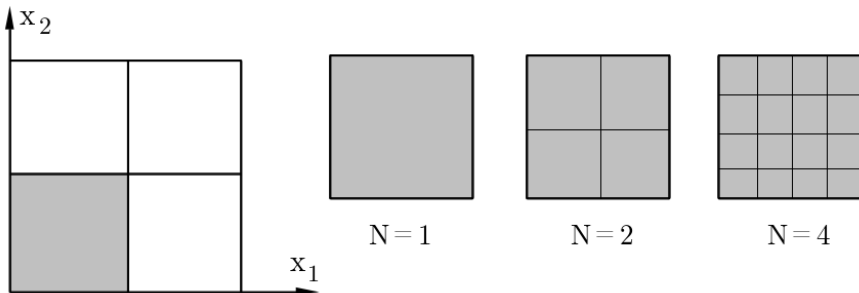
The results are summarized in the two different ways.

1. Investigation of the accuracy of the FEM for a constant mesh density and varying slenderness ratio. In this case, the quarter plate is regularly meshed with  $N = 4$  four-node elements or  $N = 2$  eight-node elements (see Fig. 6.10). The result is the ratio between the deflection  $U_3$  obtained by the present FEM and the reference thin plate solution  $U_3^a$  for an increasing length-to-thickness (slenderness) ratio  $S = a/e$ .
2. Investigation of the convergence of the FEM for a thin plate ( $S = 100$ ). In this case, the result is reported in terms of relative error  $|U_3 - U_3^a|/U_3^a$  with respect to the number  $N$  of elements used for the regular mesh of the quarter plate.

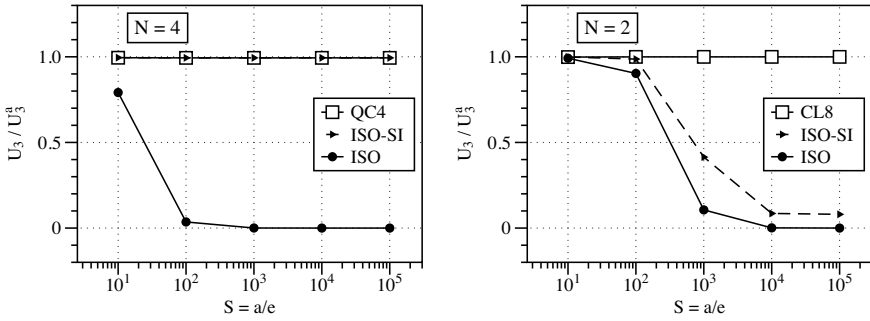
**6.4.2.1 PVD Based Elements: ED2 Model**

Figure 6.11 reports the ratio between the deflection  $U_3$  obtained by the present FEM with an ED2 model and the reference thin plate solution  $U_3^a$  for an increasing length-to-thickness (slenderness) ratio  $S = a/e$ . Results for four-node elements and a regular mesh with  $N = 4$  are given on the left, those for eight-node elements and a regular mesh with  $N = 2$  are illustrated on the right.

The full integrated ISO elements are shown to suffer a very strong locking as the plate becomes thin: the linear four-node element locks severely already for  $S \geq 10^2$ , while the quadratic eight-node element delays the severe locking for  $S \geq 10^3$ . An excellent agreement with the reference Kirchhoff-Love solution is found with the new interpolation schemes QC4 and CL8, which are thus locking-free. The selective reduced quadrature scheme is shown to be effective for the linear Lagrangean four-node element, but it does not eliminate the locking pathology for the quadratic



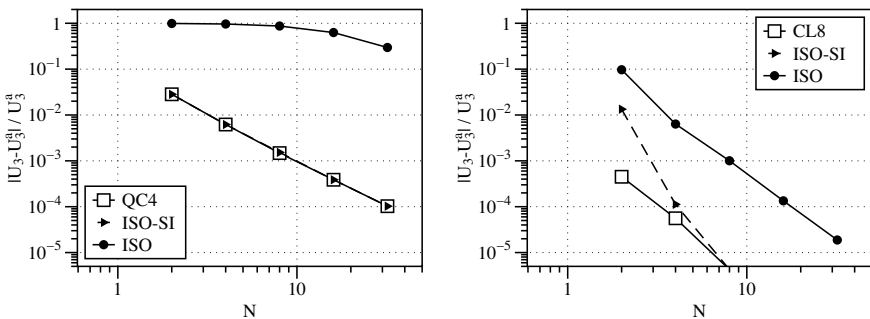
**Fig. 6.10:** Regular meshes for a quarter of the plate.



**Fig. 6.11:** Accuracy for a fixed mesh for thick to very thin plates: four-node (left) and eight-node (right) elements, ED2 model.

serendipity eight-node element: a severe locking is still found for ISO-SI eight-node element as  $S \geq 10^3$ . This difficulty is probably at the origin for the ABAQUS element S8R to be reported as suitable only for thick plates, for which the transverse shear flexibility is non-negligible.

Convergence curves for a thin plate ( $S = 100$ ) are reported in Fig. 6.12 for the four-node elements (on the left) and the eight-node elements (on the right). Concerning the four-node FE, the locking pathology is clearly visible for the isoparametric formulation (ISO) and a good convergence rate is recovered by resorting to the selective quadrature scheme (ISO-SI) and by the present QC4 interpolation. Accurate results, with relative errors of approximately  $10^{-3}$  in the transverse displacement, are obtained with  $N = 8$  elements for the quarter plate. Concerning the eight-node FE (Fig. 6.12, right), a rather satisfying convergence rate is found for  $S = 100$  and for all element formulations (ISO, ISO-SI and CL8). The new CL8 element is shown to be more accurate than the isoparametric elements, as it provides accurate results already



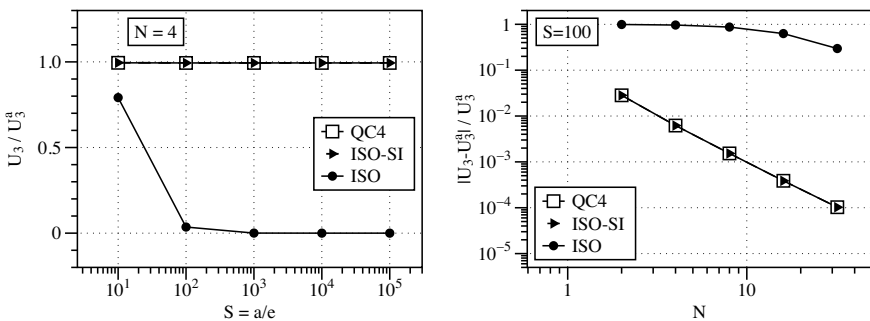
**Fig. 6.12:** Convergence of the transverse displacement for a thin plate ( $S = 100$ ): four-node (left) and eight-node (right) elements, ED2 model.

with a  $N = 2$  mesh for the quarter plate. As can be inferred from the right graphic of Fig. 6.11, the convergence rate of eight-node ISO and ISO-SI elements will be worse for thinner plates ( $S \geq 10^3$ ).

**6.4.2.2 RMVT Based Elements: EM2 and EM2c Models**

The same analysis is carried out for RMVT based mixed-hybrid elements (EM2c model) and full mixed elements (EM2 model), where only results for the four-node elements are given for the sake of brevity. Results obtained by the mixed-hybrid approach are reported in terms of accuracy with respect to the plate slenderness and in terms of convergence towards the reference Kirchhoff-Love solution in Fig. 6.13 left and right, respectively. These results confirm that the element locks if the isoparametric interpolation is used for the displacement field and the same bi-linear interpolation is employed for the transverse shear stresses. Indeed, the EM2c ISO element behaves in exactly the same manner as the ED2 ISO element. The locking pathology can be thus corrected by resorting to a selective quadrature scheme, as first pointed out in Carrera and Demasi (2002a). More interesting, the locking pathology of the mixed-hybrid elements is eliminated by adopting the QC4 interpolation scheme for the transverse shear stresses and a full quadrature.

Results obtained by the full mixed elements EM2 are reported in Fig. 6.14. These demonstrate that the ISO element does not suffer transverse shear locking if the transverse stress DOF are not condensed out at element level. ISO elements are here shown to be merely slightly less accurate than the locking-free QC4 and ISO-SI elements.



**Fig. 6.13:** Results of the shear locking test for the mixed-hybrid EM2c model.

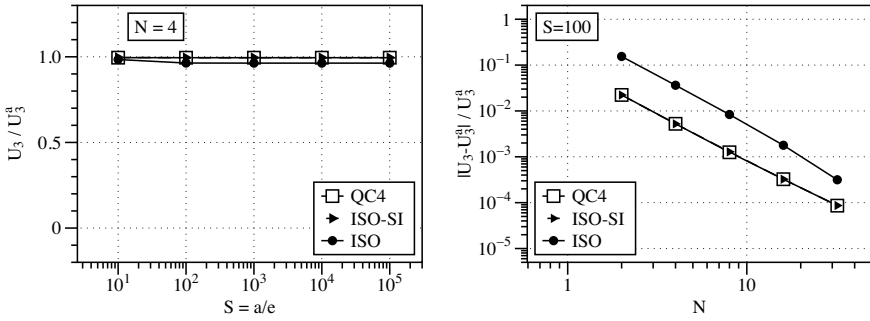


Fig. 6.14: Results of the shear locking test for the full mixed EM2 model.

### 6.4.2.3 Effectiveness of the QC4/CL8 Approach for Variable Kinematics Models

The shear locking test is carried out for various CUF-based elements in order to demonstrate the effectiveness of the proposed QC4 and CL8 approach irrespective of the employed plate kinematics. Only results for the four-node are shown, the very similar results obtained for the CL8 elements are omitted for the sake of brevity. Figure fig:validCUF-ShearLock illustrates the results obtained with several LW as well ESL models, formulated in the framework of PVD and RMVT, with the new QC4 finite element approximations. All curves are sensibly overlapped, which thus validates the proposed approach for all CUF-based variable kinematics models. In particular, for displacement-based elements, it is clearly sufficient to correct only the  $z$ -constant part of the transverse shear strain in order to eliminate the locking pathology. The independence of the FE approximation from any refinement of the FSDT kinematics has been already pointed out in D’Ottavio et al (2006).

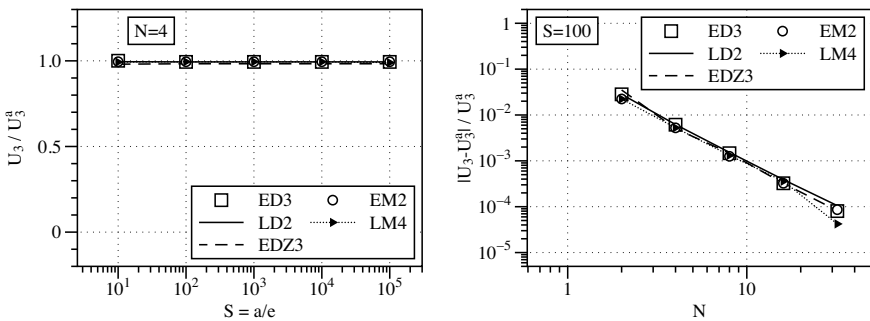


Fig. 6.15: Results of the shear locking test for various CUF models and QC4 approximation.

### 6.4.3 The Distortion Tests

In this section, the sensitivity of the present FE to the mesh distortion is illustrated on two test cases widely used in open literature, namely the square plate with distorted mesh and the circular plate.

#### 6.4.3.1 The Square Plate Test

This standard test is classically used in order to investigate the mesh sensitivity in plate bending problems. The data are given as follows:

geometry	square plate $a \times a$ with $a = 100$ and thickness $e = 1$
boundary conditions	(SA) on all sides
loading	(C)
material properties	isotropic with $E = 10.92$ and $\nu = 0.3$
mesh	$N = 2$ for the quarter plate, with the distortion parameter $s \in \{-12, -8, -4, 0, 4, 8, 12\}$ – see Fig. 6.16
results	transverse displacement $U_3 = u_3(a/2, a/2, 0)$
reference value	transverse displacement $U_3^{(0)}$ for the regular mesh ( $s = 0$ )

The distorted meshes are characterized by the parameter  $s$  defining the coordinates of the mid-node of the quarter plate, which is located in the undistorted mesh ( $s = 0$ ) at  $X_1 = X_2 = a/4$ . The parameter  $s$  may be positive or negative, as illustrated in Fig. 6.16, and it defines the coordinates of the mid-node as  $(a/4 + s, a/4 + s)$ : by taking  $a = 100$ , for the most distorted meshes ( $s = \pm 12$ ) the mid-node is hence located at  $(\pm 37, \pm 37)$ . Note that it is not usual in open literature to consider positive and negative values for the parameter  $s$ . Since a concentrated load is applied at  $X_1 = X_2 = a/2$ , the results obtained for positive and negative values of  $s$  may not be symmetric.

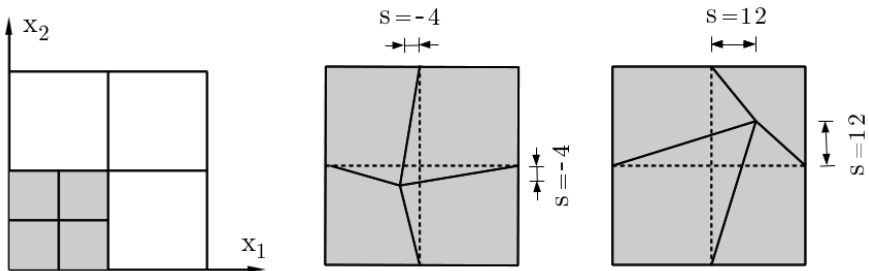


Fig. 6.16: Mesh for the quarter plate with distortion defined by the parameter  $s$ .

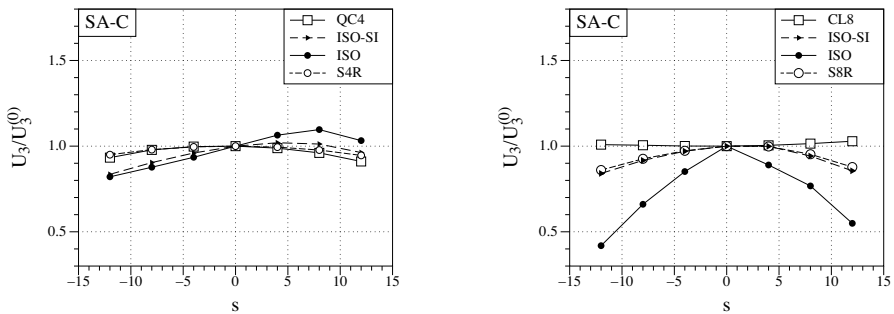


The transverse displacement  $U_3$  at the center node is normalized with respect to the value  $U_3^0$  obtained with the regular, undistorted mesh ( $s = 0$ ). Fig. 6.17 shows the results obtained by the ED2 model: on the left are reported the curves obtained by the four-node elements while on the right those obtained by the eight-node elements. The ABAQUS finite elements S4R and S8R, are included in the comparison. The results show that the proposed QC4 and CL8 are the most robust elements with respect to mesh distortion, in particular CL8 results to be practically insensitive to the mesh distortion parameter. The highest distortion sensitivity is displayed by the full-integrated ISO elements. Selective reduced quadrature elements ISO-SI perform better than the ISO elements: in the four-node case the enhancement is seen only for  $s > 0$ . The ABAQUS S4R element has very similar performances of the QC4 element, whereas the S8R element closely follows the behavior of the eight-node ISO-SI element and is thus outperformed by the proposed CL8 element.

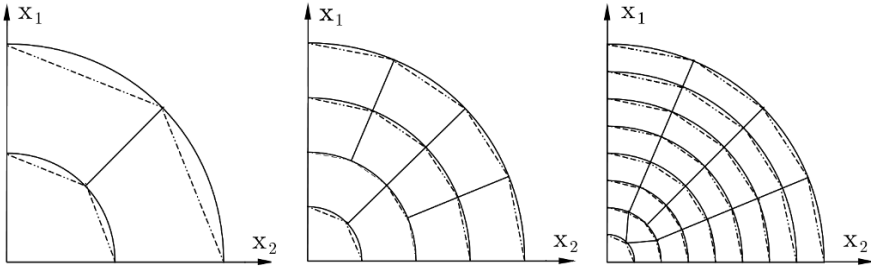
### 6.4.3.2 The Circular Plate Test

Another mesh distortion sensitivity test is considered, which concerns the bending of a clamped circular isotropic plate subjected to a uniform pressure load according to the following data:

- geometry                      circular plate of radius  $R = 5$  and thickness  $e = 0.1$
- boundary conditions      (CL) on the external perimeter
- loading                        (P)
- material properties        isotropic with  $E = 1.7472 \cdot 10^7$  and  $\nu = 0.3$
- mesh                             $N = 3, 12, 28, 60$  elements for a quarter plate – see Fig. 6.18
- results                         deflection  $U_3 = u_3(0, 0, 0)$  at the center of the plate



**Fig. 6.17:** Square plate test (SA-C): variation of the normalized central deflection with respect to the mesh distortion parameter  $s$ . Four-node (left) and eight-node elements (right), ED2 model.



**Fig. 6.18:** FE meshes with  $N = 3, 12, 28$  elements for a quarter of the circular plate: 8-node elements (continuous line) and 4-node elements (dotted line).

reference value                      Kirchhoff-Love theory  $U_3^{\text{ref}} = 0.61147 \cdot 10^{-6}$  Batoz and Dhatt (1990)

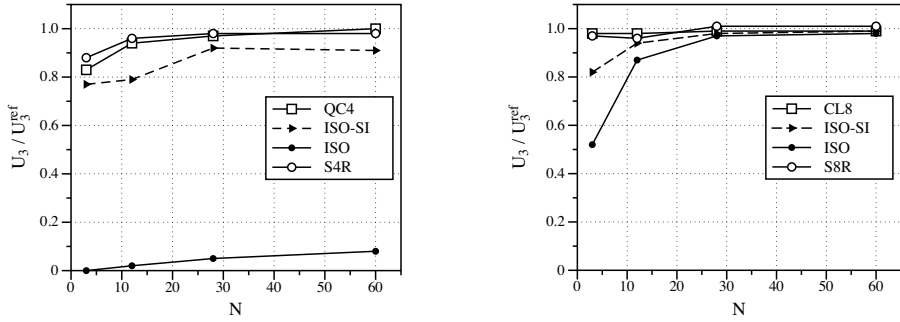
The evolution of the ratio between the central deflection and the Kirchhoff-Love solution with respect to the mesh density is reported in Fig. 6.19. The ED2 kinematics is again used and the results obtained by ABAQUS finite elements S4R and S8R are also shown for comparison.

Concerning the four-node elements (Fig. 6.19, left), it has been already shown that the ISO element suffers the distorted shapes, and for the present case it shows errors exceeding 90% even with the more refined mesh. It can be noticed that the QC4 element has a good convergence rate and its accuracy is very satisfactory. In particular, the error becomes less than 3% for  $N \geq 30$ , whereas the converged result of the four-node ISO-SI FE is still affected with an error of about 10%. The ABAQUS S4R element shows a higher accuracy than the present QC4 element for coarser meshes, but the differences between S4R and QC4 are negligible as the mesh is refined.

Observing the results for the eight-node elements (Fig. 6.19, right), it is noted that the ISO element suffers the distorted shapes, but the deflection tends towards the solution as the mesh is refined ( $N \geq 28$ ). It is further confirmed that the CL8 element is very robust, with performances that in this case are slightly better compared to those of the ABAQUS S8R element.

### 6.5 Conclusion

This paper has introduced robust FE interpolations for four-node and eight-node quadrilateral plate elements with variable kinematics expressed through Carrera’s Unified Formulation. A previous work focused on four-node PVD-based elements Le et al (2017), has been thus extended to eight-node serendipity FE approximations as well as to RMVT-based plate models. In the framework of displacement-based models, two field-consistent transverse shear strain approximations referred to as QC4



**Fig. 6.19:** Convergence study of the central deflection for the circular plate. Four-node (left) and eight-node elements (right), ED2 model.

and CL8 Polit et al (1994) have been extended to plate models of arbitrary kinematic order, including ESL and LW descriptions, by modifying only the  $z$ -constant part of the transverse shear strain. In the framework of RMVT based models, it has been shown that the full mixed formulation with isoparametric approximations does not show any shear locking pathology, but that the corresponding mixed-hybrid FEM requires an opportune correction. An enhanced mixed-hybrid FEM has been thus proposed by adopting for the transverse shear stress field the interpolation schemes resulting from the QC4 and CL8 formulations.

First results have been presented in view of assessing the robustness and accuracy of the proposed elements. For this, a number of numerical tests have been considered that are recommended whenever FE applications are proposed: eigenvalue counts to ensure the proper rank of the stiffness matrices, convergence behavior for thin and thick plates, as well as two case studies involving distorted meshes. The numerical results confirmed the superiority of the proposed FEs in comparison to classical isoparametric approaches with full or reduced integrations, i.e., they have a correct rank, are free of transverse shear locking and are less sensitive to distorted element shapes. The proposed variable kinematics FEs, implemented as a user subroutine into ABAQUS, provide a robust tool for the analysis of composite laminates, for which different models may be used for adapting the computational cost in case of thin or thick plates or whether a global or local response is required.

The preliminary results shown in this paper shall be completed by further analyses of RMVT based elements and of composite plates, including laminates and sandwich configurations. Furthermore, the optimization of the computational cost for FE models of composite structures shall be considered: on the one hand, the FE implementation of a more general variable kinematics modeling approach will be considered D’Ottavio (2016); the variable kinematics models shall, on the other hand, be effectively employed within a global-local approach that limits the use of expensive, highly accurate and quasi-3D models to small model portions.

## Appendix 1

The interpolation functions on the elementary domain are defined as follows

$$\begin{aligned}
 C_{\xi 1}(\xi, \eta) &= \frac{1}{4}(-\eta - \sqrt{3}\xi)(1 - \eta); & C_{\eta 1}(\xi, \eta) &= \frac{1}{4}(-\xi - \sqrt{3}\eta)(1 - \xi) \\
 C_{\xi 2}(\xi, \eta) &= \frac{1}{4}(-\eta + \sqrt{3}\xi)(1 - \eta); & C_{\eta 2}(\xi, \eta) &= \frac{1}{4}(\xi - \sqrt{3}\eta)(1 + \xi) \\
 C_{\xi 3}(\xi, \eta) &= \frac{1}{4}(\eta + \sqrt{3}\xi)(1 + \eta); & C_{\eta 3}(\xi, \eta) &= \frac{1}{4}(\xi + \sqrt{3}\eta)(1 + \xi) \\
 C_{\xi 4}(\xi, \eta) &= \frac{1}{4}(\eta - \sqrt{3}\xi)(1 + \eta); & C_{\eta 4}(\xi, \eta) &= \frac{1}{4}(-\xi + \sqrt{3}\eta)(1 - \xi) \\
 C_{\xi 5}(\xi, \eta) &= 1 - \eta^2; & C_{\eta 5}(\xi, \eta) &= 1 - \xi^2
 \end{aligned} \tag{6.34}$$

## Appendix 2

The non-zero terms of the  $9 \times 3$  matrices  $\bar{B}_i$  ( $i = 1, 8$ ) defining the CL8 interpolation for  $\bar{\gamma}^0$  as in Eq. (6.29) are

$$\begin{aligned}
 \bar{B}_i(1, 1) &= \sum_{I=1}^5 C_{\xi I} \left( N_i(\xi_I, \eta_I) J_{11}^{(I)}(\xi_I, \eta_I) + N_{i,\xi}^{RT}(\xi_I, \eta_I) \right) \\
 \bar{B}_i(1, 2) &= \sum_{I=1}^5 C_{\xi I} \left( N_i(\xi_I, \eta_I) J_{12}^{(I)}(\xi_I, \eta_I) + N_{i,\xi}^{ST}(\xi_I, \eta_I) \right) \\
 \bar{B}_i(8, 3) &= \sum_{I=1}^5 C_{\xi I} N_i(\xi_I, \eta_I) \\
 \bar{B}_i(4, 1) &= \sum_{J=1}^5 C_{\eta J} \left( N_i(\xi_J, \eta_J) J_{21}^{(J)}(\xi_J, \eta_J) + N_{i,\eta}^{RT}(\xi_J, \eta_J) \right) \\
 \bar{B}_i(4, 2) &= \sum_{J=1}^5 C_{\eta J} \left( N_i(\xi_J, \eta_J) J_{22}^{(J)}(\xi_J, \eta_J) + N_{i,\eta}^{ST}(\xi_J, \eta_J) \right) \\
 \bar{B}_i(9, 3) &= \sum_{J=1}^5 C_{\eta J} N_i(\xi_J, \eta_J)
 \end{aligned} \tag{6.35}$$

where  $J_{\alpha\beta}^{(p)}$  ( $p = 1, 5$ ) is the Jacobian at sampling points. The isoparametric interpolation functions for node  $i$  are denoted  $N_i$ . The functions  $N_i^{RT}$  and  $N_i^{ST}$  are given as

$$\begin{aligned}
N_{i(i=1,2,3,4)}^{RT}(\xi, \eta) &= \frac{1}{12} \left[ -J_{11}^{N_i} \xi (\xi^2 - 1)(1 + \eta_i \eta) - J_{21}^{N_i} (1 + \xi_i \xi) \eta (\eta^2 - 1) \right] \\
N_{i(i=5,7)}^{RT}(\xi, \eta) &= \frac{1}{6} \left[ J_{11}^{N_i} \xi (\xi^2 - 1)(1 + \eta_i \eta) \right] \\
N_{i(i=6,8)}^{RT}(\xi, \eta) &= \frac{1}{6} \left[ J_{21}^{N_i} (1 + \xi_i \xi) \eta (\eta^2 - 1) \right] \\
N_{i(i=1,2,3,4)}^{ST}(\xi, \eta) &= \frac{1}{12} \left[ -J_{12}^{N_i} \xi (\xi^2 - 1)(1 + \eta_i \eta) - J_{22}^{N_i} (1 + \xi_i \xi) \eta (\eta^2 - 1) \right] \\
N_{i(i=5,7)}^{ST}(\xi, \eta) &= \frac{1}{6} \left[ J_{12}^{N_i} \xi (\xi^2 - 1)(1 + \eta_i \eta) \right] \\
N_{i(i=6,8)}^{ST}(\xi, \eta) &= \frac{1}{6} \left[ J_{22}^{N_i} (1 + \xi_i \xi) \eta (\eta^2 - 1) \right]
\end{aligned} \tag{6.36}$$

where  $J_{\alpha\beta}^{N_i}$  ( $i = 1, 8$ ) is the Jacobian at nodes  $i$ .

## References

- Barut A, Madenci E, Tessler A (2013)  $C^0$ -continuous triangular plate element for laminated composite and sandwich plates using the {2,2}-Refined Zigzag Theory. *Compos Struct* 106:835–853
- Bathe KJ, Dvorkin EN (1985) A four-node plate bending element based on Mindlin/Reissner plate theory and a mixed interpolation. *Int J Numer Meth Eng* 21:367–383
- Batoz JL, Dhatt G (1990) *Modélisation des Structures par Eléments Finis*, volume 2: Poutres et Plaques. Hermès
- Batoz JL, Lardeur P (1989) A discrete shear triangular nine d.o.f. element for the analysis of thick to very thin plates. *Int J Numer Meth Eng* 28:533–560
- Belytschko T, Liu WK, Moran B (2000) *Nonlinear Finite Elements for Continua and Structures*. John Wiley & Sons, LTD, 2 edition
- Bletzinger KU, Bischoff M, Ramm E (2000) A unified approach for shear locking free triangular and rectangular shell finite elements. *Comput Struct* 75:321–334
- Botshekanan Dehkordi M, Cinefra M, Khalili SMR, Carrera E (2013) Mixed LW/ESL models for the analysis of sandwich plates with composite faces. *Compos Struct* 98:330–339
- Carrera E (1998) Evaluation of layerwise mixed theories for laminated plates analysis. *AIAA J* 36:830–839
- Carrera E (2000) Single- vs multilayer plate modelings on the basis of Reissner's mixed theorem. *AIAA J* 38:342–352
- Carrera E (2001) Developments, ideas and evaluations based upon Reissner's Mixed Variational Theorem in the modeling of multilayered plates and shells. *Appl Mech Rev* 54:301–329
- Carrera E (2003a) Historical review of zig-zag theories for multilayered plates and shells. *Appl Mech Rev* 56:287–308
- Carrera E (2003b) Theories and finite elements for multilayered plates and shells: A unified compact formulation with numerical assessment and benchmarking. *Arch Comput Meth Eng* 10:215–296
- Carrera E (2004) On the use of Murakami's zig-zag function in the modeling of layered plates and shells. *Comput Struct* 82:541–554
- Carrera E, Demasi L (2002a) Classical and advanced multilayered plate elements based upon PVD and RMVT. Part 1: Derivation of finite element matrices. *Int J Numer Meth Eng* 55(2):191–231
- Carrera E, Demasi L (2002b) Classical and advanced multilayered plate elements based upon PVD and RMVT. Part 2: Numerical implementations. *Int J Numer Meth Eng* 55(3):253–291
- Carrera E, Cinefra M, Nali P (2010) MITC technique extended to variable kinematic multilayered plate elements. *Compos Struct* 92:1888–1895

- Carrera E, Pagani A, Petrolo M (2013) Use of Lagrange multipliers to combine 1D variable kinematic finite elements. *Comput Struct* 129:194–206
- Carrera E, Cinefra M, Petrolo M, Zappino E (2014) *Finite Element Analysis of Structures through Unified Formulation*. John Wiley & Sons, Ltd
- Carrera E, Cinefra M, Lamberti A, Petrolo M (2015) Results on best theories for metallic and laminated shells including layer-wise models. *Compos Struct* 126:285–298
- Carrera E, Pagani A, Valvano S (2017) Multilayered plate elements accounting for refined theories and node-dependent kinematics. *Compos B* 114:189–210
- Chinosi C, Cinefra M, Della Croce L, Carrera E (2013) Reissner's mixed variational theorem toward MITC finite elements for multilayered plates. *Compos Struct* 99:443–452
- Cinefra M, Chinosi C, Della Croce L (2013) MITC9 shell elements based on refined theories for the analysis of isotropic cylindrical structures. *Mech Adv Mater Struct* 20:91–100
- Cinefra M, Chinosi C, Della Croce L, Carrera E (2014) Refined shell finite elements based on RMVT and MITC finite elements for the analysis of laminated structures. *Compos Struct* 113:492–497
- Demasi L (2008)  $\infty^3$  hierarchy plate theories for thick and thin composite plates: The generalized unified formulation. *Compos Struct* 84:256–270
- Demasi L (2010) Invariant finite element model for composite structures: The generalized unified formulation. *AIAA J* 48:1602–1619
- Demasi L (2012) Partially Zig-Zag advanced higher order shear deformation theories based on the Generalized Unified Formulation. *Compos Struct* 94:363–375
- Demasi L (2013) Partially Layer Wise advanced Zig Zag and HSDT models based on the Generalized Unified Formulation. *Eng Struct* 53:63–91
- D'Ottavio M (2016) A Sublaminated Generalized Unified Formulation for the analysis of composite structures and its application to sandwich plates bending. *Compos Struct* 142:187–199
- D'Ottavio M, Ballhause D, Wallmersperger T, Kröplin B (2006) Considerations on higher-order finite elements for multilayered plates based on a unified formulation. *Comput Struct* 84:1222–1235
- D'Ottavio M, Dozio L, Vescovini R, Polit O (2016) Bending analysis of composite laminated and sandwich structures using sublaminated variable-kinematic Ritz models. *Compos Struct* 155:45–62
- Feng W, Hoa SV (1998) Partial hybrid finite elements for composite laminates. *Finite Elem Anal Des* 30:365–382
- Ferreira AJM (2005) Analysis of composite plates using a layerwise shear deformation theory and multiquadrics discretization. *Mech Adv Mater Struct* 12:99–112
- Hoa SV, Feng W (1998) *Hybrid Finite Element Method for Stress Analysis of Laminated Composites*. Springer Science+Business Media, LLC, New York
- Hu H, Belouettar S, Potier-Ferry M, Daya EM (2009) Multi-scale modelling of sandwich structures using the Arlequin method - Part I: Linear modelling. *Finite Elem Anal Des* 45:37–51
- Hughes TJR (1987) *The Finite Element Method*. Prentice-Hall
- Hughes TJR, Tezduyar T (1981) Finite elements based upon Mindlin plate theory with particular reference to the four node bilinear isoparametric element. *J Appl Mech* 46:587–596
- Kulikov GM, Plotnikova SV (2016) A hybrid-mixed four-node quadrilateral plate element based on sampling surfaces method for 3D stress analysis. *Int J Numer Meth Eng* 108:26–54
- Le THC, D'Ottavio M, Vidal P, Polit O (2017) A new robust quadrilateral four-node variable kinematics plate element for composite structures. *Finite Elem Anal Des* 113:10–24
- Li MS (1989) Higher order laminated composite plate analysis by hybrid finite element method. PhD thesis, Massachusetts Institute of Technology
- MacNeal RH (1982) Derivation of element stiffness matrices by assumed strain distributions. *Nucl Eng Des* 70:3–12
- Mijuca D (2004) On hexahedral finite element HC8/27 in elasticity. *Comput Mech* 33:466–480
- Murakami H (1986) Laminated composite plate theory with improved in-plane response. *J Appl Mech* 53:661–666
- N N (2016) *Abaqus Theory Manual*. Dassault Systèmes

- Park KC, Pramono E, Stanley GM, Cabiness HA (1989) The ANS shell elements: earlier developments and recent improvements. vol 3 of *CED*, pp 217–239
- Pian THH, Li MS (1990) Stress analysis of laminated composites by hybrid finite elements. Springer-Verlag
- Pian THH, Sumihara K (1995) State-of-the-art development of hybrid/mixed finite element method. *Finite Elem Anal Des* 21:5–20
- Polit O, Touratier M, Lory P (1994) A new eight-node quadrilateral shear-bending plate finite element. *Int J Numer Meth Eng* 37:387–411
- Polit O, Vidal P, D'Ottavio M (2012) Robust  $C^0$  high-order plate finite element for thin to very thick structures: mechanical and thermo-mechanical analysis. *Int J Numer Meth Eng* 90:429–451
- Rao MK, Desai YM (2004) Analytical solutions for vibrations of laminated and sandwich plates using mixed theory. *Compos Struct* 63:361–373
- Reddy JN (1984) A simple higher-order theory for laminated composite plates. *J Appl Mech* 51:745–752
- Reddy JN (1987) A generalization of two-dimensional theories of laminated composite plates. *Comm Appl Numer Meth* 3:173–180
- Reddy JN (1993) An evaluation of equivalent-single-layer and layerwise theories of composite laminates. *Compos Struct* 25:21–35
- Reddy JN (2004) *Mechanics of Laminated Composite Plates and Shells: Theory and Analysis*. CRC Press, 2nd edition
- Reissner E (1984) On a certain mixed variational theorem and a proposed application. *Int J Numer Meth Eng* 20:1366–1368
- Robbins Jr DH, Reddy JN (1993) Modelling of thick composites using a layerwise laminate theory. *Int J Numer Meth Eng* 36:655–677
- Robbins Jr DH, Reddy JN (1996) Variable kinematic modeling of laminated composite plates. *Int J Numer Meth Eng* 39:2283–2317
- Sayyad AS, Ghugal YM (2015) On the free vibration analysis of laminated composite and sandwich plates: A review of recent literature with some numerical results. *Compos Struct* 129:177–201
- Somashekar BR, Prathap G, Babu CR (1987) A field-consistent, four-noded, laminated, anisotropic plate/shell element. *Comput Struct* 25:345–353
- Sun CT, Whitney JM (1973) Theories for the dynamic response of laminated plates. *AIAA J* 11:178–183
- Tessler A (2015) Refined zigzag theory for homogeneous, laminated composite, and sandwich beams derived from Reissner's mixed variational principle. *Meccanica* 50:2621–2648
- Timoshenko SP, Woinowsky-Krieger S (1959) *Theory of Plates and Shells*. McGraw-Hill, 2 edition
- Toledano A, Murakami H (1987) A composite plate theory for arbitrary laminate configurations. *J Appl Mech* 54:181–189
- Touratier M (1991) An efficient standard plate theory. *Int J Eng Sci* 29:901–916
- Vidal P, Polit O (2011) A sine finite element using a zig-zag function for the analysis of laminated composite beams. *Compos B* 42:1671–1682
- Wenzel C, Vidal P, D'Ottavio M, Polit O (2014) Coupling of heterogeneous kinematics and finite element approximations applied to composite beam structures. *Compos Struct* 116:177–192
- Zienkiewicz OC, Taylor RL (2000) *The Finite Element Method, volume 2: Solid Mechanics*. Butterworth-Heinemann, 5 edition

## Chapter 7

# Effect of Magnetic Field on Free and Forced Vibrations of Laminated Cylindrical Shells Containing Magnetorheological Elastomers

Gennadi Mikhasev, Ihnat Mlechka, and Svetlana Maevskaya

**Abstract** Free and forced vibrations of thin medium-length laminated cylindrical shells and panels assembled from elastic materials and magnetorheological elastomer (MRE) embedded between elastic layers are studied. The equivalent single layer model based on the generalized kinematic hypotheses of Timoshenko is used for the dynamic simulation of laminated shells. The full system of differential equations taking into account transverse shears, written in terms of the generalized displacements, is used to study free vibrations of long sandwich cylindrical shells with the MRE cores. To predict free and forced vibrations of medium-length sandwich cylindrical shells and panels, the simplified equations in terms of the force and displacement functions are utilized. The influence of an external magnetic field on the natural frequencies and logarithmic decrement for the MRE-based sandwich cylindrical shells is analyzed. If an applied magnetic field is nonuniform in the direction perpendicular to the shell axis, the natural modes of the medium-length cylindrical sandwich with the homogeneous MRE core are found in the form of functions decreasing far away from the generatrix at which the real part of the complex shear modulus has a local minimum. The high emphasis is placed on forced vibrations and their suppressions with the help of a magnetic field. Damping of medium-length cylindrical panels with the MRE core subjected to an external vibrational load is studied. The influence of the MRE core thickness, the level of an external magnetic field and the instant time of its application on the damping rate of forced vibrations is examined in details.

---

Gennadi Mikhasev · Ihnat Mlechka  
Belarusian State University, 220030 Minsk, Belarus  
e-mail: mikhasev@bsu.by, ignat.mlechka@gmail.com

Svetlana Maevskaya  
Vitebsk State University, 210030 Vitebsk, Belarus  
e-mail: svetlanamaevskaya@ya.ru



## 7.1 Introduction

Magnetorheological elastomers (MREs) belong to a new class of smart materials which due to their unique properties are gaining high interest in various areas of the structural mechanics (Gibson, 2010). MREs are composite materials consisting of a matrix (either rubbery polymer or deformed inorganic polymer) and magnetizable particles molded in this matrix. The principal mechanical characteristics of these materials are the storage and loss moduli, represented by the complex shear modulus, which are varied in a wide range when subjected to a magnetic field (Ginder, 1996; Jolly et al, 1999; Davis, 1999; Ginder et al, 2001). The MREs controllable viscoelastic properties as well as a light weight make these materials ideal to use as damping treatments or core elements in thin-walled structures experiencing an external vibrational load.

For the recent fifteen years, a considerable number of research has been carried out to observe the controllable properties and the vibration suppression capabilities of MREs embedded between elastic layers in sandwich or multilayered beams (see, among many others, Sun et al, 2003; Zhou and Wang, 2005; Howson and Zare, 2005; Zhou and Wang, 2006; Banerjee et al, 2007; Lara-Prieto et al, 2010; Korobko et al, 2012). There are much less papers on free and forced vibrations of MRE-based plates. Yeh (2013, 2014) studied the effect of different magnetic field on the modal damping and the natural frequencies for sandwich plates containing MRE cores and Aguib et al (2014); Ying et al (2014) considered forced vibrations of magnetorheological (MR) sandwich plates excited by deterministic and stochastic forces, respectively.

To the authors' best knowledge, there are only a few available papers related to the dynamic analysis of laminated shells containing cores made of a smart material with controllable elastic and rheological properties. In Yeh (2011), a three layered orthotropic cylindrical shell with an electrorheological (ER) core and outer constraining layers was considered. Introducing the complex shear modulus for the ER core and utilizing the discrete layer finite element method, the author studied the vibration and damping characteristics of the smart sandwich under different levels of applied electric fields. Mikhasev et al (2011a), applying the equivalent single layer (ESL) model for multilayered cylindrical shells, studied free vibrations of thin laminated circular cylinders with MR layers under different levels of magnetic fields. The authors concluded that an applied magnetic field may have a significant effect on the vibration characteristics of thin MRE-based laminated cylinders. An interesting effect of distortion of natural modes in a thin medium-length cylindrical sandwich containing a polarized MRE core has been captured in Mikhasev et al (2014): an applied magnetic field may result in localization of natural modes near some lines where the real part of the reduced complex shear modulus reaches a local minimum. Recently, Mikhasev et al (2011b) studied a response of a MRE-based laminated cylindrical shell with local disturbances in their surface to an applied not stationary magnetic field. It has been shown that slowly growing magnetic fields may be used with success in order to ensure the soft suppression of running localized vibrations in thin-walled structures.

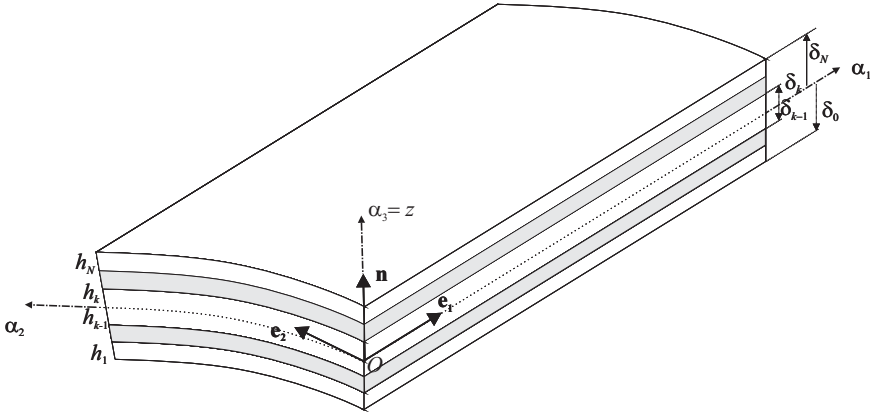
In our view, a large range of problems on free and forced vibrations of MRE-based laminated shells is not studied yet. In particular, the effect of a magnetic field on free low-frequency vibrations of medium-length cylindrical sandwich panels with MRE cores is worthy of close attention owing to a wide application of laminated panels as members of many engineering structures. Problems on the modal damping of oscillations of laminated shells with controllable MRE cores subjected to a harmonic vibrational load deserves also special attention.

A lack of detailed studies on the aforementioned and many other problems may be explained by the complexity of available models for laminated shells assembled from elastic and viscoelastic MRE laminas. In the most general terms, the known theories for multilayered shells proceed from the order of shell equations depending on a number of stacked layers (Hsu and Wang, 2005; Bolotin and Novichkov, 1980). These theories as well as available high accurate layer-wise theories (Carrera, 1999, 2002, 2003; Ferreira et al, 2011)) are rather sophisticated for practical application. The additional complexity is introduced by the coupling of the mechanical and physical (magnetic or electric) fields.

In our paper, we proceed from the idea to replace an original laminated shell containing a MRE core or layers by an equivalent single layer shell with the reduced complex moduli affected by an external magnetic field. The ESL model is expected to be more perspective for the dynamic simulation of tunable laminated thin-walled structures containing MR layers (survey articles and monographs devoted to ESL theories are, e.g., Grigolyuk and Kulikov, 1988a,b; Toorani and Lakis, 2000; Reddy, 2003; Qatu, 2004; Qatu et al, 2010). Based on the assumptions of the generalized kinematic hypothesis of Timoshenko for a whole package of a laminated shell (Grigolyuk and Kulikov, 1988b), we assume differential equations written in terms of displacements (or in terms of the force and shear functions where it is required) for the reference surface of a laminated shell as the governing equations. These equations contain coefficients depending on the complex Young's and shear moduli and the magnetic field induction as well, they being the generalization (Mikhasev et al, 2011a) of analogous equations derived in Grigolyuk and Kulikov (1988b) for elastic laminated shells. The basic purpose of the paper is to study free vibrations of sandwich cylindrical shells and panels with the MRE cores under various levels of applied external magnetic fields. The effect of a nonuniform magnetic field on the natural modes corresponding to low-frequency vibrations of a thin medium-length circular cylindrical sandwich shell containing the MRE core is also analyzed. The special attention is focused on the problem of suppression of forced vibrations in MRE panels subjected to a harmonic vibrational load under an external magnetic field.

## 7.2 Structure of Laminated Shell

Consider a thin laminated package in the form of a circular cylinder or panel of the length  $L$  (see Fig. 7.1). Let it consist of  $N$  isotropic or transversely isotropic layers



**Fig. 7.1:** Laminated cylindrical shell with a curvilinear coordinate system

characterized by thickness  $h_k$ , density  $\rho_k$ , Young's modulus  $E_k$ , shear modulus  $G_k$  and Poisson's ratio  $\nu_k$ , where  $k = 1, 2, \dots, N$ , and  $N$  is an odd number. The middle surface of any fixed layer is taken as the reference surface. We introduce a local orthogonal coordinate system by means of unit vectors  $\mathbf{e}_1$ ,  $\mathbf{e}_2$  and  $\mathbf{n} = \mathbf{e}_1 \times \mathbf{e}_2$  with an origin in the point  $O$  at the reference surface as shown in Fig. 7.1. Let  $\alpha_1$  and  $\alpha_2$  be the axial and circumferential coordinates, respectively, and  $\alpha_3 = z$  is the normal coordinate. The radius of curvature of the reference surface is  $R = 1/k_{22}$ .

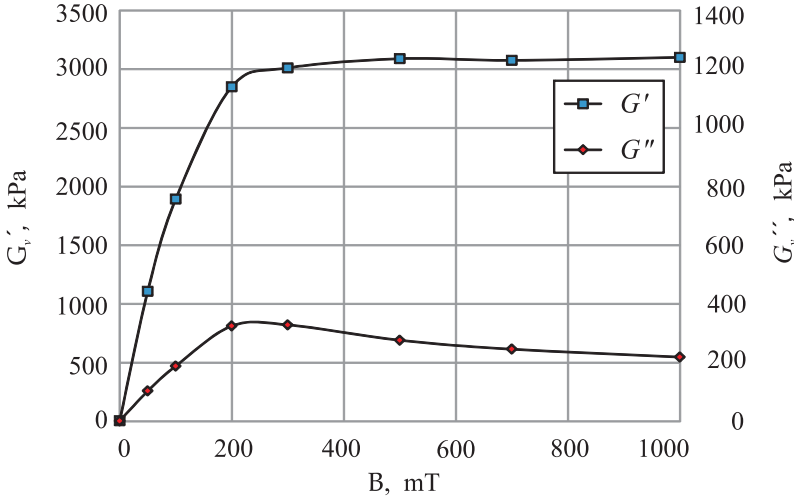
Laminas with odd numbers (numbering begins with the innermost layer) are made of an elastic material, while layers with even numbers are made of a magnetorheological elastomer (MRE) whose rheological properties depend on intensity of an applied magnetic field. For layers made of a MRE, the Young's and shear moduli,  $E_k, G_k$ , are assumed to be complex functions of the magnetic field induction  $B$ :

$$E_k = E'_k(B) + iG''_k(B), \quad G_k = G'_k(B) + iG''_k(B), \quad (7.1)$$

where  $i = \sqrt{-1}$  is the imaginary unite. If the MRE layer is considered as an isotropic material, then

$$G_k = \frac{E_k}{2(1 + \nu_k)},$$

otherwise (for a transversally isotropic layer),  $E_k$  and  $G_k$  are independent magnitudes. Here, each viscoelastic MRE layer is considered as the isotropic material with Poissons's ratio (White and Choi, 2005)  $\nu_v = 0.4$  and the shear modulus  $G_v = G'_v + iG''_v$  specified in Korobko et al (2012). For this MRE, the dependence of the storage and loss moduli,  $G'_v, G''_v$ , on the magnetic field induction  $B$  are shown in Fig. 7.2. If an applied magnetic field is non-homogeneous, then  $E_v[B(\alpha_1, \alpha_2)], G_v[B(\alpha_1, \alpha_2)]$  corresponding to the MRE layers are functions of coordinates  $\alpha_1, \alpha_2$ .



**Fig. 7.2:** Storage and loss moduli  $G'_v, G''_v$  (kPa) of the MRE vs. the magnetic field induction  $B$  (mT)

### 7.3 Basic Hypotheses

To study vibrations of multilayered shells, we will use the ESL model (Grigolyuk and Kulikov, 1988b) based on the generalized hypothesis of Timoshenko. Let  $z = \delta_k$  be the coordinate of the upper bound of the  $k^{\text{th}}$  layer,  $u_i$  and  $w$  the tangential and normal displacements of the reference surface points, respectively,  $u_i^{(k)}$  the tangential displacements of points of the  $k^{\text{th}}$  layer,  $\sigma_{i3}$  the transverse shear stresses,  $\Theta_i$  the angles of rotation of the normal  $\mathbf{n}$  about the vector  $\mathbf{e}_i$  (see Fig. 7.1). Here  $i = 1, 2; k = 1, 2, \dots, N$ .

Let us assume the following hypothesis (Grigolyuk and Kulikov, 1988b):

1. The distribution law of the transverse tangent stresses across the thickness of the  $k^{\text{th}}$  layer is assumed to be of the form

$$\sigma_{i3} = f_0(z)\mu_i^{(0)}(\alpha_1, \alpha_2) + f_k(z)\mu_i^{(k)}(\alpha_1, \alpha_2), \quad (7.2)$$

where  $f_0(z), f_k(z)$  are continuous functions introduced as follows

$$\begin{aligned} f_0(z) &= \frac{1}{h^2}(z - \delta_0)(\delta_N - z), \\ f_k(z) &= \frac{1}{h_k^2}(z - \delta_{k-1})(\delta_k - z) \end{aligned} \quad (7.3)$$

2. Normal stresses acting on the area elements parallel to the reference one are negligible with respect to other components of the stress tensor.
3. The normal deflection  $w$  does not depend on the co-ordinate  $z$ .
4. The tangential displacements are distributed across thickness of the layer package as follows:

$$u_i^{(k)}(\alpha_1, \alpha_2, z) = u_i(\alpha_1, \alpha_2) + z\theta_i(\alpha_1, \alpha_2) + g(z)\psi_i(\alpha_1, \alpha_2) \quad (7.4)$$

where

$$g(z) = \int_0^z f_0(x)dx.$$

In Eq. (7.4),  $\psi_i$  are required parameters characterizing the transverse shears in the shell. Hypothesis (7.4) permits to describe the non-linear dependence of the tangential displacements on  $z$ ; at  $g \equiv 0$  it turns into the linear Timoshenko hypothesis coinciding with the classical Kirchhoff-Love hypothesis since  $\theta_i$  are functions of the tangential displacements and derivatives of the normal deflection. Assumption (7.4) is called the generalized kinematic hypothesis of Timoshenko.

## 7.4 Governing Equations

### 7.4.1 Governing Equations in Terms of Stress Resultants and Couples

Using the variational principle and based on the aforementioned hypotheses, Grigoliuk and Kulikov have derived the equations in terms of the membrane stress resultants  $T_{ij}$  and the reduced stress couples  $\hat{L}_{ij}$ ,  $\hat{M}_{ij}$  (Grigolyuk and Kulikov, 1988b):

$$\begin{aligned} T_{1i,1} + T_{2i,2} &= q_i(\alpha_1, \alpha_2, t) - \sum_{k=1}^N \rho_k h_k \frac{\partial^2 \hat{u}_i}{\partial t^2} = 0, \quad i = 1, 2, \\ \hat{L}_{1i,1} + \hat{L}_{2i,2} &= Q_{0i}, \quad i = 1, 2, \end{aligned} \quad (7.5)$$

$$\hat{M}_{11,11} + 2\hat{M}_{12,12} + \hat{M}_{22,22} - k_{22}T_{22} = q_n(\alpha_1, \alpha_2, t) - \sum_{k=1}^N \rho_k h_k \frac{\partial^2 w}{\partial t^2} = 0,$$

where  $Z_{,i}$  designates the derivative of a function  $Z$  by  $\alpha_i$ ,  $t$  is time,  $q_i, q_n$  are the tangential and normal components of an external force,  $Q_{0i}$  is the generalized shear stress resultant. The stress resultants and couples  $T_{ij}$ ,  $Q_{0i}$ ,  $\hat{L}_{ij}$ ,  $\hat{M}_{ij}$  are linked with the normal, tangential and shear displacements  $w$ ,  $u_i, \psi_i$  by the following equations:

$$\begin{aligned}
T_{ii} &= \frac{Eh}{1-\nu^2} \left[ \hat{u}_{i,i} + \nu(\hat{u}_{j,j} + k_{22}w) \right], & T_{ij} &= \frac{Eh}{2(1+\nu)} (\hat{u}_{i,j} + \hat{u}_{j,i}), \\
\hat{M}_{ii} &= -\frac{Eh^3}{12(1-\nu^2)} \left[ \eta_3(w_{,ii} + \nu w_{,jj}) - \eta_2(\psi_{i,i} + \nu\psi_{j,j}) \right], \\
\hat{M}_{ij} &= -\frac{Eh^3}{12(1+\nu)} \left[ \eta_3 w_{,ij} - \frac{1}{2} \eta_2(\psi_{i,j} + \psi_{j,i}) \right], \\
\hat{L}_{ii} &= -\frac{Eh^3}{12(1-\nu^2)} \left[ \eta_2(w_{,ii} + \nu w_{,jj}) - \eta_1(\psi_{i,i} + \nu\psi_{j,j}) \right], \\
\hat{L}_{ij} &= -\frac{Eh^3}{12(1+\nu)} \left[ \eta_2 w_{,ij} - \frac{1}{2} \eta_1(\psi_{i,j} + \psi_{j,i}) \right], & Q_{0i} &= q_{44} \psi_i,
\end{aligned} \tag{7.6}$$

where

$$h = \sum_{k=1}^N h_k, \quad E = \frac{1-\nu^2}{h} \sum_{k=1}^N \frac{E_k h_k}{1-\nu_k^2}, \quad \nu = \sum_{k=1}^N \frac{E_k h_k \nu_k}{1-\nu_k^2} \left( \sum_{k=1}^N \frac{E_k h_k}{1-\nu_k^2} \right)^{-1} \tag{7.7}$$

are the total thickness, reduced Young's modulus and Poisson's ratio, respectively,

$$\hat{u}_i = u_i - \frac{1}{2} h c_{13} w_{,i} - \frac{1}{2} h c_{12} \psi_i \tag{7.8}$$

is the generalized displacements, and parameters  $\eta_1, \eta_2, \eta_3, c_{12}, c_{13}$  are introduced as follows:

$$\begin{aligned}
c_{12} &= \sum_{k=1}^N \xi_k^{-1} \pi_{3k} \gamma_k, & c_{13} &= \sum_{k=1}^N (\zeta_{k-1} + \zeta_k) \gamma_k, \\
\frac{1}{12} h^3 \pi_{1k} &= \int_{\delta_{k-1}}^{\delta_k} g^2(z) dz, & \frac{1}{12} h^3 \pi_{2k} &= \int_{\delta_{k-1}}^{\delta_k} z g(z) dz, \\
\frac{1}{2} h^2 \pi_{3k} &= \int_{\delta_{k-1}}^{\delta_k} g(z) dz, & \eta_1 &= \sum_{k=1}^N \xi_k^{-1} \pi_{1k} \gamma_k - 3c_{12}^2, \\
\eta_2 &= \sum_{k=1}^N \xi_k^{-1} \pi_{2k} \gamma_k - 3c_{12} c_{13}, & \eta_3 &= 4 \sum_{k=1}^N (\xi_k^2 + 3\zeta_{k-1} \zeta_k) \gamma_k - 3c_{13}^2, \\
h\xi_k &= h_k, & h\zeta_n &= \delta_n \quad (n=0, k), & q_{44} &= \frac{\left[ \sum_{k=1}^N \left( \lambda_k - \frac{\lambda_{k0}^2}{\lambda_{kk}} \right) \right]^2}{\sum_{k=1}^N \left( \lambda_k - \frac{\lambda_{k0}^2}{\lambda_{kk}} \right) G_k^{-1}} + \sum_{k=1}^N \frac{\lambda_{k0}^2}{\lambda_{kk}} G_k, \\
\lambda_k &= \int_{\delta_{k-1}}^{\delta_k} f_0^2(z) dz, & \lambda_{kn} &= \int_{\delta_{k-1}}^{\delta_k} f_k(z) f_n(z) dz, & (n=0, k).
\end{aligned} \tag{7.9}$$

In what follows, the magnitude  $G = q_{44}/h$  will be called the reduced shear modulus for the laminated package. Here, the reduced moduli  $E, \nu, G$  and parameters  $\eta_1, \eta_2, \eta_3$  are functions of the induction  $B$ .

From all variants of boundary conditions, we consider here the simply supported edges with diaphragms. In terms of displacements, stress resultants and stress couples these conditions read:

$$w = \hat{u}_2 = \psi_2 = \hat{M}_{11} = T_{11} = \hat{L}_{11} = 0 \quad \text{at} \quad \alpha_1 = 0, L. \quad (7.10)$$

### 7.4.2 Governing Equations in Terms of Displacements

Let the MRE be a homogeneous and isotropic material, and an applied magnetic field is uniform. Then the substitution of Eqs. (7.11), (7.6) into Eqs. (7.5) results in the following system of differential equations:

$$\begin{aligned} \frac{\partial^2 \hat{u}_1}{\partial \alpha_1^2} + \frac{1-\nu}{2} \frac{\partial^2 \hat{u}_1}{\partial \alpha_2^2} + \frac{1+\nu}{2} \frac{\partial^2 \hat{u}_2}{\partial \alpha_1 \partial \alpha_2} + \nu k_{22} \frac{\partial w}{\partial \alpha_1} + \frac{\rho_0(1-\nu^2)}{E} \frac{\partial^2 \hat{u}_1}{\partial t^2} &= q_1, \\ \frac{1+\nu}{2} \frac{\partial^2 \hat{u}_1}{\partial \alpha_1 \partial \alpha_2} + \frac{1-\nu}{2} \frac{\partial^2 \hat{u}_2}{\partial \alpha_1^2} + \frac{\partial^2 \hat{u}_2}{\partial \alpha_2^2} + \frac{\partial(k_{22}w)}{\partial \alpha_2} + \frac{\rho_0(1-\nu^2)}{E} \frac{\partial^2 \hat{u}_2}{\partial t^2} &= q_2, \\ \eta_2 \frac{\partial(\Delta w)}{\partial \alpha_1} - \eta_1 \left( \frac{\partial^2 \psi_1}{\partial \alpha_1^2} + \frac{1+\nu}{2} \frac{\partial^2 \psi_2}{\partial \alpha_1 \partial \alpha_2} + \frac{1-\nu}{2} \frac{\partial^2 \psi_1}{\partial \alpha_2^2} \right) + \frac{12(1-\nu^2)q_{44}}{Eh^3} \psi_1 &= 0, \\ \eta_2 \frac{\partial(\Delta w)}{\partial \alpha_2} - \eta_1 \left( \frac{\partial^2 \psi_2}{\partial \alpha_2^2} + \frac{1+\nu}{2} \frac{\partial^2 \psi_1}{\partial \alpha_1 \partial \alpha_2} + \frac{1-\nu}{2} \frac{\partial^2 \psi_2}{\partial \alpha_1^2} \right) + \frac{12(1-\nu^2)q_{44}}{Eh^3} \psi_2 &= 0, \\ \frac{h^2}{12(1-\nu^2)} \Delta \left[ \eta_3 \Delta w - \eta_2 \left( \frac{\partial \psi_1}{\partial \alpha_1} + \frac{\partial \psi_2}{\partial \alpha_2} \right) \right] \\ + \frac{k_{22}}{1-\nu^2} \left( \nu \frac{\partial \hat{u}_1}{\partial \alpha_1} + \frac{\partial \hat{u}_2}{\partial \alpha_2} + k_{22}w \right) + \frac{\rho_0}{E} \frac{\partial^2 w}{\partial t^2} &= q_n, \end{aligned} \quad (7.11)$$

where

$$\rho_0 = \sum_{k=1}^N \rho_k \xi_k$$

is the reduced density of the laminated shell.

When introducing the stress-displacement relations (7.6) into (7.10), one obtains the boundary conditions in terms of displacements:

$$w = \hat{u}_2 = \psi_2 = 0,$$

$$\begin{aligned} \eta_3 \left( \frac{\partial^2 w}{\partial \alpha_1^2} + \nu \frac{\partial^2 w}{\partial \alpha_2^2} \right) - \eta_2 \left( \frac{\partial \psi_1}{\partial \alpha_1} + \nu \frac{\partial \psi_2}{\partial \alpha_2} \right) &= 0, \\ \frac{\partial \hat{u}_1}{\partial \alpha_1} + \nu \frac{\partial \hat{u}_2}{\partial \alpha_2} + \frac{\nu}{Rw} &= 0, \end{aligned} \quad (7.12)$$

$$\eta_2 \left( \frac{\partial^2 w}{\partial \alpha_1^2} + \nu \frac{\partial^2 w}{\partial \alpha_2^2} \right) - \eta_1 \left( \frac{\partial \psi_1}{\partial \alpha_1} + \nu \frac{\partial \psi_2}{\partial \alpha_2} \right) = 0 \quad \text{at } \alpha_1 = 0, L.$$

Equations (7.11) are sufficiently complicated for analyzing both free and forced vibrations of MRE-based cylindrical shells. However, they will be useful to study free axisymmetric vibrations of circular cylindrical shells or beam-like modes of length cylinders. To predict eigenmodes corresponding to low-frequency vibrations of thin medium-length cylindrical shells, we will apply to equations of the technical shell theory.

### 7.4.3 Equations of Technical Shell Theory

Let us introduce the index of variation  $\iota$  of the stress-strain state as

$$\max\{|Z_{,1}|, |Z_{,2}|\} \sim h_*^{-\iota} Z, \quad (7.13)$$

where  $h_* = h/R$  is the dimensional thickness which is assumed as a small parameter. We will consider here the stress state which is characterized by the index of variation  $\iota = 1/2$  and the following asymptotic estimates:

$$w \sim h_* R, \quad k_{22} \sim R^{-1}, \quad u_i \ll w. \quad (7.14)$$

It is obvious that  $\hat{u}_i \ll w$  also. Let

$$\max\{\hat{u}_i\} \sim h_*^{\zeta_u} R, \quad \max\{\psi_i\} \sim h_*^{\zeta_\psi}, \quad G \sim h_*^{\zeta_G} E, \quad (7.15)$$

where  $\zeta_u, \zeta_\psi$  are the indexes of intensity of the quantities  $\hat{u}_i, \psi_i$ , respectively, and  $h_*^{\zeta_G}$  is the order of the reduced shear modulus  $G$  with regard to the reduced Young's modulus  $E$ . Then, analyzing the orders of all terms in Eqs. (7.11), we find

$$\zeta_u = 3/2, \quad \zeta_\psi = 1/2, \quad \zeta_G = 1. \quad (7.16)$$

Let  $q_i = 0$  and the inertia forces in the tangential directions be very small. Then the first two equations of system (7.5) or (7.11) become homogeneous. They are identically satisfied by the following functions:

$$T_{ij} = \delta_{ij} \Delta F - F_{,ij}, \quad (7.17)$$



where  $\delta_{ij}$  is the Kronecker delta, and  $F$  is the required stress function.

To couple the introduced stress function with the unknown displacements, we consider the strain compatibility conditions. They results in the well-known differential equation

$$\Delta^2 F - E h k_{22} w_{,11} = 0. \quad (7.18)$$

Considering the residual equations from (7.5), Grigolyuk and Kulikov (1988b) have derived the following equations:

$$\begin{aligned} D \left( 1 - \frac{\theta h^2}{\beta} \Delta \right) \Delta^2 \chi - k_{22} F_{,11} &= q_n - \rho_0 h \frac{\partial^2}{\partial t^2} \left( 1 - \frac{h^2}{\beta} \Delta \right) \chi, \\ w &= \left( 1 - \frac{h^2}{\beta} \Delta \right) \chi, \end{aligned} \quad (7.19)$$

where

$$\begin{aligned} D &= \frac{E h^3 \eta_3}{12(1-\nu^2)}, \\ \beta &= \frac{12(1-\nu^2)q_{44}}{E h \eta_1} \end{aligned} \quad (7.20)$$

are the reduced bending stiffness and shear parameter, respectively.

From the third and fourth equations of (7.11), one can find the shear displacements

$$\begin{aligned} \psi_1 &= a_{,1} + \phi_{,2}, \\ \psi_2 &= a_{,2} - \phi_{,1}, \end{aligned} \quad (7.21)$$

where

$$a = -\frac{\eta_2}{\eta_1} \frac{h^2}{\beta} \Delta \chi, \quad (7.22)$$

and  $\phi$  is the shear function which is defined from the additional equation

$$\frac{1-\nu}{2} \frac{h^2}{\beta} \Delta \phi = \phi. \quad (7.23)$$

Equation (7.23) describes the shear edge effect and should be taken into account if a simply supported edge is free of a diaphragm preventing transverse shears (Mikhasev and G., 2017). If all simply supported edges have the diaphragms, one can assume (Grigolyuk and Kulikov, 1988b)  $\phi \equiv 0$ . The correspondent boundary conditions in terms of functions  $\chi$ ,  $F$  read

$$\chi = \Delta \chi = \Delta^2 \chi = F = \Delta F = 0 \quad \text{at} \quad \alpha_1 = 0, L_1. \quad (7.24)$$

If the shell is not closed in the circumferential direction, then the boundary conditions for the simply supported edges  $\alpha_2 = 0, L_2$  with diaphragms are the same.

### 7.4.4 Error of Governing Equations

The determination of an exact error of the above equations based on the ESL model is a complicated problem. One way to estimate their error is to compare eigenvalues of some boundary-value problem on buckling or vibrations with results obtained with the help of the 3D FEM simulation. Similar comparative analysis (Mikhasev et al, 2001) has shown that accuracy of these equations is satisfactory if a shell is sufficiently thin and its vibrations occur with minor sizes of deflections or wave length. In this subsection, we aim only to give some *asymptotic* estimations of errors.

It is known that an error  $\delta_e$  of the Kirchhoff-Love hypotheses has the order  $\delta_e \sim h_*$ . It maybe expected that accepted here the generalized Timoshenko hypotheses improves an accuracy of the governing equations and results in the error  $\delta_e \sim h_*^q$ , where  $q \geq 1$ . However, as has been shown by Gol'denveiser (1961); Koiter (1966), the index of variation  $\iota$  of an expected solution may give the conclusive contribution in the estimation of an error. If  $\iota < 1$ , then within the framework of the Kirchhoff-Love hypotheses, this estimation is found as

$$\delta_e \sim \max \{h_*, h_*^{2-2\iota}\}.$$

For Eqs. (7.11) based on the generalized Timoshenko hypotheses, we have

$$\delta_e \sim \max \{h_*^q, h_*^{2-2\iota}\}, \quad (7.25)$$

where  $q \geq 1$ . The peculiarity of Eqs. (7.11) is that due to shears they have solutions with very high index of variation. So, for an elastic, isotropic and homogeneous shell with Young's and shear moduli  $E, G$  of the same asymptotic order ( $E \sim G$ ), one obtains additional integrals which account for shears and have the index of variation  $\iota = 1$ . Then  $\delta_e \sim 1$  and Eqs. (7.11) as well as Eqs. (7.18)-(7.23) become asymptotically incorrect. But if

$$G_r \sim h_*^{\zeta_G} E_r,$$

where  $\zeta_G > 0$ , then  $\iota = 1 - \zeta_G/2 < 1$ . Here,  $E_r = \Re E, G_r = \Re G$  are the real parts of the complex moduli  $E, G$  for viscoelastic shells.

Now, consider Eqs. (7.18)-(7.23) which are analogous to the well-known Mushtari-Donnell-Vlasov type equations (Mushtari and Galimov, 1961; Donnell, 1976; Wlasow, 1958). They were obtained after significant simplifications which introduced the error of an order  $h_*^{2\iota}$ . It is seen that the error of these equations is

$$\delta_e \sim \max \{h_*^{2\iota}, h_*^{2-2\iota}\}. \quad (7.26)$$

We remind that Eqs. (7.18)-(7.23) were derived under assumptions that  $\iota = 1/2$ ,  $\zeta_G = 1$ . Hence, for vibration modes with the index  $\iota = 1/2$ , one obtains the error  $\delta_e \sim h_*$ . However, Eqs. (7.18)-(7.23) can be also used to describe the *semi-momentless* dynamic stress state characterized by the index of variation  $\iota = 1/4$  for a shear pliable shell with  $\zeta_G \geq 1$ . However, for solutions having the index of variation  $\iota = 1/4$  (at  $\zeta_G = 3/2$ ), the error increases and reaches the order  $\delta_e \sim h_*^{1/2}$ .

Note also that Eqs. (7.11) and Eqs. (7.18)-(7.23) as well have been derived for cases when all the reduced moduli are constant (not dependent of coordinates  $\alpha_1, \alpha_2$ ). However, Eqs. (7.18)-(7.23) may be utilized for the analysis of low-frequency vibrations of medium-length thin laminated cylindrical shell if MRE layers are nonhomogeneous and/or an applied magnetic field is nonuniform. In Mikhasev et al (2011a) have generalized Eqs. (7.18)-(7.23) for the case when the reduced moduli  $E, G, \nu$  and shear parameters  $\eta_k, \beta$  are functions of coordinates  $\alpha_1, \alpha_2$  and the magnetic field induction  $B$  and time  $t$ . It has been also shown that if

$$y \sim R \frac{\partial y}{\partial \alpha_i},$$

where  $y$  is any of the functions  $E, G, \nu, \eta_k, \beta$  of coordinates  $\alpha_1, \alpha_2$ , and  $\iota = 1/4$ , then the generalized equations (with variable coefficients) written in terms of functions  $\chi, F, \phi$  (Mikhasev et al, 2011a) may be substituted by the simplified Eqs. (7.18)-(7.23) derived in Grigolyuk and Kulikov (1988b), these simplified equations giving the error of an order  $h_*^{1/4}$ . In what follows, Eqs. (7.18)-(7.23) will be used to analyse free vibrations of MRE sandwiches in a nonuniform magnetic field.

## 7.5 Free Vibrations of MRE-based Laminated Cylindrical Shells and Panels

### 7.5.1 Lengthy Simply Supported Cylinders

At first, let us consider Eqs. (7.11) at  $q_n = 0$ . They allow to describe any type of free vibrations of a shell of an arbitrary length. We will study here vibrations of long MRE-based cylindrical shells and show the effect of a magnetic field on the long wave modes.

For free linear vibrations, the solution of Eqs. (7.11) is written as

$$\{\hat{u}_i, \psi_i, w\} = R \{U_i(\alpha_1, \alpha_2), \Psi_i(\alpha_1, \alpha_2), W(\alpha_1, \alpha_2)\} \exp(i\Omega t), \quad (7.27)$$

where  $\Omega = \omega + i\alpha$  is the required complex natural frequency, and functions  $U_i, \Psi_i, W$  satisfying the boundary conditions (7.12) are as follows:

$$\begin{aligned} U_1 &= U_1^\circ \cos \frac{\pi n \alpha_1}{L} \cos \frac{m \alpha_2}{R}, & U_2 &= U_2^\circ \sin \frac{\pi n \alpha_1}{L} \sin \frac{m \alpha_2}{R}, \\ W &= W^\circ \sin \frac{\pi n \alpha_1}{L} \cos \frac{m \alpha_2}{R}, & & \\ \Psi_1 &= \Psi_1^\circ \cos \frac{\pi n \alpha_1}{L} \cos \frac{m \alpha_2}{R}, & \Psi_2 &= \Psi_2^\circ \sin \frac{\pi n \alpha_1}{L} \sin \frac{m \alpha_2}{R}, \end{aligned} \quad (7.28)$$

where  $n$  is a number of semi-waves in the axial direction,  $m$  is a number of waves in the circumferential direction, and  $U_i^\circ, W^\circ, \Psi_i^\circ$  are constant values.

The substitution of (7.25), (7.26) into Eqs. (7.11) yields the system of algebraic equations

$$\mathbf{A}\mathbf{X}^T = 0, \quad (7.29)$$

where  $\mathbf{X} = (U_1^\circ, U_2^\circ, W^\circ, \Psi_1^\circ, \Psi_2^\circ)$  is the five-dimensional vector, and  $\mathbf{A}$  is the  $5 \times 5$  matrix with the elements  $a_{ij}$ :

$$\begin{aligned} a_{11} &= -\delta_n^2 - \frac{1-\nu}{2}m^2 - \frac{(1-\nu^2)}{d} \frac{\Omega^2}{\omega_0^2}, & a_{12} &= \frac{1+\nu}{2}\delta_n m, \\ a_{13} &= \nu\delta_n, & a_{14} &= a_{15} = 0, & a_{21} &= \frac{1+\nu}{2}\delta_n m, \\ a_{22} &= -\frac{1-\nu}{2}\delta_n^2 - m^2 - \frac{(1-\nu^2)}{d} \frac{\Omega^2}{\omega_0^2}, & a_{23} &= -m, & a_{24} &= a_{25} = 0, \\ a_{31} &= a_{32} = 0, & a_{33} &= -\eta_2\delta_n(\delta_n^2 + m^2), \\ a_{34} &= \eta_1 \left( \delta_n^2 + \frac{1-\nu}{2}m^2 \right) + \frac{q_{44}R^2\eta_3}{D}, \\ a_{35} &= -\frac{\eta_1(1+\nu)}{2}\delta_n m, & a_{41} &= a_{42} = 0, & a_{43} &= -\eta_2 m(\delta_n^2 + m^2), \\ a_{44} &= -\frac{\eta_1(1+\nu)}{2}\delta_n m, & a_{45} &= \eta_1 \left( m^2 + \frac{1-\nu}{2}\delta_n^2 \right) + \frac{q_{44}R^2\eta_3}{D}, \\ a_{51} &= -\frac{\nu}{1-\nu^2}\delta_n, & a_{52} &= \frac{m}{1-\nu^2}, \\ a_{53} &= \varepsilon^8 g(\delta_n^2 + m^2)^2 + \frac{1}{1-\nu^2} - \frac{\Omega^2}{\omega_0^2 d}, \\ a_{54} &= -\frac{\varepsilon^8 g \eta_2}{\eta_3}\delta_n(\delta_n^2 + m^2), & a_{55} &= \frac{\varepsilon^8 g \eta_2 m}{\eta_3}(\delta_n^2 + m^2), \end{aligned} \quad (7.30)$$

where

$$\begin{aligned} \delta_n &= \frac{\pi n}{l}, & l &= \frac{L}{R}, & d &= \frac{E}{E_r^{(0)}}, & g &= \frac{\eta_3[1-(\nu_r^{(0)})^2]}{\eta_{3r}^{(0)}(1-\nu^2)}, \\ \varepsilon^8 &= \frac{h_*^2 \eta_{3r}^{(0)}}{12[1-(\nu_r^{(0)})^2]}, \\ \omega_0^2 &= \frac{E_r^{(0)}}{\rho_0 R^2}. \end{aligned} \quad (7.31)$$

Here,  $\varepsilon$  is a small parameter,  $\omega_0$  is the characteristic frequency, and  $E_r^{(0)}$ ,  $\nu_r^{(0)}$ ,  $\eta_{3r}^{(0)}$  are the real parts for the complex Young's modulus  $E$ , Poisson's ratio  $\nu$  and parameter  $\eta_3$ , respectively, calculated at the zeroth level of an applied magnetic field ( $B = 0$  mT).

The equation

$$\det \mathbf{A} = 0 \quad (7.32)$$

serves as the existence condition of a nontrivial solution of the homogeneous system (7.26). In the general case, it is a cubic equation with respect to the required frequency parameter

$$\Lambda = \frac{(1 - \nu^2)\Omega^2}{d\omega_0^2}. \quad (7.33)$$

As a particular case, we consider the axisymmetric vibrations for which

$$m = U_2^\circ = \Psi_2^\circ = 0.$$

Then, the cubic equation (7.32) degenerates into the quadratic one:

$$\Lambda^2 + (\delta_n^2 - 1 - \mu_1 \delta_n^4 r_n) \Lambda - [(1 - \nu^2)\delta_n^2 + \mu_1 \delta_n^6 r_n] = 0, \quad (7.34)$$

where

$$\mu_1 = (1 - \nu^2)\varepsilon^8 g, \quad r_n = \frac{\pi^2 + \theta K \delta_n^2}{\pi^2 + K \delta_n^2}, \quad K = \frac{\pi^2 h_*^2}{\beta}, \quad \theta = 1 - \frac{\eta_2^2}{\eta_1 \eta_3}. \quad (7.35)$$

For any fixed number  $n$ , there is only one the positive root

$$\Lambda = \frac{1}{2} \left\{ 1 - \delta_n^2 + \mu_1 r_n \delta_n^4 + [(1 - \delta_n^2 + \mu_1 r_n \delta_n^4)^2 + 4(1 - \nu^2)\delta_n^2 + 4\mu_1 r_n \delta_n^6]^{1/2} \right\}. \quad (7.36)$$

If  $\mu_1 \rightarrow 0$ , one obtains the simple formula

$$\Lambda = 1 - \delta_n^2 + \sqrt{(1 - \delta_n^2)^2 + 4(1 - \nu^2)\delta_n^2} \quad (7.37)$$

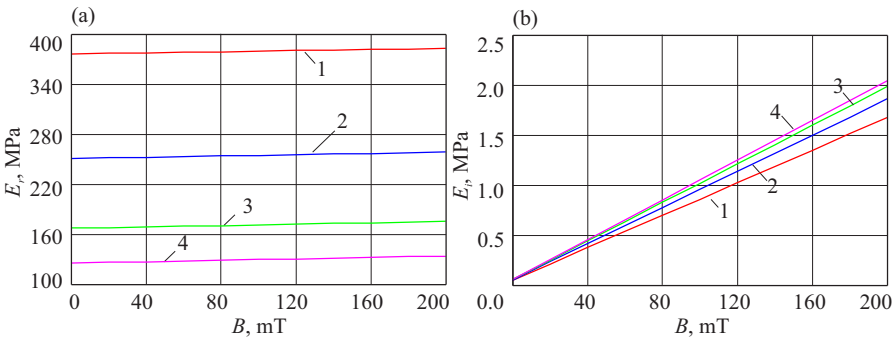
corresponding to the membrane shell theory. It is seen that the natural frequencies for the membrane modes do not depend on the shear parameter  $K$ .

As  $K \rightarrow 0$ , Eq. (7.36) gives the frequency parameter for an isotropic shell without taking into account shears. Because a parameter  $\theta$  is small, it may be concluded that the incorporation of the shear parameter  $K$  into the shell model results in the reduction of the natural frequencies for any  $\delta_n$ , the influence of  $K$  on eigenfrequencies being very weak for modes with small parameter  $\delta_n$  and becoming essential at large  $\delta_n$  and, particularly, for modes with very large number of waves  $n$  in the axial direction (and/or for a very short cylindrical shell). We note that the influence of a magnetic field on the reduced Young's modulus  $E$  is very weak and the shear parameter  $K$  is more affected by the variation of  $B$  (Mikhasev et al, 2014). Thus, changing the induction  $B$  and, in such a way, the complex shear parameter  $K$ , we can effect slightly low-frequency modes and high-frequency ones to a greater extent.

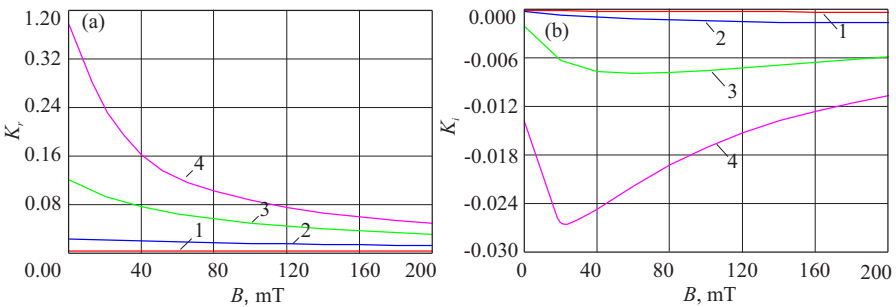
*Example 7.1.* Consider a cylindrical sandwich shell assembled from two stiffen outermost and innermost sheets and a soft MRE core. The face sheets are made of the ABS-plastic SD-0170 which is treated as an elastic material with the Young's

modulus  $E_1 = E_3 = 1.5 \cdot 10^9$  Pa, Poisson's ratio  $\nu_1 = \nu_2 = 0.4$  and density  $\rho_1 = \rho_3 = 1.4 \cdot 10^3$  kg/m<sup>3</sup>. Viscoelastic properties of the MRE are as specified in Fig. 7.2, and density is  $\rho_2 = 2.65 \cdot 10^3$  kg/m<sup>3</sup>.

In Fig. 7.3, the real and imaginary parts of the reduced Young's modulus,  $E_r = \Re E$ ,  $E_i = \Im E$ , are plotted as the functions of the magnetic field induction  $B$  for the sandwiches with the thickness  $h_1 = h_2 = 0.5$  mm of the face sheets and different thicknesses  $h_2 = 3, 5, 8, 11$  mm for the MRE core. Figure 7.4 demonstrates the behaviour of the real and imaginary parts  $K_r = \Re K$ ,  $K_i = \Im K$  of the parameter  $K$  versus the induction  $B$  for the same sandwiches with the thicknesses  $h_1, h_2$  specified above. Here, the imaginary magnitudes  $E_i$  and  $K_i$  characterize the damping capability of the MRE core embedded between two elastic sheets. It is seen that the effect of a magnetic field on  $E_r$  is very weak for all thicknesses  $h_2$  of the MRE core considered. And the function  $E_i(B)$ , demonstrating the visible dependence on  $B$ , is small with respect to  $E_r$  and its contribution to damping of vibrations is expected to be minor. Also, it may be concluded from Fig. 7.4: the thicker the MRE core is, the stronger the effect of an applied magnetic field on the shear parameter becomes.



**Fig. 7.3:** Parameters  $E_r$  (a) and  $E_i$  (b) vs. induction  $B$  for various values of thickness  $h_2 = 3$ (line1),  $5$ (2);  $8$ (3);  $11$ (4) mm of the MR core



**Fig. 7.4:** Parameters  $K_r$  (a) and  $K_i$  (b) vs. induction  $B$  for various values of thickness  $h_2 = 3$ (line1),  $5$ (2);  $8$ (3);  $11$ (4) mm of the MR core

Figure 7.5 shows the influence of the induction  $B$  on the natural frequency  $\omega = \Re\Omega$  and logarithmic decrement

$$D_l = \frac{\omega_i}{\sqrt{\omega^2 - \omega_i^2}} \tag{7.38}$$

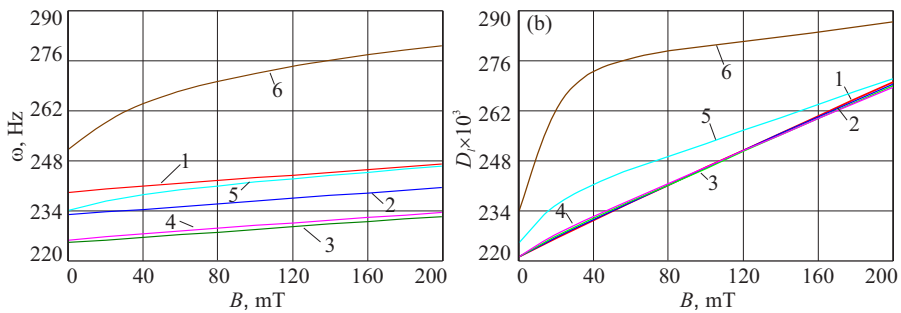
corresponding to the axially symmetric modes ( $m = 0$ ), where  $\omega_i = \Im\Omega$ . The calculations were performed by Eq. (7.36) for  $h_2 = 11$  mm,  $R = 1$  m and different values of a dimensionless parameter  $\delta_n = 0.5; 1; 3; 5; 8; 11$ . It is seen that the effect of a magnetic field on modes corresponding to small values of  $\delta_n$  (here, for  $\delta_n = 0.5; 1; 3$ ) is negligibly small, and it reveals itself for modes beginning approximately with  $\delta_n \geq 5$ , see Fig. 7.5 (b).

### 7.5.2 Medium-Length Cylindrical Panels

Consider a medium-length circular cylindrical panel with edges bounded by the curves  $\alpha_1 = 0, L_1$  and generatrices  $\alpha_2 = 0, L_2$ , where  $L_1, L_2$  are the panel length in the axial and circumferential directions, respectively. Physical parameters for all layers are assumed to be not dependent of coordinates  $\alpha_1, \alpha_2$ . To analyse free low-frequency vibrations, we consider Eqs. (7.18), (7.19), where  $q_n = 0$ .

Let all edges be simply supported and contain diaphragms. Then the natural modes with  $n$  and  $m$  semi-waves in the axial and circumferential directions are readily written down:

$$\begin{aligned} \chi &= \chi_a \exp(i\Omega t) \sin \frac{\pi n \alpha_1}{L_1} \sin \frac{\pi m \alpha_2}{L_2}, \\ F &= F_a \exp(i\Omega t) \sin \frac{\pi n \alpha_1}{L_1} \sin \frac{\pi m \alpha_2}{L_2}, \end{aligned} \tag{7.39}$$



**Fig. 7.5:** Natural frequency  $\omega$  (a) and logarithmic decrement  $D_l$  (b) vs. induction  $B$  for the axially symmetric modes and different values of a parameter  $\delta_n = 0.5$  (line 1); 1 (2); 3 (3); 5 (4); 8 (5); 11 (6)

where  $i = \sqrt{-1}$ , and  $\Omega$  is the required complex natural frequency. The substitution of (7.39) into Eqs. (7.18), (7.19) results in the following formula for eigenfrequency:

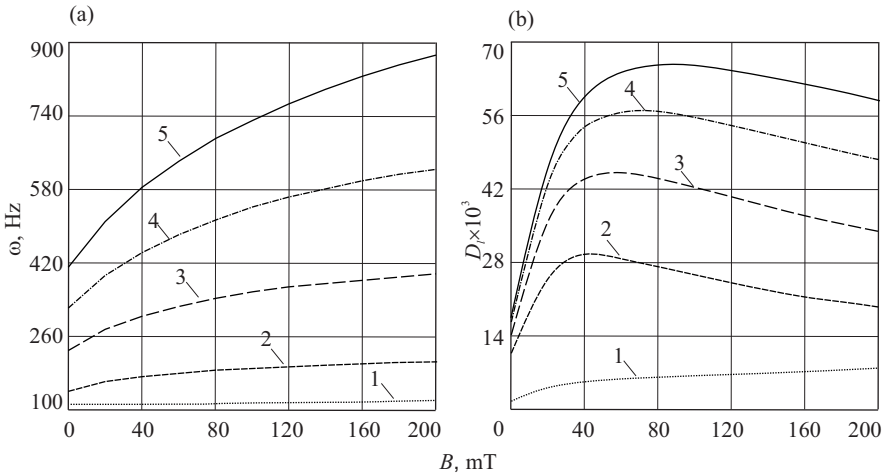
$$\Omega = \Omega_{nm} = \sqrt{\frac{E}{\rho R^2} \left\{ \frac{E}{\rho R^2} \frac{[1 + \theta K \Delta_{nm}] \Delta_{nm}^2}{1 + K \Delta_{nm}} + \frac{n^4}{l_1^4 \Delta_{nm}^2} \right\}}, \quad (7.40)$$

where

$$\eta = \frac{\pi^4 \eta_3}{(1 - \nu^2)}, \quad \Delta_{nm} = \left(\frac{n}{l_1}\right)^2 + \left(\frac{m}{l_2}\right)^2, \quad l_j = \frac{L_j}{R}. \quad (7.41)$$

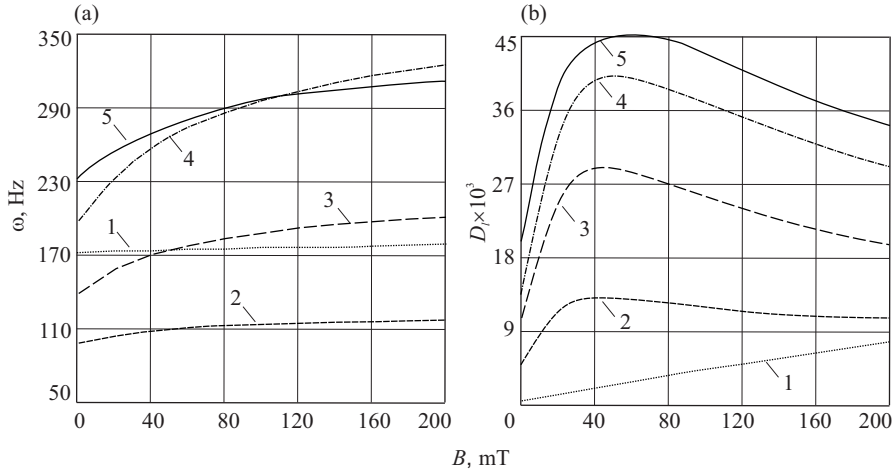
*Example 7.2.* The series of calculations of the natural frequencies  $\omega$  and logarithmic decrements  $D_l$  for cylindrical MRE-based sandwich panels with different opening angles  $\varphi_2 = L_2/R$  and the same length  $L_1 = 1$  m and radius  $R = 0.5$  m were performed. The material properties of the face sheets and MRE core are the same as in Example 7.1. Thicknesses of elastic layers and viscoelastic core are  $h_1 = h_3 = 0.5$  mm and  $h_2 = 11$  mm, respectively. Figures from 7.6 to 7.8 show the influence of the induction  $B$  on  $\omega$  and  $D_l$  corresponding to natural modes with one semi-wave ( $n = 1$ ) in the axial direction and  $m = 1; 2; 3; 4; 5$  semi-waves in the circumferential direction for the three panels with  $\varphi_2 = \pi/3, \pi/2, \pi$ .

As seen, for the panel with a small opening angle  $\varphi_2$ , the mode corresponding to the lowest eigenfrequency has the one semi-wave in both the axial and circumferential directions, and the effect of magnetic field on this mode turns out to be weak (see Fig. 7.6). For medium-length panels with a large value of  $\varphi_2$  as well as for closed



**Fig. 7.6:** Natural frequency  $\omega$  (a) and logarithmic decrement  $D_l$  (b) for cylindrical panel with the opening angle  $\varphi_2 = \pi/3$  vs. induction  $B$  for modes with one semi-wave ( $n = 1$ ) in the axial direction and  $m = 1; 2; 3; 4; 5$  semi-waves in the circumferential direction (lines 1, 2, 3, 4, 5, respectively)



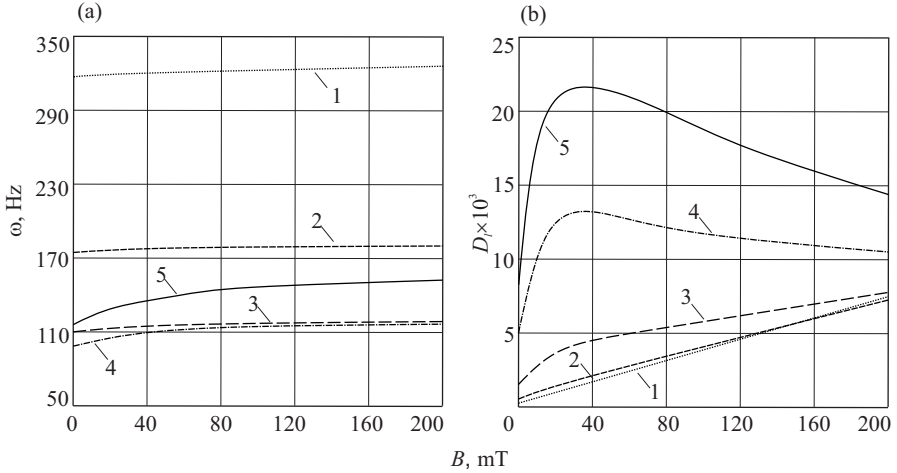


**Fig. 7.7:** Natural frequency  $\omega$  (a) and logarithmic decrement  $D_l$  (b) for cylindrical panel with the opening angle  $\varphi_2 = \pi/2$  vs. induction  $B$  for modes with one semi-wave ( $n = 1$ ) in the axial direction and  $m = 1; 2; 3; 4; 5$  semi-waves in the circumferential direction (lines 1, 2, 3, 4, 5, respectively)

cylindrical shells, the natural modes corresponding to the lowest eigenfrequencies are characterized by a number of the circumferential semi-waves of the order  $m \sim h_*^{1/4}$  (Mikhasev and Tovstik, 2009); so, for  $\varphi_2 = \pi$ , one has  $m = 4$ , although for  $\varphi_2 = \pi/3$ ,  $m = 1$ . As expected, the influence of a magnetic field on modes with a large number of semi-waves  $m$  are more essential than on modes with a small index of variation  $\iota$ . The damping capability of the MRE core is different for panels with small and large opening angles and depends on the level of an applied magnetic field: for  $\varphi_2 = \pi/3$ , the logarithmic decrement of low-frequency vibrations ( $m = 1$ ) is a slowly increasing function of  $B$  and reaches its maximum  $D_l \approx 8 \cdot 10^{-3}$  at large value of  $B = 200$  mT; and for  $\varphi_2 = \pi/3$ , the decrement for the mode with  $m = 4$  has the local maximum  $D_l \approx 13 \cdot 10^{-3}$  at a low level of an applied magnetic field ( $B \approx 35$  mT). This conclusion is important and may be used in problems on suppression of low-frequency vibration of medium-length MRE-based cylindrical panels and shells.

### 7.5.3 Vibrations of Medium-Length Cylindrical Shells in Nonuniform Magnetic Field

If any layer in a sandwich or multilayered cylindrical shell is made of a polarized MRE, then the effect of an applied magnetic may be different in various parts of a shell. Indeed, an angle between the force lines of magnetic field and alignment of magnetizable particles in a polarized MRE varies from point to point in the MR



**Fig. 7.8:** Natural frequency  $\omega$  (a) and logarithmic decrement  $D_l$  (b) for cylindrical panel with the opening angle  $\varphi_2 = \pi$  vs. induction  $B$  for modes with one semi-wave ( $n = 1$ ) in the axial direction and  $m = 1; 2; 3; 4; 5$  semi-waves in the circumferential direction (lines 1, 2, 3, 4, 5, respectively)

layer (Boczkowska et al, 2012). Even if a magnetic field is uniform, the complex shear modulus of the polarized MRE turns out to be a function of curvilinear coordinates. In this case, an applied magnetic field may result in strong distortion of eigenmodes and, particularly, in localization of natural modes in the neighborhood of a generatrix where the real part of the shear modulus has a local minimum (Mikhasev et al, 2014). In this subsection, we aim to show that a nonuniform magnetic field may lead to the same effect, that is the localization of the natural modes corresponding to low-frequency vibrations of the medium-length sandwich cylindrical shell containing a homogeneous and isotropic MRE.

Let the applied magnetic field be nonuniform so that the induction  $B(\varphi)$  in the MRE core is a function of an angle  $\varphi = \alpha_2/R$ . Then all the magneto-sensitive complex magnitudes  $\nu, \eta_3, E, \theta, \beta$  appeared in Eqs. (7.19), (7.20) are functions of  $\varphi$ . We introduce a small parameter

$$\varepsilon^8 = \frac{h_*^2 \eta_{3r}^{(0)}}{12 \left[ 1 - (\nu_r^{(0)})^2 \right]}, \quad (7.42)$$

and assume that the shell is sufficiently thin so that  $h_*$  is a quantity of the order  $\sim 0.01$  or less. In Eq. (7.42) and below, the superscript (0) means that an appropriate parameter is calculated at  $B = 0$ . Here,  $\eta_{3r} = \Re \eta_3$ ,  $\nu_r = \Re \nu$ ,  $\nu_r^{(0)} \approx 0.4$ . It is also assumed that the thickness  $h_2$  of the MRE corer is not less than 70% from the total thickness  $h$  of the shell. Then the analysis of the the magneto-sensitive complex magnitudes for the sandwich under consideration implies the following estimations (Mikhasev

et al, 2014)

$$\begin{aligned}
 v &= v_r^{(0)} \left[ 1 + \varepsilon^4 \delta v(\varphi) \right], \quad \theta_r \sim \varepsilon^3, \quad \theta_i \sim \varepsilon^4, \\
 \eta_3 &= \eta_{3r}^{(0)} \left[ 1 + \varepsilon^2 \delta \eta_3(\varphi) \right], \quad \eta_{3r}^{(0)} = \pi^{-4} \eta_r^{(0)} \left[ 1 - (v_r^{(0)})^2 \right], \\
 E_r &= E_r^{(0)} d(\varphi) = E_r^{(0)} [1 + \varepsilon d_1(\varphi)], \quad E_i/E_r^{(0)} \sim \varepsilon^4, \\
 \pi^{-2} K &= \varepsilon^2 \kappa(\varphi) = \varepsilon^2 [\kappa_0(\varphi) + i \varepsilon \kappa_1(\varphi)]
 \end{aligned} \tag{7.43}$$

at  $\varepsilon \rightarrow 0$ . In Eqs. (7.43),  $\delta v, \delta \eta_3$  and  $d_1, \kappa_0, \kappa_1$  are the complex and real functions of  $\varphi$ , respectively, so that their absolute magnitudes are quantities of the order  $O(1)$  at  $\varepsilon \rightarrow 0$ . In (7.43), the last estimate for  $K$  means that  $\zeta_G = 3/2$  (see relation (7.15)).

The solution of Eqs. (7.19), (7.20) at  $q_n = 0$  with the boundary conditions (7.24) is readily represented in the form

$$\chi = \varepsilon^{-4} R \chi^*(s, \varphi) \exp(i\Omega t), \quad F = E_r^{(0)} h R^2 F^*(s, \varphi) \exp(i\Omega t), \tag{7.44}$$

where  $s = \alpha_1/R$  is a dimensionless axial co-ordinate,  $\Omega$  is an unknown complex natural frequency, and  $\chi^*, F^*$  are dimensionless displacement and stress functions.

The substitution of (7.44) into Eqs. (7.19), (7.20) results in the following system of differential equations with respect to  $\chi^*, F^*$ :

$$\begin{aligned}
 \varepsilon^4 d(\varphi) \Delta_\varphi^2 \chi^* - \delta_n^2 F^* - \Lambda [1 - \varepsilon^2 \kappa(\varphi) \Delta_\varphi] \chi^* &= 0, \\
 \varepsilon^4 \Delta_\varphi^2 F^* + \delta_n^2 [1 - \varepsilon^2 \kappa(\varphi) \Delta_\varphi] \chi^* &= 0,
 \end{aligned} \tag{7.45}$$

where

$$\Delta_\varphi = \left( \frac{d^2}{d\varphi^2} + \delta_n^2 \right). \tag{7.46}$$

$\delta_n$  is defined by (7.31) and

$$\Lambda = \frac{\rho R^2 \Omega^2}{\varepsilon^4 E_r^{(0)}}$$

is a dimensionless frequency parameter. When deriving Eqs. (7.45) from Eqs. (7.19), (7.20), we have omitted the operator  $K\theta \Delta^3 \chi$  because of smallness of the coefficient  $K\theta$  and disregarded by very small dimensionless parameters  $\varepsilon^4 \delta v, \varepsilon^2 \delta \eta_3, E_i/E_r^{(0)}$ .

Let  $\varphi = \varphi_0$  be a generatrix where the function  $B(\varphi)$  has a local minimum. Because the storage modulus  $G'_v$  of the MRE is the increasing function of the induction  $B$  (see Fig. 7.2), then the dimensionless shear parameter  $\kappa$  satisfies the following conditions:

$$\kappa'_0(\varphi_0) = 0, \quad \kappa''_0(\varphi_0) < 0. \tag{7.47}$$

The problem is to find the minimum eigenvalue  $\Re \Lambda$  for Eq. (7.45) satisfying the conditions

$$|\chi^*|, |F^*| \rightarrow 0 \quad \text{at} \quad |\varphi - \varphi_0| \rightarrow \infty. \tag{7.48}$$

The generatrix  $\varphi = \varphi_0$  is called the weakest one. The required eigenfunctions  $\chi^*$ ,  $F^*$  satisfying (7.48) may be found in the form of asymptotic series (Mikhasev and Tovstik, 2009):

$$\begin{aligned}\chi^* &= \sum_{j=0}^{\infty} \varepsilon^{j/2} \chi_j(\zeta) \exp\{i(\varepsilon^{-1/2} p \zeta + 1/2 b \zeta^2)\}, \\ F^* &= \sum_{j=0}^{\infty} \varepsilon^{j/2} F_j(\zeta) \exp\{i(\varepsilon^{-1/2} p \zeta + 1/2 b \zeta^2)\},\end{aligned}\quad (7.49)$$

$$\Lambda = \Lambda_0 + \varepsilon \Lambda_1 + \dots, \quad (7.50)$$

where  $\zeta = \varepsilon^{-1/2}(\varphi - \varphi_0)$ ,  $p$  is the real wave parameter,  $b$  is the complex number with a positive imaginary part ( $\Im b > 0$ ), and  $\chi_j, F_j$  are polynomials in  $\zeta$ . Here the parameter  $b$  characterizes the width of an area where more intensive vibrations occur.

The substitution of (7.49), (7.50) into Eqs. (7.45) generates the sequence of algebraic equations with respect to unknown  $\chi_j, F_j, \Lambda_j$ . The stepwise consideration of these equations (see the details of this procedure in Tovstik and Smirnov, 2001; Mikhasev and Tovstik, 2009) results in the following formulae:

$$F_0 = -\delta_n^2 p^{-4} [1 + p^2 \kappa_0(\varphi_0)] \chi_0,$$

$$\lambda_r = \Re \Lambda = f^{1/2} + \frac{\varepsilon}{2f^{1/2}} \left[ \frac{(1+2m)p^3 \sqrt{-f_{pp} \kappa_0''(\varphi_0)}}{2[1+p^2 \kappa_0(\varphi_0)]} + d_1(\varphi_0) p^4 \right] + O(\varepsilon^2), \quad (7.51)$$

$$\lambda_i = \Im \Lambda = -\frac{\varepsilon f^{1/2} \kappa_1(\varphi_0) p^2}{2[1+\kappa_0(\varphi_0) p^2]} + O(\varepsilon^2), \quad b = \frac{i p^3}{1+p^2 \kappa_0(\varphi_0)} \sqrt{-\frac{\kappa_0''(\varphi_0)}{f_{pp}}},$$

where

$$f(p, \varphi_0; n) = \frac{\delta_n^4}{p^4} + \frac{p^4}{1 + \kappa_0(\varphi_0) p^2}, \quad (7.52)$$

and the wave number  $p$  is determined from the equation

$$\delta_n^{-4} \kappa_0(\varphi_0) p^{10} + 2p^8 - 2\kappa_0^2(\varphi_0) p^4 - 4\kappa_0(\varphi_0) p^2 - 2 = 0. \quad (7.53)$$

In Eq. (7.51),  $m$  is a nonnegative integer number,  $\chi_0(\zeta)$  is the Hermitian polynomial of the  $m$ th degree,  $(\dots)'$  means differentiation with respect to  $\varphi_0$ , the subscript  $p$  denotes the partial derivatives of  $f$  with respect to  $p$ . For the mode corresponding to the lowest frequencies, one needs to assume  $m = 0$ , and  $\chi_0 \equiv 1$ .

The magnitude

$$\kappa_0''(\varphi_0) = \frac{B''(\varphi_0)}{\pi^2 \varepsilon^2} \frac{dK_r}{dB} \Big|_{B=B(\varphi_0)} \quad (7.54)$$

depends on the rate of inhomogeneity of an applied magnetic field. The derivative  $dK_r/dB$  is calculated using the data presented in Fig. 7.4 (a). As seen from Eq. (7.51),

it influences on both the correction for the natural frequency and the parameter  $b$ , while the parameter  $\kappa_1(\varphi_0)$  defines the damping ratio of vibrations localized near the generatrix  $\varphi = \varphi_0$  with the lowest level of the applied magnetic field.

The following example illustrates the effect of a nonuniform magnetic field on the lowest natural frequencies and modes.

*Example 7.3.* Let the MRE-based sandwich cylindrical shell of the length  $L = 1.5$  m and radius  $R = 1$  m be in the nonuniform magnetic field. The mechanical properties and thicknesses of the face sheets and MRE core are the same as in Example 7.2. In the domain occupied by the core, the magnetic induction is assumed to be the function

$$B(\varphi) = B_0 \left[ 1 - \xi \exp(-c\varphi^2) \right], \tag{7.55}$$

where  $B_0 > 0, 0 < \xi \leq 1, c > 0$ . Then the weakest generatrix is the line  $\varphi = \varphi_0 \equiv 0$ .

Table 7.1 shows the behaviour of parameters  $p, \lambda_{r0}, \lambda_r, \lambda_i, \Im b, D_l$  with increasing the induction (parameter  $B_0$ ) and constant parameters  $c, \xi$  characterizing the rate of the magnetic field inhomogeneity. Here,  $\lambda_{r0} = \sqrt{f(p, 0; 1)}$  gives the zeroth approximation for the eigenvalue  $\Lambda$ . Then  $\Omega_0 = \sqrt{\varepsilon^4 E_r^{(0)} \lambda_{r0} / (\rho R^2)}$  is the lowest natural frequency for the shell placed in the uniform magnetic field of the induction  $B = B_0(1 - \xi)$  mT. It may be seen that increasing the magnetic field with fixed parameters  $c, \xi$  (defining the rate of inhomogeneity of magnetic field) results in increasing all parameters except the wave parameter  $p$  which shows slight decreasing. As expected, the parameter  $\Im b$ , damping ratio  $\lambda_i$  and logarithmic decrement  $D_l$  are monotonically increasing functions of the induction.

Table 7.2 demonstrates the influence of a parameter  $c$  on  $p, \lambda_{r0}, \lambda_r, \lambda_i, \Im b, D_l$  at the fixed value of  $B_0 = 80$  mT. A parameter  $c$  specifies the rate of inhomogeneity of the applied magnetic field. As seen, it does not effect on the wave parameter  $p$  and zeroth approximation  $\lambda_{r0}$  of the eigenvalue. But it essentially affects the parameter  $\Im b$ , correction  $\Lambda_1$  and the frequency parameter  $\lambda_r$  in the end. As opposed to the data from Table 7.1, the damping ratio  $\lambda_i$  and logarithmic decrement  $D_l$  are monotonically decreasing functions of  $c$ .

The above examples allow concluding that a nonuniform magnetic field may essentially disturb the low-frequency modes in thin medium-length sandwich cylinders containing a MRE core. In particular, a magnetic field not uniformly distributed in

Table 7.1: Parameters  $p, \lambda_{r0}, \lambda_r, \lambda_i, \Im b, D_l$  vs. induction  $B_0$  for the MRE shell in nonuniform magnetic field with parameters  $\xi = 0.9, c = 2$

$B_0, \text{ mT}$	$p$	$\lambda_{r0}$	$\lambda_r$	$\lambda_i$	$\Im b$	$D_l$
20	1.509	2.799	3.446	0.0114	0.197	0.0208
40	1.506	2.808	3.657	0.0126	0.262	0.0216
80	1.500	2.823	3.893	0.0143	0.331	0.0230
100	1.497	2.830	3.968	0.0148	0.351	0.0234
200	1.488	2.855	4.173	0.0159	0.394	0.0239

Table 7.2: Parameters  $p$ ,  $\lambda_{r0}$ ,  $\lambda_r$ ,  $\lambda_i$ ,  $\mathfrak{I}b$ ,  $D_l$  vs. parameter  $c$  for the MRE shell in nonuniform magnetic field with parameters  $B_0 = 80$  mT,  $\xi = 0.9$

$c$	$p$	$\lambda_{r0}$	$\lambda_r$	$\lambda_i$	$\mathfrak{I}b$	$D_l$
0.5	1.500	2.823	3.409	0.0163	0.165	0.0301
1	1.500	2.823	3.617	0.0153	0.234	0.0267
2	1.500	2.823	3.893	0.0143	0.331	0.0230
3	1.500	2.823	4.091	0.0136	0.405	0.0208
4	1.500	2.823	4.250	0.0131	0.468	0.0193

the circumferential direction can result in strong localization of modes in the shell areas where the effect of a magnetic field is weak.

## 7.6 Forced Vibrations

In this section, we consider forced vibrations of a thin medium-length sandwich cylindrical panel containing the MRE-core under the external harmonic force

$$q_n = Q^+(\alpha_1, \alpha_2) \exp(i\omega_e t) + Q^-(\alpha_1, \alpha_2) \exp(-i\omega_e t), \quad (7.56)$$

where  $0 < \omega_e$  is the frequency of excitation, and  $Q^\pm(\alpha_1, \alpha_2)$  are complex functions of the curvilinear coordinates  $\alpha_1, \alpha_2$ .

Let all the edges  $\alpha_1 = 0, L_1, \alpha_2 = 0, L_2$  be simply supported and have diaphragms preventing the edge shears, see Eqs. (7.24). Then the solution of the governing equations (7.19) may be represented in the form:

$$\begin{aligned} \chi(\alpha_1, \alpha_2, t) &= \sum_{n=1}^{\infty} \sum_{m=1}^{\infty} \sin \frac{\pi n \alpha_1}{L_1} \sin \frac{\pi m \alpha_2}{L_2} \chi_{nm}(t), \\ F(\alpha_1, \alpha_2, t) &= \sum_{n=1}^{\infty} \sum_{m=1}^{\infty} \sin \frac{\pi n \alpha_1}{L_1} \sin \frac{\pi m \alpha_2}{L_2} f_{nm}(t), \end{aligned} \quad (7.57)$$

Let us expand the functions  $Q^\pm$  into the double Fourier series

$$Q^\pm(\alpha_1, \alpha_2) = \sum_{n=1}^{\infty} \sum_{m=1}^{\infty} q_{nm}^\pm \sin \frac{\pi n \alpha_1}{L_1} \sin \frac{\pi m \alpha_2}{L_2}, \quad (7.58)$$

where

$$q_{nm}^\pm = \frac{4}{L_1 L_2} \int_0^{L_1} \int_0^{L_2} Q^\pm(\alpha_1, \alpha_2) \sin \frac{\pi n \alpha_1}{L_1} \sin \frac{\pi m \alpha_2}{L_2} d\alpha_1 d\alpha_2. \quad (7.59)$$

The substitution of Eqs. (7.56)-(7.58) into Eqs. (7.19) leads to the sequence of differential equations

$$\ddot{q}_{nm}^{\pm} + \Omega_{nm}^2 q_{nm}^{\pm} = \hat{q}_{nm}^{\pm} e^{\pm i\omega_e t}, \quad (n = 1, 2, \dots; m = 1, 2, \dots) \quad (7.60)$$

where  $\Omega_{nm}$  are the complex natural frequencies defined by (7.40), and

$$\hat{q}_{nm}^{\pm} = \frac{q_{nm}^{\pm}}{\rho h(1 + K \Delta_{nm})} \quad (7.61)$$

are the complex magnitudes depending on the complex shear parameter  $K$  introduced by Eq. (7.35).

The partial solution of Eq. (7.60) reads

$$q_p^{\pm} = \frac{\hat{q}_{nm}^{\pm}}{\Omega_{nm}^2 - \omega_e^2} e^{\pm i\omega_e t}. \quad (7.62)$$

Then the general solution of Eqs. (7.19) is

$$\chi = \chi_g + \chi_p,$$

$$\begin{aligned} \chi_g &= \sum_{n=1}^{\infty} \sum_{m=1}^{\infty} \left( c_{nm}^+ e^{i\Omega_{nm} t} + c_{nm}^- e^{-i\Omega_{nm} t} \right) \sin \frac{\pi n \alpha_1}{L_1} \sin \frac{\pi m \alpha_2}{L_2}, \\ \chi_p &= \sum_{n=1}^{\infty} \sum_{m=1}^{\infty} \left( \frac{\hat{q}_{nm}^+ e^{i\omega_e t} + \hat{q}_{nm}^- e^{-i\omega_e t}}{\Omega_{nm}^2 - \omega_e^2} \right) \sin \frac{\pi n \alpha_1}{L_1} \sin \frac{\pi m \alpha_2}{L_2}, \end{aligned} \quad (7.63)$$

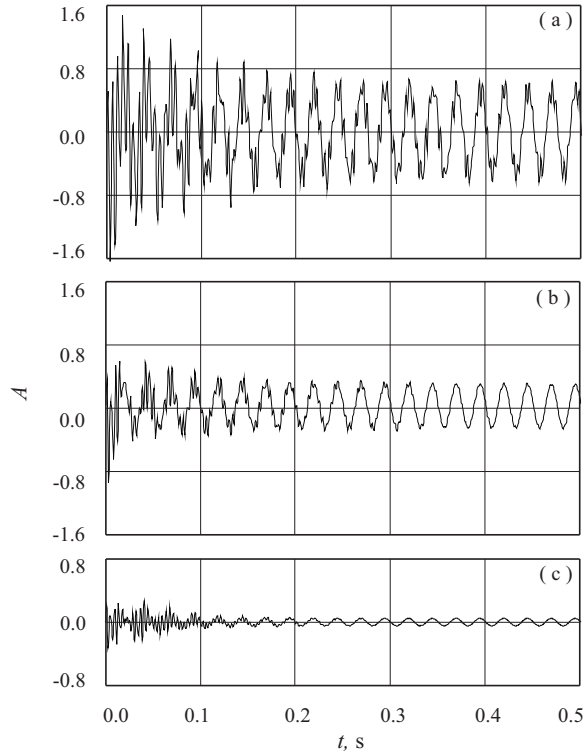
where  $c_{nm}^{\pm}$  are arbitrary complex constants which are determined from the initial conditions. If  $\omega_e = \Re \Omega_{nm}$  for any fixed  $n, m$ , then one has resonance vibrations by the mode with numbers  $n, m$ . As  $\Omega_{nm}$  is complex, the amplitude of resonance vibrations is always a bounded magnitude.

*Example 7.4.* Consider a MRE sandwich with the opening angle  $\varphi_2 = \pi$  and thickness  $h_2 = 11\text{mm}$  of the MRE core. Other geometrical and physical properties are as specified in Example 7.2. The sandwich is assumed to be motionless at  $t \leq 0$  so that

$$\chi|_{t=0} = \dot{\chi}|_{t=0} = 0. \quad (7.64)$$

Let the external force be the pulsing hydrostatic pressure  $q_n = q_a \sin \omega_e t$  (here,  $Q^{\pm} = \mp 1/2i q_a$ ) which will excite vibrations in the MRE sandwich at  $t > 0$ . On account of the linearity of equations and nil initial conditions, the amplitude  $q_a$  is not specified here. Figure 7.9 shows the scaled maximum amplitude  $A$  of forced vibrations for  $\omega_e = 40$  Hz and different values of the magnetic field induction  $B = 0$ (a), 40(b), 200(c) mT applied at  $t = 0$ . In all cases, the double infinite series in (7.63) were replaced by double finite series with 20 terms in each series. As seen, the applied external harmonic force excites the intensive vibrations in the form of the superposition of natural modes and forced vibrations. Due to viscosity of the MRE

**Fig. 7.9** Scaled maximum amplitude  $A$  of forced vibrations of MRE sandwich vs. time  $t$ (s) for different values of induction  $B$  of magnetic field applied at  $t = 0$ : (a) -  $B = 0$  mT, (b) -  $B = 40$  mT, (c) -  $B = 200$  mT



core, the excited natural modes attenuates during time with damping rate depending on the intensity of applied magnetic field, the higher the level of magnetic field is, the faster decaying of natural modes becomes. Suppression of forced vibrations of the frequency  $\omega_e = 40$  Hz are also influenced by the induction  $B$ . However, the nature of this vibration damping is another: increasing the magnetic field induction leads to increasing eigenfrequencies for all modes, see Fig. 7.6 (b), and results in fast decreasing the amplitudes

$$\sum_{n=1}^{\infty} \sum_{m=1}^{\infty} \hat{q}_{nm}^{\pm} (|\Omega_{nm}^2| - \omega_e^2)^{-1}$$

in the end.

In the above calculations, the magnetic field and external force were applied at once. Consider the next example illustrating the response of the MRE sandwich to the magnetic field and external force applied at different points of time.

*Example 7.5.* Let the initial conditions be again given by (7.64), the harmonic force  $q_n = q_a \sin \omega_e t$  is applied at  $t = 0$ , while the magnetic field of the induction  $B = 200$  mT is supplied at  $t = t_k > 0$ . The frequency  $\omega_e$  is the same as in Example 7.4. Let  $\chi^{(1)}(\alpha_1, \alpha_2, t)$  be the solution of the initial value problem (7.19), (7.64) at the interval

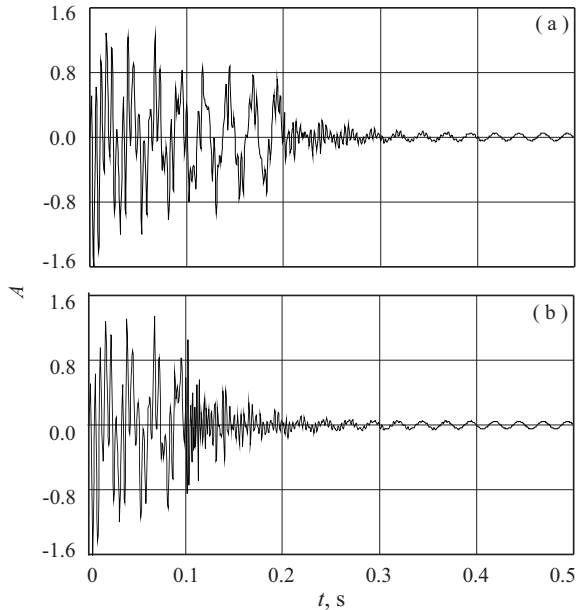


$0 \leq t \leq t_k$ . Consider the following initial conditions:

$$\chi|_{t=t_k} = \chi^{(1)}(\alpha_1, \alpha_2, t_k), \quad \dot{\chi}|_{t=t_k} = \dot{\chi}^{(1)}(\alpha_1, \alpha_2, t_k). \tag{7.65}$$

The solution of the initial value problem (7.19), (7.65) at  $t \geq t_k$  and  $B = 200$  mT is designated by  $\chi^{(2)}(\alpha_1, \alpha_2, t)$ . After applying the magnetic field at  $t = t_k$  the viscoelastic properties of the sandwich are changed instantaneously. So, to use formula (7.63) at  $t \geq t_k$ , one needs to recalculate at first all natural frequencies for the sandwich and then complex magnitudes (7.61) at  $B = 200$  mT. The parametric impact caused by the suddenly applied magnetic field is not taking into account here (see an example in Korobko et al, 2012).

Figure 7.10 shows the response of the MRE sandwich in two cases, when  $t = t_1 = 0.1$ s (a) and  $t = t_2 = 0.2$ s (b). The drawn lines at  $0 \leq t < t_k$  represent the scaled maximum amplitudes for the displacement functions  $\chi^{(1)}$  without a magnetic field, while the lines for  $t \geq t_k$  correspond to  $\chi^{(2)}$  calculated at  $B = 200$  mT. In the both cases, the application of a magnetic field results in the rapid and effective suppression of vibrations consisting of the superposition of the natural modes and the essential reduction of the forced vibrations as well. The comparison of Figs. 7.10(a) and (b) allows to conclude: for the effective suppression of excited natural modes the magnetic field should be supplied as soon as possible.



**Fig. 7.10** Response of MRE sandwich to harmonic force and magnetic field applied at different points of time  $t_k$ : (a) -  $t_k = 0.1$  s, (b) -  $t_k = 0.2$  s

## 7.7 Conclusions

The equivalent single layer theory based on the assumptions of the generalized kinematic hypotheses of Timoshenko for laminated shells was used to study both free and forced vibrations of sandwich cylindrical shells and panels containing MRE cores under various levels of applied magnetic fields. To analyze free vibrations of length cylindrical shells, the system of five differential equations accounting transverse shears and written in terms of generalized displacements was assumed as the system of governing equations. To predict free and forced vibrations of medium-length cylindrical shells and panels, the simplified equations with respect to the displacement and force functions were used.

Assuming the boundary conditions of simply supported edges with diaphragms, formulae for complex natural frequencies for both length and medium-length cylindrical shells and panels were obtained. The analysis of performed calculations for a long sandwich cylinder has shown that the influence of an applied magnetic field on the natural frequencies corresponding to modes with small numbers of waves in the axial and circumferential directions is weak. In particular, the damping effect of the MRE core turns out to be small for axially symmetric modes with number of waves in the axial direction varying from one to four. The analysis of the natural modes for medium-length cylindrical panels has revealed that the damping capability of the MRE core is different for panels with small and large opening angles and strongly depends on the level of an applied magnetic field. It has been also displayed that a nonuniform magnetic field may result in the localization of the low-frequency natural modes in the medium-length circular sandwich cylinder containing the MRE core, the localization taking place in the neighborhood of the generatrix at which the real part of the reduced shear modulus has a local minimum.

The special attention has been given to the analysis of forced vibrations of the MRE-based sandwich cylindrical panels subjected to the external pulsing pressure. The initial conditions for displacement and velocities were assumed to be zero. A solution of the initial nonhomogeneous boundary-value problem has been found in the form of series by the natural modes of the shell and represented by the sum of the general solution of homogeneous equations and the partial solution of nonhomogeneous equations. In the first example, the external force and magnetic field were applied simultaneously. Due to controllable viscosity of the MRE core, the excited natural modes corresponding to the general solution of the homogeneous equations attenuated with the damping rate depending on the induction of an applied magnetic field. The attenuation of amplitudes of forced vibrations given by the partial solution of the nonhomogeneous equations is also governed by the magnetic field, however the nature of this damping is another: it is explained by increasing the storage modulus of the MRE core under increasing the magnetic field induction. In the second example, the magnetic fields were applied at different points of time  $t_k$ . The solutions found at the segment  $0 \leq t \leq t_k$  and calculated for  $t = t_k$  were assumed then as the initial conditions for another problem considered for  $t \geq t_k$ . At that, to predict the response of the sandwich at  $t \geq t_k$ , the natural modes were recalculated taking into account the new viscoelastic properties acquired by the

shell after switching the magnetic field on. The comparative analysis of performed calculations has shown that for the effective suppression of excited vibrations the magnetic field should be supplied as soon as possible, the damping rate depending on the level of the applied magnetic field.

**Acknowledgements** The research leading to these results has received support from the People Programme (Marie Curie Actions) of the European Union's Seventh Framework Programme FP7/2007-2013/under REA grant agreement PIRSES-GA-2013-610547-TAMER. The first and second authors also acknowledge the support from both the ERASMUS+ Programme (Higher Education Mobility Agreement- 2016-2017 between Keele University, UK, and Belarusian State University, Belarus) and State Program of Scientific Investigations in Belarus "Physical Materials Science, New Materials and Technologies" (Assignment N 3.4.01).

## References

- Aguib S, Noura A, Zahloul H, Bossis G, Chevalier Y, Lançon P (2014) Dynamic behavior analysis of a magnetorheological elastomer sandwich plate. *Int J Mech Sc* 87:118–136
- Banerjee JR, Cheung CW, Morishima R, Perera M, Njuguna J (2007) Free vibration of a three-layered sandwich beam using the dynamic stiffness method and experiment. *Int J Solids Struct* 44(22):7543 – 7563
- Boczkowska A, Awietjan SF, Pietrzko S, Kurzydowski KJ (2012) Mechanical properties of magnetorheological elastomers under shear deformation. *Composites: Part B* 43:636–640
- Bolotin VV, Novichkov YN (1980) *Mechanics of Multilayer Structures* (in Russ.). Mashinostroenie, Moscow
- Carrera E (1999) Multilayered shell theories accounting for layerwise mixed description. Part 1: Governing equations. *AIAA J* 37(9):1107–1116
- Carrera E (2002) Theories and finite elements for multilayered, anisotropic, composite plates and shells. *Arch Comput Methods Engng* 9(2):87–140
- Carrera E (2003) Theories and finite elements for multilayered plates and shells: a unified compact formulation with numerical assessment and benchmarking. *Arch Comput Methods Engng* 10:215–296
- Davis LC (1999) Model of magnetorheological elastomers. *J Appl Phys* 85:3348–3351
- Donnell LH (1976) *Beams, Plates and Shells*. McGraw-Hill Inc, New York
- Ferreira AJM, Carrera E, Cinefra M, Roque CMC (2011) Analysis of laminated doubly-curved shells by a layerwise theory and radial basis functions collocation, accounting for through-the-thickness deformations. *Comput Mech* 48(1):13–25
- Gibson RF (2010) A review of recent research on mechanics of multifunctional composite materials and structures. *Comp Struct* 92(12):2793–2810
- Ginder GM (1996) Rheology controlled by magnetic fields. *Encycl Appl Phys* 16:487–503
- Ginder GM, Schlotter WF, Nichhols ME (2001) Magnetorheological elastomers in tunable vibration absorbers. In: *Proc. SPIE*. **3985**, pp 418–424
- Gol'denveiser AL (1961) *Theory of Thin Elastic Shells*. International Series of Monograph in Aeronautics and Astronautics, Pergamon Press, New York
- Grigolyuk EI, Kulikov GM (1988a) General direction of development of the theory of multilayered shells. *Mechanics of Composite Materials* 24(2):231–241
- Grigolyuk EI, Kulikov GM (1988b) *Multilayer Reinforced Shells. Calculation of Pneumatic Tires* (in Russ.). Mashinostroenie, Moscow
- Howson WP, Zare A (2005) Exact dynamic stiffness matrix for flexural vibration of three-layered sandwich beams. *J Sound Vibr* 282(3):753–767

- Hsu TM, Wang JTS (2005) A theory of laminated cylindrical shells consisting of layers of orthotropic laminae. *AIAA J* 8(12):2141–2146
- Jolly MR, Bender JW, Carlson DJ (1999) Properties and applications of commercial magnetorheological fluids. *J Intell Mater Syst Struct* 10:5–13
- Koiter WT (1966) On the nonlinear theory of thin elastic shells. *Proc Koninkl Acad Westenschap B* 69:1–54
- Korobko EV, Mikhasev GI, Novikova ZA, Zurauski MA (2012) On damping vibrations of three-layered beam containing magnetorheological elastomer. *J Intell Mater Syst Struct* 23(9):1019–1023
- Lara-Prieto V, Parkin R, Jackson M, Silberschmidt V, Keszy Z (2010) Vibration characteristics of microcantilever sandwich beams: experimental study. *Smart Mater Struct* 19(9):015,005
- Mikhasev GI, G BM (2017) Effect of edge shears and diaphragms on buckling of thin laminated medium-length cylindrical shells with low effective shear modulus under external pressure. *Acta Mech* 228(6):2119–2140
- Mikhasev GI, Tovstik PE (2009) *Localized Vibrations and Waves in Thin Shells. Asymptotic Methods* (in Russ.). FIZMATLIT, Moscow
- Mikhasev GI, Seeger F, Gabbert U (2001) Comparison of analytical and numerical methods for the analysis of buckling and vibrations of composite shell structures. In: *Proc. of "5th Magdeburg Days of Mechanical Engineering", Otto-von-Guericke-University Magdeburg, Logos, Berlin*, pp 175–183
- Mikhasev GI, Botogova MG, Korobko EV (2011a) Theory of thin adaptive laminated shells based on magnetorheological materials and its application in problems on vibration suppression. In: Altenbach H, Eremeyev V (eds) *Shell-like Structures*, Springer, Heidelberg, *Advanced Structured Materials*, vol 15, pp 727–750
- Mikhasev GI, Mlechka I, Altenbach H (2011b) Soft suppression of traveling localized vibrations in medium-length thin sandwich-like cylindrical shells containing magnetorheological layers via nonstationary magnetic field. In: Awrejcewicz J (ed) *Dynamical Systems: Theoretical and Experimental Analysis*, Springer, Switzerland, *Springer Proceedings in Mathematics & Statistics*, vol 182, pp 241–260
- Mikhasev GI, Altenbach H, Korchevskaya EA (2014) On the influence of the magnetic field on the eigenmodes of thin laminated cylindrical shells containing magnetorheological elastomer. *Compos Struct* 113:186–196
- Mushtari K, Galimov K (1961) *Nonlinear Theory of Thin Elastic Shells*. NSF-NASA, Washington
- Qatu MS (2004) *Vibration of laminated shells and plates*. Elsevier, San Diego
- Qatu MS, Sullivan RW, Wang W (2010) Recent research advances on the dynamic analysis of composite shells: 2000–2009. *Comp Struct* 93(1):14–31
- Reddy JN (2003) *Mechanics of Laminated Composite Plates and Shells: Theory and Analysis*. CRC Press, Boca Raton
- Sun Q, Zhou JX, Zhang L (2003) An adaptive beam model and dynamic characteristics of magnetorheological materials. *J Sound Vibr* 261:465–481
- Toorani MH, Lakis AA (2000) General equations of anisotropic plates and shells including transverse shear deformations, rotary inertia and initial curvature effects. *J Sound Vibr* 237(4):561–615
- Tovstik PE, Smirnov AL (2001) *Asymptotic Methods in the Buckling Theory of Elastic Shells*. World Scientific, Singapore
- White JL, Choi DD (2005) *Polyolefins: Processing, Structure, Development, and Properties*. Carl Hanser Verlag, Munich
- Wlassow WS (1958) *Allgemeine Schalentheorie und ihre Anwendung in der Technik*. Akademie-Verlag, Berlin
- Yeh JY (2011) Vibration and damping analysis of orthotropic cylindrical shells with electrorheological core layer. *Aerospace Sc Techn* 15(4):293–303
- Yeh JY (2013) Vibration analysis of sandwich rectangular plates with magnetorheological elastomer damping treatment. *Smart Mater Struct* 22(3):035,010
- Yeh JY (2014) Vibration characteristics analysis of orthotropic rectangular sandwich plate with magnetorheological elastomer. *Proc Engng* 79:378–385

- Ying ZG, Ni YQ, Ye SQ (2014) Stochastic micro-vibration suppression of a sandwich plate using a magneto-rheological visco-elastomer core. *Smart Mater Struct* 23(2):025,019
- Zhou GY, Wang Q (2005) Magneto-rheological elastomer-based smart sandwich beams with non-conductive skins. *Smart Mater Struct* 14(5):1001–1009
- Zhou GY, Wang Q (2006) Use of magneto-rheological elastomer in an adaptive sandwich beam with conductive skins. Part II: Dynamic properties. *International Journal of Solids and Structures* 43(17):5403–5420

## Chapter 8

# Impact-Induced Internal Resonance Phenomena in Nonlinear Doubly Curved Shallow Shells with Rectangular Base

Yury A. Rossikhin (†), Marina V. Shitikova, and Mohammed Salih Khalid

**Abstract** The problem of the low-velocity impact of an elastic sphere upon a nonlinear doubly curved shallow shell with a rectangular platform is investigated. The approach utilized in the present paper is based on the fact that during impact only the modes strongly coupled by some internal resonance condition are initiated. Such an approach differs from the Galerkin method, wherein resonance phenomena are not involved. Since it is assumed that shell's displacements are finite, then the local bearing of the shell and impactor's materials is neglected with respect to the shell deflection in the contact region. In other words, the Hertz's theory, which is traditionally in hand for solving impact problems, is not used in the present study; instead, the method of multiple time scales is adopted, which is used with much success for investigating vibrations of nonlinear systems subjected to the conditions of the internal resonance. The influence of impactor's mass on the phenomenon of the impact-induced internal resonance is revealed.

## 8.1 Introduction

Doubly curved panels are widely used in aeronautics, aerospace and civil engineering and are subjected to dynamic loads that can cause vibration amplitude of the order of the shell thickness, giving rise to significant non-linear phenomena (Amabili, 2005; Alijani and Amabili, 2012; Leissa and Kadi, 1971; Volmir, 1972). A review of the literature devoted to dynamic behavior of curved panels and shells could be found in Amabili and Paidoussis (2003); Amabili (2005), wherein it has been emphasized that free vibrations of doubly curved shallow shells were studied in the majority of papers either utilizing a slightly modified version of the Donnell's theory taking into

---

Yury A. Rossikhin (†) · Marina V. Shitikova · Mohammed Salih Khalid  
Research Center of Wave Dynamics, Voronezh State Technical University, Voronezh 394006, Russia  
e-mail: mvs@vgasu.vrn.ru, Khalid\_bus@yahoo.com

account the double curvature (Chia, 1988; Leissa and Kadi, 1971) or the nonlinear first-order theory of shells (Abe et al, 2000; Kobayashi and Leissa, 1995).

Large-amplitude vibrations of doubly curved shallow shells with rectangular base, simply supported at the four edges and subjected to harmonic excitation were investigated in Amabili (2005), while chaotic vibrations were analyzed in Alijani and Amabili (2012). It has been revealed that such an important nonlinear phenomenon as the occurrence of internal resonances in the problems considered in Amabili (2005); Alijani and Amabili (2012) is of fundamental importance in the study of curved shells.

In spite of the fact that the impact theory is substantially developed, there is a limited number of papers devoted to the problem of impact over geometrically nonlinear shells. Literature review on this subject could be found in Kistler and Waas (1998a,b). An analysis to predict the transient response of a thin, curved laminated plate subjected to low velocity transverse impact by a rigid object was carried out by Ramkumar and Thakar (1987), in so doing the contact force history due to the impact phenomenon was assumed to be a known linear-dependent input to the analysis. The coupled governing equations, in terms of the Airy stress function and shell deformation, were solved using Fourier series expansions for the variables.

A methodology for the stability analysis of doubly curved orthotropic shells with simply supported boundary condition and under impact load from the viewpoint of nonlinear dynamics was suggested in Zhang et al (2001). The nonlinear governing differential equations were derived based on a Donnell-type shallow shell theory, and the displacement was expanded in terms of the eigenfunctions of the linear operator of the motion equation. To analyze the influence of each single mode on the response to impact loading, only one term composed of two half-waves was used in developing the governing equation, whereas the contact force was proposed to be a sine function during the contact duration.

The review of papers dealing with the impact response of curved panels and shells shows that a finite element method and such commercial finite element software as ABAQUS or LS-DYNA and its modifications are the main numerical tools adopted by many researchers, among them: Chandrashekhara and Schoeder (1995); Liu and Swaddiwudhipong (1997); Cho et al (2000); Fu et al (2008); Fu and Mao (2008); Fu et al (2010); Gong et al (1995); Goswami (1998); Antoine and Batra (2015).

Thus, the nonlinear impact response of laminated composite cylindrical and doubly curved shells was analyzed using a modified Hertzian contact law in Chandrashekhara and Schoeder (1995) via a finite element model, which was developed based on Sander's shell theory involving shear deformation effects and nonlinearity due to large deflection. The nonlinear time dependent equations were solved using an iterative scheme and Newmark's method. Numerical results for the contact force and center deflection histories were presented for various impactor conditions, shell geometry and boundary conditions.

Later large deflection dynamic responses of laminated composite cylindrical shells under impact have been analyzed in Cho et al (2000) by the geometrically nonlinear finite element method based on a generalized Sander's shell theory with the first order shear deformation and the von Kármán large deflection assumption.

Nonlinear dynamic response for shallow spherical moderate thick shells with damage under low velocity impact has been studied in Fu and Mao (2008) by using the orthogonal collocation point method and the Newmark method to discretize the unknown variable function in space and in time domain, respectively, and the whole problem is solved by the iterative method. Further this approach was generalized for investigating dynamic response of elasto-plastic laminated composite shallow spherical shell under low velocity impact (Fu et al, 2010), and for functionally graded shallow spherical shell under low velocity impact in thermal environment (Mao et al, 2011).

The nonlinear transient response of laminated composite shell panels subjected to low velocity impact in hygrothermal environments was investigated in Swamy Naidu and Sinha (2005) using finite element method considering doubly curved thick shells involving large deformations with Green-Lagrange strains. The analysis was carried out using quadratic eight-noded isoparametric element. A modified Hertzian contact law was incorporated into the finite element program to evaluate the impact force. The nonlinear equation was solved using the Newmark average acceleration method in conjunction with an incremental modified Newton-Raphson scheme. A parametric study was carried out to investigate the effects of the curvature and side to thickness ratios of simply supported composite cylindrical and spherical shell panels.

The impact behavior and the impact-induced damage in laminated composite cylindrical shell subjected to transverse impact by a foreign object were studied in Kumar et al (2007); Kumar (2010) using three-dimensional non-linear transient dynamic finite element formulation. Non-linear system of equations resulting from non-linear strain displacement relation and non-linear contact loading was solved using Newton-Raphson incremental-iterative method. Some example problems of graphite/epoxy cylindrical shell panels were considered with variation of impactor and laminate parameters and influence of geometrical non-linear effect on the impact response and the resulting damage was investigated.

The Sander's shallow shell theory in conjunction with the Reissner-Mindlin shear deformation theory was employed in Maiti and Sinha (1996a) to develop a finite element analysis procedure to study the impact response of doubly curved laminated composite shells, in so doing the nine-noded quadratic isoparametric elements of Lagrangian family were utilized. Modified Hertzian contact law is used to calculate the contact force. Numerical results were obtained for cylindrical and spherical shells to investigate the effects of various parameters, such as radius to span ratio, span to thickness ratio, boundary condition and stacking sequence on the impact behavior of the target structure (Maiti and Sinha, 1996c,b).

A 4-noded 48 degree-of-freedom doubly curved quadrilateral shell finite element based on Kirchhoff-Love shell theory was used in Ganapathy and Rao (1998) for the nonlinear finite element analysis to predict the damage of laminated composite cylindrical and spherical shell panels subjected to low velocity impact. The large displacement stiffness matrix was formed using Green's strain tensor based on total Lagrangian approach with further utilization of an iterative scheme for solving resulting nonlinear algebraic equation by Newton-Raphson method. The load due to



low velocity impact was treated as an equivalent quasi-static load and Hertzian law of contact was used for finding the peak contact force.

Recently a new approach has been proposed for the analysis of the impact interactions of nonlinear doubly curved shallow shells with rectangular base under the low-velocity impact by an elastic sphere (Rossikhin et al, 2014). It has been assumed that the shell is simply supported and partial differential equations have been obtained in terms of shell's transverse displacement and Airy's stress function. The local bearing of the shell and impactor's materials has been neglected with respect to the shell deflection in the contact region. The equations of motion have been reduced to a set of infinite nonlinear ordinary differential equations of the second order in time and with cubic and quadratic nonlinearities in terms of the generalized displacements. Assuming that only two natural modes of vibrations dominate during the process of impact and applying the method of multiple time scales, the set of equations has been obtained, which allows one to find the time dependence of the contact force and to determine the contact duration and the maximal contact force.

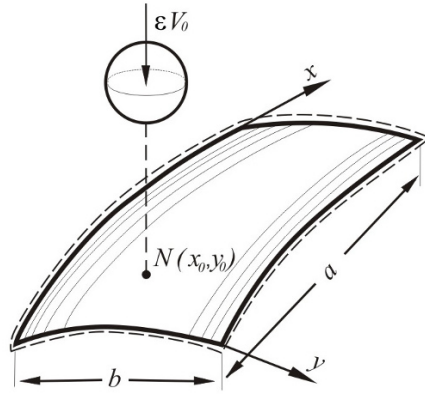
In the present paper, the approach proposed by Rossikhin et al (2014) has been generalized for studying the influence of the impact-induced internal resonances on the low velocity impact response of a nonlinear doubly curved shallow shell with rectangular platform. Such an additional nonlinear phenomenon as the internal resonance could be examined only via analytical treatment, since any of existing numerical procedures could not catch this subtle phenomenon. Impact-induced internal resonance phenomena should be studied as their initiation during impact interaction may lead to the fact that the impacted shell could occur under extreme loading conditions resulting in its invisible and/or visible damage and even failure.

## 8.2 Problem Formulation and Governing Equations

In this section, first of all we recall the problem formulation following reasoning presented in Rossikhin et al (2014, 2015). Assume that a sphere (or a body of arbitrary shape but with a rounded end) of mass  $M$  moves along the  $z$ -axis towards a thin-walled doubly curved shell with thickness  $h$ , curvilinear lengths  $a$  and  $b$ , principle curvatures  $k_x$  and  $k_y$  and rectangular base, as shown in Fig. 8.1. Impact occurs at the moment  $t = 0$  with the low velocity  $\varepsilon V_0$  at the point  $N$  with Cartesian coordinates  $x_0, y_0$ , where  $\varepsilon$  is a small dimensionless parameter.

According to the Donnell-Mushtari nonlinear shallow shell theory, the equations of motion could be obtained in terms of lateral deflection  $w$  and Airy's stress function  $\phi$  (Mushtari and Galimov, 1957)

$$\begin{aligned} \frac{D}{h} \left( \frac{\partial^4 w}{\partial x^4} + 2 \frac{\partial^4 w}{\partial x^2 \partial y^2} + \frac{\partial^4 w}{\partial y^4} \right) = \frac{\partial^2 w}{\partial x^2} \frac{\partial^2 \phi}{\partial y^2} + \frac{\partial^2 w}{\partial y^2} \frac{\partial^2 \phi}{\partial x^2} - 2 \frac{\partial^2 w}{\partial x \partial y} \frac{\partial^2 \phi}{\partial x \partial y} \\ + k_y \frac{\partial^2 \phi}{\partial x^2} + k_x \frac{\partial^2 \phi}{\partial y^2} + \frac{F}{h} - \rho \ddot{w}, \end{aligned} \quad (8.1)$$



**Fig. 8.1** Geometry of a doubly curved shallow shell.

$$\frac{1}{E} \left( \frac{\partial^4 \phi}{\partial x^4} + 2 \frac{\partial^4 \phi}{\partial x^2 \partial y^2} + \frac{\partial^4 \phi}{\partial y^4} \right) = - \frac{\partial^2 w}{\partial x^2} \frac{\partial^2 w}{\partial y^2} + \left( \frac{\partial^2 w}{\partial x \partial y} \right)^2 - k_y \frac{\partial^2 w}{\partial x^2} - k_x \frac{\partial^2 w}{\partial y^2}, \quad (8.2)$$

where  $D = \frac{Eh^3}{12(1-\nu^2)}$  is the cylindrical rigidity,  $\rho$  is the density,  $E$  and  $\nu$  are the elastic modulus and Poisson's ratio, respectively,  $t$  is time,  $F = P(t)\delta(x - x_0)\delta(y - y_0)$  is the contact force,  $P(t)$  is yet unknown function,  $\delta$  is the Dirac delta function,  $x$  and  $y$  are Cartesian coordinates, overdots denote time-derivatives,  $\phi(x, y)$  is the stress function which is the potential of the in-plane force resultants

$$N_x = h \frac{\partial^2 \phi}{\partial y^2}, \quad N_y = h \frac{\partial^2 \phi}{\partial x^2}, \quad N_{xy} = -h \frac{\partial^2 \phi}{\partial x \partial y}. \quad (8.3)$$

The equation of motion of the sphere is written as

$$M\ddot{z} = -P(t) \quad (8.4)$$

subjected to the initial conditions

$$z(0) = 0, \quad \dot{z}(0) = \varepsilon V_0, \quad (8.5)$$

where  $z(t)$  is the displacement of the sphere, in so doing

$$z(t) = w(x_0, y_0, t). \quad (8.6)$$

Considering a simply supported shell with movable edges, the following conditions should be imposed at each edge:

at  $x = 0, a$

$$w = 0, \quad \int_0^b N_{xy} dy = 0, \quad N_x = 0, \quad M_x = 0, \quad (8.7)$$

and at  $y = 0, b$

$$w = 0, \quad \int_0^a N_{xy} dx = 0, \quad N_y = 0, \quad M_y = 0, \quad (8.8)$$

where  $M_x$  and  $M_y$  are the moment resultants.

The suitable trial function that satisfies the geometric boundary conditions is

$$w(x, y, t) = \sum_{p=1}^{\bar{p}} \sum_{q=1}^{\bar{q}} \xi_{pq}(t) \sin\left(\frac{p\pi x}{a}\right) \sin\left(\frac{q\pi y}{b}\right), \quad (8.9)$$

where  $p$  and  $q$  are the number of half-waves in  $x$  and  $y$  directions, respectively, and  $\xi_{pq}(t)$  are the generalized coordinates. Moreover,  $\bar{p}$  and  $\bar{q}$  are integers indicating the number of terms in the expansion. Substituting (8.9) in (8.6) and using (8.4), we obtain

$$P(t) = -M \sum_{p=1}^{\bar{p}} \sum_{q=1}^{\bar{q}} \ddot{\xi}_{pq}(t) \sin\left(\frac{p\pi x_0}{a}\right) \sin\left(\frac{q\pi y_0}{b}\right). \quad (8.10)$$

In order to find the solution of the set of Eqs. (8.1) and (8.2), it is necessary first to obtain the solution of Eq. (8.2). For this purpose, let us substitute (8.9) in the right-hand side of Eq. (8.2) and seek the solution of the equation obtained in the form

$$\phi(x, y, t) = \sum_{m=1}^{\bar{m}} \sum_{n=1}^{\bar{n}} A_{mn}(t) \sin\left(\frac{m\pi x}{a}\right) \sin\left(\frac{n\pi y}{b}\right), \quad (8.11)$$

where  $A_{mn}(t)$  are yet unknown functions.

Substituting (8.9) and (8.11) in Eq. (8.2) and using the orthogonality conditions of sines within the segments  $0 \leq x \leq a$  and  $0 \leq y \leq b$ , we have

$$A_{mn}(t) = \frac{E}{\pi^2} K_{mn} \xi_{mn}(t) + \frac{4E}{a^3 b^3} \left(\frac{m^2}{a^2} + \frac{n^2}{b^2}\right)^{-2} \sum_k \sum_l \sum_p \sum_q B_{pqklmn} \xi_{pq}(t) \xi_{kl}(t), \quad (8.12)$$

where

$$B_{pqklmn} = pqkl B_{pqklmn}^{(2)} - p^2 l^2 B_{pqklmn}^{(1)},$$

$$B_{pqklmn}^{(1)} = \int_0^a \int_0^b \sin\left(\frac{p\pi x}{a}\right) \sin\left(\frac{q\pi y}{b}\right) \sin\left(\frac{k\pi x}{a}\right) \sin\left(\frac{l\pi y}{b}\right) \sin\left(\frac{m\pi x}{a}\right) \sin\left(\frac{n\pi y}{b}\right) dx dy,$$

$$B_{pqklmn}^{(2)} = \int_0^a \int_0^b \cos\left(\frac{p\pi x}{a}\right) \cos\left(\frac{q\pi y}{b}\right) \cos\left(\frac{k\pi x}{a}\right) \cos\left(\frac{l\pi y}{b}\right) \sin\left(\frac{m\pi x}{a}\right) \sin\left(\frac{n\pi y}{b}\right) dx dy,$$

$$K_{mn} = \left( k_y \frac{m^2}{a^2} + k_x \frac{n^2}{b^2} \right)^2 \left( \frac{m^2}{a^2} + \frac{n^2}{b^2} \right)^{-2}.$$

Substituting then (8.9)–(8.12) in Eq. (8.1) and using the orthogonality condition of sines within the segments  $0 \leq x \leq a$  and  $0 \leq y \leq b$ , we obtain an infinite set of coupled nonlinear ordinary differential equations of the second order in time for defining the generalized coordinates

$$\begin{aligned} \ddot{\xi}_{mn}(t) + \Omega_{mn}^2 \xi_{mn}(t) + \frac{8\pi^2 E}{a^3 b^3 \rho} \sum_p \sum_q \sum_k \sum_l B_{pqklmn} \left( K_{kl} - \frac{1}{2} K_{mn} \right) \xi_{pq}(t) \xi_{kl}(t) \\ + \frac{32\pi^4 E}{a^6 b^6 \rho} \sum_r \sum_s \sum_i \sum_j \sum_k \sum_l \sum_p \sum_q B_{rsijmn} B_{pqklij} \xi_{rs}(t) \xi_{pq}(t) \xi_{kl}(t) \\ + \frac{4M}{ab\rho h} \sin\left(\frac{m\pi x_0}{a}\right) \sin\left(\frac{n\pi y_0}{b}\right) \sum_p \sum_q \ddot{\xi}_{pq}(t) \sin\left(\frac{p\pi x_0}{a}\right) \sin\left(\frac{q\pi y_0}{b}\right) = 0, \end{aligned} \quad (8.13)$$

where  $\Omega_{mn}$  is the natural frequency of the  $m$ th mode of the shell vibration defined as

$$\Omega_{mn}^2 = \frac{E}{\rho} \left[ \frac{\pi^4 h^2}{12(1-\nu^2)} \left( \frac{m^2}{a^2} + \frac{n^2}{b^2} \right)^2 + K_{mn} \right]. \quad (8.14)$$

The last term in each equation from (8.13) describes the influence of the coupled impact interaction of the target with the impactor of the mass  $M$  applied at the point with the coordinates  $x_0, y_0$ .

Note that at  $M = 0$  Eqs. (8.13) are reduced to the equations describing free vibrations of shallow shells with a rectangular platform, which have been proposed in Kobayashi and Leissa (1995); Leissa and Kadi (1971) and wherein curvature effects on shallow shell vibrations, and in particular on natural frequencies (8.14), have been studied.

It is known (Anderson et al, 1994; Nayfeh, 1973a) that during nonstationary excitation of thin bodies not all possible modes of vibration would be excited. Moreover, the modes which are strongly coupled by any of the so-called internal resonance conditions are initiated and dominate in the process of vibration, in so doing the types of modes to be excited are dependent on the character of the external excitation.

Thus, in order to study the additional nonlinear phenomenon induced by the coupled impact interaction due to Eq. (8.13), we suppose that only two natural modes of vibrations are excited during the process of impact, namely,  $\Omega_{\alpha\beta}$  and  $\Omega_{\gamma\delta}$ .

Then the set of Eqs. (8.13) is reduced to the following two nonlinear differential equations (Rossikhin et al, 2014):

$$p_{11} \ddot{\xi}_{\alpha\beta} + p_{12} \ddot{\xi}_{\gamma\delta} + \Omega_{\alpha\beta}^2 \xi_{\alpha\beta} + p_{13} \xi_{\alpha\beta}^2 + p_{14} \xi_{\gamma\delta}^2 + p_{15} \xi_{\alpha\beta} \xi_{\gamma\delta} + p_{16} \xi_{\alpha\beta}^3 + p_{17} \xi_{\alpha\beta} \xi_{\gamma\delta}^2 = 0, \quad (8.15)$$

$$p_{21}\ddot{\xi}_{\alpha\beta} + p_{22}\ddot{\xi}_{\gamma\delta} + \Omega_{\gamma\delta}^2\xi_{\gamma\delta} + p_{23}\xi_{\gamma\delta}^2 + p_{24}\xi_{\alpha\beta}^2 + p_{25}\xi_{\alpha\beta}\xi_{\gamma\delta} + p_{26}\xi_{\gamma\delta}^3 + p_{27}\xi_{\alpha\beta}^2\xi_{\gamma\delta} = 0, \quad (8.16)$$

where

$$\begin{aligned} p_{11} &= 1 + \frac{4M}{\rho hab} s_1^2, & p_{22} &= 1 + \frac{4M}{\rho hab} s_2^2, & p_{12} &= p_{21} = \frac{4M}{\rho hab} s_1 s_2, \\ s_1 &= \sin\left(\frac{\alpha\pi x_0}{a}\right) \sin\left(\frac{\beta\pi y_0}{b}\right), & s_2 &= \sin\left(\frac{\gamma\pi x_0}{a}\right) \sin\left(\frac{\delta\pi y_0}{b}\right), \\ p_{13} &= \frac{8\pi^2 E}{a^3 b^3 \rho} B_{\alpha\beta\alpha\beta\alpha\beta} \frac{1}{2} K_{\alpha\beta}, & p_{14} &= \frac{8\pi^2 E}{a^3 b^3 \rho} B_{\gamma\delta\gamma\delta\alpha\beta} \left(K_{\gamma\delta} - \frac{1}{2} K_{\alpha\beta}\right), \\ p_{15} &= \frac{8\pi^2 E}{a^3 b^3 \rho} \left[ B_{\gamma\delta\alpha\beta\alpha\beta} \frac{1}{2} K_{\alpha\beta} + B_{\alpha\beta\gamma\delta\alpha\beta} \left(K_{\gamma\delta} - \frac{1}{2} K_{\alpha\beta}\right) \right], \\ p_{23} &= \frac{8\pi^2 E}{a^3 b^3 \rho} B_{\alpha\beta\alpha\beta\gamma\delta} \left(K_{\alpha\beta} - \frac{1}{2} K_{\gamma\delta}\right), & p_{24} &= \frac{8\pi^2 E}{a^3 b^3 \rho} B_{\gamma\delta\gamma\delta\gamma\delta} \frac{1}{2} K_{\gamma\delta}, \\ p_{25} &= \frac{8\pi^2 E}{a^3 b^3 \rho} \left[ B_{\alpha\beta\gamma\delta\gamma\delta} \frac{1}{2} K_{\gamma\delta} + B_{\gamma\delta\alpha\beta\gamma\delta} \left(K_{\alpha\beta} - \frac{1}{2} K_{\gamma\delta}\right) \right], \\ p_{16} &= \frac{32\pi^2 E}{a^3 b^3 \rho} \sum_i \sum_j B_{\alpha\beta i j \alpha\beta} B_{\alpha\beta \alpha\beta i j}, & p_{26} &= \frac{32\pi^2 E}{a^3 b^3 \rho} \sum_i \sum_j B_{\gamma\delta i j \gamma\delta} B_{\gamma\delta \gamma\delta i j}, \\ p_{17} &= \frac{32\pi^2 E}{a^3 b^3 \rho} \sum_i \sum_j \left( B_{\alpha\beta i j \alpha\beta} B_{\gamma\delta \gamma\delta i j} + B_{\gamma\delta i j \alpha\beta} B_{\alpha\beta \gamma\delta i j} + B_{\gamma\delta i j \alpha\beta} B_{\gamma\delta \alpha\beta i j} \right), \\ p_{27} &= \frac{32\pi^2 E}{a^3 b^3 \rho} \sum_i \sum_j \left( B_{\alpha\beta i j \gamma\delta} B_{\gamma\delta \gamma\delta i j} + B_{\gamma\delta i j \gamma\delta} B_{\alpha\beta \gamma\delta i j} + B_{\gamma\delta i j \gamma\delta} B_{\gamma\delta \alpha\beta i j} \right). \end{aligned}$$

### 8.3 Method of Solution

In order to solve a set of two nonlinear Eqs. (8.15) and (8.16), we apply the method of multiple time scales (Nayfeh, 1973b) via the following expansions:

$$\xi_{ij}(t) = \varepsilon X_{ij}^1(T_0, T_1, T_2) + \varepsilon^2 X_{ij}^2(T_0, T_1, T_2) + \varepsilon^3 X_{ij}^3(T_0, T_1, T_2), \quad (8.17)$$

where  $ij = \alpha\beta$  or  $\gamma\delta$ ,  $T_n = \varepsilon^n t$  are new independent variables, among them:  $T_0 = t$  is a fast scale characterizing motions with the natural frequencies, and  $T_1 = \varepsilon t$  and  $T_2 = \varepsilon^2 t$  are slow scales characterizing the modulation of the amplitudes and phases of the modes with nonlinearity.

Considering that

$$\frac{d^2}{dt^2} = D_0^2 + 2\varepsilon D_0 D_1 + \varepsilon^2 (D_1^2 + 2D_0 D_2),$$

where  $ij = \alpha\beta$  or  $\gamma\delta$ , and  $D_i^n = \partial^n / \partial T_i^n$  ( $n = 1, 2$ ,  $i = 0, 1$ ), and substituting the proposed solution (8.17) in (8.15) and (8.16), after equating the coefficients at like powers of  $\varepsilon$  to zero, we are led to a set of recurrence equations to various orders:

to order  $\varepsilon$

$$p_{11}D_0^2X_1^1 + p_{12}D_0^2X_2^1 + \Omega_1^2X_1^1 = 0, \quad (8.18)$$

$$p_{21}D_0^2X_1^1 + p_{22}D_0^2X_2^1 + \Omega_2^2X_2^1 = 0; \quad (8.19)$$

to order  $\varepsilon^2$

$$\begin{aligned} p_{11}D_0^2X_1^2 + p_{12}D_0^2X_2^2 + \Omega_1^2X_1^2 = & -2p_{11}D_0D_1X_1^1 - 2p_{12}D_0D_1X_2^1 \\ & - p_{13}(X_1^1)^2 - p_{14}(X_2^1)^2 - p_{15}X_1^1X_2^1, \end{aligned} \quad (8.20)$$

$$\begin{aligned} p_{21}D_0^2X_1^2 + p_{22}D_0^2X_2^2 + \Omega_2^2X_2^2 = & -2p_{21}D_0D_1X_1^1 - 2p_{22}D_0D_1X_2^1 \\ & - p_{23}(X_1^1)^2 - p_{24}(X_2^1)^2 - p_{25}X_1^1X_2^1, \end{aligned} \quad (8.21)$$

to order  $\varepsilon^3$

$$\begin{aligned} p_{11}D_0^2X_1^3 + p_{12}D_0^2X_2^3 + \Omega_1^2X_1^3 = & -2p_{11}D_0D_1X_1^2 - 2p_{12}D_0D_1X_2^2 \\ & - p_{11}(D_1^2 + 2D_0D_2)X_1^1 - p_{12}(D_1^2 + 2D_0D_2)X_2^1 - 2p_{13}X_1^1X_1^2 \\ & - 2p_{14}X_2^1X_2^2 - p_{15}(X_1^1X_2^2 + X_1^2X_2^1) - p_{16}(X_1^1)^3 - p_{17}X_1^1(X_2^1)^2, \end{aligned} \quad (8.22)$$

$$\begin{aligned} p_{21}D_0^2X_1^3 + p_{22}D_0^2X_2^3 + \Omega_2^2X_2^3 = & -2p_{21}D_0D_1X_1^2 - 2p_{22}D_0D_1X_2^2 \\ & - p_{21}(D_1^2 + 2D_0D_2)X_1^1 - p_{22}(D_1^2 + 2D_0D_2)X_2^1 - 2p_{23}X_2^1X_2^2 \\ & - 2p_{24}X_1^1X_1^2 - p_{25}(X_1^1X_2^2 + X_1^2X_2^1) - p_{26}(X_2^1)^3 - p_{27}(X_1^1)^2X_2^1, \end{aligned} \quad (8.23)$$

where for simplicity is it denoted  $X_1^1 = X_{\alpha\beta}^1$ ,  $X_2^1 = X_{\gamma\delta}^1$ ,  $X_1^2 = X_{\alpha\beta}^2$ ,  $X_2^2 = X_{\gamma\delta}^2$ ,  $\Omega_1 = \Omega_{\alpha\beta}$ , and  $\Omega_2 = \Omega_{\gamma\delta}$ .

### 8.3.1 Solution of Equations at Order of $\varepsilon$

We seek the solution of (8.18) and (8.19) in the form:

$$X_1^1 = A_1(T_1, T_2)e^{i\omega_1 T_0} + A_2(T_1, T_2)e^{i\omega_2 T_0} + \text{cc}, \quad (8.24)$$

$$X_2^1 = \alpha_1 A_1(T_1, T_2)e^{i\omega_1 T_0} + \alpha_2 A_2(T_1, T_2)e^{i\omega_2 T_0} + \text{cc}, \quad (8.25)$$

where  $A_1(T_1, T_2)$  and  $A_2(T_1, T_2)$  are unknown complex functions, cc is the complex conjugate part to the preceding terms, and  $\bar{A}_1(T_1, T_2)$  and  $\bar{A}_2(T_1, T_2)$  are their complex

conjugates,  $\omega_1$  and  $\omega_2$  are unknown frequencies of the coupled process of impact interaction of the impactor and the target, and  $\alpha_1$  and  $\alpha_2$  are yet unknown coefficients.

Substituting (8.24) and (8.25) in (8.18) and (8.19) and gathering the terms with  $e^{i\omega_1 T_0}$  and  $e^{i\omega_2 T_0}$  yield

$$\left(-p_{11}\omega_1^2 - p_{12}\alpha_1\omega_1^2 + \Omega_1^2\right)A_1 e^{i\omega_1 T_0} + \left(-p_{11}\omega_2^2 - p_{12}\alpha_2\omega_2^2 + \Omega_1^2\right)A_2 e^{i\omega_2 T_0} + \text{cc} = 0, \quad (8.26)$$

$$\left(-p_{21}\omega_1^2 - p_{22}\alpha_1\omega_1^2 + \alpha_1\Omega_2^2\right)A_1 e^{i\omega_1 T_0} + \left(-p_{21}\omega_2^2 - p_{22}\alpha_2\omega_2^2 + \Omega_2^2\alpha_2\right)A_2 e^{i\omega_2 T_0} + \text{cc} = 0. \quad (8.27)$$

In order to satisfy Eqss (8.26) and (8.27), it is a need to vanish to zero each bracket in these equations. As a result, from four different brackets we have

$$\alpha_1 = -\frac{p_{11}\omega_1^2 - \Omega_1^2}{p_{12}\omega_1^2}, \quad (8.28)$$

$$\alpha_1 = -\frac{p_{21}\omega_1^2}{p_{22}\omega_1^2 - \Omega_2^2}, \quad (8.29)$$

$$\alpha_2 = -\frac{p_{11}\omega_2^2 - \Omega_1^2}{p_{12}\omega_2^2}, \quad (8.30)$$

$$\alpha_2 = -\frac{p_{21}\omega_2^2}{p_{22}\omega_2^2 - \Omega_2^2}. \quad (8.31)$$

Since the left-hand side parts of relationships (8.28) and (8.29), as well as (8.30) and (8.31) are equal, then their right-hand side parts should be equal as well. Now equating the corresponding right-hand side parts of (8.28), (8.29) and (8.30), (8.31), we are led to one and the same characteristic equation for determining the frequencies  $\omega_1$  and  $\omega_2$ :

$$\left(\Omega_1^2 - p_{11}\omega^2\right)\left(\Omega_2^2 - p_{22}\omega^2\right) - p_{12}^2\omega^4 = 0, \quad (8.32)$$

hence it follows that

$$\omega_{1,2}^2 = \frac{\left(p_{22}\Omega_1^2 + p_{11}\Omega_2^2\right) \pm \sqrt{\left(p_{22}\Omega_1^2 - p_{11}\Omega_2^2\right)^2 + 4\Omega_1^2\Omega_2^2 p_{12}^2}}{2\left(p_{11}p_{22} - p_{12}^2\right)}. \quad (8.33)$$

Reference to relationships (8.33) shows that the frequencies of the mechanical system "target+impactor",  $\omega_1$  and  $\omega_2$ , depend on the natural frequencies of the target,  $\Omega_1$  and  $\Omega_2$ , and coefficients  $p_{11}$ ,  $p_{12}$  and  $p_{22}$ , which in their turn depend on the impactor's mass  $M$  and coordinates of the point of impact. Therefore, as the impactor mass  $M \rightarrow 0$ , the frequencies  $\omega_1$  and  $\omega_2$  tend to the natural frequencies of the shell vibrations  $\Omega_1$  and  $\Omega_2$ , respectively. Coefficients  $s_1$  and  $s_2$  depend on the numbers of the natural modes involved in the process of impact interaction,  $\alpha\beta$  and  $\gamma\delta$ , and on

the coordinates of the contact force application  $x_0$ ,  $y_0$ , resulting in the fact that their particular combinations could vanish coefficients  $s_1$  and  $s_2$  and, thus, coefficients  $p_{12} = p_{21} = 0$ .

### 8.3.2 Solution of Equations at Order of $\varepsilon^2$

Now substituting (8.24) and (8.25) in (8.20) and (8.21), we obtain

$$\begin{aligned} p_{11}D_0^2X_1^2 + p_{12}D_0^2X_2^2 + \Omega_1^2X_1^2 &= -2i\omega_1(p_{11} + \alpha_1p_{12})e^{i\omega_1T_0}D_1A_1 \\ &- 2i\omega_2(p_{11} + \alpha_2p_{12})e^{i\omega_2T_0}D_1A_2 - (p_{13} + \alpha_1^2p_{14} + \alpha_1p_{15})A_1 \left[ A_1e^{2i\omega_1T_0} + \bar{A}_1 \right] \\ &- (p_{13} + \alpha_2^2p_{14} + \alpha_2p_{15})A_2 \left[ A_2e^{2i\omega_2T_0} + \bar{A}_2 \right] \\ &- 2 \left[ p_{13} + \alpha_1\alpha_2p_{14} + (\alpha_1 + \alpha_2)p_{15} \right] A_1 \left[ A_2e^{i(\omega_1+\omega_2)T_0} + \bar{A}_2e^{i(\omega_1-\omega_2)T_0} \right] + \text{cc}, \end{aligned} \quad (8.34)$$

$$\begin{aligned} p_{21}D_0^2X_1^2 + p_{22}D_0^2X_2^2 + \Omega_2^2X_2^2 &= -2i\omega_1(p_{21} + \alpha_1p_{22})e^{i\omega_1T_0}D_1A_1 \\ &- 2i\omega_2(p_{21} + \alpha_2p_{22})e^{i\omega_2T_0}D_1A_2 - (p_{23} + \alpha_1^2p_{24} + \alpha_1p_{25})A_1 \left[ A_1e^{2i\omega_1T_0} + \bar{A}_1 \right] \\ &- (p_{23} + \alpha_2^2p_{24} + \alpha_2p_{25})A_2 \left[ A_2e^{2i\omega_2T_0} + \bar{A}_2 \right] \\ &- 2 \left[ p_{23} + \alpha_1\alpha_2p_{24} + (\alpha_1 + \alpha_2)p_{25} \right] A_1 \left[ A_2e^{i(\omega_1+\omega_2)T_0} + \bar{A}_2e^{i(\omega_1-\omega_2)T_0} \right] + \text{cc}. \end{aligned} \quad (8.35)$$

Reference to Eqs. (8.34) and (8.35) shows that the following two-to-one internal resonance could occur:

$$\omega_1 = 2\omega_2. \quad (8.36)$$

### 8.3.3 Impact-induced internal resonance $\omega_1 = 2\omega_2$

Suppose that, when the frequencies  $\omega_1$  and  $\omega_2$  are coupled by the two-to-one internal resonance (8.36), the functions  $A_1$  and  $A_2$  depend only on the time  $T_1$ . Then Eqs. (8.34) and (8.35) could be rewritten in the following form:

$$p_{11}D_0^2X_1^2 + p_{12}D_0^2X_2^2 + \Omega_1^2X_1^2 = B_1 \exp(i\omega_1T_0) + B_2 \exp(i\omega_2T_0) + \text{Reg} + \text{cc}, \quad (8.37)$$

$$p_{21}D_0^2X_1^2 + p_{22}D_0^2X_2^2 + \Omega_2^2X_2^2 = B_3 \exp(i\omega_1T_0) + B_4 \exp(i\omega_2T_0) + \text{Reg} + \text{cc}, \quad (8.38)$$

where all regular terms are designated by Reg, and

$$B_1 = -2i\Omega_1^2\omega_1^{-1}D_1A_1 - (p_{13} + \alpha_2^2p_{14} + \alpha_2p_{15})A_2^2,$$



$$B_2 = -2i\Omega_1^2\omega_2^{-1}D_1A_2 - 2[p_{13} + \alpha_1\alpha_2p_{14} + (\alpha_1 + \alpha_2)p_{15}]A_1\bar{A}_2,$$

$$B_3 = -2i\Omega_2^2\omega_1^{-1}\alpha_1D_1A_1 - (p_{23} + \alpha_2^2p_{24} + \alpha_2p_{25})A_2^2,$$

$$B_4 = -2i\Omega_2^2\omega_2^{-1}\alpha_2D_1A_2 - 2[p_{23} + \alpha_1\alpha_2p_{24} + (\alpha_1 + \alpha_2)p_{25}]A_1\bar{A}_2.$$

Let us show that the terms with the exponents  $\exp(\pm i\omega_i T_0)$  ( $i = 1, 2$ ) produce circular terms. For this purpose we choose a particular solution in the form

$$\begin{aligned} X_{1p}^2 &= C_1 \exp(i\omega_1 T_0) + \text{cc}, \\ X_{2p}^2 &= C_2 \exp(i\omega_1 T_0) + \text{cc}, \end{aligned} \quad (8.39)$$

or

$$\begin{aligned} X_{1p}^2 &= C'_1 \exp(i\omega_2 T_0) + \text{cc}, \\ X_{2p}^2 &= C'_2 \exp(i\omega_2 T_0) + \text{cc}, \end{aligned} \quad (8.40)$$

where  $C_1$ ,  $C_2$  and  $C'_1$ ,  $C'_2$  are arbitrary constants.

Substituting the proposed solution (8.39) or (8.40) in (8.37) and (8.38), we are led to the following sets of equations, respectively:

$$\begin{cases} p_{12}\omega_1^2(\alpha_1 C_1 - C_2) = B_1, \\ p_{21}\omega_1^2(-C_1 + \frac{1}{\alpha_1} C_2) = B_3, \end{cases} \quad (8.41)$$

or

$$\begin{cases} p_{12}\omega_2^2(\alpha_2 C'_1 - C'_2) = B_2, \\ p_{21}\omega_2^2(-C'_1 + \frac{1}{\alpha_2} C'_2) = B_4. \end{cases} \quad (8.42)$$

From the sets of Eqs. (8.41) and (8.42) it is evident that the determinants comprised from the coefficients standing at  $C_1$ ,  $C_2$  and  $C'_1$ ,  $C'_2$  are equal to zero, therefore, it is impossible to determine the arbitrary constants  $C_1$ ,  $C_2$  and  $C'_1$ ,  $C'_2$  of the particular solutions (8.39) and (8.40), what proves the above proposition concerning the circular terms.

In order to eliminate the circular terms, the terms proportional to  $e^{i\omega_1 T_0}$  and  $e^{i\omega_2 T_0}$  should be vanished to zero putting  $B_i = 0$  ( $i = 1, 2, 3, 4$ ). So we obtain four equations for defining two unknown amplitudes  $A_1(t)$  and  $A_2(t)$ . However, it is possible to show that not all of these four equations are linear independent from each other. For this purpose, let us first apply the operators  $(p_{22}D_0^2 + \Omega_2^2)$  and  $(-p_{12}D_0^2)$  to (8.37) and (8.38), respectively, and then add the resulting equations. This procedure will allow us to eliminate  $X_2^2$ . If we apply the operators  $(-p_{12}D_0^2)$  and  $(p_{11}D_0^2 + \Omega_1^2)$  to (8.37) and (8.38), respectively, and then add the resulting equations. This procedure will allow us to eliminate  $X_1^2$ . Thus, we obtain

$$\begin{aligned} &[(p_{11}p_{22} - p_{12}^2)D_0^4 + (p_{11}\Omega_2^2 + p_{22}\Omega_1^2)D_0^2 + \Omega_1^2\Omega_2^2]X_1^2 \\ &= [(p_{22}D_0^2 + \Omega_2^2)B_1 - p_{12}D_0^2 B_3] \exp(i\omega_1 T_0) \\ &+ [(p_{22}D_0^2 + \Omega_2^2)B_2 - p_{12}D_0^2 B_4] \exp(i\omega_2 T_0) + \text{Reg} + \text{cc}, \end{aligned} \quad (8.43)$$

$$\begin{aligned}
& \left[ (p_{11}p_{22} - p_{12}^2)D_0^4 + (p_{11}\Omega_2^2 + p_{22}\Omega_1^2)D_0^2 + \Omega_1^2\Omega_2^2 \right] X_2^2 \\
& = \left[ -p_{12}D_0^2B_1 + (p_{11}D_0^2 + \Omega_1^2)B_3 \right] \exp(i\omega_1 T_0) \\
& + \left[ -p_{12}D_0^2B_2 + (p_{11}D_0^2 + \Omega_1^2)B_4 \right] \exp(i\omega_2 T_0) + \text{Reg} + \text{cc}.
\end{aligned} \tag{8.44}$$

To eliminate the circular terms from Eqs. (8.43) and (8.44), it is necessary to vanish to zero the terms in each square bracket. As a result we obtain

$$\begin{cases} (\Omega_2^2 - p_{22}\omega_1^2)B_1 + p_{12}\omega_1^2B_3 = 0 \\ p_{12}\omega_1^2B_1 + (\Omega_1^2 - p_{11}\omega_1^2)B_3 = 0 \end{cases} \tag{8.45}$$

and

$$\begin{cases} (\Omega_2^2 - p_{22}\omega_2^2)B_2 + p_{12}\omega_2^2B_4 = 0 \\ p_{12}\omega_2^2B_2 + (\Omega_1^2 - p_{11}\omega_2^2)B_4 = 0 \end{cases} \tag{8.46}$$

From Eqs. (8.45) and (8.46) it is evident that the determinant of each set of equations is reduced to the characteristic Eq. (8.32), whence it follows that each pair of equations is linear dependent, therefore for further treatment we should take only one equation from each pair in order that these two chosen equations are to be linear independent. Thus, for example, taking the first equations from each pair and considering relationships (8.29) and (8.31), we have

$$B_1 + \alpha_1 B_3 = 0, \tag{8.47}$$

$$B_3 + \alpha_2 B_4 = 0. \tag{8.48}$$

Substituting values of  $B_1$ - $B_4$  in (8.47) and (8.48), we obtain the following solvability equations:

$$2i\omega_1 k_1 D_1 A_1 + b_1 A_2^2 = 0, \tag{8.49}$$

$$2i\omega_2 k_2 D_1 A_2 + b_2 A_1 \bar{A}_2 = 0, \tag{8.50}$$

where

$$k_i = \frac{\Omega_1^2 + \alpha_i^2 \Omega_2^2}{\omega_i^2} \quad (i = 1, 2), \quad b_1 = p_{13} + \alpha_2^2 p_{14} + \alpha_2 p_{15} + \alpha_1 (p_{23} + \alpha_2^2 p_{24} + \alpha_2 p_{25}),$$

$$b_2 = 2 \{ p_{13} + \alpha_1 \alpha_2 p_{14} + (\alpha_1 + \alpha_2) p_{15} + \alpha_2 [ p_{23} + \alpha_1 \alpha_2 p_{24} + (\alpha_1 + \alpha_2) p_{25} ] \}.$$

Let us multiply Eqs. (8.49) and (8.50) by  $\bar{A}_1$  and  $\bar{A}_2$ , respectively, and find their complex conjugates. After adding every pair of the mutually adjoint equations with each other and subtracting one from another, as a result we obtain

$$2i\omega_1 (\bar{A}_1 D_1 A_1 - A_1 D_1 \bar{A}_1) + \frac{b_1}{k_1} (A_2^2 \bar{A}_1 + \bar{A}_2^2 A_1) = 0, \tag{8.51}$$

$$2i\omega_1(\bar{A}_1 D_1 A_1 + A_1 D_1 \bar{A}_1) + \frac{b_1}{k_1}(A_2^2 \bar{A}_1 - \bar{A}_2^2 A_1) = 0, \quad (8.52)$$

$$2i\omega_2(\bar{A}_2 D_1 A_2 - A_2 D_1 \bar{A}_2) + \frac{b_2}{k_2}(A_1 \bar{A}_2^2 + \bar{A}_1 A_2^2) = 0, \quad (8.53)$$

$$2i\omega_2(\bar{A}_2 D_1 A_2 + A_2 D_1 \bar{A}_2) + \frac{b_2}{k_2}(A_1 \bar{A}_2^2 - \bar{A}_1 A_2^2) = 0. \quad (8.54)$$

Representing  $A_1(T_1)$  and  $A_2(T_1)$  in Eqs. (8.51)–(8.54) in the polar form

$$A_i(T_1) = a_i(T_1)e^{i\varphi_i(T_1)} \quad (i = 1, 2), \quad (8.55)$$

we are led to the system of four nonlinear differential equations in  $a_1(T_1)$ ,  $a_2(T_1)$ ,  $\varphi_1(T_1)$ , and  $\varphi_2(T_1)$

$$(a_1^2)^\cdot = -\frac{b_1}{k_1\omega_1} a_1 a_2^2 \sin \delta, \quad (8.56)$$

$$\dot{\varphi}_1 - \frac{b_1}{2k_1\omega_1} a_1^{-1} a_2^2 \cos \delta = 0, \quad (8.57)$$

$$(a_2^2)^\cdot = \frac{b_2}{k_2\omega_2} a_1 a_2^2 \sin \delta, \quad (8.58)$$

$$\dot{\varphi}_2 - \frac{b_2}{2k_2\omega_2} a_1 \cos \delta = 0, \quad (8.59)$$

where  $\delta = 2\varphi_2 - \varphi_1$ , and a dot denotes differentiation with respect to  $T_1$ .

From Eqs. (8.56) and (8.58) we could find that

$$\frac{b_2}{k_2\omega_2}(a_1^2)^\cdot + \frac{b_1}{k_1\omega_1}(a_2^2)^\cdot = 0. \quad (8.60)$$

Multiplying Eq. (8.60) by  $MV_0$  and integrating over  $T_1$ , we obtain the first integral of the set of Eqs. (8.56)–(8.59), which is the law of conservation of energy,

$$MV_0 \left( \frac{b_2}{k_2\omega_2} a_1^2 + \frac{b_1}{k_1\omega_1} a_2^2 \right) = K_0, \quad (8.61)$$

where  $K_0$  is the initial energy. Considering that  $K_0 = \frac{1}{2} MV_0^2$ , Eq. (8.61) is reduced to the following form:

$$\frac{b_2}{k_2\omega_2} a_1^2 + \frac{b_1}{k_1\omega_1} a_2^2 = \frac{V_0}{2}. \quad (8.62)$$

Let us introduce into consideration a new function  $\xi(T_1)$  in the following form:

$$a_1^2 = \frac{k_2\omega_2}{b_2} E_0 \xi(T_1), \quad a_2^2 = \frac{k_1\omega_1}{b_1} E_0 [1 - \xi(T_1)], \quad (8.63)$$

where  $E_0 = V_0/2$ .

It is easy to verify by the direct substitution that Eqs. (8.63) satisfy Eq. (8.62), while the value  $\xi_0 = \xi(0)$  ( $0 \leq \xi(0) \leq 1$ ) governs the energy distribution between two subsystems,  $X_1^1$  and  $X_2^1$ , at the moment of impact. Substituting (8.63) in (8.56) yields

$$\dot{\xi} = -b \sqrt{\xi}(1 - \xi) \sin \delta, \quad (8.64)$$

where

$$b = \sqrt{\frac{b_2}{k_2 \omega_2}} \sqrt{E_0}.$$

Subtracting Eq. (8.57) from the doubled Eq. (8.59), we have

$$\dot{\delta} = -b \frac{1 - 3\xi}{2 \sqrt{\xi}} \cos \delta. \quad (8.65)$$

Equation (8.65) could be rewritten in another form considering that

$$\dot{\delta} = \frac{d\delta}{d\xi} \dot{\xi},$$

or with due account for (8.64)

$$\dot{\delta} = -\frac{d\delta}{d\xi} b \sqrt{\xi}(1 - \xi) \sin \delta. \quad (8.66)$$

Substituting (8.66) in Eq. (8.65) yields

$$\sqrt{\xi}(1 - \xi) \frac{d \cos \delta}{d\xi} + \frac{1 - 3\xi}{2 \sqrt{\xi}} \cos \delta = 0. \quad (8.67)$$

Integrating (8.67), we have

$$\cos \delta = \frac{G_0}{\sqrt{\xi}(1 - \xi)}, \quad (8.68)$$

where  $G_0$  is a constant of integration to be determined from the initial conditions.

Based on relationship (8.68), it is possible to introduce into consideration the stream function  $G(\delta, \xi)$  of the phase fluid on the plane  $\delta\xi$  such that

$$G(\delta, \xi) = \sqrt{\xi}(1 - \xi) \cos \delta = G_0, \quad (8.69)$$

which is one more first integral of the set of Eqs. (8.56)–(8.59). It is easy to verify that the function (8.69) is really a stream function, since

$$v_\delta = \dot{\delta} = -b \frac{\partial G}{\partial \xi}, \quad v_\xi = \dot{\xi} = b \frac{\partial G}{\partial \delta}. \quad (8.70)$$

It is interesting to note that the stream function  $G(\delta, \xi)$  (8.69) obtained for the doubly curved shallow shell being under conditions of the two-to-one internal resonance

coincides with that for a suspension bridge subjected to the two-to-one internal resonance analyzed in Rossikhin and Shitikova (1995).

In order to find the  $T_1$ -dependence of  $\xi$ , it is necessary to express  $\sin \delta$  in terms of  $\xi$  in Eq. (8.64) with a help of relationship (8.68). As a result we obtain

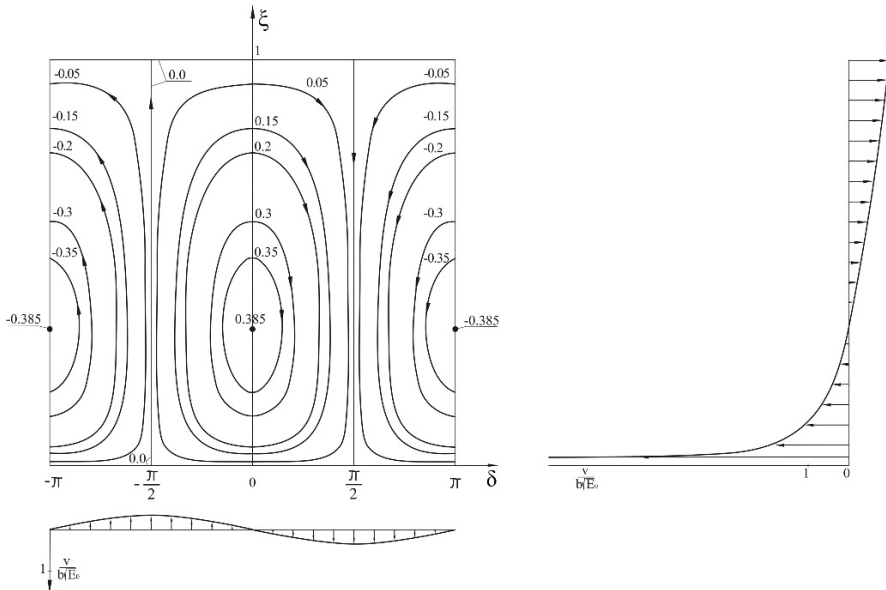
$$\dot{\xi} = -b \sqrt{\xi(1-\xi)^2 - G_0^2},$$

or

$$\int_{\xi_0}^{\xi} \frac{d\xi}{\sqrt{\xi^3 - 2\xi^2 + \xi - G_0^2}} = -bT_1, \tag{8.71}$$

where  $\xi_0$  is the initial magnitude of the function  $\xi = \xi(T_1)$ . In other words, the calculation of the  $T_1$ -dependence of  $\xi$  is reduced to the calculation of the incomplete elliptic integral in the left hand-side of (8.71).

For the case of two-to-one internal resonance (8.36), the stream-function  $G(\xi, \delta)$  is constructed according to (8.69), and its phase portrait showing the stream-lines of the phase fluid in the phase plane  $\xi - \delta$  is presented in Fig. 8.2, which for the first time was presented in Rossikhin and Shitikova (1995) for the two-to-one internal resonance during nonlinear vibrations of suspension bridges. Magnitudes of  $G$  are



**Fig. 8.2:** Phase portrait:  $\omega_1 = 2\omega_2$ .

indicated by digits near the curves which correspond to the stream-lines; the flow direction of the phase fluid elements are shown by arrows on the stream-lines.

Figure 8.2 shows that the phase fluid flows within the circulation zones, which tend to be located around the perimeter of the rectangles bounded by the lines  $\xi = 0$ ,  $\xi = 1$ , and  $\delta = \pm(\pi/2) \pm 2\pi n$  ( $n = 0, 1, 2, \dots$ ). As this takes place, the flow in each such rectangle becomes isolated. On all four rectangle sides  $G = 0$  and inside it, the value  $G$  preserves its sign. The function  $G$  attains its extreme magnitudes at the points with the coordinates  $\xi = \frac{1}{3}$ ,  $\delta = \pm\pi n$  ( $n = 0, 1, 2, \dots$ ). Stream-lines give a pictorial estimate of the connection of  $G$  with all types of the energy-exchange mechanism. Thus, the points with the coordinates  $\xi_0 = \frac{1}{3}$ ,  $\delta_0 = \pm\pi n$  ( $n = 0, 1, 2, \dots$ ) correspond to the stationary regime, since  $\dot{\delta} = 0$  and  $\dot{\xi} = 0$  according to (8.64) and (8.65). The stationary points  $\xi_0 = \frac{1}{3}$ ,  $\delta_0 = \pm\pi n$  are centers, as with a small deviation from a center, a phase element begins to move around the stationary point along a closed trajectory. Closed stream-lines correspond to the periodic change of both amplitudes and phases.

Along the lines  $\delta = \pm(\pi/2) \pm 2\pi n$  ( $n = 0, 1, 2, \dots$ ) pure amplitude modulated aperiodic motions are realized, since with an increase in time  $t$  from 0 to  $\infty$  the value  $\xi$  increases from  $\xi_0$  to 1 (along the line  $\delta = -\pi/2$ ) or decreases from  $\xi_0$  to 0 (along the line  $\delta = \pi/2$ ), and from Eq. (8.64) it follows that

$$\xi = \left[ \frac{1 + \sqrt{\xi_0} - (1 - \sqrt{\xi_0}) \exp(-b \sqrt{E_0} T_1)}{1 + \sqrt{\xi_0} + (1 - \sqrt{\xi_0}) \exp(-b \sqrt{E_0} T_1)} \right]^2, \quad (8.72)$$

$$\delta(T_1) = \delta_0 = \frac{\pi}{2} \pm \pi n, \quad n = 0, 1, 2, \dots$$

Along the line  $\xi = 1$  only phase modulated motions are realized, because when  $\xi = \xi_0 = 1$  the amplitudes  $a_1 = \text{const}$  and  $a_2 = 0$ , and from (8.64) and (8.65) we could find that

$$b \sqrt{E_0} T_1 = \ln \frac{\tan\left(\frac{\delta}{2} + \frac{\pi}{4}\right)}{\tan\left(\frac{\delta_0}{2} + \frac{\pi}{4}\right)}, \quad \xi(T_1) = \xi_0 = 1. \quad (8.73)$$

The transition of fluid elements from the points  $\xi = 0$ ,  $\delta = \pi/2 \pm 2\pi n$  to the points  $\xi = 0$ ,  $\delta = -\pi/2 \pm 2\pi n$  proceeds instantly, because according to the distribution of the phase velocity (8.70) along the section  $\delta = 0$  the magnitude of  $\mathbf{v}$  tends to infinity as  $\xi \rightarrow 0$ . The distribution of the velocity along the vertical lines  $\delta = \pm\pi n$  ( $n = 0, 1, 2, \dots$ ) has the aperiodic character, while in the vicinity of the line  $\xi = 1/3$  it possesses the periodic character.

### 8.3.3.1 Initial Conditions

In order to construct the final solution of the problem under consideration, i.e. to solve the set of Eqs. (8.56)–(8.59) involving the functions  $a_1(T_1)$ ,  $a_2(T_1)$ , or  $\xi(T_1)$ , as well as  $\varphi_1(T_1)$ , and  $\varphi_2(T_1)$ , or  $\delta(T_1)$ , it is necessary to use the initial conditions

$$w(x, y, 0) = 0, \quad (8.74)$$

$$\dot{w}(x_0, y_0, 0) = \varepsilon V_0, \quad (8.75)$$

$$\frac{b_2}{k_2 \omega_2} a_1^2(0) + \frac{b_1}{k_1 \omega_1} a_2^2(0) = E_0. \quad (8.76)$$

The two-term relationship for the displacement  $w$  (8.9) within an accuracy of  $\varepsilon$  according to (8.17) has the form

$$\begin{aligned} w(x, y, t) = & \varepsilon \left[ X_{\alpha\beta}^1(T_0, T_1) \sin\left(\frac{\alpha\pi x}{a}\right) \sin\left(\frac{\beta\pi y}{b}\right) \right. \\ & \left. + X_{\gamma\delta}^1(T_0, T_1) \sin\left(\frac{\gamma\pi x}{a}\right) \sin\left(\frac{\delta\pi y}{b}\right) \right] + O(\varepsilon^2). \end{aligned} \quad (8.77)$$

Substituting (8.24) and (8.25) in (8.77) with due account for (8.55) yields

$$\begin{aligned} w(x, y, t) = & 2\varepsilon \left\{ a_1(\varepsilon t) \cos[\omega_1 t + \varphi_1(\varepsilon t)] \right. \\ & \left. + a_2(\varepsilon t) \cos[\omega_2 t + \varphi_2(\varepsilon t)] \right\} \sin\left(\frac{\alpha\pi x}{a}\right) \sin\left(\frac{\beta\pi y}{b}\right) \\ & + 2\varepsilon \left\{ \alpha_1 a_1(\varepsilon t) \cos[\omega_1 t + \varphi_1(\varepsilon t)] \right. \\ & \left. + \alpha_2 a_2(\varepsilon t) \cos[\omega_2 t + \varphi_2(\varepsilon t)] \right\} \sin\left(\frac{\gamma\pi x}{a}\right) \sin\left(\frac{\delta\pi y}{b}\right) + O(\varepsilon^2). \end{aligned} \quad (8.78)$$

Differentiating (8.78) with respect to time  $t$  and limiting ourselves by the terms of the order of  $\varepsilon$ , we could find the velocity of the shell at the point of impact as follows

$$\begin{aligned} \dot{w}(x_0, y_0, t) = & -2\varepsilon \left\{ \omega_1 a_1(\varepsilon t) \sin[\omega_1 t + \varphi_1(\varepsilon t)] + \omega_2 a_2(\varepsilon t) \sin[\omega_2 t + \varphi_2(\varepsilon t)] \right\} s_1 \\ & - 2\varepsilon \left\{ \alpha_1 \omega_1 a_1(\varepsilon t) \sin[\omega_1 t + \varphi_1(\varepsilon t)] + \alpha_2 \omega_2 a_2(\varepsilon t) \sin[\omega_2 t + \varphi_2(\varepsilon t)] \right\} s_2 + O(\varepsilon^2). \end{aligned} \quad (8.79)$$

Substituting (8.78) in the first initial condition (8.74) yields

$$a_1(0) \cos \varphi_1(0) + a_2(0) \cos \varphi_2(0) = 0, \quad (8.80)$$

$$\alpha_1 a_1(0) \cos \varphi_1(0) + \alpha_2 a_2(0) \cos \varphi_2(0) = 0. \quad (8.81)$$

From Eqs. (8.80) and (8.81) we find that

$$\cos \varphi_1(0) = 0, \quad \cos \varphi_2(0) = 0, \quad (8.82)$$

whence it follows that

$$\varphi_1(0) = \pm \frac{\pi}{2}, \quad \varphi_2(0) = \pm \frac{\pi}{2}, \quad (8.83)$$

and

$$\cos \delta_0 = \cos [2\varphi_2(0) - \varphi_1(0)] = 0, \quad (8.84)$$

i.e.,

$$\delta_0 = \pm \frac{\pi}{2} \pm 2\pi n. \quad (8.85)$$

The signs in (8.83) should be chosen considering the fact that the initial amplitudes are positive values, i.e.  $a_1(0) > 0$  and  $a_2(0) > 0$ . Assume for definiteness that

$$\varphi_1(0) = -\frac{\pi}{2}, \quad \varphi_2(0) = -\frac{\pi}{2}. \quad (8.86)$$

Substituting now (8.79) in the second initial condition (8.75) with due account for (8.86), we obtain

$$\omega_1(s_1 + \alpha_1 s_2)a_1(0) + \omega_2(s_1 + \alpha_2 s_2)a_2(0) = E_0. \quad (8.87)$$

From Eqs. (8.76) and (8.87) we could determine the initial amplitudes

$$a_2(0) = \frac{E_0}{\omega_2(s_1 + \alpha_2 s_2)} - \frac{\omega_1(s_1 + \alpha_1 s_2)}{\omega_2(s_1 + \alpha_2 s_2)} a_1(0), \quad (8.88)$$

$$c_1 a_1^2(0) + c_2 a_1(0) + c_3 = 0, \quad (8.89)$$

where

$$c_1 = 1 + \frac{b_1 k_2 \omega_1 (s_1 + \alpha_1 s_2)^2}{b_2 k_1 \omega_2 (s_1 + \alpha_2 s_2)^2}, \quad c_2 = -\frac{b_1 k_2 (s_1 + \alpha_1 s_2) 2E_0}{b_2 k_1 \omega_2 (s_1 + \alpha_2 s_2)^2},$$

$$c_3 = \frac{b_1 k_2 E_0^2}{b_2 k_1 \omega_1 \omega_2 (s_1 + \alpha_2 s_2)^2} - \frac{k_2 \omega_2 E_0}{b_2}.$$

From Eqs. (8.88) and (8.89) it is evident that the initial magnitudes depend on the mass and the initial velocity of the impactor, on the coordinates of the point of impact, as well as on the numbers of the two modes induced by the impact.

Considering (8.84), from (8.68) we find the value of constant  $G_0$

$$G_0 = 0. \quad (8.90)$$

Reference to (8.69) shows that  $G_0$  could be zero in three cases: at  $\xi_0 = 0$ ,  $\xi_0 = 1$ , or when  $\cos \delta_0 = 0$ . The above analysis of the phase portrait has revealed that the case  $\xi_0 = 0$  is not realized. As for the case  $\xi_0 = 1$ , then the solution for the phase modulated motion takes the form of (8.73). However, for the found magnitudes of the initial phase difference  $\delta_0$  (8.85), the value of  $\tan\left(\frac{\delta_0}{2} + \frac{\pi}{4}\right)$  in (8.73) is either equal to zero or to infinity, what means that this case could not be realized as well. That is why in further treatment we will analyze only the third case, resulting in the amplitude modulated motion (8.72) with

$$\delta(T_1) = \delta_0 = \text{const}. \quad (8.91)$$

Thus, we have determined all necessary constants from the initial conditions, therefore we could proceed to the construction of the solution for the contact force.



### 8.3.3.2 Contact Force and Shell's Deflection at the Point of Impact

Substituting relationship (8.79) differentiated one time with respect to time  $t$  in (8.4), we could obtain the contact force  $P(t)$

$$P(t) = 2\epsilon M \left\{ \omega_1^2 a_1(\epsilon t) \cos[\omega_1 t + \varphi_1(\epsilon t)] + \omega_2^2 a_2(\epsilon t) \cos[\omega_2 t + \varphi_2(\epsilon t)] \right\} s_1 + 2\epsilon M \left\{ \alpha_1 \omega_1^2 a_1(\epsilon t) \cos[\omega_1 t + \varphi_1(\epsilon t)] + \alpha_2 \omega_2^2 a_2(\epsilon t) \cos[\omega_2 t + \varphi_2(\epsilon t)] \right\} s_2 + O(\epsilon^2). \quad (8.92)$$

From Eqs. (8.57) and (8.59) with due account for (8.91) it follows that

$$\varphi_1(T_1) = \text{const} = \varphi_1(0), \quad \varphi_2(T_1) = \text{const} = \varphi_2(0). \quad (8.93)$$

Considering (8.93) and (8.86), Eq. (8.92) is reduced to

$$P(t) = 2\epsilon M \omega_2^2 \left\{ 8(s_1 + \alpha_1 s_2) a_1(\epsilon t) \cos \omega_2 t + (s_1 + \alpha_2 s_2) a_2(\epsilon t) \right\} \sin \omega_2 t. \quad (8.94)$$

Substituting (8.63) in (8.94), we finally obtained

$$P(t) = 2\epsilon M \omega_2^2 \sqrt{E_0} \left\{ 8(s_1 + \alpha_1 s_2) \sqrt{\frac{k_2 \omega_2}{b_2}} \sqrt{\xi(\epsilon t)} \cos \omega_2 t + (s_1 + \alpha_2 s_2) \sqrt{\frac{k_1 \omega_1}{b_1}} \sqrt{1 - \xi(\epsilon t)} \right\} \sin \omega_2 t, \quad (8.95)$$

where the function  $\xi(\epsilon t)$  is defined by (8.72).

Since the duration of contact is a small value, what is evident from experimental data (Kistler and Waas, 1998a; Kunukkasseril and Palaninathan, 1975; Rossikhin and Shitikova, 2007), then  $P(t)$  could be calculated via an approximate formula, which is obtained from (8.94) at  $\epsilon t \approx 0$

$$P(t) \approx 16\epsilon M \omega_2^2 \left( \cos \omega_2 t + \frac{1}{8} \kappa \right) (s_1 + \alpha_1 s_2) a_1(0) \sin \omega_2 t + O(\epsilon^2), \quad (8.96)$$

where the dimensionless parameter  $\kappa$

$$\kappa = \frac{(s_1 + \alpha_2 s_2)}{(s_1 + \alpha_1 s_2)} \frac{a_2(0)}{a_1(0)} \quad (8.97)$$

is defined by the parameters of two impact-induced modes coupled by the two-to-one internal resonance (8.36), as well as by the coordinates of the point of impact and the initial velocity of impact. The deflection of the shell at the point of impact could be determined from (8.78) with due account for the found initial values of the phases

$$w(x_0, y_0, t) \approx 4\epsilon \left( \cos \omega_2 t + \frac{1}{2} \kappa \right) (s_1 + \alpha_1 s_2) a_1(0) \sin \omega_2 t + O(\epsilon^2). \quad (8.98)$$

The dimensionless time  $\tau = \omega_2 t$  dependence of the dimensionless contact force  $P^*$

$$P^*(\tau) \approx \left( \cos \tau + \frac{1}{8} \kappa \right) \sin \tau, \tag{8.99}$$

where

$$P^*(t) = \frac{P(t)}{16\varepsilon M \omega_2^2 (s_1 + \alpha_1 s_2) a_1(0)},$$

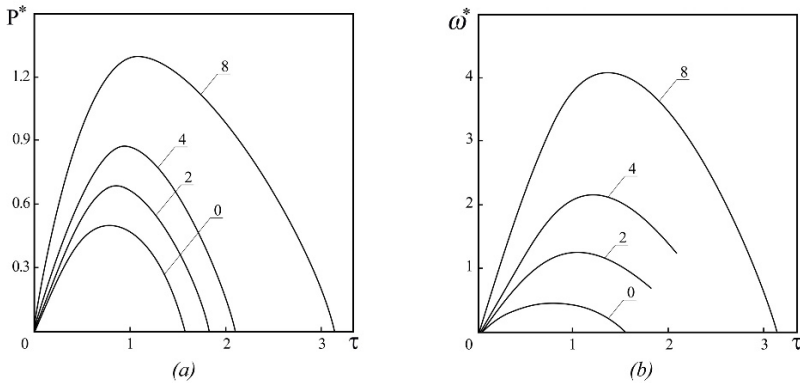
and the dimensionless deflection of the target at the point of impact

$$w^*(\tau) = \left( \cos \tau + \frac{1}{2} \kappa \right) \sin \tau, \tag{8.100}$$

where

$$w^*(t) = \frac{w(x_0, y_0, t)}{4\varepsilon (s_1 + \alpha_1 s_2) a_1(0)},$$

are shown, respectively, in Figs. 8.3 (a) and (b) for the different magnitudes of the parameter  $\kappa$ : 0, 2, 4, and 8. Figures 8.3 (a) and (b) show that the increase in the parameter  $\kappa$  results in the increase of the maximal contact force, the duration of contact, and the maximal deflection of the target at the point of impact. In other words, from Figure 3 it is evident that the peak contact force, the duration of contact and shell's deflection depend essentially upon the parameters of two impact-induced modes coupled by the two-to-one internal resonance (8.36).



**Fig. 8.3:** Dimensionless time dependence of (a) the dimensionless contact force and (b) the target deflection at the point of impact for the case of the internal resonance  $\omega_1 = 2\omega_2$ .

### 8.3.4 Solution of Equations at Order of $\varepsilon^3$

In order to study internal resonances of the order of  $\varepsilon^3$ , in further treatment we assume that  $\omega_1 \neq 2\omega_2$ . In this case in order to eliminate secular terms in Eqss (8.34) and (8.35), it is sufficient to fulfill the following equations:

$$D_1 A_1 = 0, \quad D_1 A_2 = 0, \quad (8.101)$$

whence it follows that the functions  $A_1$  and  $A_2$  are  $T_1$ -independent, i.e.,

$$A_1 = A_1(T_2), \quad A_2 = A_2(T_2). \quad (8.102)$$

To solve Eqss (8.34) and (8.35) with due account for (8.101) and (8.102), let us first apply the operators  $(p_{22}D_0^2 + \Omega_2^2)$  and  $(-p_{12}D_0^2)$  to (8.34) and (8.35), respectively, and then add the resulting equations. This procedure will allow us to eliminate  $X_2^2$ . If we apply the operators  $(-p_{12}D_0^2)$  and  $(p_{11}D_0^2 + \Omega_1^2)$  to (8.34) and (8.35), respectively, and then add the resulting equations. This procedure will allow us to eliminate  $X_1^2$ . Thus, we obtain

$$\begin{aligned} & [(p_{11}p_{22} - p_{12}^2)D_0^4 + (p_{11}\Omega_2^2 + p_{22}\Omega_1^2)D_0^2 + \Omega_1^2\Omega_2^2]X_1^2 \\ &= -[(p_{13} + \alpha_1^2 p_{14} + \alpha_1 p_{15})(p_{22}D_0^2 + \Omega_2^2) \\ & \quad - (p_{23} + \alpha_1^2 p_{24} + \alpha_1 p_{25})p_{12}D_0^2]A_1 [A_1 e^{2i\omega_1 T_0} + \bar{A}_1] \\ & \quad - [(p_{13} + \alpha_2^2 p_{14} + \alpha_2 p_{15})(p_{22}D_0^2 + \Omega_2^2) - (p_{23} + \alpha_2^2 p_{24} + \alpha_2 p_{25})p_{12}D_0^2] \\ & \quad \times A_2 [A_2 e^{2i\omega_2 T_0} + \bar{A}_2] - 2\{[p_{13} + \alpha_1 \alpha_2 p_{14} + (\alpha_1 + \alpha_2)p_{15}] (p_{22}D_0^2 + \Omega_2^2) \\ & \quad - [p_{23} + \alpha_1 \alpha_2 p_{24} + (\alpha_1 + \alpha_2)p_{25}] p_{12}D_0^2\} \\ & \quad \times A_1 [A_2 e^{i(\omega_1 + \omega_2)T_0} + \bar{A}_2 e^{i(\omega_1 - \omega_2)T_0}] + \text{cc}, \end{aligned} \quad (8.103)$$

$$\begin{aligned} & [(p_{11}p_{22} - p_{12}^2)D_0^4 + (p_{11}\Omega_2^2 + p_{22}\Omega_1^2)D_0^2 + \Omega_1^2\Omega_2^2]X_2^2 \\ &= -[(p_{23} + \alpha_1^2 p_{24} + \alpha_1 p_{25})(p_{11}D_0^2 + \Omega_1^2) \\ & \quad - (p_{13} + \alpha_1^2 p_{14} + \alpha_1 p_{15})p_{12}D_0^2]A_1 [A_1 e^{2i\omega_1 T_0} + \bar{A}_1] \\ & \quad - [(p_{23} + \alpha_2^2 p_{24} + \alpha_2 p_{25})(p_{11}D_0^2 + \Omega_1^2) - (p_{13} + \alpha_2^2 p_{14} + \alpha_2 p_{15})p_{12}D_0^2] \\ & \quad \times A_2 [A_2 e^{2i\omega_2 T_0} + \bar{A}_2] - 2\{[p_{23} + \alpha_1 \alpha_2 p_{24} + (\alpha_1 + \alpha_2)p_{25}] (p_{11}D_0^2 + \Omega_1^2) \\ & \quad - [p_{13} + \alpha_1 \alpha_2 p_{14} + (\alpha_1 + \alpha_2)p_{15}] p_{12}D_0^2\} \\ & \quad \times A_1 [A_2 e^{i(\omega_1 + \omega_2)T_0} + \bar{A}_2 e^{i(\omega_1 - \omega_2)T_0}] + \text{cc}. \end{aligned} \quad (8.104)$$

The solution of (8.103) and (8.104) has the form

$$\begin{aligned}
X_1^2 = & F_1(T_2) e^{i\omega_1 T_0} + F_2(T_2) e^{i\omega_2 T_0} + N_1 A_1^2 e^{2i\omega_1 T_0} + N_2 A_2^2 e^{2i\omega_2 T_0} \\
& + N_3 A_1 \bar{A}_1 + N_4 A_2 \bar{A}_2 + N_5 A_1 A_2 e^{i(\omega_1 + \omega_2) T_0} + N_6 A_1 \bar{A}_2 e^{i(\omega_1 - \omega_2) T_0} + \text{cc},
\end{aligned} \quad (8.105)$$

$$\begin{aligned}
X_2^2 = & \alpha_1 F_1(T_2) e^{i\omega_1 T_0} + \alpha_2 F_2(T_2) e^{i\omega_2 T_0} + E_1 A_1^2 e^{2i\omega_1 T_0} + E_2 A_2^2 e^{2i\omega_2 T_0} \\
& + E_3 A_1 \bar{A}_1 + E_4 A_2 \bar{A}_2 + E_5 A_1 A_2 e^{i(\omega_1 + \omega_2) T_0} + E_6 A_1 \bar{A}_2 e^{i(\omega_1 - \omega_2) T_0} + \text{cc},
\end{aligned} \quad (8.106)$$

where  $F_1(T_2)$  and  $F_2(T_2)$  are unknown complex functions, and coefficients  $N_i$  and  $E_i$  ( $i = 1, 2, \dots, 6$ ) are presented in Appendix.

Now substituting (8.24), (8.25), (8.105), and (8.106) in (8.20) and (8.21), we obtain (Rossikhin et al, 2015)

$$\begin{aligned}
p_{11} D_0^2 X_1^3 + p_{12} D_0^2 X_2^3 + \Omega_1^2 X_1^3 = & -[2i\omega_1(p_{11} + \alpha_1 p_{12}) D_2 A_1 \\
& + K_1 A_1^2 \bar{A}_1 + K_2 A_1 A_2 \bar{A}_2] e^{i\omega_1 T_0} \\
& - [2i\omega_2(p_{11} + \alpha_2 p_{12}) D_2 A_2 + L_1 A_2^2 \bar{A}_2 + L_2 A_1 \bar{A}_1 A_2] e^{i\omega_2 T_0} \\
& - \{M_1 A_2^3 e^{3i\omega_2 T_0} + M_2 A_1 \bar{A}_2^2 e^{i(\omega_1 - 2\omega_2) T_0}\} \\
& - R_1 A_1^2 \bar{A}_2 e^{i(2\omega_1 - \omega_2) T_0} + \text{Reg} + \text{cc},
\end{aligned} \quad (8.107)$$

$$\begin{aligned}
p_{21} D_0^2 X_1^3 + p_{22} D_0^2 X_2^3 + \Omega_2^2 X_2^3 = & -[2i\omega_1(p_{21} + \alpha_1 p_{22}) D_2 A_1 \\
& + K_3 A_1^2 \bar{A}_1 + K_4 A_1 A_2 \bar{A}_2] e^{i\omega_1 T_0} \\
& - [2i\omega_2(p_{21} + \alpha_2 p_{22}) D_2 A_2 + L_3 A_2^2 \bar{A}_2 + L_4 A_1 \bar{A}_1 A_2] e^{i\omega_2 T_0} \\
& - \{M_3 A_2^3 e^{3i\omega_2 T_0} + M_4 A_1 \bar{A}_2^2 e^{i(\omega_1 - 2\omega_2) T_0}\} \\
& - R_2 A_1^2 \bar{A}_2 e^{i(2\omega_1 - \omega_2) T_0} + \text{Reg} + \text{cc},
\end{aligned} \quad (8.108)$$

where all regular terms are designated by Reg, and coefficients  $K_i$ ,  $L_i$ ,  $M_i$ , and  $R_i$  ( $i = 1, 2, 3, 4$ ) are given in Appendix.

Reference to Eqs. (8.107) and (8.108) shows that the following three-to-one internal resonance could occur on this step:

$$\omega_1 = 3\omega_2. \quad (8.109)$$

### 8.3.4.1 Impact-Induced Three-to-One Internal Resonance

Suppose that  $\omega_1 \approx 3\omega_2$  (8.109). Then Eqs. (8.107) and (8.108) could be rewritten in the following form:

$$p_{11} D_0^2 X_1^3 + p_{12} D_0^2 X_2^3 + \Omega_1^2 X_1^3 = B_1 \exp(i\omega_1 T_0) + B_2 \exp(i\omega_2 T_0) + \text{Reg} + \text{cc}, \quad (8.110)$$

$$p_{21} D_0^2 X_1^3 + p_{22} D_0^2 X_2^3 + \Omega_2^2 X_2^3 = B_3 \exp(i\omega_1 T_0) + B_4 \exp(i\omega_2 T_0) + \text{Reg} + \text{cc}, \quad (8.111)$$

where

$$\begin{aligned}
 B_1 &= -2i\omega_1(p_{11} + \alpha_1 p_{12})D_2A_1 - K_1A_1^2\bar{A}_1 - K_2A_1A_2\bar{A}_2 - M_1A_2^3, \\
 B_2 &= -2i\omega_2(p_{11} + \alpha_2 p_{12})D_2A_2 - L_1A_2^2\bar{A}_2 - L_2A_1\bar{A}_1A_2 - M_2A_1\bar{A}_2^2, \\
 B_3 &= -2i\omega_1(p_{21} + \alpha_1 p_{22})D_2A_1 - K_3A_1^2\bar{A}_1 - K_4A_1A_2\bar{A}_2 - M_3A_2^3, \\
 B_4 &= -2i\omega_2(p_{21} + \alpha_2 p_{22})D_2A_2 - L_3A_2^2\bar{A}_2 - L_4A_1\bar{A}_1A_2 - M_4A_1\bar{A}_2^2.
 \end{aligned}$$

It could be shown in the same manner, as it has been done above for the case of the two-to-one internal resonance, that the terms with the exponents  $\exp(\pm i\omega_i T_0)$  ( $i = 1, 2$ ) produce circular terms in Eqs. (8.110) and (8.111).

In order to eliminate them, the terms proportional to  $e^{i\omega_1 T_0}$  and  $e^{i\omega_2 T_0}$  should be vanished to zero putting  $B_i = 0$  ( $i = 1, 2, 3, 4$ ). So we obtain four equations for defining two unknown amplitudes  $A_1(t)$  and  $A_2(t)$ . However, it is possible to show, once again similarly to the above case of the two-to-one internal resonance, that not all of these four equations are linear independent from each other, and therefore to obtain the following solvability equations:

$$2i\omega_1 D_2A_1 + p_1A_1^2\bar{A}_1 + p_2A_1A_2\bar{A}_2 + p_3A_2^3 = 0, \quad (8.112)$$

$$2i\omega_2 D_2A_2 + p_4A_2^2\bar{A}_2 + p_5A_1\bar{A}_1A_2 + p_6A_1\bar{A}_2^2 = 0, \quad (8.113)$$

where

$$\begin{aligned}
 p_1 &= \frac{K_1 + \alpha_1 K_3}{k_1}, & p_2 &= \frac{K_2 + \alpha_1 K_4}{k_1}, & p_3 &= \frac{M_1 + \alpha_1 M_3}{k_1}, & p_4 &= \frac{L_1 + \alpha_2 L_3}{k_2}, \\
 p_5 &= \frac{L_2 + \alpha_2 L_4}{k_2}, & p_6 &= \frac{M_2 + \alpha_2 M_4}{k_2}, & k_1 &= \frac{\Omega_1^2 + \alpha_1 \Omega_2^2}{\omega_1^2}, & k_2 &= \frac{\Omega_1^2 + \alpha_2 \Omega_2^2}{\omega_2^2}.
 \end{aligned}$$

Let us multiply Eqs. (8.112) and (8.113) by  $\bar{A}_1$  and  $\bar{A}_2$ , respectively, and find their complex conjugates. After adding every pair of the mutually adjoint equations with each other and subtracting one from another, as a result we obtain

$$2i\omega_1 (\bar{A}_1 D_2A_1 - A_1 D_2\bar{A}_1) + 2p_1A_1^2\bar{A}_1^2 + 2p_2A_1\bar{A}_1A_2\bar{A}_2 + p_3 (\bar{A}_1A_2^3 + A_1\bar{A}_2^3) = 0, \quad (8.114)$$

$$2i\omega_1 (\bar{A}_1 D_2A_1 + A_1 D_2\bar{A}_1) + p_3 (\bar{A}_1A_2^3 - A_1\bar{A}_2^3) = 0, \quad (8.115)$$

$$2i\omega_2 (\bar{A}_2 D_2A_2 - A_2 D_2\bar{A}_2) + 2p_4A_2^2\bar{A}_2^2 + 2p_5A_1\bar{A}_1A_2\bar{A}_2 + p_6 (A_1\bar{A}_2^3 + \bar{A}_1A_2^3) = 0, \quad (8.116)$$

$$2i\omega_2 (\bar{A}_2 D_2A_2 + A_2 D_2\bar{A}_2) + p_6 (A_1\bar{A}_2^3 - \bar{A}_1A_2^3) = 0. \quad (8.117)$$

Representing  $A_1(T_2)$  and  $A_2(T_2)$  in Eqs. (8.114)–(8.117) in the polar form

$$A_i(T_2) = a_i(T_2)e^{i\varphi_i(T_2)} \quad (i = 1, 2), \quad (8.118)$$

we are led to the system of four nonlinear differential equations in  $a_1(T_2)$ ,  $a_2(T_2)$ ,  $\varphi_1(T_2)$ , and  $\varphi_2(T_2)$

$$(a_1^2)' = -\frac{p_3}{\omega_1} a_1 a_2^3 \sin \delta, \quad (8.119)$$

$$2\dot{\varphi}_1 - \frac{p_1}{\omega_1} a_1^2 - \frac{p_2}{\omega_1} a_2^2 - \frac{p_3}{\omega_1} a_1^{-1} a_2^3 \cos \delta = 0, \quad (8.120)$$

$$(a_2^2)' = \frac{p_6}{\omega_2} a_1 a_2^3 \sin \delta, \quad (8.121)$$

$$2\dot{\varphi}_2 - \frac{p_5}{\omega_2} a_1^2 - \frac{p_4}{\omega_2} a_2^2 - \frac{p_6}{\omega_2} a_1 a_2 \cos \delta = 0, \quad (8.122)$$

From Eqs. (8.119) and (8.121) we could find that

$$\frac{p_6}{\omega_2} (a_1^2)' + \frac{p_3}{\omega_1} (a_2^2)' = 0 \quad (8.123)$$

Multiplying (8.123) by  $MV_0$  and integrating over  $T_2$ , we obtain the first integral of the set of Eqs. (8.119)–(8.122), which is the law of conservation of energy,

$$MV_0 \left( \frac{p_6}{\omega_2} a_1^2 + \frac{p_3}{\omega_1} a_2^2 \right) = K_0, \quad (8.124)$$

where  $K_0$  is the initial energy. Considering that  $K_0 = \frac{1}{2} MV_0^2$ , Eq. (8.124) is reduced to the following form:

$$\frac{p_6}{\omega_2} a_1^2 + \frac{p_3}{\omega_1} a_2^2 = \frac{V_0}{2}. \quad (8.125)$$

Let us introduce into consideration a new function  $\xi(T_2)$  in the following form:

$$a_1^2 = \frac{\omega_2}{p_6} E_0 \xi(T_2), \quad a_2^2 = \frac{\omega_1}{p_3} E_0 [1 - \xi(T_2)]. \quad (8.126)$$

It is easy to verify by the direct substitution that formulas (8.126) satisfy Eq. (8.125), while the value  $\xi(0)$  ( $0 \leq \xi(0) \leq 1$ ) governs the energy distribution between two subsystems,  $X_1^1$  and  $X_2^1$ , at the moment of impact.

Substituting (8.126) in (8.119) yields

$$\dot{\xi} = -bE_0(1 - \xi) \sqrt{\xi(1 - \xi)} \sin \delta, \quad (8.127)$$

where

$$b = \sqrt{\frac{\omega_1 p_6}{\omega_2 p_3}}.$$

Subtracting Eq. (8.120) from the triple Eq. (8.122), we have

$$\begin{aligned} \dot{\delta} = bE_0 \left( \frac{3}{2}\xi - \frac{1}{2}(1-\xi) \right) \sqrt{\frac{1-\xi}{\xi}} \cos \delta + E_0 \left( \frac{3p_5}{2\omega_2} - \frac{p_1}{2\omega_1} \right) \frac{\omega_2}{p_6} \xi \\ + E_0 \left( \frac{3p_4}{2\omega_2} - \frac{p_2}{2\omega_1} \right) \frac{\omega_1}{p_3} (1-\xi). \end{aligned} \quad (8.128)$$

Equation (8.128) could be rewritten in another form considering that

$$\dot{\delta} = \frac{d\delta}{d\xi} \dot{\xi},$$

or with due account for (8.127)

$$\dot{\delta} = -bE_0(1-\xi) \sqrt{\xi(1-\xi)} \frac{d\delta}{d\xi} \sin \delta. \quad (8.129)$$

Substituting (8.129) in Eq. (8.128) yields

$$\frac{d \cos \delta}{d\xi} + \frac{1-4\xi}{2\xi(1-\xi)} \cos \delta - \frac{\Gamma_1}{\sqrt{\xi(1-\xi)}} - \frac{\Gamma_2}{1-\xi} \sqrt{\frac{\xi}{1-\xi}} = 0, \quad (8.130)$$

where

$$\Gamma_1 = \frac{1}{b} \left( \frac{3p_4}{2\omega_2} - \frac{p_2}{2\omega_1} \right) \frac{\omega_1}{p_3}, \quad \Gamma_2 = \frac{1}{b} \left( \frac{3p_5}{2\omega_2} - \frac{p_1}{2\omega_1} \right) \frac{\omega_2}{p_6}.$$

Integrating (8.130), we have

$$\cos \delta = \frac{G_0}{(1-\xi) \sqrt{\xi(1-\xi)}} - \frac{\Gamma_1}{2} \sqrt{\frac{1-\xi}{\xi}} + \frac{\Gamma_2}{2} \frac{\xi}{(1-\xi)} \sqrt{\frac{\xi}{1-\xi}}, \quad (8.131)$$

where  $G_0$  is a constant of integration to be determined from the initial conditions. Based on relationship (8.131), it is possible to introduce into consideration the stream function  $G(\delta, \xi)$  of the phase fluid on the plane  $\delta\xi$  such that

$$G(\delta, \xi) = (1-\xi) \sqrt{\xi(1-\xi)} \cos \delta + \frac{\Gamma_1}{2} (1-\xi)^2 - \frac{\Gamma_2}{2} \xi^2 = G_0, \quad (8.132)$$

which is one more first integral of the set of Eqs. (8.119)–(8.122).

It is easy to verify that the function (8.132) is really a stream function, since

$$v_\delta = \dot{\delta} = -bE_0 \frac{\partial G}{\partial \xi}, \quad v_\xi = \dot{\xi} = bE_0 \frac{\partial G}{\partial \delta}. \quad (8.133)$$

In order to find the  $T_2$ -dependence of  $\xi$ , it is necessary to express  $\sin \delta$  in terms of  $\xi$  in Eq. (8.127) with a help of relationship (8.131). As a result we obtain

$$\dot{\xi} = -bE_0 \sqrt{\xi(1-\xi)^3 - \left[ G_0 - \frac{\Gamma_1}{2} (1-\xi)^2 + \frac{\Gamma_2}{2} \xi^2 \right]^2}$$

or

$$\int_{\xi_0}^{\xi} \frac{d\xi}{\sqrt{\xi(1-\xi)^3 - \left[ G_0 - \frac{\Gamma_1}{2}(1-\xi)^2 + \frac{\Gamma_2}{2}\xi^2 \right]^2}} = -bE_0T_2, \quad (8.134)$$

where  $\xi_0$  is the initial magnitude of the function  $\xi = \xi(T_2)$ . In other words, the calculation of the  $T_2$ -dependence of  $\xi$  is reduced to the calculation of the incomplete elliptic integral in the left hand-side of (8.134).

### 8.3.4.2 Phase Portraits

The qualitative analysis of the case of the three-to-one internal resonance (8.109) could be carried out with the be constructed according to (8.132) depends essentially on the magnitudes of the coefficients  $\Gamma_1$  and  $\Gamma_2$ . Let us carry out the phenomenological analysis of the phase portraits constructing them at different magnitudes of the system parameters.

- The case when  $\Gamma_1 = \Gamma_2 = 0$ .

Let us first consider the case when  $\Gamma_1 = \Gamma_2 = 0$ . Then (8.132) is reduced to

$$G(\delta, \xi) = (1 - \xi) \sqrt{\xi(1 - \xi)} \cos \delta = G_0, \quad (8.135)$$

and the stream-lines of the phase fluid in the phase plane  $\xi - \delta$  for this particular case are presented in Fig. 8.4. Magnitudes of  $G$  are indicated by digits near the curves which correspond to the stream-lines; the flow direction of the phase fluid elements are shown by arrows on the stream-lines.

Reference to Fig. 8.4 shows that the phase fluid flows within the circulation zones, which tend to be located around the perimeter of the rectangles bounded by the lines  $\xi = 0$ ,  $\xi = 1$ , and  $\delta = \pm(\pi/2) \pm 2\pi n$  ( $n = 0, 1, 2, \dots$ ). As this takes place, the flow in each such rectangle becomes isolated. On all four rectangle sides  $G = 0$  and inside it the value  $G$  preserves its sign. The function  $G$  attains its extreme magnitudes at the points with the coordinates  $\xi = \frac{1}{4}$ ,  $\delta = \pm\pi n$  ( $n = 0, 1, 2, \dots$ ).

Along the lines  $\delta = \pm(\pi/2) \pm 2\pi n$  ( $n = 0, 1, 2, \dots$ ) the solution could be written as

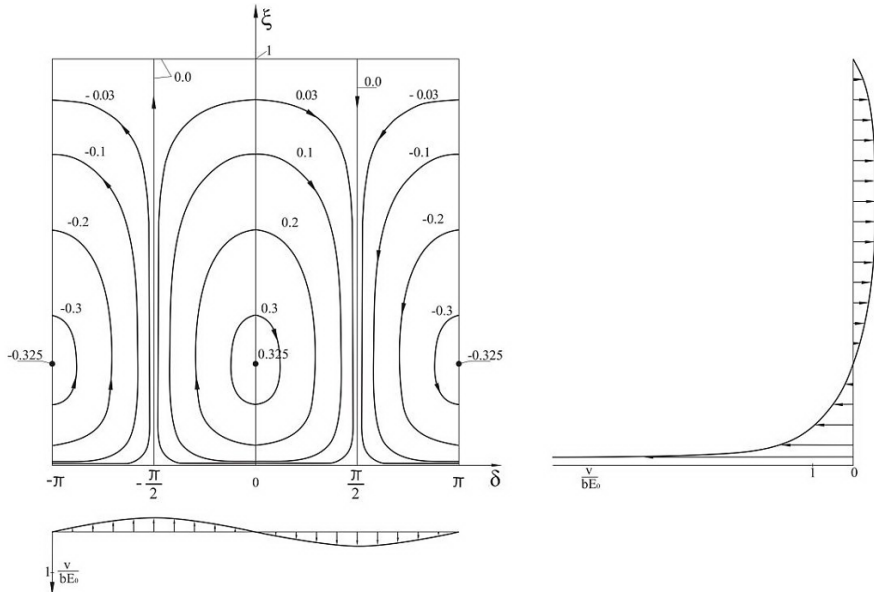
$$\xi = \left[ 1 + \frac{1}{[c_0 + f(T_2)]^2} \right]^{-1}, \quad \delta(T_2) = \delta_0 = \frac{\pi}{2} \pm \pi n, \quad n = 0, 1, 2, \dots$$

where

$$f(T_2) = -bE_0T_2, \quad c_0 = \sqrt{\frac{\xi_0}{1 - \xi_0}}.$$

Along the line  $\xi = 1$  the stationary boundary regime is realized, because when  $\xi = \xi_0 = 1$  the amplitudes  $a_1 = \text{const}$  and  $a_2 = 0$ , and from (8.127) and (8.129) it follows that  $\dot{\xi} = \dot{\delta} = 0$ . The transition of fluid elements from the points  $\xi = 0$ ,  $\delta = \pi/2 \pm 2\pi n$  to the points  $\xi = 0$ ,  $\delta = -\pi/2 \pm 2\pi n$  ( $n = 0, 1, 2, \dots$ ) proceeds instantly, because according to the distribution of the phase velocity along the section  $\delta = 0$





**Fig. 8.4:** Phase portrait for the case of 1:3 internal resonance at  $\Gamma_1 = \Gamma_2 = 0$ .

(see Fig. 8.4) the magnitude of  $\mathbf{v}$  tends to infinity as  $\xi \rightarrow 0$ . The distribution of the velocity along the vertical lines  $\delta = \pm\pi n$  has the aperiodic character, while in the vicinity of the line  $\xi = 1/4$  it possesses the periodic character.

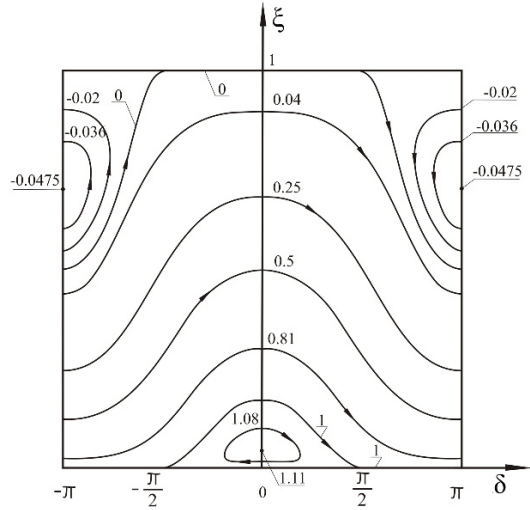
- The case when  $\Gamma_1 = 0$  and  $\Gamma_2/2 = 1$ .  
In this case, the stream-function is defined as

$$G(\xi, \delta) = \xi^{1/2}(1 - \xi)^{3/2} \cos \delta + (1 - \xi)^2 = G(\xi_0, \delta_0),$$

and Fig. 8.5 shows the streamlines of the phase fluid in the phase plane. As in the previous case, the phase fluid flows in an infinitely long channel, the boundaries of which are the straight lines  $\xi = 0$  and  $\xi = 1$ , corresponding to the phase modulated motions. In one part the streamlines are non-closed, what corresponds to the periodic change of amplitudes and the aperiodic change of phases; in another part they are closed, what corresponds to the periodic change of both amplitudes and phases. The aperiodic regime lines are the boundaries of the closed and unclosed streamline areas. From the phase portrait in Figure 5 it is seen that the circulation zones are located in a staggered arrangement by the right and left channel sides (this configuration resembles that of von Kármán staggered vortex tracks).

Each zone by the side  $\xi = 1$  is surrounded by a line with the value  $G = 0$ . This line consists of two parts connected with each other at the branch points with the coordinates  $\xi = 1, \delta = \pi/2 \pm \pi n$  ( $n = 0, 1, 2, \dots$ ). One branch of this line corresponds to the phase-modulated regime  $\xi = 1$ , and the other to the aperiodic regime,

**Fig. 8.5** Phase portrait for the case of 1:3 internal resonance at  $\Gamma_1 = 0$ , and  $\Gamma_2/2 = 1$ .



wherein  $\xi$  varies from  $\xi_{\min} = 0.5$  to  $\xi_{\max} = 1$ . At the branch point itself, the phase fluid flow velocity is equal to zero. Along the separatrix, the analytic solution can be constructed in the following form:

$$\frac{2\sqrt{2}}{1-\xi} \sqrt{(1-\xi)(2-\xi)} \Big|_{\xi_0}^{\xi} = -bE_0T_2, \quad \cos \delta = -\sqrt{\frac{1-\xi}{\xi}}.$$

The circulation zones by the side  $\xi = 0$  are surrounded by the line with the value  $G = 1$ . However, only those parts of the line  $G = 1$  which bound these zones from above and come closer to the side  $\xi = 0$  at the points  $\xi = 0, \delta = \pi/2 \pm \pi n$  belong to the domain of the fluid flow. The transition of fluid elements from the points  $\xi = 0, \delta = (\pi/2) \pm \pi n$  to the points  $\xi = 0, \delta = (3\pi/2) \pm \pi n$  proceeds instantly. The line  $G = 1$  conforms to the periodic change of the amplitudes and the aperiodic change of the phase. The separatrix  $G = 1$  is defined by the following equations:

$$\int_{\xi_0}^{\xi} \frac{d\xi}{\sqrt{\xi(1-7\xi+7\xi^2-2\xi^3)}} = \int_{\xi_0}^{\xi} \frac{d\xi}{\sqrt{\xi(0.170515-\xi)(2\xi^2-6.659\xi+5.865)}}$$

$$= -bE_0T_2, \quad \cos \delta = \frac{2-\xi}{1-\xi} \sqrt{\frac{\xi}{1-\xi}},$$

wherein  $\xi$  varies from  $\xi_{\min} = 0$  to  $\xi_{\max} = 0.170515$ . Inside the both circulation zones there are points with the extreme values of the stream-function: maximal  $G_{\max} = 1.11$  and minimal  $G_{\min} = -0.0475$ , respectively.

These points are the centers corresponding to the stable stationary regimes  $\xi = \xi_0 = 0.0443$ ,  $\delta = \delta_0 = \pm 2\pi n$  and  $\xi = \xi_0 = 0.7057$ ,  $\delta = \delta_0 = \pi \pm 2\pi n$ , respectively. Between the lines corresponding to  $G = 0$  and  $G = 1$ , unclosed streamlines are located which are in accordance with the periodic change of the amplitudes and the aperiodic change of the phase difference.

- The case when  $\Gamma_1/2 = \Gamma_2/2 = 1$ .

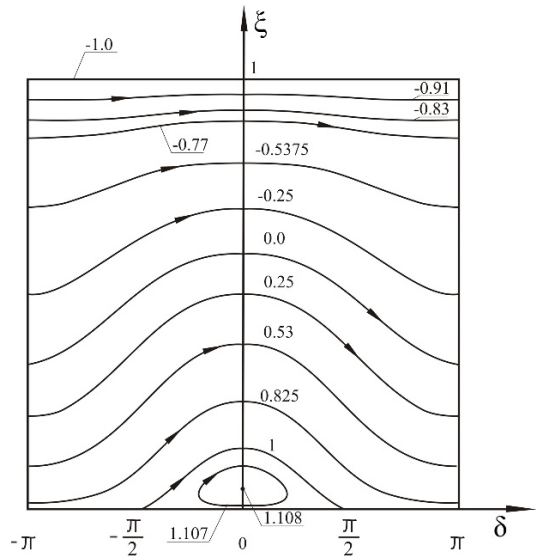
In this case, the stream-function is defined as

$$G(\xi, \delta) = \xi^{1/2}(1 - \xi)^{3/2} \cos \delta - \xi^2 + (1 - \xi)^2 = G(\xi_0, \delta_0),$$

and Fig. 8.6 shows the streamlines of the phase fluid in the phase plane.

From Fig. 8.6 it is seen that, unlike the previous case presented in Fig. 8.6, the circulation zones by the side  $\xi = 1$  and the aperiodic regime disappear. If  $\xi \rightarrow 1$ , then the streamlines level off and tend to the line  $\xi = 1$  where  $G = -1$ . If  $\xi \rightarrow 0$ , then the streamlines tend to the piecewise continuous line  $G = 1$  determined on the segments  $[-(\pi/2) \pm 2\pi n, (\pi/2) \pm 2\pi n]$ . The transition of fluid elements from the points  $\xi = 0$ ,  $\delta = (\pi/2) \pm 2\pi n$  to the points  $\xi = 0$ ,  $\delta = (3\pi/2) \pm 2\pi n$  proceeds instantly. The line  $G = 1$  conforms to the periodic change of the amplitudes and the aperiodic change of the phase difference. The separatrix  $G = 1$  is defined by the following equations:

$$\int_{\xi_0}^{\xi} \frac{d\xi}{\sqrt{\xi(1 - 7\xi + 3\xi^2 - \xi^3)}} = \int_{\xi_0}^{\xi} \frac{d\xi}{\sqrt{\xi(0.1523 - \xi)(\xi^2 - 2.8477\xi + 6.5663)}}$$



**Fig. 8.6** Phase portrait for the case of 1:3 internal resonance at  $\Gamma_1/2 = \Gamma_2/2 = 1$ .

$$= -bE_0T_2, \quad \cos \delta = \frac{2}{1-\xi} \sqrt{\frac{\xi}{1-\xi}},$$

wherein  $\xi$  varies from  $\xi_{\min} = 0$  to  $\xi_{\max} = 0.1523$ .

Inside each circulation zone there is a point with the maximal value of the stream-function  $G_{\max} = 1.108$ . These points are the centers corresponding to the stable stationary regimes  $\xi = \xi_0 = 0.04$ ,  $\delta = \delta_0 = \pm 2\pi n$ .

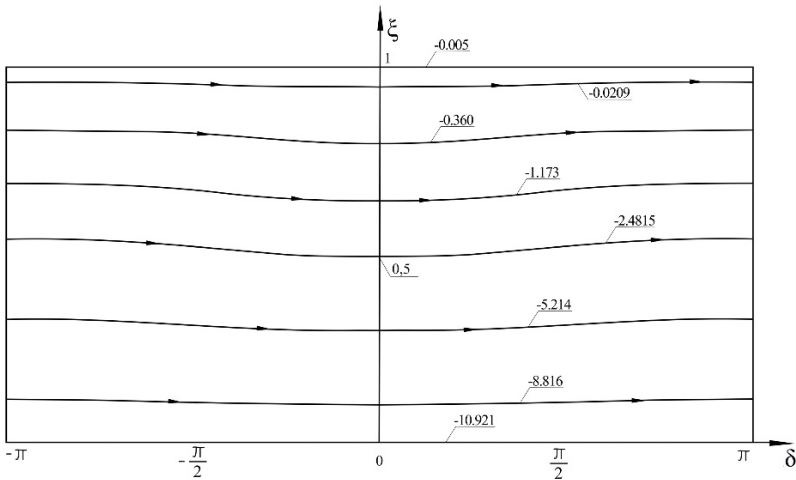
Between the lines corresponding to  $G = -1$  and  $G = 1$ , unclosed streamlines are located which are in accordance with the periodic change of the amplitudes and the aperiodic change of the phase difference.

- The case when  $\Gamma_1 = -21.84$  and  $\Gamma_2 = 0.01$ .

In this case, the stream-function is defined as

$$G(\xi, \delta) = \xi^{1/2}(1-\xi)^{3/2} \cos \delta - 0.005\xi^2 - 10.92(1-\xi)^2 = G(\xi_0, \delta_0),$$

and Fig. 8.7 shows the streamlines of the phase fluid in the phase plane. Figure 8.7 illustrates the phase portrait with only unclosed phase fluid streamlines along which the fluid flows in the direction of an increase in  $\delta$ . With  $\xi \rightarrow 0$  and  $\xi \rightarrow 1$ , the streamlines level off and tend, respectively, to the lines  $\xi = 0$  with  $G = G_{\min} = \Gamma_1/2 = -10.92$  and  $\xi = 1$  with  $G = G_{\max} = -\Gamma_2/2 = -0.005$ .



**Fig. 8.7:** Phase portrait for the case of 1:3 internal resonance at  $\Gamma_1 = -21.84$  and  $\Gamma_2 = 0.01$ .

### 8.3.4.3 Initial Conditions

In order to construct the final solution of the problem under consideration, i.e. to solve the set of Eqs. (8.119)-(8.122) involving the functions  $a_1(T_2)$ ,  $a_2(T_2)$ , or  $\xi(T_2)$ , as well as  $\varphi_1(T_2)$ , and  $\varphi_2(T_2)$ , or  $\delta(T_2)$ , it is necessary to use the initial conditions

$$w(x, y, 0) = 0, \quad (8.136)$$

$$\dot{w}(x_0, y_0, 0) = \varepsilon V_0, \quad (8.137)$$

$$\frac{P_6}{\omega_2} a_1^2(0) + \frac{P_3}{\omega_1} a_2^2(0) = E_0. \quad (8.138)$$

The two-term relationship for the displacement  $w$  (8.9) within an accuracy of  $\varepsilon$  according to (8.17) has the form

$$w(x, y, t) = \varepsilon \left[ X_{\alpha\beta}^1(T_0, T_2) \sin\left(\frac{\alpha\pi x}{a}\right) \sin\left(\frac{\beta\pi y}{b}\right) + X_{\gamma\delta}^1(T_0, T_2) \sin\left(\frac{\gamma\pi x}{a}\right) \sin\left(\frac{\delta\pi y}{b}\right) \right] + O(\varepsilon^3). \quad (8.139)$$

Substituting (8.24) and (8.25) in (8.139) with due account for (8.118) yields

$$\begin{aligned} w(x, y, t) = & 2\varepsilon \left\{ a_1(\varepsilon^2 t) \cos[\omega_1 t + \varphi_1(\varepsilon^2 t)] \right. \\ & + a_2(\varepsilon^2 t) \cos[\omega_2 t + \varphi_2(\varepsilon^2 t)] \left. \right\} \sin\left(\frac{\alpha\pi x}{a}\right) \sin\left(\frac{\beta\pi y}{b}\right) \\ & + 2\varepsilon \left\{ \alpha_1 a_1(\varepsilon^2 t) \cos[\omega_1 t + \varphi_1(\varepsilon^2 t)] + \alpha_2 a_2(\varepsilon^2 t) \right. \\ & \left. \times \cos[\omega_2 t + \varphi_2(\varepsilon^2 t)] \right\} \sin\left(\frac{\gamma\pi x}{a}\right) \sin\left(\frac{\delta\pi y}{b}\right) + O(\varepsilon^3). \end{aligned} \quad (8.140)$$

Differentiating (8.140) with respect to time  $t$  and limiting ourselves by the terms of the order of  $\varepsilon$ , we could find the velocity of the shell at the point of impact as follows

$$\begin{aligned} \dot{w}(x_0, y_0, t) = & -2\varepsilon \left\{ \omega_1 (s_1 + \alpha_1 s_2) a_1(\varepsilon^2 t) \sin[\omega_1 t + \varphi_1(\varepsilon^2 t)] + \omega_2 (s_1 + \alpha_2 s_2) \right. \\ & \left. \times a_2(\varepsilon^2 t) \sin[\omega_2 t + \varphi_2(\varepsilon^2 t)] \right\} + O(\varepsilon^3). \end{aligned} \quad (8.141)$$

Substituting (8.140) in the first initial condition (8.136) and assuming that  $a_1(0) > 0$  and  $a_2(0) > 0$ , we have

$$\cos \varphi_1(0) = 0, \quad \cos \varphi_2(0) = 0, \quad (8.142)$$

whence it follows that

$$\varphi_1(0) = \pm \frac{\pi}{2}, \quad \varphi_2(0) = \pm \frac{\pi}{2}, \quad (8.143)$$

and

$$\cos \delta_0 = \cos [3\varphi_2(0) - \varphi_1(0)] = \mp 1, \quad (8.144)$$

i.e.,

$$\delta_0 = \pm\pi(n+1) \quad (n = 0, 1, 2, \dots). \quad (8.145)$$

The signs in (8.143) should be chosen considering the fact that the initial amplitudes are positive values, i.e.  $a_1(0) > 0$  and  $a_2(0) > 0$ . Assume for definiteness that

$$\varphi_1(0) = -\frac{\pi}{2}, \quad \varphi_2(0) = -\frac{\pi}{2}. \quad (8.146)$$

Substituting now (8.141) in the second initial condition (8.137) with due account for (8.146), we obtain

$$\omega_1(s_1 + \alpha_1 s_2)a_1(0) + \omega_2(s_1 + \alpha_2 s_2)a_2(0) = E_0. \quad (8.147)$$

From Eqs. (8.138) and (8.147) we could determine the initial amplitudes

$$a_2(0) = \frac{E_0}{\omega_2(s_1 + \alpha_2 s_2)} - \frac{\omega_1(s_1 + \alpha_1 s_2)}{\omega_2(s_1 + \alpha_2 s_2)} a_1(0), \quad (8.148)$$

$$d_1 a_1^2(0) + d_2 a_1(0) + d_3 = 0, \quad (8.149)$$

where

$$d_1 = 1 + \frac{\omega_1^2(s_1 + \alpha_1 s_2)^2}{b^2 \omega_2^2(s_1 + \alpha_2 s_2)^2}, \quad d_2 = -\frac{2E_0 \omega_1(s_1 + \alpha_1 s_2)}{b^2 \omega_2^2(s_1 + \alpha_2 s_2)^2},$$

$$d_3 = \frac{E_0^2}{b^2 \omega_2^2(s_1 + \alpha_2 s_2)^2} - \frac{E_0 \omega_2}{p_6}.$$

It should be noted that the initial amplitudes depend not only on the initial velocity of the impactor, but according to (8.148) and (8.149) they are defined also by the parameters of two impact-induced modes coupled by the three-to-one internal resonance (8.109).

Considering (8.144), from (8.132) we find the value of constant  $G_0$ , which defines the trajectory of a point on the phase plane

$$G_0 = \frac{4}{V_0^2} \left[ \pm \frac{p_3}{\omega_1} \sqrt{\frac{p_3 p_6}{\omega_1 \omega_2}} a_1(0) a_2^3(0) + \frac{\Gamma_1 p_3^2}{2\omega_1^2} a_2^4(0) - \frac{\Gamma_2 p_6^2}{2\omega_2^2} a_1^4(0) \right]. \quad (8.150)$$

Thus, we have determined all necessary constants from the initial conditions, therefore we could proceed to the construction of the solution for the contact force.

#### 8.3.4.4 The Contact Force and Shell's Deflection at the Point of Contact

Now knowing  $a_1(0)$ ,  $a_2(0)$ ,  $\varphi_1(0)$ , and  $\varphi_2(0)$ , it is possible to calculate the value  $P(t)$ , which within an accuracy of  $\varepsilon$  has the form:

$$P(t) = -\varepsilon M \left[ \ddot{X}_1^1(t) s_1 + \ddot{X}_2^1(t) s_2 \right] + O(\varepsilon^3), \quad (8.151)$$

or with due account for (8.141)

$$P(t) = 2\varepsilon M \left\{ \omega_1^2 (s_1 + \alpha_1 s_2) a_1(\varepsilon^2 t) \cos [\omega_1 t + \varphi_1(\varepsilon^2 t)] + \omega_2^2 (s_1 + \alpha_2 s_2) a_2(\varepsilon^2 t) \cos [\omega_2 t + \varphi_2(\varepsilon^2 t)] \right\} + O(\varepsilon^3). \quad (8.152)$$

Considering (8.146) and (8.109), Eq. (8.152) is reduced to

$$\begin{aligned} P(t) &= 2\varepsilon M \omega_2^2 [9a_1(0)(s_1 + \alpha_1 s_2) \sin 3\omega_2 t + a_2(0)(s_1 + \alpha_2 s_2) \sin \omega_2 t] \\ &= 18M\varepsilon (s_1 + \alpha_1 s_2) \omega_2^2 a_1(0) \sin \omega_2 t \left( 3 - 4 \sin^2 \omega_2 t + \frac{1}{9} \kappa \right) + O(\varepsilon^3), \end{aligned} \quad (8.153)$$

where the dimensionless coefficient  $\kappa$  is calculated according to (8.97) and is defined by the parameters of two impact-induced modes coupled by the three-to-one internal resonance (8.109), as well as by the coordinates of the point of impact and the initial velocity of impact.

The deflection of the shell at the point of impact could be determined from (8.140) with due account for the found initial values of the phases

$$w(x_0, y_0, t) \approx 2\varepsilon (\sin \omega_1 t + \kappa \sin \omega_2 t) (s_1 + \alpha_1 s_2) a_1(0) + O(\varepsilon^2). \quad (8.154)$$

The contact force in the dimensionless form could be written as

$$P^*(\tau) = \left( \frac{3}{4} + \frac{1}{36} \kappa - \sin^2 \tau \right) \sin \tau, \quad (8.155)$$

where

$$P^*(t) = \frac{P(t)}{72\varepsilon M \omega_2^2 (s_1 + \alpha_1 s_2) a_1(0)},$$

while the dimensional deflection for the case of the three-to-one internal resonance has the form

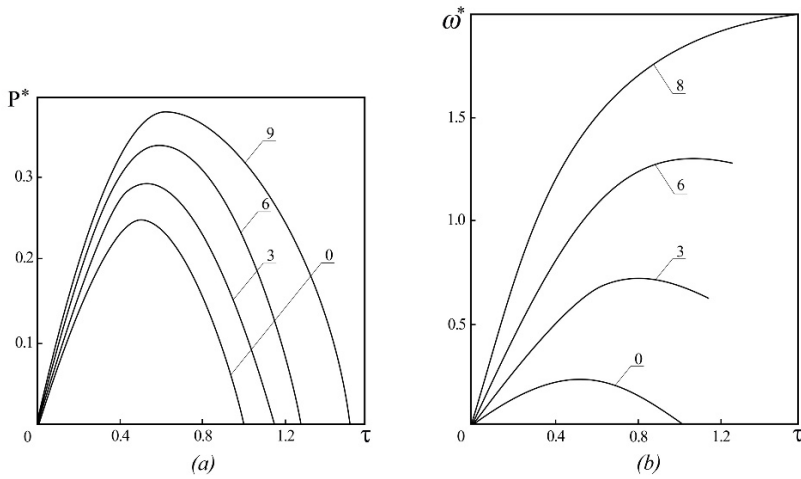
$$w^*(\tau) = \left( \frac{3}{4} + \frac{1}{4} \kappa - \sin^2 \tau \right) \sin \tau, \quad (8.156)$$

where

$$w^*(t) = \frac{w(x_0, y_0, t)}{2\varepsilon (s_1 + \alpha_1 s_2) a_1(0)}.$$

The dimensionless time  $\tau = \omega_2 t$  dependence of the dimensionless contact force  $P^*$  defined by (8.155) and of the dimensionless deflection of the target at the point of impact  $w^*$  governed by (8.156) are shown, respectively, in Fig. 8.8 (a) and (b) for the different magnitudes of the parameter  $\kappa$ : 0, 3, 6, and 9.

Reference to Fig. 8.8 shows that the increase in the parameter  $\kappa$  results in the increase of the maximal contact force, the duration of contact, as well as the peak of the shell deflection. In other words, from Figure 8 it is evident that the peak contact force and the duration of contact depend essentially upon the parameters of two impact-induced modes coupled by the three-to-one internal resonance (8.109).



**Fig. 8.8:** Dimensionless time dependence of (a) the dimensionless contact force and (b) deflection of the target at the point of impact for the case of the internal resonance  $\omega_1 = 3\omega_2$ .

## 8.4 Conclusion

In the present paper, a new approach has been proposed for the analysis of the impact interactions of nonlinear doubly curved shallow shells with rectangular base under the low-velocity impact by an elastic sphere. It has been assumed that the shell is simply supported and partial differential equations have been obtained in terms of shell's transverse displacement and Airy's stress function. The equations of motion have been reduced to a set of infinite nonlinear ordinary differential equations of the second order in time and with cubic and quadratic nonlinearities in terms of the generalized displacements.

The approach utilized in the present paper is based on the fact that during impact only two modes strongly coupled by the two-to-one or three-to-one internal resonance are initiated by the impactor. The influence of impactor's mass on the phenomenon of the impact-induced internal resonance is revealed.

Such an approach differs from the Galerkin method, wherein resonance phenomena are not involved (Zhang et al, 2001). Since it is assumed that shell's displacements are finite, then the local bearing of the shell and impactor's materials is neglected with respect to the shell deflection in the contact region. In other words, the Hertz's theory, which is traditionally in hand for solving impact problems, was not used in the present study; instead, the method of multiple time scales has been adopted, which is used with much success for investigating vibrations of nonlinear systems



subjected to the conditions of the internal resonance, as well as to find the time dependence of the contact force.

It has been shown that the time dependence of the contact force depends essentially on the position of the point of impact and the parameters of two impact-induced modes coupled by the internal resonance. Besides, the contact force depends essentially on the magnitude of the initial energy of the impactor. This value governs the place on the phase plane, where a mechanical system locates at the moment of impact, and the phase trajectory, along which it moves during the process of impact.

It is shown that the intricate  $P(t)$  dependence at impact-induced internal resonance (8.92) gives way to rather simple sine dependence, what is an accordance with a priori assumption of some researchers about a sine character of the contact force with time (Goldsmith, 1960; Gong et al, 1995; Kunukkasseril and Palaninathan, 1975; Lennertz, 1937; Zhang et al, 2001).

Table 8.1 summarizes the assumptions and principles which are the basis of the theory of impact on thin nonlinear bodies proposed in the present paper. It shows also its distinctive features in comparison with the traditional impact theory for linear thin bodies (a comprehensive review of papers in the field could be found in Rossikhin and Shitikova (2007)), which is based on the principles suggested by Timoshenko in his classical paper on the impact of an elastic sphere upon an elastic beam (Timoshenko, 1913).

Table 8.1: Comparison of main assumptions and principles used in the theories of low-velocity impact upon linear and nonlinear thin bodies

Linear thin body (target)	Nonlinear thin body (target)
1. Displacement of an impactor during the process of impact is the sum of two displacements: displacement of a target at the point of impact and local bearing of impactor and target's materials, i.e. impactor's indentation into the target 2. Local bearing is defined via the Hertzian theory 3. It is assumed that all natural modes of vibrations are generated during impact, and therefore target's displacement is expanded over all modes	1. Displacement of an impactor during the process of impact coincides with target's displacement at the point of impact; local bearing is ignored, since it is assumed that target displacement is much larger than local bearing 2. Local bearing is equal to zero 3. Under nonstationary excitation, only those modes, the natural frequencies of which satisfy certain resonant relationships (conditions of internal resonances), are generated and dominate, resulting in energy interchange between coupled modes
4. In order to obtain the solution, the method of expansion in terms of eigen functions and Hertz contact theory are employed	4. In order to obtain the solution, the method of multiple time scales in combination with different conditions of internal resonances is utilized
5. Contact force and local bearing of the impactor and target's materials are determined from nonlinear integro-differential equations	5. Contact force and target displacement at the place of contact are defined by a set of nonlinear algebraic equations

The procedure suggested in the present paper could be generalized for the analysis of impact response of plates and shells when their motions are described by three or five nonlinear differential equations.

**Acknowledgements** This research has been supported by the Ministry of Education and Science of the Russian Federation, project No. 9.5138.2017/8.9, and the first author was supported by the Ministry of Education and Science of the Russian Federation, project No. 1.4907.2017/6.7.

## References

- Abe A, Kobayashi Y, Yamada G (2000) Non-linear vibration characteristics of clamped laminated shallow shells. *J Sound Vibr* 234:405–426
- Alijani F, Amabili M (2012) Chaotic vibrations in functionally graded doubly curved shells with internal resonance. *Int J Struct Stability Dyn* 12:1250,047
- Amabili M (2005) Non-linear vibrations of doubly curved shallow shells. *Int J Non-Linear Mech* 40:683–710
- Amabili M, Paidoussis MP (2003) Review of studies on geometrically nonlinear vibrations and dynamics of circular cylindrical shells and panels, with and without fluid-structure interaction. *Appl Mech Rev* 56:349–381
- Anderson TJ, Balachandran B, H NA (1994) Nonlinear resonances in a flexible cantilever beam. *ASME J Vibr Acoustics* 116:480–484
- Antoine GO, Batra RC (2015) Low velocity impact of flat and doubly curved polycarbonate panels. *J Appl Mech* 82:041,003
- Chandrashekhara K, Schoeder T (1995) Nonlinear impact analysis of laminated cylindrical and doubly-curved shells. *J Comp Mat* 29:2160–2179
- Chia CY (1988) Nonlinear analysis of doubly curved symmetrically laminated shallow shells with rectangular platform. *Ing-Arch* 58:252–264
- Cho C, Zhao G, Kim CB (2000) Nonlinear finite element analysis of composite shell under impact. *KSME Int J* 14:666–674
- Fu YM, Mao YQ (2008) Nonlinear dynamic response for shallow spherical moderate thick shells with damage under low velocity impact (in Chinese). *Acta Materiae Compositae Sinica* 25:166–172
- Fu YM, Gao ZQ, Zhu F (2008) Analysis of nonlinear dynamic response and dynamic buckling for laminated shallow spherical thick shells with damage. *Nonlinear Dyn* 54:333–343
- Fu YM, Mao YQ, Tian YP (2010) Damage analysis and dynamic response of elasto-plastic laminated composite shallow spherical shell under low velocity impact. *Int J Solids Struct* 47:126–137
- Ganapathy S, Rao KP (1998) Failure analysis of laminated composite cylindrical/spherical shell panels subjected to low-velocity impact. *Comp Struct* 68:627–641
- Goldsmith W (1960) Impact. The theory and physical behavior of colliding solids. Arnold, London
- Gong SW, Shim VPW, Toh SL (1995) Impact response of laminated shells with orthogonal curvatures. *Comp Eng* 5:257–275
- Goswami S (1998) Finite element modelling for the impact dynamic response of composite stiffened shells. *J Reinforced Plastics Comp* 17:526–544
- Kistler LS, Waas AM (1998a) Experiment and analysis on the response of curved laminated composite panels subjected to low velocity impact. *Int J Impact Eng* 21:711–736
- Kistler LS, Waas AM (1998b) On the response of curved laminated panels subjected to transverse impact loads. *Int J Solids Struct* 36:1311–1327
- Kobayashi Y, Leissa AW (1995) Large amplitude free vibration of thick shallow shells supported by shear diaphragms. *Int J Non-Linear Mech* 30:57–66

- Kumar S (2010) Analysis of impact response and damage in laminated composite cylindrical shells undergoing large deformations. *Struct Eng Mech* 35:349–364
- Kumar S, Rao BN, Pradhan B (2007) Effect of impactor parameters and laminate characteristics on impact response and damage in curved composite laminates. *J Reinforced Plastics Comp* 26:1273–1290
- Kunukkasseril VX, Palaninathan R (1975) Impact experiments on shallow spherical shells. *J Sound Vibr* 40:101–117
- Leissa AW, Kadi AS (1971) Curvature effects on shallow shell vibrations. *J Sound Vibr* 16:173–187
- Lennertz J (1937) Beitrag zur frage nach der wirkung eines querstoßes auf einen stab. *Ing-Arch* 8:37–46
- Liu ZS, Swaddiwudhipong S (1997) Response of plate and shell structures due to low velocity impact. *ASME J Eng Mech* 123:1230–1237
- Maiti DK, Sinha PK (1996a) Finite element impact analysis of doubly curved laminated composite shells. *J Reinforced Plastics Comp* 15:322–342
- Maiti DK, Sinha PK (1996b) Finite element impact response analysis of doubly curved composite sandwich shells. Part II: Numerical results. *Int J Crashworthiness* 1:233–250
- Maiti DK, Sinha PK (1996c) Impact response of doubly curved laminated composite shells using higher-order shear deformation theories. *J Reinforced Plastics Comp* 15:575–601
- Mao YQ, Fu YM, Chen CP, Li YL (2011) Nonlinear dynamic response for functionally graded shallow spherical shell under low velocity impact in thermal environment. *Appl Math Mod* 35(6):2887–2900
- Mushtari KM, Galimov KZ (1957) *Nonlinear Theory of Thin Elastic Shells* (in Russ., English translation NASA-TT-F62, 1961). Tatknigoizdat, Kazan
- Nayfeh AH (1973a) *Nonlinear interaction: Analytical, computational, and experimental methods*. Wiley Series in Nonlinear Science, Wiley, New York
- Nayfeh AH (1973b) *Perturbation Methods*. Wiley, New York
- Ramkumar RL, Thakar YR (1987) Dynamic response of curved laminated plates subjected to low velocity impact. *ASME J Eng Mat Tech* 109:67–71
- Rossikhin YA, Shitikova MV (1995) Analysis of nonlinear free vibrations of suspension bridges. *J Sound Vibr* 186:258–282
- Rossikhin YA, Shitikova MV (2007) Transient response of thin bodies subjected to impact: Wave approach. *Shock Vibr Digest* 39:273–309
- Rossikhin YA, Shitikova MV, Salih Khalid JM (2014) Dynamic response of a doubly curved shallow shell rectangular in plan impacted by a sphere. In: Senichenkov YB, Korablev V, Chernorytski I, Korovkin N, Pozdnjkov S, Ntalianis K (eds) *Recent Advances in Mathematical Methods in Applied Sciences, Proceedings of the 2014 International Conference on Mathematical Models and Methods in Applied Sciences (MMAS'14)*, Saint Petersburg, Russia, 23–25 September, 2014, St. Petersburg, pp 109–113
- Rossikhin YA, Shitikova MV, Salih Khalid JM (2015) Low-velocity impact response of non-linear doubly curved shallow shells with rectangular base under 3:1 internal resonance. In: *Advances in Mathematics and Statistical Sciences, Proceedings of the 3rd International Conference on Mathematical, Computational and Statistical Sciences*, 22–24 February, 2015, Dubai, UAE, pp 146–155
- Swamy Naidu NV, Sinha PK (2005) Nonlinear impact behavior of laminated composite shells in hygrothermal environments. *Int J Crashworthiness* 10:389–402
- Timoshenko SP (1913) Zur Frage nach der Wirkung eines Stoßes auf einen Balken. *Zeitschrift für Mathematik und Physik* 62(1-4):198–209
- Volmir AS (1972) *Nonlinear Dynamics of Plates and Shells* (in Russ.). Nauka, Moscow
- Zhang J, van Campen DH, Zhang GQ, Bouwman V, ter Weeme JW (2001) Dynamic stability of doubly curved orthotropic shallow shells under impact. *AIAA J* 39:956–961

## Appendix

$$N_1 = - \left[ (p_{13} + \alpha_1^2 p_{14} + \alpha_1 p_{15})(\Omega_2^2 - 4\omega_1^2 p_{22}) + (p_{23} + \alpha_1^2 p_{24} + \alpha_1 p_{25})4\omega_1^2 p_{12} \right] \\ \times \left[ 16\omega_1^4 (p_{11} p_{22} - p_{12}^2) - 4\omega_1^2 (p_{11} \Omega_2^2 + p_{22} \Omega_1^2) + \Omega_1^2 \Omega_2^2 \right]^{-1}, \quad (8.157)$$

$$N_2 = - \left[ (p_{13} + \alpha_2^2 p_{14} + \alpha_2 p_{15})(\Omega_2^2 - 4\omega_2^2 p_{22}) + (p_{23} + \alpha_2^2 p_{24} + \alpha_2 p_{25})4\omega_2^2 p_{12} \right] \\ \times \left[ 16\omega_2^4 (p_{11} p_{22} - p_{12}^2) - 4\omega_2^2 (p_{11} \Omega_2^2 + p_{22} \Omega_1^2) + \Omega_1^2 \Omega_2^2 \right]^{-1}, \quad (8.158)$$

$$N_3 = - \frac{p_{13} + \alpha_1^2 p_{14} + \alpha_1 p_{15}}{\Omega_1^2}, \quad N_4 = - \frac{p_{13} + \alpha_2^2 p_{14} + \alpha_2 p_{15}}{\Omega_1^2}, \quad (8.159)$$

$$N_5 = -2 \{ [p_{13} + \alpha_1 \alpha_2 p_{14} + (\alpha_1 + \alpha_2) p_{15}] [\Omega_2^2 - p_{22}(\omega_1 + \omega_2)^2] + p_{12}(\omega_1 + \omega_2)^2 \\ \times [p_{23} + \alpha_1 \alpha_2 p_{24} + (\alpha_1 + \alpha_2) p_{25}] \} \\ \times \left[ (\omega_1 + \omega_2)^4 (p_{11} p_{22} - p_{12}^2) - (\omega_1 + \omega_2)^2 (p_{11} \Omega_2^2 + p_{22} \Omega_1^2) + \Omega_1^2 \Omega_2^2 \right]^{-1}, \quad (8.160)$$

$$N_6 = -2 \{ [p_{13} + \alpha_1 \alpha_2 p_{14} + (\alpha_1 + \alpha_2) p_{15}] [\Omega_2^2 - p_{22}(\omega_1 - \omega_2)^2] + p_{12}(\omega_1 - \omega_2)^2 \\ \times [p_{23} + \alpha_1 \alpha_2 p_{24} + (\alpha_1 + \alpha_2) p_{25}] \} \\ \times \left[ (\omega_1 - \omega_2)^4 (p_{11} p_{22} - p_{12}^2) - (\omega_1 - \omega_2)^2 (p_{11} \Omega_2^2 + p_{22} \Omega_1^2) + \Omega_1^2 \Omega_2^2 \right]^{-1}, \quad (8.161)$$

$$E_1 = - \left[ (p_{23} + \alpha_1^2 p_{24} + \alpha_1 p_{25})(\Omega_1^2 - 4\omega_1^2 p_{11}) + (p_{13} + \alpha_2^2 p_{14} + \alpha_2 p_{15})4\omega_1^2 p_{12} \right] \\ \times \left[ 16\omega_1^4 (p_{11} p_{22} - p_{12}^2) - 4\omega_1^2 (p_{11} \Omega_2^2 + p_{22} \Omega_1^2) + \Omega_1^2 \Omega_2^2 \right]^{-1}, \quad (8.162)$$

$$E_2 = - \left[ (p_{23} + \alpha_1^2 p_{24} + \alpha_1 p_{25})(\Omega_1^2 - 4\omega_2^2 p_{11}) + (p_{13} + \alpha_2^2 p_{14} + \alpha_2 p_{15})4\omega_2^2 p_{12} \right] \\ \times \left[ 16\omega_2^4 (p_{11} p_{22} - p_{12}^2) - 4\omega_2^2 (p_{11} \Omega_2^2 + p_{22} \Omega_1^2) + \Omega_1^2 \Omega_2^2 \right]^{-1}, \quad (8.163)$$

$$E_3 = - \frac{p_{23} + \alpha_1^2 p_{24} + \alpha_1 p_{25}}{\Omega_2^2}, \quad E_4 = - \frac{p_{23} + \alpha_2^2 p_{24} + \alpha_2 p_{25}}{\Omega_2^2}, \quad (8.164)$$

$$\begin{aligned}
E_5 = & -2\{[p_{23} + \alpha_1\alpha_2 p_{24} + (\alpha_1 + \alpha_2)p_{25}] [\Omega_1^2 - p_{11}(\omega_1 + \omega_2)^2] \\
& + p_{12}(\omega_1 + \omega_2)^2 [p_{13} + \alpha_1\alpha_2 p_{14} + (\alpha_1 + \alpha_2)p_{15}]\} \\
& \times [(\omega_1 + \omega_2)^4(p_{11}p_{22} - p_{12}^2) - (\omega_1 + \omega_2)^2(p_{11}\Omega_2^2 + p_{22}\Omega_1^2) + \Omega_1^2\Omega_2^2]^{-1},
\end{aligned} \tag{8.165}$$

$$\begin{aligned}
E_6 = & -2\{[p_{23} + \alpha_1\alpha_2 p_{24} + (\alpha_1 + \alpha_2)p_{25}] [\Omega_1^2 - p_{11}(\omega_1 - \omega_2)^2] \\
& + p_{12}(\omega_1 - \omega_2)^2 [p_{13} + \alpha_1\alpha_2 p_{14} + (\alpha_1 + \alpha_2)p_{15}]\} \\
& \times [(\omega_1 - \omega_2)^4(p_{11}p_{22} - p_{12}^2) - (\omega_1 - \omega_2)^2(p_{11}\Omega_2^2 + p_{22}\Omega_1^2) + \Omega_1^2\Omega_2^2]^{-1},
\end{aligned} \tag{8.166}$$

$$K_1 = 3(p_{16} + \alpha_1^2 p_{17}) + (2p_{13} + \alpha_1 p_{15})(D_1 + 2D_3) + (2\alpha_1 p_{14} + p_{15})(E_1 + 2E_3), \tag{8.167}$$

$$\begin{aligned}
K_2 = & 6p_{16} + 2\alpha_2(2\alpha_1 + \alpha_2)p_{17} + (2p_{13} + \alpha_1 p_{15})2D_4 + (2p_{13} + \alpha_2 p_{15})(D_5 + D_6) \\
& + (2\alpha_1 p_{14} + p_{15})2E_4 + (2\alpha_2 p_{14} + p_{15})(E_5 + E_6),
\end{aligned} \tag{8.168}$$

$$K_3 = 3\alpha_1(\alpha_1^2 p_{26} + p_{27}) + (2\alpha_1 p_{23} + p_{25})(E_1 + 2E_3) + (2p_{24} + \alpha_1 p_{25})(D_1 + 2D_3), \tag{8.169}$$

$$\begin{aligned}
K_4 = & 6\alpha_1\alpha_2^2 p_{26} + 2p_{27}(\alpha_1 + 2\alpha_2) + (2p_{24} + \alpha_1 p_{25})2D_4 + (2p_{24} + \alpha_2 p_{25})(D_5 + D_6) \\
& + (2\alpha_1 p_{23} + p_{25})2E_4 + (2\alpha_2 p_{23} + p_{25})(E_5 + E_6),
\end{aligned} \tag{8.170}$$

$$L_1 = 3(p_{16} + \alpha_2^2 p_{17}) + (2p_{13} + \alpha_2 p_{15})(D_2 + 2D_4) + (2\alpha_2 p_{14} + p_{15})(E_2 + 2E_4), \tag{8.171}$$

$$\begin{aligned}
L_2 = & 6p_{16} + 2\alpha_1(\alpha_1 + 2\alpha_2)p_{17} + (2p_{13} + \alpha_2 p_{15})2D_3 + (2p_{13} + \alpha_1 p_{15})(D_5 + D_6) \\
& + (2\alpha_2 p_{14} + p_{15})2E_3 + (2\alpha_1 p_{14} + p_{15})(E_5 + E_6),
\end{aligned} \tag{8.172}$$

$$L_3 = 3\alpha_2(\alpha_2^2 p_{26} + p_{27}) + (2p_{24} + \alpha_2 p_{25})(D_2 + 2D_4) + (2\alpha_2 p_{23} + p_{25})(E_2 + 2E_4), \tag{8.173}$$

$$\begin{aligned}
L_4 = & 6\alpha_1^2\alpha_2 p_{26} + 2p_{27}(2\alpha_1 + \alpha_2) + (2p_{24} + \alpha_2 p_{25})2D_3 + (2p_{24} + \alpha_1 p_{25})(D_5 + D_6) \\
& + (2\alpha_2 p_{23} + p_{25})2E_3 + (2\alpha_1 p_{23} + p_{25})(E_5 + E_6),
\end{aligned} \tag{8.174}$$

$$M_1 = p_{16} + \alpha_2^2 p_{17} + (2p_{13} + \alpha_2 p_{15})D_2 + (2\alpha_2 p_{14} + p_{15})E_2, \quad (8.175)$$

$$M_2 = 3p_{16} + \alpha_2(2\alpha_1 + \alpha_2)p_{17} + (2p_{13} + \alpha_1 p_{15})D_2 + (2\alpha_1 p_{14} + p_{15})E_2 \\ + (2p_{13} + \alpha_2 p_{15})D_6 + (2\alpha_2 p_{14} + p_{15})E_6, \quad (8.176)$$

$$M_3 = \alpha_2(\alpha_2^2 p_{26} + p_{27}) + (2p_{24} + \alpha_2 p_{25})D_2 + (2\alpha_2 p_{23} + p_{25})E_2, \quad (8.177)$$

$$M_4 = 3\alpha_1 \alpha_2^2 p_{26} + p_{27}(\alpha_1 + 2\alpha_2) + (2p_{24} + \alpha_1 p_{25})D_2 + (2\alpha_1 p_{23} + p_{25})E_2 \\ + (2p_{24} + \alpha_2 p_{25})D_6 + (2\alpha_2 p_{23} + p_{25})E_6. \quad (8.178)$$

$$R_1 = 3p_{16} + \alpha_1^2 p_{17} + (2p_{13} + \alpha_2 p_{15})D_1 + (2\alpha_2 p_{14} + p_{15})E_1 \\ + (2p_{13} + \alpha_1 p_{15})D_6 + (2\alpha_1 p_{14} + p_{15})E_6, \quad (8.179)$$

$$R_2 = 3\alpha_1^2 \alpha_2 p_{26} + p_{27}(2\alpha_1 + \alpha_2) + (2p_{24} + \alpha_2 p_{25})D_1 + (p_{25} + 2\alpha_2 p_{23})E_1 \\ + (2p_{24} + \alpha_1 p_{25})D_6 + (p_{25} + 2\alpha_1 p_{23})E_6. \quad (8.180)$$

## Chapter 9

# Ferrous Material Fill: Magnetization Channels, Layer-by-Layer and Average Permeability, Element-to-Element Field

Anna A. Sandulyak, Darya A. Sandulyak, Vera A. Ershova, and Alexander V. Sandulyak

**Abstract** For the magnetic samples of heterogeneous (including bulk) ferrous-materials, a qualitative, and according to the data on the demagnetization factor  $N$  of finely dispersed samples quantitative assessment of the volume fraction is provided for the characteristic intervals  $\gamma$  of the ferrous component. There are three intervals: the first one is  $\gamma \leq 0.2$ , the second one is  $0.2 < \gamma \leq 0.4 - 0.45$ , and the third one is  $\gamma > 0.4 - 0.45$  (up to  $\gamma \cong 0.6$  for a material filled with "densely packed" granules or grains). It should be noted that samples of heterogeneous ferrous materials within the third interval  $\gamma$ , according to the stabilization of  $N$  and its proximity to the  $N$ -value for a uniform sample (which indicates a "magnetic splicing" of the ferroelements in the heterogenous material), possess the features of a uniform magnetic sample and, therefore, they fully correspond to the notion of a quasi-uniform object. Special attention is paid to filling of granules or grains (with their inherently stable value of  $\gamma$ ) as a completely independent class of heterogeneous ferrous materials.

In order to solve the actual problems related to the determination of magnetic properties for the filling of ferroelements (granules, grains), it is preferable to use the model of selective, channeled magnetization. At the same time, the concept of this model implies obtaining necessary theoretical and experimental solutions both for the channel as a whole and for its parts (conditional cores and tube layers of different radius). In addition, such key parameters of the model as magnetic permeability of channel tube layers  $\tilde{\mu}$  and their cores  $\langle \tilde{\mu} \rangle$  (averaged data of  $\tilde{\mu}$ ) depending on their radius and intensity of magnetization field will be analyzed. It is shown the compliance of experimental data with theoretical data. The physical meaning of the parameter  $\tilde{\mu}$  reveals: it corresponds to the relative field strength  $h$  in the pores between granules.

---

Anna A. Sandulyak · Darya A. Sandulyak · Vera A. Ershova · Alexander V. Sandulyak  
Moscow Technological University, Moscow, Stromynka 20, Russia,  
e-mail: anna.sandulyak@mail.ru, d.sandulyak@mail.ru, v.ershova@mail.ru  
e-mail: a.sandulyak@mail.ru

## 9.1 Introduction. Qualitative Assessment of Typical Intervals for the Volume Fraction of a Ferrous Component

Progressive multi-purpose use of various heterogeneous ferrous materials (dispersed, with a ferrous magnetic component) (Ravnik and Hriberšek, 2013; Nielsch et al, 2002; Lacoste and Lubensky, 2001; Diguët et al, 2010; Anhalt et al, 2008; Anhalt and Weidenfeller, 2007; Schulz et al, 2010; Bottauscio et al, 2009), including solid composite and bulk (granular, acinose, powder) materials, magnetic suspensions and colloids, requires the solution of a number of physical problems. One of those problems is the determination of the averaged magnetic properties of these materials, for example, averaged (per volume) magnetic permeability and susceptibility (Ravnik and Hriberšek, 2013; Nielsch et al, 2002; Diguët et al, 2010; Anhalt et al, 2008; Anhalt and Weidenfeller, 2007; Ngo and Pileni, 2001; Schulz et al, 2010; Hultgren et al, 2005; Daniel and Corcolle, 2007; Bottauscio et al, 2009). Furthermore, the problem of obtaining information on the field between the elements of a ferrous magnetic material (in particular, between mutually contacting ferrous granules) is also in high demand, especially for magnetophoresis when magnetizable granular fill media are used as filter matrices of magnetic separators, analyzers of filter matrices of magnetic separators and analyzers of ferroimpurities disperse phase of various media (Sandulyak et al, 2015c, 2017a,c).

From the standpoint of these problems, the issue of universal modeling of such ferrous materials and their magnetization with obtaining theoretical and experimental solutions, which simultaneously cover the entire range of volume concentration of the ferrous magnetic component  $\gamma$ , i.e. within  $0 \leq \gamma \leq 1$ , is recognized as complex, and hardly solvable. This is due to specific features of ferrous material magnetization at those or other values of  $\gamma$ , i.e. at any mutual distancing of elements in the ferrous magnetic component (what determines the degree of mutual magnetic influence for the ferroelements).

More preferable is to make separately the task definition and solution of specified problems for the certain characteristic  $\gamma$  intervals. Based on the existing concepts, there should be three basic  $\gamma$  intervals that are different in their roles. The two of these are the intervals below and above the critical, percolation transition between the states of so-called "giant magnetoresistance" and "total" metallic conductivity. Another one interval corresponds to this very (not abrupt) transition. In this case, the "giant magnetoresistance" (we should note that this term is not traditional concept of conventional magnetic resistance but high electrical resistance of a heterogenous ferrous material sample in a magnetic field exposure) is inherent, of course, to samples with relatively low  $\gamma$ -values, i.e. with guaranteed mutual separation of ferroelements in it. And the state of metallic conductivity is caused by the occurrence and further increase (with increasing  $\gamma$ ) in the number of direct contacts between the ferrous elements, the emergence and increase in the number of "through target" chains of ferrous granules and ensembles of such chains, up to the limit (inherent in filling) coordination number of ferroelements.



## 9.2 Quantitative Assessment of Characteristic Intervals for the Volume Fraction of a Ferrous Component and its Values for the Filling Materials

Convincing concretization of three characteristic intervals for the volume fraction of ferrous component  $\gamma$ , mainly quantitative, directly follows from the results of the determination of demagnetization factor  $N$  for a fine-grained material sample (ferrous particles sizes are 3-100  $\mu\text{m}$  Mattei and Floc'h, 2003). Thus, this factor, as an inherent property of any magnetic sample of certain sizes and shapes, can serve as a kind of indicator for the mutual magnetic influence of ferroelements during magnetizing the sample of a heterogenous ferromaterial.

The results (Mattei and Floc'h, 2003) indeed indicate the three typical intervals of  $\gamma$ , which are given below. The first:  $\gamma \leq 0.2$ , where  $N = 0$ . The second:  $0.2 < \gamma \leq 0.4 - 0.45$ , where  $N$  is a variable increasing from zero to a certain value. The third:  $\gamma > 0.4 - 0.45$  (and up to the limit value for granular or grained filling medium:  $\gamma \cong 0.6$ ), here  $N$  maintains a stable  $N$ -value which is achieved at the end of the previous  $\gamma$  interval.

Let us give some comments to these statements.

- In the first interval with  $\gamma \leq 0.2$  the ferroelements are clearly at a significant mutual distance within the sample: for the ferroelements of conventionally spherical shape  $(\pi/6\gamma)^{1/3} = 1.4$  and more times greater than their own size. As a consequence, they are magnetized fully autonomously, practically without affecting magnetic influence on each other - with the demagnetizing factor inherent to each individual ferroelement (rather than the sample as a whole). The absence of such an influence caused by the segregation of ferroelements does not give reasons to speak here that such a sample is a magnetic body (due to the absence of  $N$  which means the lack of features for this). In this case it is just a sample representing a "set" of individual, spatially and functionally scattered ferroelements.
- In the second interval with  $0.2 < \gamma \leq 0.4 - 0.45$  (characterized by mutual approach of ferroelements, by appearing of contacts with each other), mutual magnetic influence already manifests itself judging by the fact that here  $N \neq 0$ . With increasing  $\gamma$  it is amplified and since in this interval the value of  $N$  is not yet stable (varies), we can speak here only that one gets a sample formation as a magnetic body.
- In the third interval with  $\gamma > 0.4 - 0.45$  (characterized by forming a plurality of mutual contacts between the ferroelements until reaching a maximum possible coordination number here), the mutual magnetic influence becomes so significant that, in fact, "magnetic splicing" of ferroelements takes place in the sample. In this case, it is quite possible to speak already about the fact of magnetic body formation. Such a sample according to  $N = \text{const}$  acquires properties of a uniform magnetic body (a body of a certain shape, for example, cylindrical - with a certain ratio of length to diameter). Moreover, in studies (Mattei and Floc'h, 2003) with a fine-grained sample of cylindrical shape (length  $l = 2$  cm and diameter  $d = 0.4$  cm, hence:  $l/d = 5$ ) the obtained values of  $N = 0.058 - 0.066$  were comparable with

the values of  $N = 0.04 - 0.05$  for a uniform sample of the same relative dimensions  $l/d$  (Sandulyak et al, 2015a). Such a sample can also be described as a kind of "uniform" (more accurately - quasi-uniform) sample. In this third interval there are the so-called "densely packed" (formed during filling into a container) granular or grained media, constituting a rather extensive class of industrial purpose media.

The structures of granular (grained), in particular, classical poly-spherical media lend themselves to modeling, especially for known versions of their artificial ordering. At the same time, basic parameters of such structures are determined in the most rational way, for example, packing density, porosity, co-ordination number, equivalent diameter of pores, their tortuosity, etc., only on the basis of a model with fractional (allowing the presence of conditionally fractional parts of pellet balls) cells of such structures (Sandulyak et al, 2008, 2016a,b, 2017b,d). These are the quasi-bound parallelepiped cells with vertices at the centers of eight neighboring pellet balls which completely satisfy the principle of the structure block layout as a whole. Thus, for example, the model provides quite expected (in accordance with other models) values of the volume fraction  $\gamma$  of spheres: from  $\gamma \cong 0.52$  for the simplest cubic packing of spheres to  $\gamma = 0.74$  for the packing of spheres with a more complex geometry of their relative position. Hence, the interval of possible  $\gamma$  variation for the granular (grained) packages, even for artificially ordered ones, is relatively small.

As for the actual and widely used filling of granules (grains),  $\gamma$  interval for them is further narrowed and it actually equals  $\gamma = 0.55 - 0.64$  (Sandulyak et al, 2008, 2016a,b, 2017b,d; Bennacer et al, 2013; Zhang and M., 2003; Kim and Whittle, 2006). And within this narrowed  $\gamma$  interval the value of  $\gamma$  has only a weak dependence on the overall dimensions (diameter  $D$ ) of the container, where the pellet balls with a diameter  $d$  - ranged as  $D/d = 4 - 30$  are filled (Sandulyak et al, 2016b, 2017b). For a specific value of  $D/d$  the said  $\gamma$  interval, essentially, ceases to be such, and it is degenerated into one or another particular  $\gamma$ -value. In this case, according to the obtained  $\gamma$  values (average  $\gamma \cong 0.6$ ), there is an objective reason to consider the filling of granules (grains) close to one of the ordered granules, not the most dense packing of spheres - with a simple chess-corridor order of their mutual arrangement (Sandulyak et al, 2008, 2016a,b, 2017b,d).

### **9.3 Selective (in the Form of Chains of Channels) Magnetization of Ferrous Material. Concept of Layer-Tube Channels**

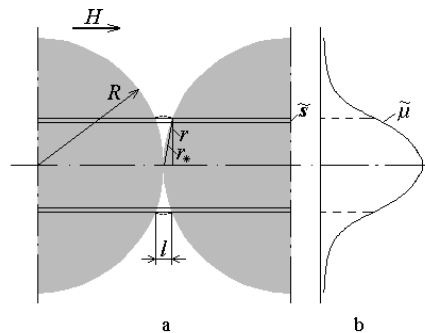
In order to solve the above-stated problems with respect to the ferrous material in the form of filling granules or grains ("densely packed", contacting each other), it is expedient to use the model of channeled magnetization of this ferrous material. In Sandulyak (1983, 1982, 1984) it was shown that granular ferrous material, in particular, the poly-ball medium is magnetized in a selective manner through efficient "elementary" channels in accordance with magnetization direction. Among the set of granules-links of the branched skeletal structure of the granular medium there are

always real straight or sinuous chains of granules corresponding to this direction. In other words, such a medium is a kind of bundle of effective "elementary" channels that penetrate the fill medium along magnetization direction.

The development of such a model is the concept in Sandulyak (1983, 1984); Sandulyak et al (2009, 2007, 2010), according to which the effective elementary channels of magnetization are not equivalent in cross-section but have a definite magnetization profile (by analogy with the profile of the fluid flow rate in a pipe). So, this channel (conducting magnetic flux), although it can in principle be characterized by averaged values of magnetic induction and permeability (Sandulyak, 1982). Nevertheless, in the cross-section significant differences in the values of these parameters can be observed.

In other words, if the effective channel is conventionally represented in the form of concentric layer-tubes, then as the radius increases, the ability to conduct the magnetic flux decreases. This is due to the fact that the magnetic resistance of each of these artificially isolated, quasi-uniform tubular layers of the channel's cross section (Fig. 9.1) is clearly not the same<sup>1</sup> (Sandulyak, 1983; Sandulyak et al, 2009). Thus, as the radius of the "incremental" tubular layer increases, its magnetic resistance increases due to the increasing distance between the surfaces of adjacent granules-links (Fig. 9.1). As a consequence, the average magnetic permeability of the layer-tubes (and induction in them) decreases, and, therefore, their ability to conduct magnetic flux decreases.

Suppose that one thin tube (Fig. 9.1a) of arbitrary radius  $r$  is selected artificially from such effective channel and is considered as quasi-uniform in length. Then we can operate with such a characteristic as the magnetic permeability of this thin tube (Sandulyak, 1983, 1984; Sandulyak et al, 2009, 2007). Naturally, tubes of different radius  $r$  will be characterized by different permeability  $\tilde{\mu}$  (due to a variable thickness of the space between the balls surfaces), which increases as the channel axis is approached and decreases as it moves away from it (Fig. 9.1b). This determines the



**Fig. 9.1** The module (segment) of the chain of the balls with dedicated elementary layered tube of the effective magnetization channel (a) and illustration of the extreme permeability profile (b) of the channel in its cross section (in the radial direction).

<sup>1</sup> Hereinafter we mean the magnetic resistance in its classical definition, i.e. as the ratio of the magnet length to its cross-section and absolute magnetic permeability, but not in the often used, mentioned earlier, interpretation of the "giant magnetoresistance" - as the relative change in the electrical resistivity under magnetic conditions.

presence of a radial, extreme by shape permeability profile  $\tilde{\mu}$  (and corresponding induction  $B$ ) for the effective channel. In this case, according to the mentioned formal analogy with the velocity profile of a fluid flow in a pipe, the analog of velocity here is, of course, magnetic induction (as the magnetic flux per area unit). As for the magnetic permeability - as induction, referred to the product  $\mu_0 H$  (where:  $\mu_0 = 4\pi 10^{-7}$  H/m - magnetic constant,  $H$  - magnetizing field strength), then such a comparison is valid up to a multiplier  $1/\mu_0 H$ .

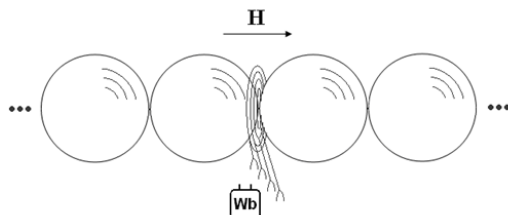
The parameters here and hereinafter (in the framework of the channeled magnetization model), namely the average permeability of the layer-tubes of an effective magnetization channel, its cores (and associated average induction in the layer-tubes and core) are amenable to the corresponding experimental determination and theoretical calculation.

#### 9.4 Data of the In-Channel (Core and Layer-Tube) Magnetic Flux, Average Induction, and Permeability

To obtain the necessary information on the magnetization channel and its features one can experimentally use, for example, magnetizable straight chain of balls (Sandulyak, 1983, 1984; Sandulyak et al, 2007, 2009). It should be like any magnet used to study the magnetic properties of its material (in this case quasi-uniform material) sufficiently long, self-sufficient to minimize the demagnetizing factor (as experiments show - with a number of balls not less than 8-10) magnetized in the solenoid with greater length.

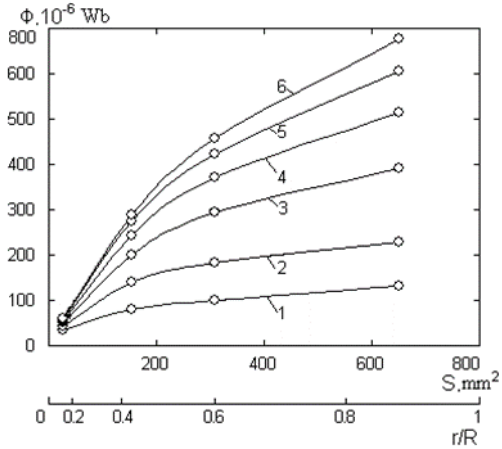
Then, using the concentric flow-measuring loops of this or that radius  $r$  (section  $s$ ) placed in the middle of this chain (Fig. 9.2) between adjacent balls of radius  $R$ , and micro-webermeter, one can obtain the data of the corresponding magnetic flux  $\Phi$  through each of these loops (Fig. 9.3). However, because of the limited dimensions of the inter-ball area where the loops are placed from considerations of obtaining data it is advisable to use balls with increased radius also as close as possible to the contact point of the granule-balls, for example,  $R = 16.65$  mm (Sandulyak, 1983, 1984; Sandulyak et al, 2007, 2009).

Measured data  $\Phi$  are the starting point for calculating the average induction  $B = \Phi/s$  in the core of a certain radius  $r$  and magnetic permeability  $\langle \tilde{\mu} \rangle = B/\mu_0 H = \Phi/s\mu_0 H$  of this core (Fig. 9.4). The use hereinafter of unusual designation of the



**Fig. 9.2** Magnetizable chain of the balls with a system of concentric flow loops located on the plane of symmetry between two central balls.

**Fig. 9.3** The magnetic flow data obtained through the use of loops in the core of different cross-section (relative radius) of the effective channel of magnetization of the chain of the balls - for different values of the intensity of the magnetizing field  $H$ , 1 -  $H = 18$  kA/m, 2 - 36, 3 - 70, 4 - 105, 5 - 140, 6 - 175.



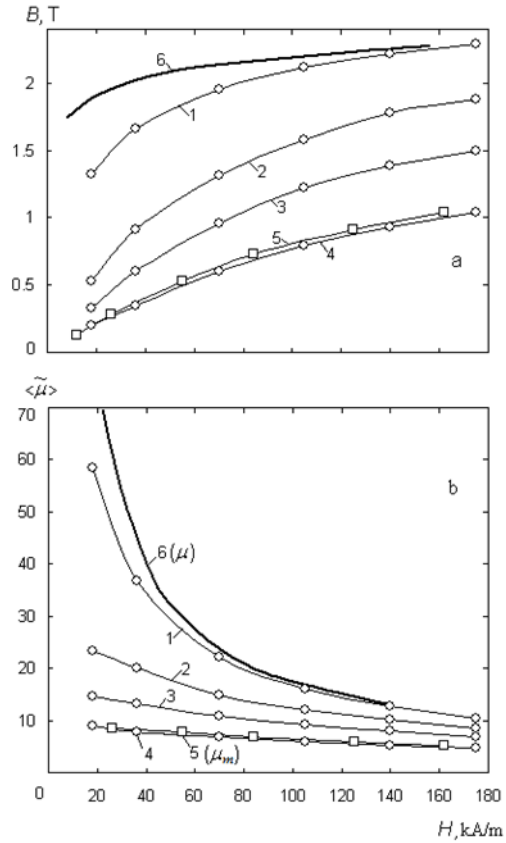
effective magnetization channel quasi-uniform core magnetic permeability, i.e.  $\langle \tilde{\mu} \rangle$ , is semantic. It corresponds to the result of averaging of this channel magnetic permeability radial profile  $\tilde{\mu}$  within limits of one or another of its cores.

In connection with the obtaining of field dependencies of induction  $B$  and permeability  $\langle \tilde{\mu} \rangle$  for various (by radius  $r$  and section  $s$ ) cores (Fig. 9.4, curves 1-4), the field dependencies of induction  $B$  and permeability  $\mu_m$  for granular filling media are of interest (Fig. 9.4, curves 5), as well as the known field dependencies of induction  $B$  and permeability  $\mu$  for a material close to the ball material - low-alloyed steel (Fig. 9.4, curves 6).

The comparison of all these dependencies clearly illustrates the quite expected fact: curves  $B$  and  $\langle \tilde{\mu} \rangle$  for the magnetization channel cores as if fill the vast "vacant" area between the curves 6 and 5 for poly-ball medium (Fig. 9.4a) and the curves 6 and 5 for the balls material (Fig. 9.4b). Indeed, as the core radius  $r$  (relative to the radius  $r/R$ ) increases, the induction and permeability curves 1-4 become similar to the corresponding curves 5 for the poly-ball medium, since in this case the core more and more reproduces the effective channel of the poly-ball medium. With decreasing  $r/R$  these curves 1-4 approach the corresponding curves 6 for the uniform metal, since for an increasingly thin core the gap between the granules decreases. In this case, in the limit ( $r/R \rightarrow 0$ ), a complete concordance of the curves can be expected. In this case, in order to obtain curves 6 in Fig. 9.4 it would be necessary to use (as it is hardly possible) such a control uniform sample that would accurately reproduce the alternation of real untempered and hardened areas (as in balls), or carry out investigations using annealed balls. At the same time, the available known curve for  $B$  (Fig. 9.4a, curve 6) is an acceptable approximation to the specific curve of our interest.

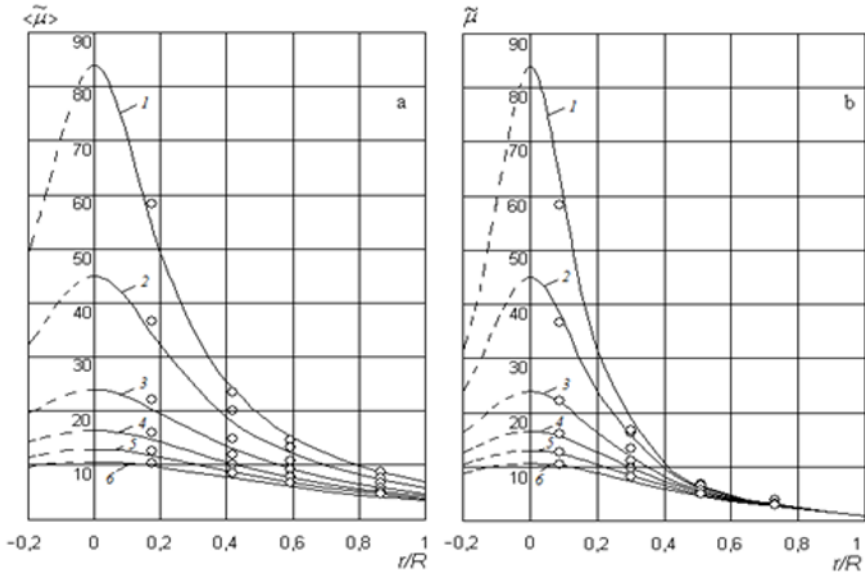
Having the field dependencies of induction  $B$  and permeability  $\langle \tilde{\mu} \rangle$  for various in-channel cores (Fig. 9.4, curves 1-4), we note a remarkable fact of the decrease in the values of  $B$  and  $\langle \tilde{\mu} \rangle$  with an increase in the radius  $r$  (relative radius  $r/R$ ) of the cores. Thus, already here, i.e. at the stage of the corresponding quantitative

**Fig. 9.4** Field dependencies of the average induction (a) in the core of radius  $r$  of the effective magnetization channel and average permeability (b) of this core ( $1 - r/R = 0.17, 2 - 0.42, 3 - 0.59, 4 - 0.87$ ), and here are the corresponding dependencies for the polishing environment (5) and low-alloy steel (6).



characterization of the cores of the magnetization channel magnetic properties (which deteriorate as they thicken) one can ascertain the existence of the radial profile of this channel magnetic properties. This is illustrated visually (in particular, in coordinates  $\langle \tilde{\mu} \rangle$  vs.  $r/R$ ) in Fig. 9.5a (points).

In addition, an indicative evidence (even more visually) of the existence of the channel magnetic properties profile is the layer-by-layer (for artificial tubes of this channel) field dependencies  $B$  and  $\tilde{\mu}$  (Fig. 9.6). They characterize the local (corresponding to a certain radius  $r$  of layer-tube) level of effective channel magnetization. To obtain these layer-by-layer field dependencies  $B$  and  $\tilde{\mu}$  (Fig. 9.6) one need, using the experimental data of magnetic fluxes  $\Phi$  (Fig. 9.3), just find the difference data  $(\Phi_{i+1} - \Phi_i)$  of fluxes between adjacent, i.e.  $(i + 1)$ th and  $i$ th concentric loops of radius  $r_{i+1}$  and  $r_i$  (cross-section  $s_{i+1}$  and  $s_i$ ). On the basis of these data it is easy to obtain the values  $B = (\Phi_{i+1} - \Phi_i)/(s_{i+1} - s_i)$ , as well as  $\tilde{\mu} = B/\mu_0 H$  (hereinafter the previously introduced designation of the layer-tube magnetic permeability is used:  $\tilde{\mu}$ ). Just such local data of induction  $B$  and permeability  $\tilde{\mu}$  at one or another distance  $r$  (relative distance  $r/R$ ) from the axis of the effective magnetization channel,



**Fig. 9.5:** The radial profile of the magnetic permeability of quasi-uniform effective magnetization channel (a) and average permeability of the core (of a certain radius) of this channel (b): 1 -  $H = 18$  kA/m, 2 - 36, 3 - 70, 4 - 105, 5 - 140, 6 - 175; points - experimental data (Figs. 9.4b and 9.6b), lines - calculation from Eqs. (9.1) and (9.5).

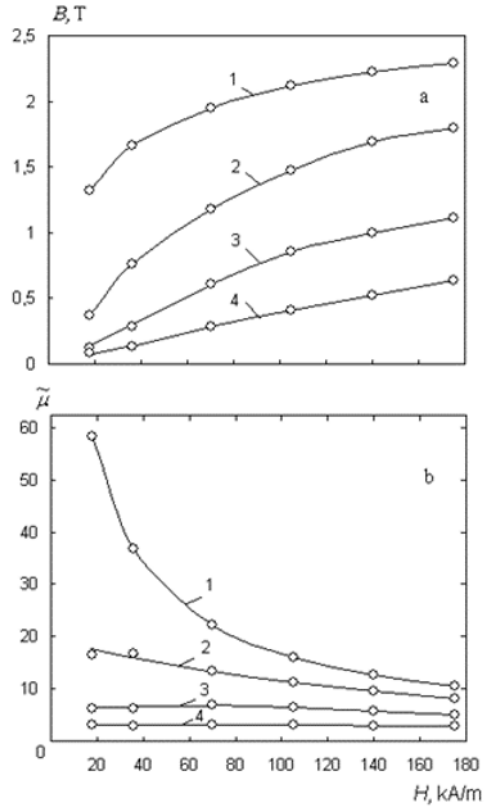
as already stated, reflects the very important property of the channel itself - radial profile of its magnetization. In particular, as it indirectly follows from the family of curves  $B$  and  $\tilde{\mu}$  decomposing by  $r/R$  (Fig. 9.6), values  $B$  and  $\tilde{\mu}$  for the effective magnetization channel decreases with increasing of  $r/R$ .

More clearly (in particular, in coordinates  $\tilde{\mu}$  of  $r/R$ ) the radial profile of the magnetic properties of the effective magnetization channel can be traced in Fig. 9.5b (points). In this case, note that despite the formal similarity, here the parameter  $r/R$  characterizes not the relative radius of the core-magnet, as it was before, but the average relative radius of the layer-tube of the effective magnetization channel (including the minimum in the experiments of a tube with zero internal radius).

### 9.5 Magnetizing Channel Layer Tubes: Local Permeability, Radial Profile

To obtain the calculated dependencies characterizing the magnetic properties of quasi-uniform layer-tubes (in particular, their magnetic permeability  $\tilde{\mu}$ ) we first note that in the space between the adjacent balls of the magnetizable chain of balls, especially at

**Fig. 9.6** The field dependencies of the average induction (a) in the layer-tube of medium radius  $r$  (between the radiuses of the cores, including the smallest core with zero internal radius) of the effective magnetization channel and the average permeability (b) of the tube layer (1 -  $r/R = 0.09$ , 2 - 0.3, 3 - 0.51, 4 - 0.73).



elevated values  $r/R$ , of course, there is a barrel-like course of magnetic force lines (Fig. 9.1a, dashed lines). In this case, according to the law of their refraction, because of relatively high values of the magnetic permeability of the balls metal these lines emerge from the ball (and enter to the ball) almost normally to its surface. At the same time, the magnetic induction vector, which is tangent to the force line, as it is known, varies not only in direction but also in magnitude. As for the numerical values of induction, at the output of the magnetic force lines from certain ball points located at a distance  $r$  from the channel axis (Fig. 9.1a) they practically correspond to the numerical values of induction at the same distance in the middle of the inter-ball space. In this sense the "form" of magnetization channel layer-tubes is actually close to cylindrical. Consequently, if we proceed from this justified simplification (Fig. 9.1a), then the problem of obtaining the calculated dependence for the radial profile of permeability  $\tilde{\mu}$  becomes completely solvable (Sandulyak, 1983, 1984; Sandulyak et al, 2007, 2009).

To do this, first, from an infinite set of thin (conditional) concentric layer-tubes of the effective magnetization channel you should select one tube (Fig. 9.1a) with radius  $r$  and small cross-section  $\tilde{s}$ , likening it to such a quasi-uniform (along the length) tube



whose magnetic resistance is equivalent to the total resistance of the corresponding real areas. In this case, the magnetic resistances of a typical link (between adjacent balls centers) of the quasi-uniform tube, section (sections) of the tube in the body of adjacent balls and section of this tube between the balls are, respectively,

$$2R/\mu_0\tilde{\mu}\delta, \quad (2R-l)/\mu_0\mu\delta, \quad l/\mu_0\delta,$$

where  $l$  - tube length between adjacent balls' surfaces (Fig. 9.1a). Secondly, it is necessary to take into account the purely geometrical constraint (Fig. 9.1a):

$$l/2R = 1 - [1 - (r/R)^2]^{0.5}$$

Then simple transformations of indicated condition for the equivalence of magnetic resistances give an expression reflecting the regularity of the change in the magnetic permeability of quasi-uniform effective magnetization channel in its radial direction

$$\tilde{\mu} = \frac{\mu}{\mu - \sqrt{1 - (r/R)^2}(\mu - 1)} \quad (9.1)$$

or, in other words, an expression for the radial profile of the channel magnetic permeability.

Figure 9.5b shows the calculated data  $\tilde{\mu}$  (lines) obtained by Eq. 9.1, revealing a bell-shaped profile  $\tilde{\mu}$  (outwardly similar to the Gaussian normal probability law). It can be seen that these calculated data  $\tilde{\mu}$  (lines) are in a good agreement with the experimental data  $\tilde{\mu}$  (points), thereby confirming validity of Eq. 9.1 that followed from the model under consideration.

It must also be said that the value  $l$  (Fig. 9.1a) for simplicity can also be expressed in terms of the distance  $r_x$  from the point of contact of the balls to the point of tube intersection with the ball surface, i.e.  $l = r_x^2/R$ , and for relatively small  $r$  it is often convenient to assume that  $r_x \cong r$ . Then an alternative to Eq. (9.1), somewhat simplified version of the formula for calculating the radial profile of the magnetic permeability of the effective magnetization channel, will follow:

$$\tilde{\mu} = \frac{\mu}{1 + 0.5(r/R)^2(\mu - 1)} \quad (9.2)$$

Values  $\tilde{\mu}$  calculated by Eqs. (9.1) and (9.2) are close, especially when  $r/R \leq 0.5$  and their difference does not exceed 3-6%.

## 9.6 Magnetization Channel Core: Average Magnetic Permeability

The calculated dependencies for the average magnetic permeability  $\langle \tilde{\mu} \rangle$  of the core with the arbitrary radius  $r$  of the effective magnetization channel can be found by typical averaging for such cases, in this case - by averaging the local (for tube

layers) values of the magnetic permeability  $\tilde{\mu}$ . In this case we can use two obvious and independent expressions for the magnetic flow through the core:

$$\Phi = \mu_0 \langle \tilde{\mu} \rangle H \pi r^2, \quad \Phi = \mu_0 H 2\pi \int_0^r \tilde{\mu} r dr, \tag{9.3}$$

from which follows necessary expression for the averaging:

$$\langle \tilde{\mu} \rangle = \frac{2}{r^2} \int_0^r \tilde{\mu} r dr \tag{9.4}$$

After the corresponding integration, taking into account Eq. (9.1) for  $\tilde{\mu}$ , follows the formula for the determining of the magnetic permeability  $\langle \tilde{\mu} \rangle$  of the certain core (radius  $r$ ) of the effective magnetization channel:

$$\langle \tilde{\mu} \rangle = \frac{2\mu}{(r/R)^2(\mu-1)} \left\{ \frac{\mu}{\mu-1} \ln \left[ \mu - (\mu-1) \sqrt{1 - \left(\frac{r}{R}\right)^2} + \sqrt{1 - \left(\frac{r}{R}\right)^2} - 1 \right] \right\} \tag{9.5}$$

Figure 9.5a shows the calculated data  $\langle \tilde{\mu} \rangle$  (lines) obtained with the use of Eq. (9.5). It can be seen that these data match previously discussed experimental data  $\langle \tilde{\mu} \rangle$  (points), thereby confirming the validity of this calculation Eq. (9.5), which followed from the model considered.

A similar integration can also be performed taking into consideration the simplified Eq. (9.2) for  $\tilde{\mu}$ , this leads to a simplified formula for  $\langle \tilde{\mu} \rangle$ :

$$\langle \tilde{\mu} \rangle \cong \frac{2\mu}{(r/R)^2(\mu-1)} \ln \left[ 1 + \frac{1}{2} \left(\frac{r}{R}\right)^2 (\mu-1) \right] \tag{9.6}$$

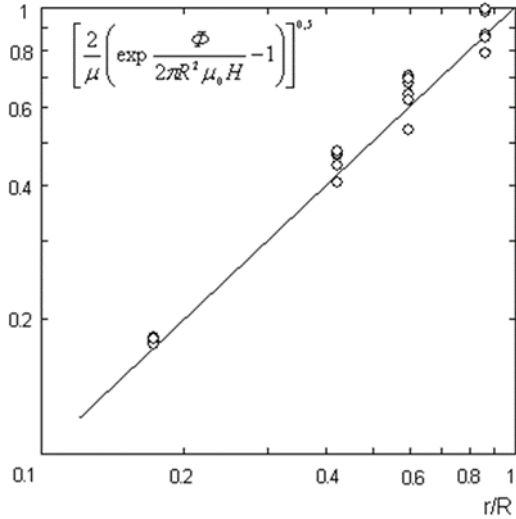
Values  $\langle \tilde{\mu} \rangle$  calculated in accordance with Eqs. (9.5) and (9.6) are close to each other. For example, for  $r/R = 0.5$ , they differ by 1-2% and even for  $r/R = 1$  - by up to 7-9%. This indicates the possibility of using (where it makes sense) a simpler Eq. (9.6) in a wide range of  $r/R$ .

If the values of the magnetic permeability of a metal  $\mu \geq 10 - 20$  are really high (as it is seen in Fig. 9.4b), Eq. (9.6) can be even more simplified by taking  $\mu \cong (\mu - 1)$ , then

$$\langle \tilde{\mu} \rangle \cong \frac{2\mu}{(r/R)^2} \ln \left[ 1 + \frac{\mu}{2} \left(\frac{r}{R}\right)^2 \right] \tag{9.7}$$

In this case the values  $\langle \tilde{\mu} \rangle$  calculated by the simplified Eq. (9.7) and the original Eq. (9.5) are sufficiently close to each other; up to the limiting experimental values  $r/R = 0.87$  they differ for not more than 3-4%.

**Fig. 9.7** Illustration of the generalization of the data in Fig. 9.3 in the coordinates according to Eq. (9.8).



### 9.7 Generalized Dependencies for Comparison of the Calculated and Experimental Data

The above-mentioned relevance between calculated and experimental data is witnessing the accuracy of the model, it can be also judged by the generalized (common) dependence. Thus, based on the first of the expressions (9.3) and obtained convenient simplified Eq. (9.7), simplified but still acceptable for the description of all the primary experimental data which is shown in Fig. 9.3, the expression for the magnetic flow  $\Phi$  in the core of the channel is written. The obtained expression presented later as:

$$\left[ \frac{2}{\mu} \left( \exp \frac{\Phi}{2\pi R^2 \mu_0 H} - 1 \right) \right]^{0.5} \cong \frac{r}{R} \tag{9.8}$$

is quite suitable for the generalization of the whole data array.

For the illustration of such generalization (in the form of common dependence) all the numerous primary experimental data of magnetic flows  $\Phi$  (Fig. 9.3) and other data included in (9.8), such as the radius of the flow-measuring loops  $r$ , the radius of balls  $R$ , the intensity of the magnetizing field  $H$ , magnetic permeability of the material of the balls  $\mu$  must be processed in the specific coordinates on which the left and right parts of Eq. (9.8) point out. In fact, the coordinates here (dimensionless) are tied to the radius of the flow-measuring loop, as seen by the right side of expression.

Indeed, in such coordinates the experimental and calculated data must obey (and in fact obey, as seen in Fig. 9.7) to the bisectrix of the right angle of this coordinate system, and this fact with such a generalized analysis confirms the validity of the considered model.

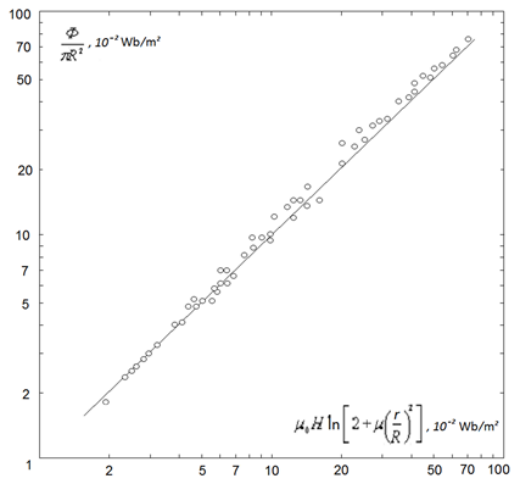
Another example of a demonstrative proof of generalization is similar to the previous one and here can be used similar approach, also using the first of Eqs. (9.3) and simplified Eq. (9.7) - to obtain such an expression:

$$\frac{\Phi}{\pi R^2} \cong 2\mu_0 H \ln \left[ 1 + \frac{\mu}{2} \left( \frac{r}{R} \right)^2 \right] \tag{9.9}$$

As seen from the left side of Eq. (9.9), the coordinates of this variant of generalization are tied to some formal induction (as a magnetic flow through a loop with radius  $r$  and which is related to the cross section of the ball).

Figure 9.8 shows that in such generalizing coordinates, the experimental and calculated data (here, in contrast to the previous version, in a more dispersed form), too, are expectedly comply with the bisectrix of the right angle of this coordinate system, which one more time confirms the validity of the considered model.

**Fig. 9.8** Illustration of the generalization of the data in Fig. 9.3 in the coordinates according to Eq. (9.9).



### 9.8 Magnetization Channel and Harness of the Channels (in the Ferromaterial Filling): Average Magnetic Permeability

One of the important consequences of Eqs. (9.5)-(9.7) is that they can be used to obtain the values of the magnetic susceptibility  $\langle \tilde{\mu} \rangle$  of the entire effective channel of magnetization (here - the straightened chain of the pellet balls). For this, in (9.5)-(9.7), we only need to take  $r/R = 1$ , i.e. to use any of these formulas:

$$\begin{aligned}
\langle \tilde{\mu} \rangle &= \frac{2\mu}{\mu-1} \left( \frac{\mu}{\mu-1} \ln \mu - 1 \right), \\
\langle \tilde{\mu} \rangle &\cong \frac{2\mu}{\mu-1} \ln \left( \frac{\mu+1}{2} \right), \\
\langle \tilde{\mu} \rangle &\cong 2 \ln \left( 1 + \frac{\mu}{2} \right)
\end{aligned} \tag{9.10}$$

Equations (9.10) can become the basis for obtaining formulas that allow the calculation of the magnetic susceptibility of the dispersed ferromaterial  $\mu_m$  (filling of granules or grains) - as a harness of the magnetization channels. For this, in Eq. (9.9) the factor 1.44 (Sandulyak et al, 2007) should be used, taking into account the difference (note - up to a constant) of the harness of the branched chain channels (in filling, for example, pellet balls, i.e. in the structure of meandering chains of granules) in the comparison with the analyzed solitary channel here (in the chain of rectified pellet balls). Then the desired formulas will be:

$$\mu_m = \frac{2.9\mu}{\mu-1} \left( \frac{\mu}{\mu-1} \ln \mu - 1 \right), \quad \mu_m \cong \frac{2.9\mu}{\mu-1} \ln \left( \frac{\mu+1}{2} \right), \quad \mu_m \cong 2.9 \ln \left( 1 + \frac{\mu}{2} \right) \tag{9.11}$$

Consequently, it becomes possible to describe analytically the magnetization curve ( $B$  vs.  $H$ ) of such a material - based on the well-known expression

$$B = \mu_m \mu_0 H, \tag{9.12}$$

but with the use of Eq. (9.11) for  $\mu_m$ . Of course, we must bear in mind that shown in (9.11) and, consequently, in the corresponding ones, written according to (9.12) with respect to (9.11), in formulas for the desired average induction  $B$ , the magnetic permeability of the substance of the balls (low-carbon steel)  $\mu$  has an individual relationship with the intensity of the magnetizing field  $H$ . This can be seen, in particular, from curve 6 in Fig. 9.4b, the data of which should be taken into account directly or by means of an additional calculation from the formula:

$$\mu = (H_\mu/H)^{0.9} \tag{9.13}$$

on the basis that the field dependencies of the magnetic permeability of steels in the post-extremal region are subject to a power-law coupling of the type (9.13) (Sandulyak et al, 2010, 2015b), up to the parameter  $H_\mu$  (here  $H_\mu = 24.4 \cdot 10^5$  A/m).

The calculated field dependencies of the induction  $B$  (magnetization curves of the spherical environment) obtained using Eqs. (9.11) - (9.13) agree with the experimental dependence (Fig. 9.4a, curve 5), which confirms the validity of these (and preceding) calculation formulas that followed from the considered model.

We note that the representation of the scattered formulas (9.11)-(9.13) in the form of one or another desired common expression was not realized here because of the obvious cumbersomeness of this expression. At the same time, it is possible to avoid such defect if in Eqs. (9.11) it is justified (as for the actually high values of  $\mu$ , as seen in Fig. 9.4b), as before, assume that  $(\mu-1) \cong \mu$ , and also  $(\mu+1) \cong \mu$ . Then, in

particular, using Eq. (9.12), the first and the second of Eqs. (9.11) and also Eq. (9.13), one can obtain such compact original formulas for calculating the magnetization curve of a granular (grainy) filling environment:

$$B = 2.9\mu_0 H \left( 0.9 \ln \frac{H_\mu}{H} - 1 \right), \quad B = 2.6\mu_0 H \ln \left( 0.46 \frac{H_\mu}{H} \right) \quad (9.14)$$

### 9.9 The Physical Meaning of the Profile Permeability. Relative Field Strength Between Ferroelements

Equations (9.1) and (9.2) for the magnetic permeability of a layer-tube  $\tilde{\mu}$  with radius  $r$ , as a matter of fact, turn to become passing decisions of one more key problem. Thus, they are formulas for calculating the field strength between ferroelements  $h$  (related to the magnetizing, i.e. external field  $H$ ) at a particular point at a distance  $r$  from the point of contact of ferroelements-balls of radius  $R$  in the area between them, and more exactly:

$$\frac{h}{H} = \tilde{\mu} = \frac{\mu}{\mu - \sqrt{1 - (r/R)^2}(\mu - 1)}, \quad \frac{h}{H} = \tilde{\mu} \cong \frac{\mu}{1 + 0.5(r/R)^2(\mu - 1)} \quad (9.15)$$

This, in particular, follows from the identical expressions for magnetic induction: in the quasi-uniform tube such as  $B = \mu_0 \tilde{\mu} H$  and in the inter-sphere region as  $B = \mu_0 h$ .

Actually, the simple expression (relation) obtained here  $\tilde{\mu} = h/H$  also reveals the physical meaning of a such parameter, inherent exclusively to the model of channeled magnetization, as a profile (local, characterizing quasi-uniform layer-tubes) magnetic permeability  $\tilde{\mu}$ . As already noted, the parameter  $\tilde{\mu}$  characterizes the relative field strength in the area between the ferroelements (granules, grains).

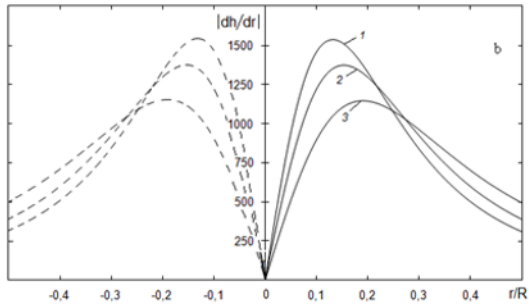
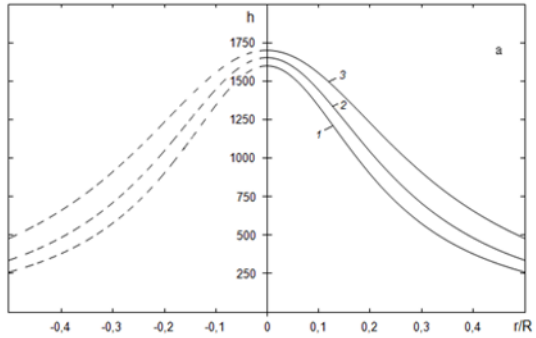
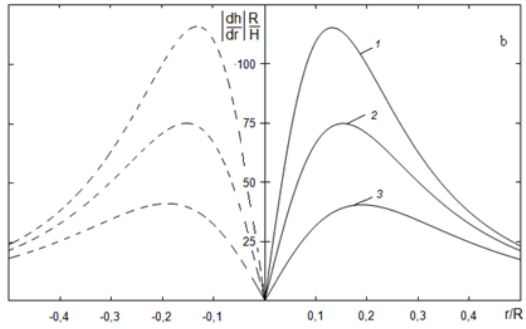
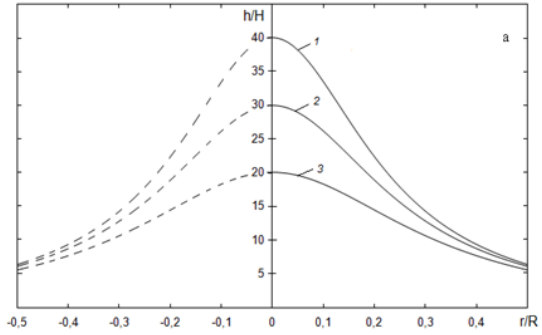
On the basis of (9.15), it is not difficult to verify (also using the data in Fig. 9.5b) which is located in the vicinity of the point of contact of the ferroelements (up to  $r/R = 0.4 - 0.5$ ):  $h \gg H$  (Fig. 9.9a). In this case, the values of the field strength between the ferroelements  $h$  can significantly differ (Fig. 9.10a) even at relatively moderate values of the magnetizing (external) field strength  $H$ .

Having the calculated Eqs. (9.15), it is not difficult to find the dependencies of the heterogeneity in the area between ferroelements (they are particular necessary for magnetophoresis problems), to be more specific, in the radial direction of the plane of symmetry, i.e. moving away along (by  $r$ ) from the point of contact of ferroelements (Fig. 9.1a) - as the derivative  $dh/dr$ :

$$\left| \frac{dh}{dr} \right| \frac{R}{H} = \frac{\mu(\mu - 1)(r/R)}{\sqrt{1 - (r/R)^2} \left[ \mu - \sqrt{1 - (r/R)^2}(\mu - 1) \right]^2} \quad (9.16)$$

$$\left| \frac{dh}{dr} \right| \frac{R}{H} = \frac{\mu(\mu - 1)(r/R)}{[1 + 0.5(r/R)^2(\mu - 1)]^2} \quad (9.17)$$

**Fig. 9.9** The relative values of the field strength  $h/H$  (a) and the heterogeneities  $|dh/dr|R/H$  (b) between the balls-elements of the chain of balls - as  $r$  is moved away from the point of contact of the balls for different magnetic field strength  $H$  (magnetic permeability of the metal of the balls  $\mu$ ), 1 -  $H = 40$  kA/m ( $\mu \cong 40$ ), 2 -  $H = 55$  kA/m ( $\mu \cong 30$ ), 3 -  $H = 85$  kA/m ( $\mu \cong 20$ ).



**Fig. 9.10** The same as in Fig. 9.9 but for absolute values of the field strength  $h$  (a) and heterogeneity  $|dh/dr|$  (b) - with a radius of ferroelements-balls  $R = 3$  mm.

An illustration of the dependencies (9.16) and (9.17) which indicates their extreme form, is shown in Fig. 9.9b. Moreover, from the simplified formula (9.17), and also using the link (9.13) and assuming, as before  $(\mu - 1) \cong \mu$ , followed by convenient expressions for the abscissa and the ordinates of the extreme:

$$\left(\frac{r}{R}\right)_{\text{extr}} = \frac{1}{\sqrt{1.5(\mu - 1)}} \cong 0.82 \left(\frac{H}{H_\mu}\right)^{0.45}, \quad (9.18)$$

$$\left(\frac{dh}{dr} \frac{R}{H}\right)_{\text{extr}} = 0.46\mu \sqrt{\mu - 1} \cong 0.46 \left(\frac{H_\mu}{H}\right)^{1.35}, \quad (9.19)$$

Equations (9.15)-(9.19) allow us to obtain important information (and to analyze it) about the field strength and its heterogeneity both in the relative, dimensionless (written here and shown in Fig. 9.9a, b), as well as in dimensional form (Fig. 9.10a, b). In the latter case, i.e. at the corresponding values of the characteristic dimensions of the ferroelements, in particular, the radius  $R$  of the pellet balls (Fig. 9.10a, b), the user receives an additional amount of necessary information: about the actual current values of the field strength and its heterogeneity, about the individual values of the ordinates and abscissas of the extremal values of heterogeneity, the width of the bands in the area of extremes, etc.

## 9.10 Conclusions

An attempt has been made to classify heterogenous, disperse ferromaterials based on the characteristic values of the volume fraction of the ferrocomponent  $\gamma$ . An estimate was made for the three expressed (especially from the position of the behavior of the demagnetizing factor of the "short" sample of such material) intervals of  $\gamma$ . In this case, such classification is due to the corresponding location of the ferroelements (including contact-less and contact), on which the degree of their mutual magnetic influence depends.

It has been established that materials in the form of fillings of ferroelements (granules, grains), as a widespread class of such ferromaterials, are characterized by practically constant value of  $\gamma \cong 0,6$ . These materials are of independent interest for research, in particular, for the purpose of determining the averaged magnetic properties (magnetic permeability, induction) and obtaining information (especially important in the field of filtering magnetophoresis) about the field between ferroelements.

Conceptually and in details (on the example of a chain of contacting balls) the productive model of the channeled magnetization of these "tightly packed" ferromaterials is stated. It allows us to establish analytical expressions and calculated dependencies (consistent with the experimental data) for the average magnetic permeability of the magnetization channel and its parts (cores, tube layers of different radius  $r$ ), and also dispersed ferromaterial as a whole (as a "harness" of branched



channels). The compliance of the results of the experiments and calculations is also illustrated in the form of generalizing dependencies.

It is shown that in the physical sense the magnetic permeability of a layer-tube with radius  $r$  of the magnetization channel characterizes the relative (related to the intensity of the magnetizing field) field strength between contacting ferroelements (for example, balls) at a distance  $r$  from their point of contact. This also makes it possible to obtain expressions characterizing the heterogeneity of the field between ferroelements.

**Acknowledgements** The research is conducted with financial support from RFFI within the frameworks of research project No 16-38-60034 mol\_a\_dk and from Russian Federation Ministry of Education and Science No 9.9626.2017.

## References

- Anhalt M, Weidenfeller B (2007) Magnetic properties of polymer bonded soft magnetic particles for various filler fractions. *Journal of Applied Physics* 101(2):023,907
- Anhalt M, Weidenfeller B, Mattei JL (2008) Inner demagnetization factor in polymer-bonded soft magnetic composites. *Journal of Magnetism and Magnetic Materials* 320(20):e844 – e848
- Bennacer L, Ahfir ND, Bouanani A, Alem A, Wang H (2013) Suspended particles transport and deposition in saturated granular porous medium: Particle size effects. *Transport in Porous Media* 100(3):377–392
- Bottauscio O, Chiampi M, Manzin A (2009) Homogenized magnetic properties of heterogeneous anisotropic structures including nonlinear media. *IEEE Transactions on Magnetics* 45(10):3946–3949
- Daniel L, Corcolle R (2007) A note on the effective magnetic permeability of polycrystals. *IEEE Transactions on Magnetics* 43(7):3153–3158
- Diguët G, Beaugnon E, Cavallé J (2010) Shape effect in the magnetostriction of ferromagnetic composite. *Journal of Magnetism and Magnetic Materials* 322(21):3337–3341
- Hultgren A, Tanase M, Felton EJ, Bhadriraju K, Salem AK, Chen CS, Reich DH (2005) Optimization of yield in magnetic cell separations using nickel nanowires of different lengths. *Biotechnol Prog* 21:509–515
- Kim YS, Whittle AJ (2006) Filtration in a porous granular medium: 2. application of bubble model to 1-d column experiments. *Transport in Porous Media* 65(2):309–335
- Lacoste D, Lubensky TC (2001) Phase transitions in a ferrofluid at magnetic-field-induced microphase separation. *Physical Review E* 64:041,506–1–041,506–8
- Mattei JL, Floc'h ML (2003) Percolative behaviour and demagnetizing effects in disordered heterostructures. *J Magnetism Magnetic Mater* 257(2-3):335 – 345
- Ngo AT, Pileni MP (2001) Assemblies of ferrite nanocrystals: Partial orientation of the easy magnetic axes. *The Journal of Physical Chemistry B* 105(1):53–58
- Nielsch K, Wehrspohn RB, Barthel J, Kirschner J, Fischer SF, Kronmüller H, Schweinböck T, Weiss D, Gösele U (2002) High density hexagonal nickel nanowire array. *Journal of Magnetism and Magnetic Materials* 249(1):234–240
- Ravnik J, Hriberšek M (2013) High gradient magnetic particle separation in viscous flows by 3D BEM. *Computational Mechanics* 51(4):465–474
- Sandulyak A, Sandulyak A, Ershova V, Polismakova M, Sandulyak D (2017a) Use of the magnetic test-filter for magnetic control of ferroimpurities of fuels, oils, and other liquids (phenomenological and physical models). *Journal of Magnetism and Magnetic Materials* 426:714–720

- Sandulyak AA, Ershova VA, Ershov DV, Sandulyak AA (2010) On the properties of short granular magnets with unordered granule chains: a field between the granules. *Solid State Physics* 52(10):2108–2115
- Sandulyak AA, Sandulyak DA, Ershova VA, Kiselev DO, Sandulyak AV (2015a) Finding out the commonalities in functional expressions for demagnetizing factor of quasi-solid and solid magnets. In: *Proceedings of the World Congress on Engineering 2015, WCE 2015, London, UK, Lecture Notes in Engineering and Computer Science, vol II*, pp 1183–1185
- Sandulyak AA, Ershova VA, Sandulyak DA, Sandulyak AV, Polismakova MN, Kiselev VA (2016a) Modeling of tubular pores in free-flowing bulk media on the basis of quasi-faceted cells of such media. *Glass and Ceramics* 73(5):190–192
- Sandulyak AA, Polismakova MN, Sandulyak AV, Sandulyak DA, Khlustikov DS (2016b) Model of quasifaceted cells and possibility of its application to free-flowing materials. *Glass and Ceramics* 72(11):420–424
- Sandulyak AA, Ershova VA, Sandulyak DA, Sandulyak AV, Polismakova MN (2017b) Fills of co-sized and different-sized granules as quasi-ordered structures. *Journal of Engineering Physics and Thermophysics* 90(2):329–335
- Sandulyak AA, Polismakova MN, Kiselev DO, A SD, Sandulyak AV (2017c) On limiting the volume fraction of particles in the disperse sample (for the tasks on controlling their magnetic properties). *Fine Chemical Technologies* 12(3):58–64
- Sandulyak AV (1982) Model' namagnichivaniya poristoy sredy (magnetization model of porous media, in Russ.). *Technical Physics* 52(11):2267–2269
- Sandulyak AV (1983) *Physicheskaya model' osagdeniya ferromagnitnykh chastiz v namagnichennoy granulirovannoy srede* (physical model of sedimentation of ferrous particles in granulated media, in Russ.). *Doklady Akademii nauk UkrSSR* (9, iss. B):49–53
- Sandulyak AV (1984) *Namagnichivaniye zepochki sharov* (magnetization of the balls chain, in Russ.). *Technical Electrodynamics* (5):102–104
- Sandulyak AV, Sandulyak AA, Ershova VA (2007) Magnetization curve of a granulated medium in terms of the channel-by-channel magnetization model (new approach). *Doklady Physics* 52(4):179–181
- Sandulyak AV, Sandulyak AA, Ershova VA (2008) Functional correction to the classical expression for the average flow velocity in a closely packed granular bed. *Theoretical Foundations of Chemical Engineering* 42(2):220–224
- Sandulyak AV, Sandulyak AA, Ershova VA (2009) On the model of channel-by-channel magnetization of a granular medium (with a radial permeability profile of a quasi-continuous channel). *Technical Physics* 54(5):743–745
- Sandulyak DA, Sandulyak AA, Kiselev DO (2015b) Granular ferromagnets: Formulas for effective magnetic permeability. In: *Proceedings of International Conference on Materials Engineering and Industrial Applications, Hong Kong*, pp 261–266
- Sandulyak DA, Slepsov VV, Sandulyak AA, Sandulyak AV, Ershova VA, Doroshenko AV (2015c) Filtration magnetophoresis process: an approach to choosing a speed regime. In: *Rudas IJ (ed) Proceedings of the 2015 International Conference on Recent Advances in Mechanics, Mechatronics and Civil, Chemical and Industrial Engineering, Zakynthos Island, Greece*, pp 72–76
- Sandulyak DA, Sandulyak AA, Ershova VA, Sandulyak AV, Kononov MA (2017d) Definition of pore tortuosity in granular medium ply based on model of quasi-faceted cells and pore-tubes. *Glass and Ceramics* 73(9):338–341
- Schulz L, Schirmacher W, Omran A, Shah SV, Böni P, Petry W, Müller-Buschbaum P (2010) Elastic torsion effects in magnetic nanoparticle diblock-copolymer structures. *J Phys: Condens Matter* 22:346,008
- Zhang DZ, M RR (2003) Effects of long and short relaxation times of particle interactions in dense and slow granular flows. In: *Proc. of ASME FEDSM' 03, 4th ASME\_JSME Joint Fluids Engineering Conference, Honolulu, Hawaii, USA, vol 1*, pp 579–582

# Chapter 10

## Modeling and Simulation of a Chemically Stimulated Hydrogel Bilayer Bending Actuator

Martin Sobczyk and Thomas Wallmersperger

**Abstract** Polyelectrolyte hydrogels are a class of smart materials which show a reversible swelling or deswelling behavior if subjected to an external stimulus, such as pH, temperature or ion concentration. Stacked layers of different hydrogels, often referred to as hydrogel layer composites, offer new possibilities to create sophisticated sensor and actuator systems on the microscale.

The numerical investigation of these systems is essential to predict and understand their complex behavior and develop devices based on hydrogel layer systems. In this contribution, a chemo-electro-mechanical multifield theory is adopted to describe the complex processes inside of the hydrogels, including migrative and diffusive ion fluxes, electrical fields and mechanical deformation due to an osmotic pressure difference.

The respective time-dependent field equations are solved on a two-dimensional domain using the Finite Element Method.

The study includes the analysis of the bending behavior of a hydrogel bilayer giving an insight into the relevant inner processes. The obtained results match with previous findings and are in excellent agreement with analytical investigations.

### 10.1 Introduction

Hydrogels are soft materials which are able to reversibly swell and deswell in water under the influence of various external stimuli. Examples for relevant stimuli are changes in pH, temperature, magnetic fields, ion concentration and electric fields as e.g. described by Qiu and Park (2001); Jeong and Gutowska (2002); Wu et al (2004); Osada and Gong (1998); Wallmersperger et al (2007). The structure of a polyelectrolyte hydrogel may be regarded as an interconnected polymer network with

---

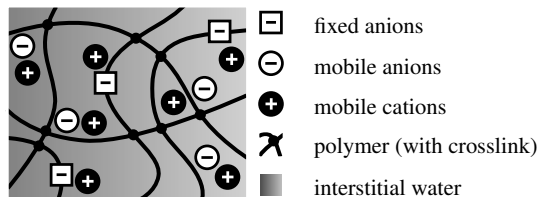
Martin Sobczyk · Thomas Wallmersperger  
Technische Universität Dresden, Institut für Festkörpermechanik, 01062 Dresden, Germany  
e-mail: martin.sobczyk@tu-dresden.de, thomas.wallmersperger@tu-dresden.de

interstitial fluid within the void of the polymer backbone. Attached to the polymer backbone polyelectrolyte ionic side chains are present, which are only able to move in connection with the overall polymer backbone. The attached ionic side chains (or functional groups) are in a large degree responsible for the swelling and deswelling properties of the hydrogel due to an osmotic pressure difference between the gel and the surrounding solution bath. As a result of the osmotic pressure difference, an uptake or release of water is observed. The microstructure of a polyelectrolyte hydrogel is schematically depicted in Fig. 10.1.

The sensoric and actoric capabilities of hydrogels are favorable for many applications, such as chemical sensors, as developed by Gerlach et al (2005) or microfluidic actuator systems as shown by Richter et al (2004, 2008). The combination of different hydrogel layers offers further possibilities to create sophisticated actuator systems like bilayer bending actuators or sensor systems which are able to respond to multiple input signals, such as temperature and salt concentration.

In the past, different groups aimed to describe the swelling and deswelling behavior of polyelectrolyte hydrogels under external stimuli theoretically. Models describing the behavior of polyelectrolyte hydrogel swelling are for example the Statistical Theory (Flory and Rehner, 1943a,b; Flory, 1956), the Theory of Porous Media (Acartürk, 2009; Ehlers et al, 2003; Leichsenring and Wallmersperger, 2017; Bluhm et al, 2016) and other continuum models (Doi, 2009; Shahinpoor, 1995; Drozdov and de Claville Christiansen, 2015; Nardinocchi and Puntel, 2017). For a review of numerical models applied to investigate the behavior of hydrogels, the reader is referred to Wu et al (2004); Ganji et al (2010). A numerical simulation to describe hydrogel layer composites was conducted by Lucantonio et al (2014), describing the bending deformation of a hydrogel composite structure where the deformation was multiplicative split into a uniform free-swelling stretch and an elastic component. Another approach to describe the hydrogel’s swelling behavior is the so-called multifield theory (Wallmersperger and Ballhause, 2008; Attaran et al, 2015; Sobczyk and Wallmersperger, 2016b). This model was introduced to compute the response of hydrogels to electric fields and was later adopted to also account for chemical stimulation. Within the framework of continuum mechanics, a coupled system of equations is formulated in order to describe the interaction of the electrical field, the movement of ions and the resulting mechanical deformation.

Goal of this paper is to predict the chemo-electro-mechanical behavior of a thin hydrogel-layer system in the configuration of a bending actuator under chemical stimulation. For this, the field equations are solved using the Finite Element Method



**Fig. 10.1** Schematic representation of the microstructure of a polyelectrolyte hydrogel.

on a two-dimensional domain. The time discretization is conducted adopting the implicit Euler Method, for the spatial discretization rectangular finite elements with linear shape functions are used.

For the description of the ion concentration distribution, a Nernst-Planck-like equation is used. The electric field and the distribution of the electric potential is evaluated using the Poisson equation for electrostatics. In order to predict the mechanical behavior of the hydrogel-layer-system, the balance of momentum is adopted.

In Sect. 10.2, the multifield theory as proposed by Sobczyk and Wallmersperger (2016b,a) is summarized. In Sect. 10.3, numerical results for the testcase of a bending actuator are given and discussed. In Sect. 10.4, a brief conclusion is drawn.

## 10.2 Chemo-Electro-Mechanical Field Formulation

In the multifield theory it is assumed, that at a local point of the hydrogel all its constituents are entirely mixed. The relevant constituents are the polymer backbone, the functional groups, interstitial fluid and free ions, cf. Fig. 10.1. Using the framework of continuum mechanics, the properties of the discrete matter (atoms) are averaged over one element and described using continuous fields. The investigated body is represented by continuously distributed material points, where at each local point only a single material point may be present.

The material behavior of hydrogels depends on the interaction of different interacting physical fields. The field variables are therefore interdependent on each other and cannot be evaluated neglecting the other. As a result, multiple field variables need to be calculated on every local point. The material properties represent the material properties of the whole representative volume element and may also be dependent on the local field variables.

The balance relations are obtained by balancing forces and moments as well as fluxes acting on a representative volume element and are evaluated in the framework of classical continuum mechanics. The balance equations are the balance of mass, the balance of linear and angular momentum balance as well as the Maxwell equations. The material laws are given by Hookean material behavior, the Poisson-Nernst-Planck equation and a linear relation between the electrical displacement and the electric field. The swelling of the hydrogel is accounted for by a decomposition of the total strain into an elastic strain and a stress-free swelling one, induced by an osmotic pressure.

In the following, the used field equation are briefly described. For further details, the reader is referred to Sobczyk and Wallmersperger (2016a,b); Wallmersperger et al (2008, 2004, 2007); Doi (2009); Doi et al (1992); Attaran et al (2015); Ballhause and Wallmersperger (2008).

### 10.2.1 Chemical Field

The distribution of mobile ions is influenced by concentration gradients and gradients of the electric potential, which lead to diffusive and migrative fluxes, respectively. The mass balance for the ion species  $\alpha$  is formulated as

$$\dot{c}^\alpha = -J_{,i}^\alpha = -(J^{\text{diff}\alpha} + J^{\text{migr}\alpha})_{,i} \quad (10.1)$$

with the migrative flux  $J^{\text{migr}\alpha}$  and the diffusive flux  $J^{\text{diff}\alpha}$  described as

$$J^{\text{migr}\alpha} = -D^\alpha \frac{F}{RT} z^\alpha c^\alpha \Psi_{,i}, \quad (10.2)$$

$$J^{\text{diff}\alpha} = -D^\alpha c_{,i}^\alpha. \quad (10.3)$$

Here,  $c$  denotes the ion concentration,  $D$  the Diffusion coefficient,  $F = 96487 \text{ C/mol}$  the Faraday constant,  $R = 8.3143 \text{ J/(mol}\cdot\text{K)}$  the universal gas constant,  $T$  the absolute temperature,  $z$  the valence of the ions and  $\Psi$  the scalar electric potential. The index  $\alpha$  displays the affiliation to the respective mobile ion species. Here, we consider mobile anions (-) and mobile cations, therefore  $\alpha = \{+, -\}$ . Throughout this contribution, the operators  $()_{,i}$  and  $\dot{()}$  denote the derivatives  $d()/dx_i$  and  $d()/dt$ , respectively.

### 10.2.2 Electrical Field

In order to describe the electrical field the Poisson equation for electrostatics

$$\Psi_{,ii} = -\frac{\rho^e}{\varepsilon^0 \varepsilon^r} \quad (10.4)$$

is used, in which the volume charge density  $\rho^e$  is described by

$$\rho^e = F \sum_{\gamma} (z^\gamma c^\gamma). \quad (10.5)$$

Here,  $\varepsilon^0 = 8.8542 \cdot 10^{-12} \text{ As/(Vm)}$  denotes the vacuum permittivity and  $\varepsilon^r$  the relative permittivity of the material. The index  $\gamma$  is used for all mobile and fixed ions. In this contribution,  $\gamma = \{+, -, \text{fc}-\}$  denotes the indices of the mobile cations (+), mobile anions (-) and fixed anions (fc-). In order to use Eq. (10.4), it is assumed, that the time derivative of the magnetic induction  $B_i$  vanishes. This assumption is adequate to use, as the propagation velocity of the electric field is much higher than the transport processes occurring in the chemical field. Therefore, the Poisson equation for electrostatics is sufficient. Magnetostatic effects are not considered in this contribution.

### 10.2.3 Mechanical Field

To determine the displacement field in the gel system, the local form of momentum balance is adopted, neglecting body forces as well as inertia terms:

$$\sigma_{ij,j} = 0. \quad (10.6)$$

It is assumed, that Hookean material behavior

$$\sigma_{ij} = E_{ijkl} \varepsilon_{kl}^{\text{el}} \quad (10.7)$$

can be used in a first approximation. In order to couple the mechanical field with the electrical and the chemical field, the total strain  $\varepsilon^{\text{tot}}$  is decomposed into an elastic strain and a stress-free swelling strain contribution, induced by an osmotic pressure difference:

$$\varepsilon_{kl}^{\text{tot}} = \varepsilon_{kl}^{\text{el}} + \varepsilon_{kl}^{\pi} \quad (10.8)$$

The swelling strain  $\varepsilon_{ij}^{\pi}$  is assumed to be proportional to the osmotic pressure difference  $\Delta\pi^{\text{osm}}$  calculated by introducing the reference concentration  $c^{\text{ref}}$ , which is an artificial degree of freedom. The swelling strain is then obtained by

$$\varepsilon_{kl}^{\pi} = \Gamma \delta_{kl} \Delta\pi^{\text{osm}} \quad (10.9)$$

and

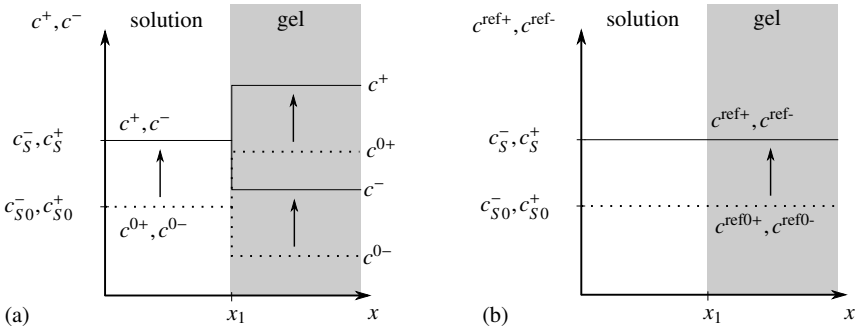
$$\Delta\pi^{\text{osm}} = RT \sum_{\alpha} (\Delta c^{\alpha} - \Delta c^{\alpha 0}) \quad \text{with} \quad \begin{cases} \Delta c^{\alpha} = c^{\alpha} - c^{\text{ref}} \\ \Delta c^{\alpha 0} = c^{\alpha} - c^{\text{ref}0} \end{cases} \quad (10.10)$$

where  $\Gamma$  is the swelling coefficient,  $\delta_{kl}$  the Kronecker Delta,  $R$  the universal gas constant,  $T$  the absolute temperature and  $c^{\alpha}$  and  $c^{\alpha 0}$  the concentration of ion species  $\alpha$  at actual and initial time. The reference concentration at initial time is denoted by  $c^{\text{ref}0}$ . It should be noted, that by definition an osmotic pressure difference can only occur, if the free movement of ions is restricted, e.g. by a semi-permeable membrane.

The reference concentration is obtained solving the equation

$$c^{\text{ref}\alpha} = \left( D^{\text{ref}\alpha} c_i^{\text{ref}\alpha} \right)_i, \quad (10.11)$$

where  $D^{\text{ref}\alpha}$  denotes the Diffusion constant of the reference concentration of the mobile ion species  $\alpha$ . The initial value of the reference concentration equals the concentration of the respective ions in the solution bath in initial state. For an illustration of the reference concentration in equilibrium, please refer to Fig. 10.2. Using this approach, the osmotic pressure difference equals the osmotic pressure difference given by the Van't Hoff law (Van't Hoff, 1888; Weiss, 1996) in equilibrium state, while the temporal development of the osmotic pressure difference is diffusion-like.



**Fig. 10.2:** Schematic representation of the ion concentration of positive ( $c^+$ ) and negative ( $c^-$ ) ions (a) and the respective reference concentrations ( $c^{\text{ref}0+}, c^{\text{ref}0+}$ ) (b) in equilibrium state. The concentrations of mobile cations and anions within the solution bath are equal; inside the gel they are unequal due to the presence of fixed charges and thus governed by the Donnan equilibrium.

Within this model, the water content or the water fluxes are not evaluated explicitly, but the swelling and deswelling behavior of the hydrogel is calculated by evaluating the osmotic pressure difference between the hydrogel and its environment.

Since the movement of the surrounding solution bath is not of interest, the balance of momentum is evaluated only in the gel domain. For this, suitable boundary conditions need to be prescribed at the interface between gel and solution bath.

### 10.2.4 Numerical Solution Procedure

In the previous section, the field equations describing the coupled chemical, electrical and mechanical behaviour of polyelectrolyte gels are formulated. In this section, a very brief description on the solution procedure is given.

To solve this coupled initial boundary value problem a numerical solution procedure is chosen. For this, the Finite Element Method is adopted. The respective field equations are formulated in the weak form using the standard continuous Galerkin procedure in space. Here, the variations of the primary variables, that are  $\delta c^\alpha$ ,  $\delta c^{\alpha\text{ref}}$ ,  $\delta \Psi$  and  $\delta u_i$  are utilized as weighting functions. Due to the nonlinear terms in the formulation, a linearization of the field problem is carried out using the standard Newton-Raphson scheme.

For the temporal discretization the unconditionally stable implicit Euler method is adopted. For the spatial discretization bilinear eight-node rectangular shell elements are implemented. The primary variables which are solved at each node are the concentration of mobile anions and cations  $c^\alpha$ , the concentration of reference anions and cations  $c^{\alpha\text{ref}}$ , the scalar electric potential as well as the displacement field  $u_i$  in  $x$ -



and y-direction. The meshing is carried out using a logarithmic mesh refinement, as e.g. described by Wallmersperger (2010).

### 10.3 Numerical Simulation of a Chemically Stimulated Bilayer

In this section the chemical stimulation of a hydrogel bending actuator with the dimensions  $L \times (b_1 + b_2)$ , where  $L = 5$  mm and  $b_1 = b_2 = b = 0.3$  mm is investigated. This configuration may for example be used as soft gripper or flapper. For this, the hydrogel-layer system is composed of two different hydrogels, each with a size of  $(L \times b)$ . The geometry parameters are summarised in Table 10.1. The gel 1 of the hydrogel-layer system is a polyelectrolyte hydrogel with a concentration of fixed anions  $c^{\text{fc}^-} = 1$  mM (Wallmersperger, 2010) and a swelling coefficient  $\Gamma = 1 \cdot 10^{-4} \text{ Pa}^{-1}$ . Gel 2 is a neutral gel and it is assumed, that it will not change its swelling state under chemical stimulation. Therefore gel 2 may be considered as an ion conducting passive structure, with  $c^{\text{fc}^-} = 0$  and  $\Gamma = 0$ . The Young's modulus of both layers is chosen as  $E = 10$  kPa (Matzelle et al, 2003). The diffusion inside of the gels is governed by the diffusion constants  $D^+ = D^- = 5 \times 10^{-10} \text{ m}^2/\text{s}$  (Acartürk, 2009) and inside of the solution bath  $D^+ = D^- = 5 \times 10^{-9} \text{ m}^2/\text{s}$  (Acartürk, 2009). The relative permittivity of the gel and the solution bath is set to  $\varepsilon^r = 80$  (permittivity of water) (Catenaccio et al, 2003; Drozdov and de Claville Christiansen, 2015). The used material parameters are summarised in Table 10.2.

The bending actuator is placed in a NaCl solution bath with an ion concentration of  $c^+ = c^- = 1$  mM (Wallmersperger et al, 2007; Wallmersperger, 2010). It is

Table 10.1: Used geometry parameters.

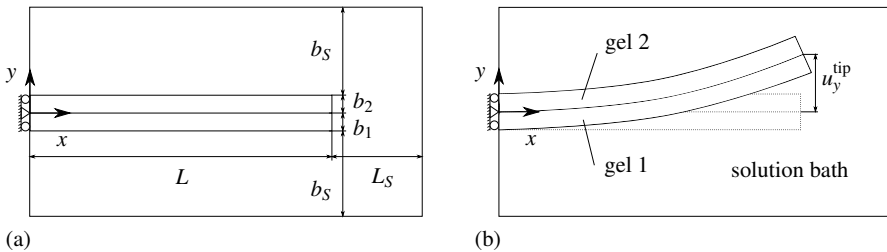
parameter	value (mm)
$L$	5
$L_S$	$2 \cdot 10^{-4}$
$b_S$	$2 \cdot 10^{-4}$
$b_1$	0.3
$b_2$	0.3

Table 10.2: Used material parameters.

material parameter	solution bath	gel 1	gel 2
Young's modulus $E$ (kPa)	-	10	10
Poisson ration $\nu$ (-)	-	0.499999	0.499999
expansion coefficient $\Gamma$ (1/Pa)	-	$1 \cdot 10^{-4}$	0
diffusion coefficient $D^+$ ( $\text{m}^2/\text{s}$ )	$5 \cdot 10^{-9}$	$5 \cdot 10^{-10}$	$5 \cdot 10^{-10}$
diffusion coefficient $D^-$ ( $\text{m}^2/\text{s}$ )	$5 \cdot 10^{-9}$	$5 \cdot 10^{-10}$	$5 \cdot 10^{-10}$
relative permittivity $\varepsilon_r$ (-)	80	80	80
fixed charge concentration $c^{\text{fc}^-}$ (mM)	0	1	0

asumed, that the system is in the respective equilibrium state. At time  $t = 0$ , the bending actuator is placed in another NaCl solution with an ion concentration of  $c^+ = c^- = 0.5 \text{ mM}$  and therefore is chemically stimulated. No external electric field is applied to the system. Throughout this investigation, one side of the bending actuator is mechanically restricted, while the other side may move freely, as depicted in Fig. 10.3a. Due to the chemical stimulation, a deflection of the bilayer actuator is anticipated as depicted in Fig. 10.3b. The numerical simulation is conducted in order to predict the bending behavior of the actuator as well as to investigate the electro-chemo-mechanical processes inside of the system.

In order to numerically analyze the described experimental setup, suitable boundary and initial conditions have to be prescribed. Around the gel system only a thin layer of solution bath is modeled, which is sufficient if the presence of the gel does not alter the concentration inside of the solution bath. Then, the concentration at the outer boundary of the thin layer of the solution bath is prescribed as Dirichlet boundary conditions with fixed values of the concentrations in the large solution bath. A mobile ion concentration  $c^+ = c^- = 0.5 \text{ mM}$ , as well as a reference concentration  $c^{+\text{ref}} = c^{-\text{ref}} = 0.5 \text{ mM}$  is prescribed there. The thin layer of the solution bath needs to be larger than the electro-chemical double layer between the gel and the solution bath, that is the respective Debye length, i.e. larger than the area in which the steep gradient between the inner and outer concentration in the numerical simulation occurs. Here, a thin layer of solution bath with a thickness of  $L_S = b_S = 2 \cdot 10^{-7} \text{ m}$  is chosen. By using this approach it is further prevented, that transport processes inside of the solution bath have a relevant influence on the response behavior of the hydrogel layer system. The boundary of the gel layer in contact to the solution bath is free of stress, that means  $\sigma_{ij}n_i = 0$ , where  $n_i$  denotes the normal vector - which is positive in outwards direction - of the respective domain. On its left side, the gel system is mechanically restricted using the boundary conditions  $u_y(x = 0, y = 0) = 0$  and  $u_x(x = 0) = 0$ . The momentum balance is only evaluated on the domain of the gel layers, and not in the solution bath. The electric potential at the outer boundary of the solution bath is set to  $\Psi = 0 \text{ V}$ .



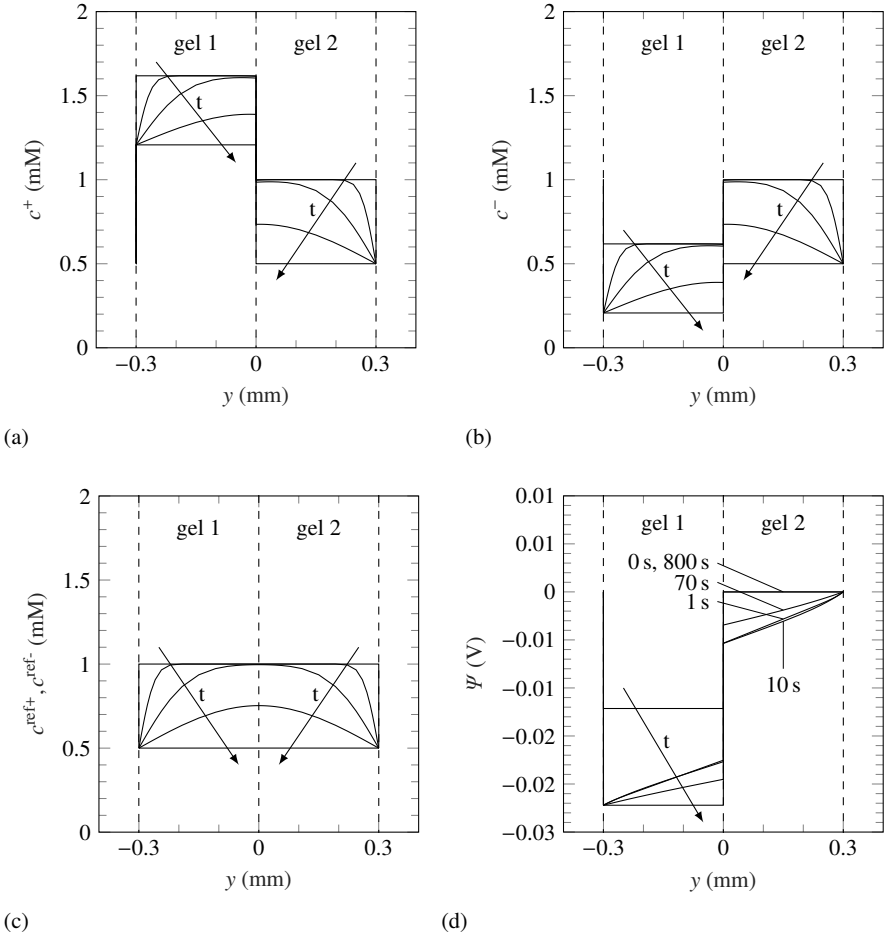
**Fig. 10.3:** Schematic representation of the investigated hydrogel layer system: (a) the system in the initial state is depicted, (b) the system during actuation is shown.

The system is defined as undeformed in initial state, that is  $u_x(t=0) = u_y(t=0) = 0$ . The initial conditions for the ion concentrations and the electric potential of the investigated system are being calculated in a foregoing stationary simulation. For this, inside of the solution bath and inside of gel 2 an ion concentration  $c^+ = c^- = 1 \text{ mM}$  is prescribed. In gel 1  $c^+ = 1.618 \text{ mM}$  and  $c^- = 0.618 \text{ mM}$  is set as initial condition. These values correlate with the Donnan equilibrium of the investigated system, in which however no information on the formation of the electro-chemical double layer is included. To obtain the initial condition of the system, on the left outer boundary of the system a no flux condition for both the positive and negative ions  $J^+ = J^- = 0$  is stipulated. On all other outer boundaries of the system a concentration of  $c^+ = c^- = 1 \text{ mM}$  is prescribed. The electric potential is given by  $\Psi = 0 \text{ V}$  in gel 2 and in the solution bath, whereas in gel 1 the electric potential is set to  $\Psi = -0.0121 \text{ V}$ . At the outer boundaries of the system, the electric potential is set to  $\Psi = 0 \text{ V}$ .

In Fig. 10.4, the development over time at  $t = 0, 1, 10, 70, 800 \text{ s}$  of the distribution of mobile ion concentrations, the reference concentration and the electric potential are depicted over  $y$  at  $x = 2.5 \text{ mm}$ . In Fig. 10.4a and 10.4b the concentration of positive and negative ions is given. With progressing time, the concentrations inside gel 1 and gel 2 are reduced from the initial equilibrium state towards the new equilibrium state. This new equilibrium state is governed by the Donnan equilibrium with respect to the concentration of fixed anions in the gel and the ion concentrations in the solution bath. Outside the boundary regions and inside gel 1 the ion concentrations in the new equilibrium yield  $c^+ = 1.207 \text{ mM}$  and  $c^- = 0.207 \text{ mM}$  with a constant electric potential  $\Psi = -0.0223 \text{ V}$ . Since no fixed charges are present in gel 2, the ion concentrations as well as the electric potential in initial state and in equilibrium state are the same as in the solution bath, i.e.  $c^+ = c^- = 1 \text{ mM}$  and  $\Psi = 0 \text{ V}$  in initial state and  $c^+ = c^- = 0.5 \text{ mM}$  and  $\Psi = 0 \text{ V}$  in equilibrium state. In Fig. 10.4c, the evolution of the reference concentration is depicted for the times  $t = 0, 1, 10, 70$  and  $800 \text{ s}$ .

The electric potential, as depicted in Fig. 10.4d, exhibits a constant value in each solution and each gel domain outside the boundary layers in equilibrium state. At the intermediate states, the electric potential in the respective domains is almost linear. Electroneutrality is fulfilled in each domain outside of the boundary layer, and therefore the curvature of the electric potential equals zero in these regions. In Fig. 10.5 it can be observed, that the electric potential differences between the solution bath and gel 1 and the differences of the electric potential between gel 1 and gel 2 are only equal for the equilibrium states, but not for the intermediate states, compare Figs. 10.5a and 10.5b. The potential differences between adjacent regions is governed by the concentration of fixed charges and mobile ions at the respective interface. Since the mobile ions need more time to reach the interface between gel 1 and gel 2 than they need to arrive at the interface between the solution bath and gel 1, the gradient of the electric potential occurs during intermediate states.

In Fig. 10.6, the steady state solution for the ion concentrations and the electric potential is given. In the steady state, gradients in the electric potential or in the concentrations disappear outside of the boundary regions. Therefore, no migrative flux  $J^{\text{mig}}$  or diffusive flux  $J^{\text{diff}}$  occurs there. Within the boundary layer, gradients in

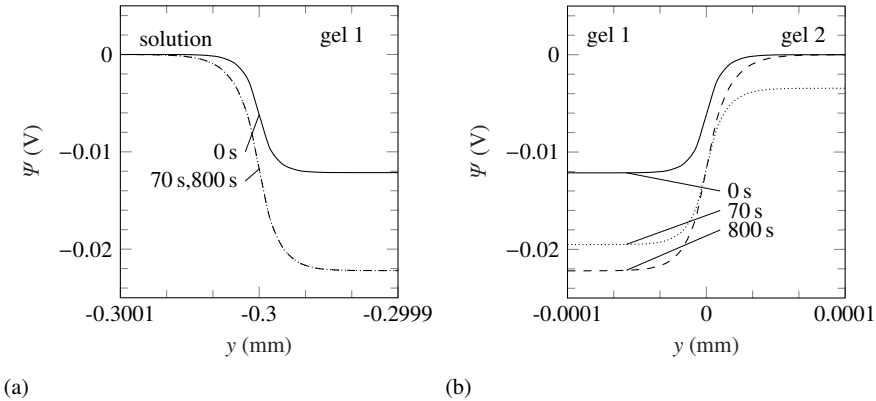


**Fig. 10.4:** Concentration of (a) positive, (b) negative and (c) reference ions and (d) electric potential over  $y$  at  $x = 2.5$  mm for the times  $t = 0, 1, 10, 70, 800$  s.

the electric potential, as well as in the concentration are present. Due to Eq. (10.1), the migrative and the diffusive flux must cancel out in steady state.

The osmotic pressure difference inside the hydrogels is calculated using Eq. (10.10). The occurring osmotic pressure difference versus  $y$  at  $x = 2.5$  mm is depicted in Fig. 10.7a for the times  $t = 0, 1, 10, 70, 800$  s. In initial state, the osmotic pressure difference is by definition equal to zero. Due to the concentration differences at the gel and solution interface, the osmotic pressure difference rises there first. Then, it propagates diffusion-like through gel 1 until it reaches its new equilibrium value

$$\lim_{t \rightarrow \infty} \Delta \pi^{osm} = 441.393 \text{ Pa.}$$



**Fig. 10.5:** Electric potential at the boundaries (a) at the left and (b) at the right side of gel 1 for the times  $t = 0, 70, 800$  s. For the chemo-electrical equilibrium states ( $t = 0$  and approximately at  $t = 800$  s), the electric potential difference between the solution bath and gel 1 is equal to the electric potential difference between gel 1 and gel 2. This is not the case for nonequilibrium states ( $t = 70$  s).

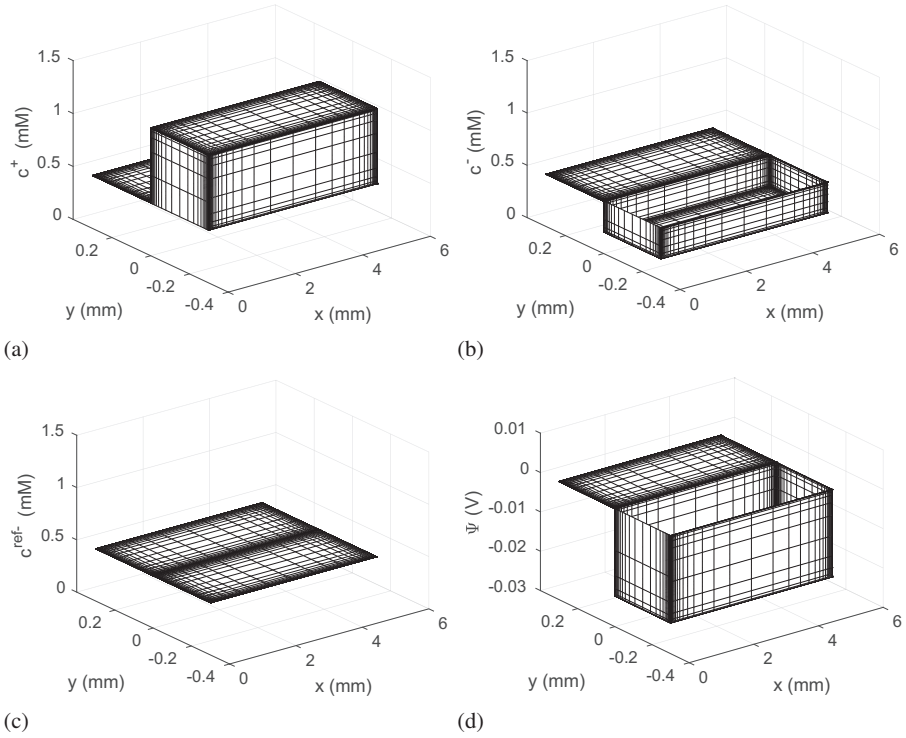
During the swelling process a negative osmotic pressure difference is observed close to gel 2. This is caused by migrative ion fluxes due to the gradient in the electric potential, compare Fig. 10.4d. With further progressing time, this effect becomes secondary compared to the diffusional fluxes and ultimately disappears due to the vanishing gradient of the electric potential. In gel 2 no osmotic pressure difference occurs, since no fixed charges are present which could restrict the free movement of ions.

With progressing time, gel 1 expands, while gel 2 is not subjected to a volumetric change. Due to this, the bending actuator behaves similar to a bi-metal subjected to thermal heating and therefore reacts with a deflection. The deflection of the gel tip  $u_y^{\text{tip}}$  is depicted versus time in Fig. 10.7b. For the steady state, the deflection of the gel layer yields

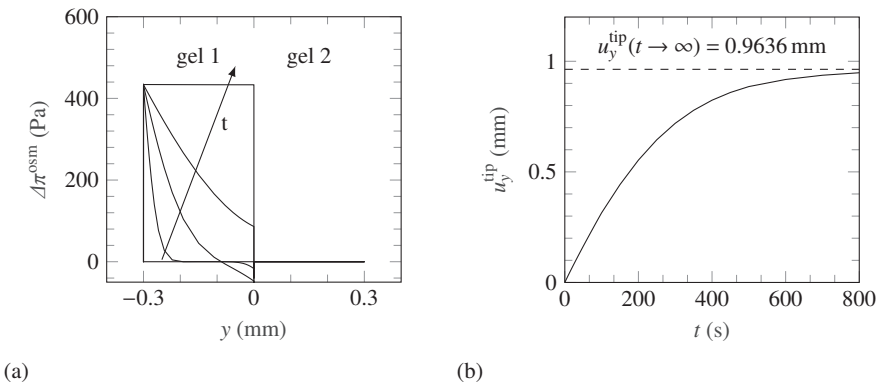
$$\lim_{t \rightarrow \infty} u_y^{\text{tip}} = 0.9636 \text{ mm.}$$

After approximately 10 minutes 95% of this maximum deflection is observed.

Due to the volumetric expansion of gel 1 and the resulting deflection of the hydrogel layer system, mechanical stresses inside the gel beam arise. In Fig. 10.8a the normal stress  $\sigma_{xx}$  is depicted on the deformed geometry for equilibrium state. Since gel 1 wants to expand and gel 2 restricts this expansion, gel 1 is subjected to a compressive and gel 2 to a tensile stress in  $x$ -direction in close proximity to the gel layer interface. A nonzero normal stress in  $y$ -direction occurs only at the tip of the bilayer as shown in Fig. 10.8b. Also shear stresses  $\sigma_{xy}$  are present only near the tip of the hydrogel layer system as can be seen in Fig. 10.8c. These results are in good

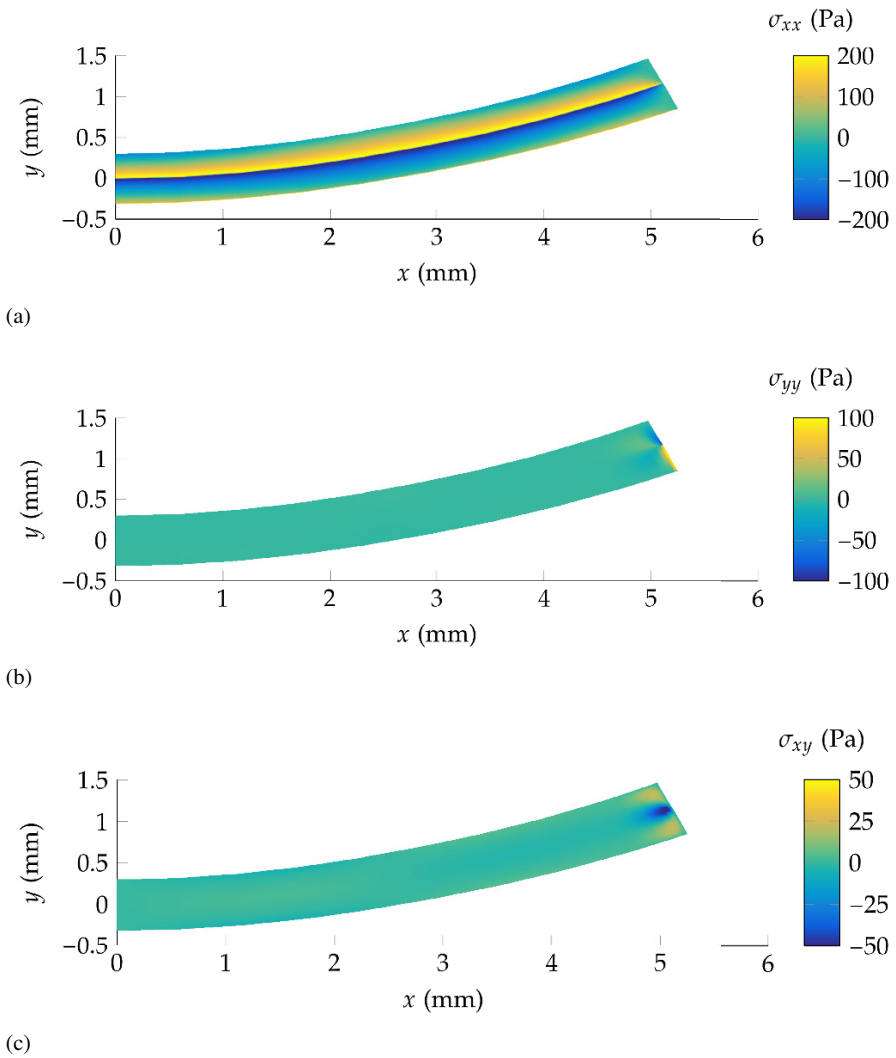


**Fig. 10.6:** 2D representation of the steady state solution for (a) the mobile cation concentration, (b) the mobile anion concentration, (c) the reference concentration and (d) the electric potential after chemical stimulation.



**Fig. 10.7:** (a) Osmotic pressure difference  $\Delta\pi^{osm}$  over  $y$  at  $x = 2.5$  mm for the time steps  $t = 0, 1, 10, 70, 800$  s and (b) deflection of the gel tip  $u_y^{tip}$  over time.

agreement with the results stated by Timoshenko investigating the stress distribution in a bi-metal thermostat (Timoshenko, 1925).



**Fig. 10.8:** Distributions of the stresses  $\sigma_{xx}$  (a),  $\sigma_{yy}$  (b) and  $\sigma_{xy}$  (c) depicted on the deformed geometry. In each picture, the upper gel is denoted as gel 1, the lower gel is denoted as gel 2, as also seen in Fig. 10.3.

## 10.4 Conclusion

In this contribution the bending as well as the electro-chemical behavior of a simple hydrogel layer composite consisting of two layers is described based on a coupled multi-field model. For this the composite - which is immersed in a solution bath - is numerically investigated in a clamped configuration and subjected to a chemical stimulation.

The multi-field model allows to investigate the reversible swelling behavior of polyelectrolyte hydrogels in time. The respective field equations describe the chemical, the electrical and the mechanical field using the electric potential, the ion concentrations and the mechanical displacements as primary variables. A simple approach to evaluate the osmotic pressure difference during swelling is presented.

It could be shown, that the bending behavior due to swelling of the hydrogel is strongly influenced by the processes in the electrical and the chemical field. The used model is able to capture the behavior of hydrogel layer composites for chemical stimulation. With this, important predictions - like the occurring stress distribution or the deformation behavior during swelling - can be evaluated. The obtained results are in excellent agreement with the analytical solution of the Donnan equilibrium. Also, the obtained results are in good agreement with previous numerical results revealing the strength of the used method. By using the proposed model, further investigations of more complex hydrogel layer systems may be obtained.

**Acknowledgements** This research has been financially supported by the German Science Foundation (DFG) in the framework of the Research Training Group *1865 Hydrogel-based Microsystems*.

## References

- Acartürk AY (2009) Simulation of charged hydrated porous materials. PhD thesis, Universität Stuttgart
- Attaran A, Brummund J, Wallmersperger T (2015) Modeling and simulation of the bending behavior of electrically-stimulated cantilevered hydrogels. *Smart Materials and Structures* 24(3):035,021
- Ballhause D, Wallmersperger T (2008) Coupled chemo-electro-mechanical finite element simulation of hydrogels: I. Chemical stimulation. *Smart Materials and Structures* 17(4):045,011
- Bluhm J, Serdas S, Schröder J (2016) Theoretical framework of modeling of ionic EAPs within the Theory of Porous Media. *Archive of Applied Mechanics* 86(1):3–19
- Catenaccio A, Daruich Y, Magallanes C (2003) Temperature dependence of the permittivity of water. *Chemical Physics Letters* 367(5):669–671
- Doi M (2009) Gel dynamics. *Journal of the Physical Society of Japan* 78(5):052,001
- Doi M, Matsumoto M, Hirose Y (1992) Deformation of ionic polymer gels by electric fields. *Macromolecules* 25(20):5504–5511
- Drozdov AD, de Claville Christiansen J (2015) Swelling of pH-sensitive hydrogels. *Phys Rev E* 91:022,305
- Ehlers W, Acartürk A, Markert B (2003) Modelling of 3-D linear viscoelastic swelling of charged tissues and gels. *PAMM* 2(1):218–219
- Flory PJ (1956) Theory of elastic mechanisms in fibrous proteins. *Journal of the American Chemical Society* 78(20):5222–5235



- Flory PJ, Rehner J (1943a) Statistical mechanics of cross-linked polymer networks I. rubberlike elasticity. *The Journal of Chemical Physics* 11(11):512–520
- Flory PJ, Rehner J (1943b) Statistical mechanics of cross-linked polymer networks II. swelling. *The Journal of Chemical Physics* 11(11):521–526
- Ganji F, Vasheghani-Farahani S, Vasheghani-Farahani E (2010) Theoretical description of hydrogel swelling: A review. *Iranian Polymer Journal* 19:375–398
- Gerlach G, Guenther M, Sorber J, Suchanek G, Arndt KF, Richter A (2005) Chemical and pH sensors based on the swelling behavior of hydrogels. *Sensors and Actuators B: Chemical* 111:555–561
- Jeong B, Gutowska A (2002) Lessons from nature: stimuli-responsive polymers and their biomedical applications. *Trends in Biotechnology* 20(7):305–311
- Leichsenring P, Wallmersperger T (2017) Modeling and simulation of the chemically induced swelling behavior of anionic polyelectrolyte gels by applying the theory of porous media. *Smart Materials and Structures* 26(3):035,007
- Lucantonio A, Nardinocchi P, Pezzulla M (2014) Swelling-induced and controlled curving in layered gel beams. *Proceedings of the Royal Society A: Mathematical, Physical and Engineering Science* 470:20140,467
- Matzelle TR, Geuskens G, Kruse N (2003) Elastic properties of poly(n-isopropylacrylamide) and poly(acrylamide) hydrogels studied by scanning force microscopy. *Macromolecules* 36(8):2926–2931
- Nardinocchi P, Puntel E (2017) Unexpected hardening effects in bilayered gel beams. *Meccanica* pp 1–10
- Osada Y, Gong JP (1998) Soft and wet materials: Polymer gels. *Advanced Materials* 10(11):827–837
- Qiu Y, Park K (2001) Environment-sensitive hydrogels for drug delivery. *Advanced Drug Delivery Reviews* 53(3):321–339
- Richter A, Howitz S, Kuckling D, Arndt KF (2004) Influence of volume phase transition phenomena on the behavior of hydrogel-based valves. *Sensors and Actuators B: Chemical* 99(2):451–458
- Richter A, Paschew G, Klatt S, Lienig J, Arndt KF, Adler HJP (2008) Review on hydrogel-based pH sensors and microsensors. *Sensors* 8(1):561–581
- Shahinpoor M (1995) Micro-electro-mechanics of ionic polymeric gels as electrically controllable artificial muscles. *Journal of Intelligent Material Systems and Structures* 6(3):307–314
- Sobczyk M, Wallmersperger T (2016a) Modeling and simulation of chemically stimulated hydrogel layers using the multifield theory. *Proc SPIE* 9798:979,810–979,810–11
- Sobczyk M, Wallmersperger T (2016b) Modeling and simulation of the electro-chemical behavior of chemically stimulated polyelectrolyte hydrogel layer composites. *Journal of Intelligent Material Systems and Structures* 27(13):1725–1737
- Timoshenko S (1925) Analysis of bi-metal thermostats. *J Opt Soc Am* 11(3):233–255
- Van't Hoff JH (1888) XII. the function of osmotic pressure in the analogy between solutions and gases. *The London, Edinburgh, and Dublin Philosophical Magazine and Journal of Science* 26(159):81–105
- Wallmersperger T (2010) Modelling and simulation of the chemo-electro-mechanical behaviour. In: Gerlach G, Arndt KF (eds) *Hydrogel Sensors and Actuators: Engineering and Technology*, Springer Series on Chemical Sensors and Biosensors, vol 6, Springer, Berlin, Heidelberg, pp 137–163
- Wallmersperger T, Ballhause D (2008) Coupled chemo-electro-mechanical finite element simulation of hydrogels: II. electrical stimulation. *Smart Materials and Structures* 17(4):045,012
- Wallmersperger T, Kröplin B, Gülch RW (2004) Coupled chemo-electro-mechanical formulation for ionic polymer gels - numerical and experimental investigations. *Mechanics of Materials* 36(5-6):411–420
- Wallmersperger T, Ballhause D, Kröplin B (2007) On the modeling of polyelectrolyte gels. *Macromolecular Symposia* 254(1):306–313

- Wallmersperger T, Wittel FK, D'Ottavio M, Kröplin B (2008) Multiscale modeling of polymer gels - chemo-electric model versus discrete element model. *Mechanics of Advanced Materials & Structures* 15(3/4):228–234
- Weiss TF (1996) *Cellular Biophysics, vol 1: Transport*. Massachusetts Institute of Technology
- Wu S, Li H, Chen JP, Lam KY (2004) Modeling investigation of hydrogel volume transition. *Macromolecular Theory and Simulations* 13:13–29

# Chapter 11

## Mathematical Modelling of Piezoelectric Generators on the Base of the Kantorovich Method

Arkadiy N. Soloviev, Valerii A. Chebanenko, and Ivan A. Parinov

**Abstract** In this chapter, applied semi-analytical theories were constructed, allowing preliminary estimations of the output characteristics of piezoelectric generators (PEG) of various configurations. The developed theories are based on the Hamiltonian principle, extended to the theory of electroelasticity. In the first part of the work, within the framework of the Euler-Bernoulli hypotheses, a model for a cantilever PEG was developed. The main model's peculiarity is the consideration of the structural features of cantilever PEGs. In the second part, a model was developed for multilayer stacked PEGs, where the energy generation process was considered as forced oscillations of an electroelastic rod. Solutions for both cases were carried out using the Kantorovich method. The adequacy of the theories obtained in both cases was verified by comparison with finite-element calculations.

### 11.1 Introduction

In recent years, research of piezoelectric transducers that convert mechanical energy into electrical energy has been actively developed. This type of transducers is called piezoelectric generator (PEG). The basic information about PEG, as well as the

---

Arkadiy Nikolaevich Soloviev

Don State Technical University, Gagarin sq., 1 &

I. I. Vorovich Institute of Mathematics, Mechanics and Computer Sciences, Southern Federal University, Milchakov st., 8A, Rostov-on-Don, Russia

e-mail: solovievarc@gmail.com

Valerii Alexandrovich Chebanenko

Southern Scientific Center of Russian Academy of Science, Chekhov st., 41, Rostov-on-Don, Russia

e-mail: valera.chebanenko@yandex.ru

Ivan Anatolievich Parinov

I. I. Vorovich Institute of Mathematics, Mechanics and Computer Sciences, Southern Federal University, Milchakov st., 8A, Rostov-on-Don, Russia

e-mail: parinov\_ia@mail.ru

problems arising in different development stages of energy harvesting devices, are given in the review papers Liu et al (2009); Liao and Sodano (2009); Han et al (2013); Chebanenko et al (2015), as well as in the monographs Erturk and Inman (2011); Elvin and Erturk (2013).

PEGs are divided into two configurations: stack and cantilever. Most of the works are devoted to the study of the characteristics of cantilever type PEGs. There are several ways of modeling PEGs: a mathematical model with lumped parameters, a mathematical model with distributed parameters and a finite element model. In Dutoit et al (2005); Dutoit and Wardle (2007); Adhikari et al (2009); Roundy and Wright (2004) the focus is on the construction of PEG models based on oscillations of a mechanical system with lumped parameters. The use of such systems is a convenient modeling approach, since it allows obtaining analytical dependencies between the output parameters of PEG (potential, power, etc.) and the electrical and the mechanical characteristics as well as the resistance of the external electric circuit.

The modeling with the use of lumped parameters provides initial representations on the problem, allowing one to use simple expressions for the description of the system. However, it is approximate and restricted to only one oscillation mode. This description does not take into account important aspects of the system.

Another type of modelling is distributed parameter modeling. Based on the Euler-Bernoulli hypotheses for beams, analytical solutions of the coupled problem have been obtained in Erturk and Inman (2008); Deng et al (2014); Soloviev et al (2017) for different configurations of cantilever type PEGs. They obtained explicit expressions for the output voltage on resistive electric loads and for console displacements. In addition, the authors studied in detail behavior of PEGs with short-circuited and open-circuited electric circuits, and the influence of piezoelectric coupling effects and flexoelectric effects Deng et al (2014); Soloviev et al (2017). Nevertheless, in these studies, the case where the piezoelectric element does not completely cover the substrate has not been considered. In Nechibvute et al (2012); Soloviev et al (2013); Solovyev and Duong (2016); Yu et al (2010) the finite element modeling of the different types of cantilever PEGs are discussed. The case where the piezoelectric element does not completely cover the substrate is easily solved by this modelling approach. Nevertheless, obtaining a semi-analytical solution for the case of incomplete covering of the substrate by a piezoelectric element is of interest.

Several papers are devoted to the investigation of stack-type PEGs based on finite element modelling Feenstra et al (2008); Baker et al (2005); Cavallier et al (2005); Shevtsov et al (2016); Solovyev et al (2016) and lumped parameter modeling Dutoit et al (2005); Zhao and Erturk (2014); Goldfarb and Jones (1999). Recently, attention has been directed to analytical studies of stack type generators. Due to the fact that the stack PEGs can carry high compression levels that allows their integration in different infrastructure objects (for example, transportable roads and rail-roads). Therefore, the necessity arises to develop mathematical models for prediction of output characteristics of PEGs.

Various models of stack type PEGs have been proposed in Zhao and Erturk (2014); Wang et al (2013). The model submitted in Zhao and Erturk (2014) depends on the initial experimental data and does not provide information about displacements. The

model proposed in Wang et al (2013) does not have such disadvantages. However, it is very tedious for analysis due to its recursive type

The above brief analysis of known works has shown that the problem of modeling PEG of various configurations with the help of analytical methods in full is not yet solved, although it is quite relevant.

## 11.2 Mathematical Modelling of PEG

### 11.2.1 The Boundary-Value Problem in the Theory of Electroelasticity

Consider a piezoelectric body of volume  $V$  bounded by a surface  $S$ , subjected to external loads and located in an electromagnetic field. External loads include mass forces  $X$  and surface loads  $p$ . The basic equations in the theory of electroelasticity are the equations of motion and the electric field equations (Vatulyan and Soloviev, 2009):

$$\begin{aligned}\sigma_{ji,j} + X_i &= \rho \ddot{u}_i, \\ D_{i,i} &= 0, \quad x \in V, t > 0,\end{aligned}\tag{11.1}$$

where  $\sigma_{ij}$  denotes the components of the stress tensor,  $X_i$  represents the components of the vector of mass forces,  $u_i$  is a components of the displacement vector,  $D_i$  stands for a component of the electric displacement vector. To these equations the constitutive laws (Vatulyan and Soloviev, 2009) are added:

$$\begin{aligned}\sigma_{ij} &= c_{ijkl}^E \varepsilon_{kl} - e_{kij} E_k, \\ D_i &= e_{ikl} \varepsilon_{kl} + \varepsilon_{ik}^S E_k,\end{aligned}\tag{11.2}$$

where  $c_{ijkl}^E$  is the tensor of elastic moduli measured at a constant electric field,  $\varepsilon_{kl}$  the components of the linear deformation tensor,  $e_{kij}$  the tensor of piezoelectric constants,  $E_k$  the components of the electric field vector, and  $\varepsilon_{ik}^S$  the tensor of dielectric constants measured at constant displacement. The components  $\varepsilon_{kl}$  and  $E_k$  are given by:

$$\begin{aligned}\varepsilon_{ij} &= \frac{1}{2} (u_{i,j} + u_{j,i}), \\ E_i &= -\varphi_{,i},\end{aligned}\tag{11.3}$$

where  $\varphi$  electrical potential.

Substituting (11.2) and (11.3) into (11.1) we obtain a system of coupled equations in which the unknowns are the displacements  $u_i$  and the electric potential  $\varphi$ :

$$\begin{aligned}c_{ijkl}^E u_{k,lj} + e_{kij} \varphi_{,kj} + X_i &= \rho \ddot{u}_i, \\ e_{ikl} u_{k,li} - \varepsilon_{ik}^S \varphi_{,ki} &= 0.\end{aligned}\tag{11.4}$$

The first equation describes the motion, and the second describes the quasistatic electric field.

Mechanical and electrical boundary conditions are added to these equations (Vatulyan and Soloviev, 2009). In the case when the electrodes are connected to an external circuit, the following condition must be added:

$$\begin{aligned} \varphi|_{S_E} &= v, \\ \iint_{S_E} \dot{D}_i n_i ds &= I, \end{aligned} \quad (11.5)$$

where  $S_E$  is the area of the electrode,  $v$  denotes the unknown potential, which is found from the second condition,  $I$  is the electric current. Thus, we have completed the formulation of the linear problem of electroelasticity.

### 11.2.2 Modeling of Cantilever Type PEGs

We consider the functional Soloviev and Vatulyan (2011)

$$\Pi = \iiint_V (H - X_i u_i) dV - \iint_S (p_i u_i + \sigma \varphi) dS, \quad (11.6)$$

where  $H$  is the electric enthalpy. The Hamiltonian principle, generalized to the theory of piezoelectricity, has the form

$$\delta \int_{t_1}^{t_2} (K - \Pi) dt = 0, \quad (11.7)$$

where  $K$  is the kinetic energy, and  $t_2 - t_1$  stands for the time interval.

Substituting (11.6) into (11.7), we obtain the following expression for the Hamiltonian principle:

$$\int_{t_1}^{t_2} dt \iiint_V (\delta K - \delta H) dV + \int_{t_1}^{t_2} dt \left[ \iiint_V X_i \delta u_i dV + \iint_S (p_i \delta u_i + \sigma \delta \varphi) dS \right] = 0. \quad (11.8)$$

The variation of the electric enthalpy in linear electroelasticity is:

$$\delta H = \sigma_{ij} \delta \varepsilon_{ij} - D_i \delta E_i. \quad (11.9)$$

The variation of the kinetic energy is

$$\delta \int_{t_1}^{t_2} K dt = -\rho \int_{t_1}^{t_2} dt \iiint_V \ddot{u}_i \delta u_i dV. \tag{11.10}$$

To these equations we add the constitutive equations (11.2).

Let us consider the case when there are no mass forces, external loads, and surface charge densities are applied. Then, taking into account the governing equations (11.2) and the equations (11.3), as well as the expressions for the variations (11.9) and (11.10), the Hamiltonian principle (11.8) takes the form

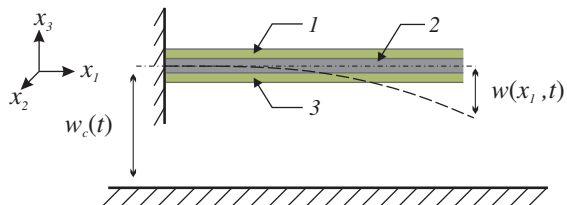
$$\int_{t_1}^{t_2} dt \iiint_V [-(c_{ijkl} u_{k,l} + e_{kij} \varphi_{,k}) \delta u_{i,j} - (e_{ikl} u_{k,l} - \varepsilon_{ik} \varphi_{,k}) \delta \varphi_{,i}] dV - \int_{t_1}^{t_2} dt \left[ \iiint_V \rho \ddot{u}_i \delta u_i dV + \iint_S \sigma \delta \varphi dS \right] = 0. \tag{11.11}$$

Let us consider the simplest bimorph design of cantilever PEG, presented in Fig. 11.1. The cantilever bimorph PEG consists of two piezoelements (Fig. 11.1 points 1 and 3) glued to the substrate (Fig. 11.1 point 2), which is clamped at one end. The thickness of the electrodes and the adhesive layer, due to the smallness of their values, can be neglected.

Since this construction is nothing more than a laminated beam, to simplify the problem, we introduce the Euler-Bernoulli hypotheses. The excitation of oscillations in PEGs, shown in Fig. 11.1, occurs through the movement of the base with respect to a certain plane. Therefore, the absolute displacement of the cantilever along the  $x_3$  coordinate will consist of displacement of the base  $w_c(t)$  and relative movement of the cantilever  $w(x_1, t)$ . Taking into account the foregoing, the displacement vector  $u$  takes the following form:

$$u = \left\{ -x_3 \frac{\partial w(x_1, t)}{\partial x_1}, 0, w(x_1, t) - w_c(t) \right\}^T. \tag{11.12}$$

The transition to the consideration of the one-dimensional case also simplifies the governing equations (11.2)



**Fig. 11.1** Bimorph cantilever PEG: 1 and 3 — piezoelements, 2 — substrate

$$\begin{aligned} \sigma_{11} &= c_{11}^{E*} \varepsilon_{11} - e_{31}^* E_3, \\ D_3 &= e_{31}^* \varepsilon_{11} + \varkappa_{33}^{S*} E_3, \end{aligned} \tag{11.13}$$

where the material constants are expressed as follows:

$$c_{11}^{E*} = \frac{1}{s_{11}^E}, \quad e_{31}^* = \frac{d_{31}}{s_{11}^E}, \quad \varkappa_{33}^{S*} = \varkappa_{33}^T - \frac{d_{31}^2}{s_{11}^E}. \tag{11.14}$$

Substituting (11.12) into (11.11), taking into account (11.13) we obtain:

$$\begin{aligned} &\int_{t_1}^{t_2} dt \iiint_V \left[ \left( -c_{11}^{E*} x_3^2 \frac{\partial^2 w(x_1, t)}{\partial x_1^2} + e_{31}^* x_3 \varphi_{,3} \right) \delta \left( \frac{\partial^2 w(x_1, t)}{\partial x_1^2} \right) \right] dV + \\ &\quad + \int_{t_1}^{t_2} dt \iiint_V \left[ \left( e_{31}^* x_3 \frac{\partial^2 w(x_1, t)}{\partial x_1^2} + \varkappa_{33}^{S*} \varphi_{,3} \right) \delta \varphi_{,3} \right] dV + \tag{11.15} \\ &\quad + \int_{t_1}^{t_2} dt \left[ \iiint_V \{ -\rho (\ddot{w}(x_1, t) - \ddot{w}_c(t)) \delta w(x_1, t) \} dV + \iint_S \sigma \delta \varphi dS \right] = 0. \end{aligned}$$

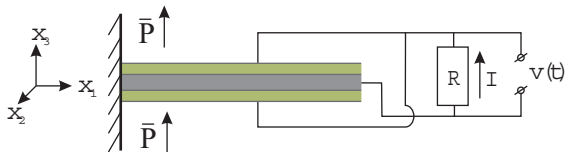
In the PEG under investigation, the polarization vector is directed along the  $x_3$  coordinate axis (see Fig. 11.2). Electrodes are applied to large sides perpendicular to the  $x_3$  axis, and therefore, it makes sense to consider only the components of the electric potential along the axis  $x_3$ .

Since the piezoelectric element is assumed to be thin and there are no free charges inside, we suggest that the electric field is distributed linearly along the thickness of the piezoceramic element:

$$\varphi = \frac{v(t)x_3}{h}, \quad \varphi_{,3} = \frac{v(t)}{h}, \tag{11.16}$$

where  $v(t)$  denotes the potential difference between the upper and lower electrode of the piezoelectric element,  $h$  is the thickness of the piezoelectric element.

Taking into account (11.16), the expression (11.15) takes the form:



**Fig. 11.2** Wiring diagram of PEG



$$\begin{aligned}
& \int_{t_1}^{t_2} dt \iiint_V \left[ \left( -c_{11}^{E*} x_3^2 \frac{\partial^2 w(x_1, t)}{\partial x_1^2} + e_{31}^* x_3 \frac{v(t)}{h} \right) \delta \left( \frac{\partial^2 w(x_1, t)}{\partial x_1^2} \right) \right] dV + \\
& \quad + \int_{t_1}^{t_2} dt \iiint_V \left[ \left( \frac{e_{31}^* x_3}{h} \frac{\partial^2 w(x_1, t)}{\partial x_1^2} + \varepsilon_{33}^{S*} \frac{v(t)}{h^2} \right) \delta(v(t)) \right] dV + \quad (11.17) \\
& \quad + \int_{t_1}^{t_2} dt \left[ \iiint_V \{ -\rho(\ddot{w}(x_1, t) - \ddot{w}_c(t)) \delta w(x_1, t) \} dV + \iint_S \frac{\sigma x_3}{h} \delta v(t) dS \right] = 0.
\end{aligned}$$

To solve the problem of forced oscillations of cantilever bimorph PEGs, we will use the Kantorovich method (Kerr and Alexander, 1968). We represent the relative displacements of a beam as a series expansion:

$$w(x_1, t) = \sum_{i=1}^N \eta_i(t) \phi_i(x_1), \quad (11.18)$$

where  $N$  is the number of modes considered,  $\eta_i(t)$  are the unknown generalized coordinates,  $\phi_i(x_1)$  denotes the known test functions that satisfy the boundary conditions.

Substituting the representation (11.18) in (11.17) and equating the coefficients with independent variations of  $\delta v$  and to zero  $\delta \eta$ , we obtain a system of differential equations describing the forced oscillations of the bimorph PEG connected to the resistor:

$$\begin{aligned}
M\ddot{\eta}(t) + D\dot{\eta}(t) + K\eta(t) - \Theta v(t) &= p, \\
C_p v(t) + \Theta^T \eta(t) &= -q, \quad (11.19)
\end{aligned}$$

where  $D = \mu M + \gamma K$  is the Rayleigh-type damping matrix, and the remaining coefficients are:

$$\begin{aligned}
 C_p &= \frac{bL}{h} \varepsilon_{33}^*, \\
 M_{ij} &= \int_0^L m\phi_i(x_1)\phi_j(x_1)dx_1, \\
 K_{ij} &= \int_0^L EI\phi_i''(x_1)\phi_j''(x_1)dx_1, \\
 p_i &= -\ddot{w}_c(t) \int_0^L m\phi_i(x_1)dx_1, \\
 \theta_i &= \int_0^L J_p\phi_i''(x_1)dx_1,
 \end{aligned}
 \tag{11.20}$$

where  $C_p$  is the electric capacity,  $M_{ij}$  denotes the elements of the mass matrix,  $K_{ij}$  are the elements of the stiffness matrix,  $\theta_i$  represents the elements of the electromechanical coupling vector,  $p_i$  are the elements of the effective mechanical load vector,  $m$  is the specific weight,  $EI$  stands for the bending stiffness,  $M$  denotes the proof mass.

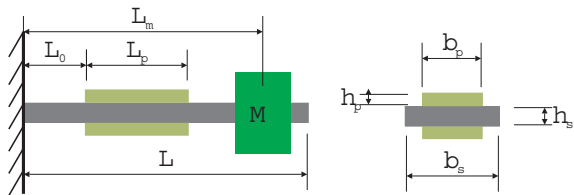
Differentiating with time the second equation in system (11.19), taking into account the fact that  $\dot{q} = I$ , we will satisfy condition (11.5). Using Ohm’s law, we obtain the equation for the electric circuit in the following form:

$$C_p\dot{v}(t) + \Theta^T\dot{\eta}(t) + \frac{v(t)}{R} = 0,
 \tag{11.21}$$

where  $R$  is the electrical resistance (the resistor on which the voltage is measured see Fig. 11.2).

Figure 11.1 shows the simplest case of a bimorph cantilever PEG, but in reality the production of such a structure is rather difficult. It becomes necessary to take into account such design features as incomplete covering of the piezoelectric element of the substrate. In addition, to adjust the resonance frequency and increase the output power, proof mass is often used. In view of the foregoing, we will consider the PEG shown in Fig. 11.3. Hereinafter, the subscripts  $p, s$  and  $m$  will denote that the variable corresponds to the piezoelectric element, substrate and mass, respectively.

**Fig. 11.3** Bimorph cantilever PEG with piezoelement and proof mass displaced relative to the clamp



The search for a solution for this design is associated with the need to divide the beam into four segments. The first segment begins at the clamp and contains to the beginning of the piezoelement. The second segment is the part of the substrate covered with a piezoelectric element. The third segment is the free part of the beam, following the piezoelement up to the attachment point of the proof mass (mass is considered as a point). The fourth segment starts right after the proof mass and contains to the end of the beam. Taking into account the division of the beam described above, the piecewise-defined function  $\phi_i(x_1)$  takes the following form:

$$\phi_i(x_1) = \begin{cases} \phi_i^{(1)}(x_1), & x_1 \leq L_0 \\ \phi_i^{(2)}(x_1), & L_0 < x_1 \leq L_p + L_0 \\ \phi_i^{(3)}(x_1), & L_p + L_0 < x_1 \leq L_m \\ \phi_i^{(4)}(x_1), & x_1 > L_m \end{cases}, \quad (11.22)$$

where  $\phi_i^{(1)}$ ,  $\phi_i^{(2)}$ ,  $\phi_i^{(3)}$ ,  $\phi_i^{(4)}$  correspond to the modes of oscillation of the first, second, third and fourth segments, respectively. We write the solution in a general form for each part of the beam:

$$\begin{aligned} \phi_i^{(1)}(x_1) &= a_{1,i} \sin(\beta_i x_1) + a_{2,i} \cos(\beta_i x_1) + a_{3,i} \sinh(\beta_i x_1) + a_{4,i} \cosh(\beta_i x_1) \\ \phi_i^{(2)}(x_1) &= a_{5,i} \sin(\beta_i x_1) + a_{6,i} \cos(\beta_i x_1) + a_{7,i} \sinh(\beta_i x_1) + a_{8,i} \cosh(\beta_i x_1) \\ \phi_i^{(3)}(x_1) &= a_{9,i} \sin(\beta_i x_1) + a_{10,i} \cos(\beta_i x_1) + a_{11,i} \sinh(\beta_i x_1) + a_{12,i} \cosh(\beta_i x_1) \\ \phi_i^{(4)}(x_1) &= a_{13,i} \sin(\beta_i x_1) + a_{14,i} \cos(\beta_i x_1) + a_{15,i} \sinh(\beta_i x_1) + a_{16,i} \cosh(\beta_i x_1). \end{aligned} \quad (11.23)$$

Next, we write down the boundary conditions:

$$\phi_i^{(1)}(0) = 0, \phi_i^{\prime(1)}(0) = 0, \phi_i^{\prime\prime(4)}(L) = 0, \phi_i^{\prime\prime\prime(4)}(L) = 0. \quad (11.24)$$

In addition, we will need the conjugation conditions for the beam segments:

$$\begin{aligned}
\phi_i^{(1)}(L_0) &= \phi_i^{(2)}(L_0) \\
\phi_i^{\prime(1)}(L_0) &= \phi_i^{\prime(2)}(L_0) \\
\phi_i^{\prime\prime(1)}(L_0) &= \frac{EI^{(2)}}{EI^{(1)}} \phi_i^{\prime\prime(2)}(L_0) \\
\phi_i^{\prime\prime\prime(1)}(L_0) &= \frac{EI^{(2)}}{EI^{(1)}} \phi_i^{\prime\prime\prime(2)}(L_0) \\
\phi_i^{(2)}(L_0 + L_p) &= \phi_i^{(3)}(L_0 + L_p) \\
\phi_i^{\prime(2)}(L_0 + L_p) &= \phi_i^{\prime(3)}(L_0 + L_p) \\
\phi_i^{\prime\prime(2)}(L_0 + L_p) &= \frac{EI^{(1)}}{EI^{(2)}} \phi_i^{\prime\prime(3)}(L_0 + L_p) \\
\phi_i^{\prime\prime\prime(2)}(L_0 + L_p) &= \frac{EI^{(1)}}{EI^{(2)}} \phi_i^{\prime\prime\prime(3)}(L_0 + L_p) \\
\phi_i^{(3)}(L_m) &= \phi_i^{(4)}(L_m) \\
\phi_i^{\prime(3)}(L_m) &= \phi_i^{\prime(4)}(L_m) \\
\phi_i^{\prime\prime(3)}(L_m) &= \phi_i^{\prime\prime(4)}(L_m) \\
\phi_i^{\prime\prime\prime(3)}(L_m) &= \phi_i^{\prime\prime\prime(4)}(L_m) - \alpha \beta^4 \phi_i^{(3)}(L_m) \\
\alpha &= \frac{M}{mL},
\end{aligned} \tag{11.25}$$

where  $EI^{(1)}$  and  $EI^{(2)}$  are bending stiffness of segments.

Adding a proof mass to the model requires considering its effect on the system of equations (11.19), since it is an additional inertial load that affects the kinetic energy. Taking into account the proof mass, the expressions for some components of (11.20) change as follows:

$$\begin{aligned}
M_{ij} &= \int_0^L m \phi_i(x_1) \phi_j(x_1) dx_1 + M \phi_i(L_m) \phi_j(L_m), \\
p_i &= -\ddot{w}_c(t) \int_0^L m \phi_i(x_1) dx_1 + M \phi_i(L_m).
\end{aligned} \tag{11.26}$$

Satisfying the boundary conditions, we obtain a homogeneous system of 16 equations with 16 unknowns:

$$\Lambda = \begin{pmatrix} a_{1,1} & \cdots & a_{1,16} \\ \vdots & \ddots & \vdots \\ a_{16,1} & \cdots & a_{16,16} \end{pmatrix}, \tag{11.27}$$

The specific weight  $m(x_1)$ , for the case under consideration, is calculated as follows:

$$m(x_1) = \rho_s A_s + 2\rho_p A_p \left( H(x_1 - L_0) - H(x_1 - L_0 - L_p) \right), \quad (11.28)$$

where  $H(x_1)$  is the Heaviside function.

The bending stiffness  $EI$  for the model under consideration is calculated as follows:

$$EI(x_1) = c_p \left[ \iint_{S_{p1}} x_3^2 dS + \iint_{S_{p2}} x_3^2 dS \right] \left( H(x_1 - L_0) - H(x_1 - L_0 - L_p) \right) + c_s \iint_{S_s} x_3^2 dS, \quad (11.29)$$

where  $c_p$  and  $c_s$  are elastic constants of piezoelements and substrate, respectively,  $S_{p1}$ ,  $S_{p2}$  and  $S_s$  are cross-section areas of upper and lower piezoelements and substrate, respectively. The function  $J_p(x_1)$  is equal to

$$J_p(x_1) = \frac{e_{31}^*}{h_p} \left( \iint_{S_{p1}} x_3 dS + \iint_{S_{p2}} x_3 dS \right) \left( H(x_1 - L_0) - H(x_1 - L_0 - L_p) \right). \quad (11.30)$$

After all the preliminary steps have been taken, we proceed directly to solving the system of equations (11.19). We assume that the excitation is harmonic:

$$\begin{aligned} w_c(t) &= \tilde{w}_c e^{i\omega t} \\ p &= \tilde{p} e^{i\omega t}. \end{aligned} \quad (11.31)$$

Then we seek the solution in the form

$$\begin{aligned} \eta(t) &= \tilde{\eta} e^{i\omega t} \\ v(t) &= \tilde{v} e^{i\omega t}. \end{aligned} \quad (11.32)$$

A tilde above a variable indicates the amplitude. After substituting (11.31) and (11.32), the system of equations (11.19) takes the form

$$\begin{aligned} \left[ -\omega^2 M + i\omega(\mu M + \gamma K) + K \right] \tilde{\eta} - \Theta \tilde{v} &= \tilde{p}, \\ \left( i\omega C_p + \frac{1}{R} \right) \tilde{v} + i\omega \Theta^T \tilde{\eta} &= 0. \end{aligned} \quad (11.33)$$

From the second equation in system (11.33) we obtain  $\tilde{v}$

$$\tilde{v} = -\frac{i\omega \Theta^T \tilde{\eta}}{i\omega C_p + \frac{1}{R}}. \quad (11.34)$$

Then we substitute (11.34) into the first equation of the system (11.32) and express  $\tilde{\eta}$

$$\tilde{\eta} = \left[ -\omega^2 M + i\omega(\mu M + \gamma K) + K + \frac{i\omega \Theta \Theta^T}{i\omega C_p + \frac{1}{R}} \right]^{-1} \tilde{p}. \quad (11.35)$$

Substituting expression for  $\tilde{\eta}$  back into (11.34), we get a new expression for  $\tilde{v}$

$$\tilde{v} = -\frac{i\omega\Theta^T}{i\omega C_p + \frac{1}{R}} \left[ -\omega^2 M + i\omega(\mu M + \gamma K) + K + \frac{i\omega\Theta\Theta^T}{i\omega C_p + \frac{1}{R}} \right]^{-1} \tilde{p}. \quad (11.36)$$

The obtained expressions (11.35) and (11.36) are solutions of the system of equations (11.33).

### 11.2.2.1 Numerical Experiment

We will consider a bimorph cantilever PEG, manufactured using the PKR-7M ceramic, which has the geometric and physical properties given in Table 11.1. The excitation of the system is given by a harmonic displacement of the base  $w_c = \tilde{w}_c e^{i\omega t}$ , whose amplitude is  $\tilde{w}_c = 0.1$  mm, and the coefficients of the modal damping are equal  $\xi_1 = \xi_2 = 0.02$ .

The first step in the research is the construction of amplitude-frequency characteristics (AFC) of displacements, potentials arising on electrodes, etc. Figure 11.4 shows the frequency response of the voltage, on the external electrodes, and the displacement of the end of the beam. In the literature (Erturk and Inman, 2011; Elvin and Erturk, 2013), the main performance characteristics of PEGs are the dependence of voltage and power on electrical resistance. Here are dependencies of the main characteristics of the PEG on the electrical resistance. All characteristics were investigated at the first resonant frequency.

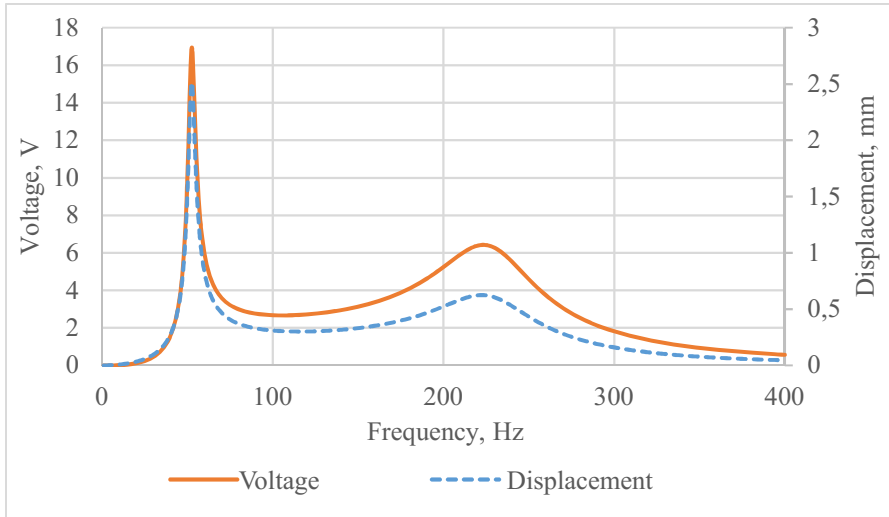
Figure 11.5 is a typical dependence of the output electric voltage on electrical resistance. With increasing resistance, the voltage rises to a certain limiting value. This limit value corresponds to the open circuit condition.

The output power is calculated by the formula:

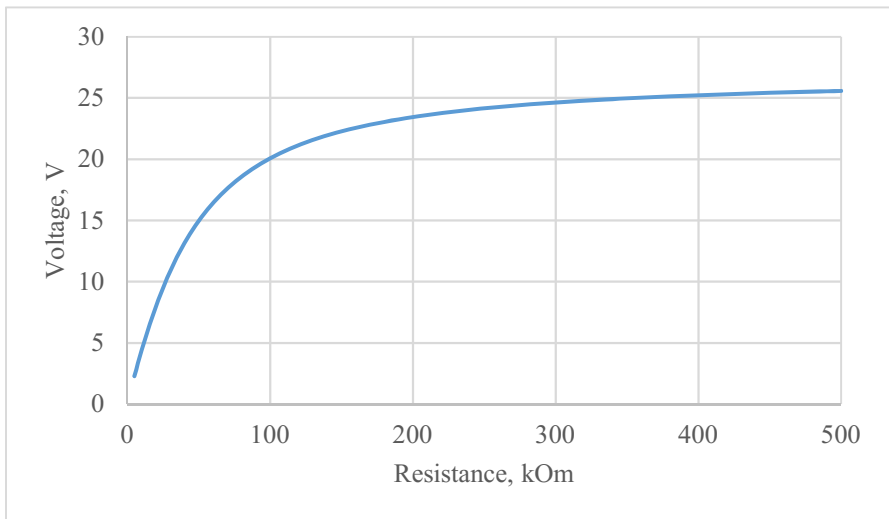
$$P = \frac{v^2}{R}. \quad (11.37)$$

Table 11.1: PEG Parameters

	Substrate	Piezoelement
Geometrical dimensions ( $L_0 \times b \times h$ )	110×10×1 mm <sup>3</sup>	56×6×0.5 mm <sup>3</sup>
Density ( $\rho$ )	1650 kg/m <sup>3</sup>	8000 kg/m <sup>3</sup>
The Young's modulus and Poisson's ratio ( $E, \nu$ )	15 GPa and 0.12	—
Elastic compliance ( $s_{11}^E$ )	—	17.5×10 <sup>-12</sup> Pa
Relative permittivity ( $\epsilon_{33}^S/\epsilon_0$ )	—	5000
Piezoelectric module ( $d_{31}$ )	—	-350 pC/N



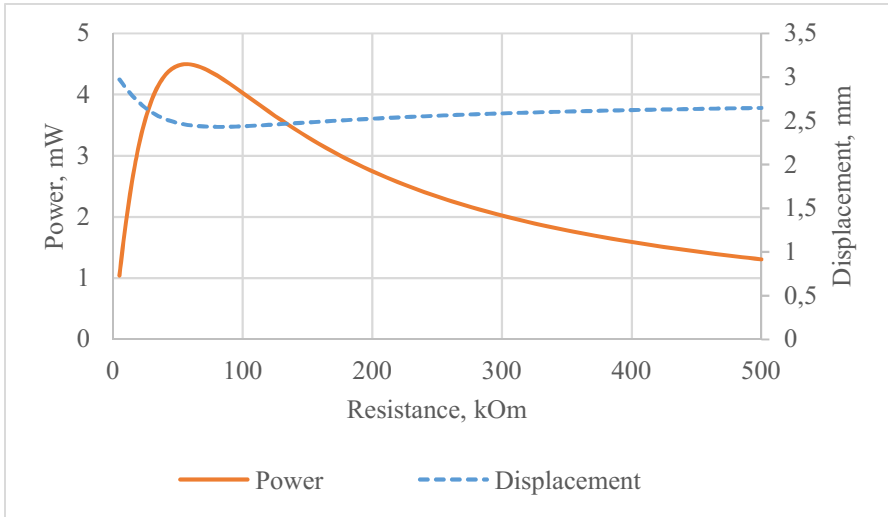
**Fig. 11.4:** Amplitude-frequency response of the voltage and the displacement of the beam’s end



**Fig. 11.5:** Dependence of voltage on electrical resistance

In addition to the dependence of the output power on the electrical resistance, we shall construct the dependence of the displacement of the end of the beam on the electrical resistance.

Figure 11.6 shows a typical dependence of output power on electrical resistance. This dependence for power is characterized by the presence of a maximum, the



**Fig. 11.6:** Dependencies of output power and displacement of the beam’s end from resistance

position of which depends on the electrical capacity of the piezoelements and the excitation frequency of the PEG. The dependence of the displacement of the free end of the beam on the electrical resistance has a minimum, the position of which coincides with the maximum of power. This indicates that the conversion of mechanical energy into electrical energy, at a given value of electrical resistance, is maximized.

### 11.2.2.2 Comparison with Finite Element

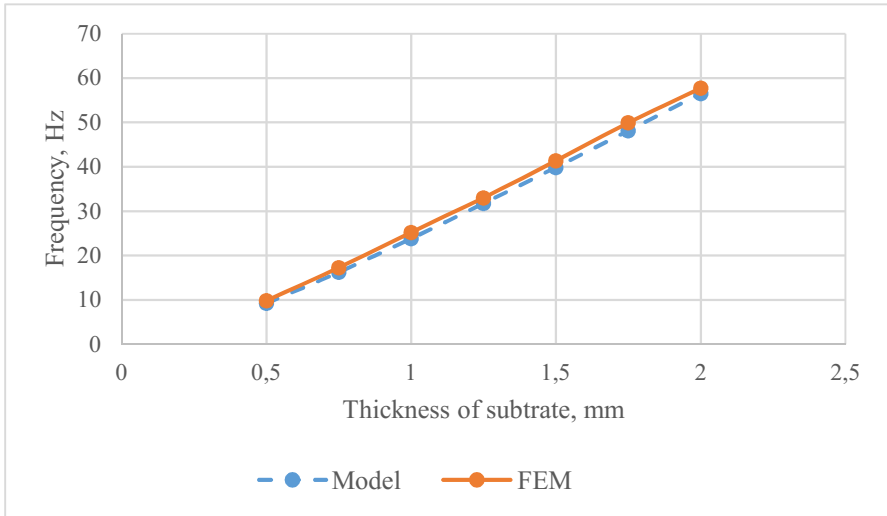
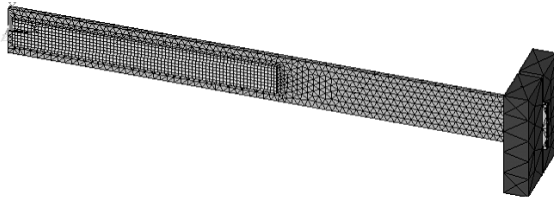
In the literature there are mathematical models of PEGs with lumped parameters. They are convenient for describing the stack type PEGs. In the case of generators of the cantilever type, they give inaccurate results. There is work in which corrective coefficients for these models are given, but they are suitable for the case when the piezoelectric element completely covers the surface of the substrate. In the case of incomplete coverage, preliminary experiments are required to identify the parameters of the five model parameters. This is the obstacle to design. Therefore, we compare the obtained mathematical model with a finite element model (cf. Fig. 11.7).

Soloviev et al (2013) deals with the finite element modeling of the laboratory model of cantilever PEG. The calculation was made for the cantilever model described at the beginning of previous paragraph. The value of the proof mass was 5 g.

Measurements were made in conditions of an open circuit when the cantilever base was excited by a displacement of 0.1 mm. Dependencies for the first resonant frequencies and the output electric potential were obtained, depending on the thick-



**Fig. 11.7** Finite element model in ANSYS

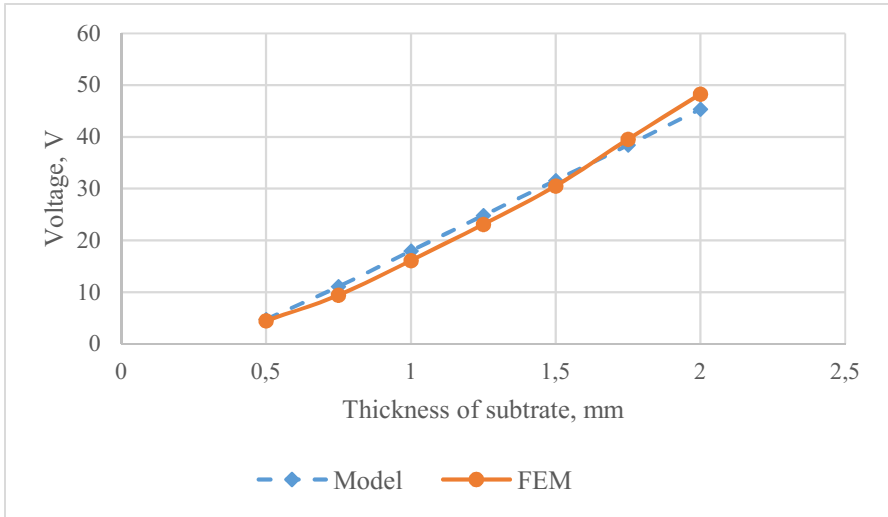


**Fig. 11.8:** Dependence of the first resonance frequency on the thickness of the substrate: dashed line — model, solid — finite element simulation

ness of the substrate. We perform similar calculations and compare the obtained data.

As can be seen from Fig. 11.8 with increasing substrate thickness, the value of the first resonant frequency also increases. The difference between the finite element calculation and the model does not exceed 5%, which indicates a sufficient accuracy of the constructed model.

From Fig. 11.9, it follows that as the thickness of the substrate increases, the value of the output electric potential increases. The difference between the finite element calculation and the model does not exceed 7%, which indicates a sufficient accuracy of the constructed model.



**Fig. 11.9:** Dependence of the output electric potential on the thickness of the substrate: dashed line — model, solid line — finite element simulation

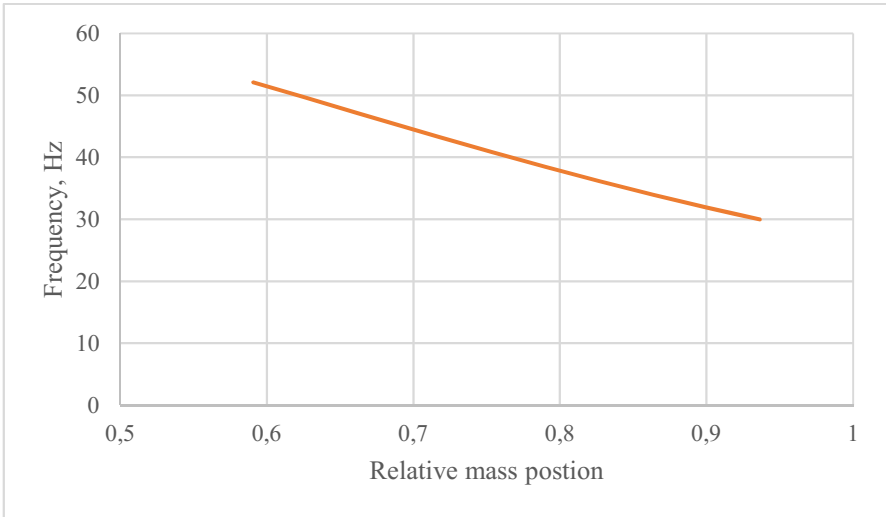
### 11.2.2.3 Parametric Studies

Next, we will investigate the dependencies of the main performance characteristics of cantilever PEGs (resonance frequency, beam tip’s displacement, output voltage and power) on the position of the proof mass, and the position of the piezoelement.

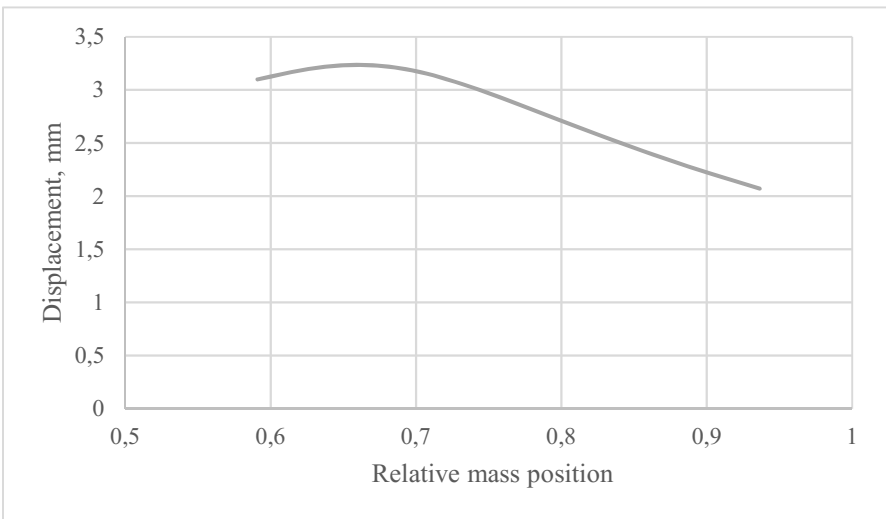
Consider the effect of the position of the proof mass  $M$  of 3 g on the performance of the PEG. As the main parameter we will use the relative position of the proof mass, i.e. normalized with respect to the coordinate of the end of the substrate.

As can be seen from Fig. 11.10 with increasing distance between clamped end and the proof mass, the first resonance frequency of the beam decreases. From Fig. 11.11 we can conclude that at some position of the proof mass, the maximum displacement of the end of the beam is achieved. From Fig. 11.12 it follows that at some position of the proof mass, there are local maxima of the output voltage and the maximum of the output power (with the optimum electrical resistance). Since the power directly depends on the electrical resistance, it makes sense to consider the value of the resistance at which power is maximal i.e. optimum electrical resistance. Figure 11.13 demonstrates that the closer the proof mass is to the end of the beam, the higher the value of the optimum electrical resistance. Analyzing the obtained data, we can conclude that there is a certain value of the position of the proof mass, at which the maximum output power is reached.

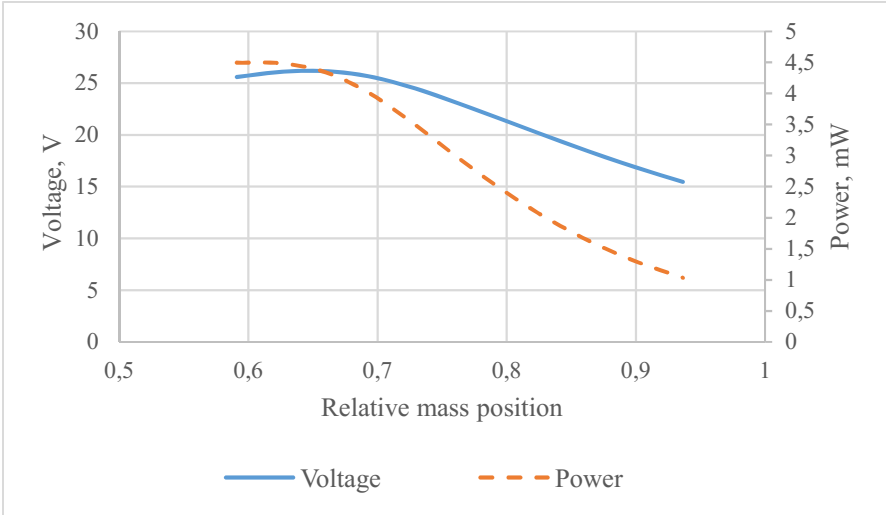
Next, we consider the case when the length of the piezoelement is fixed. We will investigate the effect of repositioning of the piezoelectric element relative to the clamped end on the performance of the PEG, taking into account the presence of the proof mass of 3 g. As the main parameter, we will use the relative offset, i.e.



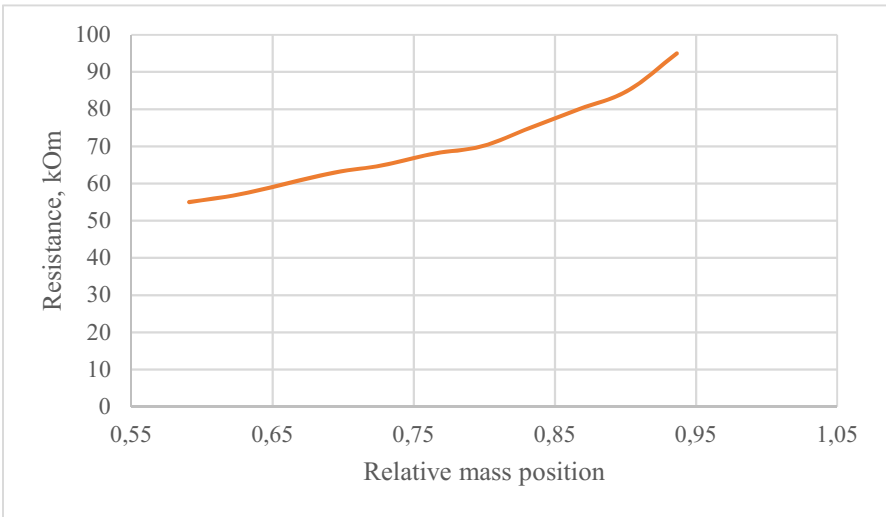
**Fig. 11.10:** Dependence of the first resonance frequency on the position of the proof mass



**Fig. 11.11:** Dependence of the displacement of the beam's end on the position of the proof mass

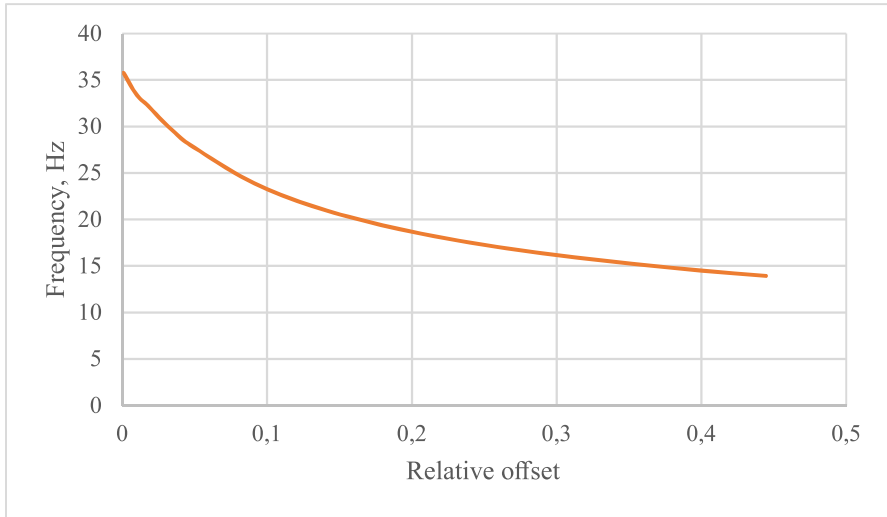


**Fig. 11.12:** Dependence of the maximum output voltage and power on the position of the proof mass



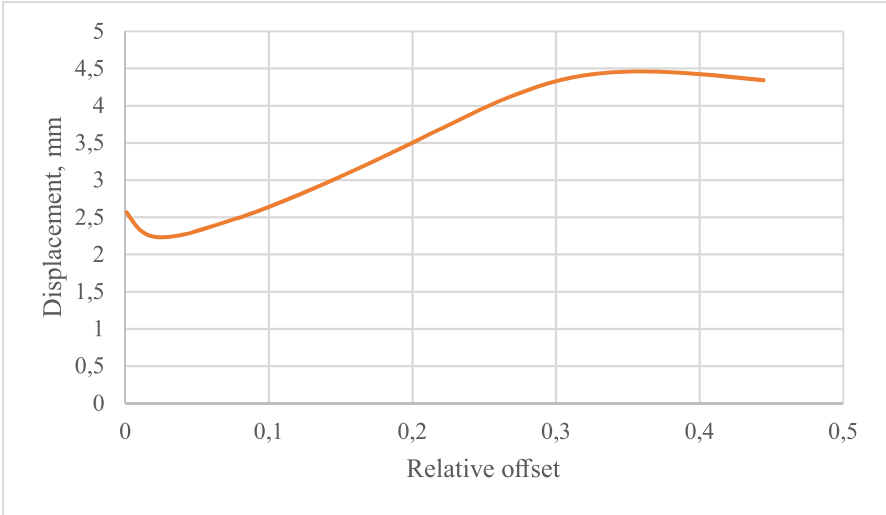
**Fig. 11.13:** Dependence of the resistance value at which the maximum power is reached, from the position of the proof mass

normalized with respect to the length of the substrate. This parameter is responsible for the coordinate of the beginning of the piezoelement. From Fig. 11.14 it can be seen that as the position of piezoelectric element becomes more indented, the first resonance frequency decreases monotonically. Figure 11.15 shows that with

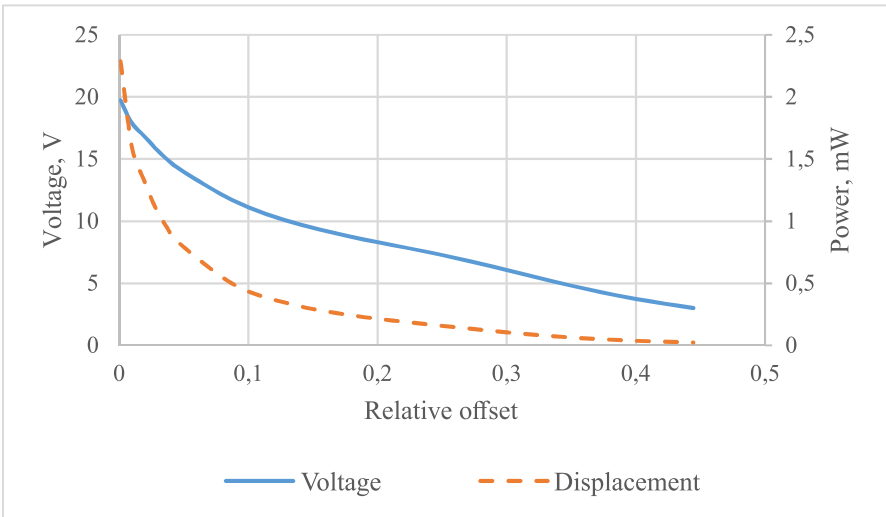


**Fig. 11.14:** Dependence of the first resonance frequency on the offset from clamp

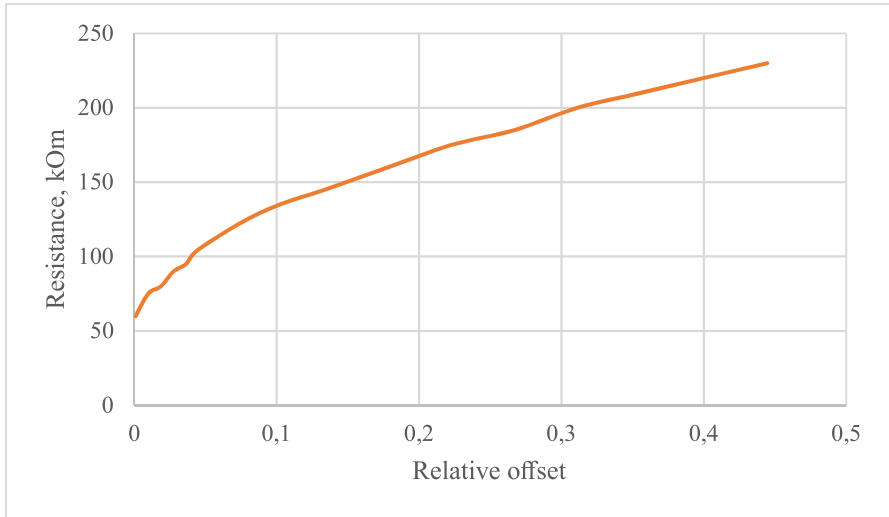
increasing offset of the piezoelectric element from the clamp displacement of the end of the beam decreases slightly at a small interval, and then increases. This may indicate that the bending stiffness of the beam near the clamping zone decreases. In Fig. 11.16 it is shown that with an increase in the piezoelectric element's offset from the clamped end, the output voltage drops noticeably. Moreover, the maximum voltage is observed when the offset is minimal. The maximum output power demonstrates similar behavior. The dependence of the value of the electrical resistance, at which the maximum power is reached, on the amount of offset of the piezoelectric element from the clamped end, depicted in Fig. 11.17, has a monotonous increasing character. The obtained data on the influence of the position of the piezoelectric element on the output characteristics of the PEG indicate that it is most advantageous from the point of view of obtaining maximum power to position the piezoelectric element near the clamp.



**Fig. 11.15:** Dependence of the displacement of the beam’s end on the position of the piezoelectric element



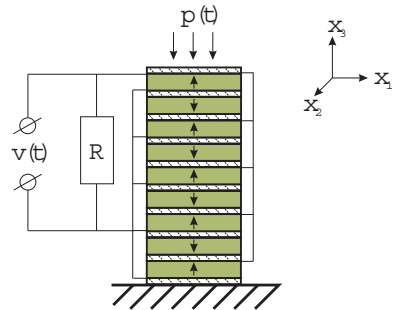
**Fig. 11.16:** Dependence of the maximum output voltage and power on the amount of indentation of the piezoelectric element from the termination



**Fig. 11.17:** Dependence of the resistance value, at which the maximum power is reached, on the offset from clamp

### 11.2.3 Modelling of Stack Type PEG

The derivation of the equations describing the behavior of the stack-type PEG, shown in Fig. 11.18, is also based on the Hamiltonian principle given earlier. This PEG is subjected to an external mechanical loading  $p(t)$  along the coordinate axis  $x_3$ .



**Fig. 11.18** Stack PEG scheme

Therefore, repeating the calculations (11.6)–(11.11), we obtain the following equation:

$$\int_{t_1}^{t_2} dt \iiint_V \left[ - (c_{ijkl} u_{k,l} + e_{kij} \varphi_{,k}) \delta u_{i,j} - (e_{ikl} u_{k,l} - \vartheta_{ik} \varphi_{,k}) \delta \varphi_{,i} \right] dV - \quad (11.38)$$

$$- \int_{t_1}^{t_2} dt \left[ \iiint_V \rho \ddot{u}_i \delta u_i dV + \iint_S (p_i \delta u_i + \sigma \delta \varphi) dS \right] = 0,$$

where, in contrast to (11.11), external loads  $p_i$  are conserved.

Let us consider the construction of PEGs of the stack type, shown in Fig. 11.18. The simplest stacked PEG consists of several piezoceramic plates connected to each other (either glued at the production stage, or stapled mechanically). The thickness of the electrodes can, due to the smallness of its values, be neglected.

After introducing the assumption of small deformations, the problem reduces to forced longitudinal vibrations of the rod along the  $x_3$  coordinate. Taking into account the foregoing, the displacement vector  $u$  takes the following form:

$$u = \{0, 0, w(x_3, t)\}^T. \quad (11.39)$$

The transition to the consideration of the one-dimensional case also simplifies the governing equations (11.2):

$$\begin{aligned} \sigma_{11} &= c_{33}^{E*} \varepsilon_{33} - e_{33}^* E_3, \\ D_3 &= e_{33}^* \varepsilon_{33} + \vartheta_{33}^{S*} E_3, \end{aligned} \quad (11.40)$$

where the material constants are expressed as follows:

$$c_{33}^{E*} = \frac{1}{s_{33}^E}, \quad e_{33}^* = \frac{d_{33}}{s_{33}^E}, \quad \vartheta_{33}^{S*} = \vartheta_{33}^T - \frac{d_{33}^2}{s_{33}^E}. \quad (11.41)$$

Substituting (11.39) into (11.38), taking into account (11.40), we obtain:

$$\begin{aligned} & \int_{t_1}^{t_2} dt \iiint_V \left[ \left( -c_{33}^{E*} \frac{\partial w(x_3, t)}{\partial x_3} + e_{33}^* \varphi_{,3} \right) \delta \left( \frac{\partial w(x_3, t)}{\partial x_3} \right) \right] dV + \\ & + \int_{t_1}^{t_2} dt \iiint_V \left[ \left( e_{33}^* \frac{\partial w(x_3, t)}{\partial x_3} + \vartheta_{33}^{S*} \varphi_{,3} \right) \delta \varphi_{,3} \right] dV + \quad (11.42) \\ & + \int_{t_1}^{t_2} dt \left[ \iiint_V \{ -\rho \ddot{w}(x_3, t) \delta w(x_3, t) \} dV + \iint_S (p_3 \delta w(x_3, t) + \sigma \delta \varphi) dS \right] = 0. \end{aligned}$$

In the studied PEG, the polarization vector is directed along the coordinate axis  $x_3$ . The electrodes are applied to the long sides of piezoceramic plates perpendicular to the axis  $x_3$ . They are connected in parallel (see Fig. 11.18). Accordingly, it makes



sense to consider only the components of the electric potential gradient along the axis  $x_3$ .

Since the piezoelements are assumed to be thin and there are no free charges inside, we assume that the electric field is distributed linearly along the thickness of each piezoceramic element:

$$\varphi = \frac{v(t)x_3}{h}, \quad \varphi_{,3} = \frac{v(t)}{h}, \quad (11.43)$$

where  $v(t)$  is the potential difference between the upper and lower electrode of the piezoelectric element,  $h$  denotes the thickness of the single piezoelectric layer. Taking into account (11.43), the expression (11.41) takes the form:

$$\begin{aligned} & \int_{t_1}^{t_2} dt \iiint_V \left[ \left( -c_{33}^{E*} \frac{\partial w(x_3, t)}{\partial x_3} + e_{33}^* \frac{v(t)}{h} \right) \delta \left( \frac{\partial w(x_3, t)}{\partial x_3} \right) \right] dV + \\ & + \int_{t_1}^{t_2} dt \iiint_V \left[ \left( \frac{e_{33}^*}{h} \frac{\partial w(x_3, t)}{\partial x_3} + \varepsilon_{33}^{S*} \frac{v(t)}{h^2} \right) \delta v(t) \right] dV + (11.44) \\ & + \int_{t_1}^{t_2} dt \left[ \iiint_V \{ -\rho \ddot{w}(x_3, t) \delta w(x_3, t) \} dV + \iint_S \left( p_3 \delta w(x_3, t) + \frac{\sigma_{x_3}}{h} \delta v(t) \right) dS \right] = 0. \end{aligned}$$

To solve the problem of forced longitudinal oscillations of stacked PEGs, we will also use the Kantorovich method. Further, repeating the calculations similarly to the derivation of equations (11.18)–(11.21), we obtain a system of differential equations describing the forced oscillations of the stacked PEG connected to the resistor:

$$\begin{aligned} M\ddot{\eta}(t) + D\dot{\eta}(t) + K\eta(t) - \Theta v(t) &= p, \\ C_p \dot{v}(t) + \Theta^T \dot{\eta}(t) + \frac{v(t)}{R} &= 0. \end{aligned} \quad (11.45)$$

Coefficients of (11.45) are equal to:

$$\begin{aligned}
C_p &= N_p \frac{bl}{h} \varepsilon_{33}^{S*}, \\
M_{ij} &= \int_0^H m \phi_i(x_3) \phi_j(x_3) dx_3, \\
K_{ij} &= \int_0^H Y \phi_i'(x_3) \phi_j'(x_3) dx_3, \\
p_i &= -p_0 \phi_i(x_3), \\
\theta_i &= \int_0^H J_p \phi_i'(x_3) dx_3, \\
Y &= \iint_S c_{33}^{E*} dS, \\
J_p &= \iint_S \frac{e_{33}^*}{h} dS,
\end{aligned} \tag{11.46}$$

where  $N_p$  is the number of piezoelectric layers,  $b$ ,  $l$  and  $h$  are the width, length and height of single piezoelement,  $H$  denotes the height of the whole stack,  $Y$  stands for the rigidity of the cross section of the stack.

Now it remains to find a set of test functions satisfying the boundary conditions. The search for test functions satisfying the boundary conditions is connected to the solution of the eigenvalue problem for the rod. We solve the problem of free vibrations of the rod shown in Fig. 11.18. Let us write out the solution in general form:

$$\phi_i(x_3) = a_{1,i} \sin(\beta_i x_3) + a_{2,i} \cos(\beta_i x_3). \tag{11.47}$$

Boundary conditions in the considered case are:

$$\phi_i(0) = 0, \quad \phi_i'(H) = 0. \tag{11.48}$$

We can find the eigenvalues  $\beta_i$  and coefficients  $a_i$ .

After this we obtain a homogeneous system of 4 equations with 4 unknowns which is given in matrix form:

$$\Lambda = \begin{pmatrix} a_{1,1} & \dots & a_{1,4} \\ \vdots & \ddots & \vdots \\ a_{4,1} & \dots & a_{4,4} \end{pmatrix} = 0. \tag{11.49}$$

This system has nonzero solutions when its determinant is zero. The determinant of the system yields a characteristic equation that needs to solve in order to compute the eigenvalues  $\beta_i$ :

$$1 + \cos \beta_i \cosh \beta_i = 0. \tag{11.50}$$

Equation (11.50) is transcendental. Therefore we will solve it with numerical methods. Knowing  $\beta_i$ , we can find the coefficients  $a_i$  for the required number of vibration modes  $N$ .

For the case of harmonic loading, obtaining the solution of the system (11.45) is analogous to the solution for harmonic loading of the cantilever PEG (11.31)-(11.36). Here, the loading of an arbitrary shape, in particular the impulse form, will be considered.

To consider a load  $p(t)$  having an arbitrary shape, we represent its amplitude values with a set of discrete values, and then interpolate it using Fourier series:

$$p(t) \cong m_0 + \sum_{k=1}^N \left[ m_k \cos\left(k \frac{2\pi t}{T}\right) + n_k \sin\left(k \frac{2\pi t}{T}\right) \right], \tag{11.51}$$

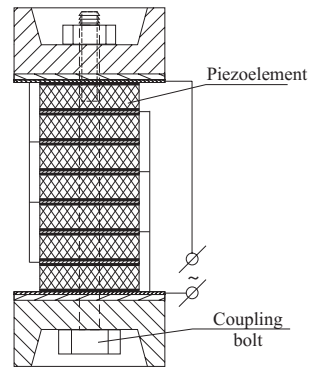
where  $m_0$  is the average value,  $T$  denotes the loading duration,  $n_k, m_k$  are Fourier coefficients.

$$m_0 = \frac{1}{T} \int_0^T p(t) dt, \quad m_k = \frac{2}{T} \int_0^T p(t) \cos\left(k \frac{2\pi t}{T}\right) dt, \quad n_k = \frac{2}{T} \int_0^T p(t) \sin\left(k \frac{2\pi t}{T}\right) dt. \tag{11.52}$$

Then, we substitute the obtained approximation (11.51) into (11.45) and solve the system numerically by the Runge-Kutta method.

### 11.2.3.1 Parametric Studies

As input parameters of the model, we use the initial data from the experiment. We will consider stack PEG, made using disk elements from ceramics PZT-19. The model of PEG considered in Fig. 11.19, is a stack of piezoelements of the ring type, connected together by a coupling bolt. Above and below are metal discs that distribute the



**Fig. 11.19** Schematic model of the stacked PEG

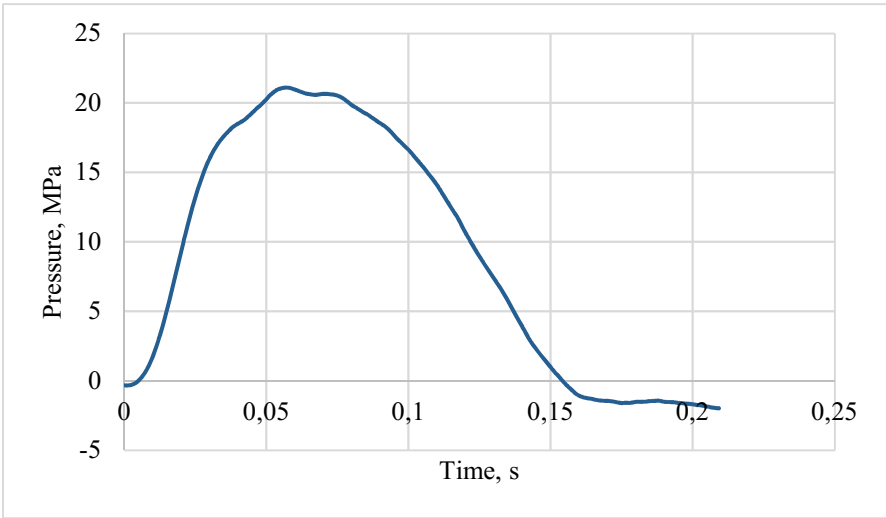
applied load evenly over the section, and protect against direct mechanical action

on the piezoelements. The metal discs are followed by an insulating spacer, which prevents electrical shorting. Between the piezoelements are located electrodes. They are connected in parallel. In order to take into account the influence of the metal core (clamping bolt) in the cross section of the PEG, we add to the rigidity of the cross section  $Y$  one more term:

$$Y = \iint_{S_p} c_{33}^{E*} dS + \iint_{S_c} c_c dS , \tag{11.53}$$

where  $S_p$  and  $S_c$  are the areas of the section of the stack and bolt, respectively,  $c_{33}^{E*}$  and  $c_c$  represent the modulus of elasticity of the piezoceramic and steel, respectively.

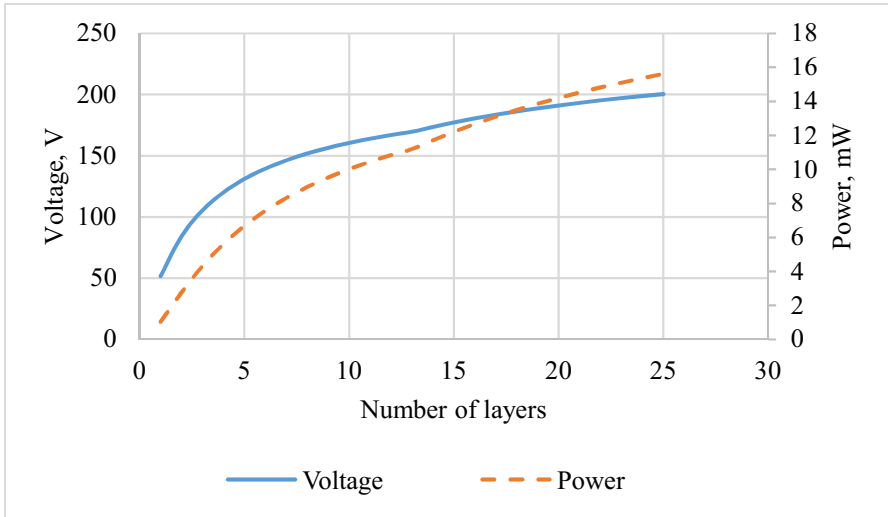
This PEG will be subjected to a pulsed loading, the shape of which is shown in Fig. 11.20. The main geometric and physical properties of the generator model



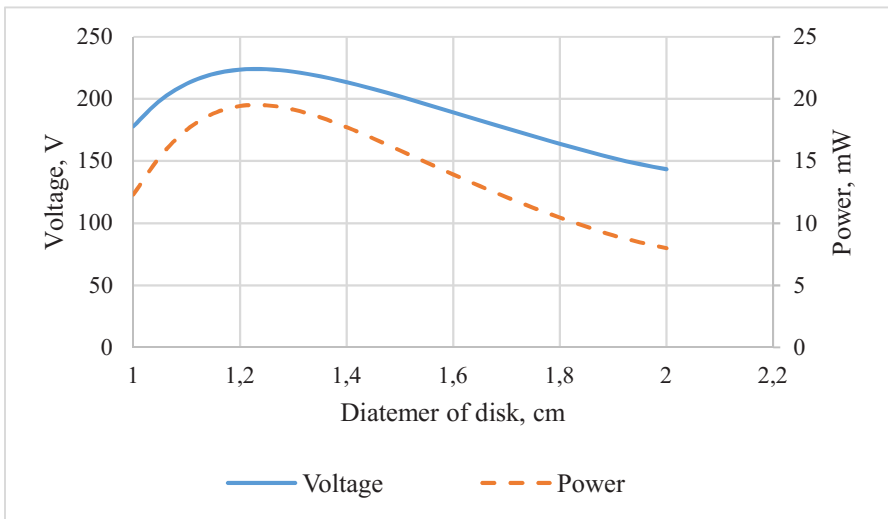
**Fig. 11.20:** Shape of the loading force

under study are given in Table 11.2. The modal damping coefficients are equal  $\xi_1 = \xi_2 = 0.02$ .

Investigations of the dependence of the main characteristics of the stacked PEG (output voltage and power) on various parameters (geometric sizes of piezoelements and the number of piezoelements) were carried out. Figure 11.21 shows the dependence of the maximum output voltage and the power on the number of layers of PEG. The geometry of the layers is assumed to be unchanged. From the above dependence, it follows that with an increase in the number of layers, the output voltage and power increase. The behavior of the obtained dependencies is similar to the behavior of the square root function. The dependence shown in Fig. 11.22, demonstrates the effect of the outer diameter of the disk on the maximum output voltage and power. It



**Fig. 11.21:** Dependence of output voltage and output power of stacked PEG on the number of layers

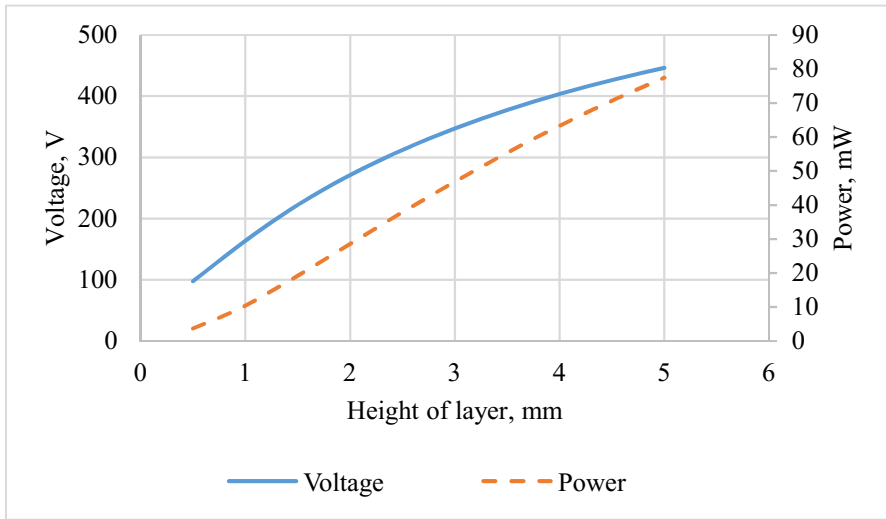


**Fig. 11.22:** Dependence of the output voltage and output power of the stacked PEG on the diameter of the piezoelectric cell

Table 11.2: PEG Parameters

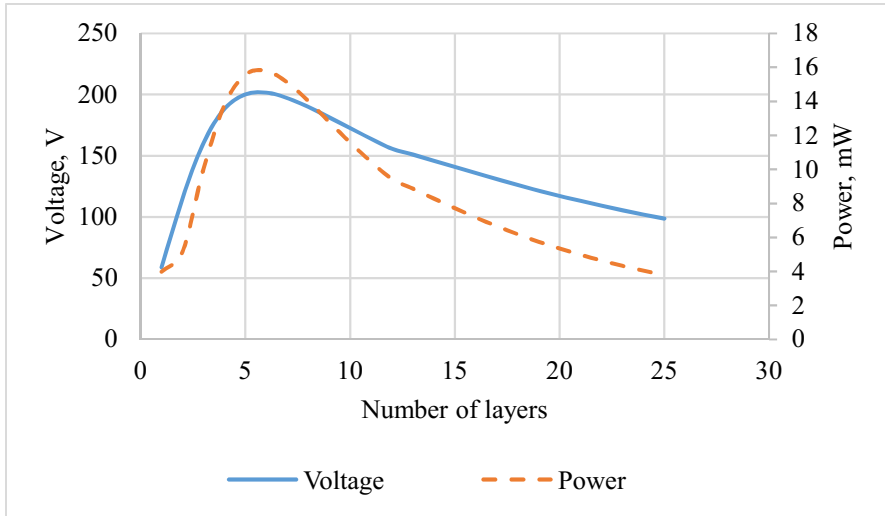
	Core	Piezoement
Geometrical dimensions( $D \times d \times h$ )	6 mm	$18 \times 8 \times 1 \text{ mm}^3$
Density ( $\rho$ )	$7800 \text{ kg/m}^3$	$7500 \text{ kg/m}^3$
The Young's modulus and Poisson's ratio ( $E, \nu$ )	210 GPa and 0.3	—
Elastic compliance ( $s_{33}^E$ )	—	$17 \times 10^{-12} \text{ Pa}$
Relative permittivity ( $\epsilon_{33}^S / \epsilon_0$ )	—	1500
Piezoelectric module ( $d_{33}$ )	—	-307 pC/N

follows from the figure that with an increase in the external diameter of the disk, the output voltage and power increase to a certain value, after which the recession occurs. From Fig. 11.23, which shows the dependence of the maximum output voltages and power on the height of each layer, it follows that as the height of the layers increases, the output voltages and power increase. This dependence is close to linear.



**Fig. 11.23:** Dependence of output voltage and output power of stacked PEG on the height of each layer

In addition, the influence of the number of layers on the output characteristics of PEG was investigated at a fixed total height of the entire piezostack. The results are shown in Fig. 11.24. It turned out that there is a number of layers, in which the output characteristics will be maximum.



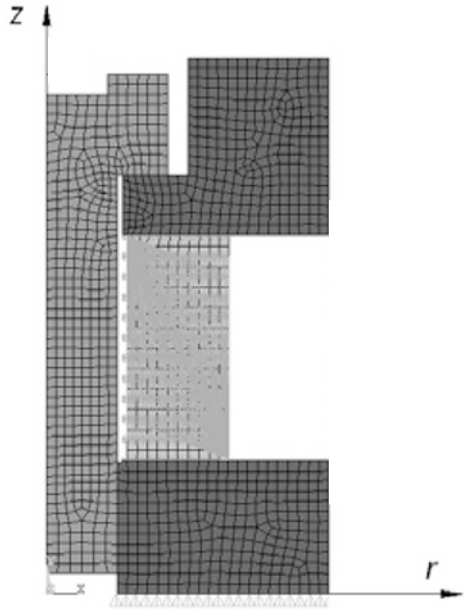
**Fig. 11.24:** Dependence of the output voltage and output power of the stacked PEG on the number of layers, provided that the height of the entire packet remains unchanged

### 11.2.3.2 Comparison With Finite Element

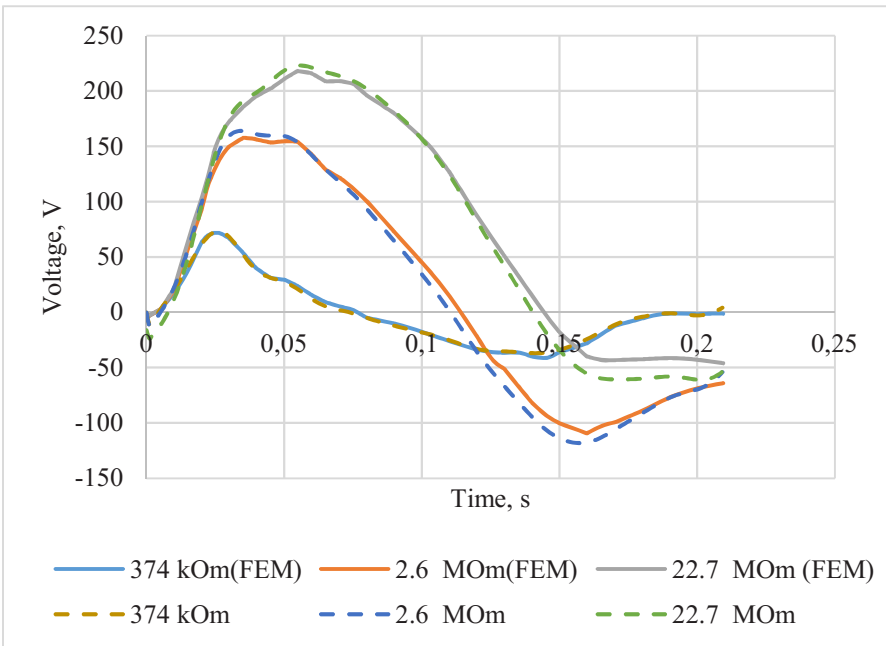
Let us compare the derived model for stack PEG with finite-element calculations. In Solovyev et al (2016), a finite element simulation of the stack PEG impulse loading experiment was carried out. In the ANSYS package, the generator model was constructed. The model is presented in Fig. 11.25. In the course of the experiment, a pulse excitation applied to the PEG was recorded, which was shown earlier in Fig. 11.20. This impulse was used in ANSYS as an excitation force. Calculation of the output electric potential was made with three values of electrical resistance: 374 kOhm, 2.6 MOhm, 22.7 MOhm. A comparison of the results obtained with finite element modeling and the analytical model is shown in Fig. 11.26. From Fig. 11.26 it follows that the model obtained coincides, with a sufficient degree of accuracy, with the finite-element calculation. The average error did not exceed 5%.

## 11.3 Summary

In this work, applied numerical theories were constructed, allowing preliminary estimations of the output characteristics of the PEG of various configurations. The developed theories are based on the Hamiltonian principle, extended to the theory of electroelasticity. The solution was carried out using the Kantorovich method. In the first part of the work, within the framework of the Euler-Bernoulli hypotheses, a



**Fig. 11.25** Axisymmetric finite element model of PEG



**Fig. 11.26:** The time dependence of the electrical potential for various electrical resistances: dashed line — model, continuous line — finite element simulation



model of a cantilever PEG was created. The main model's peculiarity is the consideration of structural features. In the second part, a model was developed for multilayer stacked PEG, where the energy generation process was considered as forced oscillations of an electroelastic rod. The adequacy of the obtained theories in both cases was verified by comparison with finite-element modelling. The characteristics of PEGs (resonant frequencies, output voltage and power) are calculated depending on geometric parameters such as the dimensions, location of piezoelements, the number of piezolayers, etc. The results are presented in the form of graphs of possible options for optimal parameters of PEG.

**Acknowledgements** This work has been supported by the Government Contract (project part 9.1001.2017/PCh, by the Russian Foundation for the Basic Research Grant 16-58-52013 MNT-a and by Russian State Mission 007-01114-16 PR (project 0256-2015-0074).

## References

- Adhikari S, Friswell MI, Inman DJ (2009) Piezoelectric energy harvesting from broadband random vibrations. *Smart Materials and Structures* 18(11):115,005
- Baker J, Roundy S, Wright P (2005) Alternative geometries for increasing power density in vibration energy scavenging for wireless sensor networks. In: 3rd International Energy Conversion Engineering Conference, American Institute of Aeronautics and Astronautics
- Cavallier B, Berthelot P, Nouira H, Foltete E, Hirsinger L, Ballandras S (2005) Energy harvesting using vibrating structures excited by shock. In: *IEEE Ultrasonics Symposium*, IEEE, vol 2, pp 943–945
- Chebanenko VA, Akopyan VA, Parinov IA (2015) Piezoelectric generators and energy harvesters: Modern state of the art. In: Parinov IA (ed) *Piezoelectrics and Nanomaterials: Fundamentals, Developments and Applications*, Nova Science Publishers, New York, pp 243–277
- Deng Q, Kammoun M, Erturk A, Sharma P (2014) Nanoscale flexoelectric energy harvesting. *International Journal of Solids and Structures* 51(18):3218–3225
- Dutoit NE, Wardle BL (2007) Experimental verification of models for microfabricated piezoelectric vibration energy harvesters. *AIAA journal* 45(5):1126–1137
- Dutoit NE, Wardle BL, Kim SG (2005) Design considerations for MEMS-scale piezoelectric mechanical vibration energy harvesters. *Integrated Ferroelectrics* 71(1):121–160
- Elvin N, Erturk A (2013) *Advances in Energy Harvesting Methods*. Springer, Heidelberg
- Erturk A, Inman DJ (2008) On mechanical modeling of cantilevered piezoelectric vibration energy harvesters. *Journal of Intelligent Material Systems and Structures* 19(11):1311–1325
- Erturk A, Inman DJ (2011) *Piezoelectric Energy Harvesting*. John Wiley and Sons, Ltd., New York
- Feenstra J, Granstrom J, Sodano H (2008) Energy harvesting through a backpack employing a mechanically amplified piezoelectric stack. *Mechanical Systems and Signal Processing* 22(3):721–734
- Goldfarb M, Jones LD (1999) On the efficiency of electric power generation with piezoelectric ceramic. *Trans ASME J Of Dyn Syst Measurement and Control* 121:566–571
- Han B, Vassilaras S, Papadias CB, Soman R, Kyriakides MA, Onoufriou T, Nielsen RH, Prasad R (2013) Harvesting energy from vibrations of the underlying structure. *Journal of Vibration and Control* 19(15):2255–2269
- Kerr AD, Alexander H (1968) An application of the extended kantovorich method to the stress analysis of a clamped rectangular plate. *Acta Mechanica* 6(2-3):180–196
- Liao Y, Sodano HA (2009) Structural effects and energy conversion efficiency of power harvesting. *Journal of Intelligent Material Systems and Structures* 20(5):505–514

- Liu Y, Tian G, Wang Y, Lin J, Zhang Q, Hofmann HF (2009) Active piezoelectric energy harvesting: General principle and experimental demonstration. *Journal of Intelligent Material Systems and Structures* 20(5):575–585
- Nechibvute A, Chawanda A, Luhanga P (2012) Finite element modeling of a piezoelectric composite beam and comparative performance study of piezoelectric materials for voltage generation. *ISRN Mater Science* ID 921361:11 pages
- Roundy S, Wright PK (2004) A piezoelectric vibration based generator for wireless electronics. *Smart Materials and Structures* 13(5):1131
- Shevtsov S, Akopyan V, Rozhkov E, Chebanenko V, Yang CC, Jenny Lee CY, Kuo CX (2016) Optimization of the electric power harvesting system based on the piezoelectric stack transducer. In: Parinov IA, Chang SH, Topolov VY (eds) *Advanced Materials: Manufacturing, Physics, Mechanics and Applications*, Springer International Publishing, Cham, pp 639–650
- Soloviev AN, Vatulyan AO (2011) Non-classical biem in electroelasticity and inverse coefficient problem. In: Parinov IA (ed) *Piezoceramic Materials and Devices*, Nova Science Publishers, New York, pp 1–51
- Soloviev AN, Parinov IA, Duong LV, Yang CC, Chang SH, Lee JCY (2013) Analysis of finite element models for piezoelectric devices of energy harvesting. In: Parinov IA, Chang SH (eds) *Physics and Mechanics of New Materials and their Applications*, Nova Science Publishers, New York, pp 335–352
- Soloviev AN, Chebanenko VA, Zakharov YN, Rozhkov EV, Parinov IA, Gupta VK (2017) Study of the output characteristics of ferroelectric ceramic beam made from non-polarized ceramics pzt-19: Experiment and modeling. In: Parinov IA, Chang SH, Jani MA (eds) *Advanced Materials: Techniques, Physics, Mechanics and Applications*, Springer International Publishing, Cham, pp 485–499
- Solovyev AN, Duong LV (2016) Optimization for the harvesting structure of the piezoelectric bimorph energy harvesters circular plate by reduced order finite element analysis. *International Journal of Applied Mechanics* 8(3):1650,029
- Solovyev AN, Duong LV, Akopyan VA, Rozhkov EV, Chebanenko VA (2016) Numerical simulation of the experiment on pulsed excitation of stack type piezoelectric generator. *Vestnik DSTU* 1(84):19–26
- Vatulyan AO, Soloviev AN (2009) *Direct and inverse problems for homogeneous and inhomogeneous elastic and electroelastic bodies (in Russ.)*. SFEDU Publishers, Rostov-on-Don
- Wang J, Shi Z, Han Z (2013) Analytical solution of piezoelectric composite stack transducers. *Journal of Intelligent Material Systems and Structures* 24(13):1626–1636
- Yu S, He S, Li W (2010) Theoretical and experimental studies of beam bimorph piezoelectric power harvesters. *J of Mechanics of Mater and Structures* 5(3):427–445
- Zhao S, Erturk A (2014) Deterministic and band-limited stochastic energy harvesting from uniaxial excitation of a multilayer piezoelectric stack. *Sensors and Actuators A: Physical* 214:58–65

## Chapter 12

# Modeling of Dielectric Elastomers Accounting for Electrostriction by Means of a Multiplicative Decomposition of the Deformation Gradient Tensor

Elisabeth Staudigl, Michael Krommer, and Alexander Humer

**Abstract** Nonlinear modeling of inelastic material behavior by a multiplicative decomposition of the deformation gradient tensor is quite common for finite strains. The concept has proven applicable in thermoelasticity, elastoplasticity, as well as for the description of residual stresses arising in growth processes of biological tissues. In the context of advanced materials, the multiplicative decomposition of the deformation gradient tensor has been introduced within the fields of electro-elastic elastomers, shape-memory alloys as well as piezoelectric materials. In the present paper we apply this multiplicative approach to the special case of dielectric elastomers in order to account for the electrostrictive effect. Therefore, we seek to include the two main sources of electro-mechanical coupling in dielectric elastomers. These are elastostatic forces acting between the electric charges and electrostriction due to intramolecular forces of the material. In particular we intend to study the significance of electrostriction for the particular case of dielectric elastomers, in the form of a thin layer with two compliant electrodes.

## 12.1 Introduction

In this work we study constitutive modeling within the field of nonlinear electro-elasticity, with special application to dielectric elastomer films. Dielectric elastomers are capable of a mechanical response upon application of an external electric field, which is why they are commonly termed electro-active polymers (EAPs). These

---

Elisabeth Staudigl · Michael Krommer  
Institute of Mechanics and Mechatronics, TU Wien, Getreidemarkt 9, A-1060 Vienna, Austria  
e-mail: elisabeth.staudigl@tuwien.ac.at, michael.krommer@tuwien.ac.at

Alexander Humer  
Institute of Technical Mechanics, Johannes Kepler University Linz, Altenbergerstraße 69, A-4040  
Linz, Austria  
e-mail: alexander.humer@jku.at

types of actuators are predicted to have a large variety of promising application fields, due to their characteristic to resist large strains while having a low stiffness and low density. These features, make them especially prone to smart or bio-inspired structural technologies e.g. artificial muscles. An EAP is typically assembled of a dielectric film sandwiched between two electrodes. When applying a potential difference to the electrode layers, they attract each other due to Coulomb forces, causing a pressure on the surface of the dielectric film, enforcing a deformation. Practical applications of this effect have been developed rather intensively, see examples such as soft and flexible keyboards (Xu et al, 2016) or artificial caterpillars demonstrated by various groups e.g. in SPIE (2017).

However, the full theoretical background of the deformation is yet not fully exploited. It has been reported, that the electric field might also interact with the dielectric layer as it gets polarized. This effect is reasoned in the micro-structure of the material, where different polarization mechanisms prevail. Therefore, we seek to include the two main sources of electro-mechanical coupling in dielectric elastomers as pointed out in Mehnert et al (2016). Polarization on the molecular level, called electrostriction, poses a process for which a full geometric nonlinear electro-mechanically coupled theory is necessary in order to model the impact of this effect adequately. Among the first theoretical works referring to electrostriction we refer to Zhao and Suo (2008), while earlier Zhenyi et al (1994) already presented experimental results.

Typical candidates for the material choice of dielectrics are silicon rubber and polyurethane elastomers, while special graft elastomers have been developed in the 1990s whose improved properties among high elastic-modulus count also the capability of nonlinear behavior at large strain regimes; therefore, a geometrical nonlinear framework is also necessary to model the mechanical behavior accurately. Theoretical works on the field of nonlinear electro-mechanical coupling date back into the 1950s. Toupin (1956) was among the first to address this field. A comprehensive presentation has later been given by Landau et al (2013); Maugin and Eringen (2012). Within the framework of nonlinear elasticity the book of Bonet and Wood (1997), has proven to be a handy reference, while special emphasis on the electric-coupling procedure can be found in the works of Dorfmann and Ogden (2005); Bustamante et al (2009a); Dorfmann and Ogden (2017) as well as in McMeeking and Landis (2004).

Constitutive modeling techniques incorporating the multiplicative decomposition of the deformation gradient tensor are quite common for finite strains. The concept has proven applicable in thermoelasticity, elastoplasticity, as well as for the description of residual stresses arising in growth processes of biological tissues (Lubarda, 2004). In the context of advanced materials, electro-elastic elastomers have been investigated in Skatulla et al (2012), shape-memory alloys in Arghavani et al (2010) and piezoelectric materials in Humer and Krommer (2015). A geometric nonlinear formulation on the constitutive modeling for the coupled electrostrictive-viscoelastic problem has been published by Ask et al (2012) using an additive decomposition of the free energy function. However, the comparison to experimental results, published by Diaconu and Dorohoi (2005); Diaconu et al (2006), suggest to put still further

investigations into this field. Bortot et al (2016); Ask et al (2015) made already use of the multiplicative decomposition of the deformation gradient tensor in their viscoelastic constitutive relation. Applications within the fields of electro-elastic coupled fields can be found in Zäh and Miehe (2015), and with special application to piezoelectricity in the works of Humer and Krommer (2015). Special interest is put on the physical bounds of the actuation at high strain magnitude. Phenomena called pull in or ceasing instability currently limit further increase in the actuation strains, as either imperfections or localization effects lead to the breakdown of the EAP. Analytical efforts to investigate these phenomena were made in Xu et al (2010), making use of the Hessian. They derived analytical expressions for the critical strain values, above which no stable stretch configuration exists any more.

This work is organized into five sections. First, we are going to introduce the basic electro-elastic coupled balance equations of continuum-mechanics, following Maugin and Eringen (2012) and the recent work of Humer et al (2017). The relevant electric quantities are reviewed and the Maxwell equations of electrostatics for dielectric materials are addressed. Within the second part, we introduce these quantities into the continuum mechanic theory in order to derive the spatial balance equations rendering the basis for the electro-mechanically coupled theory. With the spatial balance equations at hand, the material counterparts are obtained by which some preliminary constitutive relations are derived shortly, in order to demonstrate the general approach to the constitutive modeling framework. We close this part by introducing the incompressibility constraint using a Lagrange multiplier, which allows the physical interpretation of an electrostatic force. Higher order effects are then incorporated into the theory in Sect. 12.3. There, we extend the constitutive model by introducing the multiplicative decomposition of the deformation gradient. Results of the derivations show, that additional electro-mechanical coupling stresses increase the electro-elastic entanglement while still the overall physical relations can be retained. Section 12.4 provides additional background on the electrostrictive effect, unveiling the approach to include this effect into the constitutive model. In Sect. 12.5, we finally apply the resulting equations to the simple example of a homogeneous in-plane deformation of a plate. We choose this example on the one hand, as it allows for a comparison to experimental results, while on the other hand theoretical investigations allow for generalized statements on the impact of the electrostrictive effect.

## 12.2 Electromechanical Coupling by Electrostatic Force

### 12.2.1 Kinematics in Nonlinear Elasticity

Beginning with the kinematic quantities required in the framework of nonlinear continuum mechanics, we consider a material body, whose material points in the undeformed reference configuration  $V_r$  are denoted by upper case letters  $\mathbf{X}$ . Its bound-

ary is referred as  $\partial V_r$ . We consider only quasi-static, time independent deformation, which lead to a deformed current configuration, denoted by  $V$  with the boundary  $\partial V$ , and assume that a mapping function  $\chi$  exists, such that  $\mathbf{x} = \chi(\mathbf{X})$  uniquely maps the position vector of the material point into the current configuration  $\mathbf{x}$ , see Fig. 12.1. Hence the deformation gradient tensor  $\mathbf{F}$  can be defined with respect to  $\chi$  given by,

$$\mathbf{F} = \nabla_0 \mathbf{x} = \nabla_0 \chi(\mathbf{X}). \tag{12.1}$$

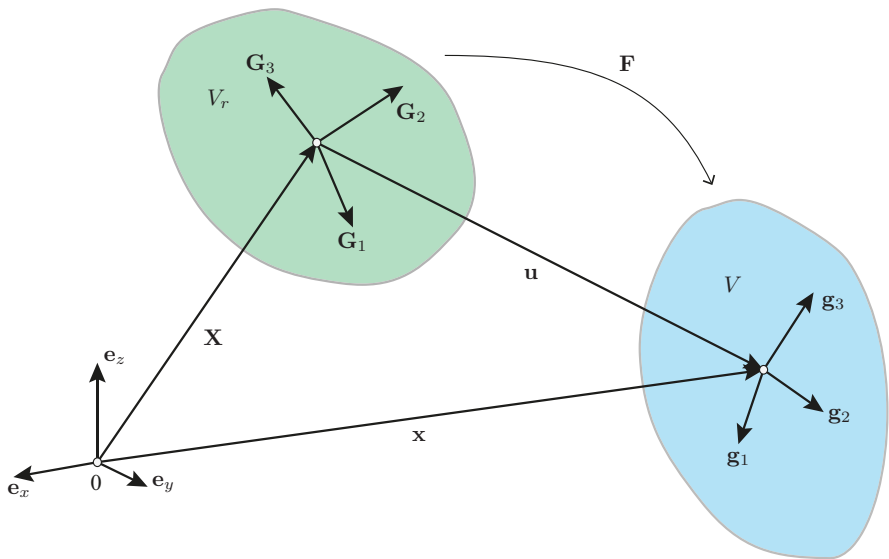
$\nabla_0$  is the differential operator with respect to the reference configuration. The volume change throughout the configuration is defined by  $J = \det \mathbf{F}$  assuming  $J > 0$  holds.

Knowing the deformation gradient tensor  $\mathbf{F}$  allows to introduce the nonlinear strain measures

$$\mathbf{B} = \mathbf{F} \cdot \mathbf{F}^T, \quad \mathbf{C} = \mathbf{F}^T \cdot \mathbf{F}, \tag{12.2}$$

where  $\mathbf{B}$  is referred to as the left, and  $\mathbf{C}$  as the right Cauchy-Green Tensor.

Orientation and position of a deformed surface element are defined by the unit outward normal vector  $\mathbf{n}$  on  $\partial V$ , while  $\mathbf{t}$  is the force per unit area on  $\partial V$ , which allows to introduce the second rank Cauchy stress tensor  $\boldsymbol{\sigma}$  through  $\boldsymbol{\sigma}^T \cdot \mathbf{n} = \mathbf{t}$ .



**Fig. 12.1:** Field mapping of a general deformable body.

### 12.2.2 Electro-Elastic Balance Laws

In order to derive the balance equations for the electro-elastic continuum, we start by defining the dependent variables within the micro-continuum, which upon statistical averaging over the continuum volume, lead to the relevant expressions of the macro-continuum. Within the continuum mechanic framework, only the quantities arising when applying external fields have to be taken into account, internal field quantities are incorporated by the concepts of electro-mechanical stress and internal energy. Upon application of an external electric field  $\mathbf{e}$ , charges  $q$  are encouraged to move slightly forming dipole-moments within the continuum; this process called polarization  $\mathbf{p}$ , see Fig. 12.2, is reflected by electrostatic volume force  $\mathbf{f}^E$ , the corresponding couple  $\mathbf{c}^E$ , and the power of the electrostatic force  $W^E$ :

$$\mathbf{f}^E = (\nabla \mathbf{e}) \cdot \mathbf{p}, \quad \mathbf{c}^E = \mathbf{p} \times \mathbf{e}, \quad W^E = \rho \mathbf{e} \cdot \frac{d}{dt} \left( \frac{\mathbf{p}}{\rho} \right) + \mathbf{f}^E \cdot \mathbf{v}. \quad (12.3)$$

#### 12.2.2.1 Maxwell Equation and Electric Body Forces

In case of electrostatics for an ideal dielectric, terms with free charges and magnetic interactions can be dropped in the Maxwell equations, which then read:

$$\nabla \cdot \mathbf{d} = 0, \quad (12.4)$$

$$\nabla \times \mathbf{e} = \mathbf{0}; \quad (12.5)$$

respectively, the *Gauss Law* and the *Faraday Law* of electrostatics. Here, we already used the electric displacement vector, defined by  $\mathbf{d} = \epsilon_0 \mathbf{e} + \mathbf{p}$ , in which  $\epsilon_0$  denotes the vacuum permittivity. One may find an exact solution for the *Faraday Law* immediately by engaging a scalar potential function  $\Phi$ , which satisfies  $\mathbf{e} = -\nabla \Phi$ ;  $\nabla$  is the differential operator with respect to the current configuration. Additionally, the fields  $\mathbf{e}$ ,  $\mathbf{p}$  and  $\mathbf{d}$  have to satisfy the jump conditions

$$\mathbf{n} \cdot \llbracket \mathbf{d} \rrbracket = 0, \quad \mathbf{n} \times \llbracket \mathbf{e} \rrbracket = \mathbf{0}. \quad (12.6)$$

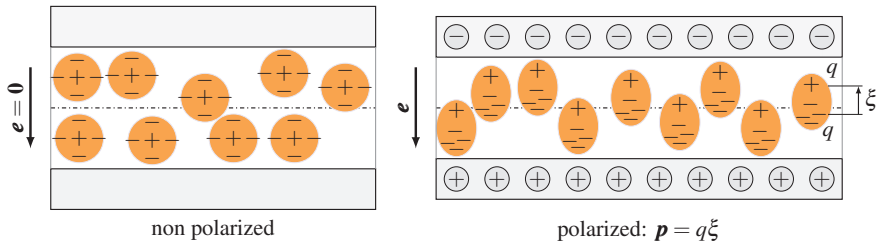


Fig. 12.2: Polarization of a continuum.

The bracketed terms denote jumps in the relevant field quantity. In case of vacuum the fields reduce to  $\mathbf{d} = \varepsilon_0 \mathbf{e}$ . Following Bustamante et al (2009b), the boundary conditions can be set as a function in  $\mathbf{p}$ :

$$\varepsilon_0 \llbracket \mathbf{e} \rrbracket = (\mathbf{n} \cdot \mathbf{p}) \mathbf{n}, \quad \llbracket \mathbf{d} \rrbracket = (\mathbf{n} \cdot \mathbf{p}) \mathbf{n} - \mathbf{p}; \quad (12.7)$$

hence, by introducing the so called Maxwell stress which is present in the free field, the jump on the boundary  $\partial V$  of a material can be defined as:

$$\llbracket \boldsymbol{\sigma}^M \rrbracket \cdot \mathbf{n} = \frac{1}{2} \varepsilon_0^{-1} (\mathbf{p} \cdot \mathbf{n})^2 \mathbf{n}. \quad (12.8)$$

### 12.2.2.2 Conservation Laws

Turning now to the equations of the theory of electro-elasticity, we start with the macroscopic law of conservation of mass  $m = \rho V$  in form of the *Continuity equation*:

$$\dot{m} = \frac{\partial \rho}{\partial t} + \nabla \cdot (\rho \mathbf{v}) = 0, \quad (12.9)$$

where  $\mathbf{v} = \dot{\mathbf{x}}$  denotes the current velocity of the continuum at the point  $\mathbf{x}$ .

For the electro-elastic coupling, the electrostatic body-force  $\mathbf{f}^E$  of the continuum is first introduced into the *Balance of linear momentum*. Hence, the momentum of a body, which is balanced by body forces  $\rho \mathbf{f}$  per unit volume, mechanical surface loads  $\mathbf{t} = \boldsymbol{\sigma}^T \cdot \mathbf{n}$  per unit area, and the effect of the electrostatic force per unit volume  $\mathbf{f}^E$  reads

$$\frac{d}{dt} \int_V \rho \mathbf{v} dV = \int_V (\rho \mathbf{f} + \mathbf{f}^E) dV + \int_{\partial V} \mathbf{t} dS \quad (12.10)$$

in its global form. Using the Gauss integral theorem, yields the local form,

$$\nabla \cdot \boldsymbol{\sigma} + \rho \mathbf{f} + \mathbf{f}^E - \rho \dot{\mathbf{v}} = \mathbf{0}. \quad (12.11)$$

In analogy to the pure mechanical case, also an electrostatic stress tensor  $\boldsymbol{\sigma}^E = \nabla \cdot \boldsymbol{\sigma}^E$  can be introduced. Adding the electrostatic stress tensor to the Cauchy stress tensor  $\boldsymbol{\sigma}$ , results in the total electro-mechanical stress tensor  $\boldsymbol{\sigma}^{tot}$ ,

$$\boldsymbol{\sigma}^{tot} = \boldsymbol{\sigma} + \boldsymbol{\sigma}^E, \quad \boldsymbol{\sigma}^E = \mathbf{e}(\varepsilon_0 \mathbf{e} + \mathbf{p}) - \frac{1}{2} \varepsilon_0 (\mathbf{e} \cdot \mathbf{e}) \mathbf{I}. \quad (12.12)$$

Furthermore, one has to incorporate the electric couple  $\mathbf{c}^E$  in the *Balance of Moment of Momentum*,

$$\frac{d}{dt} \int_V \mathbf{x} \times \rho \mathbf{v} dV = \int_V \mathbf{x} \times (\rho \mathbf{f} + \mathbf{f}^E) dV + \int_V \mathbf{c}^E dV + \int_{\partial V} \mathbf{x} \times \mathbf{t} dS. \quad (12.13)$$



This yields, in contrast to the pure mechanical theory of elasticity, a non-symmetric mechanical Cauchy stress tensor. Using the identity

$$\nabla \cdot (\mathbf{x} \times \boldsymbol{\sigma}) = \mathbf{x} \times (\nabla \cdot \boldsymbol{\sigma}) + {}^3\boldsymbol{\varepsilon} \cdot \boldsymbol{\sigma}, \quad (12.14)$$

where  ${}^3\boldsymbol{\varepsilon}$  is the third rank *Levi-Civita tensor*, and the Gauss integral theorem the local form eventually yields to the symmetry of the sum of the Cauchy stress tensor, and the polarization stress  $\boldsymbol{\sigma}^P$ :

$$\mathbf{c}^E + {}^3\boldsymbol{\varepsilon} \cdot \boldsymbol{\sigma} = \mathbf{0} \quad , \quad \mathbf{c}^E = \mathbf{p} \times \mathbf{e} = {}^3\boldsymbol{\varepsilon} \cdot \mathbf{e} \mathbf{p} = {}^3\boldsymbol{\varepsilon} \cdot \boldsymbol{\sigma}^P. \quad (12.15)$$

The last equation states, that the negative antisymmetric part of the Cauchy stress tensor is identically the antisymmetric part of the dipole moment tensor  $\boldsymbol{\sigma}^P$ . Hence,

$$\text{skew}(\boldsymbol{\sigma} + \boldsymbol{\sigma}^P) = \mathbf{0} \quad \text{and} \quad \boldsymbol{\sigma}^S = \boldsymbol{\sigma} + \boldsymbol{\sigma}^P, \quad (12.16)$$

where a symmetric stress tensor  $\boldsymbol{\sigma}^S = (\boldsymbol{\sigma}^S)^T$  has been introduced. If we now use the last part of Eq. (12.16) and insert it into the electro-mechanical stress tensor, we find the famous Maxwell stress tensor  $\boldsymbol{\sigma}^M$ :

$$\boldsymbol{\sigma}^{tot} = \boldsymbol{\sigma}^S - \boldsymbol{\sigma}^P + \boldsymbol{\sigma}^E = \boldsymbol{\sigma}^S + \boldsymbol{\sigma}^M, \quad (12.17)$$

$$\boldsymbol{\sigma}^M = \boldsymbol{\sigma}^E - \boldsymbol{\sigma}^P = \varepsilon_0 \mathbf{e} \mathbf{e} - \frac{1}{2} \varepsilon_0 (\mathbf{e} \cdot \mathbf{e}) \mathbf{I}. \quad (12.18)$$

Finally, in order to get hands on a thermodynamically consistent constitutive relation, the *Balance of Energy* for the electro-elastic body reads

$$\frac{d}{dt} \int_V \rho \left( \frac{1}{2} \mathbf{v}^2 + e \right) dV = \int_V [(\rho \mathbf{f} + \mathbf{f}^E) \cdot \mathbf{v} + \rho \mathbf{e} \cdot \dot{\boldsymbol{\pi}}] dV + \int_{\partial V} \mathbf{t} \cdot \mathbf{v} dS, \quad (12.19)$$

which upon using the balance of momentum Eq. (12.11), yields the local form:

$$\rho \dot{e} - \boldsymbol{\sigma} \cdot \cdot (\nabla \mathbf{v})^T - \rho \mathbf{e} \cdot \dot{\boldsymbol{\pi}} = 0, \quad (12.20)$$

where  $\dot{\boldsymbol{\pi}} = \frac{d}{dt} \frac{\mathbf{p}}{\rho}$ . Finally, following Maugin and Eringen (2012) we change the dependent variable by using a Legendre transform for the internal energy  $e$  in order to gain the Helmholtz free energy  $\psi = e - \frac{1}{\rho} \mathbf{e} \cdot \mathbf{p}$

$$\rho \dot{\psi} + \frac{d}{dt} \mathbf{e} \cdot \mathbf{p} - \boldsymbol{\sigma} \cdot \cdot (\nabla \mathbf{v})^T - \rho \mathbf{e} \cdot \dot{\boldsymbol{\pi}} = 0, \quad (12.21)$$

which after differentiation gives the final form of the rate of free energy:

$$\rho \dot{\psi} = \boldsymbol{\sigma} \cdot \cdot (\nabla \mathbf{v})^T - \dot{\mathbf{e}} \cdot \mathbf{p}. \quad (12.22)$$

### 12.2.3 Lagrangian (Material) Framework

Within this part the framework of the derivation of the constitutive relations is presented in a generalized state, in order to present the overall procedure. We start by transforming the relations, which were obtained previously in the current (spatial) configuration into the reference configuration, resulting into the Lagrangian (material) framework. The transformation rules of the dependent variables read:

$$\rho_0 = \rho J, \quad (12.23)$$

$$\mathcal{P} = J\mathbf{F}^{-1} \cdot \mathbf{p}, \quad (12.24)$$

$$\mathcal{E} = \mathbf{e} \cdot \mathbf{F}, \quad (12.25)$$

$$\mathbf{S} = J\mathbf{F}^{-1} \cdot \boldsymbol{\sigma} \cdot \mathbf{F}^{-T}. \quad (12.26)$$

$\boldsymbol{\sigma}$  defines the Cauchy stress tensor and  $\mathbf{S}$  the second Piola-Kirchoff stress tensor.  $\mathcal{E}$  and  $\mathcal{P}$  define the material electric field and polarization vector respectively. The electric displacement vector  $\mathbf{d}$ , transforms in the same manner as the polarization vector, using Nanson's formula  $\mathbf{n}d\mathbf{a} = J\mathbf{F}^{-T} \cdot \mathbf{N}dA$ :

$$\mathcal{D} = J\mathbf{d} \cdot \mathbf{F}^{-T}, \quad \mathcal{D} = \varepsilon_0 \mathcal{E} \cdot \mathbf{C}^{-1} + \mathcal{P}. \quad (12.27)$$

Maxwell equations can be written as

$$\mathbf{d} = \varepsilon_0 \mathbf{e} + \mathbf{p}, \quad \nabla_0 \cdot \mathcal{D} = \nabla_0 \cdot (\varepsilon_0 \mathcal{E} \cdot \mathbf{C}^{-1} + \mathcal{P}) = 0, \quad (12.28)$$

$$\nabla_0 \times \mathcal{E} = \mathbf{0}, \quad (12.29)$$

while by carefully applying the volume, surface and line element transformation rules, on can find the electrostatic material force and couple:

$$\mathcal{F}^E = (\nabla_0 \mathcal{E}) \cdot \mathcal{P}, \quad (12.30)$$

$$\mathcal{C}^E = -\mathbf{F}^{-T} \cdot \mathcal{E} \times \mathcal{P} \cdot \mathbf{F}^T. \quad (12.31)$$

Next, we write the material form of the balance of momentum, while from the balance of moment of momentum, the material form of the polarization stress tensor is derived:

$$\rho_0 \mathbf{v} = \nabla_0 \cdot (\mathbf{S} + \mathbf{S}^E) + \rho_0 \mathbf{f}, \quad (12.32)$$

$$\mathbf{S}^P = J\mathbf{F}^{-1} \cdot \mathbf{e}\mathbf{p} \cdot \mathbf{F}^{-T} = \mathbf{C}^{-1} \cdot \mathcal{E}\mathcal{P} \quad (12.33)$$

The material electrostatic stress tensor follows to

$$\mathbf{S}^E = \mathbf{C}^{-1} \cdot \mathcal{E}(\varepsilon_0 \mathcal{E} \cdot \mathbf{C}^{-1} + \mathcal{P}) - \frac{1}{2} \varepsilon_0 J(\mathcal{E} \cdot \mathbf{C}^{-1} \cdot \mathcal{E}) \cdot \mathbf{C}^{-1} \quad (12.34)$$

$$= \mathbf{C}^{-1} \cdot \mathcal{E}\mathcal{D} - \frac{1}{2} \varepsilon_0 J(\mathcal{E} \cdot \mathbf{C}^{-1} \cdot \mathcal{E}) \cdot \mathbf{C}^{-1}. \quad (12.35)$$

In order to obtain the material form of the free energy function, one has to incorporate the time rate of the right Cauchy-Green strain tensor  $\dot{\mathbf{C}} = (\dot{\mathbf{F}}^T \cdot \mathbf{F} + \mathbf{F}^T \cdot \dot{\mathbf{F}})$ , which allows to write the proper transformation of the gradient of the velocity vector  $\nabla_{\mathbf{v}} = \mathbf{F}^{-T} \cdot \frac{1}{2} \dot{\mathbf{C}} \cdot \mathbf{F}^{-1}$ . Hence, the material rate of free energy function per unit mass  $\dot{\psi}(\mathbf{C}, \boldsymbol{\mathcal{E}})$  can be written as:

$$\rho_0 \dot{\psi} = \left( \mathbf{S} + \boldsymbol{\mathcal{P}} \boldsymbol{\mathcal{E}} \cdot \mathbf{C}^{-1} \right) \cdot \frac{1}{2} \dot{\mathbf{C}} - \boldsymbol{\mathcal{P}} \cdot \dot{\boldsymbol{\mathcal{E}}}. \quad (12.36)$$

In the material form of the problem the boundary conditions are obtained by transforming the second Piola Kirchoff stress tensor to its two-field tensor counterpart  $\mathbf{P}^{tot} = \mathbf{F} \cdot \mathbf{S}^{tot}$ ,

$$\mathbf{N} \cdot \llbracket \mathbf{P}^{tot} \rrbracket = \mathbf{0}, \quad \mathbf{N} \cdot \llbracket \boldsymbol{\mathcal{D}} \rrbracket = 0, \quad (12.37)$$

and by Faraday's law  $\nabla_0 \times \boldsymbol{\mathcal{E}} = \mathbf{0}$ ,

$$\mathbf{N} \times \llbracket \boldsymbol{\mathcal{E}} \rrbracket = \mathbf{0}. \quad (12.38)$$

### 12.2.4 Constitutive Relations

In order to close the theory, the phenomenological properties of the material have to be taken into account. We consider only small gradients in the electric field and strains, which therefore allows to take the classical quadratic form of the generalized thermodynamic energy function, valid in electro-elastic bodies. The free energy function  $\psi$  is assumed to decompose additively into a mechanical part  $\psi_{me}(\mathbf{C})$ , and an electrical part  $\psi_{el}(\mathbf{C}, \boldsymbol{\mathcal{E}})$ .

However, an additional term, called augmented free energy, motivated by the presence of ponderomotive forces in vacuum is additionally incorporated. This approach is suggested in Dorfmann and Ogden (2005). In order to make a clear distinction, we indicate the sum of all free energy functions with  $\Omega$ ,

$$\Omega = \psi + \psi_{aug} = \psi_{me}(\mathbf{C}) + \psi_{el}(\mathbf{C}, \boldsymbol{\mathcal{E}}) + \psi_{aug}(\mathbf{C}, \boldsymbol{\mathcal{E}}), \quad (12.39)$$

where the dependent variables of the augmentation term  $\psi_{aug}(\mathbf{C}, \boldsymbol{\mathcal{E}})$  are introduced in accordance to the electrical free energy. Writing the rate of the augmented free energy yields

$$\dot{\Omega} = \frac{\partial \psi_{me}}{\partial \mathbf{C}} \cdot \dot{\mathbf{C}} + \frac{\partial \psi_{el}}{\partial \mathbf{C}} \cdot \dot{\mathbf{C}} + \frac{\partial \psi_{aug}}{\partial \mathbf{C}} \cdot \dot{\mathbf{C}} + \frac{\partial \psi_{el}}{\partial \boldsymbol{\mathcal{E}}} \cdot \dot{\boldsymbol{\mathcal{E}}} + \frac{\partial \psi_{aug}}{\partial \boldsymbol{\mathcal{E}}} \cdot \dot{\boldsymbol{\mathcal{E}}}, \quad (12.40)$$

or after inserting Eq. (12.36)

$$\rho_0 \dot{\Omega} = \frac{1}{2} \left( \mathbf{S} + \boldsymbol{\mathcal{P}} \boldsymbol{\mathcal{E}} \cdot \mathbf{C}^{-1} + 2\rho_0 \frac{\partial \psi_{aug}}{\partial \mathbf{C}} \right) \cdot \dot{\mathbf{C}} - \left( \boldsymbol{\mathcal{P}} - \rho_0 \frac{\partial \psi_{aug}}{\partial \boldsymbol{\mathcal{E}}} \right) \cdot \dot{\boldsymbol{\mathcal{E}}}. \quad (12.41)$$

A comparison unveils

$$\frac{\partial \psi_{me}}{\partial \mathbf{C}} = \frac{1}{2\rho_0} \mathbf{S}, \quad \frac{\partial \psi_{el}}{\partial \mathbf{C}} = \frac{1}{2\rho_0} \mathbf{S}^P, \quad -\frac{\partial \psi_{el}}{\partial \boldsymbol{\mathcal{E}}} = \frac{1}{\rho_0} \boldsymbol{\mathcal{P}}, \quad (12.42)$$

$$\frac{\partial \psi_{aug}}{\partial \mathbf{C}} = \frac{1}{2\rho_0} \mathbf{S}^M, \quad -\frac{\partial \psi_{aug}}{\partial \boldsymbol{\mathcal{E}}} = \frac{1}{\rho_0} (\boldsymbol{\mathcal{D}} - \boldsymbol{\mathcal{P}}). \quad (12.43)$$

We obtain relations for the total electric displacement and the total stress expressed by simple addition:

$$\boldsymbol{\mathcal{D}} = -\rho_0 \frac{\partial \psi_{el}}{\partial \boldsymbol{\mathcal{E}}} - \rho_0 \frac{\partial \psi_{aug}}{\partial \boldsymbol{\mathcal{E}}} = -\rho_0 \frac{\partial \Omega}{\partial \boldsymbol{\mathcal{E}}}, \quad (12.44)$$

$$\mathbf{S}^{tot} = 2\rho_0 \frac{\partial \psi_{me}}{\partial \mathbf{C}} + 2\rho_0 \frac{\partial \psi_{el}}{\partial \mathbf{C}} + 2\rho_0 \frac{\partial \psi_{aug}}{\partial \mathbf{C}} = 2\rho_0 \frac{\partial \Omega}{\partial \mathbf{C}}. \quad (12.45)$$

Still the specific form of the energy functions is missing. For the mechanical part  $\psi_{me}$  any hyperelastic strain energy function can be used. In order to define the electrical energy function, we assume the energy to take a quadratic form in  $\boldsymbol{\mathcal{E}}$ , and start by transforming the heuristic relation  $\boldsymbol{p} = \chi \boldsymbol{e}$  for the polarization vector given in the spatial framework into the material framework:

$$\boldsymbol{p} = \chi \boldsymbol{e}, \quad \boldsymbol{\mathcal{P}} = J\chi \mathbf{C}^{-1} \cdot \boldsymbol{\mathcal{E}}, \quad (12.46)$$

$$\rho_0 \psi_{el} = -\frac{1}{2} \chi \varepsilon_0 \boldsymbol{\mathcal{E}} \cdot (\mathbf{C}^{-1} \cdot \boldsymbol{\mathcal{E}}), \quad (12.47)$$

where  $\chi$  is the electric susceptibility. The augmentation term reads

$$\rho_0 \psi_{aug} = -\frac{1}{2} \varepsilon_0 J \boldsymbol{\mathcal{E}} \cdot (\mathbf{C}^{-1} \cdot \boldsymbol{\mathcal{E}}), \quad (12.48)$$

and by taking the derivative with respect to  $\mathbf{C}$ , while keeping in mind  $\frac{\partial J}{\partial \mathbf{C}} = \frac{1}{2} J \mathbf{C}^{-1}$ , we find

$$\frac{1}{2\rho_0} \mathbf{S}^P = \frac{\partial \psi_{el}}{\partial \mathbf{C}} = \frac{1}{2\rho_0} \chi \varepsilon_0 \mathbf{C}^{-1} \cdot \boldsymbol{\mathcal{E}} \boldsymbol{\mathcal{E}} \cdot \mathbf{C}^{-1}, \quad (12.49)$$

$$\frac{1}{2\rho_0} \mathbf{S}^M = \frac{\partial \psi_{aug}}{\partial \mathbf{C}} = \frac{1}{2\rho_0} \varepsilon_0 J \left( \mathbf{C}^{-1} \cdot \boldsymbol{\mathcal{E}} \boldsymbol{\mathcal{E}} - \frac{1}{2} \mathbf{I}(\boldsymbol{\mathcal{E}} \boldsymbol{\mathcal{E}} \cdot \cdot \mathbf{C}^{-1}) \right) \cdot \mathbf{C}^{-1}, \quad (12.50)$$

which are the constitutive relations for the polarization stress  $\mathbf{S}^P$  and the material Maxwell stress tensor  $\mathbf{S}^M$ . Subsequently, we obtain the polarization vector by taking the derivative with respect to  $\boldsymbol{\mathcal{E}}$ ,

$$\frac{1}{\rho_0} \boldsymbol{\mathcal{P}} = -\frac{\partial \psi_{el}}{\partial \boldsymbol{\mathcal{E}}} = \frac{1}{\rho_0} \chi \varepsilon_0 \mathbf{C}^{-1} \cdot \boldsymbol{\mathcal{E}}, \quad (12.51)$$

$$-\rho_0 \frac{\partial \psi_{aug}}{\partial \boldsymbol{\mathcal{E}}} = \varepsilon_0 J \mathbf{C}^{-1} \cdot \boldsymbol{\mathcal{E}}. \quad (12.52)$$

Here it should be noted, that the polarization stress  $\mathbf{S}^P$  can directly be obtained by multiplication with  $\boldsymbol{\mathcal{E}} \cdot \mathbf{C}^{-1}$ . Gathering all terms one can find the constitutive relation

for the electric displacement vector  $\mathbf{D} = \mathbf{P} + \varepsilon_0 J \mathbf{C}^{-1} \cdot \mathbf{E}$  to

$$\rho_0 \dot{\Omega} = \left( \mathbf{S} + \mathbf{D} \mathbf{E} \cdot \mathbf{C}^{-1} - \frac{1}{2} \varepsilon_0 J \mathbf{C}^{-1} \cdot (\mathbf{E} \mathbf{E} \cdot \mathbf{C}^{-1}) \right) \cdot \frac{1}{2} \dot{\mathbf{C}} - \mathbf{D} \cdot \dot{\mathbf{E}}. \quad (12.53)$$

The bracketed term is the total second Piola-Kirchhoff stress tensor  $\mathbf{S}^{tot}$ , which is composed of the unsymmetric mechanical second Piola-Kirchhoff stress tensor  $\mathbf{S}$ , the polarization stress  $\mathbf{S}^P$  and the symmetric Maxwell stress  $\mathbf{S}^M$ .

This renders the classical version of electro-mechanical coupling most commonly used in the field of dielectric elastomers, where the major driving mechanism is given by the electrostatic force. In case of incompressible dielectric elastomers, the deformation gradient is obliged to  $\det \mathbf{F} = J = 1$ , hence  $\dot{J} = 0$ . Therefore, the constitutive relation for the total second Piola-Kirchhoff stress tensor is constrained, and we account for the constraint by introducing a Lagrange multiplier  $p$ ,

$$\mathbf{S}^{tot} = 2\rho_0 \frac{\partial \Omega}{\partial \mathbf{C}} + p \mathbf{C}^{-1}, \quad \mathbf{D} = -\rho_0 \frac{\partial \Omega}{\partial \mathbf{E}} \quad (12.54)$$

and refer to Dorfmann and Ogden (2005) as well as to Wissler and Mazza (2005) when making the interpretation of  $p$  as taking the role of a hydrostatic pressure, which can be identified as taking a mechanical part as well as an electric part which corresponds to the electrostatic force acting on the dielectric material, in case of plane stress.

### 12.3 Electromechanical Coupling Using a Multiplicative Decomposition of the Deformation Gradient Tensor

In order to broaden the constitutive model to nonlinear effects involving electro-mechanical coupling on the constitutive level, we make use of the multiplicative decomposition of the deformation gradient tensor. This idea is adopted from the fields of thermo-elasticity and plasticity. Using this technique allows for incorporating different or even multiple phenomena and cross effects, e.g. piezoelectricity or electrostriction.

Obviously when dealing with electro-mechanical coupling, the deformation gradient is naturally decomposed into an elastic part  $\mathbf{F}_{me}$ , called the mechanical and an electric part  $\mathbf{F}_{el}$  called the electric deformation gradient tensor,

$$\mathbf{F} = \mathbf{F}_{me} \cdot \mathbf{F}_{el}, \quad (12.55)$$

where  $\mathbf{F}_{el} = \mathbf{F}_{el}(\mathbf{E})$  is assumed to solely depend on the material electric field vector  $\mathbf{E}$ .

We apply the right (Lee-type; Lee, 1969) decomposition proposed by Skatulla et al (2012) for dielectric elastomers, where the right Cauchy-Green tensor can then be expressed by  $\mathbf{C} = \mathbf{F}_{el}^T \cdot \mathbf{C}_{me} \cdot \mathbf{F}_{el}$  with the mechanical part being  $\mathbf{C}_{me} = \mathbf{F}_{me}^T \cdot \mathbf{F}_{me}$ .

It is clear, that the decomposition order puts already restrictions on the choice of dependent variables within the free energy function, resulting in a rather specific theory. Therefore, switching the order of the multiplicative decomposition to a right (Clifton-type; Clifton, 1972) decomposition, necessitates a completely different modeling approach from the very beginning.

We start the derivation of the constitutive relations analogously to the previous section 12.2, however, we drop the augmentation term temporary, the free energy function now reads  $\psi = \psi_{me}(\mathbf{C}_{me}) + \psi_{el}(\mathbf{C}, \boldsymbol{\mathcal{E}})$ , while its rate computes to:

$$\dot{\psi} = \frac{\partial \psi_{me}}{\partial \mathbf{C}_{me}} \cdot \dot{\mathbf{C}}_{me} + \frac{\partial \psi_{el}}{\partial \mathbf{C}} \cdot \dot{\mathbf{C}} + \frac{\partial \psi_{el}}{\partial \boldsymbol{\mathcal{E}}} \cdot \dot{\boldsymbol{\mathcal{E}}}. \quad (12.56)$$

Inserting  $\dot{\mathbf{C}} = \mathbf{F}_{el}^T \cdot \dot{\mathbf{C}}_{me} \cdot \mathbf{F}_{el}$  the time rate of the mechanical right Cauchy-Green tensor is:

$$\dot{\mathbf{C}}_{me} = \mathbf{F}_{el}^{-T} \cdot \dot{\mathbf{C}} \cdot \mathbf{F}_{el}^{-1} - 2\text{sym}(\mathbf{C}_{me} \cdot \dot{\mathbf{F}}_{el} \cdot \mathbf{F}_{el}^{-1}). \quad (12.57)$$

Therefore, upon applying the symmetry and cyclic permutation property of the double dot product, and after inserting  $\dot{\mathbf{F}}_{el} = \frac{\partial \mathbf{F}_{el}}{\partial \boldsymbol{\mathcal{E}}} \cdot \dot{\boldsymbol{\mathcal{E}}}$ , the first, mechanical, part of the free energy, gets:

$$\frac{\partial \psi_{me}}{\partial \mathbf{C}_{me}} \cdot \dot{\mathbf{C}}_{me} = \mathbf{F}_{el}^{-1} \cdot \frac{\partial \psi_{me}}{\partial \mathbf{C}_{me}} \cdot \mathbf{F}_{el}^{-T} \cdot \dot{\mathbf{C}} - \left( 2\mathbf{F}_{el}^{-1} \cdot \frac{\partial \psi_{me}}{\partial \mathbf{C}_{me}} \cdot \mathbf{C}_{me} \cdot \frac{\partial \mathbf{F}_{el}}{\partial \boldsymbol{\mathcal{E}}} \right) \cdot \dot{\boldsymbol{\mathcal{E}}}. \quad (12.58)$$

This allows to rewrite the rate of the free energy Eq. (12.56), such that the global form with regard to the double dot product can be restored:

$$\dot{\psi} = \left( \mathbf{F}_{el}^{-1} \cdot \frac{\partial \psi_{me}}{\partial \mathbf{C}_{me}} \cdot \mathbf{F}_{el}^{-T} + \frac{\partial \psi_{el}}{\partial \mathbf{C}} \right) \cdot \dot{\mathbf{C}} - \left( 2\mathbf{F}_{el}^{-1} \cdot \frac{\partial \psi_{me}}{\partial \mathbf{C}_{me}} \cdot \frac{\partial \mathbf{F}_{el}}{\partial \boldsymbol{\mathcal{E}}} - \frac{\partial \psi_{el}}{\partial \boldsymbol{\mathcal{E}}} \right) \cdot \dot{\boldsymbol{\mathcal{E}}}. \quad (12.59)$$

Comparing now the coefficients of this relation to the material rate of free energy from Eq. (12.36), the constitutive relations for the symmetric second Piola-Kirchhoff stress tensor as well as for the polarization vector can be obtained:

$$\mathbf{S}^S = \mathbf{S} + \boldsymbol{\mathcal{P}}\boldsymbol{\mathcal{E}} \cdot \mathbf{C}^{-1} = 2\rho_0 \mathbf{F}_{el}^{-1} \cdot \frac{\partial \psi_{me}}{\partial \mathbf{C}_{me}} \cdot \mathbf{F}_{el}^{-T} + 2\rho_0 \frac{\partial \psi_{el}}{\partial \mathbf{C}}, \quad (12.60)$$

$$\boldsymbol{\mathcal{P}} = 2\rho_0 \mathbf{F}_{el}^{-1} \cdot \frac{\partial \psi_{me}}{\partial \mathbf{C}_{me}} \cdot \mathbf{C}_{me} \cdot \frac{\partial \mathbf{F}_{el}}{\partial \boldsymbol{\mathcal{E}}} - \rho_0 \frac{\partial \psi_{el}}{\partial \boldsymbol{\mathcal{E}}}. \quad (12.61)$$

Here the pronounced coupling nature of the multiplicative decomposition becomes clear, while the second Piola-Kirchhoff stress tensor experiences a transformation by the electrical deformation gradient, the polarization vector  $\boldsymbol{\mathcal{P}}$  is now composed of two parts, an electrical one  $\boldsymbol{\mathcal{P}}_{el}$  and a coupled electro-mechanical part  $\boldsymbol{\mathcal{P}}_{coup}$ .

$$\boldsymbol{\mathcal{P}}_{el} = -\rho_0 \frac{\partial \psi_{el}}{\partial \boldsymbol{\mathcal{E}}}, \quad \boldsymbol{\mathcal{P}}_{coup} = 2\rho_0 \mathbf{F}_{el}^{-1} \cdot \frac{\partial \psi_{me}}{\partial \mathbf{C}_{me}} \cdot \mathbf{C}_{me} \cdot \frac{\partial \mathbf{F}_{el}}{\partial \boldsymbol{\mathcal{E}}}. \quad (12.62)$$

Moreover, the corresponding polarization stress  $\mathbf{S}^P = \mathbf{S}^{pol,el} + \mathbf{S}^{pol,coup}$  is again obtained by multiplication with  $\boldsymbol{\mathcal{E}} \cdot \mathbf{C}^{-1}$ :

$$\mathbf{S}^{pol,el} = \boldsymbol{\mathcal{P}}_{el} \boldsymbol{\mathcal{E}} \cdot \mathbf{C}^{-1} = -\rho_0 \left( \frac{\partial \psi_{el}}{\partial \boldsymbol{\mathcal{E}}} \right) \boldsymbol{\mathcal{E}} \cdot \mathbf{C}^{-1}, \quad (12.63)$$

$$\mathbf{S}^{pol,coup} = \boldsymbol{\mathcal{P}}_{coup} \boldsymbol{\mathcal{E}} \cdot \mathbf{C}^{-1} = \rho_0 \left( 2\mathbf{F}_{el}^{-1} \cdot \frac{\partial \psi_{me}}{\partial \mathbf{C}_{me}} \cdot \mathbf{C}_{me} \cdot \frac{\partial \mathbf{F}_{el}}{\partial \boldsymbol{\mathcal{E}}} \right) \boldsymbol{\mathcal{E}} \cdot \mathbf{C}^{-1}. \quad (12.64)$$

The symmetric Piola-Kirchoff stress tensor composes now of three parts  $\mathbf{S}^S = \mathbf{S} + \mathbf{S}^{pol,coup} + \mathbf{S}^{pol,el}$ . The term  $\mathbf{S}^{pol,el}$ , introduces the electrostatic force into the theory, since it has to fulfill the restriction

$$-\frac{\partial \psi_{el}}{\partial \boldsymbol{\mathcal{E}}} \boldsymbol{\mathcal{E}} \cdot \mathbf{C}^{-1} = 2 \frac{\partial \psi_{el}}{\partial \mathbf{C}}. \quad (12.65)$$

Due to simplicity, we choose the same free energy  $\rho_0 \psi_{el} = -\frac{1}{2} \chi \varepsilon_0 \boldsymbol{\mathcal{E}} \cdot (\mathbf{C}^{-1} \cdot \boldsymbol{\mathcal{E}})$  from Sect. 12.2, since it has already been shown to be a proper choice. The variables  $\varepsilon_0$  and  $\chi$  are the permittivity in vacuum and the electric susceptibility respectively.

The identification of the electrostatic force motivates further statements on the analysis of the electro-elastic coupling nature. As the responsible term for the electrostatic force can now be excluded, still a symmetric electro-mechanical stress tensor  $\mathbf{S}^{em} = \mathbf{S} + \boldsymbol{\mathcal{P}}_{coup} \boldsymbol{\mathcal{E}} \cdot \mathbf{C}^{-1}$  can be obtained, which upon comparison to Eq. (12.60) reads:

$$\mathbf{S}^{em} = 2\rho_0 \mathbf{F}_{el}^{-1} \cdot \frac{\partial \psi_{me}}{\partial \mathbf{C}_{me}} \cdot \mathbf{F}_{el}^{-T}. \quad (12.66)$$

By using  $\mathbf{C}_{me} = \mathbf{F}_{el}^{-T} \cdot \mathbf{C} \cdot \mathbf{F}_{el}^{-1}$ , the coupling polarization can be written as:

$$\boldsymbol{\mathcal{P}}_{coup} = \mathbf{S}^{em} \cdot \mathbf{C} \cdot \mathbf{F}_{el}^{-1} \cdot \frac{\partial \mathbf{F}_{el}}{\partial \boldsymbol{\mathcal{E}}}, \quad (12.67)$$

which after comparison to the balance of energy yields the symmetric second Piola-Kirchoff stress tensor being composed of an electromechanical part  $\mathbf{S}^{em}$  and the electrical part  $\mathbf{S}^{pol,el}$ .

$$\mathbf{S}^S = \mathbf{S} + \boldsymbol{\mathcal{P}} \boldsymbol{\mathcal{E}} \cdot \mathbf{C}^{-1} = \mathbf{S}^{em} + \mathbf{S}^{pol,el}, \quad \boldsymbol{\mathcal{P}} = \boldsymbol{\mathcal{P}}_{el} + \boldsymbol{\mathcal{P}}_{coup} \quad (12.68)$$

with the specific constitutive relations:

$$\mathbf{S}^{em} = 2\rho_0 \mathbf{F}_{el}^{-1} \cdot \frac{\partial \psi_{me}}{\partial \mathbf{C}_{me}} \cdot \mathbf{F}_{el}^{-T} \quad \text{and} \quad \mathbf{S}^{pol,el} = 2\rho_0 \frac{\partial \psi_{el}}{\partial \mathbf{C}}, \quad (12.69)$$

$$\boldsymbol{\mathcal{P}}_{el} = -\rho_0 \frac{\partial \psi_{el}}{\partial \boldsymbol{\mathcal{E}}} \quad \text{and} \quad \boldsymbol{\mathcal{P}}_{coup} = \mathbf{S}^{em} \cdot \mathbf{C} \cdot \mathbf{F}_{el}^{-1} \cdot \frac{\partial \mathbf{F}_{el}}{\partial \boldsymbol{\mathcal{E}}}. \quad (12.70)$$

In view of a proper thermodynamic presentation of the rate of the free energy, one can finally write:

$$\rho_0 \dot{\psi} = \underbrace{\mathbf{F}_{el} \cdot \mathbf{S}^{em} \cdot \mathbf{F}_{el}^T}_{=\rho_0 \dot{\psi}_{me}(\mathbf{C}_{me})} \cdot \frac{1}{2} \dot{\mathbf{C}}_{me} + \underbrace{\mathbf{S}^{pol,el}}_{=\rho_0 \dot{\psi}_{el}} \cdot \frac{1}{2} \dot{\mathbf{C}} - \mathcal{P}_{el} \cdot \dot{\mathcal{E}}. \quad (12.71)$$

Consider the case  $\mathbf{F}_{el} = \mathbf{I}$ ; then  $\mathcal{P}_{coup} = \mathbf{0}$ ,  $\mathbf{F}_{me} = \mathbf{F}$ ,  $\mathbf{C}_{me} = \mathbf{C}$  and  $\mathbf{S}^{em} = \mathbf{S}$  hold, and the previous constitutive model without constitutive coupling is found:

$$\mathbf{S} = 2\rho_0 \cdot \frac{\partial \psi_{me}}{\partial \mathbf{C}}, \quad \mathbf{S}^{pol} = \mathcal{P} \mathcal{E} \cdot \mathbf{C}^{-1} = 2\rho_0 \frac{\partial \psi_{el}}{\partial \mathbf{C}} \quad \text{and} \quad \mathcal{P} = -\rho_0 \frac{\partial \psi_{el}}{\partial \mathcal{E}}. \quad (12.72)$$

### 12.3.1 Total Stress

It remains to incorporate the contribution of the electric field in vacuum to the constitutive model. Starting at the definition for the free energy function, the objective we want to achieve is to find some global relationships which hold when incorporating the multiplicative decomposed deformation gradient. We make use of the augmentation term in Sect. 12.2 and write

$$\rho_0 \dot{\Omega} = \rho_0 \dot{\psi} - \frac{1}{2} \varepsilon_0 \mathcal{J} \mathcal{E} \cdot (\mathbf{C}^{-1} \cdot \mathcal{E}) = \rho_0 \dot{\psi} + \rho_0 \dot{\psi}_{aug}. \quad (12.73)$$

Hence, in analogy to the electric free energy, also for the augmentation term  $\psi_{aug} = \psi_{aug}(\mathbf{C}, \mathcal{E})$  holds, and the rate of the augmented free energy can be expressed as:

$$\rho_0 \dot{\Omega} = \rho_0 \dot{\psi} + \rho_0 \frac{\partial \psi_{aug}}{\partial \mathbf{C}} \cdot \dot{\mathbf{C}} + \rho_0 \frac{\partial \psi_{aug}}{\partial \mathcal{E}} \cdot \dot{\mathcal{E}}. \quad (12.74)$$

However, in few of a uniform presentation, one might be interested to further develop  $\dot{\psi}$  given in Eq. (12.59). As  $\psi_{me} = \psi_{me}(\mathbf{C}_{me}) = \psi_{me}(\mathbf{C}_{me}(\mathbf{C}, \mathcal{E}))$  holds, and by using  $\mathbf{C}_{me} = \mathbf{F}_{el}^{-T} \cdot \mathbf{C} \cdot \mathbf{F}_{el}^{-1}$  the derivative of the mechanical free energy can be expressed by

$$\begin{aligned} \frac{\partial \psi_{me}}{\partial \mathcal{E}} &= \frac{\partial \psi_{me}}{\partial \mathbf{C}_{me}} \cdot \frac{\partial \mathbf{C}_{me}}{\partial \mathcal{E}} = \frac{\partial \psi_{me}}{\partial \mathbf{C}_{me}} \cdot \frac{\partial (\mathbf{F}_{el}^{-T} \cdot \mathbf{C} \cdot \mathbf{F}_{el}^{-1})}{\partial \mathcal{E}} \\ &= -2\mathbf{F}_{el}^{-1} \cdot \frac{\partial \psi_{me}}{\partial \mathbf{C}_{me}} \cdot \left( \mathbf{C}_{me} \cdot \frac{\partial \mathbf{F}_{el}}{\partial \mathcal{E}} \cdot \mathbf{F}_{el}^{-1} \right) = -2\mathbf{F}_{el}^{-1} \frac{\partial \psi_{me}}{\partial \mathbf{C}_{me}} \cdot \mathbf{C}_{me} \cdot \frac{\partial \mathbf{F}_{el}}{\partial \mathcal{E}}, \end{aligned} \quad (12.75)$$

and furthermore,

$$\frac{\partial \psi_{me}}{\partial \mathbf{C}} = \frac{\partial \psi_{me}}{\partial \mathbf{C}_{me}} \cdot \frac{\partial \mathbf{C}_{me}}{\partial \mathbf{C}} = \frac{\partial \psi_{me}}{\partial \mathbf{C}_{me}} \cdot \frac{\partial (\mathbf{F}_{el}^{-T} \cdot \mathbf{C} \cdot \mathbf{F}_{el}^{-1})}{\partial \mathbf{C}} = \mathbf{F}_{el}^{-1} \cdot \frac{\partial \psi_{me}}{\partial \mathbf{C}_{me}} \cdot \mathbf{F}_{el}^{-T} \quad (12.76)$$

which finally gives



$$\mathbf{D} = -\rho_0 \frac{\partial \psi_{me}}{\partial \boldsymbol{\mathcal{E}}} - \rho_0 \frac{\partial \psi_{el}}{\partial \boldsymbol{\mathcal{E}}} - \rho_0 \frac{\partial \psi_{aug}}{\partial \boldsymbol{\mathcal{E}}} = -\rho_0 \frac{\partial \Omega}{\partial \boldsymbol{\mathcal{E}}}, \tag{12.77}$$

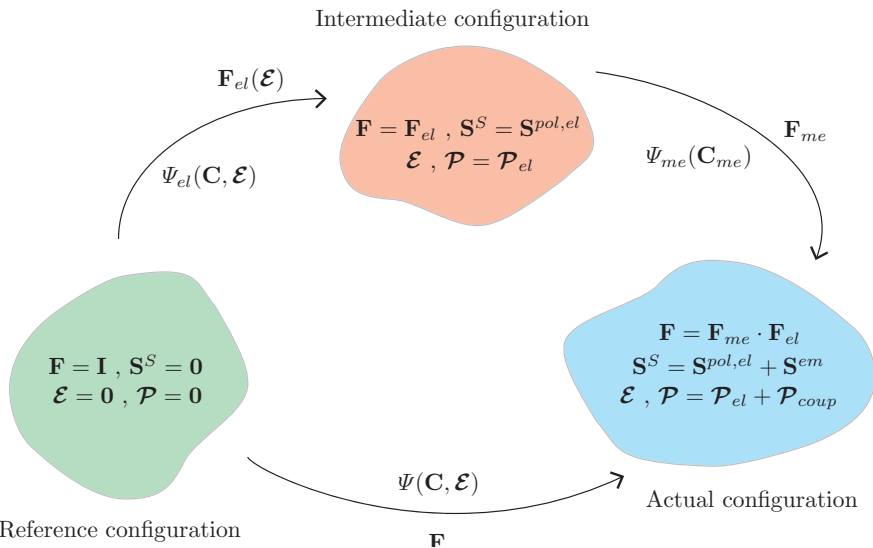
$$\mathbf{S}^{tot} = 2\rho_0 \frac{\partial \psi_{me}}{\partial \mathbf{C}} + 2\rho_0 \frac{\partial \psi_{el}}{\partial \mathbf{C}} + 2\rho_0 \frac{\partial \psi_{aug}}{\partial \mathbf{C}} = 2\rho_0 \frac{\partial \Omega}{\partial \mathbf{C}}. \tag{12.78}$$

Note, that in case of multiplicative decomposition, the electric displacement vector contains the material derivative of the mechanical free energy with respect to the electric field, this was not the case in the representation of the constitutive equations in section 12.2. Inserting the quantities into the rate of augmented free energy finally yields

$$\rho_0 \dot{\Omega} = \mathbf{S}^{tot} \cdot \frac{1}{2} \dot{\mathbf{C}} - \mathbf{D} \cdot \dot{\boldsymbol{\mathcal{E}}}. \tag{12.79}$$

### 12.3.2 Intermediate Configuration

By using a multiplicative decomposition, one equivalently introduces an intermediate configuration, see Fig. 12.3 into the deformation path, which is a result of the right Lee-type decomposition. In our case, the intermediate configuration might be adopted in case when no mechanical loads are applied, hence  $\mathbf{C}_{me} = \mathbf{I}$ , and the electro-mechanical stress, given in Eq. (12.68)



**Fig. 12.3:** The intermediate configuration is entered by instantaneously taking all mechanical loads yielding to an appealing, yet unphysical state of pure electrical origin.

$$\mathbf{S}^{em} = \mathbf{S} + \mathcal{P}_{coup} \boldsymbol{\mathcal{E}} \cdot \mathbf{C}^{-1} = 2\rho_0 \mathbf{F}_{el}^{-1} \cdot \frac{\partial \psi_{me}}{\partial \mathbf{C}_{me}} \cdot \mathbf{F}_{el}^{-T}, \quad (12.80)$$

has to vanish. This is true, because the mechanical part of the free energy  $\psi_{me}(\mathbf{C}_{me})$  per definition depends solely on the mechanical right Cauchy-Green tensor. Hence, the symmetric stress tensor  $\mathbf{S}^S$  for the intermediate configuration must be equal to the electrical polarization stress tensor  $\mathbf{S}^S = \mathbf{S}^P = \mathbf{S}^{pol,el}$ . Moreover, as the total stress tensor is  $\mathbf{S}^{tot} = \mathbf{S}^S - \mathbf{S}^P + \mathbf{S}^E = \mathbf{S}^E$  yields to  $\mathbf{S}^{tot} = \mathbf{S}^P + \mathbf{S}^M$ , hence, there exists a total stress tensor in the intermediate configuration, composed of the symmetric Maxwell stress and the unsymmetric electrical polarization stress.

Moreover, as the electro-mechanical stress tensor is composed of the second (mechanical) Piola-Kirchoff stress and the coupling polarization stress tensor  $\mathbf{S}^{em} = \mathbf{S} + \mathbf{S}^{pol,coup} = \mathbf{0}$  yields in consequence that either  $\mathbf{S} = -\mathbf{S}^{pol,coup}$  or both  $\mathbf{S}^{pol,coup} = \mathbf{0}$  and  $\mathbf{S} = \mathbf{0}$  vanish. However, in either way, the total stress tensor remains apparent because of the Maxwell stress tensor, hence the intermediate configuration cannot be a "stress-free" configuration.

This concept of different deformation path yields to three possible configurations:

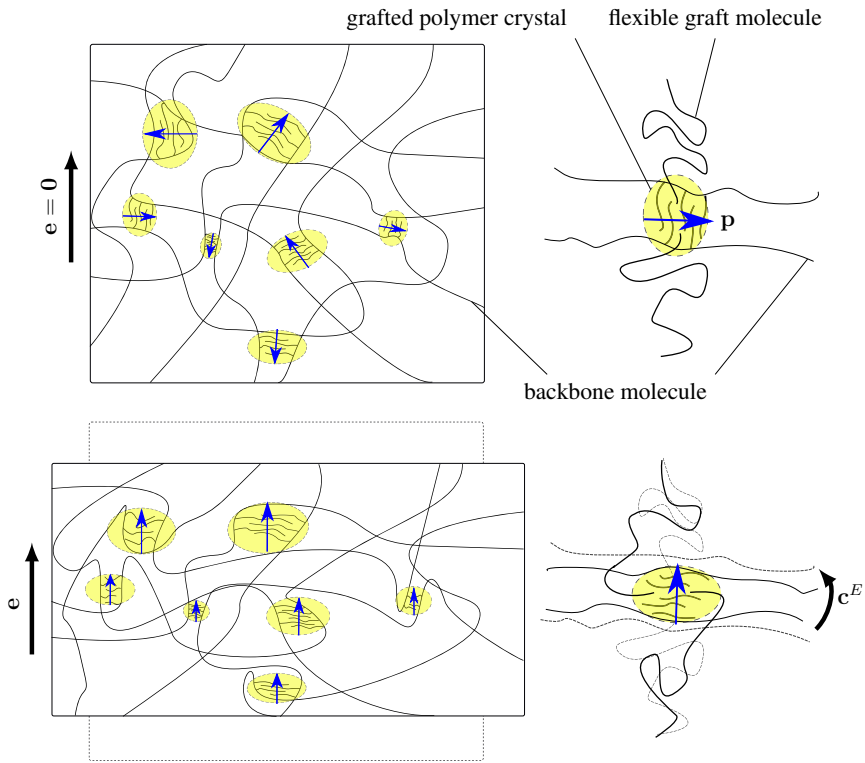
1. The unloaded reference configuration, here both the electric field vector and the polarization vector have to vanish  $\boldsymbol{\mathcal{E}} = \mathcal{P} = \mathbf{0}$ , while at the same time  $\mathbf{F} = \mathbf{I}$  is prescribed, hence this configuration is stress free  $\mathbf{S}^{tot} = \mathbf{S}^S = \mathbf{0}$ .
2. Allowing a pure electric polarization  $\mathcal{P} = \mathcal{P}_{el}$  accompanied with an electric field, yields to a configuration where stress fields  $\mathbf{S}^{tot} = \mathbf{S}^{pol,coup} + \mathbf{S}^M$  are present yielding to a deformation field characterized by  $\mathbf{F} = \mathbf{F}_{el}$ .
3. Within the actual configuration, all physical possible combination of electric and mechanic sources are present, allowing now the the symmetric electro-mechanical stress tensor  $\mathbf{S}^{em}$  to emerge. When starting in the intermediate configuration, the actual configuration is attained through the mechanical energy field  $\psi_{me}(\mathbf{C}_{me})$ . When going this path one has to keep the electric field  $\boldsymbol{\mathcal{E}}$  constant and add the coupled term to the polarization vector field  $\mathcal{P} = \mathcal{P}_{el} + \mathcal{P}_{coup}$ .

## 12.4 Electrostriction

Phenomenologically speaking, electrostriction is the quadratic response in the strain field, upon application of an electric field; hence, we write a series expansion

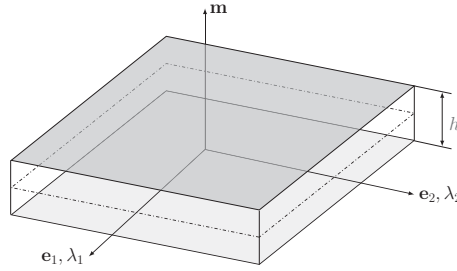
$$\boldsymbol{\varepsilon} \approx \boldsymbol{\mathcal{E}} \cdot {}^3\mathbf{e} + \boldsymbol{\mathcal{E}}\boldsymbol{\mathcal{E}} \cdot \cdot {}^4\mathbf{D} + \dots \quad (12.81)$$

for the infinitesimal strain tensor  $\boldsymbol{\varepsilon}$ , where  ${}^3\mathbf{e}$  is a third rank piezoelectric coefficient tensor, and  ${}^4\mathbf{D}$  a fourth rank electrostrictive parameter tensor. Therefore, electrostriction renders a higher order effect, which is typically considered as negligible. However, experimental results show, that among the linear electrostatic relation, also higher order effects contribute significantly to the strain field. As piezoelectricity is a special topic, in this work we restrict ourselves to electrostriction, which also depends



**Fig. 12.4:** Electrostrictive graft polymer, left deformation of the whole specimen, right reorientation of the crystal unit upon application of an electric field.

highly on the materials properties. In order to explore the origin of this effect one has to look inside the micro-structure. Materials which exhibit a distinct electrostrictive behavior carry typically polarized cells or crystalline groups within a matrix of long chained elastomer molecules. In 1998 NASA (Su et al, 1999) published results on their improved EAP material, with especially improved electrostrictive properties, called electrostrictive graft elastomer. The key ingredients are crystalline groups which are solvents in a flexible backbone polymer matrix. Upon application of an external electric field, the dipole moments within the crystal cells have to reorient, according to the induced dipole couple  $\mathbf{c}^E = \mathbf{p} \times \mathbf{e}$ . This effect is shown in Fig. 12.4. If the sign of the external field is changed, the dipole couple reorients in the other direction; hence, the cells are turned around such, that the same net deformation can be measured. As every material carries imperfections, which lead to polarized cells within the structure, every material is capable of undergoing an electrostrictive behavior. However, e.g. in silicon rubber one can barely find such micro defects,



**Fig. 12.5:** Homogeneous plate in cartesian coordinates, the unit vector in thickness direction is denoted with  $\mathbf{m}$ .

which is why the electrostrictive effect of silicon rubber (3M VHB4910) is rather small. Other materials which have drawn attention due to their distinct ability towards electrostriction are polyurethane elastomers, see experimental results in Diaconu et al (2006). We complete this introductory part by mentioning that also combinations of electrostrictive EAPs and piezoelectric copolymers exist (so called ferroelectric-electrostrictive materials), which allow the use of the piezoelectric polymer for sensing and the electrostrictive one for actuation.

In order to incorporate electrostriction into the constitutive relations in the present paper, we make use of the yet undefined electric deformation gradient tensor  $\mathbf{F}_{el}$ , which in case of electrostriction might e.g. take the form of an exponential function suggested by Skatulla et al (2012):

$$\mathbf{F}_{el} = \exp \mathbf{D}, \tag{12.82}$$

where  $\mathbf{D}$  is a proper second rank tensor, which in turn has to satisfy  $\mathbf{D} = \ln \mathbf{F}_{el}$ , such that by choosing  $\mathbf{D}$  carefully, the electric deformation gradient might become identical to the electric right stretch tensor  $\mathbf{F}_{el} = \mathbf{R}_{el} \mathbf{U}_{el} := \mathbf{U}_{el}$ , hence  $\mathbf{D}$  becomes an electrical logarithmic strain tensor  $\mathbf{E}^{el}$

$$\mathbf{D} = \ln \mathbf{U}_{el} = \mathbf{E}^{el}, \tag{12.83}$$

which then can be chosen quadratic in the material electric field vector  $\mathcal{E}$ .

### 12.4.1 Homogeneously Deformed Plate

We turn now to the case of homogeneous in plane deformation of a plate, see Fig. 12.5, in which the coordinate system is embedded such, that one unit vector  $\mathbf{m}$  is aligned with the electric field vector  $\mathcal{E} = \mathcal{E}_3 \mathbf{m}$ , acting in thickness direction. Hence the electric deformation gradient takes the form  $\mathbf{F}_{el} = \mathbf{U}_{el} = \lambda_{el}(\mathbf{I} - \mathbf{m}\mathbf{m}) + \lambda_{el,3} \mathbf{m}\mathbf{m}$ .

Therefore, the tensor  $\mathbf{D}$  is taken in the form of a diagonal tensor:

$$\mathbf{D} = c_1(\boldsymbol{\mathcal{E}} \cdot \boldsymbol{\mathcal{E}})\mathbf{mm} + c_2(\boldsymbol{\mathcal{E}} \cdot \boldsymbol{\mathcal{E}})(\mathbf{I} - \mathbf{mm}), \quad (12.84)$$

where the two parameter  $c_1$  and  $c_2$  are electrostrictive material parameter, which allow to write the electrical stretches in the form:

$$\lambda_{el} = \exp(c_2 \boldsymbol{\mathcal{E}} \cdot \boldsymbol{\mathcal{E}}) \quad , \quad \lambda_{el,3} = \exp(c_1 \boldsymbol{\mathcal{E}} \cdot \boldsymbol{\mathcal{E}}). \quad (12.85)$$

It remains now to recall and specify the augmented free energy. Starting with the mechanical free energy, we are using a neo-Hookean hyperelastic strain energy function,

$$\rho_0 \psi_{me}(\mathbf{C}_{me}) = \rho_0 \psi_{me}(I_{C_{me}}, II_{C_{me}}, III_{C_{me}}) = \frac{\mu}{2}(I_{C_{me}} - 3 - 2 \ln J_{me}) + K(\ln J_{me})^2; \quad (12.86)$$

the electrical and the augmented free energy are respectively:

$$\rho_0 \psi_{el} = -\frac{1}{2} \chi \varepsilon_0 \boldsymbol{\mathcal{E}} \cdot (\mathbf{C}^{-1} \cdot \boldsymbol{\mathcal{E}}) \quad (12.87)$$

$$\rho_0 \psi_{aug} = -\frac{1}{2} J \varepsilon_0 \boldsymbol{\mathcal{E}} \cdot (\mathbf{C}^{-1} \cdot \boldsymbol{\mathcal{E}}). \quad (12.88)$$

#### 12.4.1.1 Plane Stress

For the total stress tensor we write  $\mathbf{S}^{tot} = \mathbf{S}_2 + \boldsymbol{\tau}\mathbf{m} + \mathbf{m}\boldsymbol{\tau} + S_{33}\mathbf{mm}$ , where  $\mathbf{S}_2$  is its plane part,  $\boldsymbol{\tau}$  is the total transverse shear stress vector and  $S_{33}$  the magnitude of the total stress in direction of the unit normal vector  $\mathbf{m}$ . We use  $\mathbf{I}_2 = \mathbf{I} - \mathbf{mm}$  for the plane identity tensor. The restriction to plane stress allows to set all parts in  $\mathbf{m}$  direction zero, hence  $\mathbf{S}^{tot} = \mathbf{S}_2$ . As a consequence, shear components of the right Cauchy-Green tensor vanish; hence, it can be decomposed into an in plane part  $\mathbf{C}_2$ , and an out of plane tensor  $C_{33}\mathbf{mm}$  such that  $\mathbf{C} = \mathbf{C}_2 + C_{33}\mathbf{mm}$ . In accordance to the total right Cauchy-Green tensor, also the mechanical right Cauchy-Green tensor turns into  $\mathbf{C}_{me} = \mathbf{C}_{2,me} + C_{33,me}\mathbf{mm}$ . By using the transformation rule  $\mathbf{C}_{me} = \mathbf{F}_{el}^{-T} \cdot \mathbf{C} \cdot \mathbf{F}_{el}^{-1}$ , the invariants of  $\mathbf{C}_{me}$  turn into functions of the total right Cauchy-Green tensor, and the electric stretches.

$$I_{C_{me}} = \text{tr} \mathbf{C}_{me} = \lambda_{el}^{-2} \text{tr} \mathbf{C}_2 + \lambda_{el,3}^{-2} C_{33}, \quad (12.89)$$

$$II_{C_{me}} = \mathbf{C}_{me} \cdot \cdot \mathbf{C}_{me} = \lambda_{el,3}^{-4} C_{33}^2 + \lambda_{el}^{-4} \mathbf{C}_2 \cdot \cdot \mathbf{C}_2, \quad (12.90)$$

$$III_{C_{me}} = \det \mathbf{C}_{me} = \lambda_{el}^{-4} \lambda_{el,3}^{-2} C_{33} \det \mathbf{C}_2. \quad (12.91)$$

#### 12.4.1.2 Incompressibility

As dielectric elastomers are often considered incompressible,  $J = \det \mathbf{F} := 1$ , we have:

- $\det \mathbf{F} = \det \mathbf{F}_{el} = 1$ ,
- $\det \mathbf{C} = 1 \rightarrow C_{33} = \det \mathbf{C}_2^{-1} = III_{\mathbf{C}_2}^{-1}$ .

Turning to the electric deformation gradient tensor, the incompressibility condition already defines one of the electrostrictive material parameter  $c_1$  in terms of the second one  $c_2$ :

$$\det \mathbf{F}_{el} = 1 = \lambda_{el,3}^2 \lambda_{el,3} = \exp((c_1 + 2c_2)\mathcal{E}_3^2) = 1 \quad \rightarrow \quad c_1 = -2c_2. \quad (12.92)$$

Additionally the electric in plane stretch is a direct result of the out of plane stretch:  $\lambda_{el}^{-2} = \lambda_{el,3} = \exp(c_1\mathcal{E}_3^2)$ . For the electric free energy function the inverse total right Cauchy-Green tensor is needed, as  $\mathbf{C}^{-1} = \mathbf{C}_2^{-1} + \mathbf{C}_{33}^{-1}\mathbf{m}\mathbf{m}$  holds. Upon inserting  $\mathbf{E} = \mathcal{E}_3\mathbf{m}$  and using  $J = 1$  the electric free energy and the augmented free energy are:

$$\rho_0(\psi_{el} + \psi_{aug}) = -\frac{1}{2}\varepsilon_0(1 + \chi)\frac{\mathcal{E}_3^2}{C_{33}}. \quad (12.93)$$

For the mechanical free energy function the trace of the mechanical right Cauchy-Green tensor is needed. If we make use of  $\lambda_{el}^{-2} = \lambda_{el,3}$  and  $C_{33} = \det \mathbf{C}_2^{-1} = III_{\mathbf{C}_2}^{-1}$ , the invariants read:

$$I_{\mathbf{C}_{me}} = \lambda_{el}^{-2} \text{tr} \mathbf{C}_2 + \lambda_{el}^4 C_{33}, \quad (12.94)$$

$$II_{\mathbf{C}_{me}} = \lambda_{el}^8 C_{33}^2 + \lambda_{el}^{-4} \mathbf{C}_2 \cdot \mathbf{C}_2, \quad (12.95)$$

$$III_{\mathbf{C}_{me}} = \lambda_{el}^{-4} \lambda_{el}^4 III_{\mathbf{C}_2}^{-1} \det \mathbf{C}_2 = 1. \quad (12.96)$$

We can now write the augmented free energy for the incompressible neo-Hookean material and the plane stress case:

$$\rho_0 \Omega_2 = \frac{\mu}{2} \left( \lambda_{el}^{-2} \text{tr} \mathbf{C}_2 + \lambda_{el}^4 III_{\mathbf{C}_2}^{-1} - 3 \right) - \frac{1}{2} \varepsilon III_{\mathbf{C}_2} \mathcal{E}_3^2, \quad (12.97)$$

where we used the permittivity  $\varepsilon = \varepsilon_0(\chi + 1) = \varepsilon_r \varepsilon_0$ , with the relative permittivity  $\varepsilon_r = \chi + 1$ , and the electrical stretch  $\lambda_{el} = \exp(c_2 \mathcal{E}_3^2) = \exp((-c_1/2)\mathcal{E}_3^2)$ .

### 12.4.1.3 Electrostatic Force

We already reduced the augmented free energy to its plane counterpart, however, in order to ensure incompressibility when using the constitutive relations for the stresses one has to enforce the condition by using a Lagrange multiplier  $p$ :

$$\mathbf{S}_2 = 2\rho_0 \frac{\partial \Omega_2}{\partial \mathbf{C}_2} + p \mathbf{C}_2^{-1}, \quad (12.98)$$

where  $p$  can be obtained by making use of the plane stress condition in the three dimensional problem  $S_{33} = 0$ , keeping  $C_{33} = III_{\mathbf{C}_2}^{-1}$  in mind yields

$$S_{33} = 2\rho_0 \frac{\partial \Omega_2}{\partial C_{33}} + p C_{33}^{-1} = 0 \quad \rightarrow \quad p = -2C_{33} \rho_0 \frac{\partial \Omega_2}{\partial C_{33}}. \quad (12.99)$$

Inserting  $p$  into the plane part of the total stress tensor finds

$$\mathbf{S}_2 = 2\rho_0 \frac{\partial \Omega_2}{\partial \mathbf{C}_2} - 2C_{33}\rho_0 \frac{\partial \Omega_2}{\partial C_{33}} \mathbf{C}_2^{-1}, \quad (12.100)$$

which upon using  $C_{33} = III_{\mathbf{C}_2}^{-1}$  and the identity  $\frac{\partial III_{\mathbf{C}_2}^{-1}}{\partial \mathbf{C}_2} = -III_{\mathbf{C}_2}^{-1} \mathbf{C}_2^{-1}$  finally becomes

$$\begin{aligned} \mathbf{S}_2 &= 2\rho_0 \left( \frac{\partial \Omega_2}{\partial \mathbf{C}_2} \Big|_{C_{33}=III_{\mathbf{C}_2}^{-1}} - \frac{\partial \Omega_2}{\partial C_{33}} \Big|_{C_{33}=III_{\mathbf{C}_2}^{-1}} III_{\mathbf{C}_2}^{-1} \mathbf{C}_2^{-1} \right) \\ &= 2\rho_0 \left( \frac{\partial \Omega_2}{\partial \mathbf{C}_2} + \frac{\partial \Omega_2}{\partial C_{33}} \frac{\partial C_{33}}{\partial \mathbf{C}_2} \right) \Big|_{C_{33}=III_{\mathbf{C}_2}^{-1}}. \end{aligned} \quad (12.101)$$

This is however identical to

$$\mathbf{S}_2 = 2\rho_0 \frac{\partial \Omega_2}{\partial \mathbf{C}_2}, \quad (12.102)$$

with the plane part of the augmented free energy. Hence, for the case of plane stress, incompressibility is ensured by application of a pressure  $p$ . The externally applied electric field acting in thickness direction, however yields to a stress resultant in thickness direction whose contribution has to be balanced by the Lagrange multiplier

$$p = -2C_{33}\rho_0 \frac{\partial \Omega_2}{\partial C_{33}}, \quad (12.103)$$

which takes part of a mixed mechanical portion on the one hand, and an electrostatic Coulomb force resultant on the other hand.

In summery, the constitutive model for plane stress case yields the total stress tensor  $\mathbf{S}^{tot} = \mathbf{S}_2^{tot}$ . Because of  $\boldsymbol{\mathcal{E}} = \mathcal{E}_3 \mathbf{m}$  also the electric displacement vector has only a component in the thickness direction  $\mathcal{D}_3$ ; hence, the non-vanishing components read:

$$\mathbf{S}_2^{tot} = 2\rho_0 \frac{\partial \Omega_2}{\partial \mathbf{C}_2}, \quad \mathcal{D}_3 = -\rho_0 \frac{\partial \Omega_2}{\partial \mathcal{E}_3} = \varepsilon III_{\mathbf{C}_2} \mathcal{E}_3 - \rho_0 \frac{\partial \Omega_2}{\partial \lambda_{el}} \frac{\partial \lambda_{el}}{\partial \mathcal{E}_3}. \quad (12.104)$$

#### 12.4.1.4 Traction Boundary Condition

Within a conducting material such as the electrodes attached on top and bottom of the dielectric layer, the electric field has to vanish. Hence, there is no contribution from the Maxwell stress in thickness direction, however, at the vertical boundaries where the film and the exterior (vacuum) field share a surface, continuity in the stress field must be ensured. Denoting with subscript 2 the plane components, for the plane first Piola-Kirchoff  $[[\mathbf{P}_2^{tot}]] \cdot \mathbf{N}_2 = \mathbf{0}$  must hold, where  $\mathbf{N}_2$  is the in plane unit normal vector at the vertical edges. In addition, we claim also continuity of  $\mathbf{F}_2$  as well as  $\mathbf{S}_2^{tot}$  at the interface. For this reason, we can demand the continuity condition equivalently by taking the second Piola-Kirchoff stress, and its Maxwell stress version in air  $\mathbf{S}_2^M$ .

Let us discuss the jump condition in more detail, for the dielectric material the full contribution of the augmented free energy applies, while in the exterior field, all constituents arising from the presence of material vanish, hence the only remaining term is the augmentation term:

$$\rho_0 \Omega_{Dielectric} = \rho_0 \Omega_2, \quad \rho_0 \Omega_{exterior\ field} = \rho_0 \psi_{aug}. \quad (12.105)$$

The Maxwell stress tensor is obtained by differentiating the augmented free energy, and using  $\mathbf{C}^{-1} = \mathbf{C}_2^{-1} + C_{33}^{-1} \mathbf{m}\mathbf{m}$  with  $\boldsymbol{\mathcal{E}} \cdot \boldsymbol{\mathcal{E}} = \mathcal{E}_3^2$  and  $\boldsymbol{\mathcal{E}}\boldsymbol{\mathcal{E}} = \mathcal{E}_3^2 \mathbf{m}\mathbf{m}$ :

$$\begin{aligned} \mathbf{S}^M &= 2 \frac{\partial \psi_{aug}}{\partial \mathbf{C}} = \frac{1}{2} \varepsilon_0 J \mathbf{C}^{-1} \cdot \mathcal{E}_3 \mathcal{E}_3 \mathbf{m}\mathbf{m} \cdot \mathbf{C}^{-1} - \frac{1}{2} \varepsilon_0 J \mathbf{C}^{-1} \cdot \mathcal{E}_3^2 \cdot \mathbf{C}^{-1} \\ &= \frac{1}{2} \varepsilon_0 J C_{33}^{-2} \mathcal{E}_3^2 \mathbf{m}\mathbf{m} - \frac{1}{2} \varepsilon_0 J \mathcal{E}_3^2 C_2^{-2}, \end{aligned} \quad (12.106)$$

such that the plane part is  $\mathbf{S}_2^M = \mathbf{S}^M \cdot \mathbf{I}_2$ .

We use  $\mathbf{P}_2^{tot} = \mathbf{F}_2 \cdot \mathbf{S}_2^{tot}$  in the dielectric elastomer, and by writing the equilibrium at the surface with the plane Maxwell stress tensor  $\mathbf{P}_2^M = \mathbf{F}_2 \cdot \mathbf{S}_2^M$  the traction boundary condition is found to:

$$\mathbf{F}_2 \cdot \mathbf{S}_2^{tot} \cdot \mathbf{N}_2 = \mathbf{F}_2 \cdot \mathbf{S}_2^M \cdot \mathbf{N}_2 = -\mathbf{F}_2 \cdot \frac{1}{2} \varepsilon_0 J \mathcal{E}_3^2 C_2^{-2} \cdot \mathbf{N}_2. \quad (12.107)$$

## 12.5 Electromechanical Stability

Still, the electrostrictive material parameter  $c_1$  remains unknown, in order to define  $c_1$  one has to rely on experimental measurements. However, proper identification of a coefficient associated with electrostriction is difficult as also the strain coming from Maxwell effect is quadratic in the electric field. Hence, a direct comparison to experimental data is not possible, and a proper conversion from the measured value to the electrostrictive parameter  $c_1$  has to be applied. Diaconu and Dorohoi (2005) used a parameter  $M$  to relate the experimental dependence of the measured strain on the applied electric field. We will make use of the data set obtained there and proceed by specifying the mathematical model to the problem from the measurements.

We consider a thin plate, which is free to deform in plane upon application of an external electric field in thickness direction  $\mathcal{E}_3 = V/h$ , where  $V$  is the magnitude of the applied voltage, and  $h$  the thickness of the plate. For this problem, a spherical right Cauchy-Green tensor, with the same in plane stretches due to the homogeneous deformation, applies, hence  $\mathbf{C}_2 = C \mathbf{I}_2$  with  $C = \lambda^2$ . Where  $\lambda = \lambda_1 = \lambda_2$  denotes the principal stretch in both in-plane directions. We use  $\mathbf{I}_2 = \mathbf{I} - \mathbf{m}\mathbf{m}$  the plane identity tensor, and write the invariants for this problem,

$$I_{\mathbf{C}_2} = 2C = 2\lambda^2, \quad III_{\mathbf{C}_2} = C^2 = \lambda^4. \quad (12.108)$$



By using the neo-Hookean strain energy function, specified for incompressible materials, the expression for the augmented free energy gets,

$$\rho_0 \Omega_2 = \frac{\mu}{2} (2\lambda_{el}^{-2} \lambda^2 + \lambda_{el}^4 \lambda^{-4} - 3) - \frac{1}{2} \varepsilon \lambda^4 \mathcal{E}_3^2, \quad (12.109)$$

where  $\varepsilon = \varepsilon_0(1 + \chi) = \varepsilon_0 \varepsilon_r$ . The plane total second Piola-Kirchhoff stress tensor is obtained by using implicit differentiation, and the relation  $\partial \mathbf{C}_2 / \partial \lambda = 2\lambda \mathbf{I}_2$ :

$$\mathbf{S}_2^{tot} = 2\rho_0 \frac{\partial \Omega_2}{\partial \mathbf{C}_2} = 2\rho_0 \frac{\partial \Omega_2}{\partial \lambda} \frac{\partial \lambda}{\partial \mathbf{C}_2} = \rho_0 \frac{1}{\lambda} \frac{\partial \Omega_2}{\partial \lambda} \mathbf{I}_2. \quad (12.110)$$

Next, the contributing stress from the exterior field needs to be incorporated, by making use of the traction boundary condition  $\mathbf{F}_2 \cdot \mathbf{S}_2^{tot} \cdot \mathbf{N}_2 = \mathbf{F}_2 \cdot \mathbf{S}_2^M \cdot \mathbf{N}_2$  with  $\mathbf{F}_2 = \lambda \mathbf{I}_2$  and  $\mathbf{S}_2^M = -\frac{1}{2} \varepsilon_0 \mathcal{E}_3^2 \lambda^{-4} \mathbf{I}_2$ :

$$\rho_0 \frac{\partial \Omega_2}{\partial \lambda} \mathbf{N}_2 = -\frac{1}{2} \varepsilon_0 \mathcal{E}_3^2 \lambda^{-3} \mathbf{N}_2 \quad (12.111)$$

Integration yields the augmentation energy  $\rho_0 \Omega_2^{aug} = \frac{1}{4} \varepsilon_0 \lambda^{-2} \mathcal{E}_3^2$ , such that the traction boundary condition can be expressed by an overall plane energy function  $\bar{\Omega}_2$

$$\rho_0 \bar{\Omega}_2 = \rho_0 \Omega_2 - \rho_0 \Omega_2^{aug} = \rho_0 \Omega_2 - \frac{1}{4} \varepsilon_0 \lambda^{-2} \mathcal{E}_3^2. \quad (12.112)$$

Moreover, the traction boundary condition can be equally written in terms of a new overall second Piola-Kirchhoff type stress tensor  $\bar{\mathbf{S}}_2 \cdot \mathbf{N}_2 = 0$ , where

$$\bar{\mathbf{S}}_2 = \frac{1}{\lambda} \left( \frac{\partial \Omega_2}{\partial \lambda} + \frac{1}{2} \varepsilon_0 \lambda^{-3} \mathcal{E}_3^2 \right) \mathbf{I}_2 = \frac{1}{\lambda} \frac{\partial \bar{\Omega}_2}{\partial \lambda} \mathbf{I}_2 \quad (12.113)$$

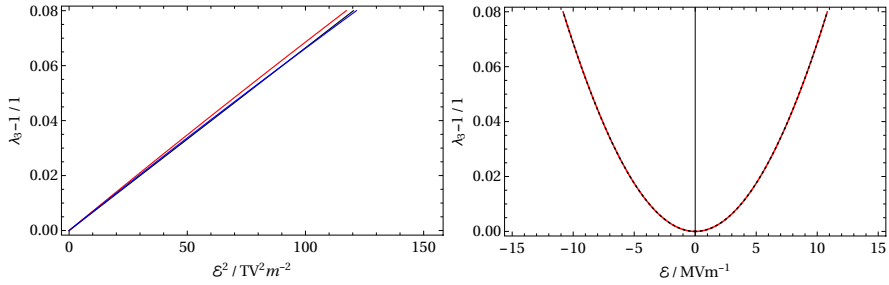
has to vanish in the whole plate. We can now proceed to the stability analyses by writing the equilibrium condition in form of the Principle of Gibbs (Ziegler, 1998)

$$\frac{\partial \bar{\Omega}_2}{\partial \lambda} = 0, \quad (12.114)$$

yielding the equilibrium stretches  $\lambda = \lambda_0$ . Furthermore, one can judge on the stability of these stretches by making use of the Dirichlet stability criterion for conservative problems,

$$\left. \frac{\partial^2 \bar{\Omega}_2}{\partial \lambda^2} \right|_{\lambda_0} > 0. \quad (12.115)$$

We proceed by specifying the overall free energy for the incompressible neo-Hookean material and write the equilibrium condition:



**Fig. 12.6:** Equilibrium Biot strain for Voltage driven actuation, left the linear course of the strain upon the square electric field, right the quadratic course upon the linear electric field. The red line corresponds to the full model, black dotted neglects Maxwell effect, black solid line linearized problem, blue line electric stretch.

$$\rho_0 \bar{\Omega}_2 = \frac{\mu}{2} (2\lambda_{el}^{-2} \lambda^2 + \lambda_{el}^4 \lambda^{-4} - 3) - \frac{1}{2} \varepsilon \lambda^4 \mathcal{E}_3^2 - \frac{1}{4} \varepsilon_0 \mathcal{E}_3^2 \lambda^{-2}, \quad (12.116)$$

$$(\lambda_{el}^{-2} \lambda - \lambda_{el}^4 \lambda^{-5}) - \lambda^3 \left( 1 - \frac{1}{4\varepsilon_r} \lambda^{-6} \right) \frac{\varepsilon}{\mu} \mathcal{E}_3^2 = 0 \quad (12.117)$$

where we have used  $\varepsilon = \varepsilon_0(1 + \chi) = \varepsilon_0 \varepsilon_r$ . Finally, we close the theoretical part by specifying the material parameter using the same polyurethane elastomer reported in Diaconu and Dorohoi (2005), with  $\varepsilon_r = 8.8$ ,  $Y = 3\mu$  and  $Y = 3.6\text{MPa}$ . Multiplication of Eq. (12.117) with  $\lambda$  and using  $\lambda^2 = \lambda_3^{-1}$ , which was obtained from the incompressibility condition, yields:

$$(\lambda_{el}^{-2} \lambda_3^{-1} - \lambda_{el}^4 \lambda_3^2) - \lambda_3^{-2} \left( 1 - \frac{1}{4\varepsilon_r} \lambda_3^3 \right) \frac{\varepsilon}{\mu} \mathcal{E}_3^2 = F(\lambda_3, \mathcal{E}_3^2) = 0. \quad (12.118)$$

In the reference, quadratic dependence of the strains was observed at low electric field strength. To ensure comparability, we approximate the equilibrium condition  $F(\lambda_3, \mathcal{E}_3^2)$  in the vicinity of  $\lambda_3 \approx 1$  and  $\mathcal{E}_3^2 \approx 0$ , leading to the linear relation

$$\varepsilon_3 = - \left( \frac{\varepsilon(1 - \frac{1}{4\varepsilon_r})}{3\mu} - c_1 \right) \mathcal{E}_3^2 = -M \mathcal{E}_3^2, \quad (12.119)$$

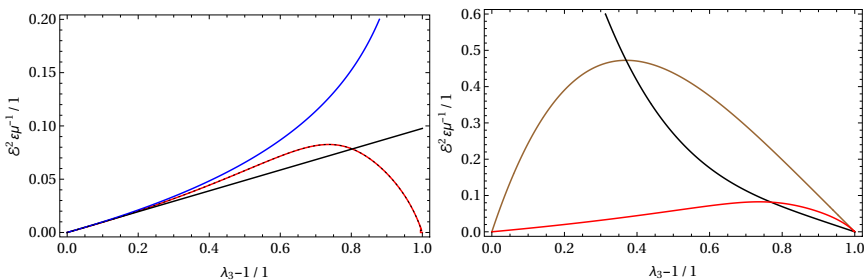
which allows for incorporating the measured value  $M$ . Diaconu and Dorohoi (2005) measured a value of  $M = 7.07 \times 10^{-16} \text{m}^2 \text{V}^{-2}$ , which is a parameter, that still carries the contribution from the Maxwell effect. Here, we have introduced the Biot strain measure  $\varepsilon_3 = \lambda_3 - 1$ . By solving the linearized system the electrostrictive parameter  $c_1 = -6.86 \times 10^{-16} \text{m}^2 \text{V}^{-2}$  can be found. Hence, the contribution of the Maxwell effect is 3.066%, which agrees well with the value 3.07% given in Diaconu and Dorohoi (2005). In Fig. 12.6, the equilibrium Biot strain against the square of the electric field (left), and right the equilibrium Biot strain against the linear electric

field is shown. Clearly, the electrostrictive behavior can be observed. On the left side, the solid red line corresponds to the strain response of the whole problem, the black line shows the linearized system given Eq. (12.119), and the blue line corresponds only to the electrical Biot strain  $\varepsilon_{el,3} = \lambda_{el}^{-2} - 1 = \exp(c_1 \mathcal{E}_3^2) - 1$ . However, for small strains, almost no difference is visible. In the right figure, the red line corresponds to the problem discussed in this paper, accounting for the Maxwell effect, while the black dotted line shows the solution of the problem if the Maxwell stress arising from the traction boundary is neglected. Results show, there is almost no difference, due to the prevailing electrostrictive effect.

Increasing the field strength and allowing also higher strains, the different curves deviate from each other, unveiling the nature of each contributor, see Fig. 12.7. In the left figure, again the red as well as the black dotted line are almost equal, as the Maxwell effect from the boundary condition is negligibly small. The black solid line is again the linear solution. Attention should be taken to the blue line, which shows the electric stretch  $\lambda_{el,3} - 1$  in thickness direction; its nature unveils the impact of the electrostrictive effect, which for the polyurethane material under consideration seems to be of great importance.

Strains of such magnitude cannot be obtained in nature, as at some point the system loses its stability. On the right hand side in Fig. 12.7 the equilibrium strains (red, black dotted and brown) and the stability margin in black are presented. The theoretical bounds of equilibrium stretches, and the corresponding field strength can be obtained by using the Dirichlet criteria and are acquired for several cases:

- Considering both Maxwell effect and electrostriction, with the following equilibrium condition, and Dirichlet stability criterion



**Fig. 12.7:** Equilibrium Biot strain considering higher electric fields, up to Biot strain = 1. On the right side, the red line corresponds to the case with electrostriction, brown line only electrostatic forces, black line stability margin. Left: red and black dotted line, equilibrium strain accounting for electrostriction with and without Maxwell boundary term, black solid line linearized strain, blue line electrical part of the Biot strain  $\varepsilon_{el,3}$ .

$$(\lambda\lambda_{el}^{-2} - \lambda^{-5}\lambda_{el}^4) - \lambda^3 \left(1 - \frac{1}{4\varepsilon_r}\lambda^{-6}\right) \frac{\varepsilon}{\mu} \mathcal{E}_3^2 = 0, \quad (12.120)$$

$$(\lambda_{el}^{-2} + 5\lambda^{-6}\lambda_{el}^4) - 3\lambda^2 \left(1 + \frac{1}{4\varepsilon_r}\lambda^{-6}\right) \frac{\varepsilon}{\mu} \mathcal{E}_3^2 = 0. \quad (12.121)$$

- Neglecting the Maxwell effect from the boundary conditions, which follows by dropping the terms with the relative permittivity.

$$(\lambda\lambda_{el}^{-2} - \lambda^{-5}\lambda_{el}^4) - \lambda^3 \frac{\varepsilon}{\mu} \mathcal{E}_3^2 = 0, \quad (12.122)$$

$$(\lambda_{el}^{-2} + 5\lambda^{-6}\lambda_{el}^4) - 3\lambda^2 \frac{\varepsilon}{\mu} \mathcal{E}_3^2 = 0. \quad (12.123)$$

- In order to draw a comparison to the impact of the electrostrictive effect the case for pure electrostatic force, shown in Krommer et al (2016):

$$(\lambda - \lambda^{-5}) - \lambda^3 \frac{\varepsilon}{\mu} \mathcal{E}_3^2 = 0, \quad (12.124)$$

$$(1 + 5\lambda^{-6}) - 3\lambda^2 \frac{\varepsilon}{\mu} \mathcal{E}_3^2 = 0. \quad (12.125)$$

The critical stretch in thickness direction is obtained by inserting  $\lambda_3 = \lambda^{-2}$ , and solving the equilibrium condition. Using this critical value thereafter in the Dirichlet criterion yields the critical electric field. For the last two discussed cases, the critical stretch  $\lambda_{crit}$  along with the critical electric field  $\mathcal{E}_{3,crit}$  are

$$\lambda_{crit,ES\ Force}^{-6} = \frac{1}{4} \rightarrow \sqrt{\frac{\varepsilon}{\mu}} \mathcal{E}_{3,crit,ES\ Force} = \frac{\sqrt{3}}{4^{\frac{2}{3}}} = 0.687, \quad (12.126)$$

$$\left(\frac{\lambda_{crit,DE}}{\lambda_{e,crit,DE}}\right)^{-6} = \frac{1}{4} \rightarrow \sqrt{\frac{\varepsilon}{\mu}} (\exp(-c_1 \mathcal{E}_{3,crit,DE}^2) \mathcal{E}_{3,crit,DE}) = \frac{\sqrt{3}}{4^{\frac{2}{3}}} = 0.687. \quad (12.127)$$

First the critical stretch and electric field for the electrostatic force is presented in Eq.(12.126). For the problem accounting for electrostriction but dropping the Maxwell effect, a very similar correlation can be found, see Eq.(12.127). However, if considering both electrostriction and Maxwell effect, the limiting criteria turn out to be more complicated

$$\lambda_{crit}^6 = \left(-1 + 8\lambda_{el,crit}^6 \varepsilon_r + \sqrt{1 - 20\lambda_{el,crit}^6 \varepsilon_r + 64\lambda_{el,crit}^{12} \varepsilon_r^2}\right) (4\varepsilon_r)^{-1}, \quad (12.128)$$

which upon using the abbreviations  $k = (-1 + 8\varepsilon_r \lambda_{el,crit}^6)$  and  $s = \sqrt{k^2 - 4\varepsilon_r \lambda_{el,crit}^6}$  yields

$$\lambda_{crit}^6 = (k + s)(4\varepsilon_r)^{-1}, \quad (12.129)$$

and

$$\sqrt{\frac{\varepsilon}{\mu}} \mathcal{E}_{crit} = \sqrt{\frac{2^{\frac{2}{3}}(\lambda_{crit}^6 - \lambda_{el,crit}^6)4\varepsilon_r}{\lambda_{el,crit}^2(k-1+s)(k\varepsilon_r^{-1} + s\varepsilon_r^{-1})^{\frac{1}{3}}}}. \tag{12.130}$$

However, as it has turned out that the Maxwell effect seems to have minimal effect on the solution, Fig. 12.7 indicates almost the same critical values, as for the case where Maxwell effect is dropped. This can be judged, as the black line giving the stability margin crosses the equilibrium lines where the tangent gets horizontally, in both cases.

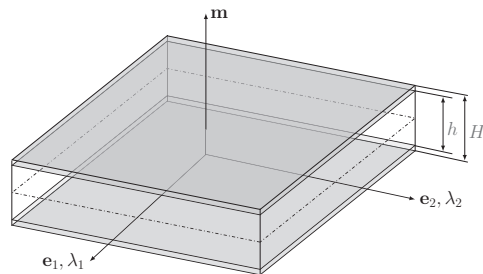
### 12.5.1 Stiffening Effect of Electrodes

Up to now, the investigations presented above, were made under the assumption, that electrodes attached to the EAP film do not interact with the EAP other than supplying an electric field. As this assumption is fairly crude, the last part is devoted to the problem of a homogeneously deformed plate with electrodes attached on top and bottom, see Fig. 12.8.

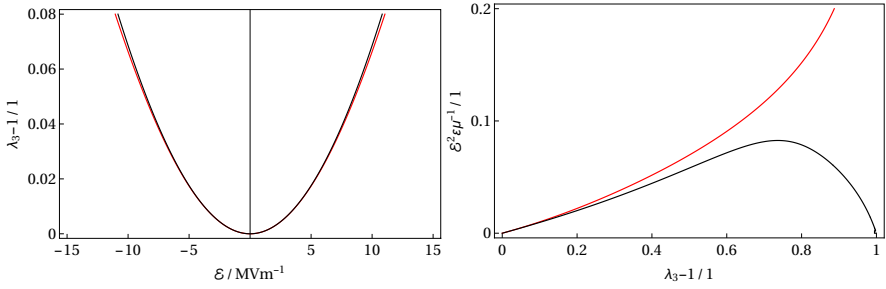
We investigate the case of compliant electrodes made of steel, hence we use a St. Venant-Kirchoff material model for the constitutive part of the electrodes. Due to the in plane deformation a membrane state of stress prevails. We use  $\varepsilon_3 = \lambda_3 - 1$ , the strain component in thickness direction as it correlates to the in plane stretches by the relation  $\lambda^2 = \lambda_3^{-1}$ .

$$u_{m,2} = \frac{1}{2}(A(\text{tr}\varepsilon_3 \text{tr}\varepsilon_3 - 2(1-\nu)\text{det}\varepsilon_3)) \quad , \quad A = \int_{-H/2}^{-h/2} \frac{Y}{(1+\nu)(1-\nu)} dz \tag{12.131}$$

$A$  denotes the tension stiffness, which is given for the lower electrode, but correspondingly applies to the upper electrode by changing the sign of the bounds.  $Y = 210 \times 10^9 \text{Nm}^{-2}$  denotes the elastic modulus, and  $\nu = 0.33$  the Poisson's ratio of steel. We incorporate the electrodes into our constitutive model of the dielectric by simply adding the strain energy  $u_{m,2}$  to the augmented free energy function  $\Omega_2$  and



**Fig. 12.8** Electro-active polyurethan plate with electrodes at the height  $\frac{1}{2}(H-h)$  attached on top and bottom.



**Fig. 12.9:** In red, the equilibrium Biot strain for the plate with electrodes, black plate problem without electrodes.

find

$$\Omega_{2,ges} = \frac{1}{2}h(-\mathcal{E}_3^2 \epsilon_0 \epsilon_r \lambda^4 + (2\lambda^2 \lambda_{el}^{-2} + \lambda^{-4} \lambda_{el}^4 - 3)\mu) + \frac{(\frac{H}{2} - \frac{h}{2})Y(\lambda^2 - 1)^2}{(1 + \nu)(1 - \nu)}. \quad (12.132)$$

As the Maxwell effect coming from the vertical boundaries has been shown to be negligible, we dropped the term, and proceed by determining the electrostrictive coefficient  $c_1$ . Again the correlation of the experimentally known data for  $M$  to our parameter  $c_1$  is found in a linear approximation of the equilibrium equation  $\frac{\partial \Omega_{2,ges}}{\partial \lambda} = 0$ , in the vicinity of  $\lambda_3 \approx 1$  and  $\mathcal{E}_3 \approx 0$  to

$$\epsilon_3 = -h(\nu^2 - 1) \left( \frac{(\epsilon + 3c_1\mu)}{h(Y + 3\mu(\nu^2 - 1)) - HY} \right) \mathcal{E}_3^2 = -M\mathcal{E}_3^2. \quad (12.133)$$

At first, the difference in the electrostrictive behavior and the stable stretch configuration is investigated. As for the experimental value  $M = 7.07 \times 10^{-16} \text{m}^2 \text{V}^{-2}$  no thickness of the sample was reported, we assumed a value of  $1 \mu\text{m}$ . The thickness of the electrodes is derived by using the relation  $H = 1,00002h$ , which results in an electrostrictive coefficient of  $c_1 = -9.94 \times 10^{-15} \text{m}^2 \text{V}^{-2}$ . Figure Fig. 12.9 shows the resulting equilibrium Biot strain, the electrostrictive behavior upon the linear electric field is still visible, furthermore, the stiffening effect of the electrodes tends to stabilize the problem (red line) as no horizontal tangent is present any more. Additionally to the single parameter set we are using so far, Diaconu et al (2006) published experimental results for another set of five different materials, given in Tab. 12.1. Again only results for small electric fields and strains are presented in Diaconu et al (2006). At this regime the results given in Fig. 12.10, upon the square electric field agree very well, however at higher fields, experimental results tend to deviate nonlinearly, which is not visible from the results of our model. The black line in Fig. 12.10 corresponds to the pure EAP model without electrodes. Finally, the results upon increasing the thickness of the electrodes by the factor 10 are presented in Fig.12.11. The electrostrictive behavior remains for a broadened electric field.

Table 12.1: Material parameter taken from Diaconu et al (2006), at an electric field of  $\mathcal{E}_3 = 4.5\text{MVm}^{-1}$

Sample	Thickness [ $\mu\text{m}$ ]	Y [MPa]	$M \times 10^{16}$ [ $\text{m}^2\text{V}^{-2}$ ]	$c_1 \times 10^{16}$	Color
1	15	6.19	3.00	2.87	Red
2	27	25.46	5.00	4.97	Green
3	33	51.03	8.00	7.89	Blue
4	49	52.39	12.28	12.27	Brown
5	110	59.5	8.92	8.91	Magenta

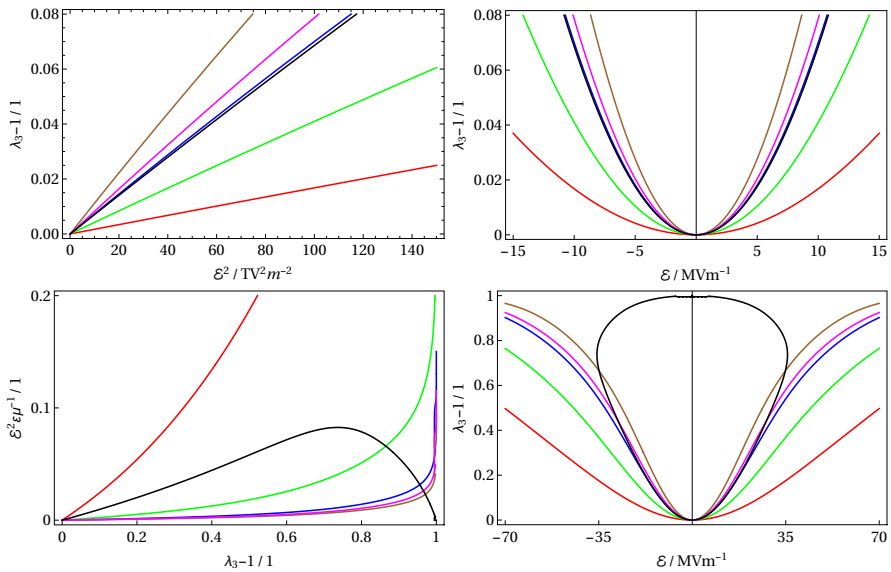
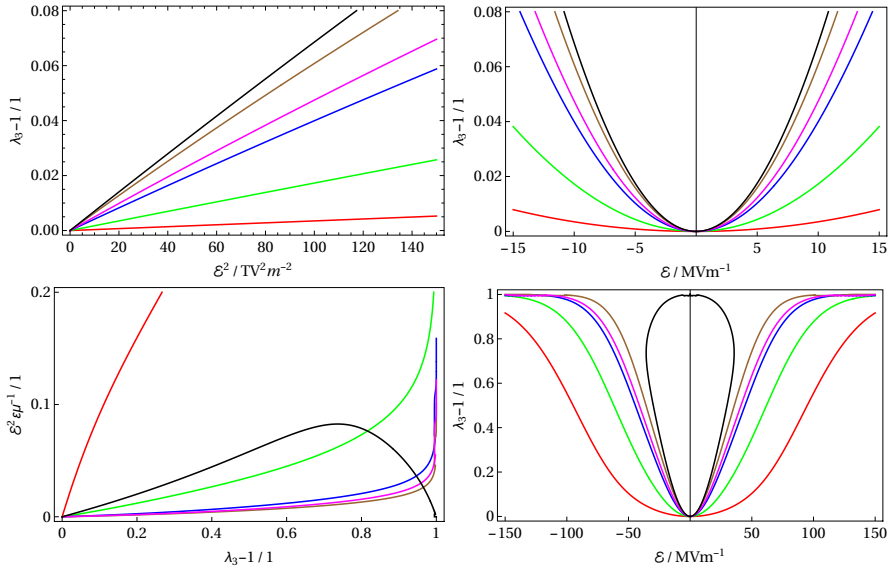


Fig. 12.10: Response at small electric fields and strains above, and at large fields bottom.

While if the thickness is decreased, the curves tend to the solution without electrodes, presented in black.

## 12.6 Conclusion and Outlook

The constitutive modeling framework in the field of nonlinear electro-elasticity has been presented in details, starting by introducing the electrostatic field quantities, the macroscopic balance equations were derived and with clear focus on the multiplicative decomposition of the deformation gradient applied to the effect of electrostriction.



**Fig. 12.11:** Increasing the thickness of the electrodes by factor 10.

The application on a simple homogeneously deformed plate unveiled, that the electrostrictive effect has a considerable effect on the actuation behavior of electroactive polymers, and can be enhanced by the choice of dielectric material. In the near future, the presented model is extended to geometrically nonlinear shells and the implementation into a geometrically nonlinear finite element code, in order to apply the model to more general problems. Special attention will be paid on the choice of the specific constitutive law for the electrical part of the deformation gradient, as this component offers access to easily incorporate different models and requires some more investigations.

**Acknowledgements** Support from the K2 area of the Linz Center of Mechatronics GmbH is gratefully acknowledged. This area is promoted as a K2 project with the project name Austrian Competence Center of Mechatronics - ACCM in the context of Competence Centers for Excellent Technologies (COMET) by BMVIT, BMWFJ and by the country Upper Austria.

## References

Arghavani J, Auricchio F, Naghdabadi R, Reali A, Sohrabpour S (2010) A 3d finite strain phenomenological constitutive model for shape memory alloys considering martensite reorientation. *Continuum Mechanics and Thermodynamics* 22(5):345–362

Ask A, Menzel A, Ristinmaa M (2012) Phenomenological modeling of viscous electrostrictive polymers. *International Journal of Non-Linear Mechanics* 47(2):156 – 165



- Ask A, Menzel A, Ristinmaa M (2015) Modelling of viscoelastic dielectric elastomers with deformation dependent electric properties. *Procedia IUTAM* 12:134–144
- Bonnet J, Wood RD (1997) *Nonlinear Continuum Mechanics for Finite Element Analysis*. Cambridge University Press, Cambridge
- Bortot E, Denzer R, Menzel A, Gei M (2016) Analysis of viscoelastic soft dielectric elastomer generators operating in an electrical circuit. *International Journal of Solids and Structures* 78:205–215
- Bustamante R, Dorfmann A, Ogden RW (2009a) Nonlinear electroelastostatics: a variational framework. *Zeitschrift für angewandte Mathematik und Physik* 60(1):154–177
- Bustamante R, Dorfmann A, Ogden RW (2009b) On electric body forces and maxwell stresses in nonlinearly electroelastic solids. *International Journal of Engineering Science* 47(11):1131–1141
- Clifton RJ (1972) On the equivalence of  $F^e F^p$  and  $\bar{F}^p \bar{F}^e$ . *Trans ASME J Appl Mech* 39(1):287–289
- Diaconu I, Dorohoi D (2005) Properties of polyurethane thin films. *Journal of Non-Linear Opto-electronics and Advanced Materials* 7(2):921–924
- Diaconu I, Dorohoi D, Ciobanu C (2006) Electromechanical response of polyurethane films with different thickness. *Rom Journ Phys* 53(1):91–97
- Dorfmann A, Ogden RW (2005) Nonlinear electroelasticity. *Acta Mechanica* 174(3):167–183
- Dorfmann L, Ogden RW (2017) Nonlinear electroelasticity: material properties, continuum theory and applications. *Proceedings of the Royal Society of London A: Mathematical, Physical and Engineering Sciences* 473(2204)
- Humer A, Krommer M (2015) Modeling of piezoelectric materials by means of a multiplicative decomposition of the deformation gradient. *Mechanics of Advanced Materials and Structures* 22(1-2):125–135
- Humer A, Krommer M, Staudigl E (2017) Nonlinear electro-elasticity for piezoelectric materials and structures using a multiplicative decomposition of the deformation gradient. In: 8th ECCOMAS Thematic Conference on Smart Structures and Materials, pp 1316–1328
- Krommer M, Vetyukov Y, Staudigl E (2016) Finite deformations of thin plates made of dielectric elastomers: Modeling, numerics and stability. *Journal of Intelligent Material Systems and Structures*
- Landau LD, Bell JS, Kearsley MJ, Pitaevskii LP, Lifshitz EM, Sykes JB (2013) *Electrodynamics of Continuous Media*. Elsevier, London
- Lee EH (1969) Elastic-plastic deformation at finite strains. *Trans ASME J Appl Mech* 36(1):1–6
- Lubarda VA (2004) Constitutive theories based on the multiplicative decomposition of deformation gradient: Thermoelasticity, elast-plasticity, and biomechanics. *Applied Mechanics Review* 57(4):95–108
- Maugin GA, Eringen AC (2012) *Electrodynamics of Continua, vol I: Foundations and Solid Media*. Springer, New York
- McMeeking RM, Landis CM (2004) Electrostatic forces and stored energy for deformable dielectric materials. *Trans ASME Journal of applied Mechanics* 72(4):581–590
- Mehnert M, Hossain M, Steinmann P (2016) On nonlinear thermo-electro-elasticity. *Proceedings of the Royal Society of London A: Mathematical, Physical and Engineering Sciences* 472(2190)
- Skatulla S, Sansour C, Arockiarajan A (2012) A multiplicative approach for nonlinear electro-elasticity. *Computer Methods in Applied Mechanics and Engineering* 245-246:243 – 255
- SPIE (2017) Spie special event. EAP-in-Action Session and Demonstrations, Vol. 19, SPIE Smart Structures NDE
- Su J, Harrison JS, St Clair TL, Bar-Cohen Y, Leary S (1999) Electrostrictive graft elastomers and applications. In: *MRS Symposium Proceedings*, Boston, pp 1–6
- Toupin R (1956) The elastic dielectric. *Journal of Rational Mechanics and Analysis* 5(6):849–915
- Wissler M, Mazza E (2005) Modeling of a pre-strained circular actuator made of dielectric elastomers. *Sensors and Actuators A: Physical* 120(1):184–192
- Xu BX, Müller R, Klassen M, Gross D (2010) On electromechanical stability analysis of dielectric elastomer actuators. *Applied Physics Letters* 97(16):162,908
- Xu D, Tairyeh A, Anderson IA (2016) Stretch not flex: programmable rubber keyboard. *Smart Materials and Structures* 25(1):015,012

- Zäh D, Miehe C (2015) Multiplicative electro-elasticity of electroactive polymers accounting for micromechanically-based network models. *Computer Methods in Applied Mechanics and Engineering* 286:394–421
- Zhao X, Suo Z (2008) Electrostriction in elastic dielectrics undergoing large deformation. *Journal of Applied Physics* 104(12):123,530
- Zhenyi M, Scheinbeim JJ, Lee JW, Newman BA (1994) High field electrostrictive response of polymers. *Journal of Polymer Science Part B: Polymer Physics* 32(16):2721–2731
- Ziegler F (1998) *Mechanics of Solids and Fluids*, 2nd edn. Springer, Vienna, New York

# Chapter 13

## Mechanics of Axially Moving Structures at Mixed Eulerian-Lagrangian Description

Yury Vetyukov

**Abstract** We discuss a series of methods of the mathematical modelling of large deformations of axially moving strings, beams and plates. Both uni-axial and looped trajectories of motion are considered, which allows the application of these methods to such practically important problems as rolling mills or belt drives. Based on the principles of Lagrangian mechanics, we transform the variational formulations of structural mechanics to problem-oriented exact kinematic descriptions with mixed spatial and material coordinates. The discretization of an intermediate domain results in a consistent non-material finite element formulation with particles of continuum flowing across the mesh. This allows avoiding numerically induced oscillations in the solution, while keeping the discretization fine where necessary, e.g. in the regions of contact.

### 13.1 Introduction

Axially moving structures are frequently used in engineering as an intrinsic part of many technical solutions. It is not surprising that they have long attracted the attention of mechanical engineers. Practical relevance, technical difficulties in maintaining the desired regime of motion, non-trivial and even sometimes counter-intuitive behavior are coupled with challenges, intrinsic to the theoretical investigation of such systems.

The mathematical modeling is traditionally based on a spatial (Eulerian) kinematic description, see review papers by Chen (2005); Marynowski and Kapitaniak (2014). Considering the unknown displacements, forces and other mechanical fields as functions of a fixed coordinate in the axial direction simplifies the analysis, as the problem needs to be solved in a fixed control domain only and the boundary

---

Yury Vetyukov

Institute of Mechanics and Mechatronics, Vienna University of Technology, Getreidemarkt 9, 1060 Vienna, Austria

e-mail: [yury.vetyukov@tuwien.ac.at](mailto:yury.vetyukov@tuwien.ac.at)

conditions are applied at fixed points. The common difficulty is that the basic equations of structural mechanics are generally available in the Lagrangian form, where the variables are observed in material points. The present contribution is focused on consistently solving this issue by transforming the equations to new problem-specific coordinates.

Below, in Sect. 13.2, we demonstrate the transformation of the equations to the spatial form in a simple linear case, when the relation between the material and the spatial coordinates is known in advance. In nonlinear problems, many authors adopt certain kinematical simplifications and derive the mathematical model in the spatial frame from scratch (Ghayesh et al, 2013; Kong and Parker, 2005), or rely upon other known equations from the literature. Thus, the models of Wickert (1992); Mote (1966) are often applied. While numerous fascinating and practically important results were obtained in this way, accurate modelling of large deformations of axially moving structures requires exact treatment of geometrically nonlinear effects both in the elastic response as well as in the inertial properties with an established structural mechanics theory in the background. Despite growing interest of researchers (Humer, 2013; Humer and Irschik, 2009, 2011; Eliseev and Vetyukov, 2012; Pechstein and Gerstmayr, 2013; Vetyukov et al, 2017b), developing efficient and reliable techniques of transforming the general equations of motion to a new spatial form remains a challenging problem.

In statics of flexible solids, modelling of a discretized system is convenient with the principle of minimality of the potential energy. For a given finite element (or global Ritz) approximation one simply integrates the total strain energy and energy of external forces as functions of generalized coordinates, and the derivatives of these functions constitute the equations. An extension to dynamics is traditionally accomplished with Lagrange's equations of motion of the second kind; the kinetic energy becomes a quadratic form of generalized velocities. The approach is particularly straightforward when combined with the material description of the kinematics of deformation and motion. Considering mechanical fields as functions of coordinates in the reference configuration is advantageous because an elastic body keeps "memory" of its undeformed state. Moreover, dealing with the same material volume ensures the validity of the variational principle and the corresponding equations. Modern applications pose challenging problems of computational modelling of fluid-structure interaction, material forming processes, etc. Similar to fluid mechanics it becomes more efficient to observe the processes at given points in space, which gave birth to the so-called Arbitrary Lagrangian-Eulerian (ALE) formulations. This family of methods features control volumes, which are moving in a problem-oriented manner relative to both the spatial actual state as well as the reference configuration (Donea et al, 2004). In their traditional form, ALE methods imply accounting for the advection of material in the local forms of the constitutive and balance equations. Although their applications in structural mechanics are presently sparse, we can mention the works by Hong and Ren (2011); Yang et al (in press). The authors of the mentioned papers make use of a redundant set of degrees of freedom in a finite element model with additional constraints. This flexible formulation results in a differential-algebraic system of equations, which needs to be integrated over time.

In this chapter, we systematically discuss the application of a novel kinematic description of thin axially moving structures, which undergo finite deformations superimposed upon the gross nominal motion. The main results were partially presented by the author previously in Vetyukov (2017); Vetyukov et al (2016). The presented work in progress is currently actively developed towards the consistent model of dry friction with stick and slip phenomena in the zones of contact of the axially moving continua with pulleys and drums.

### 13.2 Linear Waves in a Moving String

We begin with the simple example of waves, running in a moving string. A particle of a string is identified by a material (Lagrangian) coordinate  $s$ . We assume small transverse deflection  $w$  and constant tension force and write

$$\begin{aligned} \partial_t^2 w &= c^2 \partial_s^2 w, \\ \partial_s w &\equiv \left. \frac{\partial w}{\partial s} \right|_{t=\text{const}}, \quad \partial_t w \equiv \left. \frac{\partial w}{\partial t} \right|_{s=\text{const}} \end{aligned} \tag{13.1}$$

for a dynamic process over time  $t$  with the wave velocity  $c$ . The mechanical field  $w$  is considered at a given material point  $s$ , and the wave equation features a material time derivative  $\partial_t$ , which is typical for the Lagrangian formulation. In mathematical physics, one conventionally considers (13.1) with boundary conditions. Our string is moving axially between two spatially fixed points, and the boundary conditions need to be posed in time varying material points  $s_{1,2}(t)$ . Moving boundary conditions make the problem essentially more difficult and challenging for solving by either the established methods of mathematical physics or numerical techniques of finite differences or finite elements.

Assuming a constant velocity  $v$  of the gross axial motion, we find simple relations between the material coordinate  $s$  and the spatial one  $x$ , along which the string is moving, see Fig. 13.1:

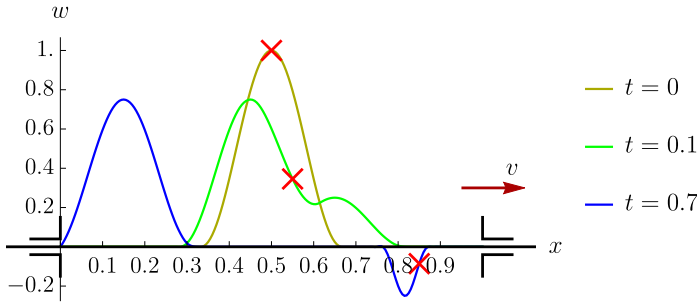
$$x = s + vt. \tag{13.2}$$

In the following, we will mainly deal with the Eulerian form of equations, in which the unknown fields are observed at a given spatial coordinate  $x$ . Derivatives with respect to time and space need to be transformed from the material to the spatial form:

$$\partial_s w = \partial_x w \equiv w', \quad \partial_t w = \dot{w} + vw', \quad \dot{w} \equiv \left. \frac{\partial w}{\partial t} \right|_{x=\text{const}}. \tag{13.3}$$

We introduce a shortened notation: a prime means a derivative with respect to  $x$  and a dot denotes a time derivative at given  $x$ .

Applying Eqs. (13.3) twice, we transform the wave equation (13.1) to the Eulerian form and arrive at an equivalent boundary value problem with the new pair of variables  $x$  and  $t$ :



**Fig. 13.1:** Wave travelling in a moving string at three different instances of time; crosses mark the same material particle

$$\ddot{w} + 2v\dot{w}' = (c^2 - v^2)w'', \quad u|_{x=0,l} = 0. \tag{13.4}$$

The boundary conditions are imposed at fixed points  $x = 0$  and  $x = l$ , the latter being the length of the control domain. The equation appears to be more complicated, but the boundary value problem may be solved either analytically in the form of infinite series (van Horssen and Ponomareva, 2005), or, even easier, numerically using the method of finite differences. The example solution for the following values of parameters and the smooth initial state

$$c = 1, \quad l = 1, \quad v = 0.5;$$

$$t = 0: \quad \dot{w} = 0, \quad w = \begin{cases} w_0(1 + \cos(6\pi(x/l - 1/2)))/2, & l/3 < x < 2l/3 \\ 0, & x < l/3 \text{ or } x > 2l/3 \end{cases} \tag{13.5}$$

$$w_0 = 1$$

is shown for three instances of time in Fig. 13.1; SI system of units will be used throughout the Chapter. The chosen large sample value of the amplitude  $w_0$  lies certainly far beyond the range of applicability of the geometrically linear wave equation (13.1). The string is moving, and the sequential positions of a material point, which is originally in the middle of the string, are marked in Fig. 13.1 by a cross. We see two waves of unequal intensities, travelling with the velocities  $c + v$  and  $c - v$  respectively to the right and to the left and reflecting from the end points. From (13.4) we conclude that the type of the partial differential equation changes when  $v$  grows above  $c$ , which means loss of stiffness and dynamic instability.

### 13.3 Large Vibrations of an Axially Moving String

The mathematical model for large vibrations of an axially moving string or a beam was presented by the author in Vetyukov (2017). The key points of the analysis

are discussed below, we restrict the presentation to the string case without bending stiffness.

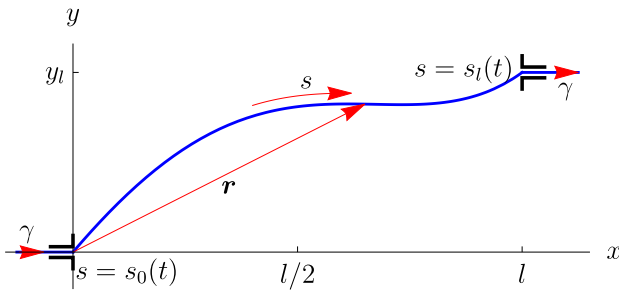
We consider the planar motion of a string across a given domain, see Fig. 13.2. The material enters the domain at the left end  $x = 0$  and leaves it at the right one  $x = l$  with the same rate  $\gamma$ . This material length of the string per time unit is essentially different from the spatial velocity of the particles in the axial direction. Such kind of kinematically prescribed influx or outflux of the material may be implemented using a timing belt and a toothed pulley. It means that the total material length of the string, which remains in the control volume of the considered problem, remains constant.

The kinematically prescribed time-varying transverse deflection of the end point

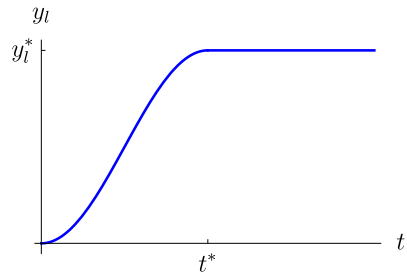
$$y_l(t) = \begin{cases} \frac{1}{2}y_l^* \left(1 - \cos \frac{\pi t}{t^*}\right), & t \leq t^* \\ y_l^*, & t > t^* \end{cases} \tag{13.6}$$

brings the system into a complicated in-plane motion with coupled axial and transverse dynamics when  $\dot{y}_l$  is not small, see Fig. 13.3 for a plot of (13.6).

Although the equations of string dynamics at finite deformations are well established at Lagrangian description (Eliseev, 2006; Eliseev and Vetyukov, 2012), it is a numerically challenging task to solve them with the boundary conditions moving across the material domain. Thus, an attempt to impose kinematic constraints at



**Fig. 13.2:** Vibrations of an axially moving string with kinematically prescribed transverse motion of the right end



**Fig. 13.3** Kinematically prescribed transverse coordinate of the right end of the moving string

moving points of a finite element mesh leads inevitably to numerically induced oscillations in the solution. Therefore, in the following we will use the principle of virtual work as a starting point and transform the equations to a more advantageous problem-specific kinematic description.

For the material description, we consider the displacement from an initially straight horizontal reference configuration

$$\mathbf{u} = u_x \mathbf{i} + u_y \mathbf{j} \quad (13.7)$$

being a function of the material coordinate  $s$  and time  $t$ , such that the actual position vector of a particle is

$$\mathbf{r} = x\mathbf{i} + y\mathbf{j} = s\mathbf{i} + \mathbf{u}, \quad x = s + u_x, \quad y = u_y; \quad (13.8)$$

the unit vectors in the directions of the coordinate axes are respectively called  $\mathbf{i}$  and  $\mathbf{j}$ . The longitudinal strain measure reads

$$\varepsilon = |\partial_s \mathbf{r}| - 1 = \sqrt{(\partial_s(s + u_x))^2 + (\partial_s u_y)^2} - 1. \quad (13.9)$$

The strain energy  $U$  per unit material length  $s$  is a quadratic function of the strain,

$$U = \frac{1}{2} b \varepsilon^2, \quad (13.10)$$

in which  $b$  is the tension stiffness.

### 13.3.1 Mixed Eulerian-Lagrangian Description of the Kinematics of Motion

Further exploiting the simple idea of the mixed Eulerian-Lagrangian description, we change the variable. Instead of the unknown fields  $u_x(s, t)$ ,  $u_y(s, t)$ , we seek the material coordinate and the transverse displacement as functions of the axial spatial coordinate and time:

$$s = s(x, t) = x - u_x(x, t), \quad u_y = u_y(x, t). \quad (13.11)$$

The presentation (13.11) is incapable of describing the formation of loops, at which several material points have the same coordinate  $x$ . However, we gain more efficiency in the analysis of practically relevant problems with large vibration amplitudes.

Again introducing short notation for the derivatives with the pair of variables  $x, t$  similar to (13.3) and using

$$ds = dx - du_x = (1 - u'_x)dx, \quad \partial_s(\dots) = (1 - u'_x)^{-1}(\dots)', \quad (13.12)$$



we rewrite the strain measure (13.9) to the spatial form

$$\varepsilon = \frac{\sqrt{1 + u_y'^2}}{1 - u_x'} - 1. \quad (13.13)$$

Now we address the velocity of a particle and compute it in the mixed description, in which a convective term comes into play:

$$\begin{aligned} \partial_t x &= \partial_t u_x(x, t) = \dot{u}_x + u_x' \partial_t x \quad \Rightarrow \quad \partial_t x = \frac{\dot{u}_x}{1 - u_x'}, \\ \mathbf{v} &= \partial_t \mathbf{u}(x, t) = \dot{\mathbf{u}} + \mathbf{u}' \partial_t x = \dot{\mathbf{u}} + \mathbf{u}' \frac{\dot{u}_x}{1 - u_x'}. \end{aligned} \quad (13.14)$$

The acceleration results into

$$\mathbf{w} = \dot{\mathbf{v}} + \mathbf{v}' \frac{\dot{u}_x}{1 - u_x'}. \quad (13.15)$$

### 13.3.2 Mixed Form of the Variational Equation of Virtual Work

The boundaries of the active material segment of the string, which is currently in the control domain, vary over time with the known rate:

$$s_0(t) \leq s \leq s_l(t), \quad \dot{s}_0 = \dot{s}_l = -\gamma. \quad (13.16)$$

We restrict the presentation to the simple case of known rates of the material influx and outflux and begin with the material form of the variational equation of virtual work for the active segment of the string:

$$\int_{s_0}^{s_l} (\rho \mathbf{w} \cdot \overset{\circ}{\delta} \mathbf{u} + \overset{\circ}{\delta} U) ds = 0. \quad (13.17)$$

With  $\overset{\circ}{\delta}$  we denote a material variation, i.e. a variation of a mechanical field in a given material point. Owing to the kinematic nature of the boundary conditions, we state that the variation  $\overset{\circ}{\delta} \mathbf{u}$  vanishes at the current boundaries, and there is no virtual work produced by the interaction forces with the parts of the continuum outside the active domain.

Using the mathematics similar to (13.14), we relate the material variation  $\overset{\circ}{\delta}$  at fixed material point and the spatial one  $\delta$  at given  $x$ :

$$\overset{\circ}{\delta} \varphi = \delta \varphi + \varphi' \frac{\delta u_x}{1 - u_x'}; \quad (13.18)$$

$\varphi$  is any mechanical field, which can be considered as a function of both, the material and the spatial coordinates. Transforming the elastic term in (13.17) to the spatial form is simply:

$$\int_{s_0}^{s_l} \delta \circ U \, ds = \delta U^\Sigma, \quad U^\Sigma = \int_{s_0}^{s_l} U \, ds = \int_0^l U(1 - u'_x) \, dx. \quad (13.19)$$

The distributed strain energy  $U$  remains a quadratic form (13.10) of the strain measures (13.13). The inertial term in (13.17) reads

$$\int_{s_0}^{s_l} \rho \mathbf{w} \cdot \delta \circ \mathbf{u} \, ds = \int_0^l \rho \mathbf{w} \cdot ((1 - u'_x) \delta \mathbf{u} + \mathbf{u}' \delta u_x) \, dx; \quad (13.20)$$

besides (13.12) we also used the transformation rule for the variations (13.18). Substituting (13.19) and (13.20) in (13.17), we obtain a non-material variational equation

$$\int_0^l \rho \mathbf{w} \cdot ((1 - u'_x) \delta \mathbf{u} + \mathbf{u}' \delta u_x) \, dx + \delta U^\Sigma = 0. \quad (13.21)$$

The latter can be used in a numerical procedure with a suitable Ritz-Galerkin approximation of the unknown displacement  $\mathbf{u}(x, t)$ . More elegance, simplicity in implementation and efficiency can be reached by transforming the equation to the form of Lagrangian equations of motion of the second kind for a given approximation of the unknown displacements.

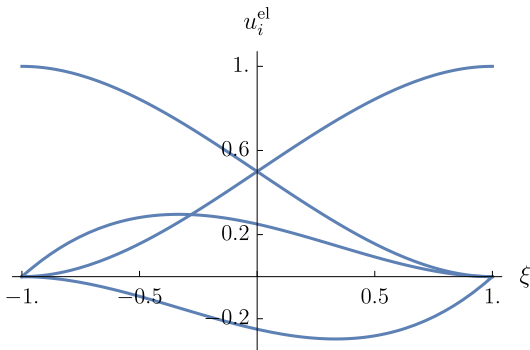
### 13.3.3 Finite Element Approximation

The finite element approximation of the unknown field of displacements is set in the form

$$\mathbf{u}(x, t) = \sum_{k=0}^n (u_k(x) q_{k,1}(t) \mathbf{i} + u_k(x) q_{k,2}(t) \mathbf{j}) = \sum_{k=0}^n \sum_{\alpha=1}^2 \mathbf{u}_{k,\alpha}(x) q_{k,\alpha}(t). \quad (13.22)$$

Both cartesian components are independently represented by piecewise-cubic shape functions  $u_k(x)$ , which allows achieving  $C^1$  inter-element continuity with the corresponding fine rate of mesh convergence. With equal finite element sizes and a local coordinate  $\xi$  on each finite element, which varies from  $-1$  to  $1$ , we have a linear mapping from  $\xi$  to  $x$  and use four cubic shape functions  $u_i^{\text{el}}(\xi)$  (Fig. 13.4) with the properties

**Fig. 13.4** Cubic shape functions, which provide  $C^1$  inter-element continuity



$$\begin{aligned}
 u_i^{\text{el}}|_{\xi=-1} &= \delta_{1,i}, \quad \partial_\xi u_i^{\text{el}}|_{\xi=-1} = \delta_{2,i}, \quad u_i^{\text{el}}|_{\xi=1} = \delta_{3,i}, \quad \partial_\xi u_i^{\text{el}}|_{\xi=1} = \delta_{4,i}; \\
 \delta_{j,i} &= \begin{cases} 1, & i = j; \\ 0, & i \neq j; \end{cases}
 \end{aligned}
 \tag{13.23}$$

the four conditions uniquely determine four coefficients of cubic polynomials, which often find use in the models of classical rods and shells (Vetyukov, 2014b, 2012). The global shape functions  $u_k(x)$  are constructed from the local ones  $u_i^{\text{el}}(\xi)$ , degrees of freedom  $q_{k,\alpha}$  determine either the value or the derivative of the corresponding component of  $\mathbf{u}$  in a node. Each node has now four degrees of freedom, and  $n$  is twice the number of nodes in the finite element model. The boundary conditions in the first and the last nodes,

$$\dot{u}_x|_{x=0,l} = \gamma, \quad u_y|_{x=0} = 0, \quad u_y|_{x=l} = y_l(t)
 \tag{13.24}$$

kinematically prescribe some of the functions  $q_{k,\alpha}$ , which thus deleted from the set of active degrees of freedom in the model.

### 13.3.4 Lagrange’s Equation of Motion of the Second Kind

The dynamic part of Eq. (13.21) can be represented in terms of the kinetic energy of the control domain

$$T^\Sigma = \int_0^l \frac{1}{2} \rho \mathbf{v} \cdot \mathbf{v} (1 - u'_x) dx.
 \tag{13.25}$$

In Vetyukov (2017) it was rigorously proved, that the Lagrange’s equation of motion of the second kind

$$\frac{d}{dt} \left( \frac{\partial T^\Sigma}{\partial \dot{q}_{k,\alpha}} \right) - \frac{\partial T^\Sigma}{\partial q_{k,\alpha}} = - \frac{\partial U^\Sigma}{\partial q_{k,\alpha}}
 \tag{13.26}$$

retains validity in the considered case of non-material control volume, provided that the shape functions of the active degrees of freedom vanish at both ends:

$$\mathbf{u}_{k,\alpha}(0) = \mathbf{u}_{k,\alpha}(l) = 0, \quad (13.27)$$

which is the case for kinematic boundary conditions at hand.

### 13.3.5 Example Solution

The finite element scheme including the time integration was implemented in the *Wolfram Mathematica*<sup>1</sup> environment. With  $n_{el}$  being the number of elements in the model, we have  $n_{el} + 1$  nodes with  $4(n_{el} + 1)$  degrees of freedom  $q_{k,\alpha}$ , 4 of which are prescribed by the boundary conditions and excluded from the active set. The total strain energy (13.19) and kinetic energy (13.25) were computed using a Gaussian quadrature rule with 3 integration points per element. Substituting further the known time variations for the kinematically prescribed degrees of freedom, we construct the system of second order differential equations for the transient dynamics in the form (13.26). With the values of the numerical parameters, initial values and time derivatives of degrees of freedom we integrate the equations over time using standard *NDSolve* routine. Setting the option *Method* -> {"*EquationSimplification*" -> "*Residual*"} allows *Mathematica* to treat the problem as a system of differential-algebraic equations and to use the corresponding solver, which is more efficient and robust in the present case. The obtained results are ready for post-processing.

At first, we considered the linear problem of wave propagation in a moving string, discussed in the motivational example, Sect. 13.2. Setting the numerical values and the initial conditions in accordance with (13.5), we were able to reproduce the results of Fig. 13.1 with a high level of accuracy even using small  $n_{el}$ .

The numerical experiments presented below feature the following parameters of the model with large deformations:

$$\begin{aligned} l = 1, \quad b = 1, \quad \rho = 1, \quad \gamma = 0.1 \text{ or } \gamma = 0.05, \\ \varepsilon_0 = -0.1, \quad t^* = 5, \quad y_l^* = 0.4. \end{aligned} \quad (13.28)$$

Scalability of the model allows testing the numerical scheme for unit tension stiffness and inertia. The structure is pre-stressed, and the initial tension strain

$$\varepsilon_0 = \frac{s_l - s_0 - l}{s_l - s_0} \quad (13.29)$$

determines the material length of the active part of the string  $s_l - s_0$ , whose length does not change during the simulation. In the beginning, the structure is moving steadily with

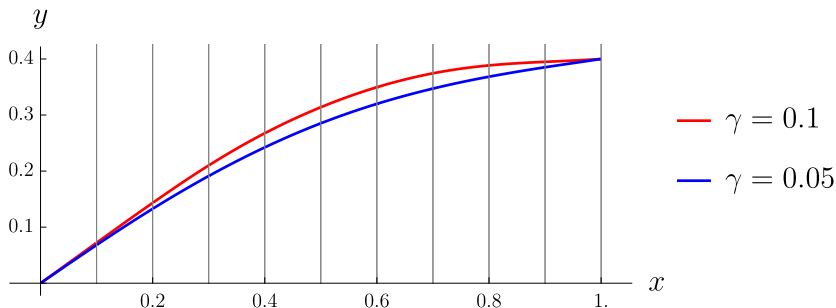
<sup>1</sup> <https://www.wolfram.com/mathematica/>

$$t = 0 : \quad \dot{\mathbf{u}} = \gamma \mathbf{i}, \quad \mathbf{u}' = -\frac{\varepsilon_0}{1 - \varepsilon_0} \mathbf{i}. \tag{13.30}$$

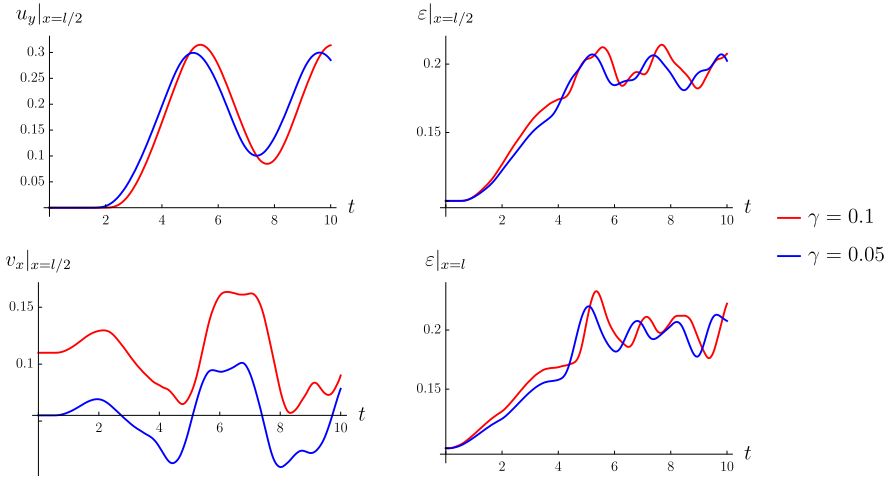
The initial velocity of transverse waves is determined by the pre-tension and for the given numerical parameters can be estimated as  $\sqrt{0.1}$  (square root of the tension divided by the linear density), which is comparable to the rate of material supply  $\gamma$ . The transverse motion of the right end  $y_l(t)$  according to (13.6) increases the general tension level and the wave velocity over the time period  $0 \leq t \leq t^*$ .

Taking  $n_{el} = 10$ , we sequentially solved the transient problem for both axial transport rates  $\gamma$ , given in (13.28); a simulation takes about 10-15 seconds of CPU time with a modern desktop computer with an Intel i7 CPU 2.3 GHz. The computed deformed configurations of the structure for the time instant  $t = 10$  are presented in Fig. 13.5. The curves here are simple plots of  $u_y$  in dependence on the axial coordinate  $x$ , the domains of the finite elements are indicated by gray vertical lines, and the nodes of the finite element model reside on this lines. More informative are the time histories of characteristic variables, which are shown for both solutions in Fig. 13.6. In the middle point of the domain  $x = l/2$  we observe the time variation of the transverse displacement  $u_y$ , of the strain  $\varepsilon$  and of the axial component of the velocity of particles  $v_x$ ; we also present the time variation of the strain  $\varepsilon$  in the end point of the domain  $x = l$ . The starting values of the velocity  $v_x$  are not equal to  $\gamma$  because of the pre-strain. We notice that the strain at the right end immediately responds to the growing  $y_l(t)$ , but it takes some time before the influence in the middle point is observed.

For the demonstration of the rapid mesh convergence, extension to the case of a beam with the bending stiffness and modelling dynamic instability at growing velocity of axial motion we refer to Vetyukov (2017). The formulation was also validated by successfully comparing the results in Fig. 13.6 against a lumped particles simulations at Lagrangian description, which featured thousands of particles in contrast to just a few number of degrees of freedom in the presented model, see the above reference for the details of comparison.



**Fig. 13.5:** Deformed structure in the control volume at  $t = 10$  for two values of the axial transport rate



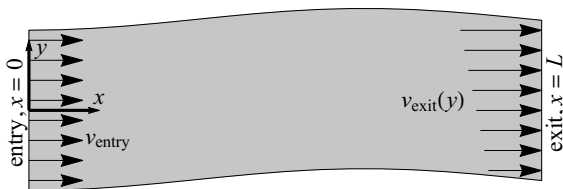
**Fig. 13.6:** Time histories of the transverse deflection, strain and axial velocity in the middle point of the control domain as well as of the strain in the end point for two values of the axial transport rate

### 13.4 Finite Deformations of an Axially Moving Plate

We proceed to modelling finite deformations and bending of an elastic plate moving across a given domain and present the results, which were presented in Vetyukov et al (2016) under the terms of the Creative Commons Attribution 4.0 International License (<http://creativecommons.org/licenses/by/4.0/>). Previous attempts to obtain a model for an axially moving deformable plate (Ghayesh et al, 2013; Banichuk et al, 2010) did not account for particular kinematic conditions at the boundaries of the domain in the form of time and space variations of the prescribed velocity profiles. These effects are particularly relevant in applications of hot rolling, strip coiling or belt drive simulations.

In this section we discuss a mathematical description for finite deformations of a thin plate, which is moving between two parallel lines, see Fig. 13.7. This gross axial motion takes place in the direction of the  $x$ -axis (called in the following axial direction) from left to right. Velocities of the plate at the entry to the domain  $x = 0$

**Fig. 13.7** Deformable plate moving in the axial direction ( $x$ ) with kinematically prescribed velocities; the velocity profile at the exit from the domain is varying in the transverse direction ( $y$ )



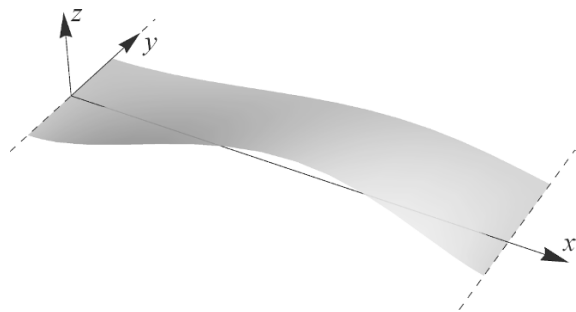
and at the exit from it  $x = L$  are kinematically prescribed and equal respectively  $v_{\text{entry}}$  and  $v_{\text{exit}}$ . In a transient process, a non-constant profile of the velocity  $v_{\text{exit}}(y)$  results in the deformation of the plate in its plane  $xy$  and subsequent buckling in the out-of-plane direction of the  $z$ -axis. This kind of undesired behavior may happen during the metal rolling process, paper production, etc., which makes the respective methods of analysis practically relevant.

The proposed Eulerian-Lagrangian formulation is motivated by computational difficulties that are inherent in conventional finite element modeling of the deformation of the plate. As a Lagrangian finite element mesh propagates across the domain in the course of a simulation, kinematic boundary conditions need to be imposed at the interior of the finite elements. This typical "variational crime" leads to numerically induced oscillatory behavior of the stressed state of the plate and this would not allow for accurate presentation of its bending, which is tightly coupled with the in-plane stresses. While extended finite element formulations (Moës et al, 1999) or a mortar approach (De Lorenzis et al, 2011) could theoretically be applied to solving the issue, an elegant and efficient alternative is to preserve the finite element mesh from moving in the axial direction. This guarantees that the boundaries of the active domain, at which the displacements need to be prescribed for each time step, remain aligned with the boundaries of the finite element mesh.

At present, we restrict the consideration to the constant profile of the velocity of material production  $v_{\text{entry}}$  and aim at modeling the evolution of finite deformations of an elastic plate under quasistatic assumptions. Further extensions of the approach are discussed in the concluding remarks below. Further extensions of the approach are discussed below in Sect. 13.5.

### 13.4.1 Kinematic Description

Consider a plate as a two-dimensional material surface axially moving across a domain, bounded by two lines, see Fig. 13.8. Rolling of a sheet of metal, paper production or motion of a conveyor belt are typical examples of such a structure. At each time instant, the plate is clamped at the lines of contact: there are no out-of-plane



**Fig. 13.8** Deformable plate, moving across a domain, bounded by two lines (dashed): three-dimensional view

displacements in the direction of the  $z$  axis at  $x = 0$  and  $x = L$  nor does the plate rotate about these lines. The material is produced in a fixed segment  $-w/2 \leq y \leq w/2$  at  $x = 0$ , such that the plate is here centered and has a fixed width  $w$ . The second line of contact, where the plate is leaving the domain, may travel in the transverse direction, see discussion in Sect. 13.4.5.

For the sake of mathematical description, we introduce an infinitely long *reference configuration*, see Fig. 13.9. Particles of the plate are identified by their material coordinates  $\overset{\circ}{x}$  and  $\overset{\circ}{y}$ , i.e., by the reference position vector

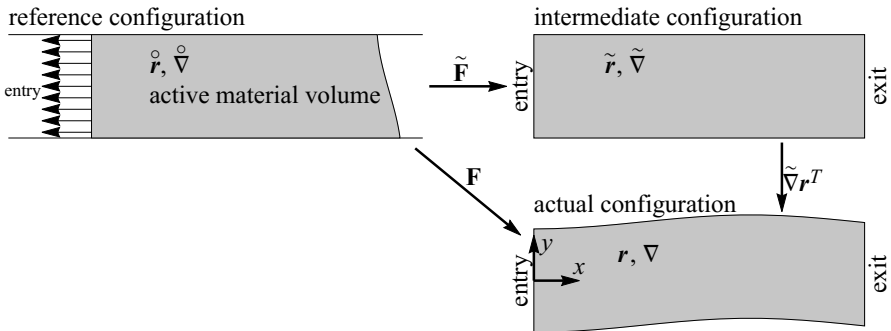
$$\overset{\circ}{r} = \overset{\circ}{x}\mathbf{i} + \overset{\circ}{y}\mathbf{j}, \quad -w/2 \leq \overset{\circ}{y} \leq w/2 \tag{13.31}$$

with  $\mathbf{i}$ ,  $\mathbf{j}$  and  $\mathbf{k}$  being the unit base vectors of the global cartesian frame. In the *actual state* we consider just the particles, which are currently residing in the domain  $0 \leq x \leq L$ . In the reference configuration these particles form a planar manifold, which will be called *active material volume* in the following (depicted grey in Fig. 13.9), and which is thus a pre-image of the actual state. Between the time instants  $t$  and  $t + dt$ , a material layer of the length  $v_{\text{entry}}dt$  enters the domain from the left. As  $v_{\text{entry}} = \text{const}$ , it means that the left boundary of the active material volume (which is a pre-image of the line  $x = 0$ ,  $-w/2 \leq y \leq w/2$  in the actual configuration) is moving across the stress free reference configuration to the left with the velocity  $v_{\text{entry}}$ , the mathematical form of this statement being (13.71).

The Lagrangian description, at which the actual configuration is defined by a mapping from  $\overset{\circ}{r}$  to the actual place of a particle

$$\mathbf{r} = x\mathbf{i} + y\mathbf{j} + z\mathbf{k}, \tag{13.32}$$

remains efficient as long as the active material volume is known (and suitable for being discretized in numerical simulations). This is not the case for the problem at hand, and it is efficient to decompose the mapping into two steps by introducing an additional spatially fixed *intermediate configuration*. This rectangular domain with



**Fig. 13.9:** Configurations involved in the mathematical description of the kinematics of the plate



the position vector

$$\tilde{\mathbf{r}} = \tilde{x}\mathbf{i} + \tilde{y}\mathbf{j}, \quad 0 \leq \tilde{x} \leq L, \quad -w/2 \leq \tilde{y} \leq w/2 \quad (13.33)$$

differs from the reference state by the axial displacement  $u_x$  only:

$$\tilde{\mathbf{r}} = \mathring{\mathbf{r}} + u_x\mathbf{i}, \quad \tilde{x} = \mathring{x} + u_x, \quad \tilde{y} = \mathring{y}. \quad (13.34)$$

At the same time, the transverse displacement  $u_y$  and the out-of-plane displacement  $u_z$  differ in the actual configuration from the intermediate one:

$$\mathbf{r} = \tilde{\mathbf{r}} + u_y\mathbf{j} + u_z\mathbf{k}, \quad x = \tilde{x}, \quad y = \tilde{y} + u_y, \quad z = u_z. \quad (13.35)$$

Now, as

$$\tilde{x} = x, \quad \tilde{y} = \mathring{y}, \quad (13.36)$$

the left and the right boundaries of the intermediate configuration (13.33) map onto the lines of contact of the plate  $x = 0$  and  $x = L$ . We thus introduce the mapping from the active material volume in the reference configuration to the actual state implicitly in the form

$$\mathring{\mathbf{r}} = \mathring{\mathbf{r}}(\tilde{\mathbf{r}}), \quad \mathbf{r} = \mathbf{r}(\tilde{\mathbf{r}}), \quad (13.37)$$

which guarantees the conformity of the domains.

### 13.4.2 Deformation and Strain Energy

Treating displacements

$$\mathbf{u} = u_x\mathbf{i} + u_y\mathbf{j} + u_z\mathbf{k} \quad (13.38)$$

as primary variables, we seek them as functions of the place in the intermediate configuration:

$$\mathbf{u} = \mathbf{u}(\tilde{\mathbf{r}}) = \mathbf{r} - \mathring{\mathbf{r}}. \quad (13.39)$$

The quasistatic simulations below are based on the principle of stationarity of the total strain energy of the active volume of the plate for each time instance. For a classical (transverse shear-rigid) Kirchoff plate model (Eliseev, 2006; Eliseev and Vetyukov, 2010; Vetyukov, 2014b), the strain energy depends on the two symmetric *strain tensors*

$$\mathbf{E} = \frac{1}{2}(\mathbf{F}^T \cdot \mathbf{F} - \mathbf{I}_2), \quad (13.40)$$

$$\mathbf{K} = \mathbf{F}^T \cdot \mathbf{b} \cdot \mathbf{F}.$$

The first strain measure  $\mathbf{E}$  describes the membrane (in-plane) deformation of the plate, while the second one  $\mathbf{K}$  is responsible for its bending. The *gradient of deformation* is the transposed gradient of the position vector of the actual state with respect to the reference one:

$$\begin{aligned} \mathbf{F} &= \overset{\circ}{\nabla} \mathbf{r}^T, \\ \overset{\circ}{\nabla} &= \mathbf{i} \frac{\partial}{\partial \overset{\circ}{x}} + \mathbf{j} \frac{\partial}{\partial \overset{\circ}{y}} \equiv \mathbf{i} \partial_{\overset{\circ}{x}} + \mathbf{j} \partial_{\overset{\circ}{y}}. \end{aligned} \quad (13.41)$$

The in-plane *identity tensor* is

$$\mathbf{I}_2 = \mathbf{i}\mathbf{i} + \mathbf{j}\mathbf{j} = \overset{\circ}{\nabla} \overset{\circ}{\mathbf{r}}, \quad (13.42)$$

and the second metric tensor of the actual configuration

$$\mathbf{b} = -\nabla \mathbf{n} \quad (13.43)$$

which is the negative gradient of the *unit normal vector*  $\mathbf{n}$  to the actual surface of the plate (Stoker, 1989; Ciarlet, 2005). We recall the relation between the differential operators of the reference and of the actual states,

$$\overset{\circ}{\nabla} = \mathbf{F}^T \cdot \nabla, \quad (13.44)$$

and rewrite the second equality in (13.40):

$$\mathbf{K} = -\overset{\circ}{\nabla} \mathbf{n} \cdot \mathbf{F}. \quad (13.45)$$

Now, the displacement (13.39) is a field over the intermediate configuration, which does not allow us to directly compute the strain tensors using (13.40). We aim at *transforming the above kinematic relations* from the material description featuring derivatives with respect to the coordinates in the reference state *to the differential operator of the intermediate configuration*

$$\tilde{\nabla} = \mathbf{i} \partial_{\tilde{x}} + \mathbf{j} \partial_{\tilde{y}}. \quad (13.46)$$

For a two-stage mapping from the reference configuration to the actual one, the total deformation gradient is a product

$$\mathbf{F} = \tilde{\nabla} \mathbf{r}^T \cdot \overset{\circ}{\nabla} \tilde{\mathbf{r}}^T, \quad (13.47)$$

which is mathematically equivalent to the chain rule of differentiation of a function of multiple arguments. We introduce the gradient of deformation from the reference configuration to the intermediate one

$$\tilde{\mathbf{F}} = \overset{\circ}{\nabla} \tilde{\mathbf{r}}^T = \left( \mathbf{I}_2 - \mathbf{i} \tilde{\nabla} u_x \right)^{-1}. \quad (13.48)$$

Indeed, using a relation between the differential operators analogous to (13.44) and recalling (13.34), we write

$$\begin{aligned} \overset{\circ}{\nabla} &= \tilde{\mathbf{F}}^T \cdot \tilde{\nabla}, \\ \mathbf{I}_2 = \overset{\circ}{\nabla} \overset{\circ}{\mathbf{r}} &= \tilde{\mathbf{F}}^T \cdot \tilde{\nabla} (\tilde{\mathbf{r}} - u_x \mathbf{i}) = \tilde{\mathbf{F}}^T \cdot \left( \mathbf{I}_2 - \tilde{\nabla} u_x \mathbf{i} \right) \quad \Rightarrow \quad (13.48). \end{aligned} \quad (13.49)$$

The inverse of an in-plane tensor in (13.48) is again an in-plane one, and the total deformation gradient  $\mathbf{F}$  can now be computed for any field of displacements (13.39), known in the intermediate configuration (13.33).

While this is sufficient for the membrane strains  $\mathbf{E}$  in (13.40), further mathematics is needed to compute the tensor of bending strains  $\mathbf{K}$ . Using the first relation in (13.49), we rewrite (13.45) as

$$\mathbf{K} = \tilde{\mathbf{F}}^T \cdot \tilde{\mathbf{K}} \cdot \tilde{\mathbf{F}}, \quad (13.50)$$

in which a symmetric tensor

$$\tilde{\mathbf{K}} = -\tilde{\nabla} \mathbf{n} \cdot \tilde{\nabla} \mathbf{r}^T \quad (13.51)$$

is introduced.

The vector of unit normal is easy to compute with the known relation  $\mathbf{r}(\tilde{\mathbf{r}}) = \mathbf{r}(\tilde{x}\mathbf{i} + \tilde{y}\mathbf{j})$ . Considering a surface, parametrized by coordinates  $x$  and  $y$ , we write

$$\mathbf{n} = \frac{\partial_{\tilde{x}} \mathbf{r} \times \partial_{\tilde{y}} \mathbf{r}}{|\partial_{\tilde{x}} \mathbf{r} \times \partial_{\tilde{y}} \mathbf{r}|}. \quad (13.52)$$

From (13.35) we see, that  $\mathbf{n}$  at a given point of the intermediate configuration does not depend on the field  $u_x(\tilde{\mathbf{r}})$ . Now we apply  $\tilde{\nabla}$  to both sides of the identity

$$\tilde{\nabla} \mathbf{r} \cdot \mathbf{n} = (\mathbf{i} \partial_{\tilde{x}} \mathbf{r} + \mathbf{j} \partial_{\tilde{y}} \mathbf{r}) \cdot \mathbf{n} = 0 \quad (13.53)$$

and arrive at an alternative form of (13.51), which shows the symmetry of  $\tilde{\mathbf{K}}$  more clear:

$$\tilde{\nabla} \tilde{\nabla} \mathbf{r} \cdot \mathbf{n} = -\tilde{\nabla} \mathbf{n} \cdot \tilde{\nabla} \mathbf{r}^T = \tilde{\mathbf{K}}. \quad (13.54)$$

The above general nonlinear kinematic relations may be simplified when particular deformations or coupling terms are negligible. Thus, in a *geometrically linear model* just small deformations are assumed to be superposed upon a regular axial motion of the plate, and linearizing we arrive at the conventional strains of the classical plate theory:

$$\mathbf{E} \approx \boldsymbol{\varepsilon} = \nabla(u_x \mathbf{i} + u_y \mathbf{j})^S, \quad \mathbf{K} \approx \boldsymbol{\kappa} = \nabla \nabla u_z. \quad (13.55)$$

In a linear theory, one does not need to differentiate between  $\nabla$  and  $\tilde{\nabla}$ , and conventional finite element models of a plate may be applied. However, in this linear formulation the in-plane stresses are decoupled from the bending of the plate, which makes it inapplicable for studying buckling behavior.

Returning to the fully nonlinear model, we write the strain energy of a plate per unit area of its reference configuration as a quadratic form of the strains (Eliseev and Vetyukov, 2010):

$$U = \frac{1}{2} (A_1 (\text{tr} \mathbf{E})^2 + A_2 \mathbf{E} \cdot \mathbf{E} + D_1 (\text{tr} \mathbf{K})^2 + D_2 \mathbf{K} \cdot \mathbf{K}). \quad (13.56)$$

Thus, we assume that the local strains remain small, which does not exclude large overall deformations of a thin structure. For a homogeneous isotropic plate with the

thickness  $h$ , Young's modulus  $E$  and Poisson's ratio  $\nu$ , the stiffness coefficients are

$$A_1 = \frac{E\nu h}{1-\nu^2}, \quad A_2 = \frac{Eh}{1+\nu}, \quad D_1 = \frac{h^2}{12}A_1, \quad D_2 = \frac{h^2}{12}A_2. \quad (13.57)$$

Now, we need to integrate the strain energy over the intermediate configuration. The change of variables is to be accounted for,

$$d\tilde{x}d\tilde{y} = (\det \tilde{\mathbf{F}})^{-1}d\tilde{x}d\tilde{y} \quad (13.58)$$

with

$$(\det \tilde{\mathbf{F}})^{-1} = 1 - \partial_{\tilde{x}}u_x, \quad (13.59)$$

see Eq. (13.48). Finally, the total strain energy of the active material volume reads

$$U^\Sigma = \int_0^L d\tilde{x} \int_{-w/2}^{w/2} (1 - \partial_{\tilde{x}}u_x) U d\tilde{y}. \quad (13.60)$$

In the absence of external loading,  $U^\Sigma$  will be at minimum in a state of stable static equilibrium provided that the set of material particles is fixed. Although we are dealing with an open system, and particles are continuously entering and leaving the active material volume, this condition is fulfilled at each time step of a quasistatic simulation owing to the kinematic nature of the boundary conditions at both ends of the domain, see the discussion in Sect. 13.4.5.

### 13.4.3 Finite Element Scheme

In a numerical scheme, we need to compute the total strain energy  $U^\Sigma$  and its derivatives for a given approximation of displacements  $\mathbf{u}(\tilde{\mathbf{r}})$ . Similar to the above one-dimensional case (13.22), we have applied a four-node  $C^1$ -continuous finite element approximation, which is based on the idea of a Bogner-Fox-Schmit rectangle with bi-cubic shape functions, see Vetyukov (2014a,b). A regular mesh was introduced in the intermediate configuration with  $n_x \times n_y$  elements in the axial direction and in the transverse one, respectively. With twelve degrees of freedom at each node (vector of displacement, its two derivatives with respect to the local coordinates on the element and one mixed second-order derivative) we guarantee the continuity of both  $\mathbf{u}$  and  $\mathbf{n}$  across the boundaries of the element. Now, the first strain measure  $\mathbf{E}$  is continuous and the second one  $\mathbf{K}$  may undergo discontinuities of the first kind, which is sufficient for the regularity of the integral (13.60).

At each time instant we fix the values of displacements at the boundaries  $x = 0$  and  $x = L$  according to (13.75). Along with the condition of clamping  $\mathbf{n} = \mathbf{k}$ , this results in kinematic constraints for some of the degrees of freedom. Seeking for a stable equilibrium, we minimize  $U^\Sigma$  with respect to remaining degrees of freedom

of the model  $e$  with the help of a quasi-Newton scheme, which requires computing derivatives of the kind

$$\frac{\partial U^\Sigma}{\partial e} = \int_0^L d\bar{x} \int_{-w/2}^{w/2} \left( (1 - \partial_{\bar{x}} u_x) \frac{\partial U}{\partial e} - \frac{\partial(\partial_{\bar{x}} u_x)}{\partial e} U \right) d\bar{y}. \quad (13.61)$$

A Gaussian integration rule with  $3 \times 3$  points per element is used, and at each integration point we compute

$$\frac{\partial U}{\partial e} = (A_1 I_2 \text{tr} E + A_2 E) \cdot \frac{\partial E}{\partial e} + (D_1 I_2 \text{tr} E + D_2 E) \cdot \frac{\partial K}{\partial e}. \quad (13.62)$$

The difficulty lies at evaluating the derivatives of the strain measures with respect to  $e$ . Writing

$$\frac{\partial E}{\partial e} = F^T \cdot \frac{\partial F}{\partial e}, \quad \frac{\partial F}{\partial e} = \frac{\partial \tilde{\nabla} \mathbf{r}^T}{\partial e} \cdot \tilde{\mathbf{F}} + \tilde{\nabla} \mathbf{r}^T \cdot \frac{\partial \tilde{\mathbf{F}}}{\partial e}, \quad (13.63)$$

we see that either the first or the second term remain in the last expression depending on the kind of degree of freedom under consideration. Indeed,

$$\frac{\partial \tilde{\nabla} \mathbf{r}^T}{\partial e} = \left( \tilde{\nabla} \frac{\partial(u_y \mathbf{j} + u_z \mathbf{k})}{\partial e} \right)^T, \quad (13.64)$$

which vanishes if  $e$  is a degree of freedom of axial motion. Considering now the second term in Eq. (13.62), we write

$$\frac{\partial K}{\partial e} = \tilde{\mathbf{F}}^T \cdot \frac{\partial \tilde{\mathbf{K}}}{\partial e} \cdot \tilde{\mathbf{F}} + 2\tilde{\mathbf{F}}^T \cdot \tilde{\mathbf{K}} \cdot \frac{\partial \tilde{\mathbf{F}}}{\partial e}. \quad (13.65)$$

Again, either the first or the second term needs to be treated depending on the kind of  $e$ .

Although programming the computation according to Eqs. (13.62)-(13.65) is feasible, it would be a challenging task to obtain the second-order derivatives in an algorithmic manner. In the present study, we used a system of computer algebra and first computed the first and the second order derivatives of the strain measures with respect to the local geometric characteristics

$$\partial_{\bar{x}} \mathbf{u}, \quad \partial_{\bar{y}} \mathbf{u}, \quad \partial_{\bar{x}}^2 \mathbf{u}, \quad \partial_{\bar{y}}^2 \mathbf{u}, \quad \partial_{\bar{x}} \partial_{\bar{y}} \mathbf{u}. \quad (13.66)$$

The resulting expressions were exported as automatically generated C# code into the in-house finite element simulation software. Now, the derivatives of (13.66) with respect to the nodal degrees of freedom are just the shape functions of a finite element, and the element's stiffness matrix and force vector  $\tilde{\mathbf{F}}$  are easily computed using the chain rule.

### 13.4.4 Benchmark Problem

The kinematic formulation and the resulting finite element scheme were validated on a simple benchmark problem. Consider a plate of a trapezoidal shape. The width of the plate is  $w$ , while the other two edges have lengths  $L$  and  $L + u_{x0}$  as in Fig. 13.10. The right (inclined) edge is clamped and kinematically rotated such, that it becomes parallel to the left one, which is also clamped. Depending on the magnitude of  $u_{x0}$ , the resulting deformation of the plate in its own plane may become unstable and lead to the out-of-plane buckling as depicted in the figure by the surface with the grid lines on it.

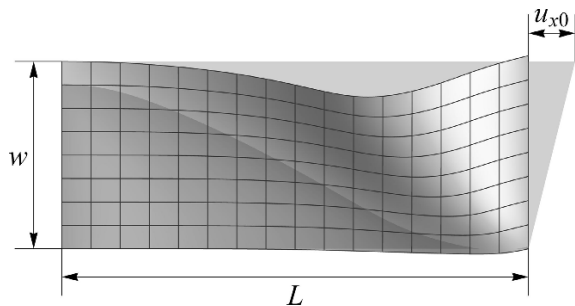
As the deformed configuration is bounded between two parallel lines, the problem is perfectly suitable for the mixed Eulerian-Lagrangian description. At the same time, a solution with the conventional Lagrangian finite elements with the same approximation (Vetyukov, 2014a) is readily available, which allows comparing the solutions and thus testing the new numerical scheme.

Using SI system of units here and in the following, we summarize the parameters of the considered model:

$$L = 1, \quad w = 0.4, \quad u_{x0} = 0.1, \quad h = 5 \cdot 10^{-3}, \quad E = 2.1 \cdot 10^{11}, \quad \nu = 0.3. \quad (13.67)$$

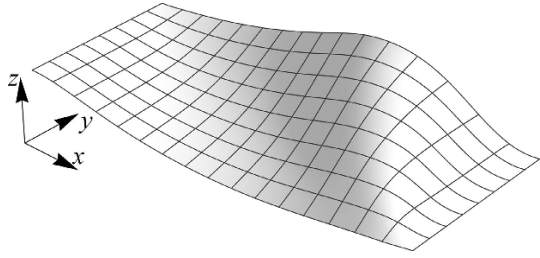
Seeking for a static equilibrium, we considered an intermediate configuration  $0 \leq x \leq L, -w/2 \leq \tilde{y} \leq w/2$  and prescribed  $u_x$  and  $u_y$  at the edge  $x = L$  such, that its pre-image in the reference state  $\hat{r}$  would correspond to the given undeformed geometry and the length of the rotated edge is preserved. The out-of-plane buckling was promoted by imposing a small gravity force in the first iteration of the quasi-Newton minimization scheme, which was then released for the rest of iterations.

In accordance with Eq. (13.35), the transverse grid lines of the finite element mesh, shown in the deformed state in Fig. 13.10 remain parallel to the  $y$ -axis. The surface of the plate in the supercritical state after buckling may be better observed from an isometric viewpoint as shown in Fig. 13.11. We studied the mesh convergence and compared the solutions with the proposed mixed Eulerian-Lagrangian description and with the conventional Lagrangian finite elements by finding the maximal and the



**Fig. 13.10** Undeformed geometry of a trapezoidal plate and its postbuckling configuration after the inclined edge is kinematically rotated

**Fig. 13.11** Deformed configuration of a trapezoidal plate, kinematically loaded in its own plane



minimal values of the displacement  $u_z$ , which are observed at the edges  $\tilde{y} = \pm w/2$  of the plate. The results of the comparison, which are summarized in Table 13.1, clearly demonstrate that both formulations converge to the same solution.

Table 13.1: Mesh convergence and comparison of the mixed Eulerian-Lagrangian and traditional Lagrangian frameworks for a benchmark problem

Discretization, $n_x \times n_y$	Mixed E.-L.		Lagrangian	
	min $u_z$	max $u_z$	min $u_z$	max $u_z$
$4 \times 2$	-0.05851	0.18428	-0.07322	0.18138
$8 \times 4$	-0.05546	0.18319	-0.05831	0.18256
$16 \times 8$	-0.05496	0.18277	-0.05527	0.18259
$32 \times 16$	-0.05493	0.18274	-0.05490	0.18262

### 13.4.5 Time Stepping and Boundary Conditions

Time rates of mechanical entities need to be considered in a quasistatic simulation. We need to differentiate between the velocity of a particle  $\dot{\mathbf{u}}$  with the *material time derivative*

$$(\dots) \equiv \left. \frac{\partial(\dots)}{\partial t} \right|_{\tilde{\mathbf{r}}=\text{const}} \tag{13.68}$$

and the time rate  $\partial_t \mathbf{u}$  with the *local derivative* at a given point in the intermediate configuration defined as

$$\partial_t(\dots) \equiv \left. \frac{\partial(\dots)}{\partial t} \right|_{\tilde{\mathbf{r}}=\text{const}} \tag{13.69}$$

The general relation between the material and the local time derivatives with the known convective term reads

$$\dot{\mathbf{u}} = \frac{d\mathbf{u}(\tilde{\mathbf{r}}(\tilde{\mathbf{r}}, t), t)}{dt} = \partial_t \mathbf{u} + \dot{\tilde{\mathbf{r}}} \cdot \tilde{\nabla} \mathbf{u} = \partial_t \mathbf{u} + \dot{u}_x \mathbf{i} \cdot \tilde{\nabla} \mathbf{u} = \partial_t \mathbf{u} + \dot{u}_x \partial_{\tilde{x}} \mathbf{u}. \tag{13.70}$$

Observing the time evolution of nodal variables, we need to deal with the local time derivatives as the nodes of the finite element mesh are fixed in the intermediate

configuration. As discussed after Eq. (13.31), the left boundary of the active material volume moves across the reference state with a known velocity, which means that the local time rate of  $\mathbf{u}$  is known at the left edge:

$$x = 0: \quad \partial_t \dot{\mathbf{r}} = -v_{\text{entry}} \mathbf{i} \Rightarrow \partial_t \mathbf{u} = v_{\text{entry}} \mathbf{i}. \quad (13.71)$$

On the opposite, at the right boundary we know the actual velocities of the particles, with which they move across the line of contact:

$$x = L: \quad \dot{\mathbf{u}} = v_{\text{exit}} \mathbf{i}, \quad \dot{u}_x = v_{\text{exit}} \Rightarrow \partial_t \mathbf{u} = v_{\text{exit}} (\mathbf{i} - \partial_{\bar{x}} \mathbf{u}). \quad (13.72)$$

This explains the fact that the right line of contact will move in the transverse direction as long as  $\partial_{\bar{x}} \mathbf{u}$  has a non-zero component in the direction of the  $y$ -axis (the  $z$  component is always zero owing to the condition of clamping). Indeed, in Fig. 13.7 the plate is slightly inclined immediately before  $x = L$  and it is easy to imagine, that in the next time instant a new cross-section of the plate with greater values of  $y$  will arrive at the line of contact. *Stationary motion* of the plate with

$$\mathbf{u} = \mathbf{u}_s(\bar{\mathbf{r}}) + v_{\text{entry}} t \mathbf{i} \quad (13.73)$$

is possible only when the static deformation  $\mathbf{u}_s$  fulfills

$$\begin{aligned} x = 0: \quad \mathbf{u}_s = 0, \quad \mathbf{k} \cdot \partial_{\bar{x}} \mathbf{u}_s = 0; \\ x = L: \quad v_{\text{entry}} \mathbf{i} = v_{\text{exit}} (\mathbf{i} - \partial_{\bar{x}} \mathbf{u}_s) \Rightarrow \partial_{\bar{x}} \mathbf{u}_s = \left(1 - \frac{v_{\text{entry}}}{v_{\text{exit}}}\right) \mathbf{i}. \end{aligned} \quad (13.74)$$

These boundary conditions allow seeking the stationary solution by solving just a single static problem.

We turn back to the problem of evolution of the deformation of the plate in time. The strategy of computing the solution  $\mathbf{u}^{(k+1)}$  in the end of a time step  $t^{(k+1)} = (k+1)\tau$  for a known state of the plate  $\mathbf{u}^{(k)}$  in the beginning of the time step  $t^{(k)} = k\tau$  comprises the following two stages.

1. First we compute new displacements at the left and right boundaries of the domain,

$$x = 0, L: \quad \mathbf{u}^{(k+1)} = \mathbf{u}^{(k)} + \tau \partial_t \mathbf{u}, \quad (13.75)$$

in which the local time derivatives are determined by (13.71) and (13.72). This sort of explicit time integration requires a moderately small time step size and has a clear advantage: with known displacements  $u_x$  at  $x = 0, L$  we have a fixed material volume for the end of the time step, which allows finding the equilibrium by seeking  $\arg \min U^\Sigma$ . In practice, updating the nodal variables according to the incremental boundary conditions (13.75) requires a derivative of the velocity profile  $v'_{\text{exit}}(y)$  as the nodal unknowns comprise not only displacements, but also their derivatives in the transverse direction.

2. As soon as the kinematic constraints are applied for some of the degrees of freedom of the nodes at the left and right boundaries of the domain, we proceed



to the quasi-Newton iterative scheme and seek the values of the rest of degrees of freedom in the model by minimizing the total strain energy (13.60). At each iteration we compute the force vector by the derivatives  $\partial U^\Sigma / \partial e$ , and the stiffness matrix is evaluated only when the rate of convergence at the previous iteration was unsatisfactory. Converged iterations provide us with the new equilibrium state  $\mathbf{u}^{(k+1)}$ .

### 13.4.6 Simulation of a Moving Plate

We considered a plate with the width  $w$ , length  $L$  and material properties as in the benchmark test (13.67). As the behavior of the system depends strongly on the ratio between the membrane and the bending stiffness of the plate, we considered two values of its thickness and started with a thick plate with  $h = 0.02$ . Velocities at the boundaries were chosen as follows:

$$v_{\text{entry}} = 5, \quad v_{\text{exit}} = 5 + 1y. \tag{13.76}$$

Note that the mean value of the exit velocity varies when the line of contact is moving in the transverse direction. Thus, the linear component in  $v_{\text{exit}}$  rotates the cross-section of the plate at  $x = L$  clockwise, which "pushes" the line of contact in the positive direction of  $y$ -axis: its mean transverse displacement

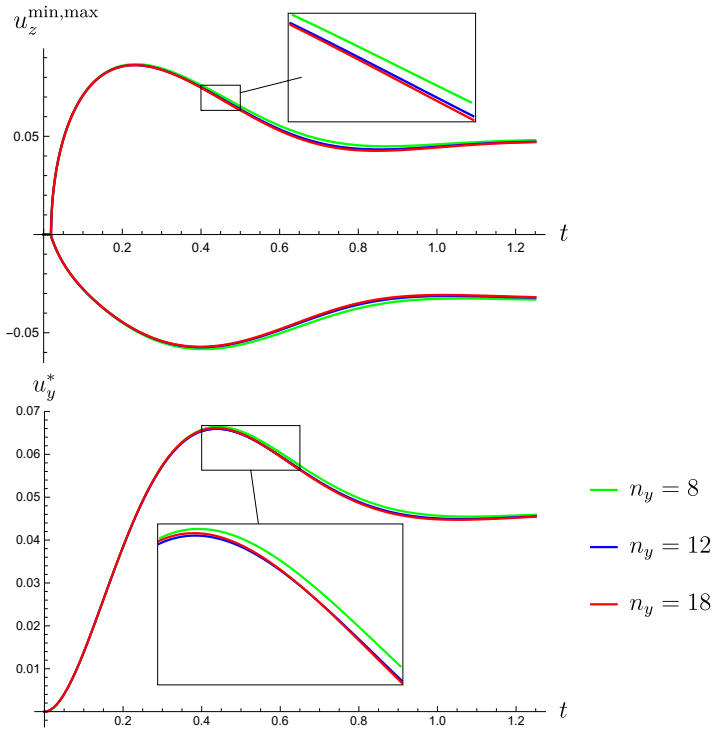
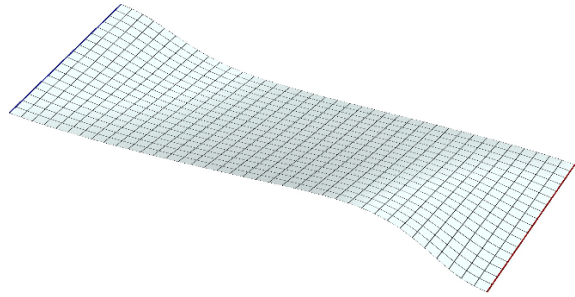
$$u_y^* = \frac{1}{w} \int_{-w/2}^{w/2} u_y|_{\tilde{x}=L} d\tilde{y} \tag{13.77}$$

grows in time. The mean value of  $v_{\text{exit}}$  increases as well, and a tension force appears in the plate. However, the part of the plate near  $\tilde{y} = -w/2$  is compressed in the axial direction, which (along with the shear deformation owing to the motion of the line of contact) may result in the instability of the plane configuration.

We integrated over the time span  $0 \leq t \leq 1.25$  with the step size  $\tau = 0.00125$ , which allowed avoiding instability in the explicit time integration of the boundary conditions for finer meshes. Experiments showed that further reduction of the time step size results in nearly identical solutions. Varying the number of finite elements in the transverse direction  $n_y$ , we kept the length to width aspect ratio of the elements  $(L/n_x)/(w/n_y) \approx 1.2$ .

The computed configuration of the plate at  $t = 0.4$  with  $n_y = 18$  is shown in Fig. 13.12. As discussed after (13.76), the linear component in  $v_{\text{exit}}$  leads to a growing in-plane deformation, which soon initiates the out-of-plane buckling of the plate. The computed time histories of the maximal and the minimal (negative) displacements  $u_z$  as well as of the mean transverse displacement of the line of contact  $u_y^*$  are shown in Fig. 13.13 for three levels of mesh refinement. Besides rapid mesh convergence and transition to a stationary regime, we clearly observe the time instant of buckling

**Fig. 13.12** Deformed configuration of the thick plate at  $t = 0.4$  computed with 18 finite elements in the transverse direction

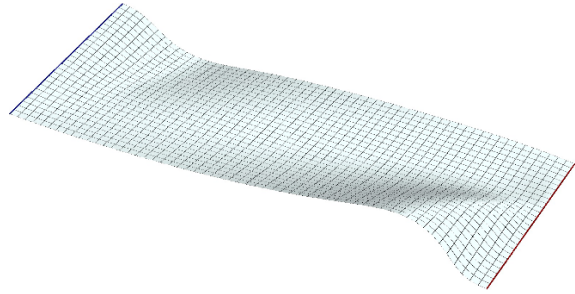


**Fig. 13.13:** Time histories of the maximal and minimal out-of-plane displacements  $u_z$  and the mean transverse displacement of the right edge  $u_y^*$  of the thick plate, computed with sequentially refined finite element models

of the plate, at which in-plane equilibria with  $u_z = 0$  become unstable and non-zero values of  $u_z^{\min}$ ,  $u_z^{\max}$  are produced in the simulation.

A thin plate with  $h = 0.01$  has significantly lower bending stiffness in comparison to the membrane one, which makes the simulation more challenging from the numerical point of view. The deformed surface, presented in Fig. 13.14, is less smooth than the previous one in Fig. 13.12. Lines with high curvature ("folds") may now

**Fig. 13.14** Thin plate at  $t = 0.4$  computed with 27 finite elements in the transverse direction, the "folds" are observable in the deformation pattern

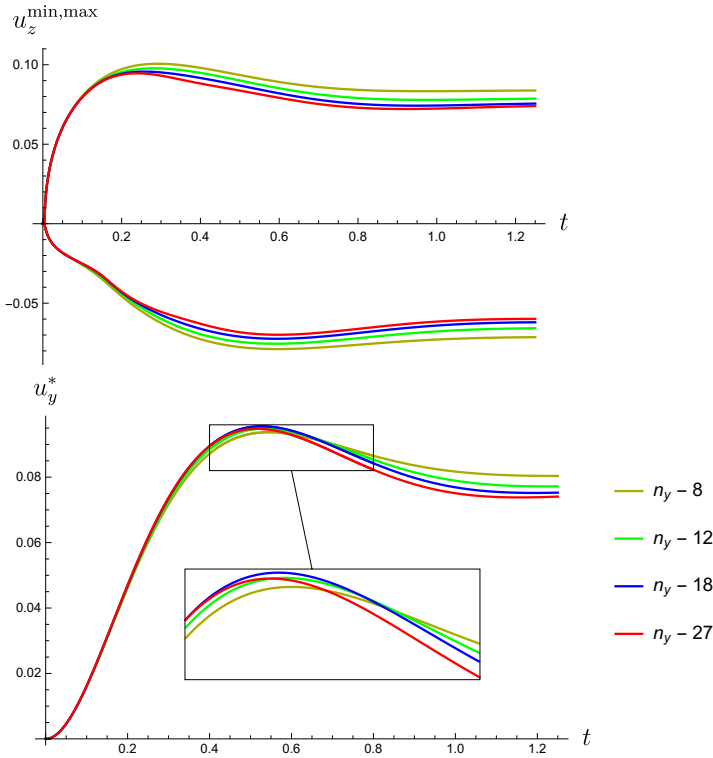


be observed, which require dense finite element meshes to be accurately resolved. In particular, the boundary layer near  $x = L$  tends to demonstrate a complicated deformation pattern. The effect is getting more pronounced for yet thinner plates (as the one, considered in the benchmark test in Sect. 13.4.4). Nevertheless, the solution with  $n_y = 27$  finite elements in the transverse direction is quite accurate, as it may be concluded from the time histories, shown in Fig. 13.15. Earlier buckling of the thin shell may also be observed.

### 13.5 Mixed Eulerian-Lagrangian Formulation in the Analysis of a Belt Drive

The belt drive is a very common technical solution. Mathematical modelling of its behavior is, however, often a challenging task at Lagrangian description, as the particles of the belt are permanently moving from the free spans to the contact zones and back. Our interest is commonly focused on the time history of mechanical fields in a particular point in space rather than on following them in a given material point of the belt. As it is typical for axially moving structures, Lagrangian (material) kinematic description is not an optimal choice for this sort of problems, in particular for numerical methods with spatial discretization. Purely Eulerian (spatial) (Eliseev and Vetyukov, 2012; Vetyukov et al, 2017b) or mixed Eulerian-Lagrangian (Vetyukov et al, 2016, 2017a) formulations are advantageous as we discretize the problem in a domain-specific manner. Exact solutions of the problem of an extensible belt moving between the pulleys with dry friction law of contact were provided by Rubin (2000); Bechtel et al (2000); Morimoto and Iizuka (2012) for stationary regimes of motion. Leamy (2005) as well as Kim et al (2011) considered perturbations of stationary motion, which should allow studying transient regimes with sufficiently small and slow deviations from a given steady one. Hong and Ren (2011) suggested a mixed finite element formulation, which combines Lagrangian nodes with Arbitrary Lagrangian-Eulerian ones using constraint conditions, typical for Multibody Systems Dynamics, and which can theoretically be applied to the considered class of problems.

In the present section, we discuss, how the previously used mixed Eulerian-Lagrangian kinematic description can be transferred to the looped motion of a

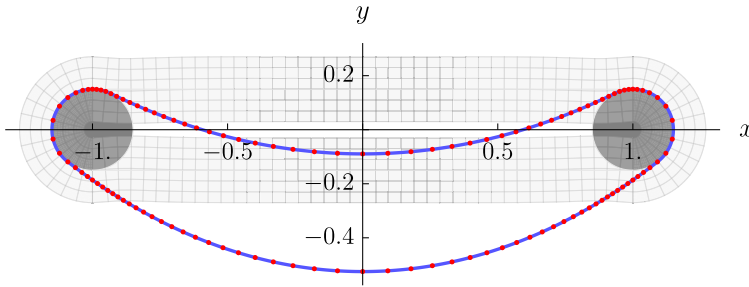


**Fig. 13.15:** Time histories of the maximal and minimal out-of-plane displacements  $u_z$  and the mean transverse displacement of the right edge  $u_y^*$  of the thin plate

belt drive with transverse deflections and frictional contact with the pulleys. This preliminary presentation of the ongoing research work is restricted to static solutions of the contact problem with no frictional interaction and shall serve as a basis for the future analysis of moving systems. For a semi-analytical study of the problem of contact of a belt with the pulleys with the account of bending and shear effects we refer to Belyaev et al (2017).

### 13.5.1 Problem Statement

We consider a flexible belt with the tension stiffness  $b$ , which is stretched on two identical rigid pulleys with radius  $R$  and is hanging in the field of gravity  $g$ , see Fig. 13.16. With the distance between the centers of the pulleys  $H$ , we denote by  $\lambda$  the ratio between the shortest possible contour of the belt  $L$  and its material length  $L_{\text{mat}}$ :



**Fig. 13.16:** Weakly pre-tensed rubber belt, hanging on two pulleys in the field of gravity; the curvilinear coordinate system is plotted in the background

$$L_{\text{mat}} = \lambda L, \quad L = 2H + 2R. \tag{13.78}$$

In the following, we mainly focus on the case  $\lambda > 1$ , such that the belt is under tension just because of the gravity force. This situation is mostly challenging for the mathematical modelling.

As the pulley radius  $R$  is small compared to the distance  $H$ , it is certainly advantageous to keep the finite element discretization finer near the contact zones; larger elements can be used in the free spans to reduce the number of unknowns. This is feasible with the use of the mixed Eulerian-Lagrangian kinematics, which is demonstrated below on the simple example of seeking just a single equilibrium configuration of the hanging belt.

### 13.5.2 Problem-Specific Coordinate System

Splitting the spatial coordinates into a Eulerian and a Lagrangian one for a looped belt requires a looped coordinate system. The classical polar or elliptical coordinates would have too high distortions for longer belt drives with large  $H$  and small  $R$ . Therefore, we decided to develop a problem-specific coordinate system, which consists of 6 separately defined zones, see Fig. 13.17 for the geometrical parameters

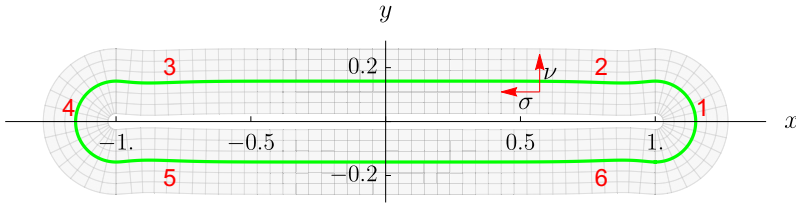
$$H = 2, \quad R = 0.15. \tag{13.79}$$

The position vector of a point in space  $\mathbf{r}$  is determined by two curvilinear coordinates  $\sigma$  and  $\nu$ :

$$\mathbf{r} = \mathbf{g}(\sigma) + \nu \mathbf{n}(\sigma). \tag{13.80}$$

Here

- $\mathbf{g}(\sigma)$  is a generatrix of the coordinate system; it is a  $C^2$  continuous curve in the plane in the plane  $xy$ , which is defined piecewise analytically over 6 segments, see details below;



**Fig. 13.17:** Coordinate lines of the used curvilinear coordinate system with numbered analytical segments in the piece-wise presentation of the generatrix, which is plotted by a green line

- $\mathbf{n}$  is the unit outer normal vector to the generatrix:

$$\mathbf{n} \cdot \mathbf{g}' = 0, \quad \mathbf{n} \cdot \mathbf{n} = 1; \tag{13.81}$$

$\mathbf{n}$  is  $C^1$  continuous, which makes  $\mathbf{r}$  also  $C^1$  continuous everywhere and the metric of the resulting coordinate system is then  $C^0$  continuous;

- $\sigma$  is a circumferential coordinate in the direction of gross axial motion of the belt,  $\nu$  is a coordinate in the normal direction.

We choose polar coordinates in the segments 1 and 4 with  $x > H/2$  and  $x < -H/2$  coinciding with the outer half-circles of the pulleys. The analytical expressions for other four segments involve exponents, which provide the necessary continuity and which turn into ordinary Cartesian coordinates at a significant distance from the contact zones.

The coordinate lines of the coordinate system are orthogonal, and in each segment and in each point we compute scalar products

$$\partial_\sigma \mathbf{r} \cdot \partial_\nu \mathbf{r} = 0, \quad \partial_\nu \mathbf{r} \cdot \partial_\nu \mathbf{r} = 1, \quad \partial_\sigma \mathbf{r} \cdot \partial_\sigma \mathbf{r} = \Lambda(\sigma, \nu). \tag{13.82}$$

The metric coefficients of the coordinate system form a diagonal matrix, and the component in the circumferential direction reads

$$\Lambda = \Lambda_0(\sigma) + 2\Lambda_1(\sigma)\nu + \Lambda_2(\sigma)\nu^2, \tag{13.83}$$

$$\Lambda_0 = \mathbf{g}' \cdot \mathbf{g}', \quad \Lambda_1 = \mathbf{g}' \cdot \mathbf{n}', \quad \Lambda_2 = \mathbf{n}' \cdot \mathbf{n}'.$$

The metric is continuous owing to the achieved  $C^2$  smoothness of the generatrix, and the single coefficients  $\Lambda_{0,1,2}$  may be pre-computed in the integration points of the finite elements, in which  $\sigma = \text{const}$ . In segments 1, 4 with polar coordinates  $x \leq -H/2$  and  $x \geq H/2$  we have  $\Lambda_0 = 1, \Lambda_1 = 0, \Lambda_2 = 1$ . More complicated expressions need to be used in  $-H/2 < x < H/2$ , which, however, result in  $\Lambda \approx 1$  far away from the pulleys, where the coordinates are almost Cartesian.

It remains to notice, that the generatrix  $\mathbf{g}(\sigma)$  is constructed such, that in each point  $\sigma$  is the arc coordinate of the projection of the point onto the undistorted contour

of the belt, and at the free spans we have  $d\sigma = \pm dx$ . Finally, the function  $\mathbf{g}(\sigma)$  is periodic, and we have

$$\mathbf{r}(\sigma, \nu) = \mathbf{r}(\sigma + L, \nu). \quad (13.84)$$

### 13.5.3 Mixed Lagrangian-Eulerian Kinematic Description

Particles of the belt are identified by the material coordinate  $s$ . The belt is looped, which means that coordinates  $s$  and  $s + L_{\text{mat}}$  correspond to the same material point.

At material (Lagrangian) description, we would consider the curvilinear coordinates as functions of the material one:

$$\mathbf{r} = \mathbf{r}(\sigma(s), \nu(s)). \quad (13.85)$$

The proposed mixed Eulerian-Lagrangian description rests upon the change of variable:

$$s = s(\sigma). \quad (13.86)$$

We observe the material particles, which cross spatial coordinate lines  $\sigma = \text{const}$ . The position vector reads

$$\mathbf{r} = \mathbf{r}(\sigma, \nu(\sigma)). \quad (13.87)$$

Again, all mechanical entities are periodic functions of  $\sigma$  with the only exception being the material coordinate, for which holds

$$s(\sigma + L) = s(\sigma) + L_{\text{mat}}. \quad (13.88)$$

### 13.5.4 Finite Element Approximation and Energy

As discussed in Sect. 13.3.3, the cubic finite element approximation in the domain

$$0 \leq \sigma \leq L \quad (13.89)$$

provides us with the  $C^1$  continuous approximation of

$$s(\sigma), \quad \nu(\sigma). \quad (13.90)$$

As each node has fixed coordinate  $\sigma_k$ , we mesh all six segments of the coordinate system individually. The periodicity conditions are ensured by looping the finite element mesh, i.e., by uniting the degrees of freedom at nodes at  $\sigma = 0$  and  $\sigma = L$ . Instead of directly using the condition (13.88) on such a mesh, we account for the jump in  $s$  on the very last finite element when computing the derivatives.

In contrast to (13.9), here we use the Green-Lagrangian strain measure

$$\varepsilon = \frac{1}{2} (\partial_s \mathbf{r} \cdot \partial_s \mathbf{r} - 1); \quad (13.91)$$

see Eliseev and Vetyukov (2012) for a discussion of the difference between the possible strain measures in mechanics of strings. Transforming (13.91) to the new kinematic description (13.90), we use the rule of differentiating inverse and implicit functions along with the metric (13.82) and compute

$$\varepsilon = \frac{\Lambda + v'^2 - s'^2}{2s'^2}; \quad (13.92)$$

the prime means a derivative with respect to  $\sigma$ . Using again a quadratic approximation for the strain energy of the belt per its material length, we write its total mechanical energy in the field of gravity as an integral over the spatial coordinate  $\sigma$ :

$$U^{\mathcal{E}} = \int_0^L \frac{1}{2} b \varepsilon^2 s' d\sigma + \int_0^L \rho g \mathbf{r} \cdot \mathbf{j} s' d\sigma \quad (13.93)$$

with  $\mathbf{j}$  being the unit vector of the vertical cartesian axial  $y$ ,  $\rho$  the density per unit material length and  $g$  the free fall acceleration.

Using the simple penalty formulation for the normal contact of the belt and the pulleys, we find the equilibrium by minimizing

$$U^{\mathcal{E}} + P \rightarrow \min, \quad P = \int_0^L \frac{1}{2} K \gamma^2 d\sigma. \quad (13.94)$$

Here,  $K$  is the high penalty stiffness and  $\gamma$  is the penetration depth, which vanishes as long as the point of the belt does not touch a pulley.

### 13.5.5 Simulation Results

In the numerical example we consider a soft rubber belt with the square cross-section of the size  $5 \cdot 10^{-3}$ , which is by 1% longer than the contour between the pulleys, and use the following parameters of the problem:

$$b = 12.5, \quad \rho = 0.03, \quad g = 9.8, \quad K = 2 \cdot 10^5, \quad \lambda = 1.01. \quad (13.95)$$

We used a non-homogeneous mesh with smaller elements near the points, in which the belt touches the pulleys. The minimization (13.94) started with the initial approximation  $s = \sigma$ ,  $v = 0$  and resulted in the configuration, shown in Fig. 13.16. In the equilibrium state we have the total strain energy of the belt approximately 0.0534, the potential of the field of gravity  $-0.252$  and the penalty term resulted into a very small



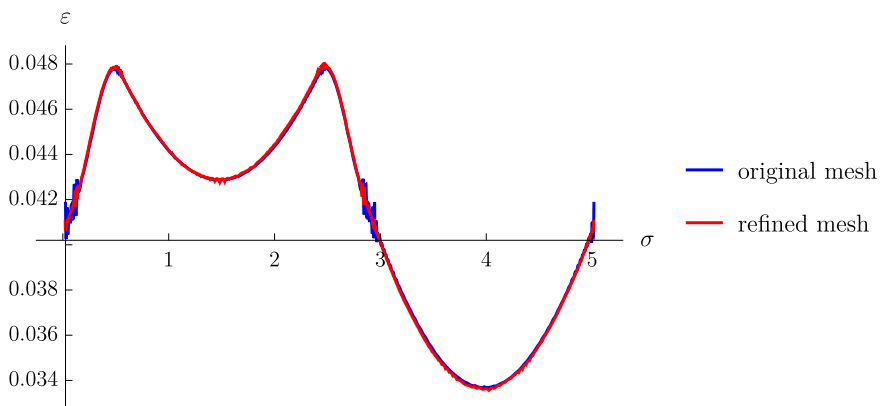
value  $P \approx 3.89 \cdot 10^{-5}$ , which means that the penalty stiffness factor is sufficiently high.

In Fig. 13.18 we demonstrate the computed distribution of strain along the belt. Locking (inability of the finite element approximation to represent the exact solution) results in irregularities, which appear mostly near the upper points of the pulleys. Dividing each element into two, we arrived at a much more regular solution for a refined mesh (red line in the figure).

We additionally validated the results by integrating the contact force, which acts on the pulleys from the side of the belt. The vertical component of the integrated force, which acts on the left pulley results approximately to  $-0.734268$ , while the half of the weight of the belt is  $\rho g L_{\text{mat}}/2 = 0.73381$ . Good correspondence was also achieved for the horizontal component of the contact force at the left pulley, which results into  $0.9968$  after integration. Computing the strains in the middle points of the upper and lower free spans of the belt, finding the respective tension forces according to  $Q = b\varepsilon \sqrt{1 + 2\varepsilon}$  (for the particularity of computing the force with the Green-Lagrangian strain measure we refer to Eliseev and Vetyukov (2012)) and adding both we arrive at  $0.9941$ .

### 13.5.6 Work in Progress and Outlook

While it is too early to present the preliminary results of modelling the motion of the belt with rotating pulleys and dry friction in detail, it can already be stated that the resulting time histories of the strains in different points of the belt are remarkably smooth, in particular in comparison with the attempts to achieve the same solutions using Lagrangian kinematic description. Step-like discontinuities appear when the



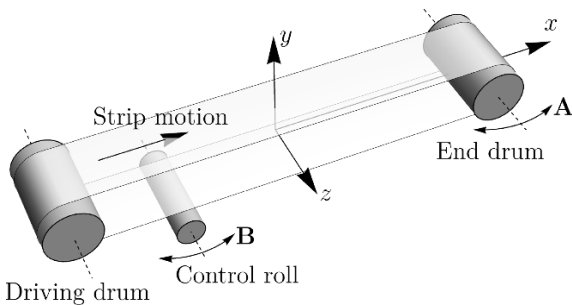
**Fig. 13.18:** Computed distribution of strain along the hanging belt for the original mesh and for the refined one

contact state in a neighboring integration point switches from stick to slip as the zone of creep of the belt is growing (Rubin, 2000; Reynolds, 1874). The mesh convergence is very satisfactory.

The discussed above kinematics and simulation strategy may be applied to significantly more challenging problems, like e.g. modelling the motion of an endless steel belt between two rotating drums, Fig. 13.19. Being efficient in such technological processes as food industry, production of laminates, casting of optical films, etc., such belts often suffer from lateral run off during the motion because of intrinsic unsymmetries in the geometry, orientation of drums, temperature distribution, etc. Reliable mathematical modelling, which is necessary for the model-based design of a controller (Fig. 13.20) is particularly challenging for weakly tensed belts because of the high membrane and low bending stiffness along with the very hard contact conditions. Preliminary results of a non-material finite element simulation of a steel belt using a shell model and a three-dimensional curvilinear coordinate system, which is the extension of the one in Fig. 13.17, are shown in Fig. 13.21. Imperfect geometry of the belt is accounted for using the multiplicative decomposition from the undeformed state to the reference one (Vetyukov et al, 2017a), and then we apply the mixed Eulerian-Lagrangian kinematic description to prevent the mesh from motion in the circumferential direction. We observe the effects, known from the practical experience: skew hanging of the belt, partial loss of contact with the drums (indicated by missing integration points in the figure) and lateral run-off during the motion.

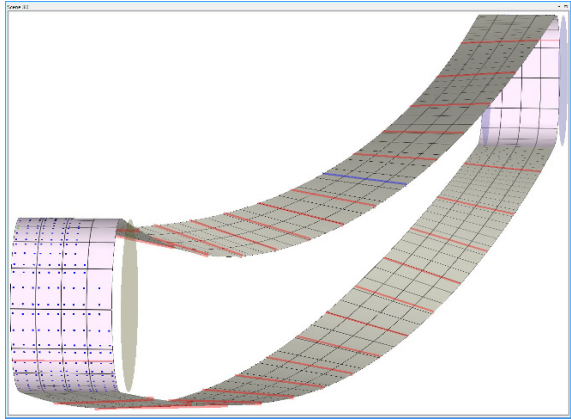


**Fig. 13.19** Endless steel belt, moving between two rotating drums



**Fig. 13.20** Controlling the motion of an endless steel belt

**Fig. 13.21** Non-material finite element simulation of a moving steel, which is running off in the lateral direction because of the imperfect geometry



Currently, the research work is focused on the consistency of the analysis of the effects of the dry friction with stick and slip phenomena.

**Acknowledgements** The support of the author from the Austrian Science foundation FWF in the framework of the collaboration with the research team of the project "Eulerian Mechanics of Belts" [grant number I2093-N25] is gratefully acknowledged.

## References

- Banichuk N, Jeronen J, Neittaanmäki P, Tuovinen T (2010) On the instability of an axially moving elastic plate. *International Journal of Solids and Structures* 47:91–99
- Bechtel SE, Vohra S, Jacob KI, Carlson CD (2000) The stretching and slipping of belts and fibers on pulleys. *ASME Journal of Applied Mechanics* 67:197–206
- Belyaev AK, Eliseev VV, Irschik H, Oborin EA (2017) Contact of two equal rigid pulleys with a belt modelled as cosserat nonlinear elastic rod. *Acta Mechanica* in press
- Chen LQ (2005) Analysis and Control of Transverse Vibrations of Axially Moving Strings. *ASME Applied Mechanics Reviews* 58:91–116
- Ciarlet P (2005) An introduction to differential geometry with applications to elasticity. *Journal of Elasticity* 1-3(78/79):1–215
- De Lorenzis L, Temizer I, Wriggers P, Zavarise G (2011) A large deformation frictional contact formulation using NURBS-based isogeometric analysis. *International Journal for Numerical Methods in Engineering* 87(13):1278–1300
- Donea J, Huerta A, Ponthot JP, Rodriguez-Ferran A (2004) Arbitrary Lagrangian-Eulerian Methods. In: Stein E, de Borst R, Hughes T (eds) *Encyclopedia of Computational Mechanics*, vol 1: Fundamentals, John Wiley & Sons, Ltd, chap 14
- Eliseev V, Vetyukov Y (2012) Effects of deformation in the dynamics of belt drive. *Acta Mechanica* 223:1657–1667
- Eliseev VV (2006) *Mechanics of Deformable Solid Bodies* (in Russian). St. Petersburg State Polytechnical University Publishing House, St. Petersburg
- Eliseev VV, Vetyukov Y (2010) Finite deformation of thin shells in the context of analytical mechanics of material surfaces. *Acta Mechanica* 209(1-2):43–57

- Ghayesh MH, Amabili M, Païdoussis MP (2013) Nonlinear dynamics of axially moving plates. *Journal of Sound and Vibration* 332(2):391–406
- Hong D, Ren G (2011) A modeling of sliding joint on one-dimensional flexible medium. *Multibody System Dynamics* 26:91–106
- van Horssen WT, Ponomareva SV (2005) On the construction of the solution of an equation describing an axially moving string. *Journal of Sound and Vibration* 287(1-2):359–366
- Humer A (2013) Dynamic modeling of beams with non-material, deformation-dependent boundary conditions. *Journal of Sound and Vibration* 332:622–641
- Humer A, Irschik H (2009) Onset of transient vibrations of axially moving beams with large displacements, finite deformations and an initially unknown length of the reference configuration. *ZAMM Zeitschrift für Angewandte Mathematik und Mechanik* 89(4):267–278
- Humer A, Irschik H (2011) Large deformation and stability of an extensible elastica with an unknown length. *International Journal of Solids and Structures* 48:1301–1310
- Kim D, Leamy MJ, Ferri AA (2011) Dynamic Modeling and Stability Analysis of Flat Belt Drives Using an Elastic/Perfectly Plastic Friction Law. *ASME Journal of Dynamic Systems, Measurement, and Control* 133:1–10
- Kong L, Parker RG (2005) Steady mechanics of belt-pulley systems. *ASME Journal of Applied Mechanics* 72:25–34
- Leamy MJ (2005) On a perturbation method for the analysis of unsteady belt-drive operation. *ASME Journal of Applied Mechanics* 72(4):570–580
- Marynowski K, Kapitaniak T (2014) Dynamics of axially moving continua. *International Journal of Mechanical Sciences* 81:26–41
- Moës N, Dolbow J, Belytschko T (1999) A finite element method for crack growth without remeshing. *International Journal for Numerical Methods in Engineering* 46(1):1278–1300
- Morimoto T, Iizuka H (2012) Rolling contact between a rubber ring and rigid cylinders: Mechanics of rubber belts. *International Journal of Mechanical Sciences* 54:234–240
- Mote JCD (1966) On the nonlinear oscillation of an axially moving string. *Journal of Applied Mechanics* 33:463–464
- Pechstein A, Gerstmayr J (2013) A Lagrange-Eulerian formulation of an axially moving beam based on the absolute nodal coordinate formulation. *Multibody System Dynamics* 30:343–358
- Reynolds O (1874) On the efficiency of belts or straps as communicators of work. *The Engineer* 38:396
- Rubin M (2000) An exact solution for steady motion of an extensible belt in multipulley belt drive systems. *Journal of Mechanical Design* 122:311–316
- Stoker JJ (1989) *Differential Geometry*. Wiley Classics Library, Wiley
- Vetyukov Y (2012) Hybrid asymptotic-direct approach to the problem of finite vibrations of a curved layered strip. *Acta Mechanica* 223(2):371–385
- Vetyukov Y (2014a) Finite element modeling of Kirchhoff-Love shells as smooth material surfaces. *ZAMM* 94(1-2):150–163
- Vetyukov Y (2014b) *Nonlinear Mechanics of Thin-Walled Structures. Asymptotics, Direct Approach and Numerical Analysis*. Foundations of Engineering Mechanics, Springer, Vienna
- Vetyukov Y (2017) Non-material finite element modelling of large vibrations of axially moving strings and beams. *Journal of Sound and Vibration* submitted
- Vetyukov Y, Gruber PG, Krommer M (2016) Nonlinear model of an axially moving plate in a mixed Eulerian-Lagrangian framework. *Acta Mechanica* 227:2831–2842
- Vetyukov Y, Gruber PG, Krommer M, Gerstmayr J, Gafur I, Winter G (2017a) Mixed Eulerian-Lagrangian description in materials processing: deformation of a metal sheet in a rolling mill. *International Journal for Numerical Methods in Engineering* 109:1371–1390
- Vetyukov Y, Oborin E, Krommer M, Eliseev V (2017b) Transient modelling of flexible belt drive dynamics using the equations of a deformable string with discontinuities. *Mathematical and Computer Modelling of Dynamical Systems* 23(1):40–54
- Wickert JA (1992) Nonlinear vibration of a traveling tensioned beam. *International Journal of Non-Linear Mechanics* 27(3):503–517

Yang S, Deng Z, Sun J, Zhao Y, Jiang S (in press) A variable-length beam element incorporating the effects of spinning. *Latin American Journal of Solids and Structures*

## Chapter 14

# A software platform for the analysis of porous die-cast parts using the finite cell method

Mathias Würkner, Sascha Duczek, Harald Berger, Heinz Köppe, Ulrich Gabbert

**Abstract** Due to the die-cast technology the manufactured parts contain unavoidable imperfections such as cavities and pores with a length scale much smaller than the size of the produced parts. Such imperfections can reduce the load bearing capacity as well as the lifetime of a part and, consequently, have to be taken into consideration during the design process. But, to include the huge amount of small scale pores in a classical finite element simulation requires an extremely refined mesh and results in a computational effort, which may exceed the capacity of today's computer hardware. An alternative approach is the application of the finite cell method (FCM), which can operate with non body-fitted hexahedral or tetrahedral meshes, meaning that the finite element mesh does not have to be aligned to the geometry of the structural part. The pores are taken into account in form of a STL data set (STL: standard tessellation language) coming from computed tomography (CT) or other sources, such as from a cast simulation procedure.

The paper deals with the development of a software platform, which combines the FCM with the widely used commercial finite element package Abaqus. The overall workflow along with specific implementational details are discussed. Finally, academic benchmark problems are used to verify the developed software platform.

### 14.1 Introduction

The development of light-weight designs in the automotive industry contributes to fulfill the EU regulations to reduce the fuel consumption as well as the carbon dioxide and nitrogen oxide emissions of combustion engines. But, also in electric vehicles the light-weight design is essential, because it contributes to an increase of the vehicle's

---

Mathias Würkner · Sascha Duczek · Harald Berger · Heinz Köppe · Ulrich Gabbert  
Institute of Mechanics, Otto von Guericke University of Magdeburg, Universitätsplatz 2,  
39106 Magdeburg, e-mail: mathias.wuerkner@ovgu.de, sascha.duczek@ovgu.de, harald.berger@ovgu.de, heinz.koeppel@ovgu.de, ulrich.gabbert@ovgu.de

range. In general a weight reduction can be achieved by optimizing the design of the part and by changing the deployed material. The application of aluminium die-cast in connection with an optimized design fulfils the requirements for a light-weight and cost effective product. But die-cast parts show an inherent and unavoidable amount of imperfections, such as cavities and pores. A wide range of changeable parameters are available to reduce the porosity, such as a large amount of setting parameters at the die-cast machines, the thermal cycling of the manufacturing process, the amount of applied spray etc.; for details see the research results presented in (Ambos et al, 2013a).

The location, the shape, the number and the distribution of pores have a great influence on the durability and strength properties of die-cast parts. The information are available today provided by fast computed tomography (CT) scans, which are used to investigate the pore morphology in detail (Ambos et al, 2013a,b; Oberdorfer et al, 2014; Rehse et al, 2013). CT scans help to identify and to quantify the location, the size and the volume of pores. Besides the 3D coordinates of each voxel measured with a CT scan also a gray value, the so called Hounsfield scale, is assigned. From these data a STL file is derived, which represents a triangular surface tessellation, originally developed for the stereolithography process. Finally, each pore is described by a surface mesh of triangles. This topological description can be used for further steps in a finite element analysis of die-cast parts with pores. At pores high stress concentrations often occur, which may facilitate a crack initiation. Therefore, the calculation of stress concentration at the most significant pores of die-cast parts under real operating conditions is of great interest. For the overall simulation the FEM is usually used and applied to the ideal construction without regarding pores. To take into account the pores we propose to apply the finite cell method (FCM). In the following it is assumed, that the pores are given in form of a STL data set. The main difference of the FCM to the classical FEM is the concept of embedding the original or physical domain into a larger domain creating a simpler geometrical shape (Ramière et al, 2007; Saul'ev, 1963). The finite cell method (FCM) combines the so called fictitious domain approach with the FEM especially in case of higher order finite elements (Duczek et al, 2015, 2016; Düster et al, 2008; Parvizian et al, 2007; Zander et al, 2012; Rank et al, 2009).

The FCM can be interpreted as an extension of the classical FEM. If a finite element model (FE model) of the ideal geometry of a construction (without inhomogeneities such as pores) is given and additionally CT scans or STL data sets containing informations on the pore morphology are provided, the FCM can be used to calculate the stress field taking into account the real geometry of the pores. Consequently, for an industrial application it would be helpful to combine the FCM with the FEM based on commercially available software tools (Ansys, Abaqus, etc.).

The paper deals with the development of such a software platform combining the FCM with the FEM and using a STL file containing the inhomogeneities in order to calculate the displacements and stresses based on a FE model of the ideal geometry. The platform uses data interfaces and offers a flow chart, so that the complete analysis process can be performed automatically.

The paper is organized as follows. In Sect. 14.2 some basic information about the

FCM are briefly given. This also includes the main differences to the classical FEM. Then the platform concept is described in Sect. 14.3. In Sect. 14.4 some information and trouble shootings according to the STL data derived from CT measurements are discussed. In Sect. 14.5 the platform is tested by analyzing some academic test examples, which demonstrate the capability of handling the complete analysis process. The paper finishes with a summary and an outlook to further development steps.

## 14.2 The Finite Cell Method

Numerical methods are most preferred for solving nonlinear and complex physical problems. In engineering applications the FEM is one of the most popular methods. The basic idea of the method is to divide the physical domain of the considered problem into smaller subdomains, the so called finite elements (FEs), where in each of these domains the unknown solution is approximated by an ansatz function including a field of unknown variables, the so called degrees of freedom (DOFs). These unknowns are determined by solving a system of equations.

The finite cell method (FCM) is a numerical method, which is strongly related to the FEM. The FCM can be interpreted as an extension of the FEM and belongs to the class of fictitious domain methods (Düster et al, 2008; Parvizian et al, 2007). In the following a brief description and the fundamental equations of the FCM are presented. In addition the differences in relation to the classical FEM are emphasized. For further informations and explanations regarding the FEM and the FCM the reader is referred to other literature (Düster et al, 2008; Parvizian et al, 2007; Zienkiewicz and Taylor, 2000; Bathe, 2002; Duczec, 2014).

### 14.2.1 Fundamentals of the Finite Cell Method

Let us focus on a 3D problem of linear elasticity. It is assumed, that the problem is given by

$$-\operatorname{div} \underline{\underline{\tilde{\sigma}}} = \underline{f} \quad (14.1)$$

on a domain  $\Omega$ .  $\underline{\underline{\tilde{\sigma}}}$  denotes the second order Cauchy stress tensor. The right-hand side of the equation characterizes the body loads. Due to linear elasticity and the general use of Cartesian coordinate systems the more convenient Voigt notation is used, describing the stresses and strains in vector form. In the following vector and matrix form quantities are highlighted by a single and double underline, respectively. In order to solve a boundary value problem the boundary conditions have to be formulated. The boundary of  $\Omega$ , denoted with  $\partial\Omega$ , is split into a Dirichlet boundary, denoted  $\Gamma_D$ , and two Neumann boundaries, denoted  $\Gamma_N$  and  $\Gamma_0$ . It holds  $\partial\Omega = \Gamma_D \cup \Gamma_N \cup \Gamma_0$  and  $\Gamma_D \cap \Gamma_N \cap \Gamma_0 = \emptyset$ . The boundary conditions are given as follows



$$\underline{u} = \underline{0} \quad \text{on } \Gamma_D, \tag{14.2}$$

$$\underline{t} = \underline{\bar{t}} \quad \text{on } \Gamma_N, \tag{14.3}$$

$$\underline{t} = \underline{0} \quad \text{on } \Gamma_0, \tag{14.4}$$

where  $\underline{u}$  are the displacements and  $\underline{t}$  are the tractions. Adding a bar over a letter means that the quantity is prescribed. Using the Bubnov-Galerkin method the weak form of the boundary value problem is derived. Multiplying Eq. (14.1) with a test function  $\underline{v}$ , which is zero on the boundary  $\Gamma_D$ , and afterwards performing an integration over  $\Omega$  results in a weak form of the equilibrium. Using the multidimensional integration by parts and taking into account the boundary conditions Eqs. (14.2)-(14.4) the weak form can be rewritten as

$$\int_{\Omega} (\underline{D}\underline{v})^T \underline{\sigma} d\Omega - \int_{\Gamma_N} \underline{v}^T \underline{\bar{t}} d\Gamma - \int_{\Omega} \underline{v}^T \underline{f} d\Omega = 0. \tag{14.5}$$

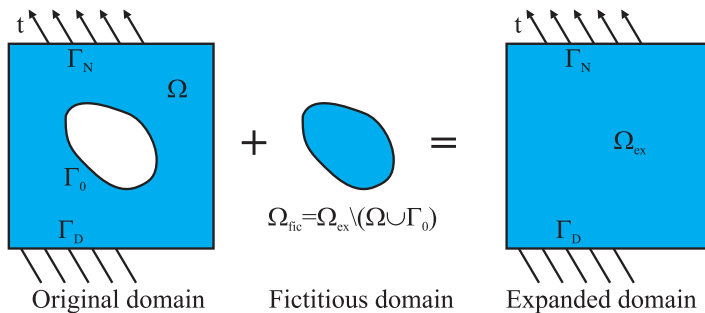
Here  $\underline{\sigma}$  denotes the stresses in the Voigt notation. The quantity  $\underline{D}$  denotes the matrix of differential operators, which relates the displacements to the strains in the Voigt notation as

$$\underline{D}\underline{u} = \underline{\varepsilon}. \tag{14.6}$$

Using the constitutive law of linear elasticity the weak form changes to

$$\int_{\Omega} (\underline{D}\underline{v})^T \underline{C}\underline{D}\underline{u} d\Omega - \int_{\Gamma_N} \underline{v}^T \underline{\bar{t}} d\Gamma - \int_{\Omega} \underline{v}^T \underline{f} d\Omega = 0. \tag{14.7}$$

Here  $\underline{C}$  is the elasticity matrix in the Voigt notation. Instead of solving the physical problem on the original domain an expanded domain is used in the FCM, denoted with  $\Omega_{\text{ex}}$  (see Fig. 14.1). The additional domain, also called fictitious domain and denoted with  $\Omega_{\text{fic}}$ , is chosen in such a way, that  $\Omega_{\text{ex}}$  can be characterized by a simpler geometric structure. For further investigations we assume, as shown in Fig. 14.1, that the fictitious domain is completely enclosed by the original domain. In case of



**Fig. 14.1:** Expansion of the original domain by a fictitious domain

investigating die-cast parts such a fictitious domain represents a pore.

Using the expansions  $\underline{u}_{\text{ex}}$  and  $\underline{v}_{\text{ex}}$  and additionally the continuity conditions related to displacements and tensions on the boundary  $\Gamma = \partial\Omega \cap \partial\Omega_{\text{fic}}$  the weak form can be written as

$$\int_{\Omega_{\text{ex}}} \left( \underline{D}_{\underline{v}_{\text{ex}}} \right)^T \underline{C}_{\underline{ex}} \underline{D} \underline{u}_{\text{ex}} d\Omega - \int_{\Gamma_{\text{N}}} \underline{v}_{\text{ex}}^T \bar{t} d\Gamma - \int_{\Omega_{\text{ex}}} \underline{v}_{\text{ex}}^T \underline{f} d\Omega = 0. \quad (14.8)$$

Here  $\underline{C}_{\underline{ex}}$  denotes the modified elasticity matrix defined by

$$\underline{C}_{\underline{ex}} = \alpha(\underline{x}) \underline{C}, \quad (14.9)$$

where

$$\alpha(\underline{x}) = \begin{cases} 1.0 & \forall \underline{x} \in \Omega, \\ 0.0 & \forall \underline{x} \in \Omega_{\text{fic}}. \end{cases} \quad (14.10)$$

With respect to further investigations related to the numerical integration it is mentioned, that the value of  $\alpha$  in  $\Omega_{\text{fic}}$  should be replaced by a sufficiently small value representing numerical zero. This avoids severe ill-conditioning of the global stiffness matrix in the upcoming discretization process. To simplify the problem we further assume, that body loads are absent. Therefore the last term of Eq. (14.8) is neglected in further investigations.

In the FEM the domain  $\Omega$  is divided into finite elements, where in the FCM the expanded domain  $\Omega_{\text{ex}}$  is partitioned. Due to similarities in the discretization process of the FCM and the FEM the used elements in the FCM are currently called finite cells, which helps to distinguish between the two methods for further explanations (Düster et al, 2008; Parvizian et al, 2007). In general the finite cells differ from the classical finite elements by the fact, that they do not have to be adapted to the real physical geometry or inner boundaries, for instance caused by different material regions. This gives the opportunity to use a more simplified discretization grid. Very promising cases would be uniform grids of rectangularly shaped cells in 2D or hexahedrally shaped cells in 3D (see Fig. 14.2).

Let us just concentrate on the first term of Eq. (14.8). Assuming  $\Omega_{\text{ex}}$  is completely divided into  $M$  finite cells the term can be changed to

$$\sum_{c=1}^M \int_{\Omega_c} \left( \underline{D}_{\underline{v}_{\text{ex}}} \right)^T \underline{C}_{\underline{ex}} \underline{D} \underline{u}_{\text{ex}} d\Omega. \quad (14.11)$$

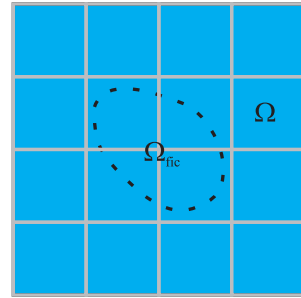
The second term can be treated in a similar way.

In similarity to the FEM the displacement  $\underline{u}_{\text{ex}}$  is approximated in each cell using so called shape functions

$$\underline{u}_{\text{ex}} = \underline{N} \hat{\underline{u}}. \quad (14.12)$$

Here  $\underline{N}$  and  $\hat{\underline{u}}$  are the matrix of shape functions and the vector of unknown variables, the so called DOFs, respectively. Using  $\underline{v}_{\text{ex}} = \underline{N} \hat{\underline{v}}$ , Eqs. (14.11) and (14.12) the

**Fig. 14.2** Uniform finite cell grid of an expanded 2D domain consisting of quadratically shaped cells (right side of the figure); the occupied domain of the  $c$ -th finite cell is denoted by  $\Omega_c$  (left side of the figure)



following system of equations can finally be derived for each finite cell

$$\underline{\underline{K}} \underline{\hat{u}} = \underline{F}. \tag{14.13}$$

By assembling the system of equations of all finite cells the global system of equations is derived as

$$\underline{\underline{K}}^A \underline{\hat{u}}^A = \underline{F}^A. \tag{14.14}$$

The FCM is an extension of the FEM, which gives the opportunity of defining a compatible finite cell for each finite element. This also assures the possibility of creating a hybrid mesh consisting of both finite elements and finite cells. In the following such a mesh is called FE-FC mesh.

### 14.2.2 Numerical Integration

For the evaluation of  $\underline{\underline{K}}$  and  $\underline{F}$  in Eq. (14.13) integrals have to be calculated. In the classical FEM, due to mapping transformations using a reference element, the integrand is in general non-polynomial. The integration cannot be analytically performed in most of the cases. Therefore, numerical integration methods are used. For common finite elements as in commercial software tools (Abaqus, Ansys, etc.) the Gaussian quadrature is applied. This approach converges fast for sufficiently smooth integrands, but not for discontinuous ones. Referring to Fig. (14.2) and Eq. (14.11), for the finite cells the integrand is discontinuous due to the jump in the elasticity matrix. That is why in the FCM an adaptive integration scheme is used in order to capture this discontinuity in an appropriate way.

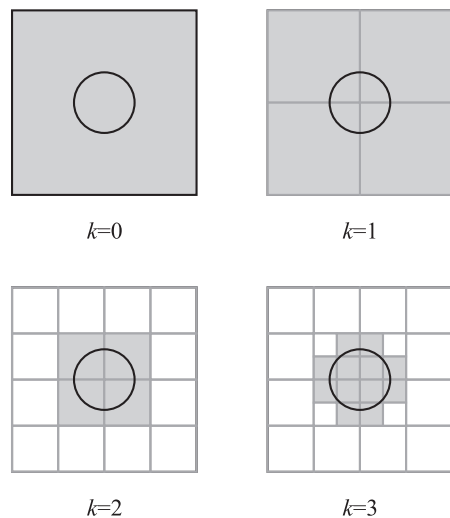
In the following, the case of discontinuous material properties is discussed. This means, the cell contains the joint boundary of the fictitious and the original domain. A common Gaussian quadrature for solving the integrals would be an inappropriate approach. Instead a composed integration is used. This integration procedure is characterized by subdividing the domain of the cell, using a subdivision scheme. In the following a quadtree subdivision procedure for the 2D case will be explained. Referring to Fig. 14.3 it is assumed, that a cell is cut by the boundary of the region.

The subdivision level, denoted with  $k$ , is zero at the beginning. For  $k = 1$  the domain of the cell is split into four equal-sized subdomains, which are called subcells in the following. In order to establish the level  $k = 2$  each of the four subcells is checked, whether it contains the boundary or not. If it is true the domain of the subcell is split further into four smaller subcells. In Fig. 14.3 the subcells, which have to be divided, are marked with a gray color filling. Higher subdivision levels are obtained by following the previously explained procedure until the integration is converged. In case of 3D finite cells an octree-subdivision scheme is used. Here the cells are split into eight subcells. Detailed information, such as the integration weights and points of the Gaussian quadrature, can be taken from Duczek (2014).

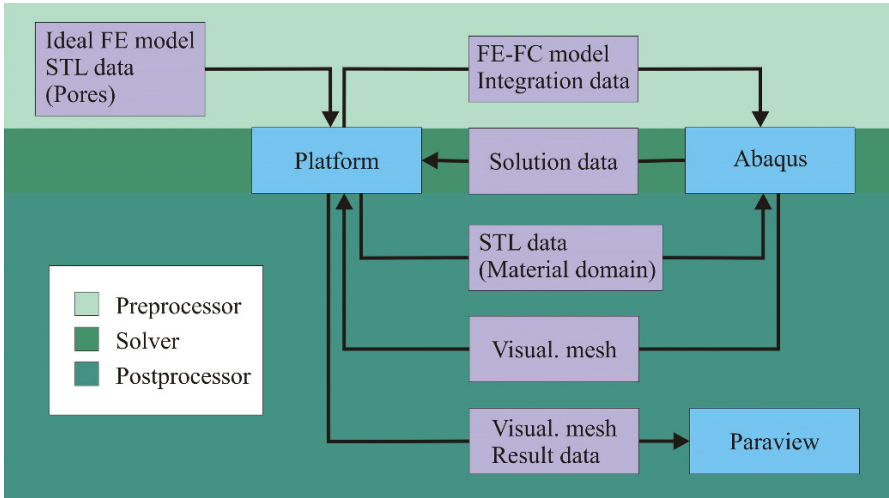
### 14.3 Concept of the Software Platform

For developing the software platform concept the programming software tool Matlab is used. The platform combines the FCM and the interaction of its interface to an appropriate commercial software tool in order to establish a complete workflow of creating the FC model, solving the problem and evaluating its strains and stresses. In this regard the programming of the platform is split into three sections. These are the preprocessor, the solver and the post processor (see Fig. 14.4).

The preprocessor deals with the creation of the FC model. In the following it is assumed, that a sample of an ideal die-cast part (without pores) is already given as a FE model and the information of the pores are separately provided in form of a STL data set. This data set contains the topology of the surface triangulation of the pores as well as the locations of the corner vertices of the triangles. The mesh of the FE model is used to perform the FC discretization. The finite elements are replaced



**Fig. 14.3** Schematic sketch of a quadtree subdivision procedure, where the fictitious domain is represented by a circular region; cells/subcells containing at least parts of this region are highlighted in light gray



**Fig. 14.4:** Flow chart of the developed software platform

by finite cells. In general, as mentioned in Sect. 14.2, the expanded domain, here represented by the ideal die-cast part, can be discretized with cells. According to the adaptive numerical integration a distinction of two cases has to be considered: (i) the integration point is in the physical region and (ii) the integration point is in the fictitious domain. The numerical integration of cells completely located in the real domain ( $\alpha = 1.0$ ) are treated as in standard finite elements. Cells, which are completely located in the fictitious domain ( $\alpha = 0.0$ ), are removed from the model, which results in a lower effort in solving the system of equations. Only those finite cells have to be treated separately, whose domain contains the boundary of the fictitious domain, i.e. the material discontinuity Eq. (14.9). The resolution of this discontinuity in the numerical integration, controllable by the subdivision level  $k$ , has to be fine enough to reduce the integration error sufficiently.

For the sake of clarity, the finite elements belonging to the real domain do not have to be replaced by finite cells, since the numerical treatment of cells and elements is identical. These elements can be kept. The resulting FE-FC model does not differ in a numerical sense from the corresponding pure FC model.

The usage of the platform is tied to the condition, that the initial FE mesh has to be either hexahedral or tetrahedral. Due to the numerical accuracy a hexahedral mesh is to be preferred. In industrial application the geometry of a part is in general very complex. Therefore, most existing meshes are tetrahedral meshes, which are simpler to create. Using compatible finite cells the FE-FC model is established with regard to the initial FE model. The hybrid model and the data set for numerical integration (integration weights and points) of the cells given in an appropriate format are transferred via the software platform to a commercial FE tool, such as Abaqus. In Abaqus for instance, the possibility of applying user-defined subroutines (UEL

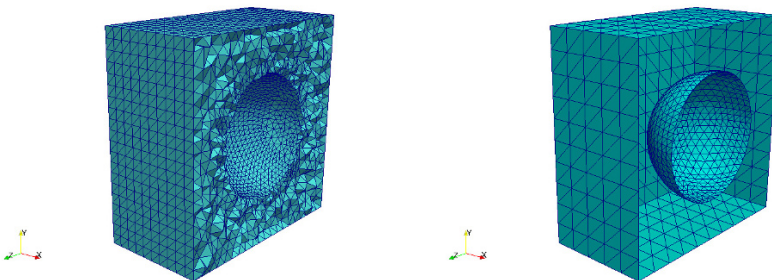
subroutines) is used to incorporate the special FCM part, which is needed to create and to solve the overall global system of equations.

The postprocessor of the software platform deals with the subsequent treatment of the vector of unknowns, i.e. the displacement at all nodes of the FE-FC mesh. These solution data are transferred to the software platform. In combination with the previously saved FE-FC model it is possible to calculate the displacements, strains and stresses at any point. For the purpose of visualizing those quantities on the FE-FC point grid a problem occurs, since points of the grid lie in the fictitious domain, which in case of representing a pore causes visualization artifacts. For this reason a grid of points is created, where all the points belong to a body-fitted mesh, the so called visualization mesh. The displacements, strains and stresses are calculated at the points of the visualization mesh by using the data from the FC-FE solution. In order to generate the visualization mesh the surface triangulation based on the FE model of the ideal die-cast part in combination with the STL data set of the pores is transferred to Abaqus and a mesh consisting of 4-node tetrahedra is created. Alternatively, the surface triangulation and its grid of points can be used for the visualization (see Fig. 14.5).

The actual visualization of strains and stresses is performed by using a data interface to the open source software ParaView. Executing ParaView and transferring the calculated results in an appropriate format provides the opportunity to an interactive evaluation of the displacements, strains and stresses.

## 14.4 Trouble Shooting the STL Data Set

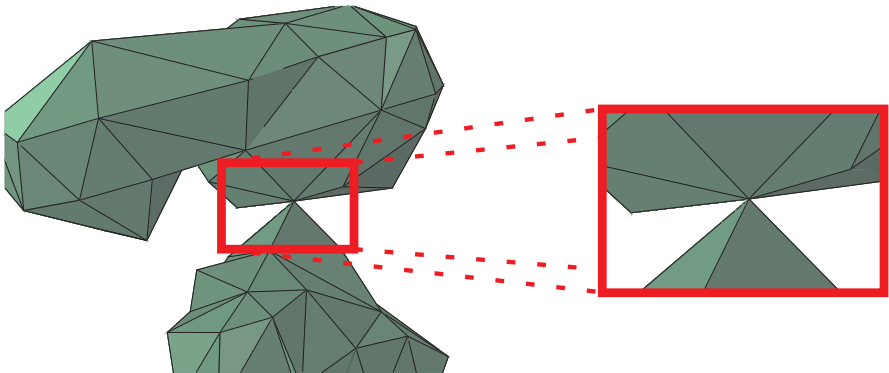
First used in stereolithography CAD software nowadays the STL format is supported by almost every CAD software. The file format can be either Ascii or binary. As mentioned in Sect. 14.3 a STL data set is used in the preprocessor of the developed platform. This data set contains in the case of die-cast parts the pore morphology



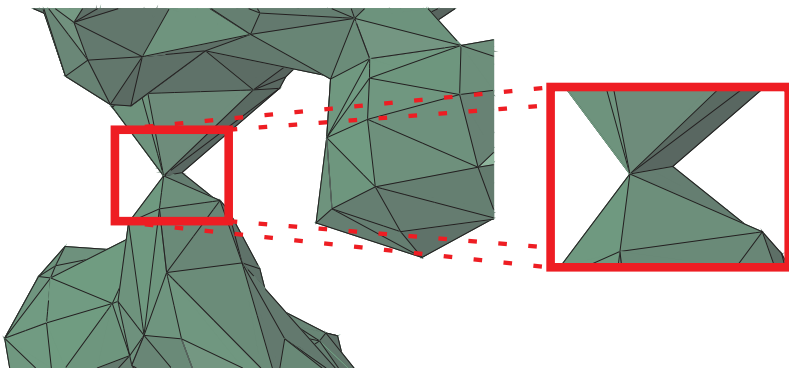
**Fig. 14.5:** Samples of visualization meshes: 3D tetrahedral mesh (left) and a surface triangulation mesh (right)

in form of a surface triangulation described by normals and point locations. The simplicity of the STL format using unstructured triangular facets often causes errors in the 3D meshing procedure. Overlapping of facets, incorrect normal directions, unclosed surface descriptions, etc. are not prevented by the format. Also closed surface triangulations can be connected to each other, as for instance by a line segment or a point (see Figs. 14.6 and 14.7), which complicates the unique identification of surface objects. Therefore, a mesh repair or a remeshing procedure is absolutely essential for FEM or FCM applications. However, this is a highly complex issue and topic of several publications (Bechet et al, 2002; Attene, 2014).

The repair mechanisms for STL data included in the software platform is still under development; a reorienting of the normals of facets is already included.



**Fig. 14.6:** Problems of identifying pores: Closed surface triangulations of pores connected to each other by a point



**Fig. 14.7:** Problems of identifying pores: Closed surface triangulations of pores connected to each other by a line segment

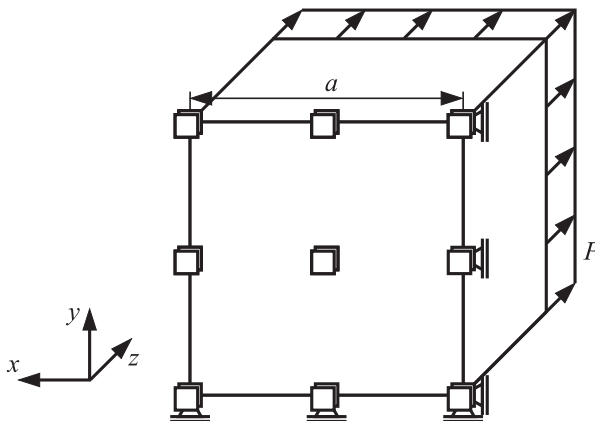
## 14.5 Verification of the Software Platform

In this section the developed platform is tested with help of some academic test cases. The objective of these investigations is to demonstrate the capability of the developed software platform of performing the complete analysis process.

The first example deals with a cube ( $a = 10\text{m}$ ), in which a centrally located ellipsoidal pore is embedded. The material is aluminium (see Table 14.1). A tensile load  $P = 100\text{N/m}^2$  is applied on the surface of the cube normal to the positive  $z$ -direction (see Fig. 14.8). On the opposite surface the displacements in  $z$ -direction are constrained to zero. In addition the displacements in  $x$ - and  $y$ -direction are also constrained to zero at two edges of this surface, respectively. These boundary conditions ensure enabled transverse contraction.

In order to verify the calculated quantities by using the developed software platform a reference FE analysis (Abaqus) is performed. The applied body-fitted FE model consists of 180325 tetrahedral elements (764424 DOFs) of second polynomial order (10-node tetrahedral elements; see Fig. 14.9) and is used to evaluate the computations. In comparison, the FE-FC model is based on a  $25 \times 25 \times 25$  hexahedral FE mesh (204828 DOFs). Both simulations employ elements with an identical polynomial order. The subdivision level was set to  $k = 3$ .

Figures 14.10 and 14.11 show some results related to the developed software platform and to the purely Abaqus-based simulations, respectively. The depicted results are the displacement magnitudes (left side of the figures) and the von Mises stresses (right side of the figures). Due to the boundary conditions we can observe a band of stress concentrations at the surface of the ellipsoidal pore. It can be summarized, that the results of both analyses are in very good agreement.

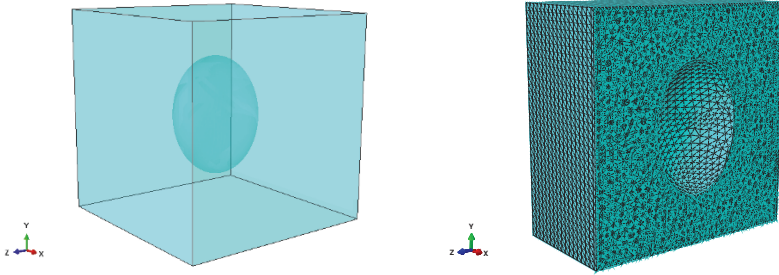


**Fig. 14.8:** Model definition: Boundary conditions, loads and dimensions

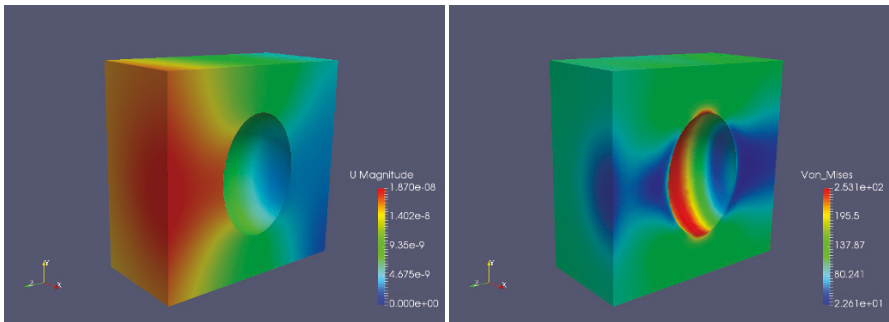


Table 14.1: Material properties

Material	Young's modulus [N/mm <sup>2</sup> ]	Poisson's ratio
Aluminium	70000	0.33

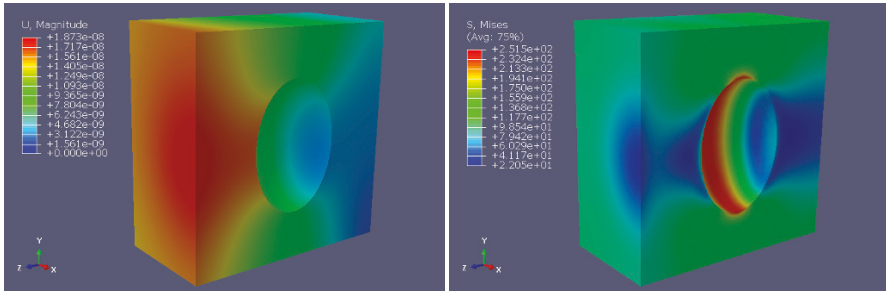


**Fig. 14.9:** Geometrical model of a cube with a centrally embedded ellipsoidal pore (left) and a sectional view of the corresponding FE model with a body-fitted finite element mesh



**Fig. 14.10:** Displacement magnitudes and von Mises stresses calculated with help of the developed software platform and a coarse FE-FC mesh of  $25 \times 25 \times 25$  hexahedral elements

Next we consider an example with more than one inclusion. As shown in Fig. 14.12 a cube ( $a = 10\text{m}$ ) with four randomly distributed embedded ellipsoidal pores is investigated. Note that, all pores have different volumes and sizes. As in the previous example a body-fitted FE model (Abaqus) is used as reference model. The model consists of 300864 tetrahedral elements (1263081 DOFs) with a polynomial order of two. The FE-FC model is again based on a  $25 \times 25 \times 25$  hexahedral FE mesh (204828



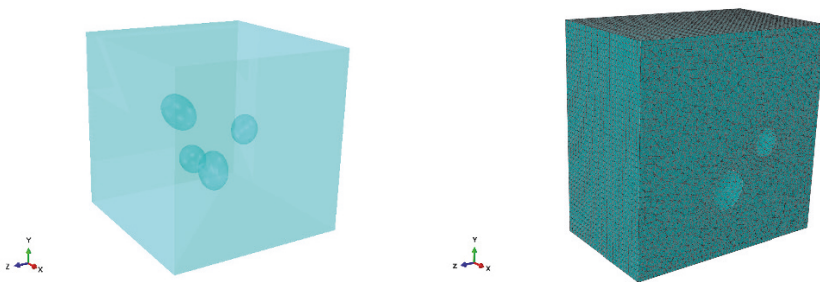
**Fig. 14.11:** Displacement magnitude and von Mises stresses calculated with the help of a body-fitted finite element mesh

DOFs) with an identical polynomial order. The integration subdivision level is set to  $k = 4$ .

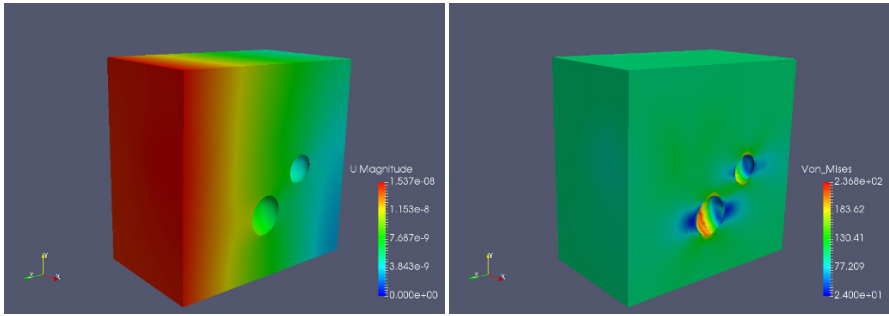
In Figs. 14.13 and 14.14 the results related to the developed software platform and to the pure Abaqus model are shown, respectively. While the displacement magnitudes are in good agreement the von Mises stresses show some small differences, with a maximum value of about 6%. Nevertheless it has to be pointed out, that the model related the developed software platform only uses almost one twentieth of the element number of the reference model.

### 14.6 Summary and Outlook

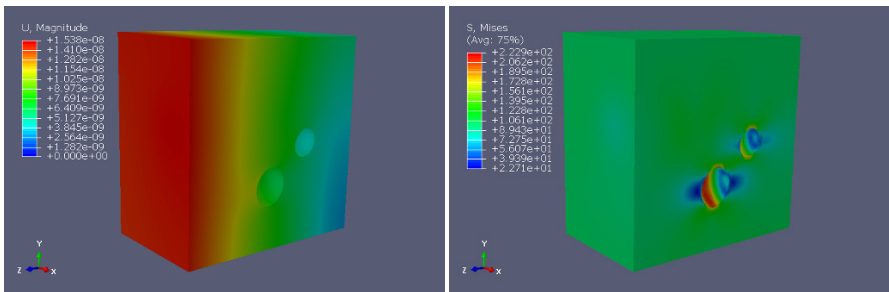
The current paper deals with the development of a software platform using the FCM and the STL format in order to calculate displacements, strains and stresses of die-cast parts. The platform contains a complete flow chart of the analysis. The ideal



**Fig. 14.12:** Geometrical model of a cube with four randomly distributed embedded ellipsoidal pores and a sectional view of the corresponding FE model with a body-fitted finite element mesh



**Fig. 14.13:** Displacement magnitudes and von Mises stresses calculated with the developed platform



**Fig. 14.14:** Displacement magnitudes and von Mises stresses calculated with Abaqus

geometry given in form of a FE model and the pore morphology given in the STL format deal as initial informations for the platform. The usage of interfaces to several software tools (Abaqus, ParaView) helps the platform to assure the capability of performing a complete analysis process. The representation of the results can be interactively performed by using ParaView, where the results are based on a point grid belonging to a visualization mesh. This visualization mesh contains either a 3D point grid related to the real geometry or a grid related to the boundary surface of the real geometry.

The platform and its flow chart is verified with the help of two academic test problems. Their results, such as displacements and stresses, calculated by the platform are compared to results of body-fitted FE models, which are used as reference. Despite of much smaller numbers of DOFs compared to the reference models they are in good agreement with the calculated quantities of the FE models.

In the future, the platform and its flow chart will be tested on real die-cast part, which contains pores lying in a critical region of the part. Also improvements according to the trouble shootings with the STL format will be included in the platform.

**Acknowledgements** The authors gratefully acknowledge the support provided by the European Regional Development Fund (German: Europäischer Fonds für regionale Entwicklung–EFRE) and the Investitionsbank Saxony-Anhalt related to the project number ZS/2016/04/78125.

## References

- Ambos E, Anders U, Schalk S, Bullick M, Reinhart C, Matzen HU, Besser W (2013a) Gussteilprüfung auf einem neuen Niveau: Neue Ergebnisse über den Einsatz schneller Computertomografen in Druckgiessereien. *Giesserei Erfahrungsaustausch* 11/12:8–15
- Ambos E, Besser W, Teuber S, Brunke O, Neuber D, Stuke I, Lux H (2013b) Einsatz der schnellen Computertomographie zur Porositätsbewertung an Druckgussteilen. *Giesserei-Rundschau* 60:14–22
- Attene M (2014) Direct repair of self-intersecting meshes. *Graphical Models* 76:658–668
- Bathe KJ (2002) *Finite-Elemente-Methoden*. Springer-Verlag
- Bechet E, Cuilliere JC, Trochu F (2002) Generation of a finite element MESH from stereolithography (STL) files. *Computer-Aided Design* 34:1–17
- Duczek S (2014) Higher Order Finite Elements and the Fictitious Domain Concept for Wave Propagation Analysis. *VDI Fortschritt-Berichte Reihe 20 Nr. 458*, URL <http://edoc2.bibliothek.uni-halle.de/urn/urn:nbn:de:gbv:ma9:1-5434>
- Duczek S, Berger H, Ambos E, Gabbert U (2015) Eine neue Methode zur Berücksichtigung des Einflusses der Porosität in Al-Druckgussteilen auf die Festigkeit - Ein Beitrag zum Leichtbau. *Gießerei-Rundschau* 62:222–227
- Duczek S, Duvigneau F, Gabbert U (2016) The finite cell method for tetrahedral meshes. *Finite Elements in Analysis and Design* 121:18–32
- Düster A, Parvizian J, Yang Z, Rank E (2008) The finite cell method for three-dimensional problems of solid mechanics. *Computational Methods in Applied Mechanics and Engineering* 197:3768–3782
- Oberdorfer B, Habe D, Kaschnitz E (2014) Bestimmung der Porosität in Al-Gussteilen mittels CT und ihres Einflusses auf die Festigkeitseigenschaften. *Giesserei-Rundschau* 61:138–141
- Parvizian J, Düster A, Rank E (2007) Finite cell method: h- and p-extension for embedded domain problems in solid mechanics. *Computational Methods in Applied Mechanics and Engineering* 41:121–133
- Ramière I, Angot P, Belliard M (2007) A fictitious domain approach with spread interface for elliptic problems with general boundary conditions. *Computational Methods in Applied Mechanics and Engineering* 196:766–781
- Rank E, Düster A, Schillinger D, Yang Z (2009) The finite cell method: High order simulation of complex structures without meshing. In: Yuan Y, Cui JZ, Mang H (eds) *Computational Structural Engineering*, Springer Science+Business Media B.V.
- Rehse C, Schmicker D, Maaß A, Bähr R (2013) Ein Bewertungskonzept für computertomographisch ermittelte Porositäten in Gussteilen hinsichtlich ihrer Auswirkung auf die lokale Beanspruchbarkeit des Bauteils. *Giesserei-Rundschau* 60:106–110
- Saul'ev VK (1963) On solution of some boundary value problems on high performance computers by fictitious domain method. *Siberian Mathematical Journal* 4:912–925
- Zander N, Kollmannsberger S, Ruess M, Yosibash Z, Rank E (2012) The finite cell method for linear thermoelasticity. *Computers and Mathematics with Application* 64:3527–3541
- Zienkiewicz OC, Taylor RL (2000) *The Finite Element Method - Volume 2: Solid Mechanics*. Butterworth-Heinemann

# Chapter 15

## Refined One-Dimensional Models for the Multi-Field Analysis of Layered Smart Structures

Enrico Zappino and Erasmo Carrera

**Abstract** The analysis of layered structures requires the use of numerical tools that are able to describe the complex behavior that can appear at the interface between two different materials. The use of the Finite Element Method can only lead to accurate results if the kinematic assumptions of the structural models allow complex deformation fields to be evaluated, and as a consequence classical models are often ineffective in the analysis of such structures. The use of the Carrera Unified Formulation provides a general tool that can be used to derive refined one-dimensional models in a compact form. The use of a refined kinematic description over the cross-section of an element leads to accurate results even when multi-field problems are considered, that is when complex stress fields appear. A comprehensive derivation of a class of refined one-dimensional models, which are able to deal with multilayer structures and multi-field problems, is presented in this section. Thermal and piezoelectric effects are considered, and a fully coupled thermo-piezo-elastic model is presented. Finally, some benchmarks are shown in order to verify the accuracy of the presented models.

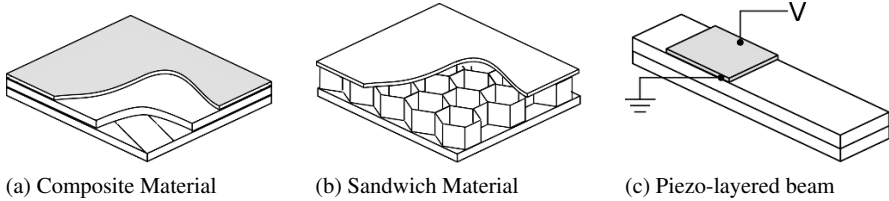
### 15.1 Introduction

The development of innovative structures requires the use of numerical tools that are able to deal with the complexities introduced by innovative materials. Laminated materials are used extensively in all engineering fields, and they can appear in many different forms. The most common layered structures are made up of composite materials, see Fig. 15.1a, that exploit the orthotropic properties of the fiber reinforced layers to increase the stiffness of the structural component in the desired direction. When the weight of the structure is one of the design parameters, the use of sandwich

---

Enrico Zappino · Erasmo Carrera  
*Mul<sup>2</sup>Team*, Politecnico di Torino, Corso Duca degli Abruzzi 24, Torino, Italy,  
e-mail: [enrico.zappino@polito.it](mailto:enrico.zappino@polito.it), [erasmo.carrera@polito.it](mailto:erasmo.carrera@polito.it)

© Springer Nature Singapore Pte Ltd. 2018  
H. Altenbach et al. (eds.), *Analysis and Modelling of Advanced Structures and Smart Systems*, Advanced Structured Materials 81,  
[https://doi.org/10.1007/978-981-10-6895-9\\_15](https://doi.org/10.1007/978-981-10-6895-9_15)



**Fig. 15.1:** Examples of layered structures.

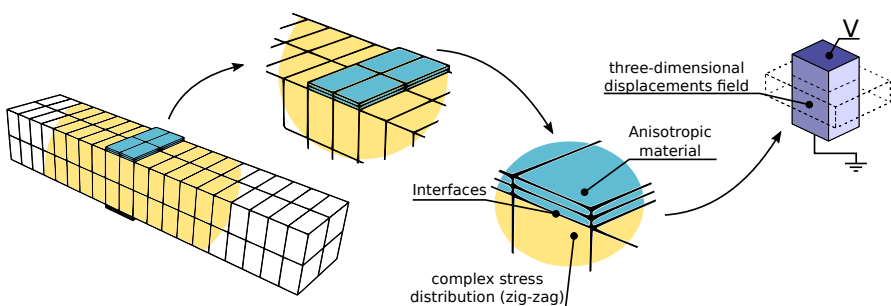
materials, see Fig. 15.1b, may lead to an improvement in the bending resistance without increasing the total weight of the structure. Sandwich materials exploit a thick soft core and two external skins. The core, in addition to absorbing the shear load, increases the distance of the skins from the neutral axis. Another example of layered material is that used in smart structures, see Fig. 15.1c. In this case, a layer or a patch of active material, e.g. piezoelectric material, is bonded onto a structure with the purpose of exploiting the piezo-elastic effect as an actuator or a sensor. Piezo-layered structures have become very important over the last few decades because they are at the basis of the development of MEMS (Micro Electro-Mechanical Systems) devices. The present work has focused on piezo-layered structures, although it is common to find piezoelectric patches on composite materials and sandwich panels.

The analysis of layered beam structures involves evaluating complex stress fields. When the Euler-Bernoulli (Euler, 1744) beam model is used, it is accepted that the solution can only be considered accurate for slender bodies and isotropic materials, that is, it cannot be applied to layered structures. If moderately stubby structures are considered the model proposed by Timoshenko (1921) has to be used to include shear effects, and in this case, the use of a shear correction factor, see Timoshenko (1921); Cowper (1966); Dong et al (2010), is required to overcome the approximation of a constant shear distribution over the cross-section. Even though the Timoshenko model is more accurate than the Euler-Bernoulli theory, neither of these classical models is suitable for the stress analysis of layered structures because they are not able to properly describe the layers interfaces. The introduction of refined structural models allows the limitations introduced by the fundamental assumptions of the classical models to be overcome and the stress singularities due to local effects to be dealt with. Carrera (1997a) pointed out that the analysis of layered structures requires a numerical model that is able to fulfill the  $C_z^0$  requirement, that is, the continuity of the transversal stress component has to be ensured to obtain reliable results.

Many refined one-dimensional models have been proposed over the last few decades, e.g. the use of warping functions, as proposed by Vlasov (1984), which allows the cross-section deformation to be included in beam models. Cross-sectional warping plays an essential role in thin-walled structures, as shown in the work by Friberg (1985); Ambrosini (2000), where the warping function approach was used. Schardt (1966) proposed a one-dimensional model for the thin-walled structures analysis where the displacement field was considered as an expansion around the mid-

plane of the thin-walled cross-section. This approach, which is called the generalized beam theory (GBT), was also used by Davies and Leach (1994); Davies et al (1994), and an extension to the analysis of composite material was proposed by Silvestre et al (2002). The Variation Asymptotic Method, VAM, proposed by Berdichevsky (1976), uses a characteristic cross-section parameter to build an asymptotic expansion of the solution. The application of this approach to one-dimensional structures can be seen in the work by Giavotto et al (1983). Volovoi (1999); Yu et al (2002); Yu and Hodges (2004) have extended this method to composite materials and beams with arbitrary cross-sections.

All these methods allow the accuracy of one-dimensional models to be improved. The development of these models has been crucial in the design of innovative structures that make use of innovative materials. One of these applications is the development of piezoelectric devices. Figure 15.2 shows how the analysis of a piezo-layered structure requires many aspects to be taken into account, such as the material interfaces and the orthotropy of the material. The piezoelectric effect has been known since the 19<sup>th</sup> century, when the Curie brothers first noticed it. This effect pertains to the conversion of mechanical to electrical energy and vice-versa. The use of piezoelectric materials in structural design is very interesting because of their properties, and a great deal of effort has been made to include the piezoelectric contribution in structural models. Crawley and Luis (1987); Bailey and Hubbard (1985) considered the piezoelectric contribution as an additional strain which had to be added to the inactive structure. Classical structural models were used extensively to analyze piezoelectric materials; as shown by Sarvanos and Heyliger (1999) in their review. In the past, classical three-dimensional (Dong et al, 2006; Xu and Koko, 2004), two-dimensional (Kim and Kim, 2005; Moitha et al, 2004) and one-dimensional models were used to study structures with piezoelectric effects. The use of refined structural models improves the accuracy of the stress and strain fields, especially when complex structures, such as multi-layered structures, are considered. A great deal of effort has been focused on the extension of these models to the analysis of piezoelectric materials. One of the most critical points is the interface between the structure and piezoelectric patches, as shown by (Zhou and Tiersten, 1994). The introduction of shear effects (see Caruso et al, 2003; Kumar and Narayanan,



**Fig. 15.2:** Example of a piezo-layered structure.

2007; Kusculuoglu and Royston, 2005; Liu et al, 2004; Vasques and Rodrigues, 2006), makes it possible to have a more accurate description of the stress field of the problem. More refined approaches have been proposed in the last few years (see Zhou et al, 2000; Moita et al, 2005; Vidal et al, 2011); in these cases, a first order theory has been considered. Carrera (1997b); Robaldo et al (2006); Carrera et al (2007) proposed the use of refined two-dimensional models for the analysis of multi-layered structures, including piezoelectric materials. The use of a refined model over the whole structural domain requires more computational costs than those necessary. The best solution would be to use refined models only in the region in which they are required and classical models elsewhere. The problem of mixing or joining different structural models is a well-known topic in literature as shown by Kim et al (1997). Biscani et al (2012) proposed an approach that is able to increase the accuracy of the model, but only where the piezoelectric elements are located. The coupling between of piezo-ceramic and metallic materials can be a problematic when the device has to operate at high temperatures. The large difference between the thermal expansion coefficients (CTE) could lead to large deformations, which in turn could overcome the stroke of the actuator. Accurate numerical models may be used to predict the behavior of these devices, and they can be used in the design process. The use of classical beam models for the thermo-piezo-elastic analysis of multilayer structures can be found in the work by Tzou and Ye (1994); Ahmad et al (2006). (Carrera and Robaldo, 2007) presented a class of refined two-dimensional models for the accurate analysis of plates and shells including thermal and piezoelectric effects.

A unified approach to the development of refined one-dimensional models, which is suitable for multi-field analyses is presented in the following pages. The structural model is based on the Carrera Unified Formulation (CUF), a numerical tool that can be used to derive any order of structural model in a compact and unified form. CUF was firstly developed for two-dimensional models by Carrera (2003) and was extended to the thermal-elastic problem by Carrera (2000); Robaldo et al (2005). The piezo-elastic formulation was introduced by Robaldo et al (2006). The fully coupled piezo-thermo-mechanical expansion of the CUF was presented by Carrera and Boscolo (2007). This numerical approach was extended to the one-dimensional model by Carrera et al (2010, 2011b, 2012a,b), more details can be found in the books by Carrera et al (2014a, 2011a).

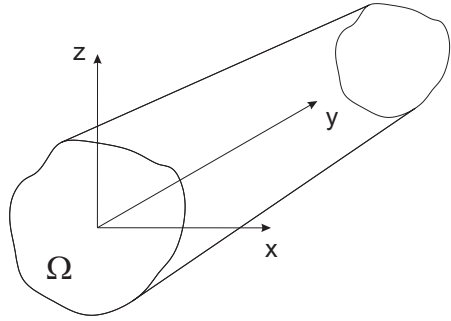
The displacement field above the cross-section was described in the work by Carrera and Petrolo (2012) through the use of Lagrange-type polynomials. The extension of this model to a multi-field analysis was presented by Miglioretti et al (2014) for the piezo-mechanical problem, and was used by Zappino et al (2016).

## 15.2 Thermo-Piezo-Elastic One-Dimensional Model

This section presents the refined one-dimensional model used in the following analyses. The coordinate reference frame is shown in Fig. 15.3. The displacement three-dimensional field is described using the vector  $\mathbf{u}$ :



**Fig. 15.3** Beam reference system.



$$\mathbf{u}^T = \{u_x, u_y, u_z\} \tag{15.1}$$

In the thermo-piezo-elastic formulation, in addition to the mechanical variables, also the temperature variation,  $\vartheta$ , and the electric potential,  $\phi$ , must be considered. The solution of the thermo-piezo-elastic problem requires to define five quantities in each point:

$$\mathbf{u}^T = \{u_x, u_y, u_z, \vartheta, \phi\} \tag{15.2}$$

where vector  $\mathbf{u}$  contains the unknown quantities.

### 15.2.1 Kinematic Approximation

The one-dimensional approximation requires to assume a known displacement field, a temperature variation and a electric potential over the cross-section. Different formulation can be used, in the following pages a review of the classical models and the details of the refined kinematic assumptions used in the present work are presented.

#### 15.2.1.1 Classical Beam Models

Classical beam models are subject to a number of fundamental assumptions that limit the use of these models to a small number of applications.

The Euler-Bernoulli beam theory, EBBT, does not consider shear effects and the warping of the cross-section, which is considered rigid in- and out-of-plane. The displacement field of the cross-section can be written as:

$$\begin{aligned} u_x &= u_{x1} \\ u_y &= u_{y1} + x \frac{\partial u_{z1}}{\partial y} + z \frac{\partial u_{x1}}{\partial y} \\ u_z &= u_{z1} \end{aligned} \tag{15.3}$$

This model has only three degrees of freedom, DOF, over the cross-section because the rotation of the cross-section is considered as the derivatives of the rigid translation.

The Timoshenko beam theory, TBT, includes the effects of the shear but it is considered constant over the cross-section. In this case, the displacement field of the cross-section can be written as:

$$\begin{aligned} u_x &= u_{x_1} \\ u_y &= u_{y_1} + x u_{y_2} + z u_{y_3} \\ u_z &= u_{z_1} \end{aligned} \quad (15.4)$$

The TBT has five DOFs, because the cross-sectional rotation is a free parameter. The use of these models is limited to slender (EBBT) and moderately slender (TBT) bodies, because the fundamental assumptions are only verified for these geometries. In the present form these models can be used to describe the bending of prismatic beam. The torsional effects can be included considering the contributions introduced by de Saint-Venant (1856) or, in the case of thin-walled structures, by Vlasov (1984).

The use of refined one-dimensional models allows the range of applicability of these models to be extended to a large number of applications. In this work the refined one-dimensional models derived from using the CUF are used to build node-dependent kinematic one-dimensional models. A brief review of these models is presented in the following section.

### 15.2.1.2 Refined One-Dimensional Models

The one-dimensional approximation requires a known displacement field to be assumed over the cross-section. A function expansion can be used to describe properly the behavior of the beam cross-section. This approach, suggest by Washizu (1968), leads to write the three-dimensional displacement field as:

$$\mathbf{u} = \mathbf{u}_\tau(y)F_\tau(x, z), \quad \tau = 1 \dots M. \quad (15.5)$$

where  $F_\tau(x, z)$  is the function expansion over the cross-section,  $\mathbf{u}_\tau(y)$  is the unknown vector along the beam axis, and  $M$  is the number of terms in the functions expansion  $F_\tau(x, z)$ . The choice of the functions expansion allows the kinematic of the model to be modified. A number of possible choices were presented by Carrera et al (2014c). In the present work Taylor and Lagrange expansions are considered, more details are reported in the next sections.

The displacements approximation introduced in Eq. (15.5) leads to a one-dimensional problem. The solution of this problem can be obtained using the Finite Element Method, FEM, which allows the system of partial derivative functions to be reduced to an algebraic system. FEM approximates the axial unknowns  $\mathbf{u}_\tau(y)$  using the one-dimensional shape functions  $N_i$ , that is, the displacement field assumes the formulation:

$$\mathbf{u} = \mathbf{u}_{i\tau} N_i(y) F_\tau(x, z), \quad \tau = 1 \dots M; \quad i = 1 \dots N_n. \tag{15.6}$$

where  $N_i$  are the shape functions introduced by the FE model,  $N_n$  is the number of nodes of the element and  $\mathbf{u}_{i\tau}$  are the nodal unknowns. The virtual variation of the displacement can be written as:

$$\delta \mathbf{u} = \delta \mathbf{u}_{js} N_j(y) F_s(x, z), \quad s = 1 \dots M; \quad j = 1 \dots N_n. \tag{15.7}$$

### 15.2.1.3 Taylor Expansion Models (TE)

The one-dimensional TE model consists of an expansion that uses 2D polynomials  $x^m z^n$ , as  $F_\tau$ , where  $m$  and  $n$  are positive integers. For instance, the second-order displacement field is:

$$\begin{aligned} u_x &= u_{x_1} + x u_{x_2} + z u_{x_3} + x^2 u_{x_4} + xz u_{x_5} + z^2 u_{x_6} \\ u_y &= u_{y_1} + x u_{y_2} + z u_{y_3} + x^2 u_{y_4} + xz u_{y_5} + z^2 u_{y_6} \\ u_z &= u_{z_1} + x u_{z_2} + z u_{z_3} + x^2 u_{z_4} + xz u_{z_5} + z^2 u_{z_6} \end{aligned} \tag{15.8}$$

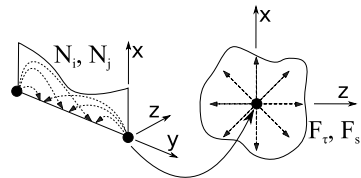
Figure 15.4 shows a representation of a two nodes element based on the TE expansion. In this case, the  $F_\tau$  and  $F_s$  functions are used to expand the solution from the beam node to the cross-section.

### 15.2.1.4 Lagrange Expansion Models (LE)

In the case of LE models, Lagrange polynomials are used to build refined one-dimensional models. The iso-parametric formulation is exploited to deal with arbitrary cross-section shaped geometries. For instance, the linear interpolation functions are:

$$\begin{aligned} F_1 &= \frac{1}{4} (1 - \xi)(1 - \eta); \quad F_2 = \frac{1}{4} (1 + \xi)(1 - \eta); \\ F_3 &= \frac{1}{4} (1 + \xi)(1 + \eta); \quad F_4 = \frac{1}{4} (1 - \xi)(1 + \eta) \end{aligned} \tag{15.9}$$

where  $\xi$  and  $\eta$  are the coordinates in the natural reference system. Equation (15.9) coincides with the linear Lagrange polynomial in two dimensions. In this paper a quadratic element with nine nodes, LE9, is used. When LE is used the unknowns are only the displacements of the cross-sectional nodes.



**Fig. 15.4** A two-nodes beam based on the Taylor expansion.

Figure 15.5 shows a representation of a two nodes element based on the LE. In this case the  $F_\tau$  and  $F_s$  functions are used to expand the solution from the cross-sectional nodes to the cross-section area.

This approach is very effective when layered structure are considered. Fig. 15.6 shows a layered beam, the beam has two layer but there is a patch at one end, that is, in that area three layer are present. Figure 15.6 shows how each layer can be represented with a different element over the cross section. This approach allow the accuracy of the results to be increased because a zig-zag displacement field can be predicted.

### 15.2.2 Geometrical Relations

The geometrical relations in the case of the thermo-piezo-elastic model allow the strain ( $\boldsymbol{\epsilon}$ ), the spatial thermal variations ( $\boldsymbol{\theta}$ ) and the electric field ( $\boldsymbol{E}$ ) to be evaluated. The strain vector,  $\boldsymbol{\epsilon}$ , can be written as:

$$\boldsymbol{\epsilon}^T = \{ \epsilon_{xx} \ \epsilon_{yy} \ \epsilon_{zz} \ \epsilon_{xz} \ \epsilon_{yz} \ \epsilon_{xy} \} = \mathbf{D}_u \mathbf{u} \tag{15.10}$$

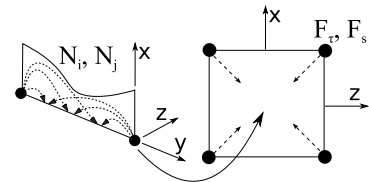
where  $\mathbf{D}_u$  is:

$$\mathbf{D}_u^T = \begin{bmatrix} 0 & 0 & \partial_z & \partial_x & \partial_y & 0 \\ 0 & \partial_y & 0 & 0 & \partial_z & \partial_x \\ \partial_x & 0 & 0 & \partial_z & 0 & \partial_y \end{bmatrix} \tag{15.11}$$

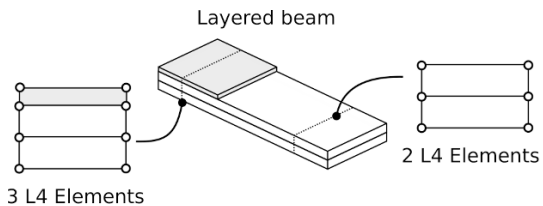
The spatial temperature variation,  $\boldsymbol{\theta}$ , can be written as:

$$\boldsymbol{\theta} = \left\{ \frac{\partial \vartheta}{\partial x} \ \frac{\partial \vartheta}{\partial y} \ \frac{\partial \vartheta}{\partial z} \right\}^T = \mathbf{D}_\vartheta \vartheta \tag{15.12}$$

where  $\vartheta$  is the temperature and  $\mathbf{D}_\vartheta$  is:



**Fig. 15.5** A two-nodes beam based on the Lagrange expansion.



**Fig. 15.6** Example of the cross-sectional discretization of a layered structure.

$$\mathbf{D}_\vartheta^T = \left[ \partial_x \partial_y \partial_z \right] \quad (15.13)$$

The electric field,  $\mathbf{E}$ , can be expressed as:

$$\mathbf{E} = \left\{ \frac{\partial \phi}{\partial x} \frac{\partial \phi}{\partial y} \frac{\partial \phi}{\partial z} \right\}^T = \mathbf{D}_\phi \phi \quad (15.14)$$

where  $\mathbf{D}_\phi$  is equal to  $\mathbf{D}_\vartheta$ . The symbol  $\partial$  stands for partial derivative, that is:  $\partial_x = \frac{\partial}{\partial x}$ ,  $\partial_y = \frac{\partial}{\partial y}$  and  $\partial_z = \frac{\partial}{\partial z}$

### 15.2.3 Constitutive Relations

The constitutive equation for the thermo-piezo-elastic model have been derived in according with the work presented by Carrera et al (2008).

The stress,  $\boldsymbol{\sigma}$  can be written in the following form:

$$\boldsymbol{\sigma} = \mathbf{C}\boldsymbol{\varepsilon} - \boldsymbol{\lambda}\vartheta - \mathbf{e}\mathbf{E} \quad (15.15)$$

The first contribution comes from the Hook's law and derives from the mechanical problem.

$$\begin{Bmatrix} \sigma_{xx} \\ \sigma_{yy} \\ \sigma_{zz} \\ \sigma_{xz} \\ \sigma_{yz} \\ \sigma_{xy} \end{Bmatrix} = \begin{bmatrix} C_{11} & C_{12} & C_{13} & 0 & 0 & C_{16} \\ C_{21} & C_{22} & C_{23} & 0 & 0 & C_{26} \\ C_{31} & C_{32} & C_{33} & 0 & 0 & C_{36} \\ 0 & 0 & 0 & C_{44} & C_{45} & 0 \\ 0 & 0 & 0 & C_{54} & C_{55} & 0 \\ C_{61} & C_{62} & C_{63} & 0 & 0 & C_{66} \end{bmatrix} \begin{Bmatrix} \epsilon_{xx} \\ \epsilon_{yy} \\ \epsilon_{zz} \\ \epsilon_{xz} \\ \epsilon_{yz} \\ \epsilon_{xy} \end{Bmatrix} \quad (15.16)$$

The second term,  $\boldsymbol{\lambda}\vartheta$ , comes from the thermo-mechanical coupling. The vector  $\boldsymbol{\lambda}$  can be written as:

$$\boldsymbol{\lambda} = \mathbf{C}\boldsymbol{\alpha} = \mathbf{C}\{\alpha_1 \alpha_2 \alpha_3 0 0 0\}^T \quad (15.17)$$

Where  $\mathbf{C}$  is the matrix with the elastic coefficients of the material, and  $\boldsymbol{\alpha}$  is the vector of the thermal expansion coefficients. The last term,  $\mathbf{e}\mathbf{E}$ , comes from the electro-mechanical coupling. The matrix  $\mathbf{e}$  contains the piezoelectric stiffness coefficients and can be written as:

$$\mathbf{e} = \mathbf{C}\mathbf{d} = \mathbf{C} \begin{bmatrix} 0 & 0 & 0 & 0 & d_{15} & 0 \\ 0 & 0 & 0 & d_{24} & 0 & 0 \\ d_{31} & d_{32} & d_{33} & 0 & 0 & 0 \end{bmatrix}^T \quad (15.18)$$

where  $\mathbf{d}$  is the matrix of the piezoelectric coefficients.

The electric displacement,  $\mathbf{D}$ , can be written in the following form:

$$\mathbf{D} = \mathbf{e}\boldsymbol{\varepsilon} + \boldsymbol{\chi}\mathbf{E} + \mathbf{p}\vartheta \quad (15.19)$$

The first term,  $\mathbf{e}\boldsymbol{\varepsilon}$ , comes from the electro-mechanical coupling. The second contribution,  $\boldsymbol{\chi}\mathbf{E}$ , is due to the electric problem,  $\boldsymbol{\chi}$  is to the dielectric permittivity matrix of the material:

$$\boldsymbol{\chi} = \begin{bmatrix} \chi_{11} & \chi_{12} & 0 \\ \chi_{21} & \chi_{22} & 0 \\ 0 & 0 & \chi_{33} \end{bmatrix} \quad (15.20)$$

The last term,  $\mathbf{p}\vartheta$ , comes from the thermo-electric problem and  $\mathbf{p}$  is the vector of the pyro-electric coefficients.

The last constitutive equation describe the heat flux,  $\mathbf{h}$ :

$$\mathbf{h} = \boldsymbol{\kappa}\boldsymbol{\theta} \quad (15.21)$$

where  $\boldsymbol{\kappa}$  is the conductivity coefficients matrix:

$$\boldsymbol{\kappa} = \begin{bmatrix} \kappa_{11} & \kappa_{12} & 0 \\ \kappa_{21} & \kappa_{22} & 0 \\ 0 & 0 & \kappa_{33} \end{bmatrix} \quad (15.22)$$

### 15.2.4 Governing Equation

The governing equation can be written using the virtual displacements principle, PVD:

$$\delta L_{int} = \delta L_{ext} \quad (15.23)$$

where  $\delta L_{int}$  is the variation of the internal work while,  $\delta L_{ext}$  is the variation of the external work.

In explicit form the PVD can be written as:

$$\delta L_{int} = \int_V (\delta \boldsymbol{\varepsilon}^T \boldsymbol{\sigma} - \delta \boldsymbol{\theta}^T \mathbf{h} - \delta \mathbf{E}^T \mathbf{D}) dV = \delta L_{ext} \quad (15.24)$$

If geometrical and constitutive equation are substituted in Eq. (15.24) the following equation is obtained:

$$\begin{aligned} \delta L_{int} = \int_V & (\delta \boldsymbol{\varepsilon}^T \mathbf{C} \boldsymbol{\varepsilon} - \delta \boldsymbol{\varepsilon}^T \boldsymbol{\lambda} \vartheta - \delta \boldsymbol{\varepsilon}^T \mathbf{e} \mathbf{E} + \delta \boldsymbol{\theta}^T \boldsymbol{\kappa} \boldsymbol{\theta} \\ & - \delta \mathbf{E}^T \mathbf{e} \boldsymbol{\varepsilon} - \delta \mathbf{E}^T \boldsymbol{\chi} \mathbf{E} - \delta \mathbf{E}^T \mathbf{p} \vartheta) dV \end{aligned} \quad (15.25)$$

If the kinematic approximation introduced before is used the terms that compose the variation of the internal work can be written in matrix form.

The first term,  $\delta \boldsymbol{\varepsilon}^T \mathbf{C} \boldsymbol{\varepsilon}$ , represents the mechanical problem. The strain can be expressed in term of derivatives of the displacements, moreover the displacements can be written using the shape functions  $N_i$  and  $F_\tau$ .

$$\int_V \delta \mathbf{\epsilon}^T \mathbf{C} \mathbf{\epsilon} = \delta \mathbf{q}_{js}^T \int_V N_j F_s \mathbf{I} \mathbf{D}_u^T \mathbf{C} \mathbf{D}_u \mathbf{I} F_\tau N_i dV \mathbf{q}_{ui\tau} = \delta \mathbf{q}_{js}^T \mathbf{k}_{uu}^{ij\tau s} \mathbf{q}_{ui\tau} \quad (15.26)$$

$\mathbf{k}_{uu}^{ij\tau s}$  is the fundamental nucleus of size  $3 \times 3$  of the stiffness matrix of the pure mechanical problem.  $\mathbf{q}_{ui\tau}$  is the part of the unknown vector related to the mechanical variables.

The term  $\delta \mathbf{\epsilon}^T \boldsymbol{\lambda} \vartheta$  can be written as:

$$\int_V \delta \mathbf{\epsilon}^T \boldsymbol{\lambda} \vartheta = \delta \mathbf{q}_{js}^T \int_V N_j F_s \mathbf{I} \mathbf{D}_u^T \boldsymbol{\lambda} \mathbf{I} F_\tau N_i dV \mathbf{q}_{\vartheta i\tau} = \delta \mathbf{q}_{js}^T \mathbf{k}_{u\vartheta}^{ij\tau s} \mathbf{q}_{\vartheta i\tau} \quad (15.27)$$

$\mathbf{k}_{u\vartheta}^{ij\tau s}$  is the fundamental nucleus of size  $3 \times 1$  of the stiffness matrix of the thermo-elastic problem.  $\mathbf{q}_{\vartheta i\tau}$  is the part of the unknown vector related to the thermal variable.

The term  $\delta \mathbf{\epsilon}^T \mathbf{e} \mathbf{E}$  can be written as:

$$\int_V \delta \mathbf{\epsilon}^T \mathbf{e} \mathbf{E} = \delta \mathbf{q}_{js}^T \int_V N_j F_s \mathbf{I} \mathbf{D}_u^T \mathbf{e} \mathbf{D}_\phi \mathbf{I} F_\tau N_i dV \mathbf{q}_{\phi i\tau} = \delta \mathbf{q}_{js}^T \mathbf{k}_{u\phi}^{ij\tau s} \mathbf{q}_{\phi i\tau} \quad (15.28)$$

$\mathbf{k}_{u\phi}^{ij\tau s}$  is the fundamental nucleus of size  $3 \times 1$  of the stiffness matrix of the piezo-elastic problem.  $\mathbf{q}_{\phi i\tau}$  is the part of the unknown vector related to the electrical variable.

The term  $\delta \boldsymbol{\theta}^T \boldsymbol{\kappa} \boldsymbol{\theta}$  can be written as:

$$\int_V \delta \boldsymbol{\theta}^T \boldsymbol{\kappa} \boldsymbol{\theta} = \delta \mathbf{q}_{js}^T \int_V N_j F_s \mathbf{I} \mathbf{D}_\theta^T \boldsymbol{\kappa} \mathbf{D}_\theta \mathbf{I} F_\tau N_i dV \mathbf{q}_{\theta i\tau} = \delta \mathbf{q}_{js}^T \mathbf{k}_{\theta\theta}^{ij\tau s} \mathbf{q}_{\theta i\tau} \quad (15.29)$$

$\mathbf{k}_{\theta\theta}^{ij\tau s}$  is the fundamental nucleus of size  $1 \times 1$  of the stiffness matrix of the pure thermal problem.

The term  $\delta \mathbf{E}^T \mathbf{e} \boldsymbol{\epsilon}$  can be written as:

$$\int_V \delta \mathbf{E}^T \mathbf{e} \boldsymbol{\epsilon} = \delta \mathbf{q}_{\phi js}^T \int_V N_j F_s \mathbf{I} \mathbf{D}_\phi^T \mathbf{e} \mathbf{D}_u \mathbf{I} F_\tau N_i dV \mathbf{q}_{ui\tau} = \delta \mathbf{q}_{\phi js}^T \mathbf{k}_{\phi u}^{ij\tau s} \mathbf{q}_{ui\tau} \quad (15.30)$$

$\mathbf{k}_{\phi u}^{ij\tau s}$  is the fundamental nucleus of size  $1 \times 3$  of the stiffness matrix of the piezo-elastic problem.

The term  $\delta \mathbf{E}^T \boldsymbol{\chi} \mathbf{E}$  can be written as:

$$\int_V \delta \mathbf{E}^T \boldsymbol{\chi} \mathbf{E} = \delta \mathbf{q}_{\phi js}^T \int_V N_j F_s \mathbf{I} \mathbf{D}_\phi^T \boldsymbol{\chi} \mathbf{D}_\phi \mathbf{I} F_\tau N_i dV \mathbf{q}_{\phi i\tau} = \delta \mathbf{q}_{\phi js}^T \mathbf{k}_{\phi\phi}^{ij\tau s} \mathbf{q}_{\phi i\tau} \quad (15.31)$$

$\mathbf{k}_{\phi\phi}^{ij\tau s}$  is the fundamental nucleus of size  $1 \times 1$  of the stiffness matrix of the pure electric problem.

The term  $\delta \mathbf{E}^T \mathbf{p} \vartheta$  can be written as:

$$\int_V \delta \mathbf{E}^T \mathbf{p} \vartheta = \delta \mathbf{q}_{\phi j s}^T \int_V N_j F_s \mathbf{I} \mathbf{D}_{\phi}^T \mathbf{p} \mathbf{D}_{\theta} \mathbf{I} F_{\tau} N_i dV \mathbf{q}_{\theta i \tau} = \delta \mathbf{q}_{\phi j s}^T \mathbf{k}_{\phi \theta}^{i j \tau s} \mathbf{q}_{\theta i \tau} \quad (15.32)$$

$\mathbf{k}_{\phi \theta}^{i j \tau s}$  is the fundamental nucleus of size  $1 \times 1$  of the stiffness matrix of the pyro-electric problem.

All the fundamental nucleus can be assembled together in fundamental nucleus of the multi-field problem:

$$\delta L_{int} = \delta \mathbf{u}_{j s}^T \overbrace{\left[ \begin{array}{c|c|c} \mathbf{k}_{uu} & \mathbf{k}_{u\theta} & \mathbf{k}_{u\phi} \\ \hline \dots & \vdots & \vdots \\ \dots & \vdots & \vdots \\ \dots & \vdots & \vdots \\ \dots & \vdots & \vdots \\ \dots & \vdots & \vdots \\ \dots & \vdots & \vdots \\ \dots & \vdots & \vdots \\ \dots & \vdots & \vdots \\ \dots & \vdots & \vdots \end{array} \right]}^{\mathbf{k}^{i j \tau s}} \mathbf{u}_{i \tau} \quad (15.33)$$

The contributions  $\mathbf{k}_{\theta \phi}$  and  $\mathbf{k}_{\theta u}$  can be neglected when an external temperature is imposed as boundary condition, as in the present paper. As can be seen in Eq. (15.33), when the multi-field case is considered the nucleus is no more symmetric, as a consequence the global stiffness matrix loses the properties that come from the symmetry, this can reduce the efficiency of the numerical solution and an appropriate solver must be used.

### 15.2.5 Loading Vector

The virtual work due to the load  $\mathbf{P} = \{P_x, P_y, P_z, P_{\theta}, P_{\phi}\}$  can be expressed as:

$$\delta L_{ext} = \int_V \delta \mathbf{u}^T \mathbf{P} dV \quad (15.34)$$

Considering the displacement function the external work can be written as:

$$\delta L_{ext} = \delta \mathbf{u}_{s j}^T \int_V F_s^j N_j \mathbf{P} dV = \delta \mathbf{u}_{s j}^T \cdot \mathbf{p}_{s j} \quad (15.35)$$

where  $\mathbf{p}_{s j}$  is the expression of the fundamental nucleus of the load vector.



### 15.2.6 Rotation and Assembly of the Fundamental Nucleus

The analysis of complex structures requires finite elements to be rotated in any direction and the stiffness to be computed in a given reference system, that is, the displacements have to be expressed in the same, global reference system. The matrices can be written in the global reference system using a rotation matrix, with respect to the local reference system. The rotation matrices are:

$$\mathbf{\Lambda}_x = \begin{bmatrix} 1 & 0 & 0 \\ 0 & \cos(\theta) & \sin(\theta) \\ 0 & -\sin(\theta) & \cos(\theta) \end{bmatrix}, \tag{15.36}$$

$$\mathbf{\Lambda}_y = \begin{bmatrix} \cos(\phi) & 0 & \sin(\phi) \\ 0 & 1 & 0 \\ -\sin(\phi) & 0 & \cos(\phi) \end{bmatrix}, \tag{15.37}$$

$$\mathbf{\Lambda}_z = \begin{bmatrix} \cos(\xi) & -\sin(\xi) & 0 \\ \sin(\xi) & \cos(\xi) & 0 \\ 0 & 0 & 1 \end{bmatrix} \tag{15.38}$$

where  $\theta$ ,  $\phi$  and  $\xi$  are the rotation angles around the  $x$ ,  $y$ , and  $z$  axis, as shown in Fig. 15.7. The displacement vector in the global reference system,  $\mathbf{u}_{glob}$ , can be written as:

$$\mathbf{u}_{glob} = \mathbf{\Lambda}_x \mathbf{\Lambda}_y \mathbf{\Lambda}_z \mathbf{u}_{loc} = \mathbf{\Lambda} \mathbf{u}_{loc} \tag{15.39}$$

Therefore, the mechanical part of the fundamental nucleus in the global reference system becomes:

$$\mathbf{k}_{uu_{glob}}^{ij\tau s} = \mathbf{\Lambda}^T \mathbf{k}_{uu_{loc}}^{ij\tau s} \mathbf{\Lambda} \tag{15.40}$$

The coupling terms can be rotated using the following equations:

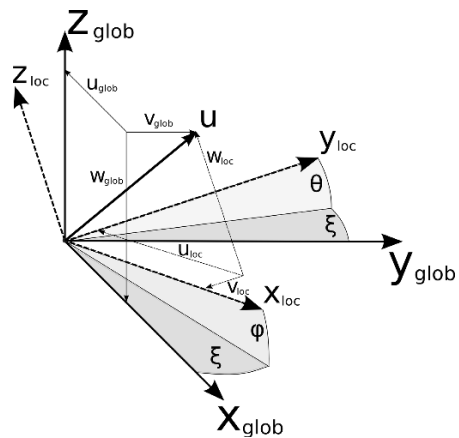


Fig. 15.7 Representation of the rotation angles.

$$\mathbf{k}_{u\Theta_{glob}}^{ij\tau s} = \mathbf{\Lambda}^T \mathbf{k}_{u\Theta_{loc}}^{ij\tau s} \tag{15.41}$$

$$\mathbf{k}_{u\phi_{glob}}^{ij\tau s} = \mathbf{\Lambda}^T \mathbf{k}_{u\phi_{loc}}^{ij\tau s} \tag{15.42}$$

$$\mathbf{k}_{\phi u_{glob}}^{ij\tau s} = \mathbf{k}_{\phi u_{loc}}^{ij\tau s^T} \mathbf{\Lambda} \tag{15.43}$$

The terms  $\mathbf{k}_{\phi\phi}$ ,  $\mathbf{k}_{\phi\theta}$  and  $\mathbf{k}_{\theta\theta}$  are related to scalar fields therefore do not need to be rotated. Once all the elements have been expressed in the same reference system, the global stiffness matrix can be assembled using the classical FEM approach.

### 15.2.7 The Stiffness Matrix Assembly

The fundamental nuclei introduced in the previous section, that are discussed extensively in Carrera et al (2014b), can be used as bricks to build the matrix of the complete structure. Figure 15.8 shows the procedure used to build the stiffness matrix, starting from the fundamental nucleus. The loops on  $\tau$  and  $s$  allow to build the stiffness matrix at the node level while the loops on  $i$  and  $j$  make it possible to create the stiffness matrix at the element level. The assembly on the global stiffness matrix can be done summing the stiffness of the nodes shared by more then one element.

## 15.3 Numerical Results

The results obtained using the previously introduced structural model are reported in this section. The structural model has been assessed, and the results have been compared with those presented in literature using classical approaches. The Piezo-elastic model has been assessed considering the benchmark proposed by Zhang and

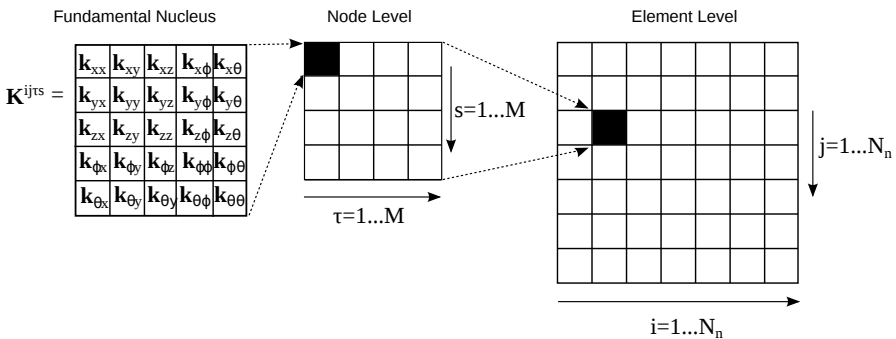


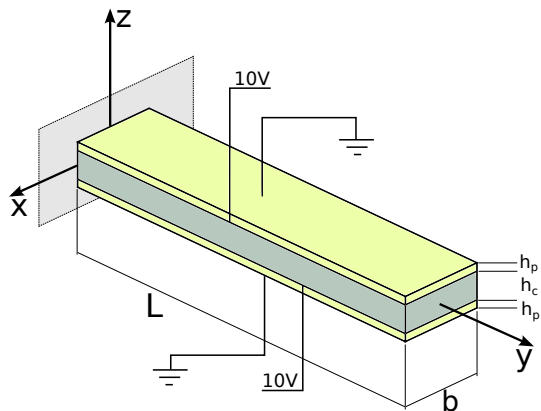
Fig. 15.8: Stiffness matrix assembly.

Sun (1996b). A second case, a beam with piezo-patches, has been considered and the results have been compared with those by Kpeky et al (2017). Finally, the results from the thermo-piezo-elastic model have been compared with those by Tzou and Ye (1994).

### 15.3.1 Piezo-Elastic Model Assessment

A piezo-elastic model has been assessed in this section. The sandwich beam considered in the analysis is shown in Fig. 15.9. The beam has a length,  $L$ , of 0.1 m, a thickness of the metallic core,  $h_c$ , of 16 mm and two external piezo-patches which have a thickness,  $h_p$ , equal to 1 mm. The width is considered equal to 1 m. A potential of 10 V is applied to the face of the interface between the piezoelectric patch and the internal core, while, the external free faces have a potential set equal to 0 V. The piezoelectric patches are polarized in the  $z$  direction. The properties of the piezoelectric material used in the patches are reported in Table 15.1, while the properties of the aluminum alloy used in the core are reported in Table 15.2.

The displacements due to the applied voltage, have been evaluated. The results have been compared with those of Zhang and Sun (1996b). Figure 15.10 shows the vertical displacement of the beam along the length of the beam. The results are in agreement with those present in literature. This assessment proves that the present beam formulation is able to provide an accurate description of piezo-elastic coupling.



**Fig. 15.9** Geometry of the sandwich beam used in the piezo-elastic assessment

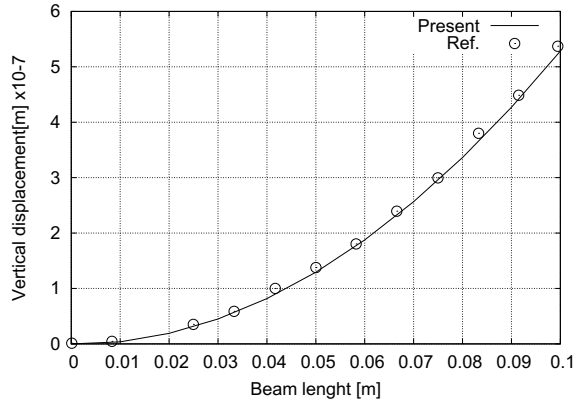
Table 15.1: Material properties of PZT-5H

$C_{11}, C_{22}, C_{33}$	$C_{12}$	$C_{13}, C_{23}$	$C_{44}, C_{55}, C_{66}$	$e_{15}, e_{24}$	$e_{31}, e_{32}$	$e_{33}$	$\chi_{11}, \chi_{22}$	$\chi_{33}$
[GPa]	[GPa]	[GPa]	[GPa]	[C/m <sup>2</sup> ]	[C/m <sup>2</sup> ]	[C/m <sup>2</sup> ]	[F/m]	[F/m]
126	79.5	84.1	23.0	17.0	-6.5	23.3	$1.503 \times 10^{-8}$	$1.30 \times 10^{-8}$

Table 15.2: Aluminum alloy 1 material properties

aluminum alloy 1	
Mechanical properties	
$E$	70.3 GPa
$\nu$	0.345

Fig. 15.10 Vertical displacement of the beam along the y-axis.



### 15.3.2 Cantilever Beams with Piezo-Patches

A cantilevered beam with two piezo-patches has been considered in this section. Benchmark cases of this type have been studied by various researchers such as Sun and Zhang (1995); Zhang and Sun (1996a); Benjeddou et al (1997), as well as Kpeky et al (2017). The beam geometry is shown in Fig. 15.11.

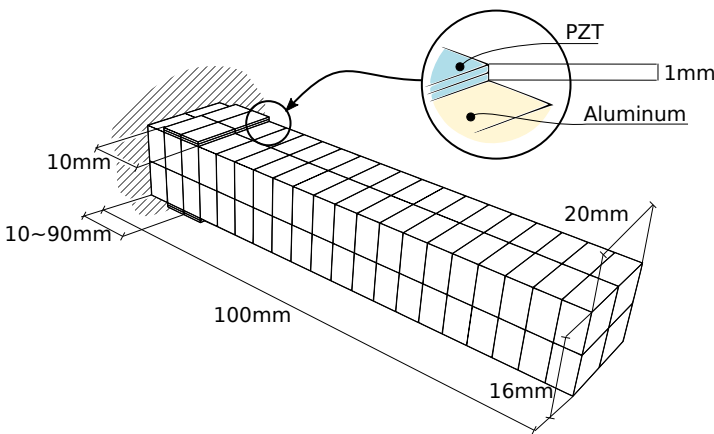


Fig. 15.11: Geometrical feature of slender beams with piezo-patches.

The piezoelectric components are poled in the thickness direction  $z$ . A voltage equal to  $\Delta\phi = \phi_{bottom} - \phi_{top} = 10$  V has been applied for the upper patch and  $\Delta\phi = -10$  V for the lower one to actuate the beam. The piezoelectric components are made of PZT-5H, whose material coefficients are listed in Table 15.1, The substrate structures employ aluminum which has the Young modulus  $E = 70.3$  GPa and a Poisson ratio  $\nu = 0.345$ . Two cases are considered:

- *Case A*: the piezo-patches cover the whole length of the beam;
- *Case B*: the piezoelectric components have a length  $c = 0.01$  m and variable positions along the axial direction from  $d = 0.01$  m to  $d = 0.09$  m.

The numerical results for *Case A* were obtained with uniform LE nodal kinematics, denoted as “12LE9”, which discretizes the cross-section into 12 sub-domains. It should be noted that when Lagrange expansions are adopted to describe the kinematics on a cross-section of a beam, each expansion term possesses specific physical coordinates. The structure is divided into 20 beam elements along the longitudinal direction, and each element has 4 FEM nodes. The obtained results have been compared with the solutions provided by Benjeddou et al (1997); Kpeky et al (2017) as well as with those obtained from ABAQUS 3D modelling. The ABAQUS models employ eight layers of C3D20R mechanical brick elements and another eight layers of C3D20RE piezoelectric brick elements, uniformly distributed  $8 \times 40$  ( $x \times y$ ) along each layer. The results given by Benjeddou et al (1997) were obtained using a beam element model in which the displacement assumptions were layer-wisely defined (in other words the Bernoulli-Euler theory was used for the faces while the Timoshenko theory was adopted for the cores), and displacement continuity was enforced at the layer interfaces. Kpeky et al (2017) reached their solution through solid-shell piezoelectric elements, that is, SHB8PSE and SHB20E.

The variation in deflection along the beam axis at the central cross-sectional point (lines A) and at one of the upper corners (lines B) are shown in Fig. 15.12 for *Case A*. Table 15.3 compares the deflection on two sets of locations on the free-end cross-sections. The current solution for the shear configuration in *Case A* shows good agreement with those of Benjeddou et al (1997); Kpeky et al (2017).

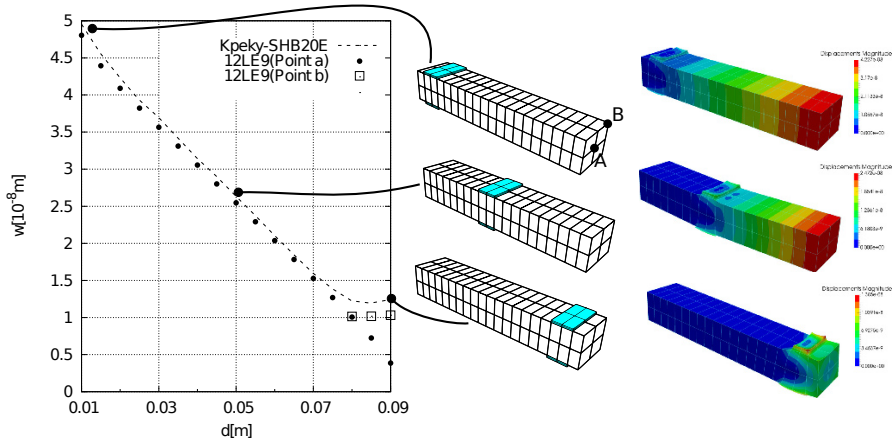
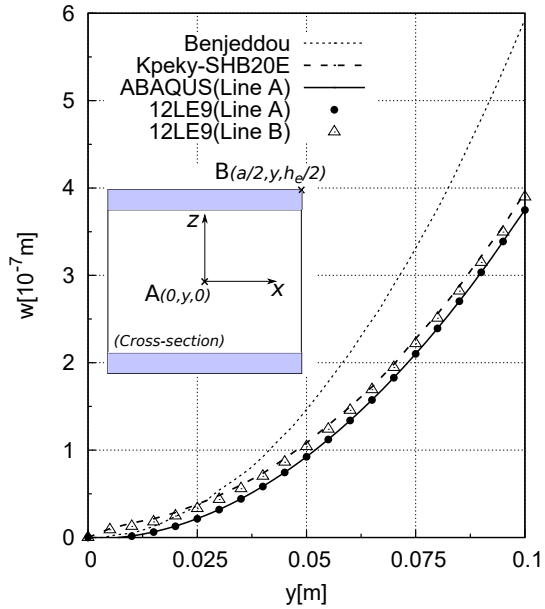
The models with the same uniform 12LE9 sectional kinematics were also applied to obtain the numerical solutions to *Case B*, and the results are shown in Fig. 15.13. It can be observed that the results based on 12LE9 are in good agreement with the reference solutions taken from literature (Kpeky et al, 2017).

A frequency response analysis, in which the patches were closer to the beam root, has been performed using the present model. In this case, the two patches were used

Table 15.3: Tip deflection of the cantilevered beam in *Case A*

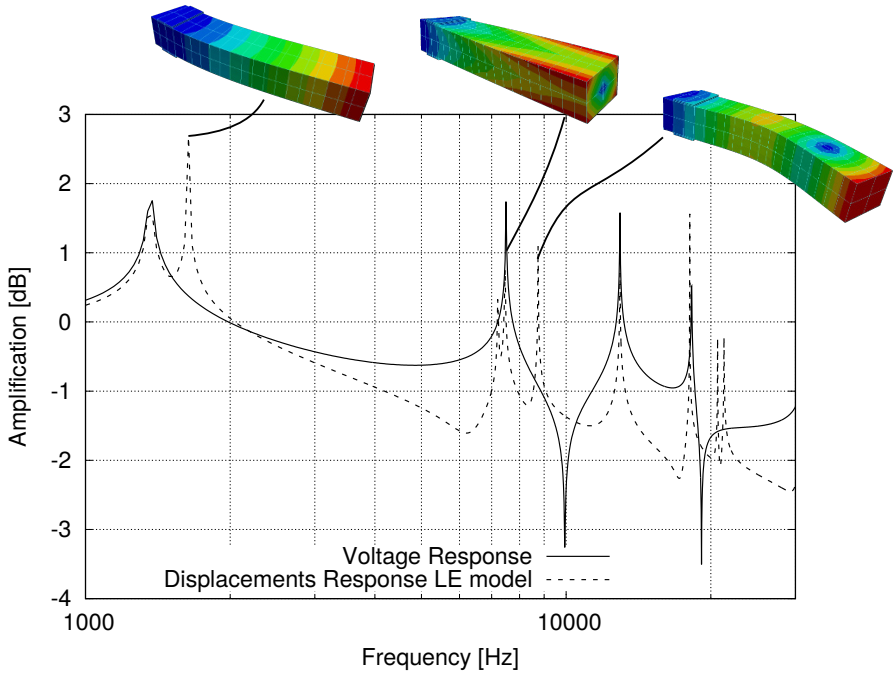
	$w[10^{-7} \text{ m}]$	
	$(0, b, 0)$	$(\frac{a}{2}, b, \frac{h_c}{2})$
ABAQUS	3.749	3.913
12LE9	3.748	3.897

**Fig. 15.12** Vertical displacement along the beam beam, piezo-patches cover the entire length (*Case A*).



**Fig. 15.13:** Tip deflection of the cantilever beams with piezo-patches in *Case B*.

as sensors and an external force was applied at the tip of the beam. Figure 15.14 shows the frequency response of the cantilevered beam. The dashed line shows the mechanical response, and it can be seen that it identifies the natural frequencies of the structure reported in Table 15.4. The solid line represents the electric response evaluated on the outer surface of the piezo-patch. It can be seen that the resonances of the electric response just appear when the mechanical modes stretch the piezo-patches during the deformation. In the other cases the deformation does not produce an electric response.



**Fig. 15.14:** Frequency response of the cantilever beams with piezo-patches

Table 15.4: First six natural frequency of the cantilever beams with piezo-patches

Natural Frequency LE Model	
1	1363.1
2	1637.2
3	7214.3
4	7460.0
5	8744.9
6	12941.5

### 15.3.3 Thermo-Piezo-Elastic Model Assessment

The fully coupled thermo-piezo-elastic model has been assessed in this section. The structure reported in Fig. 15.15 has been considered. This is once again a sandwich beam but with the following dimensions:  $L$  equal to 1 m,  $b$  equal to 0.0508 m, the core thickness,  $h_c$ , equal to 3.36 mm and the thickness of two external piezo-patches,  $h_p$ , equal to 0.254 mm.

The internal core has the properties that are reported in Table 15.5, while the external piezoelectric patches have been built using the same material that was used in the previous assessment, that is PZT-5H. The thermal properties of this material are reported in Table 15.6.

**Fig. 15.15** Geometry of the sandwich beam used in the thermo-piezo-elastic assessment

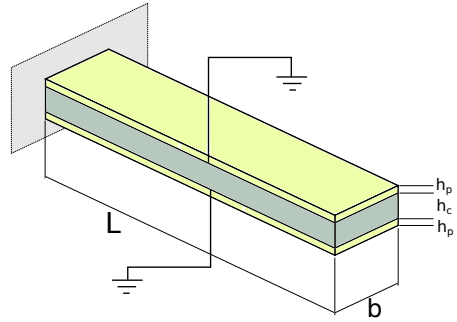


Table 15.5: Aluminum alloy 2 material properties

aluminum alloy 1		
Mechanical properties		
$E$	68.95	GPa
$\nu$	0.292	-
Thermal properties		
$\alpha$	$11 \times 10^{-6}$	$^{\circ}\text{C}^{-1}$

Table 15.6: PZT-5H material thermal properties

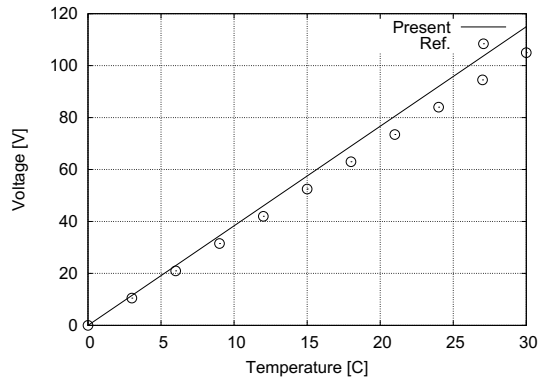
PZT-5H	
Thermal properties	
$\lambda_1$	$2 \times 10^5 \text{ Nm}^2 \text{ }^{\circ}\text{C}^{-1}$
$\lambda_2$	$2 \times 10^5 \text{ Nm}^2 \text{ }^{\circ}\text{C}^{-1}$
$\lambda_3$	$-2.7 \times 10^5 \text{ Nm}^2 \text{ }^{\circ}\text{C}^{-1}$
Pyro-electric properties	
$p_3$	$25 \times 10^{-6} \text{ Cm}^2 \text{ }^{\circ}\text{C}^{-1}$

The structure is subjected to a homogeneous thermal environment, that is, at each point the same value of temperature has been imposed. An electric potential of 0 V as been considered at the interfaces between the core and the patches, as shown in Fig. 15.15. The voltage of the external layer faces, due to the deformation caused by the thermal load, has been evaluated. The results have been compared with those of Tzou and Ye (1994).

Figure 15.16 shows the variation of the electric potential at different temperatures. It is possible to see that there is a linear correlation between the temperature and the potential. The small difference between the present results and the reference values is due to the different kinematic model that has been adopted. While the reference results were obtained using classical models, the present approach takes into account a *quasi* three-dimensional deformation that produces a slightly higher potential.



**Fig. 15.16** Upper face potential at different temperature.



## 15.4 Conclusions

The multi-field analysis of layered structures requires the use of refined structural models. Finite elements based on a layer-wise approach are able to describe the complex displacement fields due to the variations in the material properties at each layer. In these cases, it is important to have a *zig-zag* capability in the kinematic description, that is, the  $C_z^0$  requirement can be fulfilled. The refined one-dimensional models presented in the present work uses a Lagrange expansion over the cross-section that allows each layer to be described with an independent expansion, or Lagrange element. The computational model has been developed in the framework of the Carrera Unified Formulation, which allows refined structural models to be derived in compact form. The results shown in the present work highlight the following points:

- the present one-dimensional model can provide three-dimensional results in the case of thermo-piezo-elastic analysis;
- the present model can deal with the analysis of layered structures with piezo-patches;
- both sensor and actuator patches can be considered;
- the computational costs can be reduced with respect to full three-dimensional models.

In short the present formulation can be considered a valid option for the multi-field analysis of layered structures.

## References

- Ahmad SN, Upadhyay CS, Venkatesan C (2006) Electro-thermo-elastic formulation for the analysis of smart structures. *Smart Materials and Structures* 15(2):401
- Ambrosini R (2000) A modified Vlasov theory for dynamic analysis of thin-walled and variable open section beams. *Engineering Structures* 22(8):890–900

- Bailey T, Hubbard J (1985) Distributed piezoelectric polymer active vibration control of a cantilever beam. *AIAA Journal* 8:605–611
- Benjeddou A, Trindade M, Ohayon R (1997) A unified beam finite element model for extension and shear piezoelectric actuation mechanisms. *Journal of Intelligent Material Systems and Structures* 8(12):1012–1025
- Berdichevsky VL (1976) Equations of the theory of anisotropic inhomogeneous rods. *Dokl Akad Nauk* 228:558–561
- Biscani F, Nali P, Belouettar S, Carrera E (2012) Coupling of hierarchical piezoelectric plate finite elements via arlequin method. *Journal of intelligent materials systems and structures* 23:749
- Carrera E (1997a)  $C_2^0$  Requirements – Models for the two dimensional analysis of multilayered structures. *Composite Structure* 37:373–384
- Carrera E (1997b) An improved reissner-mindlin-type model for the electromechanical analysis of multilayered plates including piezo-layers. *Journal of Intelligent Material Systems and Structures* 8:232–248
- Carrera E (2000) An assessment of mixed and classical theories for thermal stress analysis of orthotropic multilayered plates. *Journal of Thermal Stresses* 23:797–831
- Carrera E (2003) Theories and finite elements for multilayered plates and shells: A unified compact formulation with numerical assessment and benchmarking. *Archives of Computational Methods in Engineering* 10:215–297
- Carrera E, Boscolo M (2007) Hierarchic multilayered plate elements for coupled multifield problems of piezoelectric adaptive structures: Formulation and numerical assessment. *Archives of Computational Methods in Engineering* 14(4):383–430
- Carrera E, Petrolo M (2012) Refined beam elements with only displacement variables and plate/shell capabilities. *Meccanica* 47:537–556
- Carrera E, Robaldo A (2007) Extension of reissner mixed variational principle to thermopiezelasticity. *Atti della Accademia delle Scienze di Torino Classe di Scienze Fisiche Matematiche e Naturali* 31:27–42
- Carrera E, Boscolo M, Robaldo A (2007) Hierarchic multilayered plate elements for coupled multifield problems of piezoelectric adaptive structures: Formulation and numerical assessment. *Archives of Computational Methods in Engineering* 14(4):383–430
- Carrera E, Brischetto S, Nali P (2008) Variational statements and computational models for multifield problems and multilayered structures. *Mechanics of Advanced Materials and Structures* 15(3-4):182–198
- Carrera E, Giunta G, Nali P, Petrolo M (2010) Refined beam elements with arbitrary crps-section geometries. *Computers and Structures* 88:283–293
- Carrera E, Gaetano G, M P (2011a) *Beam Structures, Classical and Advanced Theories*. John Wiley & Sons
- Carrera E, Petrolo M, Nali P (2011b) Unified formulation applied to free vibrations finite element analysis of beams with arbitrary section. *Shock and Vibrations* 18(3):485–502
- Carrera E, Petrolo M, Varello A (2012a) Advanced beam formulations for free vibrations analysis of conventional and joined wings. *Journal of Aerospace Engineering* 25(2):282–293
- Carrera E, Zappino E, Petrolo M (2012b) Advanced elements for the static analysis of beams with compact and bridge-like sections. *Journal of structural engineering* 56:49–61
- Carrera E, Cinefra M, Petrolo M, Zappino E (2014a) Comparisons between 1d (beam) and 2d (plate/shell) finite elements to analyze thin walled structures. *Aerotecnica Missili & Spazio The journal of Aerospace Science, Technology and Systems* 93(1-2)
- Carrera E, Cinefra M, Petrolo M, Zappino E (2014b) *Finite Element Analysis of Structures Through Unified Formulation*. John Wiley & Sons
- Carrera E, Filippi M, Zappino E (2014c) Free vibration analysis of laminated beam by polynomial, trigonometric, exponential and zig-zag theories. *Journal of Composite Materials* 48(19):2299–2316
- Caruso G, Galeani S, Menini L (2003) Active vibration control of an elastic plate using multiple piezoelectric sensors and actuators. *Simulation modelling practice and theory* 11:403–419

- Cowper GR (1966) The shear coefficient in Timoshenko's Beam Theory. *Journal of Applied Mechanics* 33(2):335–340
- Crawley E, Luis J (1987) Use of piezoelectric actuators as elements of intelligent structures. *AIAA Journal* 25:1373–1385
- Davies JM, Leach P (1994) First-order generalised beam theory. *Journal of Constructional Steel Research* 31(2-3):187–220
- Davies JM, Leach P, Heinz D (1994) Second-order generalised beam theory. *Journal of Constructional Steel Research* 31(2-3):221–241
- Dong SB, Alpdogan C, Taciroglu E (2010) Much ado about shear correction factors in Timoshenko beam theory. *International Journal of Solids and Structures* 47(13):1651–1665, DOI 10.1016/j.ijsolstr.2010.02.018
- Dong XJ, Meng G, Peng JC (2006) Vibration control of piezoelectric actuators smart structures based on system identification technique. *Journal of sound and vibration* 297:680–693
- Euler L (1744) *De curvis elasticis. Methodus inveniendi lineas curvas maximi minimive proprietate gaudentes, sive solutio problematis iso-perimetrci lattissimo sensu accepti.* Bousquet & Socios, Lausanne & Geneva
- Friberg PO (1985) Beam element matrices derived from Vlasov's theory of open thin-walled elastic beams. *International Journal for Numerical Methods in Engineering* 21:1205–1228
- Giavotto V, Borri M, Mantegazza P, Ghiringhelli G, Carmaschi V, Maffioli GC, Mussi F (1983) Anisotropic beam theory and applications. *Computers & Structures* 16(1):403–413
- Kim J, Varadan VV, Varadan VK (1997) Finite element modelling of structures including piezoelectric active devices. *International journal for numerical methods in engineering* 832:817–832
- Kim TW, Kim JH (2005) Optimal distribution of an active layer for transient vibration control of an flexible plates. *Smart Material and Structures* 14:904–916
- Kpeky F, Abed-Meraim F, Boudaoud H, Daya EM (2017) Linear and quadratic solid-shell finite elements shb8pse and shb20e for the modeling of piezoelectric sandwich structures. *Mechanics of Advanced Materials and Structures* pp 1–20
- Kumar K, Narayanan S (2007) The optimal location of piezoelectric actuators and sensors for vibration controls of plate. *Smart Material and Structures* 16:2680–2691
- Kusculuoglu ZK, Royston TJ (2005) Finite element formulation for composite plates with piezoceramic layers for optimal vibration control applications. *Smart Material and Structures* 14:1139–1153
- Liu G, Dai K, Lim K (2004) Static and vibration control of composite laminates integrated with piezoelectric sensors and actuators using radial point interpolation method. *Smart Material and Structures* 14:1438–1447
- Miglioretti F, Carrera E, Petrolo M (2014) Variable kinematic beam elements for electro-mechanical analysis. *Smart Structures and Systems* 13(4):517–546
- Moita J, Soares C, Soares C (2005) Active control of forced vibration in adaptive structures using a higher order model. *Composite Structures* 71:349–355
- Moitha J, Correia I, Soares C, Soares C (2004) Active control of adaptive laminated structures with bonded piezoelectric sensors and actuators. *Computer and Structures* 82:1349–1358
- Robaldo A, Carrera E, Benjeddou A (2005) Unified formulation for finite element thermoleastic analysis of multilayered anisotropic composite plates. *Journal of Thermal Stresses* 28:1031–1064
- Robaldo A, Carrera E, Benjeddou A (2006) A unified formulation for finite element analysis of piezoelectric adaptive plates. *Computers & Structures* 84(22):1494–1505
- de Saint-Venant A (1856) *Mémoire sur la Torsion des Prismes, avec des considérations sur leur flexion, ainsi que sur l'équilibre interieur des solides élastiques en général, et des formules pratiques pour le calcul de leur résistance à divers efforts s'exerçant simultanément.* Académie des Sciences de l'Institut Impérial de Frances 14:233–560
- Sarvanos D, Heyliger P (1999) Mechanics and computational models for laminated piezoelectric beams, plate, and shells. *Applied Mechanics Review* 52(10):305–320
- Schardt R (1966) Eine Erweiterung der Technischen Biegetheorie zur Berechnung Prismatischer Falwerke. *Der Stahlbau* 35:161–171

- Silvestre N, N S, Camotim D (2002) First-Order Generalised Beam Theory for Arbitrary Orthotropic Materials. *Thin-Walled Structures* 40(9):791–820
- Sun C, Zhang X (1995) Use of thickness-shear mode in adaptive sandwich structures. *Smart Materials and Structures* 4(3):202
- Timoshenko SP (1921) On the corrections for shear of the differential equation for transverse vibrations of prismatic bars. *Philosophical Magazine* 41:744–746
- Tzou HS, Ye R (1994) Piezothermoelasticity and precision control of piezoelectric systems: Theory and finite element analysis. *Journal of Vibration and Acoustics* 116(4):489–495
- Vasques C, Rodrigues J (2006) Active vibration of smart piezoelectric beams: comparison of classical and optimal feedback control strategies. *Computer and Structures* 84:1459–1470
- Vidal P, D'Ottavio M, Thaier M, Polit O (2011) An efficient finite shell element for the static response of piezoelectric laminates. *Journal of intelligent materials systems and structures* 22:671
- Vlasov VZ (1984) *Thin Walled Elastic Beams*, 2nd edn. National Technical Information Service, Jerusalem
- Volovoi VV (1999) Asymptotic theory for static behavior of elastic anisotropic I-beams. *International Journal of Solids and Structures* 36(7):1017–1043, DOI 10.1016/S0020-7683(97)00341-7
- Washizu K (1968) *Variational methods in elasticity and plasticity*. Oxford: Pergamon Press
- Xu S, Koko T (2004) Finite element analysis and design of actively acontrolled piezoelectric smart structure. *Finite element in Analysis and Design* 40:241–262
- Yu W, Hodges DH (2004) Elasticity Solutions Versus Asymptotic Sectional Analysis of Homogeneous, Isotropic, Prismatic Beams. *Journal of Applied Mechanics* 71(1):15
- Yu W, Volovoi VV, Hodges DH, Hong X (2002) Validation of the variational asymptotic beam sectional analysis (VABS). *AIAA Journal* 40:2105–2113
- Zappino E, Carrera E, Rowe S, Mangeot C, Marques H (2016) Numerical analyses of piezoceramic actuators for high temperature applications. *Composite Structures* 151:36 – 46
- Zhang X, Sun C (1996a) Formulation of an adaptive sandwich beam. *Smart Materials and Structures* 5(6):814
- Zhang XD, Sun CT (1996b) Formulation of an adaptive sandwich beam. *Smart Materials and Structures* 5(6):814
- Zhou X, Chattopadhyay A, Gu H (2000) Dynamic response of smart composites using a coupled thermo-piezoelectric-mechanical model. *AIAA Journal* 38:1939–1948
- Zhou YS, Tiersten HF (1994) An elastic analysis of laminated composite plates in cylindrical bending due to piezoelectric actuators. *Smart Materials and Structures* 3(3):255